Lecture Notes in Electrical Engineering 794

Aritra Acharyya
Arindam Biswas
Palash Das *Editors*

# Generation, Detection and Processing of Terahertz Signals

Springer

# Lecture Notes in Electrical Engineering

## Volume 794

The book series *Lecture Notes in Electrical Engineering* (LNEE) publishes the latest developments in Electrical Engineering - quickly, informally and in high quality. While original research reported in proceedings and monographs has traditionally formed the core of LNEE, we also encourage authors to submit books devoted to supporting student education and professional training in the various fields and applications areas of electrical engineering. The series cover classical and emerging topics concerning:

- Communication Engineering, Information Theory and Networks
- Electronics Engineering and Microelectronics
- Signal, Image and Speech Processing
- Wireless and Mobile Communication
- Circuits and Systems
- Energy Systems, Power Electronics and Electrical Machines
- Electro-optical Engineering
- Instrumentation Engineering
- Avionics Engineering
- Control Systems
- Internet-of-Things and Cybersecurity
- Biomedical Devices, MEMS and NEMS

For general information about this book series, comments or suggestions, please contact leontina.dicecco@springer.com.

To submit a proposal or request further information, please contact the Publishing Editor in your country:

**China**

Jasmine Dou, Editor (jasmine.dou@springer.com)

**India, Japan, Rest of Asia**

Swati Meherishi, Editorial Director (Swati.Meherishi@springer.com)

**Southeast Asia, Australia, New Zealand**

Ramesh Nath Premnath, Editor (ramesh.premnath@springernature.com)

**USA, Canada:**

Michael Luby, Senior Editor (michael.luby@springer.com)

**All other Countries:**

Leontina Di Cecco, Senior Editor (leontina.dicecco@springer.com)

**** This series is indexed by EI Compendex and Scopus databases. ****

More information about this series at http://www.springer.com/series/7818

Aritra Acharyya · Arindam Biswas · Palash Das
Editors

# Generation, Detection and Processing of Terahertz Signals

Springer

*Editors*
Aritra Acharyya
Department of Electronics
and Communication Engineering
Cooch Behar Government Engineering
College
Cooch Behar, West Bengal, India

Arindam Biswas
School of Mines and Metallurgy
Kazi Nazrul University
Asansol, West Bengal, India

Palash Das
Department of Electronics
and Communication Engineering
Cooch Behar Government Engineering
College
Cooch Behar, West Bengal, India

ISSN 1876-1100 ISSN 1876-1119 (electronic)
Lecture Notes in Electrical Engineering
ISBN 978-981-16-4946-2 ISBN 978-981-16-4947-9 (eBook)
https://doi.org/10.1007/978-981-16-4947-9

# Preface

The terahertz (THz) frequency band gap or 'THz gap' is the most untouched and unexplored portion of the entire radio frequency (RF) spectrum. This band (0.30–10.0 THz) lies between the millimeter-wave (mm-wave (RF)) and infrared (IR (optical)) bands, which means THz band includes the tremendously high-frequency (THF) band (i.e., 0.30–3.0 THz) and extends up to the starting of the far-IR band (i.e., 10.0 THz). Therefore, the researchers are nowadays trying to uncover the technologies from both sides, i.e., from both RF and optical spectrums, in order to explore the THz band and to develop devices and circuits for realizing the THz systems. The mm-wave spectrum is already in use in 5th generation (5G) mobile communication technology. The THz spectrum will play a vital role in next-generation mobile communication technologies (i.e., 6G and onward). The primary advantage of THz communication is that the ultra-high speed of data transfer can be achieved in this spectrum; i.e., uses of additional techniques for spectral efficiency enhancement are not required. Moreover, from the perspective of wireless transmission, a smaller wavelength of THz signals helps those to achieve greater directivity, smaller free-space diffraction, etc.; in this regard, THz communication is much advantageous than the mm-wave wireless communication. On the other hand, unlike the IR or visible light communication systems, THz communication is not very much hampered by the alignment issues, scintillation, ambient light interface, atmospheric turbulence, fog, etc. There is a high chance of achieving ultra-high bandwidth with ultra-low-latency communication systems by using the THz spectrum in the near future. However, one prominent limitation of long-haul THz communication is the considerable amount of absorption of THz signals in water vapor molecules at and beyond 1.0 THz. Other than the communication, the THz frequency band is also under huge demand in different other sectors like medical, pharmaceutical sectors, food diagnostics, industrial quality inspection, bio-sensing, bio-imaging, remote sensing, spectroscopy, astronomy, etc. Due to the lower photon energy of the THz waves as compared to X-ray photons, the THz frequency band is much secure and effective for remote inspection of historical artifacts, highly sensitive semiconductor devices, historical paintings, historical structures, etc. This book contains detailed descriptions and associated discussions regarding different generation, detection and signal processing techniques for the electrical and optical signals within the THz frequency

spectrum (0.30–3.0 THz). It includes detailed reviews of some recently developed electronic and photonic devices for generating and detecting THz waves, potential materials for implementing THz devices and circuits, some newly developed systems and methods associated with THz wireless communication, THz antennas and some cutting-edge techniques associated with the THz signal and image processing. The proposed book covers a very vast audience from basic science to engineering and technology experts as well as learners. This could eventually work as a textbook for engineering students or science master's programs and for researchers. This book also serves a common public interest by presenting new methods for data evaluation, medical diagnosis, etc., to improve the quality of life in general, with a better integration into society.

Cooch Behar, West Bengal, India — Aritra Acharyya
Asansole, West Bengal, India — Arindam Biswas
Cooch Behar, West Bengal, India — Palash Das

# Contents

# Editors and Contributors

## About the Editors

**Dr. Aritra Acharyya** is currently working at Department of Electronics and Communication Engineering, Cooch Behar Government Engineering College, Harinchawra, Ghughumari, West Bengal, 736170, India, as Assistant Professor. He was born in 1986. He received B.E. and M.Tech. degrees from IIEST, Shibpur, India, and Institute of Radio Physics and Electronics, University of Calcutta, India, in the years 2007 and 2010, respectively. Finally, he obtained Ph.D. degree from Institute of Radio Physics and Electronics, University of Calcutta, in the year 2016. His research interests are high-frequency semiconductor devices, nano-structures, semiconductor physics, transport phenomena, quantum mechanics, optoelectronics, etc. He has published 81 research papers in peer-reviewed national and international journals, 60 research papers in national and international conference proceedings, and several book chapters. He also authored and edited six and three numbers of books, respectively.

**Dr. Arindam Biswas** is Assistant Professor, School of Mines and Metallurgy, Kazi Nazrul University, Asansol, Burdwan, West Bengal, 713340, India. He was born in West Bengal, India, in 1984. He received M.Tech. degree in Radio Physics and Electronics from University of Calcutta, India, in 2010 and Ph.D. from NIT Durgapur in 2013. He was Postdoctoral Researcher at Pusan National University, South Korea, with prestigious BK21PLUS Fellowship, Republic of Korea. He got Visiting Professor at Research Institute of Electronics, Shizouka University, Japan. He has been selected for IE(I) Young Engineer Award: 2019–2020 in Electronics and Telecommunication Engineering discipline, Institute of Engineers, India. Dr. Biswas has ten years' of experience in teaching research and administration. Presently, Dr. Biswas is working as Assistant Professor in School of Mines and Metallurgy at Kazi Nazrul University, Asansol, West Bengal, India. He has 48 technical papers in different journals and 30 conference proceedings and six books, one edited volume and one book chapter with international repute. Dr. Biswas received research grant from Science and Engineering Research Board, Government of India, under Early Career Research Scheme for research in Terahertz-based GaN Source. He also received Research Grant from Centre of Biomedical Engineering, Tokoyo Medical and Dental University in association with RIE, Shizouka University, Japan, for study of biomedical THz imaging based on WBG semiconductor IMPATT source. Presently, Dr. Biswas is serving as Associate Editor of Cluster Computing, Springer (SCI Indexed), and as Guest Editor of Nanoscience and Nanotechnology-Asia (Scopus Indexed), Recent Patent in Material Science (Scopus Indexed), Bentham Science Publisher. Dr. Biswas has produced four Ph.D. students in different topics of applied optics and high-frequency semiconductor device. He has organized and chaired difference International Conferences in India and abroad. His research interest is in carrier transport in low-dimensional system and electronic device, nonlinear optical communication, and THz semiconductor source. Dr. Biswas acted as Reviewer for reputed journals, Member of the Institute of Engineers (India), and Regular Fellow of Optical Society of India (India).

**Dr. Palash Das** is currently working at Cooch Behar Government Engineering College as Assistant Professor. He did his M.S. and Ph.D. from IIT Kharagpur and B.Tech. from Kalyani Government Engineering College, West Bengal, India. His current research interest involves GaN optical devices, GaN HEMT, HRXRD of GaN/AlGaN thin film, ideation of new device structures, simulation and modeling, and simulation tool development using Visual Basic 6, automated measurement instrument development with embedded hardware and visual basic-based software. He is currently guiding one Ph.D. scholar working on GaN optical devices for intra-device communication applications. He has guided around 15 B.Tech. projects as well. Palash is owning one US patent and three Indian patents; he authored 11 journal papers, 19 conference papers, and two book chapters. He developed a few software to simulate/demonstrate/measure certain semiconductor physical characteristics. He recently developed one measurement instrument product for automated I-V characterization of electronic devices.

## Contributors

**Aritra Acharyya** Department of Electronics and Communication Engineering, Cooch Behar Government Engineering College, Cooch Behar, West Bengal, India

**Daksh Agarwal** Department of Materials Science and Engineering, University of Pennsylvania, Philadelphia, PA, USA;
Currently At Lam Research Corporation, Fremont, CA, USA

**Bilal Aghoutane** ISO Laboratory, Ibn Tofail University, Kenitra, Morocco

**Gufran Ahmad** Department of Electrical Engineering, Dayalbagh Educational Institute, Agra, India

**Amit Banerjee** Physics Department, Bidhan Chandra College, Asansol, West Bengal, India

**J. P. Banerjee** Institute of Radio Physics and Electronics, University of Calcutta, Kolkata, India

**T. Basu** Department of Basic Science and Humanities, Institute of Engineering and Management & University of Engineering and Management, Kolkata, India

**Rabindranath Bera** Department of Electronics & Communication Engineering, Sikkim Manipal Institute of Technology, Sikkim Manipal University, Majitar, Rangpo, East Sikkim, Sikkim, India

**Suporna Bhowmick** Department of Electronics and Communication Engineering, RCC Institute of Information Technology, Kolkata, India

**Arindam Biswas** Centre for Organic Spin-Tronics and Optoelectronics Devices (COSOD) and Mining Engineering Department, Kazi Nazrul University, Asansol, Burdwan, West Bengal, India;
Mining Engineering Department, Centre for Organic Spin-Tronics and Optoelectronics Devices (COSOD), Kazi Nazrul University, Asansol, Burdwan, West Bengal, India

**S. Chakrabarti** Department of Computer Science and Engineering, Institute of Engineering and Management & University of Engineering and Management, Kolkata, India

**B. Chatterjee** Department of Computer Science and Engineering, University of Engineering and Management, Jaipur, Rajasthan, India

**Subhashri Chatterjee** International Center for Materials Nanoarchitectectonics (MANA), National Institute for Material Science (NIMS), Tsukuba, Japan;
Graduate School of Chemical Sciences and Engineering, Hokkaido University, Sapporo, Japan

**Dilip Kumar Choudhary** Department of ETC, G H Raisoni College of Engineering, Nagpur, Maharashtra, India

**P. K. Das** Department of Basic Science and Humanities, Institute of Engineering and Management & University of Engineering and Management, Kolkata, India

**Palash Das** Department of Electronics and Communication Engineering, Cooch Behar Government Engineering College, Cooch Behar, West Bengal, India

**Pampa Debnath** Department of Electronics and Communication Engineering, RCC Institute of Information Technology, Kolkata, India

**Arpan Deyasi** Department of Electronics and Communication Engineering, RCC Institute of Information Technology, Kolkata, India

**Ritam Dutta** Center of Intelligent Systems and Robotics - ITER, Siksha 'O' Anusandhan (Deemed to be University), Odisha, India

**Mohammed EL Ghzaoui** Faculty of Sciences, Sidi Mohammed Ben Abdellah University, Fes, Morocco

**Hanan El Faylali** ISO Laboratory, Ibn Tofail University, Kenitra, Morocco

**Anuva Ganguly** Institute of Radio Physics and Electronics, University of Calcutta, Kolkata, India

**Dilip Kumar Gayen** Department of Computer Science & Engineering, College of Engineering & Management, Kolaghat, KTPP Township, Medinipur, West Bengal, India

**K. P. Ghatak** Department of Basic Science and Humanities, Institute of Engineering and Management & University of Engineering and Management, Kolkata, India

**Anirudhha Ghosal** Institute of Radio Physics and Electronics, University of Calcutta, Kolkata, India

**Monisha Ghosh** Department of Electronics and Communications Engineering, Supreme Knowledge Foundation Group of Institution, Mankundu, Hooghly, West Bengal, India

**Jayabrata Goswami** Institute of Radio Physics and Electronics, University of Calcutta, Kolkata, India

**S. Kanungo** Department of Electrical and Electronics Engineering, Birla Institute of Technology and Science, Shameerpet, Hyderabad, Telangana, India

**M. P. Karthikeyan** Department of Computer Science, PPG College of Arts and Science, Coimbatore, India

**Hare Krishna** Department of ECE, RTC Institute of Technology, Ranchi, Jharkhand, India

**Bidyut Kumar Kundu** School of Applied Sciences, Centurion University of Technology and Management, Bhubaneswar, Odisha, India

**Sandipan Mallik** Department of Electronics and Communication Engineering, National Institute of Science and Technology, Berhampur, Odisha, India

**Jamal Mestoui** Faculty of Sciences, Sidi Mohammed Ben Abdellah University, Fes, Morocco

**M. Mitra** Department of Electronics and Telecommunication Engineering, Indian Institute of Engineering Science and Technology, Shibpur, Howrah, West Bengal, India

**Kousik Mukherjee** Department of Physics, Banwarilal Bhalotia College, Asansol, India;
Centre of Organic Spintronics and Optoelectronic Devices (COSOD), Kazi Nazrul University, Asansol, Burdwan, West Bengal, India

**Prajukta Mukherjee** Department of Electrical Engineering, Cooch Behar Government Engineering College, Cooch Behar, West Bengal, India

**S. J. Mukhopadhyay** Department of Electronics and Telecommunication Engineering, Indian Institute of Engineering Science and Technology, Shibpur, Howrah, West Bengal, India

**Nitai Paitya** Department of Computer Science and Engineering, Sikkim Manipal Institute of Technology, Sikkim Manipal University, Sikkim, India

**J. Pal** Department of Physics, Meghnad Saha Institute of Technology, Nazirabad, Anandapur, Kolkata, India

**R. Paul** Department of Computer Science and Engineering, Institute of Engineering and Management & University of Engineering and Management, Kolkata, India

**Pragti** School of Basic Sciences, Discipline of Chemistry, Indian Institute of Technology Indore, Indore, India

**Debabrata Samanta** Department of Computer Science, CHRIST (Deemed to be) University, Bangalore, Karnataka, India

**Angsuman Sarkar** Department of Electronics and Communication Engineering, Kalyani Government Engineering College, Kalyani, Nadia, India

**Prashant Kumar Singh** University College of Engineering and Technology (UCET), VBU, Hazaribag, Jharkhand, India

**Shashank Kumar Singh** University College of Engineering and Technology (UCET), VBU, Hazaribag, Jharkhand, India

**Shivendra Pratap Singh** Department of Electronics and Communication Engineering, National Institute of Science and Technology, Berhampur, Odisha, India

**Anjini Kumar Tiwary** Department of ECE, Birla Institute of Technology, Mesra, Jharkhand, India

# Introduction to Generation, Detection and Processing of Terahertz Signals


**Aritra Acharyya, Arindam Biswas, and Palash Das**

**Abstract** In this preparatory chapter, a brief introduction to the generation, detection and processing of terahertz (THz) signals is given. Short descriptions of prospective applications of THz signals as well as some state-of-the-art electronic and photonic devices have also been included in this chapter. A chapter-wise overview of the entire book has been incorporated at the end of this introductory chapter.

**Keywords** Generation · Detection · Materials · Signal processing · Terahertz · Terahertz antenna · Terahertz-gap · Wireless communication

## 1 Introduction

The terahertz (THz) frequency band or 'THz-gap' is the most untouched and unexplored portion of the entire radio-frequency (RF) spectrum. This band (0.3–10 THz) lies between the millimeter-wave (mm-wave (RF)) and infrared (IR (optical)) bands; which means, THz band includes the tremendously high frequency (THF) band (i.e. 0.3–3 THz) and extends up to the starting of the far-IR band (i.e. 10 THz). Therefore, the researchers are now-a-days trying to uncover the technologies from both sides, i.e. from both RF and optical spectrums, in order to explore the THz band and to develop devices and circuits for realizing the THZ systems. The mm-wave spectrum is already in use in 5th generation (5G) mobile communication technology [1, 2]. The THz spectrum will play a vital role in next generation mobile communication technologies (i.e. 6G and onwards) [3–8]. The primary advantage of THz communication is that the ultra-high speed of data transfer can be achieved in this spectrum; i.e. uses of additional techniques for spectral efficiency enhancement are not required). Moreover, from the perspective of wireless transmission, smaller wavelength of THz

A. Acharyya (✉) · P. Das
Department of Electronics and Communication Engineering, Cooch Behar Government Engineering College, Harinchawra, Ghughumari, Cooch Behar, West Bengal 736170, India

A. Biswas
Centre for Organic Spin-Tronics and Optoelectronics Devices (COSOD) and Mining Engineering Department, Kazi Nazrul University, Asansol, Burdwan, West Bengal 713340, India



A. Acharyya et al. (eds.), *Generation, Detection and Processing of Terahertz Signals*, Lecture Notes in Electrical Engineering 794,
https://doi.org/10.1007/978-981-16-4947-9_1

signals help those to achieve greater directivity, smaller free-space diffraction, etc.; in this regard, THz communication is much advantageous than mm-wave wireless communication. On the other hand, unlike the IR or visible light communication systems, THz communication is not very much hampered by alignment issues, scintillation, ambient light interface, atmospheric turbulence, fog, etc. [9, 10]. There is a high chance of achieving ultra-high bandwidth with ultra-low latency communication systems by using THz spectrum in near future [11]. However, one prominent limitation of long-haul THz communication is the considerable amount of absorption of THz signals in water vapour molecules at and beyond 1 THz.

Other than the communication, the THz frequency band is also under huge demand in different other sectors like medical, pharmaceutical sectors, food diagnostics, industrial quality inspection, bio-sensing, bio-imaging, remote sensing, spectroscopy, astronomy, etc. [12–21]. Due to the lower photon energy of THz waves as compared to X-ray photons, THz frequency band is much secure and effective for remote inspection of historical artefacts, highly sensitive semiconductor devices, historical paintings, historical structures, etc. [22].

## 2 Latest Developments in THz Technologies

Several technological challenges associated with the generation, detection and processing of the THz signals result limited amount of efforts among the researchers to explore the 0.3–10 THz frequency spectrum; as a result of it, this unexplored spectrum is referred to as the 'THz-gap' as mentioned in the earlier section. Due to the limited amount of power output of the THz sources and low sensitivity of THz detectors, the development of THz communication system is still underdeveloped [23, 24]. Moreover, the resolution of THz imaging within the range of 0.3–5 THz is significantly low as compared to the X-ray imaging, due to the longer wavelength of the THz signals within the said frequency range [25]. In order to achieve higher imaging resolution, frequencies greater than 5 THz have to be used for the said purpose. But efficient generation of high-power 5–10 THz signals is a highly challenging task. The saturation drift velocity of the charge carriers in the base semiconductor materials used to fabricate the electronic and optoelectronic devices operational within this frequency range must be significantly high. Also, the breakdown field of these materials must be very high in order to achieve high THz power from those devices. Some wide bandgap (WBG) materials like GaN, SiC, diamond, etc. and some two-dimensional (2-D) carbon-based nano0materials like carbon nanotubes (CNTs), graphene nano ribbons (GNRs), etc., show immense potentialities in this regard [26–30]. Examples of some promising semiconductor based THz sources are given below:

(a) Quantum cascade lasers,
(b) Negative differential resistance (NDR) diodes,
(c) Impact avalanche transit time (IMPATT) diodes,

(d) Heterostructure field effect transistors (HFTs),
(e) Resonant tunneling diodes (RTDs),
(f) GUNN diodes,
(g) High electron mobility transistors (HEMTs), etc.

One extraordinary technique for generating intense THz pulses of picoseconds duration is the optical rectification technique [31] which utilizes the nonlinear optical method. Some examples of optical nonlinear crystals which are used for optical rectification are DAST, DSTMS, OH-1, etc. [32]. State-of-the-art lithography controlled etching techniques, advanced techniques to fabricate micro-electro-mechanical systems (MEMS) enable the modern researchers to achieve excellent surface quality, moderate grain size (>100 nm) and extremely low surface roughness (20 nm) [33], while fabricating THz vacuum electronic device (VED) sources with transverse circuit dimensions of the order of sub-mm range [34–38]. Significantly high-power capability of THz VED sources is highly promising for numerous applications in THz science and technology range [34–36]. Some other potential non-semiconductor based THz devices are given by

(a) Accelerator-based THz sources,
(b) Photoconductive devices,
(c) Backward wave oscillators (BWOs) [37],
(d) Free electron lasers [38],
(e) Frequency multiplication devices [39],
(f) Gas lasers, etc.

All the above-mentioned devices are operational at room temperature.

On the other hand, detection of THz signals is a very challenging task due to the unavailability of sufficiently sensitive THz detectors. However, rapid research works since last two decades provided a few promising THz detectors, which are already commercially available. Some examples of those are given by

(a) Schottky barrier diodes (SBDs) [40],
(b) Photoconductive folded dipole antenna,
(c) Micro-bolometer [41, 42],
(d) Bolometer,
(e) Pyroelectric detectors,
(f) Hot electron bolometer [43],
(g) Field effect transistors (FETs) [44], etc.

Realization of system-level THz technologies essentially requires compact and systematic signal processing techniques. Recent advances in THz signal processing techniques, modelling of channel, noise, etc., are creating new horizons for system-level development of THz science and technology [45].

## 3 Overview of the Book

This book contains detailed descriptions and associated discussions regarding different generation, detection and signal processing techniques for the electrical and optical signals within the THz frequency spectrum (0.3–10 THz). It includes detailed reviews of some recently developed electronic and photonic devices for generating and detecting THz waves, potential materials for implementing THz passive circuits, some newly developed systems and methods associated with THz wireless communication, THz antennas and some cutting-edge techniques associated with the THz signal and image processing. The book covers a very wide range of readers from basic science to technological experts as well as students. This book can be considered as a text book for under graduate, post graduate and doctoral students and also for scientists.

Chapter-wise organization of the entire book is as follows. The absorption cross-section of double quantum well triple barrier structure is analytically computed in Chapter "Investigating Absorption Cross Section and Oscillator Strength for Double Quantum Well with Pöschl-Teller Potential", where the authors have used Pöschl-Teller potential geometry considering the intra-band transition between ground and first excited states. Chapter "Channel Characterization and CE-OFDM Modulation for Terahertz System" describes the channel characterization and constant envelope orthogonal frequency division multiplexing modulation for THz systems. Detailed descriptions of some state-of-the-art applications of THz antennas are presented in Chapter "Investigation on Antennas for Terahertz Applications". Some important aspects of all optical encryption and decryption circuits are discussed in Chapter "All-Optical Encryption and Decryption Circuit". Chapter "Gallium Oxide-Based IMPATT Sources for THz Applications" describes the potentialities of gallium oxide as possible base material for high-power THz sources. The concept of optical exclusive-OR gate based on THz optical asymmetric de-multiplexer and quantum dot semiconductor optical amplifier is the subject matter of Chapter "All Optical XOR Gate Using Quantum Dot Semiconductor Optical Amplifier Based Terahertz Optical Asymmetric Demultiplexer (TOAD)". Chapter "Generation, Detection and Analysis of Sub-Terahertz Over the Air (OTA) Test Bed for 6G Mobile Communication Use Cases" demonstrates the generation, detection and analysis of sub-terahertz over the air (OTA) test bed for 6G mobile communication system. The recent advancements in THz imaging and its modern applications are summarized in Chapter "THz Image Processing and Its Applications". The static analysis of single gate tunnel field effect transistors based on indium arsenide channel material is presented in Chapter "A DC Analysis of Single Gate TFET Using InAs as Channel Material". Emergence of avalanche transit time oscillators as THz sources is beautifully summarized from its inception to the state-of-the-art in Chapter "Cutting-Edge Technologies for Terahertz Wave Generation: A Brief History from the Inception Till the Present State of The Art". An approximate model for analyzing newly proposed lateral avalanche transit time source based THz oscillator has been elaborated in Chapter "An Approximate Model for Analyzing Four-Terminal Lateral

Single-Drift IMPATT Based THz Radiators". Some state-of-the-art simulation techniques for analyzing the THz avalanche transit time oscillators have been described in Chapter "On Some Modern Simulation Techniques for Studying THz ATT Sources". Chapter "Studies on Sub-Terahertz Performance of Avalanche Transit Time Sources" describes the THz performance of silicon, indium phosphide, gallium arsenide and silicon carbide based avalanche transit time sources. Studies on some heterojunction material systems suitable for THz applications are presented in Chapter "Search of a Suitable Heterojunction Material System for Terahertz Wave Generation". Applications of Si ~ 3C-SiC heterostructures in high frequency electronics up to the THz spectrum are briefly discussed in Chapter "Applications of Si~3C-SiC Heterostructures in High-Frequency Electronics up to the Terahertz Spectrum". The detailed static and dynamic analysis of a proposed novel Indium Arsenide (InAs)/Silicon (Si) heterojunction based dual gate triple metal *p-i-n* tunneling graphene nanoribbon field effect transistor (DG-TM-TGNFET) has been reported in Chapter "Novel InAs/Si Heterojunction Dual-Gate Triple Metal P-I-N Tunneling Graphene Nanoribbon Field Effect Transistor (DG-TM-TGNFET) For High-Frequency Applications". Chapter "Design and Simulation of Microstrip Antenna for Terahertz Applications" deals with the design and simulation of microstrip antennas for THz applications. The recent trends in the applications of THz science and technology in different fields of biomedication engineering are described in Chapter "Trends in Terahertz Biomedical Applications". Finally, the Chapters "The Elastic Constants in Opto-electronic Materials Under Terahertz Frequency" and "Screening Length, Terahertz Frequency and Opto-electronic Compounds" described the elastic constants and screening lenghths of some potential electronic material systems at THz spectrum.

## References


1. Xiao M, Mumtaz S, Huang Y, Dai L, Li Y, Matthaiou M, Karagiannidis GK, Björnson E, Yang K, Chih-Lin I, Ghosh A (2017) Millimeter wave communications for future mobile networks. IEEE J Sel Areas Commun 35(9):1909–1935
2. Rangan S, Rappaport TS, Erkip E (2014) Millimeter-wave cellular wireless networks: potentials and challenges. Proc IEEE 102(3):366–385
3. Akyildiz IF, Jornet JM, Han C (2014) TeraNets: ultra-broadband communication networks in the terahertz band. IEEE Wireless Commun 21(4):130–135
4. Akyildiz IF, Jornet JM, Han C (2014) Terahertz band: next frontier for wireless communications. Phys Commun 12:16–32
5. Kleine-Ostmann T, Nagatsuma T (2011) A review on terahertz communications research. J Infrared Millimeter Terahertz Waves 32(2):143–171
6. Chen Z, Ma X, Zhang B, Zhang Y, Niu Z, Kuang N, Chen W, Li L, Li S (2019) A survey on terahertz communications. China Commun 16(2):1–35
7. Huang K, Wang Z (2011) Terahertz terabit wireless communication. IEEE Commun Mag 12(4):108–116
8. Song H, Nagatsuma T (2011) Present and future of terahertz communications. IEEE Trans THz Sci Technol 1(1):256–263
9. Grobe L, Paraskevopoulos A, Hilt J, Schulz D, Lassak F, Hartlieb F, Kottke C, Jungnickel V, Langer K (2013) High-speed visible light communication systems. IEEE Commun Mag 51(12):60–66

10. Pathak PH, Feng X, Hu P, Mohapatra P (2015) Visible light communication, networking, and sensing: a survey, potential and challenges. IEEE Commun Surv Tuts 17(4):2047–2077
11. Rappaport TS, Xing Y, Kanhere O, Ju S, Madanayake A, Mandal S, Alkhateeb A, Trichopoulos GC (2019) Wireless communications and applications above 100 GHz: opportunities and challenges for 6G and beyond. IEEE Access 78(7):729–757
12. Siegel PH (2002) Terahertz technology. IEEE Trans Microwave Theor Tech 50(3):910–928
13. Martyniuk P, Antoszewski J, Martyniuk M, Faraone L, Rogalski A (2014) New concepts in infrared photodeector designs. Appl Phys Rev 1, 041102-1-35
14. Woodward RM, Cole BE, Wallace VP, Pye RJ, Arnone DD, Linfield EH, Pepper M (2002) Terahertz pulse imaging in reflection geometry of human skin cancer and skin tissue. Phys Med Biol 47:3853–3863
15. Nagel M, Bolivar PH, Brucherseifer M, Kurz H, Bosserhoff A, Buttner R (2002) Integrated THz technology for label-free genetic diagnostics. Appl Phys Lett 80(1):154–156
16. Karpowicz N, Zhong H, Zhang C, Lin KI, Hwang JS, Xu J, Zhang XC (2005) Compact continuous-wave subterahertz system for inspection applications. Appl Phys Lett 86 (5), 054105-1-3
17. Yamamoto K, Yamaguchi M, Miyamaru F, Tani M, Hangyo M (2004) Non-invasive inspection of c-4 explosive in mails by terahertz time-domain spectroscopy. J Appl Phys 43(3B):L414–L417
18. Kawase K, Ogawa Y, Watanabe Y, Inoue H (2003) Non-destructive terahertz imaging of illicit drugs using spectral fingerprints. Opt Express 11(20):2549–2054
19. Joerdens C, Koch M (2008) Detection of foreign bodies in chocolate with pulsed terahertz spectroscopy. Opt Eng 47 (3), 037003-1-5
20. Tonouchi M (2007) Cutting-edge terahertz technology. Nat Photonics 1:97–105
21. Prince JL, Links J (2006) Medical imaging signals and systems. 2nd edn. Pearson Prentice Hall, Upper Saddle River
22. Dandolo CLK, Jepsen PU (2016) Wall painting investigation by means of non-invasive terahertz time-domain imaging (THz-TDI): inspection of subsurface structures buried in historical plasters. J Infrared Millimeter Terahertz Waves 37:198–208
23. Chen S-L, Chang Y-C, Zhang C, Ok JG, Ling T, Mihnev MT, Guo TBNLJ (2014) Efficient real-time detection of terahertz pulse radiation based on photoacoustic conversion by carbon nanotube nanocomposite. Nat Photonics 8:537–542
24. Sirtori C (2002) Bridge for the terahertz gap. Nature 417:132–133
25. Saleh BEA, Teich MC (2007) Fundamentals of photonics, 2nd edn. Wiley, New York, p 1200
26. Biswas A, Sinha S, Acharyya A, Banerjee A, Pal S, Satoh H, Inokawa H (2018) 1.0 THz GaN IMPATT source: effect of parasitic series resistance. J Infrared Millimeter Terahertz Waves 39(10):954–974
27. Acharyya A, Banerjee JP (2014) Prospects of IMPATT devices based on wide bandgap semiconductors as potential terahertz sources. Appl Nanosci 4:1–14
28. Acharyya A, Banerjee S, Banerjee JP (2013) Potentiality of semiconducting diamond as base material of millimeter-wave and terahertz IMPATT devices. J Semiconductors 35(3), 034005-1-11
29. Acharyya A (2019) Three-terminal graphene nanoribbon tunable avalanche transit time sources for terahertz power generation. Physica Status Solidi (a) 216(18), 1900277
30. Acharyya A (2019) 1.0–10.0 THz radiation from graphene nanoribbon based avalanche transit time sources. Physica Status Solidi (a) 216(7):1800730
31. Yeh KL, Hoffmann MC, Hebling J, Nelson KA (2007) Generation of 10 μJ ultrashort terahertz pulses by optical rectification. Appl Phys Lett 90:171121
32. Hauri CP, Ruchert C, Vicario C, Ardana F (2011) Strong-field single-cycle THz pulses generated in an organic crystal. Appl Phys Lett 99:161116
33. Kirley MP, Booske JH (2015) Terahertz conductivity of copper surfaces. IEEE Trans Terahertz Sci Technol 5:1012–1020
34. Booske JH (2008) Plasma physics and related challenges of millimeter-wave-to-terahertz and high power microwave generation. Phys Plasmas 15:16–20

35. Barker RJ, Booske JH, Luhmann NC, Nusinovich GS (eds) (2005) Modern microwave and millimeter wave power electronics, Wiley, New York
36. Booske JH, Dobbs RJ, Joye CD, Kory CL, Neil GR, Park GS, Park J, Temkin RJ (2011) Vacuum electronic high power terahertz sources. IEEE Trans Terahertz Sci Technol 1:52–75
37. He W et al. (2015) Generation of broadband terahertz radiation using a backward wave oscillator and pseudospark-sourced electron beam. Appl Phys Lett 107:133501
38. Gavrilov NG, Knyazev BA, Kolobanov EI, Kotenkov VV, Kubarev VV, Kulipanov GN, Matveenko AN, Medvedev LE, Miginsky SV, Mironenko LA, Oreshkov AD, Ovchar VK, Popik VM, Salikova TV, Scheglov MA, Serednyakov SS, Shevchenko OA, Skrinsky AN, Tcheskidov VG, Vinokurov NA (2007) Status of the Novosibirsk highpower terahertz FEL Nucl. Instrum Methods Phys Res A 575(1–2):54–57
39. Virginia Diodes Inc Virginia Diodes, Inc—Frequency multipliers. (last accessed April 2021) Available from: http://vadiodes.com/en/frequency-multipliers
40. Han R et al (2013) Active terahertz imaging using Schottky diodes in CMOS: Array and 860-GHz pixel. IEEE J Solid-State Circuits 48:2296–2308
41. Grant JP et al (2013) A monolithic resonant terahertz sensor element comprising a metamaterial absorber and micro-bolometer. Laser Photon Rev 7(6):1043–1048
42. Carranza IE, Grant JP, Gough J, Cumming D (2017) Terahertz metamaterial absorbers implemented in cmos technology for imaging applications: scaling to large format focal plane arrays. IEEE J Sel Top Quantum Electron 23(4):4700508
43. Dobrovolsky V, Sizov F (2007) Room temperature, or moderately cooled, fast THz semiconductor hot electron bolometer. Semicond Sci Technol 22:103–106
44. Boppel S et al (2012) IEEE 12th topical meeting on silicon monolithic integrated circuits RF systems. SiRF 2012, pp 77–80
45. Sarieddeen H, Alouini MS, Al-Naffouri TY (2020) an overview of signal processing techniques for terahertz communications. TechRxiv, Preprint. https://doi.org/10.36227/techrxiv.12363359.v1.

# Investigating Absorption Cross Section and Oscillator Strength for Double Quantum Well with Pöschl-Teller Potential


**Arpan Deyasi, Suporna Bhowmick, Pampa Debnath, and Angsuman Sarkar**

**Abstract** Absorption cross section of triple barrier double quantum well structure is analytically computed with Pöschl-Teller potential geometry considering the intra-band transition from ground to first excited state. Peak values of absorption cross section are noted which reflects active area for optical transitions has dimensions in sub-micron range. Structural parameters are varied to compute the possible variation of that cross section, taking into account the first order band nonparabolicity. Oscillator strength is also calculated as a function of incident wavelength which indicates the statistical possibility of transition is higher with increasing wavelength between those two quantum states. Simulated findings are compared with the data available for rectangular well which speaks in favor of the Pöschl-Teller geometry owing to lower energy spreading and higher peak value. Results stand in favor of the present potential configuration as proposed in the paper, and therefore can be utilized for design of quantum well-based photonic detector.

**Keywords** Pöschl-Teller potential · Absorption cross section · Oscillator strength · Double quantum well · Depth parameter · Width parameter

## 1 Introduction

Research on nanostructure devices are progressed in last two decades mostly due to the advantage of low-noise electronic properties [1, 2]. Simultaneously the photonic properties offered have received high attention due to the immense possibility of making improved transmitter, receiver and sensors [3–5]. Among different quantum

A. Deyasi (✉) · S. Bhowmick · P. Debnath
Department of Electronics and Communication Engineering, RCC Institute of Information Technology, Canal South Road, Kolkata 700015, India

A. Sarkar
Department of Electronics and Communication Engineering, Kalyani Government Engineering College, Kalyani, Nadia 741235, India
e-mail: angsumansarkar@ieee.org



A. Acharyya et al. (eds.), *Generation, Detection and Processing of Terahertz Signals*, Lecture Notes in Electrical Engineering 794,
https://doi.org/10.1007/978-981-16-4947-9_2

well structures, though quantum dot based devices are preferred [6, 7] for applications, but quantum well structures are comparatively easy to realize experimentally [8], and theoretical workers can easily support the findings through analytical/numerical investigations [9, 10]. Among various quantum well geometries, Pöschl-Teller configuration has attracted interest to researchers due to its unique features of exhibiting Bose-Einstein condensation at 39 K [11]. Also, it already exhibits higher operating frequency for optical applications. Therefore, it becomes essential to further investigate the geometry subject to the operation at higher THz region.

In recent years, novel works are published on optical properties of quantum well modulators [12]. Semi-parabolic quantum wells are considered for peak value calculation of absorption coefficient using density matrix approach [13]. In this specific structure, effects of external conditions are very recently investigated [14] for computation of non-linear absorption coefficients. One electron core-shell spherical quantum dots are analyzed [15] for the same purpose. Researchers also demonstrated the role of material composition [16] on the non-linear coefficients for quantum ring-type structure.

A few relevant works on investigation of absorption coefficient of quantum well-based devices are already reported [17, 18], and works are extended for superlattice structures [19]. However, most of the works are calculated considering rectangular geometry, which is ideal, and henceforth, loses significance when practical results are obtained. A few reports are published on Gaussian [20], parabolic [21] wells, though devoid of tunability property of the shape and size of well. In this context, Pöschl-Teller configuration carries huge significance as it is the first quantum well which can be tailored in terms of depth and breadth.

Earlier, absorption cross section of triangular quantum wire is reported [22, 23] by different workers in correction with various detector applications. Concurrently, similar works are reported for superlattice structure [24, 25]. It may be noted that role of band structure becomes critical for this computation [26], as well as the shape of potential profile [27]. Therefore, for accurate calculation, several important factors, as well as the band structure, should be included, and there lies success of this evaluation.

The two concerned properties in this chapter, namely oscillator strength, and absorption cross section, signify the probability of transition between two states, and the area required for that action, respectively. Therefore, findings of these two properties carry significance from application point-of-view, when they are considered for detector design at nanometric level. Incorporation of realistic band structure, as well as lineshape function, adds importance to the proposal. Here lies the novelty of the work.

## 2 Motivation of the Proposed Work

For optical detector design, absorption coefficient is the most important parameter. However, oscillator strength is also equally important as it determines the statistical probability of the transport of carriers between the quantum levels. Henceforth, a simultaneous determination of both properties is the subject of interest for researchers. However, for nanoelectronic devices, area of the device is one of the prime concerns for optical applications, and henceforth, the cross section for the absorption becomes significant. Coefficient of absorption is already measured several times and reported, whereas cross section and corresponding oscillator strength become less investigated. Henceforth, these two properties are considered primarily for the investigation.

Moreover, shape of the potential profile becomes also important as far as device performance is concerned. Most of the works are based on the ideal rectangular well profile, which can't be implemented in practical point-of-view. Henceforth, various critical geometries and profiles are considered thereafter, like triangular, parabolic, Gaussian, etc. Latest candidate in this list is the Pöschl-Teller, which has significance in low temperature applications. Combining with the previous concept on properties to be investigated, title of the present manuscript becomes critically important at present-day concept.

## 3 Mathematical Formulation

Analysis of optical properties begin with the calculation of absorption coefficient [28], which can be put in a generalized manner as

$$\alpha(\omega) = \frac{q^2 h}{\varepsilon c n_r m^{*2} V} \frac{1}{\hbar\omega} \sum_{u,v} \left|\langle u|p_z|v\rangle^2\right| \delta(E_v - E_u - \hbar\omega)(f_{FD}^u - f_{FD}^v), \quad (1)$$

where Fermi–Dirac distributions $(f_{FD}^u, f_{FD}^v)$ are invoked for quantization properties.

The function $\sum_{u,v} \left|\langle u|p_z|v\rangle^2\right|$ indicates the overlap function between the consecutive states calculated over the momentum variable inside conduction band, $E_u$ and $E_v$ are corresponding energy functions. Other variables have meanings as per convention. Introducing lineshape function [28], we get

$$\alpha(\omega) = \frac{\rho_s \pi q^2 h}{4\pi \varepsilon c n_r m^* W_w} o_{n,m} \delta(\Delta E_{v,u} - \hbar\omega), \quad (2)$$

where $W_w$ is the quantum well length, $\rho_s$ denotes 2D charge density, $O_{n,m}$ is the oscillator strength between the two consecutive quantum levels.

Oscillator strength is a function of quantized dimension as [28]

$$o_{21} = \frac{4\pi}{m^* h\omega}\left[\frac{4h}{3\pi W_w}\right]^2. \tag{3}$$

After computing oscillator strength, absorption cross section is estimated using the following equation

$$\sigma_{v,u} = \frac{q^2 T}{2\varepsilon_0 m^* nc} o_{v,u}\left[1 + T^2\left(2\pi\frac{E - \Delta E_{v,u}}{h}\right)^2\right]^{-1}, \tag{4}$$

where '$T$' denotes relaxation time.

## 4 Results and Discussions

Using Eqs. (3) and (4), oscillator strength and absorption cross section are respectively computed and plotted for Pöschl-Teller potential configuration of the DQWTB system in presence of externally applied electric field directed along dimensional confinement. The oscillator strength depends only on the width of the quantum well. Figure 1 shows the variation of the oscillator strength for Pöschl-Teller quantum well configuration. The oscillator strength monotonically increases with wavelength.

But while increasing well width, oscillator strength decreases. Higher well width reduces the quantum confinement which results in the reduction in eigenenergies. This, in turn, changes the separation between energy values, hence the oscillator strength decreases. Using Eq. (4), absorption cross section is computed and plotted for the structure. Considering band nonparabolicity, the eigenenergies are obtained. Result is calculated in presence of bias and peak position is determined with respect to the energy. For validation of the result, the simulated behavior is compared with that obtained for ideal rectangular well structure.

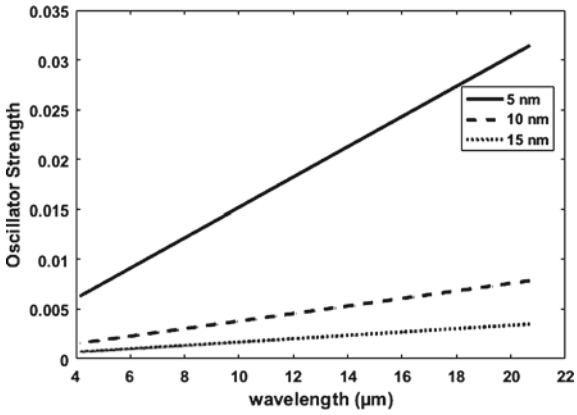


**Fig. 1** Oscillator strength for Pöschl-Teller potential for three different well dimensions

Figure 2 shows the variation of absorption cross section for different well widths. Reduction of quantum confinement drastically reduces the profile. Lowering the quantum well dimension enhances quantum confinement, which, in turn, increases eigenvalue. Thus the peaks appear at higher energy states. From the equation, it can be noted absorption cross section is directly proportional to the oscillator strength, which again inversely proportional to the well width thus it reduces for higher well width.

Similar type of investigation is carried out for the contact barrier and middle barrier width, which are represented in Figs. 3 and 4 simultaneously. The increment in sandwich layer width results in significant change in the magnitude of intersubband transition though the Eigen energy peaks appear in closer distances. The value of absorption cross section increases with the increase in dimension. In Fig. 3, it is seen that higher contact barrier width makes higher quantum energy level, which causes

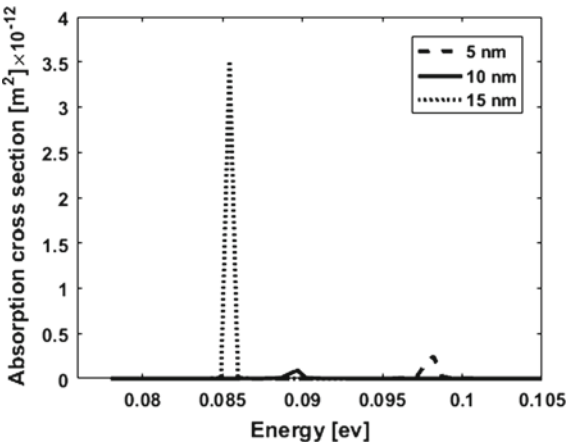


**Fig. 2** Absorption cross section of Pöschl-Teller potential for three different well dimensions

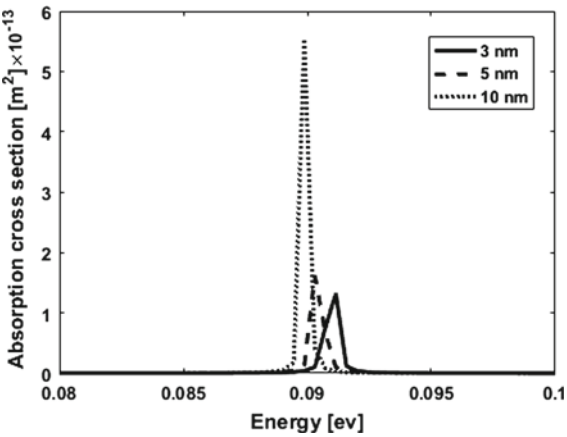


**Fig. 3** Absorption cross section of Pöschl-Teller potential for three different contact barrier widths

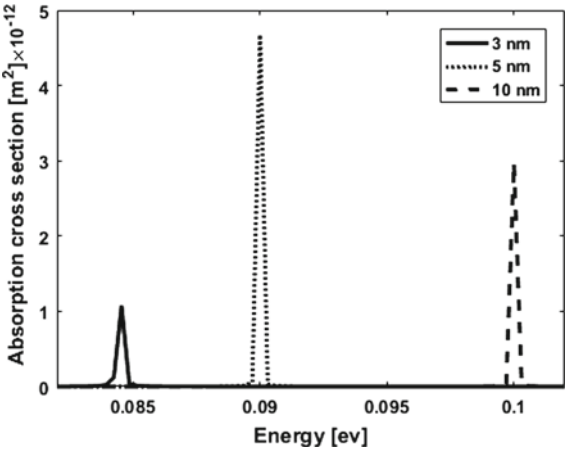


**Fig. 4** Absorption cross section of Pöschl-Teller potential for three different middle barrier widths

change in peak magnitude. According to the eigenenergy states, the peak appears at different energy values. The peak values are listed in Table 1.

Similar simulation is carried out for the depth parameter and width parameter, which are represented in Figs. 5 and 6 respectively (also see Table 2). Figure 7 shows the comparison between the ideal potential well structure and Pöschl-Teller potential well geometry. It can be noted that the peak value achieved for Pöschl-Teller potential is significantly high with respect to that achieved in rectangular well.

**Table 1** Peak value of absorption cross section for different structural dimensions

| Name of parameter | Dimension [nm] | $E_1$ [eV] | $E_2$ [eV] | $\Delta E_{21}$ [eV] | Peak value of absorption cross section ($m^2$) × $10^{-12}$ |
|---|---|---|---|---|---|
| Well width | 5 | 0.04203 | 0.14 | 0.09797 | 0.02485 |
| | 10 | 0.04253 | 0.132 | 0.08947 | 0.097 |
| | 15 | 0.04453 | 0.13 | 0.08547 | 3.514 |
| Contact barrier width | 3 | 0.08303 | 0.174 | 0.09097 | 0.040 |
| | 5 | 0.07153 | 0.162 | 0.09047 | 0.013 |
| | 10 | 0.04253 | 0.1325 | 0.08997 | 0.0538 |
| Middle barrier width | 3 | 0.04503 | 0.1295 | 0.08447 | 1.07 |
| | 5 | 0.04253 | 0.1325 | 0.08997 | 4.676 |
| | 10 | 0.03753 | 0.1375 | 0.09997 | 2.976 |

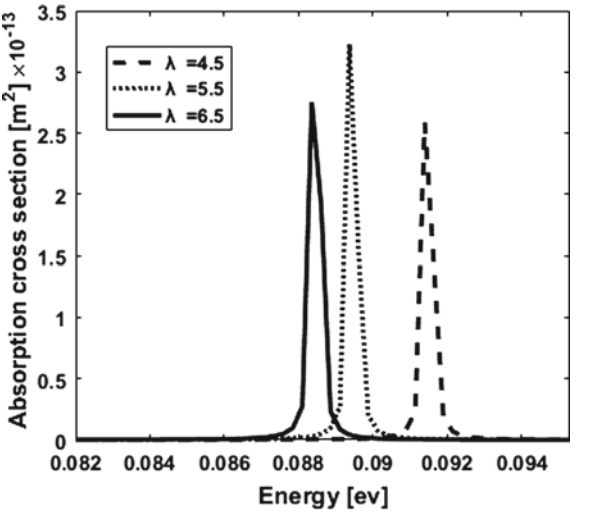


**Fig. 5** Absorption cross section of Pöschl-Teller potential for three different depth parameters

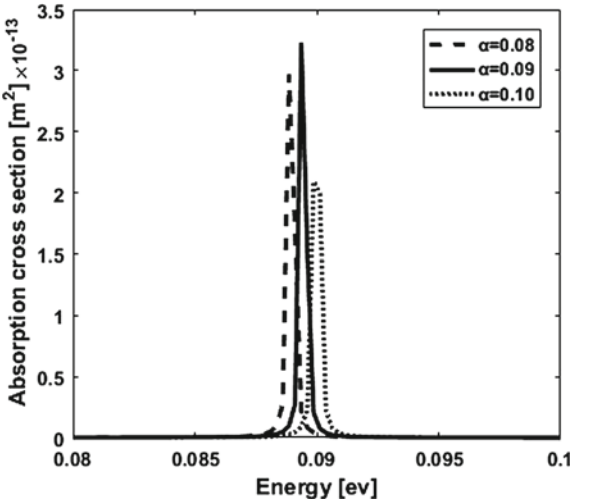


**Fig. 6** Absorption cross section of Pöschl-Teller potential for three different breadth parameters

**Table 2** Peak value of absorption cross section for depth and width parameter

| Name of parameter | Dimension [nm] | $E_1$ [eV] | $E_2$ [eV] | $\Delta E_{21}$ [eV] | Peak value of absorption cross section ($m^2$) × $10^{-12}$ |
|---|---|---|---|---|---|
| Width parameter | 0.08 | 0.07053 | 0.1595 | 0.08897 | 0.02969 |
| | 0.09 | 0.04253 | 0.132 | 0.08947 | 0.03227 |
| | 0.1 | 0.00703 | 0.0970 | 0.08999 | 0.02093 |
| Depth parameter | 4.5 | 0.01005 | 0.1905 | 0.18045 | 0.02588 |
| | 5.5 | 0.08203 | 0.1705 | 0.08847 | 0.03227 |
| | 7.5 | 0.04253 | 0.1325 | 0.08997 | 0.02753 |

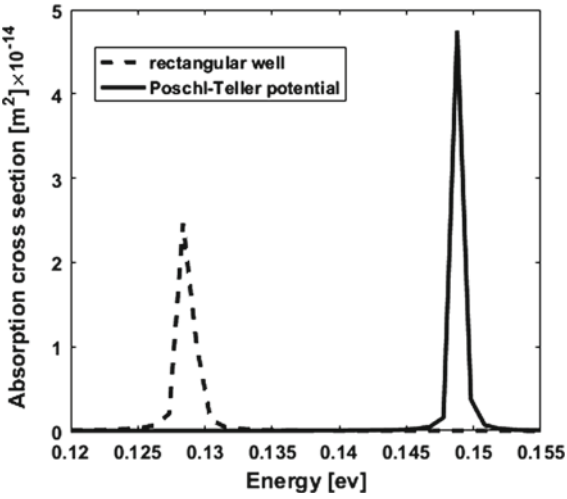


**Fig. 7** Comparative study of absorption coefficient between Pöschl-Teller potential with rectangular well

## 5 Summary

The theoretical analysis showed that Pöschl-Teller potential provides 1.7 times higher cross section peak than rectangular geometry when other designs and external parameters are kept same. Also, energy bandwidth for the present configuration exhibits 29% less energy bandwidth. Combining these two features, it can be considered as a potential candidate for detector design. It may also be noted that tuning of design parameters (width and depth) does not affect greatly the cross section magnitude (less than 1% variation), which is really important from operational point-of-view. Position of the peak and its magnitude significantly depend on structural parameters, as evident from the simulation. Therefore, for specific applications, choice of design, as well as structural parameters, become essential along with the operating wavelength to get higher oscillator strength.

## References

1. Lin SH, Feng DJY, Lee ML, Lay TS, Sun TP, Kuan CH (2012) Double-barrier superlattice infrared photodetector integrated with multiple quantum-well infrared photodetector to improve performance. Int J Electrochem Sci 7:5746–5753
2. Lu ZG, Liu JR, Song CY, Weber J, Mao Y, Chang SD, Ding HP, Poole PJ, Barrios PJ , Poitras D, Janz S , O'Sullivan M (2018) High performance InAs/InP quantum Dot 34.462-GHz C-band coherent comb laser module. Opt Exp 26(2):2160–2167
3. Wan Y, Inoue D, Jung D, Norman JC, Shang C, Gossard AC, Bowers JE (2018) Directly modulated quantum dot lasers on silicon with a milliampere threshold and high temperature stability. Photonics Res 6(8):776–781

4. Suganuma T, Ghosh S, Kazi M, Kobayashi R, Nakano Y, Tanemura T (2018) Monolithic InP stokes vector receiver with multiple-quantum-well photodetectors. J Lightwave Technol 36(5):1268–1274
5. Alves RA, Costa JC, Gomes M, Silva NA, Guerreiro A (2017) Quantum wires as sensors of the electric field: a model into quantum plasmonics. 25th optical fiber sensors conference, pp 1–4
6. Vinasco JA, Radu A, Kasapoglu E, Restrepo RL, Morales AL, Feddi E, Mora-Ramos ME, Duque CA (2018) Effects of geometry on the electronic properties of semiconductor elliptical quantum rings. Sci Rep 8:13299
7. Kumar S, Biswas D (2007) Effects of a Gaussian size distribution on the absorption spectra of III-V semiconductor quantum dots. J Appl Phys 102:084305
8. Lu F, Bhattacharya I, Sun H, Tran TTD, Ng KW, Malheiros-Silveria GN, Chang-Hasnain C (2017) Nanopillar quantum well lasers directly grown on silicon and emitting at silicon-transparent Wavelengths. Optica 4(7), 717–723
9. Belov PA, Khramtsov ES (2017) The binding energy of excitons in narrow quantum wells. IOP Conf Ser J Phys 816:012018
10. Kaatuzian H, Kojori HS, Zandi A, Kohandani R (2013) Effects of Quantum well size alteration on excitonic population oscillation slow light devices properties. Opt Photonics J 3:298–304
11. Sarath R, Vinodkumar PC (2015) Bose-einstein condensation in generalized Pöschl-Teller potential. PRAMANA J Phys 85(1):77–89
12. Li EH, Choy WCH (1998) Optical properties of interdiffused quantum well modulators. Conference on optoelectronic and microelectronic materials and devices, 14–16 Dec 1998, Perth, WA, Australia, pp 1–4
13. Karimi MJ, Keshavarz A, Poostforush A (2011) Linear and nonlinear intersubband optical absorption of finite and infinite semi-parabolic quantum wells. Mod Phys Lett B 25(7):497–507
14. You J-F, Zhao Q, Zhang Z-H, Yuan J-H, Guo K-X, Feddi E (2019) The effect of temperature, hydrostatic pressure and magnetic field on the nonlinear optical properties of AlGaAs/GaAs semi-parabolic quantum well. Int J Mod Phys B 33(27):1950325
15. Kostic R, Stojanovic D (2020) Intersubband transitions in spherical quantum dot quantum well nanoparticle. Opt Quant Electron 52:285
16. Kehili MS, Sellami R, Mansour AB, Melliti A (2020) Manipulation of linear and nonlinear optical properties of GaSb quantum ring in AlGaAs/GaAs/AlGaAs quantum well and AlAs/GaAs/InGaAs/AlAs double quantum well. Opt Quant Electron 52:321
17. Dey A, Neogi A, Maiti B, Chandra D (2012) Simple analysis of the interband absorption coefficient of bulk and quantum well of nonparabolic semiconductors with application to $Hg_{1-x}Cd_xTe$ material. J Optoelectron Adv Mater 14(3–4):210–218
18. Lever L, Hu Y, Myronov M, Liu X, Owens N, Gardes FY, Marko IP, Sweeney SJ, Ikonic Z, Leadley DR, Reed GT, Kelsal RW (2011) Modulation of the absorption coefficient at 1.3 μm in Ge/SiGe multiple quantum well heterostructures on silicon. Opt Lett 36(21):4158–4160
19. Giannoccaro G, Leonardis FD, Passaro VMN (2015) A computational approach of optical absorption in semiconductor quantum dot superlattices. IEEE 15th international conference on nanotechnology, pp 1–4
20. Sarkar D, Deyasi A (2016) Comparative analysis of absorption coefficient for parabolic and Gaussian quantum wells for photodetector application. Adv Ind Eng Manage 5(2):197–201
21. Sarkar D, Deyasi A (2016) Oscillator strength of Gaussian double quantum well for intersubband transition. Springer Proc Phys Adv Opt Sci Eng 53:433–438
22. Khordad R, Tafaroji S, Katebi R (2012) Quantum wire with triangle cross section: optical properties. Commun Theor Phys 57(6):1076–1080
23. Deyasi A, Das NR (2014) Oscillator strength and absorption cross-section of core-shell triangular quantum wire for intersubband transition. Proceedings in Physics: Advances in Optical Science and Engineering: 2nd international conference on optoelectronics and applied optics 166(78):629–635
24. Geiregat P, Omari A, Justo Y, Van Thourhout D, Hens Z (2013) Absorption enhancement in 2D nanocrystal superlattices through near-field dipolar coupling: a novel optical phenomenon at the nanoscale. CLEO: 2013, OSA Technical Digest, paper QTu1A.7

25. Kundu P, Ghosh P, Deyasi A (2014) Analytical computation of absorption coefficient for intersubband transition in MQW structure. Lecture notes in electrical engineering: international conference on computational advancement in communication circuits and systems, part 6: Advances in devices and circuit 335(35):321–329
26. Sarkar D, Deyasi A (2016) Calculating absorption coefficient of Gaussian double quantum well structure with band nonparabolicity for photodetector in microwave spectra. Found Front Comput Commun Electr Eng 47:225–229
27. Bhowmick S, Chakraborty D, Guha D, Chakraborty B, Debnath P, Deyasi A (2021) Computation of absorption coefficient for Pöschl-Teller potential in double quantum well structure for photodetector applications. Springer: Lecture notes in electrical engineering: 4th international conference on microelectronics, computing & communication systems 26:317–327
28. Manasreh O (2015) Semiconductor Heterojunctions and Nanostructures. The McGraw Hill Companies, 1st edn. New York

# Channel Characterization and CE-OFDM Modulation for Terahertz System


**Mohammed EL Ghzaoui and Jamal Mestoui**

**Abstract** In wireless communication systems, the transmission channel constitutes the medium separating the transmitter from the receiver. Due to the growing demand for wireless systems in terms of data rate, it is necessary to look for new technology to support this need. Nowadays, The interest of Terahertz (THz) technology is growing increasingly. Indeed, THz technology indeed has the potential to provide ultra-fast data rate of Terabit-per-second (Tbps), Reliable Low Latency Communications and multimedia applications for wireless communication systems. However, the transmission channel at Terahertz bands poses more complexity than the currently used sub-30 GHz bands. The increase in the carrier frequency led to a high path loss. In this direction, Constant envelope Orthogonal Frequency Division Multiplexing (CE-OFMD) modulation is used in this work to increase the quality of transmission in terms of the Bit Error Rate (BER). Thus, In order to develop the THz system and effectively exploit the advantages of this technology, it is essential to know the properties of the radio channel in THz Band than to implement the THz channel in the transmission chain based on CE-OFDM. To do that, an accurate model for THz channel have to be expected by taking into account the effect of both the scattering loss and atmospheric attenuation which are the main characteristics of THz channels. The proposed model in this chapter is based on the Saleh-Valenzuela (S-V) statistical model which combines the concepts of "clusters" and AOA (Angle Of Arrival). In order to validate the proposed model, simulations of frequency channel response and time domain channel are carried out. It has been demonstrated from simulation that the performance of the THz system depends on the transmission windows. For this reason, we used CE-OFDM over these transmission windows to improve the performance of THz system.

**Keywords** OFDM · CE-OFDM · BER · SNR · THz · Channel modeling · Wireless communication systems

M. EL Ghzaoui (✉) · J. Mestoui
Faculty of Sciences, Sidi Mohammed Ben Abdellah University, 30050 Fes, Morocco

J. Mestoui
e-mail: j.mestoui@edu.umi.ac.ma



A. Acharyya et al. (eds.), *Generation, Detection and Processing of Terahertz Signals*, Lecture Notes in Electrical Engineering 794,
https://doi.org/10.1007/978-981-16-4947-9_3

## 1 Introduction

The rapid and continuous growth of wireless telecommunications market is creating an increasing number of needs. Among these needs are the needs to have broadband, provide a high quality of service, make the most of the available frequency resource, and design state-of-the-art equipment. In fact, low, medium, and high frequencies have been used extensively to meet this need and to offer several types of services [1–3]. As the needs grew, the low frequencies began to be saturated so went to higher frequency bands like 4G technology that supports few Gbps as data rate is requested [4]. To more increase the coverage and data rate 5G technology is used [5, 6].

Today, researchers are focused on terahertz technology. Among the techniques exploited in Terahertz bands are the OFDM (Orthogonal Frequency Division Multiplexing) modulation. This modulation technique has demonstrated great potential that has positioned it among the reliable solutions for future wireless telecommunications networks [7–10]. However, the implementation of the OFDM system in the THz system requires more strictness at the levels of digital-to-analog converters (DACs) at the transmitter and the analog -to- digital converters (ADC) receiver level [11, 12]. The DAC cuts all samples that exceed certain maximum amplitude. Locale this level is a trade-off between the cutoff probability and the quantization noise level. However, lower PAPR will increase SNR and allow low resolution to be used at DAC levels [13]. So, for high efficiency, the HPA (High Power Amplifier) must work in its saturation zone, unfortunately, it is in this zone that the most severe non-linearities occur, which are sources of distortions (intermodulation, spectral rise, etc.) of the transmitted signals. These effects are important when the signals to be amplified have high PAPR [14–16]. The use of HPA [13] in its saturation zone causes intermodulation products, distortions within the band, secondary lobe lifts that generate interferences between channels, and an increase in the bit error rate (TEB). There are a multitude of proposals to deal with this problem of non-linearities, a state-of-the-art is given in [17, 18], each of them reduces the PAPR but proves more or less effective depending on the type of signals and/or the context of transmission of information. A potential solution for reducing PAPR in OFDM systems is to use the constant envelope OFDM system (CE-OFDM) [19]. In addition, using continuous phase modulation in the CE-OFDM system, the PAPR can be reduced to 0 dB [20]. Although CPM modulation has a minimal spectral efficiency compared to non-constant envelope modulations, it functions with a little complexity, so the performance of this modulation is favorable thanks to a minimal PAPR and its robustness against the amplitude variation and thermal noise which is the noise most presence in wireless channels.

This chapter is devoted to a general presentation of multi-carrier transmission techniques such as CE-OFDM modulation. So, this chapter will be devoted to the application of the CE-OFDM modulation on a Terahertz Channel. Indeed, we will implement the simulation results of the transfer functions in the communication chain based on the CE-OFDM modulation, to see the effect of the different parameters of the CE-OFDM modulation on the performance of the communication chain. The comparison in terms of TEB of the modulation OFDM and CE-OFDM on a real

Terahertz channel will be given. Therefore, the main objective of this thesis is the reduction of transmission errors under the data rate constraint and the robustness of multi-carrier THz systems, so that they can be used effectively in home networks.

This document is divided into 3 main parts, giving a logical and chronological overview of the work carried out during this chapter. The first part is devoted to the study of the THz channel. The goal is both to understand the THz technology, as well as to define the organization of data exchanges on the network. A very large throughput imposes a large bandwidth and if this bandwidth "covers" part of the spectrum with dips (due to multiple paths), there is a total loss of information for the corresponding frequency. The channel is then called "selective" in frequency. To overcome the problem of frequency selectivity of the channel, it is chosen to use the modulation CE-OFDM. It is a modulation process that allows digital data to be transmitted in a multi-path channel while ensuring a good compromise between performance and spectral occupancy. This technique will be dealt with in part two. In the third and last part, we will implement the CE-OFDM technique in the THz context. Roughly speaking, this chapter will first define the phenomena important for the analysis of a propagation channel and its statistical modeling. We will then study the implementation of transmission techniques on this kind of Channel.

## 2 Propagation Channel

The environment in which a communication system emits represents its propagation channel. We present in this part the problems generally encountered in wireless channels, some channel models, and finally the proposed module for THz bands.

### *2.1 Propagation Phenomena*

During wireless transmission, the transmitted waves or signals are usually affected by three types of physical phenomena: reflection, diffraction, and diffusion.

- Reflection occurs when the transmitted signal encounters large obstacles compared to its wavelength. It could be a building, land, or many other obstacles. In this case, the signal is returned to the source instead of continuing its propagation to the receiver.
- Diffraction occurs when the signal is obstructed by an irregular, sharp surface or with a small aperture. The signal is thus broadcast by crossing an obstacle. Generally, the waves from this diffraction are used to establish further paths between the transmitter and the receiver in case of direct non-visibility.
- Diffusion is a physical phenomenon that forces the radiation of an electromagnetic wave to deviate from the direct path by one or more local obstacles having reduced dimensions compared to the wavelength of the transmitted signal. These barriers

are called broadcasters. As examples, we can cite foliage, traffic signs, and street lamps.

The propagation of a radio signal meets these different phenomena whose intensity varies according to the environment. All of these phenomena make the prediction of behavior very complex. One of the unique features in a wireless channel is the "fading". It is the change in the amplitude and phase of the signal with time and frequency. Unlike additive noise that is regularly responsible for signal degradation, fading is non-additive. It can be caused by multi-path fading or shadowing obstacles.

## *2.2 Large-Scale Fading*

It is produced by the loss of signal propagation depending on the distance and shading of objects such as buildings, vegetation.

### 2.2.1 Propagation Losses

The losses of propagation at THz frequency are much more severe than that recorded in the low frequencies [21]. To this are added other losses related to oxygen absorption and rain. As an example: absorption due to oxygen reaches its peak at 60 GHz with 15 dB per km and only 10 dB per km for the 8 GHz width band centered around 60 GHz. With such spread losses and huge absorption, providing a wireless gigabit link with a good link budget is a real challenge at this frequency, this makes it a better candidate for indoor applications more than the external one.

### 2.2.2 Shadowing

Because of the variation in the medium, the power received is different from the average for a given distance, which affects the overall propagation losses. Several results of measurements made around 60 GHz showed that shading follows a normal log distribution. Let us remember from this part that medium propagation losses and shading are considered Fading on a large scale.

## *2.3 Small-Scale Fading*

Small-scale fading is about the rapid change in the transmitted symbol. The rapid variation is due to constructive and destructive interference of multi-paths when the mobile is moving a short distance. Small-scale fading consists of two independent mechanisms. The time spread of the signal and the time variation of the behavior

of the propagation channel. The temporal variation of the channel causes a Doppler shift. To measure it, we look at the spectral enlargement of the signal caused by the relative movement of the receiver with respect to the transmitter. Doppler shift is a function of the speed of the receiver. It has an impact on the description of the channel, in fact, thanks to it we can tell whether the channel is slow Fading, or fast fading.

## *2.4 Channel Models*

Channel characteristics are important parameters to consider when conducting a performance study. Among the most relevant we will note the losses of spread, and fainting in the long or short term. Throughout this chapter, we consider the configuration of a single input and a single output (SISO). Two types of channel models can be listed:

- Channel models for indoor
- Channel models for outdoor.

In this chapter, we are interested only in the internal model of transmission channel.

### 2.4.1 Internal Channel Model

These are cases where the green neck surface is small. As an example, we can talk about offices, kiosk, mines, and many more the list is not exhaustive. Due to the fact that the environment is usually closed by walls or walls, the power tends to be uniform. Signal components in all directions are received with the same power. In an internal environment, the channel is usually static or varies very little due to the low mobility of the terminals inside the building. Typically, a static channel refers to an environment in which conditions do not change during data transmission at a given time and place. This definition is the opposite of that of a time-varying environment in which people or objects around the transmitter move all the time even if the environment itself is at rest. Another case exists, that almost stationary is when the degree of temporal variation of the environment is small relative to the length of the transmitted symbol. In the majority of the literature, internal channels are taken under stationary or quasi-stationary assumptions. We consider these same assumptions throughout our paper.

## 3 Proposed Model for the THz Channel

Several empirical models of the THz channel transfer function have been defined in the literature. In [22, 23], THz channel model is given. Some measurements of the channel transfer function are obtained by using a vector network analyzer (VNA) [24]. In [25], a channel response of THz channel were examined. The impulse response of THz channel on the full terahertz band (0.1–10.0 THz) is analyzed in [26]. In [27] the Influence of antenna misalignment under LOS conditions was studied.

### *3.1 NLOS Configuration*

In the THz system, signal propagation depends not only on the direct path between the transmitter and receiver but also on the additional paths. This multi-trip scenario is clearly illustrated in Fig. 1 for the case of a multi-path channel.

The channel consists of three segments (1), (2), and (3) with respective lengths l1, l2, and l3. For reasons of simplification of the model, it will be assumed that points A and C are adapted to the transmission channel, which means will have no loss at these two points.

Because of numerous reflections, the number of paths loss tends to Infinity ((A → B → C, A → B → D → B → C, … etc.). The assignment of all coefficients of reflections and transmissions can be performed for each path di in the form of weight factor gi. The value of the parameter gi is always less than or equal to a given that it is the result of a product combination of the coefficients of reflections and transmissions of the paths. When several transmissions and reflections occur along the channel, then the weight factor will be small. In addition, if long journeys are considered, then the contribution of the signal propagating on these paths will be minimal compared to the overall propagation of the signal given the significant attenuation on these paths.

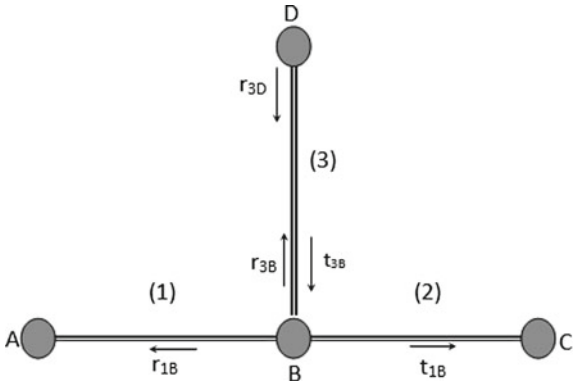


**Fig. 1** Multi-path propagation model

The delay $\tau_i$ of the path can be calculated from the dielectric constant $\varepsilon_r$ of the insulating materials, the celerity $c$ (or phase velocity $v_p$) and the lengths $l_i$ of the bonds forming the path $d_i$, as follows:

$$\tau_i = \frac{d_i\sqrt{\in_r}}{c} = \frac{d_i}{v_p} \tag{1}$$

Losses due to distance produces attenuations $A\ (f,\ d_i)$ which increases with frequency and length $d_i$. The signal therefore encompasses all existing components on the route. Thus the channel transfer function can be written in the following form:

$$H(f)_{/NLOS} = \sum_{i=1}^{N} g_i A(f, d_i) e^{2j\pi\tau_i} \tag{2}$$

For the study of the propagation signal in a complicated networks, is carried out a partitioning of the form schematized in Fig. 1.

## *3.2 LOS Configuration*

The signal attenuation on the THz environment contains two parts: multi-path losses and transmission channel length losses. To mathematically formulate the LOS component of the channel, we begin with the molecular absorption coefficient $\gamma(f, T_k, p)$ which depend on the primary parameters $f, T_k, p$. Thus, the frequency response H(F) in the case of LOS configuration is expressed as follows:

$$H(f, d)_{/LOS} = \frac{c}{4\pi f d} \exp\left(-\frac{1}{2}\gamma(f, T_k, p)d\right) \exp(-j2\pi f\tau) \tag{3}$$

where $d$ is the distance that separates the transmitter from receiver.

The transfer function of the THz channel H(f) when taking both LOS and NLOS configurations can be modeled as a function of the frequency by:

$$H(f, d) = H(f, d)_{/LOS} + H(f, d)_{/NLOS} \tag{4}$$

$$H(f, d) = \frac{c}{4\pi f d} \exp\left(-\frac{1}{2}\gamma(f, T_k, p)d\right) \exp(-j2\pi f\tau) + \sum_{i=1}^{N} g_i A(f, d_i) e^{2j\pi\tau_i} \tag{5}$$

where $\gamma(f, T_k, p)$ is the molecular absorption coefficient and $e^{-2j\pi f\frac{d_i}{v_p}}$ represent the retard of the channel.

**Table 1** Transfer Function model parameters

| Parameters | Signification |
|---|---|
| $I$ | Number of paths (the short-term path is that of index i = 1) |
| $a_0$, $a_1$ | Attenuation parameters |
| $K$ | Exponent of the attenuation factor ($0.2 \leq k \leq 1$) |
| $g_\mathrm{i}$ | Weighing factor |
| $d_\mathrm{i}$ | Path length $i$ |
| $\tau_\mathrm{i}$ | Path delay $i$ |
| $\Gamma$ | Molecular absorption coefficient |

Equation (5) represents the proposed model that describes the complex transfer function of a THz channel. Using this model, and in a frequency range of 300 GHz to 1 THz, the majority of the effects characterizing transmission on this type of line can be modeled by a minimum number of parameters. The following Table 1 summarizes the different parameters of the model.

Finally, the impulse response of the channel $h(\tau)$ is obtained from the transfer function $H(f)$ by Inverse Fourier transform:

$$h(\tau) = \int_{-\infty}^{+\infty} H(f) e^{2\pi j f \tau} df \tag{6}$$

## *3.3 Noise Encountered for THz-Based Transmissions*

In addition to the distortions caused by the channel responses on the form of the signals propagated on the wireless channels, it is also necessary to consider as a disruptive element the part of noise, taken in the broad sense of the term, which is added to the useful energy transmitted. Unlike most communication channels, the noise present at the input of a THz receiver is not reduced to the only contribution of thermal noise, also called AWGN (Additive White Gaussian Noise).

### 3.3.1 Colorful Background Noise

This type of noise is caused by the addition of many sources of noise. Its spectral energy density varies with frequency and also with variations in time. This type of noise results from the superposition of a wide variety of low-intensity noise sources present in the THz environment. Its power level varies on the scale of minutes or even hours. As opposed to white noise which has a uniform power spectral density, the background noise encountered here is a colored noise which displays a clear frequency dependence mainly in the very low part of the spectrum.

#### 3.3.2 Noise from Other Application Uses Neighboring Frequencies

This type of noise often appears in the form of an amplitude-modulated sinusoidal signal and occupies the sub-bands corresponding to large and medium-wave scattering: generally is an amplitude-modulated sine signal caused by the input of broadcast stations. it changes slowly with time.

## 4 Transmission Chain for Wireless Systems

During a transmission based on THz bands, the reflections will result in multiple paths. Since there are many possible paths connecting the transmitter to the receiver, interference phenomena will occur, the propagation channel will be characterized by the transfer function $H$. If $H(f)$ has, in the useful band, significant fluctuations in amplitude and/or phase will result in a deformation of the signal that it will be necessary to correct, which introduces the notion of Equalization of the channel. To be able to transmit information, the carrier frequency is obviously modulated, and let's calls Bu the useful or necessary bandwidth. If the Bu signal useful band is much smaller than the consistency band, the transfer function is practically frequency independent (flat channel), otherwise, the channel will be frequency-selective and Inter-symbol interference will occur in the time domain.

### *4.1 Baseband Signal*

Let $x(t)$ be the signal emitted around a carrier frequency f_c in general, whatever the modulation chosen, the signal can be put in the form: $x(t) = A(t)\cos(2\pi f_c t + \varphi)$.

Figure 2 shows the different steps of formatting the information at the time of transmission and then the processing required at reception to estimate the transmitted data with a minimum probability of error.

### *4.2 Description of the Transmission Channel*

#### 4.2.1 Source Coding

Source coding allows you to limit the number of binary elements necessary to represent the information contained in the source message. It is a compression operation that appeals to the theory of information, i.e., it compresses the transmitted data and eliminates unnecessary redundancies in the message in order to decrease the rate, said "useful" information to be transmitted.

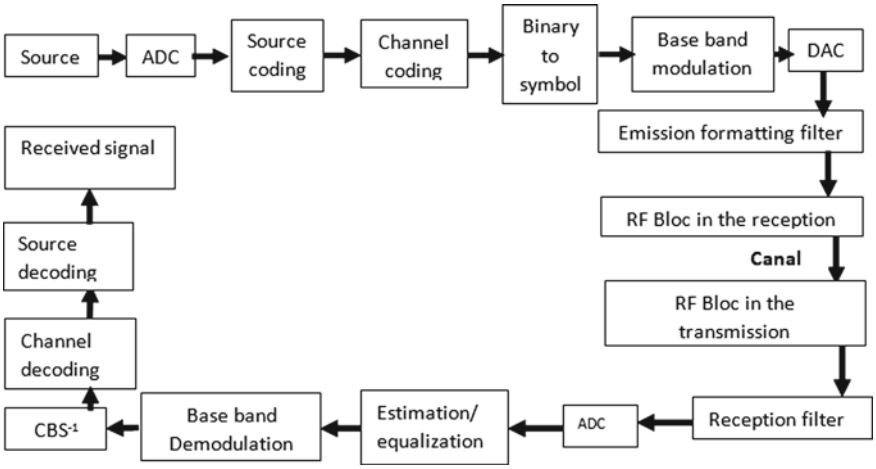


**Fig. 2** Communication chain for wireless system

### 4.2.2 Channel Coding

On a frequency-selective channel, information carried by subcarriers affected by deep fainting is lost to the receiver. In order to prevent the binary error rate from being too high, the use of error correcting codes is indispensable. The error correction code, introduced at the transmission before the modulator, makes it possible to detect and correct errors that occur during transmission through redundancy of information. The problem of choosing codes depends, among other things, on the nature of the errors introduced by the transmission channel and in particular on their probability of occurrence. Thus, two categories of errors are distinguished, grouped errors and random errors. To correct these errors there are two types of coding, block coding, and convolutional coding. Finally, in memory channels that generate packet errors, interleaving, and de-interleaving techniques are associated with encoding functions. Thus, in reception, de-interlacing makes it possible to obtain an error statistic more favorable to the decoding process.

### 4.2.3 Symbol Binary Coding

Binary symbol encoding is the step that generates a discrete signal from the digital data. Each CK element of this signal is called a symbol, can be real or complex, and is associated with one or more bits from the information source. We then define a second flow rate on the channel, the symbol flow, which is the number of symbols transmitted per unit of time. It is measured in Baud and is equal to the bit rate divided by the number of bits represented by each symbol.

### 4.2.4 Baseband Modulation

In digital communications, therefore, after channel coding, a baseband modulation is introduced which is akin to a transformation of binary symbols into complex symbols. Since the allocated transmission bands are low with respect to throughput, multi-state modulations (M-arg.) were developed, associating to each group of $M$ binary symbols of duration $t_b$ a complex symbol of duration $T_s = T_b \log 2(M)$, the choice of M depends on the spectral efficiency $\eta = D/Bp$ (bits/s/Hz). The choice of this spectral efficiency must be as important as possible in order to transmit a maximum throughput in a minimum bandwidth. The other criteria (there is the susceptibility to noise, which must be low which implies a distance between the generated symbols as large as possible and the instantaneous powers transmitted by the symbols). In general, for M-state modulation, n bits per symbol will be associated with $n = \log 2(M)$.

If we represent the position of the bits or symbols in the complex plane translating the possible values of the signal, we obtain the constellation, corresponding. To associate a set of bits with a symbol, Gray's encoding is often used. This is because it offers the advantage of distributing the symbols in the complex plane in such a way that two adjacent symbols differ only by one bit. Return to this point later.

### 4.2.5 Filtering

The shaping filter and a low-pass filter whose role is to eliminate secondary lobes of the transmitted spectrum in order to meet the spectral template imposed by the standards. Since the symbols are complex, two digital-to-analog converters will be used to make the signal compatible with the next analog part.

### 4.2.6 RF Module

The spectrum of the baseband signal is transposed to that of the channels authorized for the intended application. Note that sometimes the transposition is not performed directly around the carrier frequency but in stages, using transpositions around intermediate frequency.

## *4.3 Brief Presentation of the Receiving Chain*

The RF module includes the bandpass filter and the low noise amplifier. The signal is then transposed into a baseband, sometimes in several steps, using a complex demodulator that restores the phase and quadrature components of the signal.

The adapted filter present at the output of this demodulator is adapted to the waveform of the transmitted signal. At the sampling time corresponding to the symbol

period, this low-pass filter maximizes the power of the received signal relative to the power of the noise, ideally, cancels the interference between symbols related to low-pass filtering. This filter is identical to the formatting filter used at the broadcast. At this level of the chain, we also find the carrier recovery module based on the principle of the Phase-Locked Loop enslaved on a local oscillator. The analog-to-digital converter samples the signal at the filter output suitable for the symbol period.

As we have reported signal will suffer from powerless deformations during its propagation if its bandwidth is greater than the consistency band of the channel, which corresponds to the case of a frequency-selective channel. It is then necessary to introduce an equalizer in the receiving chain, which is a filter adapted to the channel thus allowing to compensate for variations in the transfer function of the channel or, in the time domain, to reduce the interference between symbols. In this module two parts have distinguished the estimation of the channel and the equalizer of the receiver, to extract the complex impulse response of the channel from which the coefficients of the equalizer will be deduced. At the output of the equalizer, the estimated symbols are decoded, which also allows to retrieve the necessary symbol clock during the sampling steps.

Finally, the channel and source decoding modules perform the inverse operations of those applied to the transmitted bits.

## 5 Constant Envelope OFDM

### *5.1 Description of the CE-OFDM Signal*

The OFDM signal can be expressed by:

$$m(t) = \sum_{i} \sum_{k=1}^{N} I_{i,k} q_k(t) \tag{7}$$

with $I_{i,k}$ corresponds to the symbol associated with a point of the constellation m-QAM or PSK and $q_k(t)$ are the orthogonal subcarriers. The OFDM signal is transposed around the carrier frequency $f_c$.

$$y(t) = \Re\left\{m(t)e^{j2\pi f_c t}\right\} = A_m \cos[2\pi f_c t + \phi_m(t)] \tag{8}$$

With $f_c$ is the carrier frequency and $A_m = |m(t)|$ and $\phi_m(t) = \arg[m(t)$. For the real values of $m(t)$ we have $\phi_m(t) = 0$ and $y(t)$ are simplified to a signal amplitude modulation. This mean, the data must be modulated as amplitude modulation (PAM). The signal of the CE-OFDM modulation can be writing by:

$$s(t) = Ae^{j\alpha m(t)} \tag{9}$$

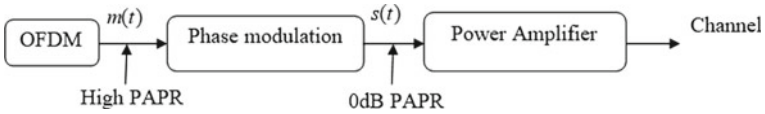


**Fig. 3** Modification of OFDM modulation to obtain CE-OFDM modulation

With $\alpha$ is a constant. The transpose signal for actual values of $m(t)$ is given by:

$$y(t) = \cos[2\pi f_c t + \alpha m(t)] \tag{10}$$

So $y(t)$ is phase modulation.

The CE-OFDM signal is performed by a transformation of the OFDM signal. The OFDM signal is passed through a phase modulator to obtain a constant envelope modulation with PAPR = 0 dB.

Figure 3 illustrates how we can obtain a CE-OFDM signal from a OFDM signal. This method will transform the OFDM signal with a high PAPR to a constant envelope signal with PAPR = 0 dB. 0 dB will allow the signal to be amplified with the HPA without producing transmission errors.

As has been proved before, the CE-OFDM modulation [28] requires that the OFDM signal must be real which mean $\phi_m(t) = 0$. So, the subcarriers $q_k(t)$ used in CE-OFDM must be real values. There are three possibilities to expresses the value of subcarriers $q_k(t)$.

In The first possibility, we express the wave as cosines function.

So for $k = 1, 2,...,N$, we have:

$$q_k(t) = \begin{cases} \cos \frac{\pi kt}{T_s} & 0 \le t \le T_s \\ 0 & \text{ailleurs} \end{cases} \tag{11}$$

For the second possibility, sine function will be used.

So for $k = 1, 2,...,N$, we have:

$$q_k(t) = \begin{cases} \sin \frac{\pi kt}{T_s} & 0 \le t \le T_s \\ 0 & \text{ailleurs} \end{cases} \tag{12}$$

The third possibility is that the wave will be represented by both cosine and sine waveforms. In this case the expression of $q_k(t)$ is given by the following relation:

$$q_k(t) = \begin{cases} \cos \frac{\pi kt}{T_s} & 0 \le t \le T_s \quad k < N \\ \sin \frac{\pi kt}{T_s} & 0 \le t \le T_s \; k > N/2 \\ 0 & \text{ailleurs} \end{cases} \tag{13}$$

The implementation of the above equations can be implemented by known algorithms. Equation (11) can be implemented by a DCT (Discrete Cosine Transform),

Eq. (12) can be implemented using the DST (Discrete Sine Transform), and Eq. (13) can be implemented by attacking the DfT (Discrete Fourier Transform).

For each case in the above possibility, the orthogonality condition must be verified:

$$\int_{iT_B}^{(i+1)T_B} q_{k1}(t - iT_B)q_{k2}(t - iT_B)dt = \begin{cases} E_q & k_1 = k_2 \\ 0 & k_1 \neq k_2 \end{cases} \tag{14}$$

where

$$E_q = \frac{T_B}{2}$$

So, the baseband signal of the CE-OFDM is expressed as:

$$s(t) = Ae^{j\phi(t)} \tag{15}$$

where $A$ is the amplitude of CE-OFDM baseband signal.

The phase of the signal during the $i$th block in the time interval it_ $iT_B \leq t < (i+1)T_B$ is given by the following expression:

$$\phi(t) = \theta_i + 2\pi h c_N \sum_{k=1}^{N} I_{i,k} q_k(t - iT_B) \tag{16}$$

The term phase memory is used in conjunction with the unwrapper phase in the receiver to ensure phase continuity and consequently good spectral efficiency [29]. The parameter h is the modulation index, N is the number of subcarriers, $I_{i,k}$ represents the symbols from the constellation PAM, $T_B$ is the duration of the $i$th block and $q_k(t)$ represents the subcarriers, the normalization constant $c_N$, is given by $c_N = \sqrt{\frac{2}{N\sigma_I^2}}$ with $\sigma_I$ is the variance,

$$\sigma_I^2 = E\left\{\left|I_{i,k}\right|^2\right\} = \frac{1}{M}\sum_{l=1}^{M}(2l - 1 - M)^2 \tag{17}$$

$$\sigma_I^2 = \frac{M^2 - 1}{3} \tag{18}$$

and the variance of the phase of the signal that is shown in [13] is given by $\sigma_\phi^2 = (2\pi h)^2$ which is always according to the modulation index.

The signal energy $E_s$ and bite energy $E_b$, are given by the following relationships:

$$E_s = A^2 T_B \tag{19}$$

$$E_b = \frac{E_s}{N \log_2(M)} \tag{20}$$

To guarantee the continuity of the phase the memory term must be expressed by:

$$\theta_i = K \sum_{l=0}^{\infty} \sum_{k=1}^{N} [I_{i-l,k} A_b(k) - I_{i-1-l,k} A_e(k) \tag{21}$$

where $K = 2\pi h c_N$, $A_b(k) = q_k(0)$, $A_e(k) = q_k(T_B - \varepsilon)$,$\varepsilon \to 0$.

The benefit of continuous phase CE-OFDM modulation (CE-OFDM-CPM) is that the CE-OFDM-CPM signal has good spectral properties [100].

## 5.2 Spectral Efficiency

The bandwidth of the OFDM signal $W$ is defined as double the largest frequency of subcarriers, so the bandwidth of $m(t)$ is given by:

$$W = 2\frac{N}{2T_B} = \frac{N}{T_B} \tag{22}$$

The bandwidth of the CE-OFDM signal depends on the modulation index, the effective bandwidth for the signal $s(t)$ can be greater than $W$. The RMS (Root-mean-Square) bandwidth is obtained from the results of analog phase modulation which is detailed in references [30, 31],

$$B_{\text{rms}} = \sigma_{\emptyset} W = 2\pi h W \tag{23}$$

As was set in (23), the RMS bandwidth can be less than W. the desired bandwidth for the signal $s(t)$ is therefore:

$$B_s = \max(2\pi h, 1) W \tag{24}$$

The power spectral density of the CE-OFDM signal can be estimated easily by Welch method for average periodogram. Figure 4 gives the spectral density of the CE-OFDM signal for different values of the modulation index.

From Fig. 4 it can be seen that the modulation index controls the spectral occupancy of the CE-OFDM modulation. But it should be noted that for small values of h the system performance is poor in terms of transmission errors. This is why the system designer must study spectral occupancy since the modulation index controls the performance of the system. From Fig. 4 it is noted that the spectral density of CE-OFDM is constant in the range where f/W < 0.8. To calculate the spectral efficiency of the CE-OFDM signal, the rate of the CE-OFDM modulation must be defined. For

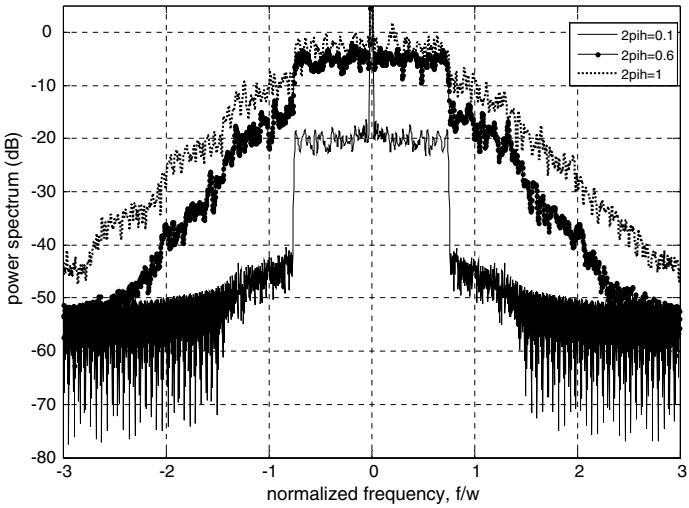


**Fig. 4** Power spectral density of CE-OFDM-CPM. $N = 512$

an uncoded CE-OFDM modulation, it is defined by:

$$R = \frac{N \log_2(M)}{T_B} \tag{25}$$

Using the relation (24) as the effective bandwidth of the CE-OFDM signal, the spectral effectiveness of this signal is represented by:

$$\eta = \frac{R}{B_s} = \frac{\log_2(M)}{\max(2\pi h, 1)} \frac{b}{s} \cdot H \tag{26}$$

## *5.3 Frequency Domain Equalization FDE*

Figure 5 gives a block diagram of FDM equalization. The distortions caused by the transmission channel are rectified with equalization [28] (Figs. 6 and 7).

## *5.4 Multi-path Diversity of the CE-OFDM System*

To comprehend why CE-OFDM enhances the performance on multi-path channels (compared to single-path channels) when OFDM does not, it is best to reason in the frequency domain. The frequency domain is frequency diversity. In fact, OFDM

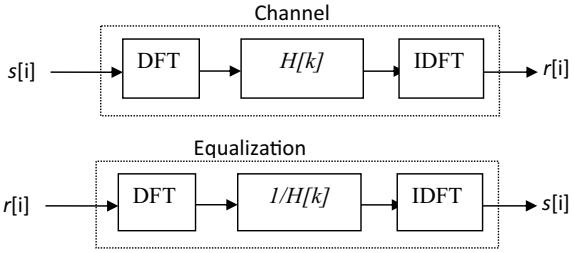


**Fig. 5** FDE diagram

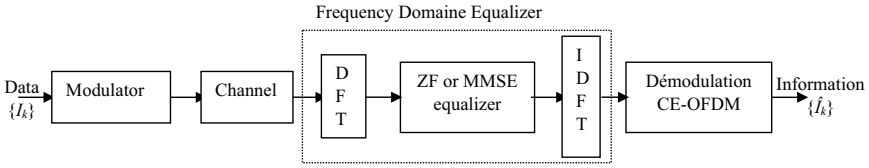


**Fig. 6** Modulation and demodulation with FDE

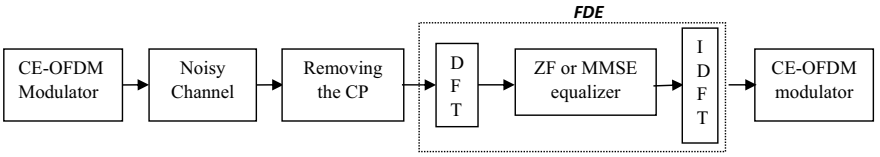


**Fig. 7** CE-OFDM modulation Bloc diagram with cyclic prefix and FDE

transforms a frequency-selective channel into a flat channel by dividing the channel into the sub-channels such that the passband of the signal will be less than the channel's consistent band (sub-channels bandwidth). The CE-OFDM signal with $\theta_i = 0$, can be expressed in the form:

$$s(t) = Ae^{j\sigma_\phi m(t)} \tag{27}$$

$$s(t) = A\sum_{n=0}^{\infty}\left[\frac{(j\sigma_\phi)^n}{n!}\right]m^n(t) \tag{28}$$

where

$$m(t) = c_N \sum_i \sum_{k=1}^{N} I_{i,k} q_k(t - iT_B) \tag{29}$$

$m(t)$ is the normalized signal.

$$s(t) \approx A\left[1 + j\sigma_\phi m(t) - \frac{\sigma_\phi^2}{2}m^2(t) - j\frac{\sigma_\phi^3}{6}m^3(t) + \cdots\right] \tag{30}$$

The term in maximum order causes the scattering of the data symbol in the frequency domain [29].

The phase modulator mixes and diffuses symbols in the frequency domain nonlinear and excessively, which gives the CE-OFDM system the potential to exploit frequency diversity in the channel.

$$s(t) \approx 1 + j\sigma_\phi m(t) \tag{31}$$

The CE-OFDM signal does not have the propagation of the data symbols in the frequency domain obtained the maximum order term. So it can be said that CE-OFDM exploits the frequency diversity when the modulation index is large and does not exploit it when the modulation index is small.

## 6 Simulation Results

In this section, we studied the performance of the CE-OFDM-CPM modulation on a THz channel. The main problem of transmission over the THz bands is the frequency selectivity of the channel as well as LOS components. The developed model in this chapter will be used to analyze the performance of the CE-OFDM modulation.

### *6.1 Simulation of the Proposed Channel Model*

Figure 8 shows a simulation of the model proposed in the band [300 GHz-1 THz], this simulation is carried out using MATLAB software. It is observed that the transfer function has a decreasing power with frequency, and the impulse response (B) corresponds to a set of multiple paths. For frequencies above 600 GHz, attenuations tend to increase. But in the case where the frequencies are less than 500 GHz the attenuation is practically the same. Thus, the transfer function for the frequencies 740 and 860 GHz undergoes consequent fainting up to −68 dB and 70 dB respectively. Therefore, the change in frequency leads to strong disturbances in the transfer function. Very significant fainting occurs at certain frequencies. Their location depends on the frequency. The analysis of these results leads to a band classification, according to their influence on the signal transmitted in the frequency range of the THz channel. Bands such as (720–805 GHz, 855–875 GHz, and 900–942 GHz) cause severe attenuations of the transmitted signal.

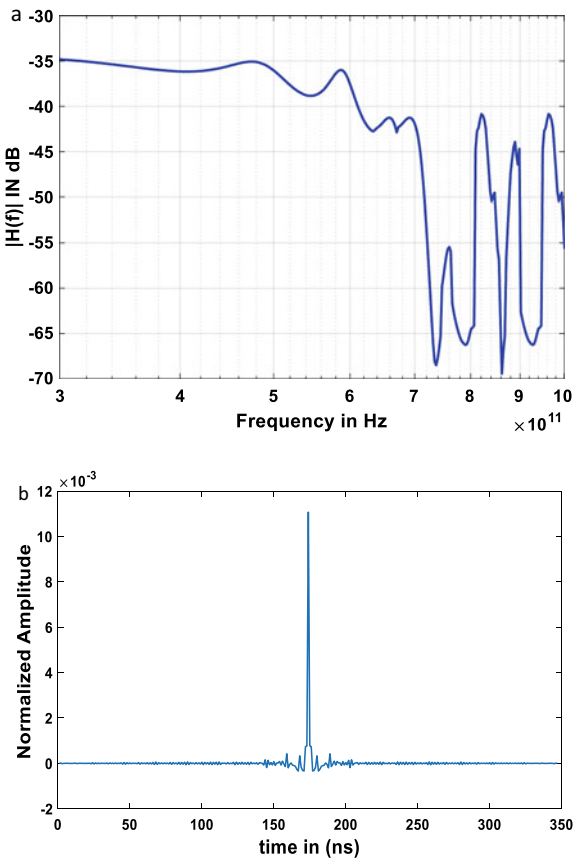


**Fig. 8** Simulation of the proposed model, transfer function (-a-), impulse response (-b-)

In Fig. 9 we depicted the Total Path Loss of the proposed channel. It can be observed that there are some bands where the path loss is higher. So, it is recommended to avoid these bands when implementing a THz system. The presented answers will be used in the simulations carried out later, as representative samples of the behavior of the THz channel. Given the lack of a clear relationship regarding the linear attenuation of the wireless channel, these responses will often be normalized in order to obtain parametric results according to the signal to noise ratio (SNR) of reception.

## *6.2 CE-OFDM Performance on the THz Channel*

The CE-OFDM-CPM technique can be seen as a mapping of the OFDM signal in the unit circle to get a PAPR of 0 dB. The OFDM signal is transformed by continuous phase modulation into a low PAPR signal, before transmitting it into the HPA. At

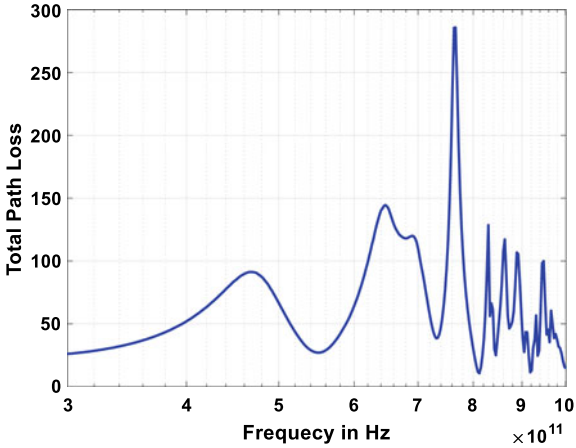


**Fig. 9** Total path loss

reception, an inverse operation is performed by phase demodulation and then an OFDM demodulation is performed as shown in Fig. 10. PM at reception is a real-world operation of the CE-OFDM-CPM receiver and that is why it is interesting to use the CE-OFDM-CPM modulation in practice.

CE-OFDM-CPM demodulation at reception essentially consists of Phase demodulation in the discrete domain followed by OFDM demodulation. The received signal is first passed into a finite impulse response filter.

The CE-OFDM modulation is like the conventional OFDM modulation, with a period $T_B$ of the CE-OFDM block, which must be greater than the maximum delay of the impulse response of the channel. A duration guard interval $T_g \geq \tau_{\max}$ is inserted between blocks of CE-OFDM to eliminate interference between symbols (ISI). At the receiver, the received signal $r(t)$ is sampled at the frequency $f_{\text{sa}} = \frac{1}{T_{\text{sa}}}$, the guard interval is removed and the CE-OFDM symbols without processing in the time domain. The expression of the signal received at discrete time can be modeled as follows:

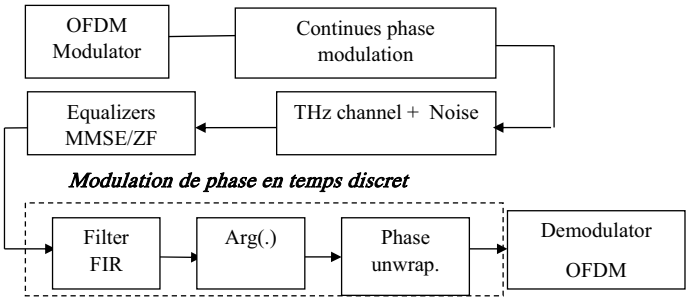


**Fig. 10** Block diagram of the CE-OFDM-CPM system

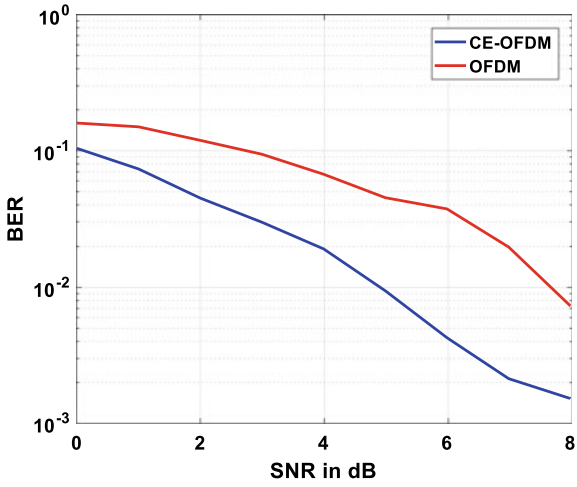


**Fig. 11** OFDM versus CE-OFDM over THz channel

$$r_p[i] = r[i] = \sum_{l=0}^{N_c-1} h[l]s[i-l] + n[i], \quad i = 0, \ldots\ldots\ldots\ldots\ldots, N_B - 1 \tag{32}$$

With $s[i]$ the CE-OFDM signal, $h[l]$ is the channel response of the THz channel and $n[i]$ is the impulse noise that is most present in the THz channel. This noise is produced by devices that are connected to the network. It should be noted that the deleted samples are $\{r[i]\}_{i=-N_g}^{-1}$. The transmission of the cyclic prefix causes the convolution of the signal with the propagation channel to be equivalent to a circular convolution. Thus,

$$r_p[i] = \frac{1}{N_{\text{DFT}}} \sum_{k=0}^{N_{\text{DFT}}-1} H[k]S[k]e^{j\frac{2\pi k}{N_{\text{DFT}}}}, \quad i = 0 \ldots\ldots\ldots, N_B - 1 \tag{33}$$

Figure 11 presented a comparison between OFDM and CE-OFDM. We can note from this figure that when the SNR increases the BER tends to decrease. Moreover, CE-OFDM outperforms conventional OFDM. As here, we are interested in analyzing the performance of THz system at a short distance the SNR must be feeble as possible. That is why we are interested in the band of 0–8db for SNR values.

## *6.3 Frequency Equalization*

Inter-symbol interference is one of the major obstacles to obtaining reliable digital communications when the transmission channel is frequency selective. Frequency

selectivity produces Inter-symbol interference, which causes high BER. To compensate for this loss of information, a frequency equalization is introduced at the reception. It should be noted that equalization is simplified thanks to the insertion of the cyclic prefix for transmissions based on conventional OFDM. But for transmission based on CE-OFDM equalizers are introduced in the frequency domain (FDE). These equalizers are frequently used, because of their simplicity and good performance. For our transmission chain which is based on the CE-OFDM modulation, the channel effect is simplified by an IDFT, then a multiplication vector, and DFT. Linear equalization techniques such as Zero Forcing (ZF), which minimizes interference between symbols, and MMSE which minimizes the mean square error between the transmitted signal and its estimation, can be used. The output of the FDE is given by:

$$\hat{x}[i] = \frac{1}{N_{\mathrm{DFT}}} \sum_{k=0}^{N_{\mathrm{DFT}}-1} R_p[k] C[k] e^{j\frac{2\pi k}{N_{\mathrm{DFT}}}}, \quad i = 0 \ldots\ldots\ldots, N_B - 1 \tag{34}$$

where $R_p[k]$ is the DFT of $r[i]$ and $C[k]$ is the correction terme, which is given by:

For ZF (zero forcing),

$$C[k] = \frac{1}{H[k]} \quad k = 0, 1 \ldots\ldots\ldots\ldots\ldots.., N_{\mathrm{DFT}} - 1 \tag{35}$$

And for the MMSE equalization (minimum mean-squared error) the correction term $\{c[k]\}$ is defined by:

$$C[k] = \frac{H^*[k]}{|H[k]|^2 + \left(\frac{E_b}{N_0}\right)^{-1}} \quad k = 0, 1 \ldots\ldots\ldots\ldots\ldots.., N_{\mathrm{DFT}} - 1 \tag{36}$$

A comparison between ZF and MMSE equalizer in CE-OFDM over THz is given in Fig. 12. It can be noted that the performance of the two equalizers is slightly the same. Bit for SNR more than 5 dB MMSE equalizer performs better than the ZF one (Fig. 12).

## 7 Summary

In this chapter, we have presented a new form of OFDM modulation namely the CE-OFDM modulation which is a constant envelope modulation (PAPR = 0 dB). We before studied this modulation in the context of THz. From the results of the simulations, we found that the CE-OFDM modulation is more efficient than the conventional OFDM modulation.

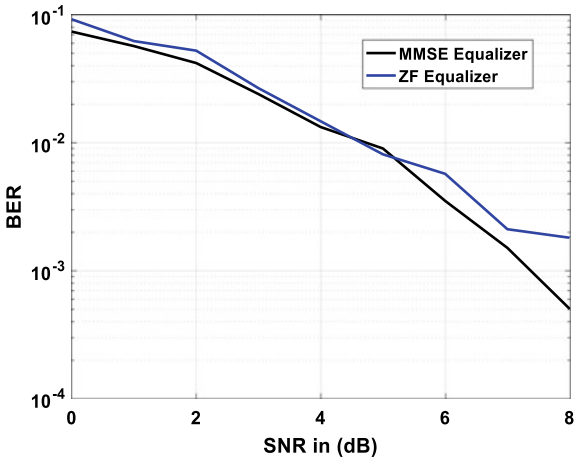


**Fig. 12** Performance comparison between ZF and MMSE equalizer in CE-OFDM modulation

## References


1. Mule SB, Manna GC, Nathani N (2015) Comparison of spectral efficiency of mobile OFDM-WiMAX technology with GSM and CDMA for cognitive radio usage. Procedia Comput Sci 49:274–281
2. Raihani H, Benbassou A, El Ghzaoui M, Belkadid J (2017) Performance evaluation of a passive UHF RFID tag antenna using the embedded T-Match structure. In: International conference on wireless technologies, embedded and intelligent systems (WITS), Fez, pp 1–6. https://doi.org/10.1109/WITS.2017.7934636
3. Lee Y-H, Tseng H-W, Lee W-C, Lin J-Y, Jan Y-G, Tsao H-W (2012) The measurement and analysis of WiMAX base station signal coverage. Prog Electromagn Res C 25:223–232
4. Bouhlel A, Sakly A, Mansouri N (2015) Performance comparison of DWT based MIMO OFDM and FFT based MIMO OFDM. Procedia Comput Sci 73:266–273
5. Ghazaoui Y, El Alami A, El Ghzaoui M, Das S, Baradand D, Mohapatra S (2020) Millimeter wave antenna with enhanced bandwidth for 5G wireless application. J Instrum 15
6. Aghoutane B et al (2020) Analysis, design and fabrication of a square slot loaded (SSL) Millimeter-wave patch antenna array for 5G applications. J Circuits, Syst Comput. https://doi.org/10.1142/S0218126621500869
7. Yli-Kaakinen J, Levanen T, Palin A, Renfors M, Valkama M (2020) Generalized fast-convolution-based filtered-OFDM: techniques and application to 5G new radio. IEEE Trans Signal Process 68:1213–1228
8. Li J, Bala E, Yang R (2014) Resource block filtered-OFDM for future spectrally agile and power efficient systems. Physical Commun 14:36–55
9. Sur SN, Sharma P, Saikia H, Banerjee S, Singh AK (2020) OFDM Based RADAR-communication system development. Procedia Comput Sci 171:2252–3226
10. Pollet T, Van Bladel M, Moeneclaey M (1995) BER sensitivity of OFDM systems to carrier frequency offset and Wiener phase noise. IEEE Trans Commun 43(2/3/4):191–193
11. Dahlman E, Parkvall S, Skold J (2018) 5G NR: The next generation wireless access technology . Academic, New York, NY, USA
12. Levanen T et al (2019) Transparent Tx and Rx waveform processing for 5G new radio mobile communications. IEEE Wireless Commun 26(1):128–136
13. El Ghzaoui M, Hmamou A, Foshi J, Mestoui J (2020) Compensation of non-linear distortion effects in MIMO-OFDM systems using constant envelope OFDM for 5G applications. J Circuits, Syst Comput 29(16):2050257

14. Zhang T, Qiao S, Zhong F, Guo SX (2017) Gaussian matrix based PAPR reduction scheme for DCO-OFDM systems. Optik 145:513–518
15. Sandoval F, Poitau G, Gagnon F (2017) Hybrid peak-to-average power ratio reduction techniques: review and performance comparison. IEEE Access 5:27145–27161
16. Rahmatallah Y, Mohan S (2013) Peak-to-average power ratio reduction in OFDM systems: a survey and taxonomy. IEEE Commun Surv Tutorial 15(4):1567–1592
17. Liang C-P, Jong J-H, Shark WE, East JR (1999) Nonlinear amplifier effects in communications systems. IEEE Trans Microwave Theory Tech 47(8):1461–1466
18. Costa E, Midrio M, Pupolin S (1999) Impact of amplifier non linearities on OFDM transmission system performance. IEEE Commun Lett 3(2):37–39
19. Tanand J, Stüber GL (2002) Constant envelope multi-carrier modulation. In: Proceedings of the IEEE Milcom, Anaheim, pp 607–611
20. Belkadid J, Benbassou A, El Ghzaoui M (2013) PAPR reduction in CE-OFDM system for numerical transmission via PLC channel. Int J Commun Antenna Propag (IRECAP) 3(5):267–272
21. El Ghzaoui M, Das S (2020) Data transmission with terahertz communication systems. In: Biswas A, Banerjee A, Acharyya A, Inokawa H, Roy J (eds) Emerging trends in terahertz solid-state physics and devices. Springer. https://doi.org/10.1007/978-981-15-3235-1_9
22. Fu J, Juyal P, Zajić A (2020) Modeling of 300 GHz chip-to-chip wireless channels in metal enclosures. IEEE Trans Wireless Commun 19(5):3214–3227
23. Choi Y, Choi J, Cioffi J (2013) A geometric-statistic channel model for THz indoor communications. J Infrared, Millimeter, Terahertz Waves 34:456–467
24. Cheng C, Sangodoyin S, Zajić A (2020) THz cluster-based modeling and propagation characterization in a data center environment. IEEE Access 8:56544–56558
25. Kokkoniemi J, Lehtomäki J, Umebayashi K, Juntti M (2015) Frequency and time domain channel models for nanonetworks in terahertz band. IEEE Trans Antennas Propag 63(2):678–691
26. Tsujimura K, Umebayashi K, Kokkoniemi J, Lehtomäki J, Suzuki Y (2018) A causal channel model for the terahertz band. IEEE Trans Terahertz Sci Technol 8(1):52–62
27. Ekti A, Boyaci A, Alparslan A, Ünal İ, Yarkan S Gorcin A, Arslan H, Uysal, M (2017) Statistical modeling of propagation channels for terahertz band. arXiv:1707.09740v1
28. Mestoui J, El Ghzaoui M, Hmamou A, Foshi J (2019) BER performance improvement in CE-OFDM-CPM system using equalization techniques over frequency-selective channel. Procedia Comput Sci 151:1016–1021
29. Thompson SC, Ahmed AU, Proakis JG, Zeidler JR, Geile M (2008) Constant envelope OFDM. IEEE Trans Commun 56(8):108–120
30. Roberts H (1977) Angle modulation. Peter Peregrinus Ltd., London
31. Thompson SC (2004) Spectral estimation of digital signaling using the welch method [Online]. Available: http://zeidler.ucsd.edu/~sct/holdings/welch/

# Investigation on Antennas for Terahertz Applications


**Bilal Aghoutane, Mohammed EL Ghzaoui, and Hanan El Faylali**

**Abstract** Terahertz (THz) antennas are achievements benefit in many applications. The interest of THz technology has been growing steadily since the creation of Terahertz Interest Group in 2008. By its unique characteristics, THz technology indeed has the potential to provide very high-data rate for wireless communication system. However, the atmospheric absorption presents in THz communication system cause high path losses. Using high gain antennas can compensate the increased path loss. Indeed, antennas are the most essential part of any wireless communication system. Thus, antenna designs for THz bands create new challenges for the researchers. In fact, the design of very high gain, directive and wideband THz antenna is very challenging and promising tasks. In this chapter, we present some advantages of antennas for THz radio communication system. Firstly, we expose the fundamental principles of the theory of antennas as well that the general characteristics of the antenna systems realized with a certain number of radiators. We will analyze antenna's systems by studying their characteristics. Steps for designing an antenna will be given. All this information may guide the user in choosing the configuration that will best respond his needs. A single-element antenna with new geometry is proposed in this contribution. The proposed microsrip slot antenna with defected ground having a circle shaped fractal and comprise a microstrip with corporate feed network operating at 5 THz which is considered as Terahertz band. The proposed antenna has the highest bandwidth of about 12.2 THz (3.6–15.8 THz) with a gain of 5.6 dBi. The designing and simulation are performed using High-Frequency Structure Simulator (HFSS). The simulation output shows a high bandwidth, enhanced gain and minimum VSWR (Voltage Standing Wave Ratio) value at THz band, which would be an excellent candidate for THz wireless communication.

**Keywords** Wireless systems · Terahertz · Gain · Bandwidth · VSWR (Voltage Standing Wave Ratio)

B. Aghoutane · H. E. Faylali
ISO Laboratory, Ibn Tofail University, Kenitra, Morocco

M. EL Ghzaoui (✉)
Faculty of Sciences, Sidi Mohamed Ben Abdellah University, 30050 Fes, Morocco



A. Acharyya et al. (eds.), *Generation, Detection and Processing of Terahertz Signals*, Lecture Notes in Electrical Engineering 794,
https://doi.org/10.1007/978-981-16-4947-9_4

# 1 Introduction

Communication brings together all the techniques for transmitting data. At a time when speed of execution is coveted, scientists and engineers are trying to develop and make systems capable of operating at increasingly high speeds. With the current development of communication and broadband, many parts of the electromagnetic spectrum are saturated. In this sense, the terahertz domain (THz), because of its high frequencies and rarely attributed, arouses a certain interest. However, the main difficulty associated with its use lies in the lack of compact, powerful and inexpensive sources and detectors. Over time, scientists and engineers have exploited the frequency bands of the electromagnetic spectrum. Starting with the visible spectrum, they gradually developed sources and detectors operating at lower or higher frequencies. However, the frequency band between 0.1 and 30 THz that is to say between 0.01 and 3 mm in wavelength, called terahertz (THz) has been little used. This frequency band is shown in Fig. 1. The THz band is located between microwaves and infrared, and marks the boundary between two physical domains: electronics for microwaves on one side, infrared optics on the other.

It is only in the last twenty years that this area has been exploited [1]. One reason is the lack of compact sources and detectors, which are powerful enough and inexpensive at the same time. THz radiation offers great scientific interests, especially because of its physical properties. In addition, it is useful in many areas of application including imaging and spectroscopy [2], biology and medicine [3], security [4, 5] and communication [6–8].

- Terahertz Communication and Advantages

Demand for short-range wireless communication has doubled every 18 months over the past 30 years [9]. In the years 1984, the speed of a wireless network was around 1 kbps, it was 100 Mbps in 2009, and it is estimated that it will be between 5 and 10 Gbps

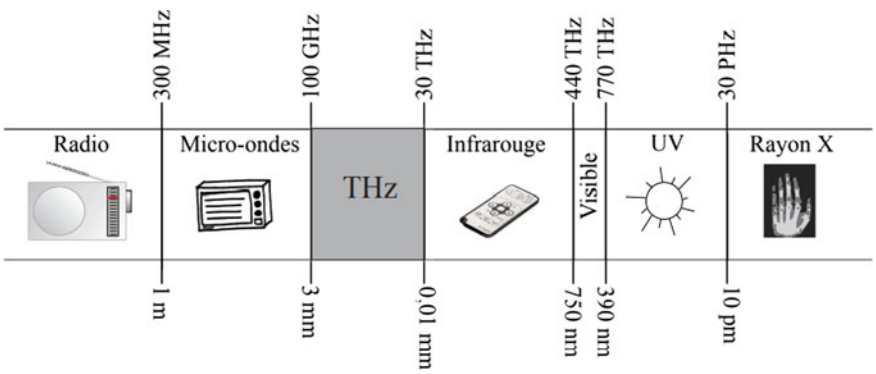


**Fig. 1** Detail of the fields of the electromagnetic spectrum. THz is located between microwaves and infrared

by ten years. In order to reach this 10 Gbps rate, the carrier frequency must be greater than 0.100 THz. For the past ten years, several research and industrial institutes have been studying the THz domain, ranging from 0.1 to 20 THz, in order to be able to use it in higher-speed communication [10]. Wireless communication systems currently marketed operating with a carrier frequency of between 2.4 GHz (standard Wi-Fi standard IEEE 802.11a from 1999) and 5 GHz (standard Wi-Fi standard IEEE 802.11bgn from 2009) approximately. Several THz communications projects have been submitted with transmitters and receivers that operate at 60 GHz [11–13]. A 2007 Koch [14] article suggests that THz communication systems will replace current Wi-Fi systems in the years 2017–2023 [15]. The THz communication system, with speeds Gbps or more, will allow a wide variety of broadband applications [16] such as the extension of the wireless network with broadband, high-definition television [17], cell phone [18], etc.

Terahertz frequencies are currently untapped and unallocated above 275 GHz. Thus, the frequency band between 275 and 1 THz is available for the development of very high-speed communications. The attenuation in the atmosphere is related to the frequency of the propagated waves [19] and peaks of resonances of chemical elements constituting it. The rotation of water molecules is responsible for many absorption peaks in the terahertz range; however, some frequency bands are usable and listed in Table 1. Frequency above 1 THz is not listed due to the many absorption peaks that render these frequencies unusable for high speed, long-range communications. The attenuation of terahertz waves in the atmosphere involves the use of reliable, but also robust and compact terahertz sources for their use in real conditions.

Very high-speed wireless communications can be applied to short or long-range communications. Very short-range transmissions find applications in electronic systems. The increase in frequency impacts the losses undergone by the signal in the interconnections increasing the consumption of the device and the thermal effects, while limiting the performance. Wireless communications distances of a few centimeters with high-data rates are an alternative to the electrical interconnections used in circuits operating at frequencies above a few GHz [20].

High speed, short-range wireless communications, over distances of less than 1 m, can be used for fast downloading of data such as magazines or high-definition movies

**Table 1** Frequency bands with its attenuation and supported bandwidth up to 1 THz

| Frequency band (GHz) | Bandwidth (GHz) | Attenuation (dB/Km) |
|---|---|---|
| 215–315 | 100 | 2–4 |
| 330–365 | 35 | 5 |
| 390–435 | 45 | 9 |
| 450–515 | 65 | 11–12 |
| 625–725 | 100 | 11 |
| 790–900 | 110 | 12 |
| 925–950 | 25 | 15 |

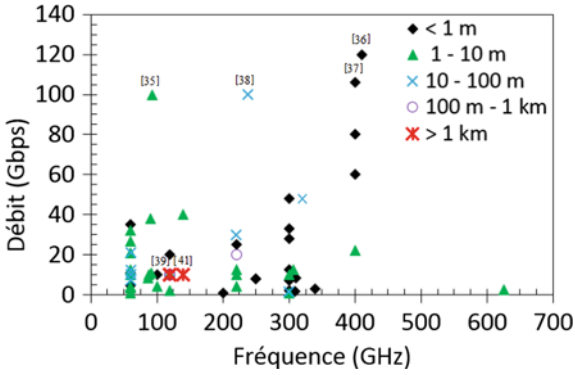


**Fig. 2** State of the art of wireless communications in the 60 GHz–1 THz frequency band for speeds greater than 1 Gbps

by passing a download terminal [21]. By increasing the range from 1 to 100 m, these applications can extend to a room or building involving spatially distinct channel communications [22]. Record speeds between 100 and 120 Gbps are reported in the literature [23–26]. The corresponding distances are between 0.5 and 20 m. The performance of wireless communications between 60 and 1 THz is shown in Fig. 2.

Wireless communications over distances greater than 100 m, at high speed, serve the back-haul network. The natural evolution of the network is to replace microwave sources with higher-frequency sources. In the longer term, a convergence toward terahertz frequencies and sources are to be considered in order to meet the speed requirements. Data rates of 10 Gbps are reported in the literature at frequencies 120 and 140 GHz for distances reaching, respectively, 5.8 and 1.5 km [27–29].

In some cases, THz communication offers several advantages over microwave and infrared systems. Here's a summary of those benefits:

- THz communication offers the ability to increase throughput and bandwidth, compared to microwave systems and can be used to simultaneously transmit multiple high-definition channels [30, 31],
- Under certain atmospheric conditions, THz waves are less attenuated than infrared waves. Atmospheric attenuation then has a different impact on THz or infrared communication depending on the conditions meteorological [32]. Recent experimental measurements have shown that THz is more robust than infrared in the presence of rain, dust fog or in the presence of air turbulence [33, 34],
- THz frequency band is not yet assigned [14]. In the United States, the band 0.275–0.300 THz is reserved for mobile communication. In Europe, frequencies above 0.275 GHz are available for communication.

- Recent work

A hexagonal fractal antenna with fed by a microstrip line has been proposed operating at over the region of 0.2–11.5 THz in [35]. The antenna possess a bandwidth of 0.2 THz–11.5 THz and VSWR $\leq$ 2. To achieve super wideband performance, a fractal radiator with defected irregular ground plane and backed plane loading can be

used. The hexagonal fractal antenna has reached an average peak gain of 10.82 dB, moreover the dimension of the antenna is 800 × 600 $\mu m^2$ in the area. In [36], a compact MIMO antenna for WBAN has proposed with two nodes are both linear arrays. It has achieved a dimension of the antenna of 35 × 36 $\mu m^2$ in the area with functioning at THz frequency 8.84 THz. The proposed antenna has achieved 8.2 dB of gain. A compact circular patch antenna has been offered in [37]. Therefore, the proposed antenna has achieved 4.8 dB and 5.3 dB of gain at 2.2 THz and 3.2 THz, respectively, with dual-band characteristic for WBAN at terahertz. In [38], an on-chip antenna had proposed with exciting by an aperture fed mechanism, and the prototype has a 15-element array comprising circular and rectangular patches. The proposed antenna has achieved a bandwidth across 0.290 THz–0.316 THz with a gain of 11.71 dBi and radiation efficiency of 70.8%. Moreover, the dimension of the antenna is 20 × 3.5 $mm^2$ in the area. In [39], a plasmonic microstrip antenna has proposed with SSP characteristics for UWR THz application. The proposed antenna possess wideband of about 5 THz operates from 0.1 to 20 THz with gain is about 12–25 dB at frequency band. A microstrip antenna had been proposed for THz application with linear scaling technique in [40], and the antenna operates from 4.9 to 5.9 THz with bandwidth is 1 THz with dimension of the antenna 30 × 25 $\mu m^2$ in the area.

The aim of this chapter work is to set up an antenna integrated, inexpensive and intended for high-speed wireless THz communication. In this work, an antenna coupled to a selective to THz application has been proposed with slot loaded of 2.1958 × 15.8465 $\mu m^2$ and 10.979 × 3.1693 $\mu m^2$ in the rectangular patch. Also, on the right of patch is loaded with added a parasitic triangle resonator of ≈10.08 $\mu m^2$. It has been designed on Roger RT/duroid with a dielectric permittivity of 10.2. The designed antenna operates from 3.6 to 15.8 THz with multi bands for THz application (Fig. 3; Table 2).

## 2 Antenna Characteristics

### *2.1 Radiation Resistance*

This is the loss of power related to the electromagnetic wave radiated by the antenna. The total power radiated by the antenna through a sphere of radius R is given by [41]:

$$P_r = \frac{k^2}{32\pi^2} Z \frac{(Il)^2}{r^2} \int_0^{\pi} 2\pi r^2 \sin^2\theta \sin\theta d\theta \tag{1}$$

where

$$Z = \sqrt{\frac{\mu_0}{\varepsilon_0}} \approx 377\Omega \tag{2}$$

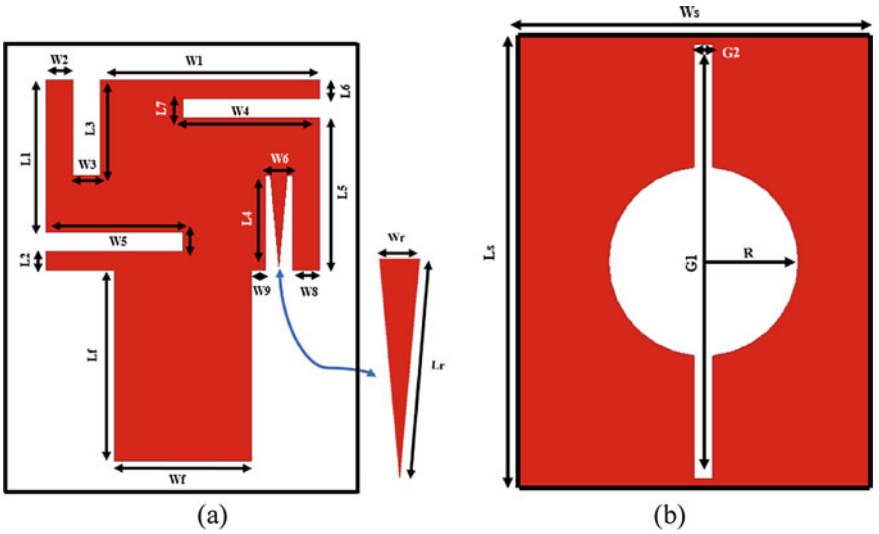


**Fig. 3** Proposed antenna geometry. **a** Top view, **b** bottom view

**Table 2** The optimized dimensions of the proposed antenna (in μm)

| Parameters | $W_1$ | $W_2$ | $W_3$ | $W_4$ | $W_5$ |
|---|---|---|---|---|---|
| Dimensions | 25.3544 | 3.1693 | 3.1693 | 15.8465 | 15.8465 |
| Parameters | $W_6$ | $W_8$ | $W_9$ | $W_f$ | $W_r$ |
| Dimensions | 3.1693 | 3.1693 | 1.58465 | 15.8465 | 1.92325 |
| Parameters | $W_s$ | $G_1$ | $G_2$ | $R$ | $L_s$ |
| Dimensions | 37.693 | 45.916 | 2 | 10 | 47.916 |
| Parameters | $L_1$ | $L_2$ | $L_3$ | $L_4$ | $L_5$ |
| Dimensions | 17.5664 | 2.1958 | 10.979 | 10.979 | 17.5664 |
| Parameters | $L_6$ | $L_7$ | $L_8$ | $L_f$ | $L_r$ |
| Dimensions | 2.1958 | 2.1958 | 2.1958 | 21.958 | 18,528,025 |

The result of the integration gives:

$$P_r = \frac{k^2}{12\pi^2} Z(Il)^2 \tag{3}$$

Let be again, by relating the size of the antenna to the wavelength l:

$$P_r = \frac{\pi}{3} \frac{l^2}{\lambda^2} Zl^2 \tag{4}$$

The power is proportional to the square of the intensity, which allows us to consider that the antenna has a resistance, called radiation resistance whose value is given with respect to the effective intensity $I_{\text{eff}}$:

$$P_r = R_r I_{\text{eff}} = R_r \frac{1}{2} I^2 \tag{5}$$

$$R_r = \frac{2\pi}{3} Z \frac{l^2}{\lambda^2} \approx 800 \frac{l^2}{\lambda^2} \tag{6}$$

A quick calculation gives an order of magnitude of the resistance of a dipole. If the ratio of the size of the dipole to the wavelength is 1/10, the radiation resistance is 8Ω. It is also noted that the smaller the size of the dipole, the lower the radiated power.

## 2.2 Efficiency of an Antenna

Let ($P_e = P_a$) be the power supply of an antenna. This power is transformed into a radiated power Pr. In the direction of emission, the radiated power is less than the power supply [42]. The antenna is an imperfect transformer. There are losses during the transformation of energy, as in any system. The efficiency of the antenna is defined by

$$\eta = \frac{P_r}{P_e} \tag{7}$$

$$\eta = \frac{R_r}{R_r + R_j} \tag{8}$$

Upon receipt, the transformation takes place in the opposite direction. The $P_{\text{rad}}$ power received on the receiver is less than the $P_a$ power radiated arriving on the antenna.

## 2.3 Radiation Intensity

The radiation intensity $K$ is defined in W/sr, which is independent of r but varies according to the direction:

$$K(\theta, \phi) = \langle P(r, \theta, \phi) \rangle r^2 = \frac{E^2(r, \theta, \phi)}{2\eta_0} r^2 = \frac{E_\theta^2(r, \theta, \phi) + E_\phi^2(r, \theta, \phi)}{2\eta_0} r^2 \tag{9}$$

$\eta_0$ is the intrinsic impedance of the vacuum (the propagation medium) or about 120π.

It is possible to obtain the total power emitted < $P_t$ > by integrating $K(\theta,\phi)$ on the 4π sr. This follows directly from the integral of the scalar product of the power density on a closed surface, by choosing a sphere, we maximize the scalar product at any point because:

$$\langle P \rangle = \langle P_r \rangle a_r \quad \text{and} \quad dS = dSa_r$$

So,

$$\langle P_r \rangle = \oint_s \langle P(r, \theta, \phi) \rangle dS$$

$$dS = r^2 \sin(\theta) d\theta d\phi$$

$$\langle P_t \rangle = \oint_{4\pi} K(\theta, \phi) d\Omega$$

$$d\Omega = \sin(\theta) d\theta d\phi$$

## 2.4 Directivity and Gain

As it was written earlier, the antenna does not emit power evenly in all directions. So the antenna has a capacity:

- To concentrate the power in order to favor certain directions in emission;
- The directivity $d(\theta, \phi)$ of an antenna in one direction therefore represents the ratio of the intensity of the radiation in this direction to the average intensity $K_{\text{moy}}$ that is to say that would be obtained if the power was emitted uniformly in all directions by an isotropic antenna $K_{\text{iso}} = K_{\text{moy}} = (\langle P_t \rangle)/4\pi$:

$$D(\theta, \phi) = \frac{K(\theta, \phi)}{K_{\text{moy}}} = \frac{4\pi K(\theta, \phi)}{\langle P_t \rangle} = \frac{4\pi K_{\max} K_n(\theta, \phi)}{K_{\max} \Omega_n} = \frac{4\pi}{\Omega_a} K_n(\theta, \phi) \quad (10)$$

The directional gain or more simply gain $G(\theta,\phi)$ of the antenna, often confused with directivity, represents the same thing taking into account losses [43]. It therefore defined relative to the power at the input < Pin > rather than < Pt > . Efiency of 100% makes directivity and gain are identical:

$$G(\theta, \phi) = \varepsilon_r D(\theta, \phi) \quad (11)$$

## 2.5 Impedance of an Antenna

Antenna input impedance is called the impedance seen at the input of this component. She is represented by:

$$Z_A = R_A + jX_A \tag{12}$$

The input resistor RA represents a dissipation term. It is related, on the one hand, to the radiated power and on the other hand, to the power lost by Joule effect.

$$R_A = R_r + R_j \tag{13}$$

If RJ < < < Rr, we get an optimal antenna operation. However, the losses by Joule effect can represent significant values depending on the geometry of the antenna. Losses in the mass plane are also to be taken into account.

The definition of the dissipated power in an antenna is given by:

$$P_e = \frac{1}{2} R_A I_A^2 \tag{14}$$

## 2.6 Reflection Coefficient

The antenna can be modeled by an impedance $Z_t$. The antenna is always connected to the modulator by a transmission line as shown in Fig. 4.

The current and voltage along the line can be expressed by the following relationships with A and B are constants.

$$V(I) = A \cdot e^{j\beta l} + B \cdot e^{-j\beta l}$$

$$I(I) = \frac{1}{R_c}\left(A \cdot e^{j\beta l} - B \cdot e^{-j\beta l}\right)$$

At the load level ($I = 0$), Ohm's law applies:

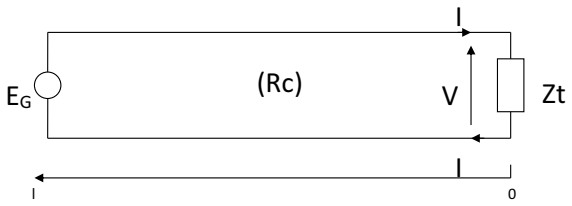


**Fig. 4** Equivalent circuit

$$V(0) = A + B \quad \text{and} \quad I(0) = \frac{1}{R_c}(A - B)$$

$$V(0) = Z_t I(0)$$

$$\frac{V(0)}{I(0)} = Z_t = R_c \frac{A + B}{A - B}$$

The reflection coefficient, denoted S11, expresses the ratio of complex amplitudes B to A: it is a complex number that therefore expresses the reflection effect, in modulus (intensity of reflection, zero to total) and in phase (phase shift of the reflected voltage relative to the incident voltage, at the point of reflection).

We note that

$$S_{11} = \rho e^{j\varphi} = \frac{B}{A} \tag{15}$$

So

$$Z_t = R_c \frac{1 + S_{11}}{1 - S_{11}}$$

Which is equivalent to

$$S_{11} = \frac{Z_t - R_c}{Z_t + R_c} \tag{16}$$

## *2.7 Notion of Reduced Impedance*

One is positioned in any abscissa l, different from 0 (a common place on the line between the source and the termination). The line has a characteristic resistance $R_c$. At this abscissa, there is a certain voltage $V$(l) and a certain current $i$(l). These two magnitudes are the result of overlays of incident and reflected flows.

We can define

$$Z(l) = \frac{V(l)}{I(l)}$$

Which mean

$$\Gamma(l) = \frac{Z(l) - R_c}{Z(l) + R_c}$$

The expressions of $V(l)$ and $I(L)$ then allow to write $Z(l)$ and $Z(L)$ as a function of ZT and Rc:

$$Z(l) = R_c \frac{Z_t + j R_c \ tg\beta l}{R_c + j Z_t \ tg\beta l}$$

$Z(l)$ is named impedance reduced to the abscissa l. This relationship is fundamental to solve adaptation problems in particular, but also to "manufacture" reactive elements (processes widely used in microwave electronics). In addition, the reduced impedance $Z(l)$ is the impedance equivalent to the set consisting of the downstream of the line and its termination (it is somehow the input impedance of the line section of length L terminated by $Z_t$). From the point of view of the upstream and therefore the source, there is no difference between the initial line (reality) and the equivalent line terminated by $Z(l)$. This concept is fundamental for the adaptation of the line. We also find:

$$\Gamma(l) = \Gamma \ e^{-2j\beta l}$$

where

$$\Gamma = \frac{Z_t - R_c}{Z_t + R_c}$$

## 2.8 Reflection Coefficient in Decibel:

If the characteristic impedance of the propagation line is $Z_c$ and the input impedance of the antenna $Z_A$, then the signal reflects on the input of the antenna with a coefficient $S_{11}$ whose expression is:

$$S_{11} = \frac{Z_{\text{in}} - Z_c}{Z_{\text{in}} + Z_c}$$

$$P_A = P_s\left(1 - |S_{11}|^2\right)$$

where

$$V(l) = A \cdot e^{j\beta l}\left(1 + \Gamma \cdot e^{-2j\beta l}\right)$$

We find most of the time, the values expressed in decibels:

$$|S_{11}|_{dB} = 20 \log|S_{11}| \tag{17}$$

The maximum power transmitted to the antenna is obtained when the impedance of the generator is equal to the combined impedance of the antenna. It corresponds to a transmission parameter of the distribution matrix (S21) close to 1 and a reflection coefficient (S11) close to 0 (in linear values). Adaptation mean that S11 = 0 dB. It is assumed that a good adaptation is obtained when the reflection coefficient is less than −10 dB. In practice, either we will seek to design the antenna in such a way that it has an impedance equal to $Z_c$ at the working frequency, or we will have at the input of the antenna an impedance transformation circuit which will modify the input impedance of the antenna seen from the source and ensure the impedance adaptation.

## *2.9 Voltage Standing Wave Ratio (VSWR)*

In antenna application notes, antenna adaptation is often characterized by the ROS or VSWR. When the antenna is less adapted, the reflection of a part of the incident wave and the addition with the incident wave lead to the appearance of a standing wave in the line that connects the antenna to the source (or receiver) [44].

## *2.10 The Steps of Designing a Patch Antenna*

The dimensions of the patch are usually in the order of half wavelength. The choice of length is guided by the resonance frequency to be given to the antenna. Since the ground plane cannot be infinite, it can be equal to three or four times the wavelength, which sometimes represents too large a footprint. A smaller ground plane will lead to a change in the properties of the antenna. The characteristics of the substrate affect those of the antenna. In general, its permittivity must be low, and it must be of negligible thickness in front of the wavelength and have low losses (we characterize the losses of a dielectric by the tangent of losses denoted tan δ. A typical value is around 10-3).

## *2.11 Sizing a Rectangular Patch Antenna*

As a summary, here is a procedure for designing a rectangular patch antenna. This can be used for a first sizing. The optimization can then be done using an electromagnetic simulator. The input data are: the substrate (electrical permittivity, loss tangent, thickness) and the operating frequency. The thickness of the substrate must be such that it satisfies the following equation. We consider a perfect and infinite plane of mass.

$$h \leq \frac{c}{4f\sqrt{\varepsilon_r - 1}}$$

Calculation of patch width:

$$W = \frac{\lambda_0}{2}\sqrt{\frac{2}{1+\varepsilon_r}}$$

$$\lambda_0 = \frac{c}{F_{res}}$$

Calculation of effective wavelength $\lambda_e$ and effective dielectric constant $\varepsilon_e$:

$$\lambda_e = \frac{c}{f\sqrt{\varepsilon_e}}$$

$$\varepsilon_e = \frac{\varepsilon_r + 1}{2} + \frac{\varepsilon_r - 1}{2}\left(1 + \frac{12h}{W}\right)^{-0.5}, \frac{W}{h} \geq 1$$

Calculation of patch length extension ΔL:

$$\Delta L = 0.412\frac{(\varepsilon_e - 0.3)}{(\varepsilon_e - 0.258)} + \frac{\frac{W}{h} + 0.264}{\frac{W}{h} + 0.8}$$

In practice, we find

$$0.05\frac{\lambda_e}{2} \leq \Delta L \leq 0.01\frac{\lambda_e}{2}$$

Calculation of patch length L:

$$L = L_e - 2\Delta L = \frac{\lambda_e}{2} - 2\Delta L$$

Calculation of the position of the feeding point: from this equation.

$$R_{\text{pos}} = R_{in}\cos^2\left(\frac{\pi x}{L}\right)$$

$$x = \frac{L}{\pi}\arccos\left(\sqrt{\frac{R_{\text{pos}}}{R_{\text{in}}}}\right)$$

The effect of the position of the feeding point can be taken into account and determined from the above equation.

## 3 Design and Optimization of Antenna

The proposed antenna configuration designed on Roger RT/duroid substrate [45–48] with the dimension of $47.916 \times 37.693\ \mu m^2$ is presented in Fig. 3. The antenna geometry comprises five iterations of rectangular slot loaded of $2.1958 \times 15.8465\ \mu m^2$ and $10.979 \times 3.1693\ \mu m^2$ in the rectangular patch. Also, on the right of patch is loaded with added a parasitic triangle resonator of $\approx 10.08\ \mu m^2$. Furthermore, the $p$ ground plane of proposed geometry is loaded with a modified slot and a parasitic rectangular ring resonator [49]. The geometrical dimensions of the basic patch from its operating frequency can be calculated as follows [50]:

$$W_p = \frac{c}{2 f_c \sqrt{\frac{\varepsilon_{\text{relative}}+1}{2}}} \tag{18}$$

$$\varepsilon_{\text{eff}} = \frac{\varepsilon_{\text{relative}}+1}{2} + \frac{\varepsilon_{\text{relative}}-1}{2}\left(\frac{1}{\sqrt{1+12\left(\frac{h}{W_p}\right)}}\right) \tag{19}$$

$$\Delta L = 0.421h\frac{(\varepsilon_{\text{eff}}+0.3)\left(\frac{W_p}{h}+0.264\right)}{(\varepsilon_{\text{eff}}-0.258)\left(\frac{W_p}{h}+0.8\right)} \tag{20}$$

$$L_p = \frac{c}{2 f_c \sqrt{\varepsilon_{\text{eff}}}} - 2\Delta L \tag{21}$$

where $W_p$ and $L_p$ represent patch's width and length, respectively, $h$ is the height of the substrate, and $\varepsilon_{\text{eff}}$ and $\varepsilon_{\text{relative}}$ are the effective and relative permittivity of substrate, respectively. $c$, $f_c$ and $\Delta L$ are the speed of light, central frequency and the effective length, respectively. The main feed line is matched by an impedance of 50 Ω. For adaptation, we can use the following transmission line equations [50].

For $\frac{W_f}{H} \leq 1$,

$$Z_0 = \frac{60}{\varepsilon_{\text{reff}}} \ln\left[\frac{8H}{W_f} + \frac{W_f}{4H}\right] \tag{22}$$

where

$$\varepsilon_{\text{reff}} = \frac{\varepsilon_r+1}{2} + \frac{\varepsilon_r-1}{2}\left(\frac{1}{\sqrt{1+12\frac{H}{W_f}}} + 0.04\left(1-\frac{W_f}{H}\right)^2\right) \tag{23}$$

For $\frac{W_f}{H} \geq 1$,

$$Z_0 = \frac{120\pi\sqrt{\varepsilon_{\text{reff}}}}{\frac{W_f}{H} + 1.393 + 0.667\ln\left(\frac{W_f}{H} + 1.444\right)} \tag{24}$$

where

$$\varepsilon_{\text{reff}} = \frac{\varepsilon_r + 1}{2} + \frac{\varepsilon_r - 1}{2}\left(\frac{1}{\sqrt{1 + 12\frac{H}{W_f}}} + 0.04\left(1 - 12\frac{H}{W_f}\right)^{-\frac{1}{2}}\right) \tag{25}$$

where $W_f$ is the width of the feed line, and $Z_0$ is the characteristic impedance of the transmission line. For calculation of the width and length $L_f$ of the feed network, Eqs. 9–11 are used.

$$W_f = \frac{2h}{\pi}\left(B - 1\ln(2B - 1) + \frac{\varepsilon_r - 1}{2\varepsilon_r}\left[\ln(B - 1) + 0.39 - \frac{0.61}{\varepsilon_r}\right]\right) \tag{26}$$

$$L_f = \frac{\lambda}{4\sqrt{\varepsilon_{\text{reff}}}} \tag{27}$$

$$B = \frac{60\pi^2}{Z_0\sqrt{\varepsilon_r}} \tag{11}$$

where $B$ is a constant used in the inverse design formula, expressed in Eq. (9) for a microstrip line of a given characteristic impedance. Generally, the notch frequency can be obtained by using the following equation [51]:

$$f_{\text{notch}} = \frac{c}{4L\sqrt{\varepsilon_{\text{re}}}} \tag{28}$$

where $L$ is the total length of the embedding slit, $\varepsilon_{\text{re}}$ is the effective dielectric constant, and c is the speed of the light. The antenna design and evolution are depicted in Fig. 2 and Table 1, respectively.

## 4 Simulation Results

The antenna design is realized in five intermediate steps as shown in Fig. 5. At first, a rectangular monopole with conventional ground plane (Ant I) is designed. In case of Ant III, patch is loaded also with a rectangular slot from the top and the bottom. To this, we add a triangular stub to the partial patch plane to achieve Ant VI geometry. In successive design steps, and the last steps Ant V, the ground plane is loaded with a modified slot comprising a circle and rectangle shaped.

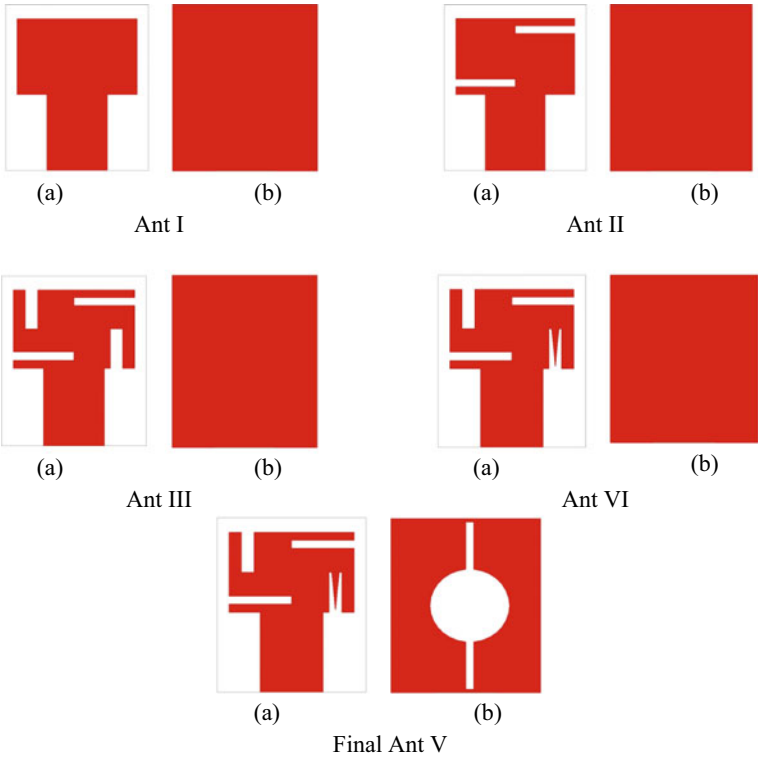


**Fig. 5** Antenna geometry steps. **a** Top view, **b** bottom view

Simulation results are performed to analyze the performance of the proposed antenna. In this direction, the antenna performance is determined in terms of S11, return loss VSWR, gain, bandwidth and current distribution. The simulated S11 of the proposed antenna has been comprised in Fig. 6. The antenna V has high bandwidth as well as high gain with high return loss. This high performance is obtained because of the partial patch and ground to achieve a bandwidth of 12.2THz (3.6–15.8 THz) for terahertz frequency band, which has been achieved by the optimization of the antenna geometry steps. The VSWR value of proposed antenna is of about 1.9 which mean that our antenna has good impedance matching. Table 3 summarizes the antennas performance in terms of VSWR (also see Fig. 7). It can be noted that Ant I and Ant II have a bandwidth near to 3.4 THz/For Ant III and Ant IV, bandwidth of 4.6 THz (3.6–7.8 THz) and 10.1 THz (3.6–13.7 THz) can be achieved, respectively. However, Ant V has the highest bandwidth 12.2 THz (3.6–15.8 THz) as well as the highest gain over the others cases. For this reason, this antenna will be considered in this work.

The variations of the real and imaginary parts of the antenna input impedance in close proximity to 50 Ω and 0 Ω, respectively, are demonstrated in Fig. 8.

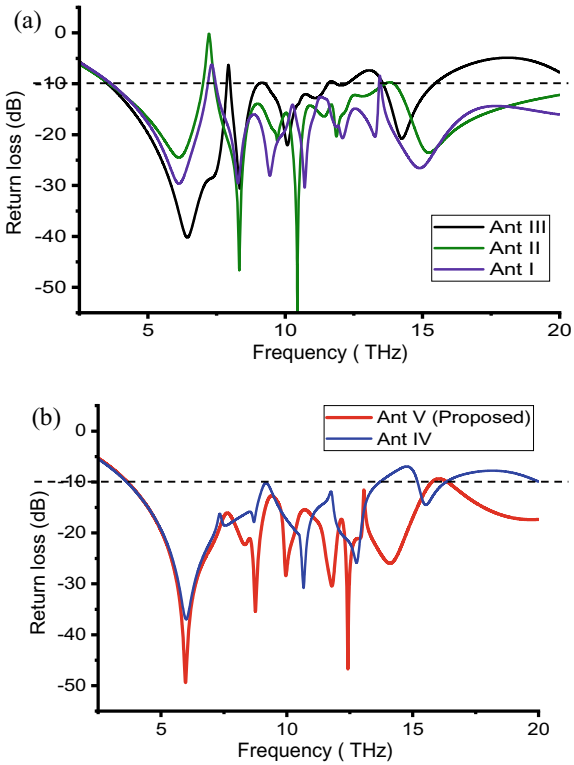


**Fig. 6** Comparison return loss. **a** between Ant I, Ant II and Ant III, **b** between Ant IV and Ant V

**Table 3** Performance of antenna design steps

| Design Steps | Bandwidth (THz) | Gain (dBi) |
|---|---|---|
| Ant I | [3.7−7.1] = 3.4 | 1.9 |
| Ant II | [3.6−6.9] = 3.3 | 4.5 |
| Ant III | [3.6−7.8] = 4.6 | 4.6 |
| Ant IV | [3.6−13.7] = 10.1 | 5.1 |
| Ant V (Proposed) | [3.6−15.8] = 12.2 | 5.6 |

The radiation pattern E plane and H plane of the proposed an antenna is presented in Fig. 9, at frequencies of 10, 12, 14 and 17 THz. The beam maximum was detected at +60°, as depicted in Fig. 9e, f. Similarly, 2D radiation patterns for antenna exhibit maximum radiation at −90° as shown in Fig. 9c. For jointly planes, the radiation patterns are found to be deformed omni-directional through slight stabilization at all frequencies. The surface current distribution of the proposed antenna has been illustrated in Fig. 10 at six different frequencies. It can be noticed from Fig. 10b, the current distribution is around 5106.8 A/m at center frequency, and on the other, the same amount of current accumulates as shown in Fig. 10a, c, e, f is above 3401.7 A/m.

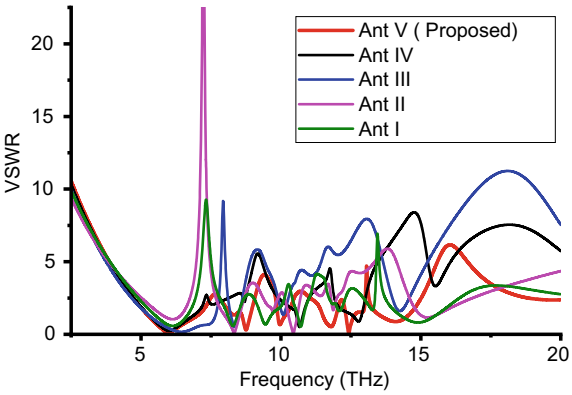


**Fig. 7** VSWR characteristics of antenna design steps

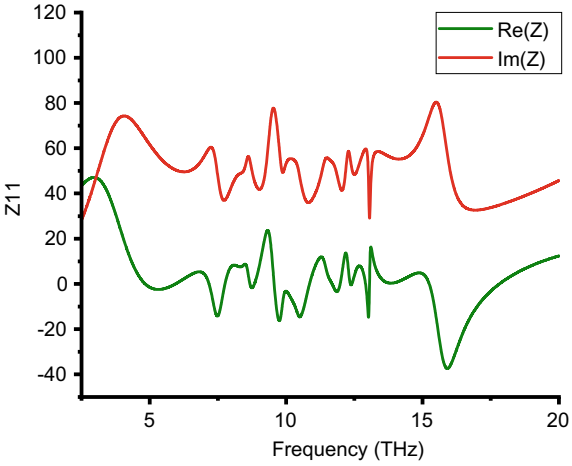


**Fig. 8** Real and Imaginary of the proposed antenna's input impedance

The 3-dimensional (3D) radiation patterns of the proposed antenna are simulated by using the commercial ANSYS HFSS as depicted in Fig. 11. The simulation radiation patterns for Ant V were acquired at 5 THz, 8 THz, 10 THz, 12 THz, 14 THz and 17 THz as illustrated in Fig. 11a, b, c, d, e, f, respectively.

## 5 Summary

In this chapter, antenna theory is presented in order to define the antenna characteristics which play a deterministic role in antenna design. We performed some steps in order to design an appropriate antenna for suitable application. In this direction, we designed a single-element antenna with new geometry. The antenna is designed with defected ground having a circle shaped fractal and comprise a microstrip with

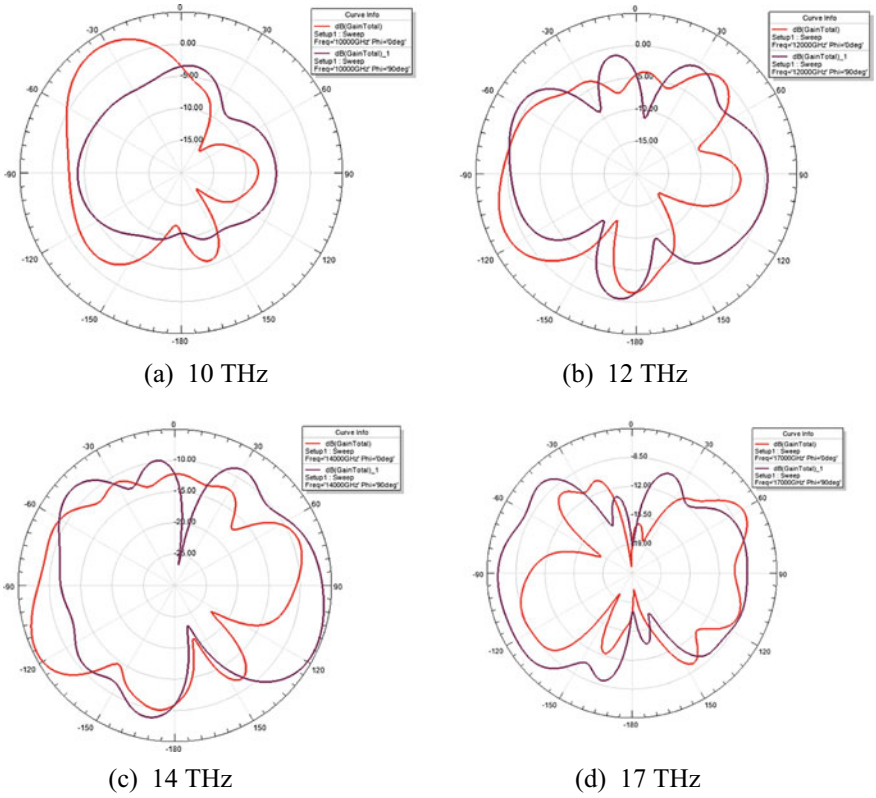

(a) 10 THz (b) 12 THz

(c) 14 THz (d) 17 THz

**Fig. 9** Radiation patterns of the proposed antenna

corporate feed network operating at 5 THz which is considered as Terahertz band. The proposed antenna has the highest bandwidth of about 12.2 THz (3.6–15.8 THz) with a gain of 5.6 dBi. HFSS software is used to simulate the proposed antenna. It has been found that the return loss is minimal, high bandwidth, enhanced gain and minimum VSWR (Voltage Standing Wave Ratio) value at THz band, which would be an excellent candidate for THz wireless communication.

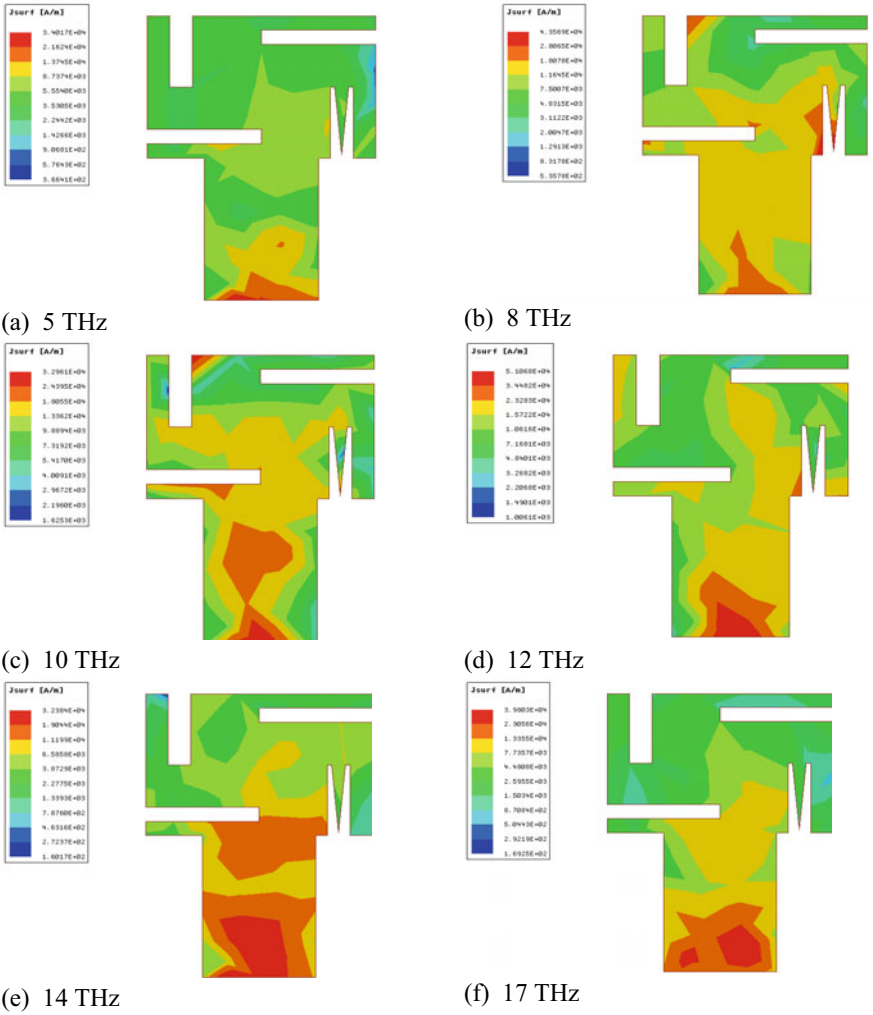


**Fig. 10** Current distribution of the proposed antenna

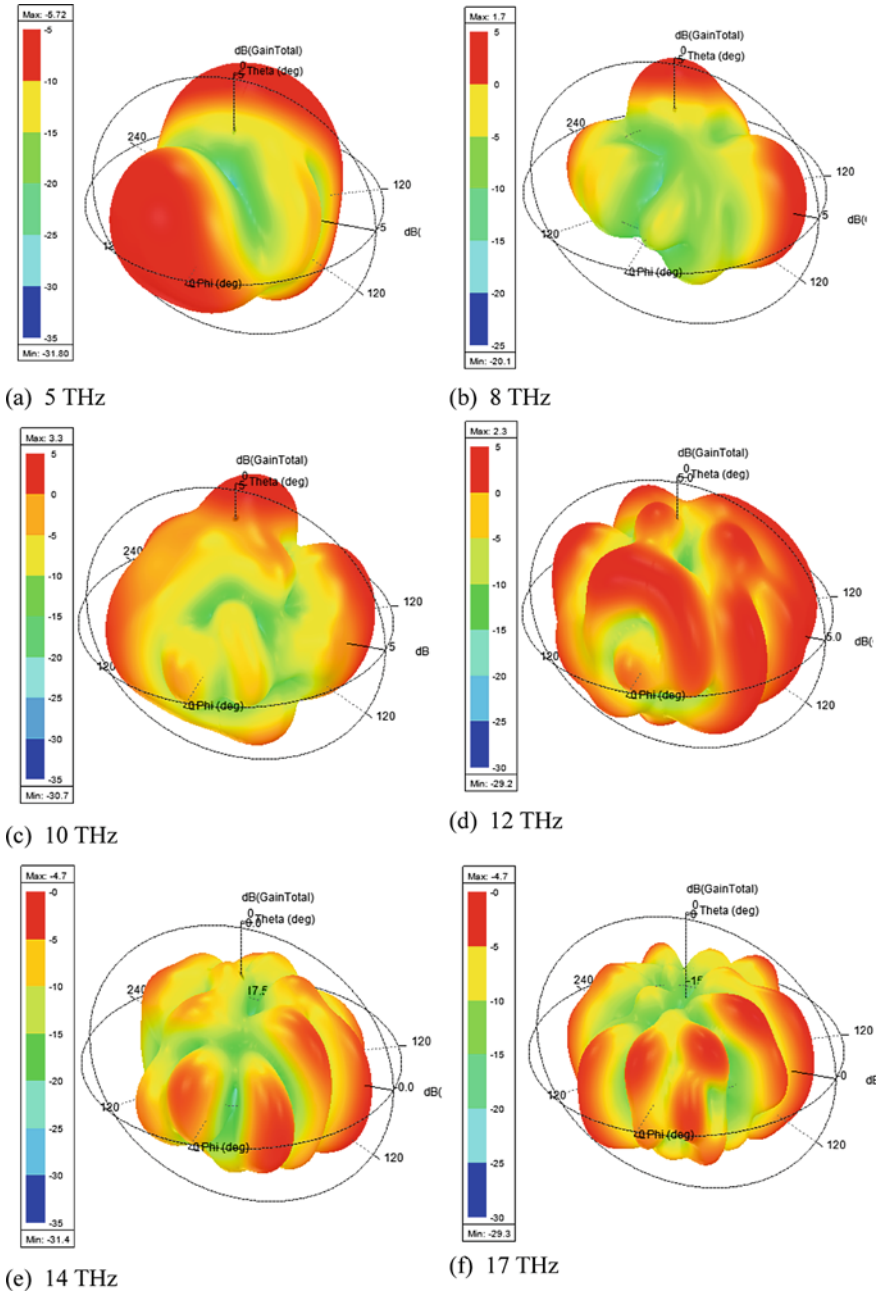


**Fig. 11** Gain 3D of the proposed antenna

## References


1. Woolard DL, Brown ER, Pepper M, Kemp M (2005) Terahertz frequency sensing and imaging: a time of reckoning future applications? Proc IEEE 93:1722–1743
2. Wang K, Mittleman D (2004) Metal wires for terahertz wave guiding. Nature 432(7015):376–379
3. Siegel PH (2004) Terahertz technology in biology and medicine. IEEE Trans Microw Theory Tech 52(10):2438–2447
4. Kemp MC, Taday PF, Cole BE, Cluff JA, Fitzgerald AJ, Tribe WR (2003) Security applications of terahertz technology. Proc SPIE 5070:44–52
5. Tribe WR, Newnham DA, Taday PF, Kemp MC (2004) Hyden object detection: security application of terahertz technology. Proc SPIE 5354:44–52
6. Blin S, Teppe F, Tohme L, Hisatake S, Arakawa K, Nouvel P, Coquillat D, Pénarier A, Torres J, Varani L, Knap W, Nagatsuma T (2012) Plasma-wave detectors for terahertz wireless communication. IEEE Electron Device Lett 33(10):1354–1356
7. Song H, Nagatsuma T (2011) Present and future of terahertz communications. IEEE Trans Terahertz Sci Technol Publ Inf 1(1):256–263
8. Federici J, Moeller L (2010) Review of terahertz and subterahertz wireless communications. J Appl Phys 107(11):111101
9. Cherry S (2005) The net effect: as China's Internet gets a much-needed makeover, will the new network promote freedom or curtail it? IEEE Spectr 42(6):38–44
10. Kurner T (2012) Towards future THz communications systems. Terahertz Sci Technol 5(1):11–17
11. Heidemann R, Hofstetter R, Schmuck H (1994) Fibre-optic technologies for 30/60 GHz picocellular PCN and mobile systems. In: 1994 IEEE MTT-S international microwave symposium digest (Cat. No. 94CH3389–4)
12. Reynolds SK, Floyd BA, Pfeiffer UR, Beukema T, Grzyb J, Haymes C, Gaucher B, Soyuer M (2006) A silicon 60-GHz receiver and transmitter chipset for broadband communications. IEEE J Solid-State Circuits 41:2820–2829
13. Pfeiffer UR, Grzyb J, Liu D, Gaucher B, Beukema T, Floyd BA, Reynolds SK (2006) A chip-scale packaging technology for 60-GHz wireless chipsets. IEEE Trans Microw Theory Tech 54(8):3387–3396
14. Koch, M (2007) Terahertz communications: a 2020 vision. In: Terahertz frequency detection and identification of materials and objects (vol 4). Springer, Netherlands 325–338
15. El Ghzaoui M, Das S (2020) Data transmission with terahertz communication systems. In: Biswas A, Banerjee A, Acharyya A, Inokawa H, Roy J (eds) Emerging trends in terahertz solid-state physics and devices. Springer. https://doi.org/10.1007/978-981-15-3235-1_9
16. Piesiewicz R, Jemai M, Koch M, Kurner T (2005) THz channel characterization for future wireless gigabit indoor communication systems. SPIE 5727, terahertz and gigahertz communications, California, pp 166
17. Hirata A, Nagatsuma T, Kosugi T, Takahashi H, Yamaguchi R, Shimizu N, Kukutsu N, Murata K, Kado Y, Ikegawa H, Nishikawa H, Nakayama T (2007) 10-Gbit/s wireless communications technology using sub-terahertz waves. In: SPIE 6772, terahertz physics, devices, and systems II, p 67720B, Boston
18. Akyildiz IF, Jornet JM, Han C (2014) Terahertz band: Next frontier for wireless communications. Phys Commun 12:16–32
19. Siles GA, Riera JM, Garcia-del-Pino G (2015) Atmospheric attenuation in wireless communication systems at millimeter and THz frequencies [Wireless Corner]. IEEE Antennas Propag Mag 57(1):48–61
20. T. L. Gouguec TL, Martin PM (2017) A 45 GHz wireless transmission for a wireless interconnect network-on-board. In: 2017 IEEE 21st workshop on signal and power integrity (SPI), pp 1–2

21. Song HJ et al (2016) Demonstration of 20-Gbps wireless data transmission at 300 GHz for KIOSK instant data downloading applications with InP MMICs. In: 2016 IEEE MTT-S international microwave symposium (IMS), pp 1–4
22. Petrov V, Kokkoniemi J, Moltchanov D, Lehtomaki J, Koucheryavy Y, Juntti M (2017) Last meter indoor terahertz wireless access: performance insights and implementation roadmap. arXiv:1708.02963 [cs], août.
23. Dogadaev A, Monroy IT (2011) Challenges and capacity analysis of 100 Gbps optical fibre wireless links in 75–110 GHz band. In: IEEE Photonic Society 24th annual meeting, 2011, pp 268–269
24. Jia S et al (2017) 120 Gb/s multi-channel THz wireless transmission and THz receiver performance analysis. IEEE Photonics Technol Lett 29(3):310–313
25. Jia S et al (2018) 0.4 THz photonic-wireless link with 106 Gb/s single channel bitrate. J Lightwave Technol 36(2):610–616
26. Koenig S et al (2013) Wireless sub-THz communication system with high data rate. Nat Photonics 7(12):977–981
27. Kosugi T, Takahashi H, Hirata A, Murata K (2013) Broadband InP MMICs for 120 GHz wireless data communications. In: 2013 IEEE 13th topical meeting on silicon monolithic integrated circuits in RF systems, p 30–32
28. Hirata A et al (2010) 5.8-km 10-Gbps data transmission over a 120-GHz-band wireless link. In: 2010 IEEE international conference on wireless information technology and systems, p 1–4
29. Wang C, Lin C, Chen Q, Lu B, Deng X, Zhang J (2013) A 10-Gbit/s wireless communication link using 16-QAM modulation in 140-GHz band. IEEE Trans Microw Theory Tech 61(7):2737–2746
30. Hirata A, Harada M, Nagatsuma T (2003) 120-GHz wireless link using photonic techniques for generation, modulation, and emission of millimeter-wave signals. J Lightwave Technol 21(10):2145–2153
31. Piesiewicz R, Kleine-Ostmann T, Krumbholz N, Mittleman D, Koch M, Schoebei J, Kurner T (2007) Short-range ultra-broadband terahertz communications: concepts and perspectives. IEEE Antennas Propag Mag 49(6):24–39
32. Federici J, Moeller L (2010) Review of terahertz and subterahertz wireless communications
33. Federici JF, Ma J (2014) Comparison of terahertz versus infrared free-space communications under identical weather conditions. In: International conference on infrared, millimeter, and terahertz waves, IRMMW-THz, Tucson
34. Ma J, Moeller L, Federici JF (2014) Experimental comparison of terahertz and infrared signaling in controlled atmospheric turbulence. In: International conference on infrared, millimeter, and terahertz waves, IRMMW-THz, Tucson
35. Singhal S, Jaiverdhan (2019) Hexagonal fractal antenna for super wideband terahertz applications. Optik 206:163615
36. Rubani Q, Gupta SH, Rajawat A (2020) A compact MIMO antenna for efficient WBAN, operating at terahertz frequency. Optik 207:164447
37. Rubani Q et al (2019) Design and analysis of circular patch antenna for WBAN atterahertz frequency. Optik 185:529–536
38. Alibakhshikenari M et al (2020) High-gain on-chip antenna design on silicon layer with aperture excitation for terahertz applications. IEEE Antennas Wirel Propag Lett 19(9):1576–1580
39. Hussein A et al (2020) UWB THz plasmonic microstrip antenna based on graphene. TELKOMNIKA 18(1):30–36
40. Kaustubh et al (2019) A linear-scaling technique for designing a THz antenna from a GHz microstrip antenna or slot antenna. Optik 199:163331
41. Ghazaoui Y, El Alami A, El Ghzaoui M, Das S, Baradand D, Mohapatra S (2020) Millimeter wave antenna with enhanced bandwidth for 5G wireless application. J Instrum 15:122–132
42. El Ghzaoui M, Hmamou A, Foshi J, Mestoui J (2020) Compensation of non-linear distortion effects in MIMO-OFDM systems using constant envelope OFDM for 5G applications. J Circuits, Syst Comput 29(16):2050257

43. Mestoui J, El Ghzaoui M, Hmamou A, Foshi J (2019) BER performance improvement in CE-OFDM-CPM system using equalization techniques over frequency-selective channel. Procedia Comput Sci 151:1016–1021
44. Raihani H, Benbassou A, El Ghzaoui M, Belkadid (2017) Performance evaluation of a passive UHF RFID tag antenna using the embedded T-Match structure. In: 2017 International conference on wireless technologies, embedded and intelligent systems (WITS), Fez, pp 1–6. https://doi.org/10.1109/WITS.2017.7934636
45. Abdullah M et al (2020) Performance analysis of line feeding microstrip patch antenna using different layers of substrate materials for terahertz (THz) applications. IOSR J Electr Electroni Eng 14(7):18–24
46. Aghoutane B, Faylali HE, Das S, Elghzaoui M (2019) Design of a high gain 2*1 patch array for fifth generation wireless applications. In: 2019 7th Mediterranean Congress of telecommunications (CMT), Fès, Morocco, pp 1–4. https://doi.org/10.1109/CMT.2019.8931351
47. Yang X, Zhang B, Fan Y, Zhong FQ, Chen Z (2010) Design of improved CMRC structure used in terahertz subharmonic pumped mixer. In: 2010 IEEE 12th international conference on communication technology, Nanjing, pp 559–562. https://doi.org/10.1109/ICCT.2010.5688912
48. Aghoutane B, Meskini N, Elghzaoui M, Faylali HE (2018) Millimeter-wave microstrip antenna array design for future 5G cellular applications. In: 2018 International conference on electronics, control, optimization and computer science (ICECOCS), Kenitra, pp 1–4. https://doi.org/10.1109/ICECOCS.2018.8610507
49. Aghoutane B et al (2021) Analysis, design and fabrication of a square slot loaded (SSL) millimeter-wave patch antenna array for 5G applications. J Circuits, Syst Comput 30(12):1–12. https://doi.org/10.1142/S0218126621500869
50. Balanis CA (2016) Antenna theory: analysis and design, 4th edn. Wiley, Hoboken, NJ
51. Ye L-H, Chu Q-X (2010) 3.5/5.5lGHz dual band-notch ultra-wideband slot antenna with compact size. Electron Lett 46:325. https://doi.org/10.1049/el.2010.2722

# All-Optical Encryption and Decryption Circuit


**Dilip Kumar Gayen**

**Abstract** In modern times, there is a huge demand for high speed communication and optical circuits can serve us the purpose very well. There have been many approaches to design optical circuits. However, whenever we think of communication, we must think about security. Hence, the need for an encryption and decryption circuit becomes inevitable for optical communication. In order to achieve our goal, we use terahertz optical asymmetric demultiplexer (TOAD)-based optical switch for the designing of the encryption and decryption circuit. The main advantage of this is that it performs the operation in terahertz range also same circuit use as encryption and decryption operations.

**Keywords** Optical encryption and decryption · Semiconductor optical amplifier · Optical communication

## 1 Introduction

Presently, a day high velocity all-optical rationale entryways are critical gadgets in optical organizations. All-optical rationale entryways execute fundamental sign preparing capacity. They additionally fit for exchanging recovery and header acknowledgment preparing in photonic exchanging hubs [1–3]. Unrest has been achieved in all-optical data preparing framework. This insurgency has been made with the assistance of the disclosure of ultra-rapid all-optical switches dependent on cross phase modulation. Among various optical switches, the terahertz optical asymmetric demultiplexer (TOAD) successfully joins quick exchanging time, high reiteration rate, and low force utilization [4–7]. The innovation of coordinating a few frequencies onto a comparable fiber is called frequency division multiplexing (WDM). The rule of WDM used in simultaneousness with optical speakers has a result in correspondence interfaces that grant fast interchanges among clients on the planet's nations. There are numerous difficulties of fiber optic correspondence. The

D. K. Gayen (✉)
Department of Computer Science & Engineering, College of Engineering & Management, Kolaghat, KTPP Township, Purba Medinipur, Medinipur, West Bengal 721171, India



A. Acharyya et al. (eds.), *Generation, Detection and Processing of Terahertz Signals*, Lecture Notes in Electrical Engineering 794,
https://doi.org/10.1007/978-981-16-4947-9_5

innovation of incorporated optics and present-day optical strands happens in the field of optical hardware and segments [8]. All-optical adder's configuration dependent on plasmonics and photonic precious stone for cutting edge super first optical processors which give scaled down actual impression of the gadgets attributable to the tight optical imprisonment. By the by, the cycle of creation engaged with the plasmonic-based plans alongside the misfortune caused at the metal are among the restricting highlights [9]. The optical utilization of Walsh-Hadamard codes turns significant for optical CDMA to take care of different issue. For this, the plans need the utilization of nonlinear optics equipped for controlling multi-esteemed signs. To accomplish this objective, all-optical TOAD-based plan of Walsh-Hadamard codes have been investigated [10]. J. Wang et al. have proposed all-optical rationale entryway at 40 Gbit/s dependent on the fell entirety and contrast recurrence age utilizing intermittently poled lithium niobate waveguide [11]. TOAD-based switches can be utilized as cascading has been shown by B. C. Wang [12]. Along these lines, TOAD-based exchanging framework is widely used to create tree design for performing two-input rationale tasks and single-digit number-crunching activities in every optical area. In this chapter, we have proposed and depict the all-optical encryption and decoding tasks utilizing TOAD-based optical switch. We have used both the transmitted and reflected port of the device.

## 2 TOAD Switch

The fundamental circuit of TOAD-based switch is appeared in Fig. 1a [4, 7]. Here, a semiconductor optical amplifier (SOA) is put lopsidedly in a circle. TOAD could be a lone arm interferometer. It uses a semiconductor optical amplifier (SOA) that is put unevenly arranged in a fiber circle. The fiber circle jointed at the base by an optical 50:50 coupler. Approaching input/incoming pulse (IP) of frequency $\lambda_1$ separates into

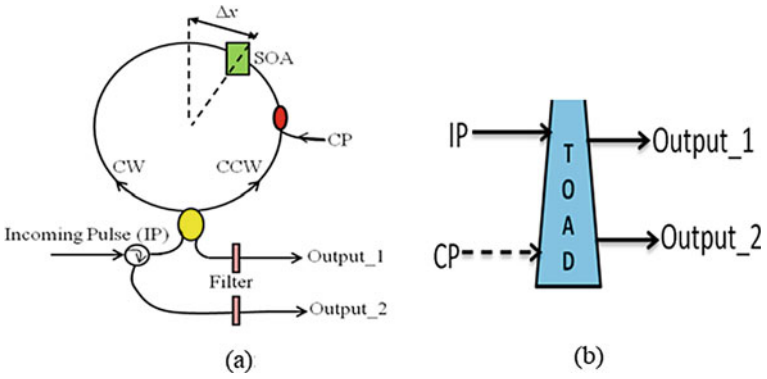


**Fig. 1** **a** All-optical TOAD-based switch and **b** block diagram of TOAD

two comparable parts. One is counter clockwise (CCW) parts and other is clockwise (CW) parts. These two parts spread around the circle reverse approach to each other and reconsolidate at this comparable coupler. Depending upon the segment, the phase difference between CW and CCW produce constructive or destructive interference. This phase difference can be made by applying beat light emission of frequency $\lambda_2$, which is implanted through a coupler affixed in the fiber circle as given in Fig. 1a. A Gaussian control pulse (CP) of full-width half greatest, data signals applied at practically same time. As SOA is put unevenly in the fiber circle by distance $\Delta x$, CW and CCW multiply two unique occasions through SOA. By then, the relative phase distinction among CW and CCW happens. Contingent on the phase different ($\Delta\Phi$) constructive or destructive impedance happens besides sends through the upper or lower port separately. The power at upper moreover, lower port can be imparted as [4–6]. The block outline of a TOAD-based switch is showed up in Fig. 1b.

$$\text{Power}_{\text{output\_1}} = \frac{\text{Power}_{\text{IP}}}{2}\left\{ \begin{array}{c} G_{\text{CW}}(t) + \text{G}_{\text{CCW}}(t) - 2 * \text{sqrt}[G_{\text{CW}}(t) * G_{\text{CCW}}(t)] \\ * \cos(\Delta\Phi) \end{array} \right\} \tag{1}$$

$$\text{Power}_{\text{output\_2}} = \frac{\text{Power}_{\text{IP}}}{2}\left\{ \begin{array}{c} G_{\text{CW}}(t) + G_{\text{CCW}}(t) + 2 * \text{sqrt}[G_{\text{CW}}(t) * G_{\text{CCW}}(t)] \\ * \cos(\Delta\Phi) \end{array} \right\} \tag{2}$$

## 3 All-Optical Encryption and Decryption

All-optical encryption and decryption circuit with the help of TOADs is designed. The circuits are designed theoretically and verified through numerical simulations. Here, encryption of 4-bit valid data at a time and the decryption circuit will be almost same as the encryption circuit, i.e., when we feed the output (encrypted data) of the encryption circuit to the input of the decryption circuit, we will get back our original signal. For the encryption and security purpose, we add 4 extra bits as the most significant bits (MSB) to the original 4-bit data which will be the least significant bits (LSB) and will then feed it to the encryption circuit. Let 1010 be our valid 4-bit data, and we feed 01001010 to the encryption where MSB 4-bit (0100) are extra added bits and LSB 4-bit (1010) is valid data. Now, the output from encryption circuit is 01010001 and that is given as the input to the same circuit (decryption circuit), and we will get back the original input which is 01001010 where the least significant 4-bits (1010) is the valid 4-bit data. Table 1 shows the truth table of 8-bit encryption circuit. The input to the encryption circuit is $x_7x_6x_5x_4x_3x_2x_1x_0$ ($x_7-x_4$ are extra added bits and $x_3-x_0$ are valid data bits) and the corresponding outputs from the encryption are $y_7y_6y_5y_4y_3y_2y_1y_0$. From Table 1 and by using Karnaugh, map we can deduce the following expressions for encryption circuit.

**Table 1** Truth table for the encryption circuit

| Input (to encryption circuit) $[x_7x_6x_5x_4x_3x_2x_1x_0]$ | Output (from encryption circuit) $[y_7y_6y_5y_4y_3y_2y_1y_0]$ |
|---|---|
| 0100 0001 | 0101 1010 |
| 0100 0010 | 0101 1001 |
| 0100 0011 | 0101 1000 |
| 0100 0100 | 0101 0111 |
| 0100 0101 | 0101 0110 |
| 0100 0110 | 0101 0101 |
| 0100 0111 | 0101 0100 |
| 0100 1000 | 0101 0011 |
| 0100 1001 | 0101 0010 |
| 0100 1010 | 0101 0001 |
| 0100 1011 | 0101 0000 |
| 0100 1100 | 0100 1111 |
| 0100 1101 | 0100 1110 |
| 0100 1110 | 0100 1101 |
| 0100 1111 | 0100 1100 |

$$y_7 = x_7,\ y_6 = x_6,\ y_5 = x_5,\ y_4 = \overline{x_4 + x_3x_2},\ y_3 = x_3x_2 + \overline{x_3} \cdot \overline{x_2},\ y_2 = x_2,$$
$$y_1 = \overline{x_1} \quad \text{and} \quad y_0 = \overline{x_0} \tag{3}$$

The circuit diagram of encryption circuit is shown in Fig. 2. To design this circuit, we use 9-TOADs-based optical switches namely T1 to T9. Incoming signals are feed to circuit from constant pulse light sources. For the switches T1 and T3, control signals are $x_7$ and $x_5$. Here, we consider the input as 01001010 ($x_7x_6x_5x_4x_3x_2x_1x_0$). As $x_7 = x_5 = 0$, i.e., control pulse (CP) is absence for the switches T1 and T3, therefore according to switching principle of TOAD-based switch only the output_2 (lower port) receives the light and no light receives at output_1 (upper port). Hence, the value of $y_7$ and $y_5$ will be 0.

For the switch T2, CP is present as $x_6 = 1$. Hence, light reaches to $y_6$, i.e., $y_6 = 1$. Now for the switches T4 and T5, CPs is zero and one as $x_4 = 0$ and $x_3 = 1$, respectively. The switches T6 and T7 receive the same control pulse from $x_2$. As $x_2 = 0$, both the switches receive the CP as 0. As $x_3 = 1$, the incoming light emerges from output_1 (upper port) of T5 and falls on T6 only. So switch T6 becomes active and switch T7 becomes inactive. For the switch T6, CP is 0 (as $x_2 = 0$) so no light comes out from output_1 (upper port). With the help of beam splitter, fraction of light from output_1 of T6 is combined with $x_4$ to act as a control signal for switch T4. Now for the switch T4, control signal is absent (as $x_4 = 0$ and output_1 (T6) = 0) so incoming pulse reaches to output_2 (lower port). Hence, $y_4$ becomes 1. As the switch T7 is inactive; therefore, no light reaches to output_1 (upper port) and output_2 (lower port). For this reason, $y_3$ is 0 and $y_2$ is 0. For the switch T8, CP

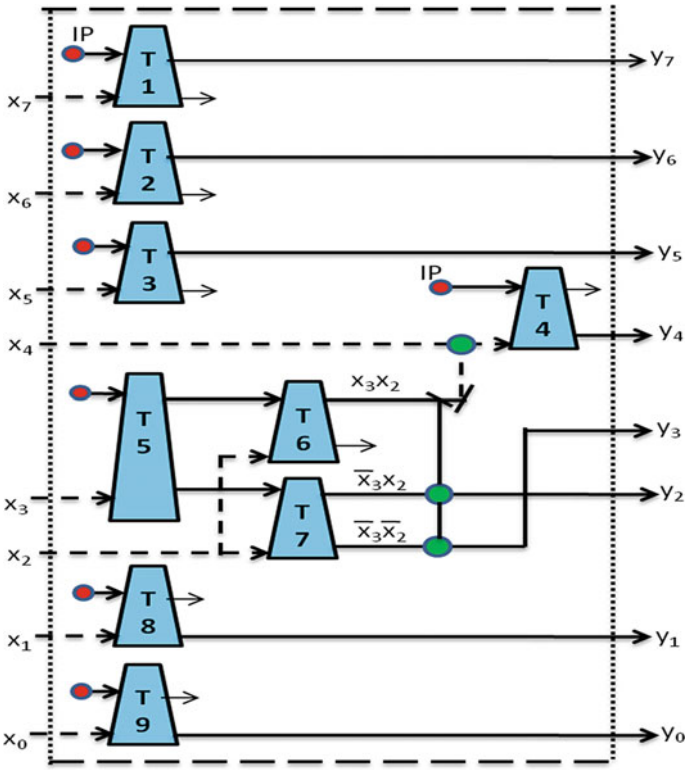


**Fig. 2** All-optical encryption circuit, where $x_7x_6x_5x_4x_3x_2x_1x_0$: inputs, $y_7y_6y_5y_4y_3y_2y_1y_0$: outputs, T1-T9: TOAD-based optical switches, ●: incoming pulse (IP), /: beam splitter and ●: beam combiner

is 1 (as $x_1 = 1$), as a result no light reaches to output_2 (lower part) so $y_1$ is 0. But for the switch T9, CP is 0 (as $x_0 = 0$), subsequently light reaches to output_2 (lower part) so $y_0$ is 1. Hence, final output is 01010001($y_7y_6y_5y_4y_3y_2y_1y_0$) that verifies the truth of the encryption circuit.

Table 2 shows the truth table of 8-bit decryption circuit. The input to the decryption circuit is $y_7y_6y_5y_4y_3y_2y_1y_0$ and the corresponding output from the decryption is $x_7x_6x_5x_4x_3x_2x_1x_0$. From Table 2 and by using Karnaugh map, we can deduce the following expressions for decryption circuit.

$$x_7 = y_7,\ x_6 = y_6, x_5 = y_5, x_4 = \overline{y_4 + y_3y_2},\ x_3 = y_3y_2 + \overline{y_3} \cdot \overline{y_2},$$
$$x_2 = y_2,\ x_1 = \overline{y_1} \quad \text{and} \quad x_0 = \overline{y_0} \tag{4}$$

The circuit diagram of decryption circuit is shown in Fig. 3. To design this circuit, we use 9-TOADs based optical switches namely T1 to T9. Incoming signals are feed to circuit from constant pulse light sources. Here we consider the input as

**Table 2** Truth table for the decryption circuit

| Input (to the decryption circuit) $[y_7y_6y_5y_4y_3y_2y_1y_0]$ | Output (from the decryption circuit) $[x_7x_6x_5x_4x_3x_2x_1x_0]$ |
|---|---|
| 0101 1010 | 0100 0001 |
| 0101 1001 | 0100 0010 |
| 0101 1000 | 0100 0011 |
| 0101 0111 | 0100 0100 |
| 0101 0110 | 0100 0101 |
| 0101 0101 | 0100 0110 |
| 0101 0100 | 0100 0111 |
| 0101 0011 | 0100 1000 |
| 0101 0010 | 0100 1001 |
| 0101 0001 | 0100 1010 |
| 0101 0000 | 0100 1011 |
| 0100 1111 | 0100 1100 |
| 0100 1110 | 0100 1101 |
| 0100 1101 | 0100 1110 |
| 0100 1100 | 0100 1111 |

01010001 ($y_7y_6y_5y_4y_3y_2y_1y_0$) which is received from output of the encryption circuit. Optical attenuators are used in every input to adjust the power of control pulse. In switches T1 and T3 control signals are $y_7$ and $y_5$. Control pulse (CP) is absence for the switches T1 and T3 as $y_7 = y_5 = 0$. According to switching, principle of TOAD based switch only the output_2 (lower port) receives the light and no light receives at output_1 (upper port). Thus, the value of $x_7$ and $x_5$ will be 0.

For the switch T2, CP is present as $y_6 = 1$. For this reason, light reaches to $x_6$, i.e., $x_6 = 1$. In switches T4 and T5, CPs are zero and one as $y_4 = 1$ and $y_3 = 0$. The switches T6 and T7 receive the same control pulse from $y_2$. As $y_2 = 0$, both the switches receive the CP as 0. Since $y_3 = 0$, the incoming light emerges from output_2 (lower port) of T5 and falls on T7 only. So switch T6 becomes inactive and no light comes out from output_1 (upper port). With the help of beam splitter, fraction of light from output_1 of T6 is combined with $y_4$ to act as a control signal for switch T4. At present for the switch T4, control signal is present (as $y_4 = 1$) subsequently no incoming pulse reaches to output_2 (lower port). Hence, $x_4$ becomes 0. In the switch T7, CP is 0 (as $y_2 = 0$) consequently light reaches to only output_2 (lower port). Subsequently, $x_3$ is 1 and $x_2$ is 0. In switch T8, CP is 0 (as $y_1 = 0$), as a result light reaches to output_2 (lower part) so $x_1$ is 1. But for the switch T9, CP is 1 (as $y_0 = 1$), then no light reaches to output_2 (lower part) so $x_0$ is 0. Therefore, final output is 01001010 ($x_7x_6x_5x_4x_3x_2x_1x_0$) that verifies the truth of the encryption circuit.

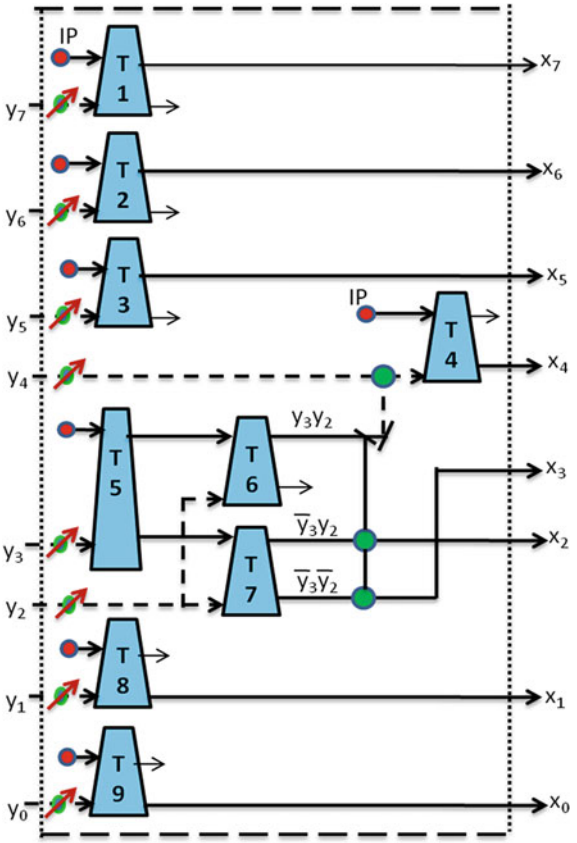


**Fig. 3** All-optical decryption circuit, where $y_7y_6y_5y_4y_3y_2y_1y_0$: inputs, $x_7x_6x_5x_4x_3x_2x_1x_0$: outputs, T1-T9: TOAD based optical switches, ●: incoming pulse (IP), /: beam splitter, ➶: variable optical attenuator and ●: beam combiner

## 4 Numerical Results

To check the action of this proposed circuit, mathematical reproduction with MATLAB has been performed utilizing various boundaries utilized in recreations and analysis of different papers [13–15]. The reproduced input and output waveforms for three different arrangements of information for encryption circuit are given in Fig. 4a–c .Here, input waveforms are addressed by arrangements of beats of explicit piece time of 50 ps and the sufficiency relates to power or force of light in milliwatt (mW). During the time stretch from 0 to 400 ps, each info gets the worth mix 0 as well as 1 and the comparing reproduced output waveforms in a similar time period are appeared at terminals $y_0$ through $y_7$. The reproduced input and output waveforms for three different arrangements of information for decryption circuit are given in Fig. 5a–c.

Here, input waveforms are addressed by arrangements of beats of explicit piece time of 50 ps and the sufficiency relates to power or force of light in milliwatt (mW). During the time stretch from 0 to 400 ps, each info gets the worth mix 0 as well

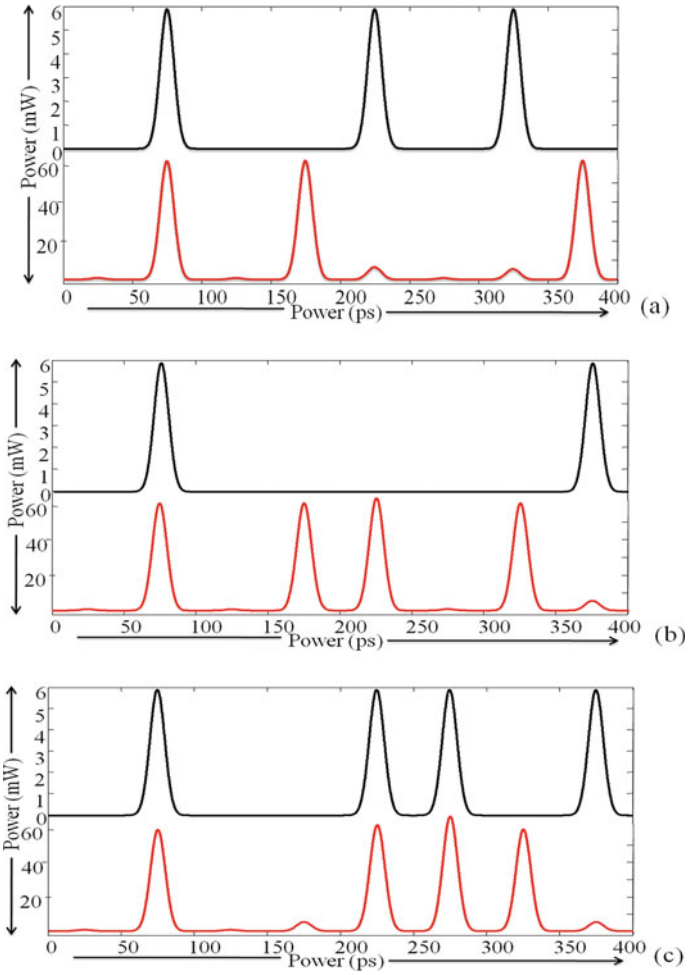


**Fig. 4** Input and output waveforms for encryption circuit, **a** input is 01001010, encrypted output is 01010001, **b** input is 01000001, encrypted output is 01011010 and **c** input is 01001101, encrypted output is 01001110

as 1 and the comparing reproduced output waveforms in a similar time period are appeared at terminals $x_0$ through $x_7$.

The eye-chart is the superposition of the outputs for the redundancy time of the sources of info, i.e., inputs shifts from 1 to 0 or 0 to 1. Figure 6 is anything but a traditional eye-graph since they are not as useful as in debasing impacts, ordinarily saw in the highlight point correspondence joins, for example, clamor source, are added by the finder and optical filaments. This graph is known as a pseudo-eye-chart. An eye-chart with huge eyes demonstrates a reasonable transmission with a

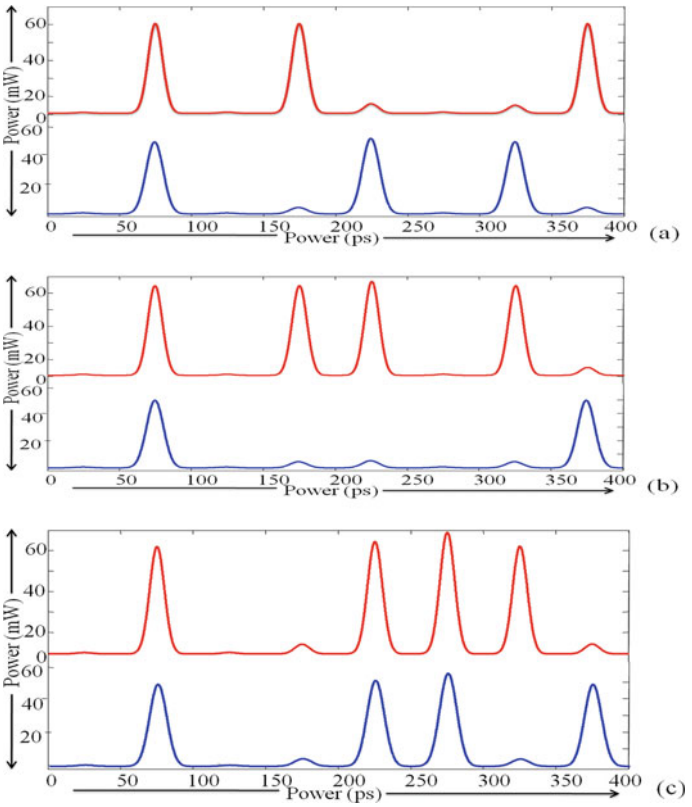


**Fig. 5** Input and output waveforms for decryption circuit, **a** input is 01010001, decrypted output is 01001010, **b** input is 01011010, decrypted output is 01000001 and **c** input is 01001110, decrypted output is 01001101

**Fig. 6** Pseudo-eye-chart

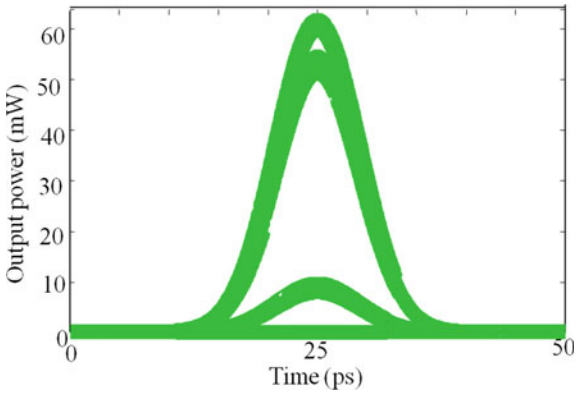

low piece rate. Here, the value of pseudo-eye-chart is almost 91.05%. This worth demonstrates very great reaction at the output terminals.

## 5 Summary

This is a new technique especially designed for the encryption of optical signal through the use of TOAD. The addition of extra bits and then encryption of the data makes the transmission highly secure from data theft or hacking. This is a very simple technique as the same optical circuit is serving as the encryption and decryption with minor changes. This technique can be developed further for overcoming the limitations and further simplification of the circuit if possible to encrypt more inputs with lesser overhead and cost.

## References

1. Suzuki M, Uenohara H (2009) Invesigation of all-optical error detection circuitusing SOA-MZI based XOR gates at 10 Gbit/s. Electron Lett 45(4):124–125
2. Minh HL, Ghassemlooy Z, Ng WP (2008) Characterization and performance analysis of a TOAD switch employing a dual control pulse scheme in high speed OTDM demultiplexer. IEEE Commun Lett 12(4):316–318
3. Li G (2009) Recent advances in coherent optical communication. Adv Opt Photonics 1(2):279–307
4. Sokoloff JP, Prucnal PR, Glesk I, Kane M (1993) A terahertz optical asymmetric demultiplexer (TOAD). IEEE Photonics Technol Lett 5(7):787–790
5. Wang H, Wu J, Lin J (2005) Performance analysis on terahertz optical asymmetric demultiplexer with assist light injection. Optics Commun 256:83–97
6. Parolari P, Boffi P, Marazzi L, Martinelli M (2003) Two-stage sagnac demultiplexer. J Lightwave Technol 21(8):1808–1812
7. Zoiros KE, Vardakas J, Houbavlis T, Moyssidis M (2005) Investigation of SOA-assisted Sagnac recirculating shift register switching characteristics. Int J Light Electron Optics 116(11):527–541
8. Kareem FQ, Zeebaree SRM, Dino HI, Sadeeq MAM, Rashid ZN, Hasan DA, Sharif KH (2021) A survey of optical fiber communications: challenges and processing time influences. Asian J Res Comput Sci 7(4):48–58
9. Goswami K, Mondal H, Sen M (2021) A review on all-optical logic adder: heading towards next-generation processor. Optics Commun 483:126668
10. Mandal AK (2017) Full-optical TOAD based Walsh-Hadamard code generation. Opt Quant Electron 49:290
11. Wang J, Sun J, Sun Q (2007) Single-PPLN-based simultaneous half-adder, half-subtracter, and OR logic gate: proposal and simulation. Opt Express 15(4):1690–1699
12. Wang BC, Baby V, Tong W, Xu L, Friedman M, Runser RJ, Glesk I, Prucnal P (2002) A novel fast optical switch based on two cascaded terahertz optical asymmetric demultiplexers (TOAD). Opt Express 10(1):15–23
13. Zoiros KE, Papadopoulos G, Houbavlis T, Kanellos GT (2006) Theoretical analysis and performance investigation of ultra-fast all-optical Boolean XOR gate with semiconductor optical amplifier-assisted Sagnac interferometer. Optics Communications 258(2):114–134

14. Zoiros KE, Houbavlis T, Kalyvas M (2004) Ultra-high speed all-optical shift registers and their applications in OTDM networks. Opt Quant Electron 36(11):1005–1053
15. Zoiros KE, Avramidis P, Koukourlis CS (2008) Performance investigation of semiconductor optical amplifier based ultra-fast nonlinear interferometer in nontrivial switching mode. Opt Eng 47(11):115006–115011

# Gallium Oxide-Based IMPATT Sources for THz Applications


**S. J. Mukhopadhyay, S. Kanungo, Aritra Acharyya, and M. Mitra**

**Abstract** The potency of terahertz (THz) impact ionization avalanche transit time (IMPATT) diodes based on ultra-wide bandgap semiconductor material β-Gallium oxide ($Ga_2O_3$) has been investigated here. A large signal simulation technique is considered to probe the DC and high-frequency features of single drift region (SDR) β-$Ga_2O_3$ IMPATTs formulated to operate at 0.5 THz. Simulated outcome focuses that the SDR β-$Ga_2O_3$ IMPATTs are able to deliver remarkably greater RF power as well as higher DC to RF conversion efficacy at the aforesaid frequency compared to the conventional Si and InP material-based double drift region (DDR) IMPATT sources.

**Keywords** β-$Ga_2O_3$ · IMPATTs · SDR · RF output power · THz

## 1 Introduction

This is beyond doubt to all that IMPATT device has proved its capability of generating adequate RF power at higher frequency band stating from microwave upto THz [1–7]. The terahertz sources have multiple practical exercises in several domains [8–12]. Silicon being the majorly used substance for IMPATT source is competent of producing RF power upto 0.5 THz [7, 13]. There are some other semiconductors like InP ($E_g = 1.35$ eV at 300 K), 4H-SiC ($E_g = 3.23$ eV at 300 K), 6H-SiC ($E_g = 2.86$ eV

S. J. Mukhopadhyay (✉) · M. Mitra
Department of Electronics and Telecommunication Engineering, Indian Institute of Engineering Science and Technology, Shibpur, Howrah, West Bengal, India

S. Kanungo
Department of Electrical and Electronics Engineering, Birla Institute of Technology and Science, Pilani, Shamirpet-Keesara Road, Jawahar Nagar, Shameerpet, Hyderabad, Telangana 500078, India
e-mail: sayan.kanungo@hyderabad.bits-pilani.ac.in

A. Acharyya
Department of Electronics and Communication Engineering, Cooch Behar Government Engineering College, Ghughumari, Harinchawra, Cooch Behar, West Bengal 736170, India



A. Acharyya et al. (eds.), *Generation, Detection and Processing of Terahertz Signals*, Lecture Notes in Electrical Engineering 794,
https://doi.org/10.1007/978-981-16-4947-9_6

at 300 K), 3C-SiC ($E_g$ = 2.36 eV at 300 K), Wz-GaN ($E_g$ = 3.40 eV at 300 K) have exhibited enormous potentialities as the base materials of IMPATT sources operating at such high frequency regime [14–20]. Here, the authors have explored the potentiality of ultra-wide bandgap semiconductor, i.e., β-$Ga_2O_3$ ($E_g$ = 4.85 at 300 K) as a substrate material of SDR IMPATT diodes operating at 0.5 THz. Because of larger bandgap, stability, and reachability to get large diameter bulk, β-$Ga_2O_3$ turns out to be a brilliant substrate for high frequency and power applications.

A well-approved large-signal model has been formulated here to carry out DC and high-frequency properties of SDR β-$Ga_2O_3$ IMPATTs intended to operate at the aforesaid frequency. Ultimately, the large-signal RF performance of SDR β-$Ga_2O_3$ IMPATTs is compared here to that of IMPATT sources based on Si, InP with a view to ensuring the superiority of SDR β-$Ga_2O_3$ over those traditional base materials.

## 2 Structure, Material, Fabrication, and Simulation

In this section, structure of the device and corresponding substance parameters, fabrication, and simulation method have been presented.

### *2.1 Structure*

The one-dimensional model (1-D) model of $p^+nn^+$ structure SDR IMPATT exhibited in Fig. 1 is considered for the simulation purpose. The space charge layer width is 0.4950 μm. Doping concentrations of highly doped regions ($N_{n+}$ and $N_{p+}$) are considered as 5.0 × $10^{25}$ $m^{-3}$. The doping concentration of n-layer (i.e., $N_D$) is adjusted to optimize the static (DC) properties of the device such as avalanche and drift layer widths, breakdown voltage so that the device can be able to provide larger power with significantly greater conversion efficacy. The diameter ($D_j$) of the device is usually considered as 10 μm. Optimized structural parameters of the device are exhibited in Table 1.

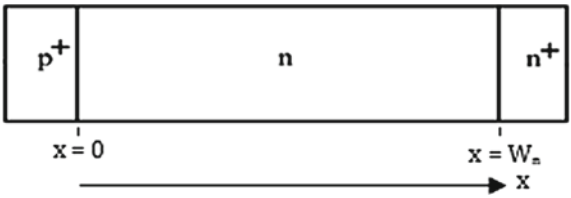


**Fig. 1** Representation of 1-D SDR IMPATT

**Table 1** Optimized design parameters of 0.5 THz SDR β-$Ga_2O_3$ IMPATTs

| $W_n$ (μm) | 0.495 |
|---|---|
| $N_D$ ($\times 10^{23}$ $m^{-3}$) | 2.000 |
| $N_A$ ($\times 10^{23}$ $m^{-3}$) | 2.000 |
| $N_{n+}$ ($\times 10^{25}$ $m^{-3}$) | 5.000 |
| $N_{p+}$ ($\times 10^{25}$ $m^{-3}$) | 5.000 |
| $D_j$ (μm) | 10.00 |

## 2.2 Material

The field dependence of ionization rate of electrons in β-$Ga_2O_3$ has been subsumed in the large signal program via reported data [21]. Similarly, the drift velocities of charge carriers in β-$Ga_2O_3$ are included in the simulation by utilizing data focused in published literature [22]. Other important material parameters such as mobility, relative dielectric constant, thermal conductivity of β-$Ga_2O_3$ are taken from recently published reports [23, 24].

## 2.3 Fabrication

Gallium oxide focuses on five different components: monoclinic, rhombohedral, defective spinel, cubic, and orthorhombic, and is represented as β-, α-, γ-, δ-, and ε-$Ga_2O_3$, respectively, [25]. Among the crystal structures, β-phase is the most stable structure and can be enhanced with melting growth techniques that facilitate the acquisition of larger, smaller sizes, costing one site. Single crystal $Ga_2O_3$ bulks combined with melted growth techniques such as czochralski, floating space, and film-based growth strategies (EFG) are highlighted elsewhere [23]. Among these, EFG has the advantage over other methods used to produce large quantities of crystal wafers. The epitaxial growth of small $Ga_2O_3$ films, with several modes such as molecular beam epitaxy (MBE), halide vapor phase epitaxy (HVPE), metal-organic chemical vapor deposition, and mist chemical vapor deposition reported in the literature published [23].

## 2.4 Simulation

The non-sinusoidal voltage excitation strategy [26] is presented here to scrutinize DC (static) and large signal properties of SDR β-$Ga_2O_3$ IMPATT diodes formulated to operate at 0.5 THz. The aforesaid parameters of β-$Ga_2O_3$ depicted previously are taken as the inputs of the simulation program developed in MATLAB domain. The simulated outcome provides important static (DC) and high frequency parameters, discussed in the following section.

## 3 Results and Discussion

Here in this article DC and large signal characteristics of SDR β-$Ga_2O_3$ IMPATT diode have been studied at operating frequency of 0.5 THz. The simulations have been accomplished for the bias current densities ranging from $1.8 \times 10^8$ A/m$^2$ to $2.6 \times 10^8$ A/m$^2$. The range of bias current density has been taken for the diode for which the diode holds negative conductance.

### *3.1 DC and Large Signal Performance of Device*

Variations of static (DC) and high-frequency parameters like maximum electric field ($\xi_P$), breakdown voltage ($V_B$), avalanche zone voltage ($V_A$), avalanche layer width ($x_a$), avalanche frequency resonance (fa), optimum frequency (fp), peak magnitude conductance (|Gp|), susceptance (Bp), peak Quality factor ($Q_p$), magnitude of negative resistance ($|Z_R|$), large signal efficacy ($\eta_L$) and RF ($P_{RF}$) power output, etc., of the device with the bias current ($J_0$) density are plotted in Fig. 2. It is evident that as the current density increases, $V_B$, $V_{A,}$ and $x_a$ increases as shown in Figs. 2a–c. As higher current density results in a larger electric field which reduces transit time of the carriers, so fa and fp increase slightly (see Fig. 2d). In addition, the magnitude of negative conductance and susceptance also increases with the current range of selections (see Fig. 2e).

It is revealed in Fig. 2g, h that the $Q_p$ and $\eta_L$ of the device decreases with the current density when the $Z_R$ magnitude increases with increasing current density leading to an increase in DC to RF power output as shown in Fig. 2f, i. RF performance measurement data for SDR β-Ga2O3 IMPATTs are not available in published publications as a result, comparisons cannot be performed with generated data. The observations are given in tabular format (see Table 2).

### *3.2 Co-Relative Study with IMPATT Sources Based on Si and InP*

It is interesting to note from Table 3 below that SDR β-$Ga_2O_3$ IMPATT diodes having the ability of generating much higher RF power ($P_{RF}$) as compared to their DDR Si and InP counterparts at 0.5 THz. Thus, β-$Ga_2O_3$ is the most suitable material over traditional base semiconductor materials like Si/InP for fabricating SDR IMPATTs at THz frequencies.

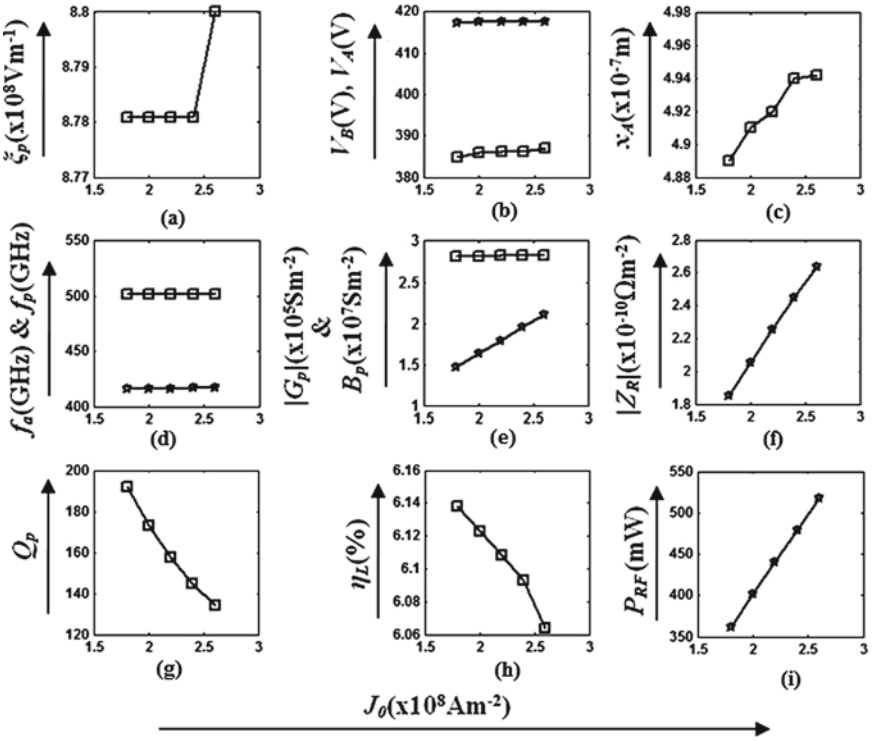


**Fig. 2** Variations of some DC and large signal parameters of 0.5 THz SDR β-$Ga_2O_3$ IMPATTs with bias current density

**Table 2** DC and large-signal characteristics of SDR β-$Ga_2O_3$ IMPATTs

| Bias current density $J_0$ (x$10^8$A/m$^2$) | 1.8 | 2.0 | 2.2 | 2.4 | 2.6 |
|---|---|---|---|---|---|
| ζp (×$10^8$ V/m) | 8.7809 | 8.7809 | 8.7809 | 8.7809 | 8.8009 |
| Breakdown voltage (V) | 417.419 | 417.152 | 416.892 | 416.622 | 417.465 |
| Avalanche voltage drop (V) | 384.930 | 386.077 | 385.835 | 386.280 | 383.548 |
| $x_A$ (×$10^{-7}$ m) | 4.890 | 4.910 | 4.910 | 4.920 | 4.870 |
| $f_a$ (GHz) | 416.50 | 416.50 | 416.50 | 416.60 | 416.60 |
| fp (GHz) | 501.90 | 501.90 | 502.00 | 502.00 | 502.10 |
| Gp (×$10^5$ Sm$^{-2}$) | −1.470 | −1.631 | −1.790 | −1.950 | −2.098 |
| Bp (×$10^7$ Sm$^{-2}$) | 2.8190 | 2.8190 | 2.8196 | 2.8196 | 2.8201 |
| $Z_R$ (×$10^{-10}$ Ωm$^{-2}$) | −1.8503 | −2.0524 | −2.2524 | −2.4520 | −2.6383 |
| Quality factor (−Q) | 191.701 | 172.826 | 157.452 | 144.584 | 134.391 |
| $P_{RF}$ (mW) | 362.230 | 401.275 | 439.996 | 478.534 | 517.019 |
| Efficiency $\eta_L$ (%) | 6.138 | 6.123 | 6.108 | 6.093 | 6.064 |

**Table 3** DC to RF power output of DDR Si, InP, and SDR β-$Ga_2O_3$ IMPATTs

| Base material | Simulated data of $P_{RF}$ (mW) |
|---|---|
| Si (DDR) | 89.61[26] |
| InP (DDR) | 141.93[26] |
| β-$Ga_2O_3$(SDR) | 517.00 |

## 4 Summary

The potential of THz SDR IMPATTs based on β-$Ga_2O_3$ is transferred to this paper. Complete DC and large-signal properties were achieved in the SDR β-$Ga_2O_3$ IMPATT diode designed to operate at 0.5 THz. The mimicry result revealed that SDR β-$Ga_2O_3$ IMPATTs were able to produce greater RF power at THz frequency compared to their traditional counterparts, namely DDR Si and InP IMPATTs. Observations presented in this article will assist in the manufacture of THz SDR β-$Ga_2O_3$ IMPATT diodes.

## References

1. Midford TA, Bernick RL (1979) Millimeter wave CW IMPATT diodes and oscillators. IEEE Trans Microwave Theor Tech 27(5):483–492
2. Luy JF, Casel A, Behr W, Kasper E (1987) A 90-GHz double-drift IMPATT diode made with Si MBE. IEEE Trans Electron Devices 34(5):1084–1089
3. Wollitzer M, Buchler J, Schafflr F, Luy JF (1996) D-band Si-IMPATT diodes with 300 mW CW output power at 140 GHz. Electron Lett 32(2):122–123
4. Dalle C, Rolland P, Lieti G (1990) Flat doping profile double-drift silicon IMPATT for reliable CW high power high-efficiency generation in the 94-GHz window. IEEE Trans Electron Devices 37(1):227–236
5. Seidel TE, Davis RE, Iglesias DE (1971) Double-Drift-region ion implanted millimetre wave IMPATT diodes. Proc IEEE 59(8):1222–1228
6. Mukhopadhyay SJ, Acharyya A, Mitra M (2020) Relative study on MM-wave performance of Group IV-IV and III-V materials based IMPATT sources. IETE J Res 66(3):1–11
7. Mukhopadhyay SJ, Ghivela GC, Sengupta J, Mitra M (2019) Prospects and potentiality of diamond based DDR IMPATTs in THz Regime. Int J Electron Lett 7(3):36–46
8. Siegel PH (2007) THz instruments for space. IEEE Trans Antenn Propag 55:2957–2965
9. Grischkowsky D, Keiding S, Exter M, Fattinger C (1990) Far-infrared time-domain spectroscopy with terahertz beams of dielectrics and semiconductors. J Opt Soc Am B 7(10):2006–2015
10. Debus C, Bolivar PH (2007) Frequency selective surfaces for high sensitivity terahertz sensing. Appl Phys Lett 91:184102
11. Yasui T, Yasuda T, Sawanaka K, Araki T (2005) Terahertz paintmeter for noncontact monitoring of thickness and drying progress in paint film. Appl Opt 44:6849
12. Stoik CD, Bohn MJ, Blackshire JL (2008) Nondestructive evaluation of aircraft composites using transmissive terahertz time domain spectroscopy. Opt Express 16(21):17039–17051
13. Acharyya A, Banerjee JP (2014) Prospects of IMPATT devices based on wide bandgap semiconductors as potential terahertz sources. Appl Nanosci 4:1–14
14. Eisele H, Chen CC, Munns GO, Haddad GI (1996) The potential of InP IMPATT diodes as high-power millimeter-wave sources: First experimental results. IEEE MTT-S international microwave symposium digest, vol 2. 17–21 June, USA, p 529

15. Mukherjee M, Banerjee S, Banerjee JP (2010) Dynamic characteristics of III-V and IV-IV semiconductor based transit time devices in the terahertz regime: a comparative analysis. Terahertz Sci Technol 3:98
16. Mukherjee M, Mazumder N, Roy SK, Goswami K (2007) Terahertz frequency performance of double drift IMPATT diode based on opto-sensitive semiconductor. In: Proceedings of Asia-Pacific microwave conference. Thailand, 11–14 Dec, pp 1–4
17. Pearton SJ, Ren F, Zang AP, Lee KP (2000) Fabrication and performance of GaN electronic devices. Mater Sci Eng 30(3):55–212
18. Meng CC, Liao GR (1999) Analysis of millimeter-wave GaN IMPATT oscillator at elevated temperature. Microw Opt Technol Lett 23:257
19. Yuan L, James A, Cooper JA, Melloch MR, Webb KJ (2001) Experimental demonstration of a silicon carbide IMPATT oscillator. IEEE Electron Device Lett 22:266
20. Vassilevski KV, Zorenko AV, Zekentes K, Tsagaraki K, Bano E, Banc C, Lebedev A (2001) 4H-SiC IMPATT diode fabrication and testing. technical digest of international conference on SiC and related materials. Tsukuba, Japan, p 713
21. Ghosh K, Singisetti U (2018) Impact ionization in β-$Ga_2O_3$. J Appl Phys 124:085707
22. Earton SJ, Yang J, Cary P, Ren F, Kim J, Tadjer MJ, Mastro M (2018) A review of $Ga_2O_3$ materials, processing and devices. Appl Phys Rev 5:011301
23. Higashiwaki M, Sasaki K, Murakami H, Kumagai Y, Koukitu A, Kuramata A, Masui T, Yamakoshi S (2016) Recent progress in $Ga_2O_3$ power devices. Semicond Sci andTechnol 31:11
24. Akyol F (2020) Simulation of β-$Ga_2O_3$ vertical schottky diode based photodetectors revealing average hole mobility of 20 $cm^2V^{-1}s^{-1}$. J Appl Phys 127:074501
25. Roy R, Hill VG, Osborn EF (1952) Polymorphism of $Ga_2O_3$ and the system $Ga_2O_3$-$H_2O$. J Am Chem Soc 74:719
26. Acharyya A, Mallik A, Banerjee D, Ganguli S, Das A, Dasgupta S, Banerjee JP (2014) IMPATT devices based on group III-V compound semiconductors: Prospects as potential terahertz radiators. HKIE Transactions 21(3):135

# All Optical XOR Gate Using Quantum Dot Semiconductor Optical Amplifier Based Terahertz Optical Asymmetric Demultiplexer (TOAD)


**Kousik Mukherjee**

**Abstract** All Optical XOR gate based on Terahertz Optical Asymmetric Demultiplexer (TOAD) using Quantum Dot Semiconductor Optical Amplifier (QDSOA) is the subject matter of this chapter. The operating speed of the proposed gate is 1 Tb/s. QDSOA is a versatile gain medium and has advantages in terms of gain recovery, patterning effect, amplified spontaneous emission (ASE) noise, etc. The XOR gate is simulated using MATLAB and analyzed by calculating Extinction ratio (ER), Contrast ratio (CR), and quality factor (Q). The bit error rate (BER) is also calculated to show proper operation of the logic for optical communication applications. The XOR gate is characterized by pseudo eye diagram also. Relative eye opening of more than 90% is calculated shows clear transmission of the bits.

**Keywords** Optical logic · Quantum dot SOA · TOAD · ASE noise

## 1 Introduction

All optical signal processing (AOSP) is the demand of modern communication systems (AOSP). Due to transparency, reconfigure-ability and tenability AOSP potentially increase the network flexibility [1]. Besides these advantages to avail high bandwidth high speed operations optical techniques should be employed. Moreover, multidimensional properties like amplitude, phase, frequency, and polarization of an optical signal can be modulated simultaneously to provide more degrees of freedom [1]. For AOSP, nonlinear optical properties are important components which can be used to manipulate different properties of an optical signal. The important nonlinearities include Four Wave Mixing (FWM), Sum and Difference frequency generation (SFG & DFG) successively, Cross Gain modulation (XGM), Cross phase modulation (XPM), etc. Semiconductor Optical Amplifier (SOA) is a versatile gain

K. Mukherjee (✉)
Department of Physics, Banwarilal Bhalotia College, Asansol, India

Centre of Organic Spintronics and Optoelectronic Devices (COSOD), Kazi Nazrul University, Asansol, Burdwan, West Bengal 713340, India



A. Acharyya et al. (eds.), *Generation, Detection and Processing of Terahertz Signals*, Lecture Notes in Electrical Engineering 794,
https://doi.org/10.1007/978-981-16-4947-9_7

medium showing various nonlinearities as mentioned above. SOAs are very attractive nonlinear devices for applications in AOSP due to their multifunctional applications [2]. Few important applications include Optical transmission [3, 4], logic gates [5, 6], wavelength converter [7], optical switch [8], and other network applications [9]. Quantum dot SOA (QDSOA) uses quantum dots in the active region find applications in pattern effect free amplification and wavelength conversion [10] which enables QDSOA to be used in high performance amplifiers and all optical switches in AOSP. Over the conventional SOAs (bulk or quantum well structure), QDSOAs have many advantages. These advantages include shorter time for gain recovery, patterning effect free operation, higher gain bandwidth, etc. [11–13]. These enable QDSOA as a potential candidate for all optical signal processing at Tb/s speed or more [13, 14]. Therefore in last two decades or more lots of QDSOA based designs of logic gates, and processors have been proposed [13–20]. Mach Zehnder Interferometer (MZI) structure is very popular in designing such devices [14, 16, 18, 19]. An MZI requires two identical QDSOAs with perfect balance of phase and gain for its operation which is very difficult to attain [15, 17]. Moreover, use of two QDSOAs makes the designs complex in hardware also. Terahertz Optical Asymmetric Demultiplexer (TOAD) is another interferometric switch but uses only a single active element like SOA [21]. Recently QDSOA is utilized to design all optical digital to analog converters (DAC) [22] with high values of dynamic range and low absolute error. Therefore, TOAD based designs have lower complexities and since single SOAs are used there are no such problems like MZI. As an ultra-speed switching device TOAD using quantum dot SOAs may become an important alternative [23]. TOAD based on QDSOA in place of conventional SOA is an important alternative for the design of optical logic devices [24]. Works [25–28] deals with the design of XOR gate using TOAD with conventional SOA. This chapter deals with the operation of a TOAD using QDSOAs and design of XOR gate using this TOAD for the first time to the best of author's knowledge. The rest of the chapter is organized as follows:

(a) Section 2: Structure and working of QDSOA
(b) Section 3: Structure of QDSOA based TOAD
(c) Section 4: Mathematical Modeling
(d) Section 5: Working Principle of the XOR gate
(e) Section 6: Results and Discussions
(f) Section 7: Summary.

## 2 Structure and Working of the QDSOA

Figure 1 shows self assembled InGaAs quantum dots on GaAs substrate is used to design the QDSOA. The wetting layer is grown with Stranski–Kranstanow mode [10]. Typical dot sizes are 10–20 nm [25], and repeated layers of such dots provide sufficient gain. There are two types of model: one state and two state for gain of the QDSOA. In the former case, only ground state transitions are considered but in

later model both excited states and ground states are considered. In Sect. 4, two state model of QDSOA is described.

## 3 Terahertz Optical Asymmetric Demultiplexer (TOAD)

TOAD is a device with Tb/s operating speed and requires low (<1 pJ) optical power for switching [21]. In this work, an SOA is used as nonlinear element asymmetrically placed in a nonlinear loop mirror configuration. A simplified diagram is shown in Fig. 1 using quantum dot SOA as nonlinear element. Here $C_p$ is the control pulse which modifies the QDSOA gain. This, in turn, controls the probe or data signal ($P_{in}$) components (denoted by $P_{cw}$ and $P_{ccw}$) amplification and phase. These two counter propagating signals passes the QDSOA at different times and experiences different time dependent gain and acquire a phase difference which depends on time and control power. These signals come out of two ports $P$ and $Q$ after constructive and destructive interferences. If $G_u$ be the unsaturated gain and $G_t$ be the time dependent gain of the QDSOA, then output from the constructive and destructive interference port $P$ and $Q$ are given by $O_P = \frac{P_{in}}{4}\left(G_t + G_u + 2\sqrt{G_t G_u}\text{Cos}\Phi\right)$ and $O_Q = \frac{P_{data}}{4}\left(G_t + G_u - 2\sqrt{G_t G_u}\text{Cos}\Phi\right)$ respectively. The phase difference is $\Phi = -0.5\,\alpha\,\ln(G_t/G_u)$.

In the absence of control signal, gains of QDSOAs are not saturated and $G_t = G_u$, and results in zero phase difference between the counter propagating signals $P_{cw}$ and $P_{ccw}$ is zero. This corresponds to $O_P = G_u\,P_{in}$ and $O_Q = 0$. When control is present with a prefixed intensity caused gain saturation such that $G_t = G_{sat} << G_u$, and a phase change of $\pi$ happens. This makes $O_P = (\sqrt{G_u} - \sqrt{G_{sat}})P_{in}/4$, and $O_P = (\sqrt{G_u} + \sqrt{G_{sat}})P_{in}/4$. Therefore, light switches from constructive port ($P$) to destructive port ($Q$). Figure 2 shows TOAD based switch using QDSOA and is called QDSTOAD switch designed and analyzed in the work by Mukherjee [23, 24]. This type of switching can be utilized to design any ultra-fast all optical logic gate and devices. In this chapter in Sect. 4, the XOR gate is designed using this switch and analyzed using mathematical modeling described in Sect. 3.

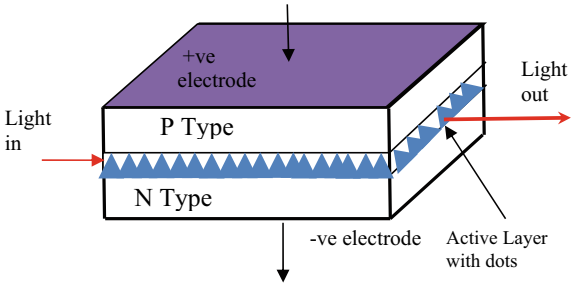


**Fig. 1** QDSOA structure

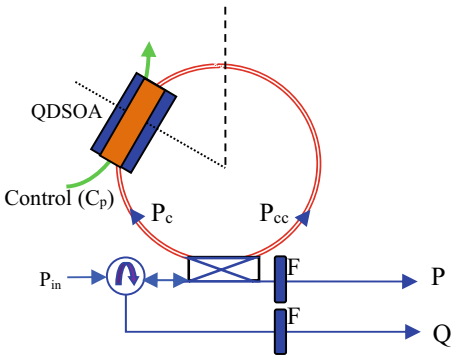


**Fig. 2** TOAD based on QDSOA

## 4 Mathematical Modeling of the QDSOA

QDSOA based TOAD works on the principle of XGM and XPM in QDSOA. These effects can be modeled by the rate equations [13–20, 22–25]:

$$\frac{\partial f}{\partial t} = \frac{(1-f)h}{\tau_{21}} - \frac{f(1-h)}{\tau_{12}} + \frac{f^2}{\tau_{1R}} - \frac{L_w g_{\max}(2f-1)P}{N_Q A_{\text{eff}} h\nu} \tag{1}$$

$$\frac{\partial h}{\partial t} = -\frac{h}{\tau_{2w}} - \frac{N(1-h)L_w}{\tau_{w2}N_Q} + \frac{(1-f)h}{\tau_{21}} - \frac{f(1-h)}{\tau_{12}} \tag{2}$$

$$\frac{\partial N}{\partial t} = \frac{J}{eL_w} - \frac{N(1-h)}{\tau_{w2}} + \frac{N_Q h}{\tau_{2w}L_w} - \frac{N}{\tau_{wR}} \tag{3}$$

$$\frac{\partial P}{\partial z} = \frac{\left[g_{\max}(2f-1) - \alpha_{\text{int}}\right]P}{A_{\text{eff}} h\nu} \tag{4}$$

$$\frac{\partial \varphi}{\partial z} = -0.5\alpha g_{\max}(2f-1) \tag{5}$$

where $N$ denotes electron density in the wetting layer, $f$ and $h$ represent electron occupation probabilities of ground state and excited state. Table 1 shows details of other parameters of Eqs. (1)–(5).

Set of coupled Eqs. (1)–(5) are solved numerically using fourth order Runge Kutta method with parameters shown in Table 1. The time dependent gain is calculated as $G_t = \exp\left[(g_{\max}(2f-1) - \alpha_{\text{int}})L\right]$, where $L$ represents length of the QDSOA. The equations are first transformed into a retarded frame by $\tau = t - z/v_g$. The spatio-temporal grid size is taken to be 0.05 μm ps.

**Table 1** Parameters used for simulations [22–24]

| |
|---|
| $(\tau_{wR}) = 0.2$ ns, the Spontaneous lifetime in the WL |
| $(\tau_{w2}) = 3$ ps, Relaxation time of electron from the WL to ES |
| $(\tau_{21}) = 0.16$ ps, Relaxation time of electron from ES to GS |
| $(V_g) = 8.3 \times 10^7$ m/s, Group velocity |
| $(\tau_{2w}) = 1$ ns, Escape time of electron from ES to WL |
| $(\tau_{12}) = 1.2$ ps, Escape time of electron from GS to ES |
| $(\tau_{1R}) = 0.4$ ns, Radiative lifetime (spontaneous) in Quantum Dot |
| $g_{max} = 14$ cm$^{-1}$, Material gain coefficient, |
| $\alpha_{int} = 2$ cm$^{-1}$, internal loss |
| Injection current density, $J = 1$ kA/cm$^2$ |
| $L_w = 250$ nm, active layer effective thickness |
| $N_Q = 5.0 \times 10^{10}$, Transparency current density |
| $A_{eff} = 0.75$ μm$^2$, Effective area |

## 5 Working Principle of the XOR Gate

Figure 3 shows the XOR gate based on two QDSTOAD. The destructive port outputs of these two are combined to get the desired XOR gate.

The XOR gate works as follows:

Condition #1. Inputs A and B are both low i.e., '0', output of both the QDSTOADs are zero, resulting a low or '0' output.

Condition #2. Input A is '0', and B is '1', nonzero output from QDSTOAD#1 result in a high output.

Condition #3. If A is '1', and B is '0', nonzero output from QDSTOAD#2 results in a high output.

Condition #4. If both A and B are '1', low output from both the QDSTOADs makes the final output low or '0'.

This explains the operation of the XOR gate.

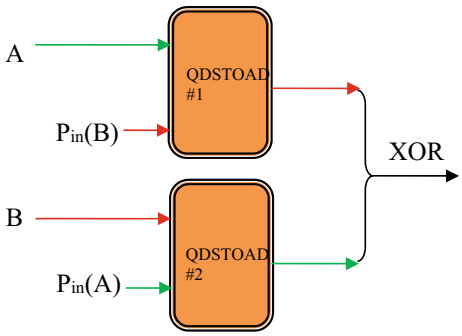


**Fig. 3** QDSTOAD based XOR gate

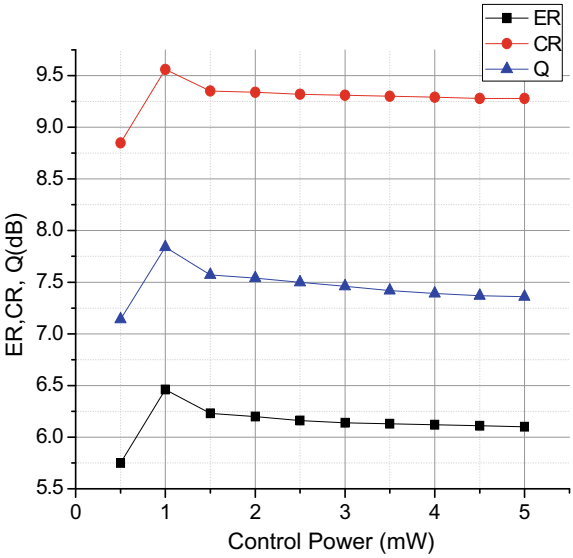


**Fig. 4** ER, CR, and QF versus control power

## 6 Results and Discussions

For the analysis of the QDSTOAD based XOR gate ER, CR, and QF are calculated and plotted with control power in Fig. 4. These parameters are defined as: ER = $10\log(P^1{}_{\min}/P^0{}_{\max})$dB, CR = $10\log(P^1{}_{\text{av}}/P^0{}_{\text{av}})$dB, AM = $10\log(P^1{}_{\max}/P^1{}_{\min})$dB, and $Q = (P^1{}_{\text{av}} - P^0{}_{\text{av}})/(s_1 + s_0)$, where ($P^1{}_{\max}$, $P^1{}_{\min}$, $P^1{}_{\text{av}}$, $s_1$) and ($P^0{}_{\max}$, $P^0{}_{\min}$, $P^0{}_{\text{av}}$, $s_0$) are highest, lowest, average, and standard deviations of high (1) and low (0) states respectively.

It is found that all these parameters show a maximum value for control power of 1 mW. Next simulations use this control power. Figure 5 shows input output bit patterns for the proposed XOR gate. The pattern shows a clear distinction between low and high states of logic in QDSTOAD based XOR gate. The ER, CR, and QF have maximum values of 6.5 dB, 7.8 dB, and 9.6 dB respectively.

The amplified spontaneous emission noise (ASE) has no significant effect on ER, CR, and QF and is clear from Fig. 6. For $N_{\text{sp}} = 0$ to 10, very small variations of ER and CR is found. The QF is almost constant for noise variations. This is one of the advantages of TOAD based devices.

## 7 Summary

All optical QDSTOAD is used to design an XOR gate at operating speed of 1 Tb/s. The analysis of ER, CR, and QF shows overall satisfactory performance of the device. The ASE noise dependence is not significant. The operation can be improved by

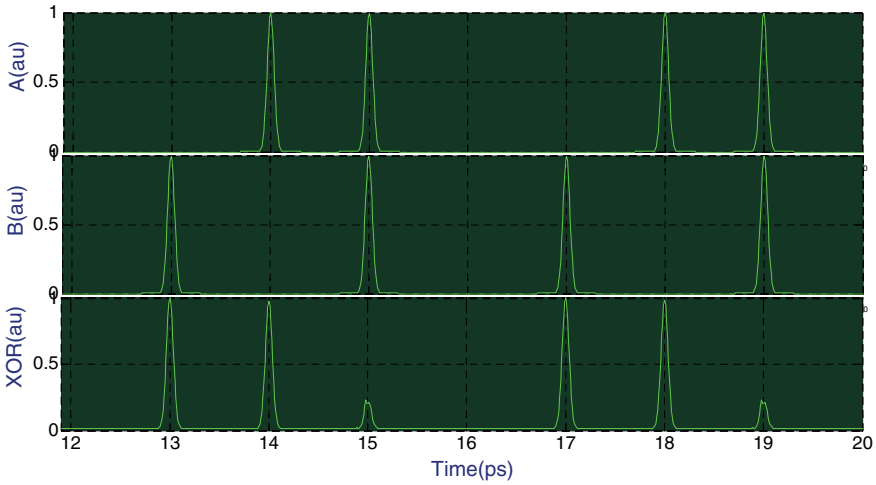


**Fig. 5** Input output bit patterns

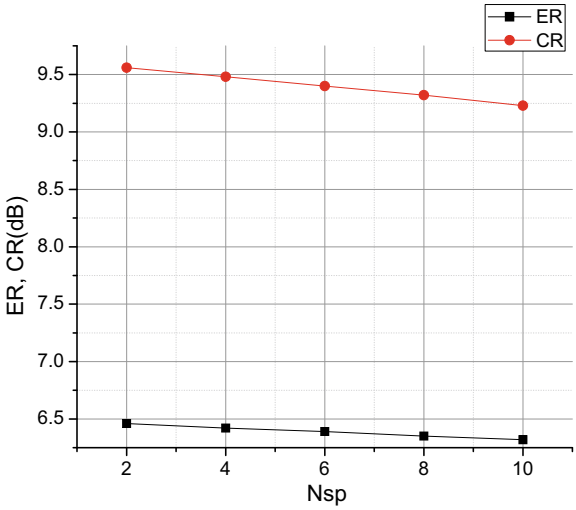


**Fig. 6** Variation of ER, CR with ASE noise factor $N_{sp}$

modifications of the structure of the QDSTOAD described above. The device may be used to construct half adder, full adder, parity checker, and generator in the future.

## References


1. Willner AE et al (2019) All-optical signal processing techniques for flexible networks. J Lightwave Technol 37(1):21–35
2. Udvary E, Berceli T (2009) Multifunctional SOAs in optical communication systems. In: 11th International conference on transparent optical networks, Azores, pp 1–4. https://doi.org/10.1109/ICTON.2009.5185045
3. Ortiz-Cornejo J, Morel P, Azou S, Pardiñas-Mir J (2020) A numerical assessment of an effective envelope-tracking semiconductor optical amplifier design for coherent-optical OFDM transmission. Opt Commun 454:124474
4. Rizou ZV, Zoiros KE (2017) Performance analysis and improvement of semiconductor optical amplifier direct modulation with assistance of microring resonator notch filter. Opt Quant Electron 49:119
5. Maji K, Mukherjee K, Raja A et al (2020) Numerical simulations of an all-optical parity generator and checker utilizing a reflective semiconductor optical amplifier at 200 Gbps. J Comput Electron 19:800–814
6. Sasikala V, Chitra K (2020) Performance analysis of multilogic all-optical structure based on nonlinear signal processing in SOA. J Opt 49:208–215. https://doi.org/10.1007/s12596-020-00608-4
7. Prashant P, Baveja P et al (2013) All-optical semiconductor optical amplifier-based wavelength converters with sub-mW pumping. IEEE Photon Technol Lett 25(1):78–80
8. Stabile R (2017) Towards large-scale fast reprogrammable SOA-based photonic integrated switch circuits. Appl Sci 7:920–922
9. Li Q, Wang Z, Wang H, Cui C, Wu C (2019) Artificial neuron based on nonlinear polarization rotation in a semiconductor optical amplifier. Opt Commun 435:405–408
10. Sugawara M, Ebe H, Hatori N, Isha M (2004) Theory of signal amplification and processing by quantum dot semiconductor optical amplifier. Phys Rev B 69:235332
11. Yazbeek HA, Belyaev P, Tkachenko IM, Hamze MM (2020) Multi-electrode quantum-dot semiconductor optical amplifier as an intensity modulator of signals in optical communication systems. J Phys Conf Ser IOP publishing 1560
12. Flayyih, Al Khursan H (2013) Theory of four wave mixing in quantum dot semiconductor optical amplifiers. J Phys D, Appl Opt 46:122–125
13. Rostami A, Baghban H, Nejad A, Qartavol RM, Saghai HR (2010) Tb/s optical logic gates based on quantum-dot semiconductor optical amplifiers. IEEE J Quant Electron 46(3):354–360
14. Kotb A, Guo C (2020) All optical NOR and XNOR logic gates at 2Tb/s based on two photon absorption in quantum dot semiconductor optical amplifiers. J Quant Electron 52(30):545–549
15. Dimitradou E, Zoiros KE (2013) All-optical XOR gate using single quantum-dot SOA and optical filter. J Lightwave Technol 31(23):3013–3021
16. Dimitradou E, Zoiros KE (2013) On the feasibility of 320 Gb/s all optical AND gate using quantum dot semiconductor optical amplifier based Mach Zehnder interferometer. Prog Electromag Res 50:113–140
17. Komatsu K, Hosoya G, Yashima H (2018) All Optical NOR gate using a single quantum dot SOA assisted an optical filter. Opt Quant Electron 50(131):1–18
18. Salehi MR, Taherian SF (2014) Performance analysis of high speed all optical Subtractor using a quantum dot semiconductor optical amplifier based Mach Zehnder amplifier. J Opt Soc Korea 18(1):65–70
19. Mi SC, Wang HL, Zhang SY, Gong Q (2020) Research of all optical NAND gates based on quantum dot semiconductor optical amplifiers cascaded connection XGM and XPM. Optik 202:163551
20. Lu G, Zhang H, Xing Z, Akahane K, Cheng Z, Liu T, Sakamoto T, Yamamoto N (2020) PAM4 receiver based on quantum-dot SOA preamplifier for short-reach applications. In: Conference on lasers and electro-optics, OSA technical digest (Optical Society of America, 2020), paper JTu2E.18

21. Sokoloff et al (1993) A terahertz optical asymmetric demultiplexer. IEEE Photon Technol Lett 5(7):787–790
22. Mukherjee K (2021) A terabit-per-second all-optical four-bit digital-to-analog converter using quantum dot semiconductor optical amplifiers. J Comput Electron. https://doi.org/10.1007/s10825-021-01675-x
23. Mukherjee K (2020) Tera-hertz Optical Asymmetric Demultiplexer (TOAD) using quantum dot semiconductor optical amplifier. In: Proceedings of EMNSD (2020), Central Institute of Technology, Kokrajhar, Assam, India 15–16 Dec, 2020
24. Mukherjee K, Dutta S, Roy S et al (2021) All-optical digital to analog converter using terahertz optical asymmetric demultiplexer based on quantum dot semiconductor optical amplifier. Opt Quant Electron 53:242–250
25. Dutta NK, Qiang W (2013) Semiconductor optical amplifiers (Chap. 10), 2nd ed. World Scientific, Singapore
26. Wang Y (2009) An all optical XOR logic gate for NRZ based on TOAD. In: PIERS Proceedings, Beijing, China, March 23–27 (2009)
27. Chattopadhyay T (2011) Eliminating the additional input beam in all-optical XOR gate using Terahertz Optical Asymmetric Demultiplexer (TOAD) based interferometer: a theoretical analysis. Opt Commun 122(16):1486–1491
28. Maji K, Mukherjee K (2019) Performance analysis of optical logic XOR gate using dual-control Terahertz Optical Asymmetric Demultiplexer (DCTOAD). In: 2019 Devices for Integrated Circuit (DevIC), 23-24 March, 2019, Kalyani, India, pp 1–4

# Generation, Detection and Analysis of Sub-Terahertz Over the Air (OTA) Test Bed for 6G Mobile Communication Use Cases


**Rabindranath Bera**

**Abstract** After successful deployment of 5G mobile, the 6G mobile research works have been initiated worldwide. In the year 2019, 6G Summit was organized at Finland. This ignites the industries and academia further to extend their R&D efforts towards 6G. Presently they are exploring the use of D-Band with radio carrier frequencies between 110 and 170 GHz for 6G mobile communications and automotive radar applications. Rohde & Schwarz and IHP started to build their first R&D Test BED with D-band frequencies for automotive radar and 6G use cases. The similar 5G-6G-IoT Wireless Solutions using Sub-Terahertz and Millimetre wave Radio was also initiated by the author and his team members both at Calcutta University and Sikkim Manipal University, India. The radio wave propagation study and the system development by the author and his group are subdivided into two categories. Category 1 of system development with radio carrier frequencies less than 100 GHz are useful for 5G IoT use cases as formulated by 3GPP in release 15/16. Category 2 with radio carrier at 140 GHz in Sub-Terahertz band will be useful for 6G-IoT use cases. This chapter will focus on discussion for category 2 of system development by the author. This will include 6G mobile communication in the form of 6G Test Bed at 140 GHz of carrier and also active remote sensing in the form of radar at 140 GHz. Thus, the Sub-Terahertz OTA 6G Test bed developed by the author is highly useful in 5G-6G-IoT Wireless Solutions. In future, the solution in the form of useful products will help our society towards a smarter world.

**Keywords** OTA · LNA · Sub-Terahertz · UM-MIMO · FBMC · OFDM · PAPR · PMCW · RCS · SISO · MIMO · COMP

R. Bera (✉)
Department of Electronics & Communication Engineering, Sikkim Manipal Institute of Technology, Sikkim Manipal University, Majitar, Rangpo, East Sikkim, Sikkim 737136, India



A. Acharyya et al. (eds.), *Generation, Detection and Processing of Terahertz Signals*, Lecture Notes in Electrical Engineering 794,
https://doi.org/10.1007/978-981-16-4947-9_8

## 1 Introduction

The next generation of future mobile cellular networks is 6G. It has the capacity to support new and unknown services having changing requirements. There should be utilization of 6G in the real world by the year 2030. New services are holographic and critical communications with swift response. In 6G there is an opening for Terahertz spectrum [1]. In Industry 4.0, industrial automation requires 0.1 ms latency at 1-10-9 reliability [1]. 6G will provide a connection to everything having an intelligent connection which includes centralized intelligence (Forward), local Intelligence (Access) and Terminal Intelligence (Data).

In 6G, a new fabric of digital services are enabled which includes human senses and ambient data in the fusion of virtual and physical worlds [2]. In 5G, there is a requirement for time synchronization to microseconds and low latency levels but it will reach within 6G [2]. To shift from 5 to 6G, there is a need for a cross functional programme of technology and scientific research which includes 4 Dimensional video, Large intelligent surfaces, Direct satellite to user through beam forming satellite, Ultra (Massive) antenna arrays for distributed (hybrid) MIMO, exceptionally low latency Artificial Intelligence (AI) and Ultra high accuracy, Terahertz sensing [2].

The update of past trends of 5G will be 6G which consists of densification, higher rates, massive antennas and emerging trends. These include new services and recent revolution in wireless devices, e.g. smart wearable, implants, Extended Reality (XR) devices [3]. The driving trends of 6G technology [3] includes the following:

- More bits, more spectrum and more reliability
- From Areal to Volumetric spectral and Energy Efficiency
- Emergence of smart surfaces and environments
- From Self Organizing Networks (SON) to self-sustaining networks
- Convergence of communications, computing control [1], localization and sensing (3CLS).

The 6G Service classes [3] include:

- Mobile broadband Reliable Low Latency Communication
- Massive URLLC (Ultra Reliable Low Latency Communication)
- Human-centric Service
- Multi-purpose 3 CLS and Energy services.

Enabling of MBRLLC (Mobile Broadband Reliable Low Latency Communication) and mobility management at high frequency millimetre wave bands and beyond Terahertz is the first step towards 6G [3]. In 6G, there are transitions from “Connected Things” to “Connected Intelligence”. There are various features in 6G which are given below by the following points [4]:

- Very high data rates up to 1 Tb/s
- Very high energy efficiency with the ability to support battery free IoT devices.
- Massive low latency control (less than 1 ms end-to-end latency)

- Very broad frequency bands (73–140 GHz and 1–3 THz)
- Connected intelligence with machine learning capability [1].

To make the communications reliable and efficient, having the combination of channel and hardware impairments, a massive number of design parameters are needed to be controlled and optimized [4]. Hardware impairments include amplifier distortion, local oscillator leakage and fading, interference, etc. are channel impairments.

The ability of 6G technology is the connection of everything, integration of different technologies having applications, support of holographic, haptic, space and underwater communication. In 6G, there will be the development of Internet of Everything extending the Internet of Things (IoT) in 5G [5]. In 5G, there is introduction of Artificial Intelligence (AI), automation and smart cities. In 6G, these technologies are integrated. The crucial role in 6G is the Terahertz band which ranges from 0.1 to 10 THz [5]. In Terahertz band, there will be the support of the development of minuscule cells in nanometre to micrometre dimensions delivering high speed communications having the coverage area up to 10 m and the "Internet of Nano Things" will be created [5]. The new proposal for 6G communication is Unmanned Aerial Vehicles (UAV) [5]. In 6G, the new umbrella term is Extended Reality (XR) which includes Virtual Reality (VR), Augmented Reality (AR) and Mixed Reality (MR). Extended Reality (XR) is the combination of Virtual and Real worlds. For Extended Reality (XR), 6G is very useful, supporting efficient connectivity, high data rate, high reliability, high resolution and low latency [5]. There will be the usage of spectrum sharing which allows the users to facilitate the sharing of the same spectrum by solving the problem of spectrum requirements in 6G. Terahertz band provides high data rates, high frequencies and high antenna gain compensating high path loss of Terahertz propagation. For Terahertz band communication, the implementation of new modulation and coding techniques is mandatory. For the implementation of new modulation and coding techniques, there is a need for the design of new transmitters and receivers which operate on high frequency band.

The requirements in 6G wireless communication include broadband frequency band, opportunistic data rate, opportunistic latency, massive Machine Type Communication (mMTC), super reliable Machine Type Communication, self-X network, super precision operating system, super precision positioning, scalability, super Energy Efficiency, connectivity in 3 Dimensional coverage, integration with satellites and Software Defined Networking (SDN) [6]. Here Self-X means Self Learning, Self Reconfiguration, Self Optimization, Self-Healing, Self Organization, Self Aggregation and Self Protection [6]. In 6G wireless communication, human-to-human, human-to-machine and machine-to-machine will be enabled in an intelligent way. In 6G mobile communication, there should be the expectation of casting the high technical standard of new spectrum and energy efficient transmission techniques [7]. The expectation of 6G mobile communication is the development of the existing wireless technologies and achievement of the enhanced system performance [7, 8]. The data rate in 6G will be from 100 to 1000 times faster than the 5G technology. In 6G networks, hundred gigabits per second will be upgraded to Terabit per second.

It is possible after the use of multi-band high spread spectrum, i.e. combination of the use of 1–3 GHz band, millimetre wave band (30–300 GHz) and Tera Hertz band (0.06–10 THz). In comparison to 5G, there is connection of trillion-level objects in 6G wireless technology. In 6G, the frequency will be above 100 GHz, new radio will validate little explored frequency sources such as millimetre wave and Terahertz bands to overcome spectrum scarcity and provide wideband width from hundreds of megahertz to several gigahertz and even to Terahertz. The big data-driven network is 6G as it is expected to support high data rates with heterogeneity in applications, devices and networks. Some of the physical layer security techniques in 5G can be utilized in 6G networks such as low-density parity check (LDPC)-based secure massive MIMO, secure millimetre wave techniques is suitable for UM-MIMO and THz band applications.

In comparison to 5G, there is an achievement of superior performance and more performance metrics. In 5G, the peak data rate is 20 Gbps, while in 6G, the data rate will be ranging from 1 to 10 Tbps. The spectrum efficiency will increase 3 to 5 times than the previous stage [9]. There is an increase in connection density 10–100 times according to the use of heterogeneous networks, diverse communication scenarios, large number of antennas and wide bandwidth [9]. For specific cases, the latency will be less than 1 ms. The energy efficiency will be 10 times better in comparison to 5G. Here the capacity should be 10,000 times of the 5G system. The connection density is 107 devices/km$^2$.

## *1.1 6G Waveform*

Radio wave propagation through wireless channels and its channel impacts are severe in degrading the performance of mobile communication. To restore the performance from channel impairments due to wave reflection, scattering and other multipath phenomena, LTE based 4G mobile waveform is doubly modulated. The 1st modulation is preferably QAM modulation where the data is converted to complex symbol having In-phase and Quadrature components. Multi Carrier Modulation (MCM) is a very popular 2nd level modulation technique after QAM based modulation which will subdivide the broadband symbols into several narrowband sub carrier to carry the symbols further and thus is highly useful in compensating channel impairments. MCM has evolved further into two major waveforms upgradation namely (i) OFDM (ii) FBMC. OFDM is targeted for 4G/5G mobile whereas FBMC for 6G [10].

OFDM is facilitated with orthogonality in subcarrier which is too difficult to maintain at the receiver leading to the problem of 'loss of orthogonality'. It results in carrier offset and a particular sub carrier at the receiver is deviated from the peak response. As a result, signal reception of the particular sub carrier has deviated from peak reception and additional leakage/interference from the neighbouring subcarrier are also getting into the received signal. Thus OFDM has following disadvantages:

(i) Imperfect synchronization causes loss of orthogonality which degrades performance.
(ii) Signal is the sum of a huge number of subcarriers with large PAPR, this leads to amplifier inefficiency.
(iii) Subcarrier inter-modulation must be reduced in order to maintain a low noise floor both in and out of band.

The above OFDM problems can be improved by (i) introducing window function that roll-off gently after OFDM modulator and (ii) by incorporating filter bank before the IFFT process at the transmitter and putting the similar filter bank pair within the receiver. Thus FBMC waveform is evolving as 6G waveform having all the three folded solutions to basic OFDM problems.

## *1.2 MC Methods [11]*

**Method 1: Filtered Multitoned (FMT)** [12]: FMT is similar to GFDM (Generalized Frequency Division Multiplexing) where at the transmitter, QAM symbols are passed through up sampler, raised cosine filter banks before the IFFT process for sub carrier generation with subcarrier bands having no overlap. $H(f)$ and $H^*(f)$ are a pair of root-Nyquist filters used in the transmitter and receiver respectively.

**Method 2: Staggered Modulated Multitoned (SMT)** [13]: SMT is further improvement in OFDM process where consecutive subcarriers are allowed to overlap in time staggered fashion with maximum time offset of T/2 [T being the Frame period]. By this process, complex symbol feeding to the OFDM IFFT process will be Offset QAM instead of QAM. The spectral efficiency is thus improved to a great extent. Here use of $H(f)$ and $H^*(f)$ guarantees separation of data symbols at the receiver.

**Method 3: Cosine Modulated Multitoned (CMT)** [14] uses pulse amplitude modulated (PAM) symbols instead of Offset QAM symbols thereby, its use cases are majorly restricted to DSL (Digital Subscriber Line) based cable or fibre optic communication instead of wireless communication. CMT also allows overlap of adjacent bands. Here also $H(f)$ and $H^*(f)$ guarantees separation of data symbols at the receiver.

Thus, OFDM is limited to 4G/5G mobile waveform uses but FBMC with its guaranteed data recovery features is highly useful for 6G mobile communication. 6G is also looking for further waveform upgradation and new scheme of waveforms. The Overall improvements at the physical layer of 6G using further technological innovations can be compared with reference to 5G technologies and use cases and tabulated as in the following Table 1.

Following a similar concept as in Table 1 towards the allocation of Frequency band for 6G mobile, Rohde & Schwarz and IHP started to build their first R&D Test BED with D-band frequencies for automotive radar and 6G use cases [15].

**Table 1** Difference between 5 and 6G at the physical layer

| Features | 5G | 6G |
|---|---|---|
| Frequency band | • Sub 6 GHz<br>• mm wave for fixed access | • Sub 6 GHz<br>• mm wave for mobile access<br>• Exploration to THZ band (110 to 170 GHz) [D Band]<br>• Non-RF bands (Optical, VLC, etc.) |
| Data rate | 20 Gbps (Maximum) | 1 Tbps |
| End to end latency | 5 ms (Radio: 1 ms) | Less than 1 ms (Radio: 0.1 ms) |
| Waveform | CP-OFDM with windowing | FBMC |
| Smart antenna | • MIMO<br>• Beam formation | • Massive MIMO<br>• Beam formation |
| Use cases | • eMBB<br>• URLLC<br>• mMTC | • MBRLLC<br>• mURLLC |

## *1.3 Use of D Band Sub-Terahertz Wave for Radar Based Sensing in Autonomous Vehicles*

Recently, the Market and Technology trends of 'radar and wireless for automotive' is reviewed by M/S Yole [12]. SAE, the Society of Automotive Engineers, a US based professional association and standard developing, has evolved six levels of driving automation from assisted drive to automated drive. More numbers of sensors including automotive radar are required to be mounted on vehicles for automotive drive. Radar should have low cost, size, weight and power (CSWaP) capabilities with highest resolution enabling a chipset for automotive radar use cases whose antenna beams will surround the vehicles for 360° as shown in Fig. 1 with 120° radiation coverage by each radar and full coverage of 360° using 4 MIMO radars mounted at the four corners of a vehicle. Radar development has the challenges like (i) Super resolution using more than 1 GHz of radar bandwidth and also (ii) ensuring very low false alarm. 2018–2025 Radar and wireless technology review for automotive forecasts that radar market expected to almost double by 2025 as compared to 5G/6G based connectivity market [16].

## *1.4 Need for Integrated Radar and Communication System*

Applications of Radar, developed mainly for military purposes, has now expanded to remote sensing, vehicular applications like Automatic Cruise Control, Autonomous Emergency Braking, etc. and is usually operational at the millimetre wave frequency range [16]. On the other hand, the new innovations in wireless communications have made the carrier frequencies almost inadequate. So there is a need to move towards

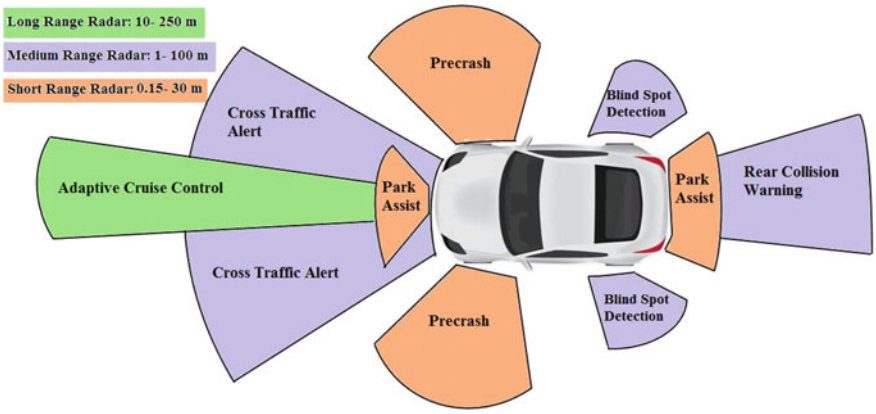


**Fig. 1** Automotive radar use cases whose antenna beams will surround the vehicles for 360° for safety operation

millimetre wave frequency bands allocated for Radar systems, which is still not fully utilized [17]. Also, there is a need to limit the excess electromagnetic emissions. Thus coexisting Radar and communication systems on mm-wave frequency band is quite essential. Such integrated system provides effective utilization of frequency band, smaller size of hardware which is essential for implementation on a vehicle and thus lowered cost [17]. Recently, various industrial and academic research is being conducted regarding the convergence of sensing and communication systems similar to U. S. DARPA (Defense Advanced Research Projects Agency) [16]. The main objective of Autonomous vehicles is to ensure safe and reliable driving with reduced accident rates and they use sensors like Radar and communication techniques for obtaining information about the road scenario. Main challenges for this joint system is the waveform design and fulfilling performance criteria of both communications and Radar functionalities. The two technologies can coexist in various ways as explained next.

## *1.5 Using Same Frequency Spectrum*

In this method, transmitters of Radar and communication operate in the same frequency band. An integrated design of Radar waveforms and codebook of communication system is developed to maintain the performance criterion of both coexisting systems [16]. In order to minimize mutual interference, transmit waveforms are optimized which will increase the signal to interference and noise ratio (SINR) at each receiver. Another method to minimize interference, is done at the Rx by exchanging channel response and SINR with the transmitter, to maintain maximum SINR for both Radar and communication receivers [18].

## 1.6 Coexistence Using Cognitive Characteristics Page

In this case, either Radar or communication is prioritized and pilot signals are used for channel state estimation and feedback this information to the subsystems [12]. Algorithms having lower computational complexities are required to design cognitive waveforms. Machine learning is beneficial to learn about the frequency spectrum, determining underused spectrum and using it [18]. This can also help to classify Radar targets, recognize automatic waveform and antenna characteristics.

## 1.7 Coexistence by Sharing Same Hardware

No spectrum sharing is done for this joint Radar communication system. This is mainly based on different methods of information embedding into Radar waveforms and communication waveforms performing Radar functions. Embedding information into Radar waveforms include methods like phase modulation based or, amplitude modulation based [16, 19]. Communication waveforms can also be used to perform Radar functionalities. The 802.11ad standard adopted for 5G wireless systems and millimetre waves in 28 and 60 GHz bandwidths can be utilized for Radar applications.

## 1.8 Dual Function Radar Communication Systems (DFRC)

In this co-design method, the two subsystems share the same hardware resources and same spectrum. So this system performs Radar and communication functions with common transmit and receive units, same bandwidth and joint dual-function waveforms [20]. DFRC can be useful in autonomous vehicles that need to obtain information of a rapidly changing scenario.

In Fig. 2 [21], the Blue coloured source vehicle transmits 6G signal to the pink coloured target vehicle. The target echo generated is used by source vehicle to derive the range, velocity and angular position of the target vehicle. Also, it shows that vehicle-to-everything (V2X) communication is an enabler for integrated Radar and communication. This V2X denotes 6G communication between source vehicle and other vehicles, or pedestrians or roadside units.

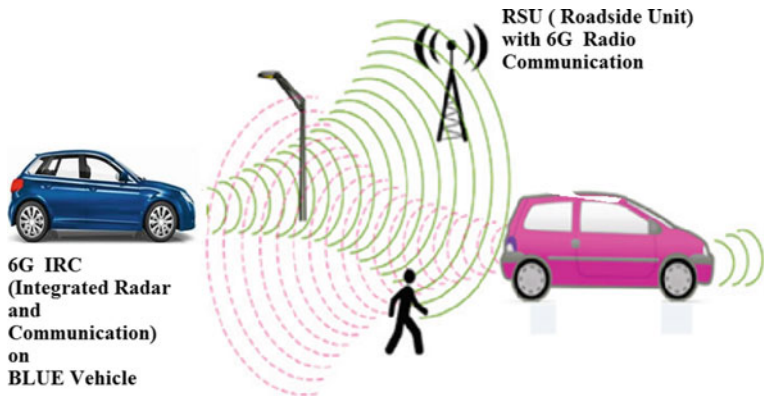


**Fig. 2** A 6G Integrated Radar and Communication (IRC) system on Vehicle where the system is sensing and Communicating at the same time and at the same frequency

### *1.9 Formulation of Research Works by the Author*

With the above reviews on recent trends on 6G based next generation mobile cellular networks and associated technologies towards a smarter world and vertical industries, the author and his group members are highly motivated and engaged in indigenous system development ranging from 10 to 140 GHz operational radio frequency, financially supported by Govt. of India since the year 1988. The Radio system development includes (i) Communication systems (ii) Radars (iii) Radiometers and is really a challenging activity so far a developing country like India is concerned. Present use cases of the above systems are 5G-6G-IoT applications for industrial IoT, Autonomous Electric Vehicles with 5G/6G and automotive radar and other areas of remote sensing. Further, they are working towards the upgradation of the above systems to 220 GHz and Terahertz region to cater for new use cases in 6G area. The above activities are similar to NYU WIRELESS activities [22]. NYU WIRELESS is a leading research centre that is pursuing 6G wireless and beyond with cutting edge work in propagation measurement and modelling above 95 GHz.

## 2 Sub-Terahertz Over the Air (OTA) Test Bed

The author is further motivated by the above 6G_IRC system mounted within the smart vehicle where their research works on (i) Communication system, (ii) Radar may be integrated into an autonomous vehicle as shown in Fig. 2. Presently, they are intended to develop the 'sub-terahertz over the air (OTA) test bed using 140 GHz radio' and utilize the same for the use cases as depicted in Fig. 3.

Therefore, the Chapter is organized as follows. The present status of 6G wireless, radar and integrated radar and communication with both millimetre wave and sub

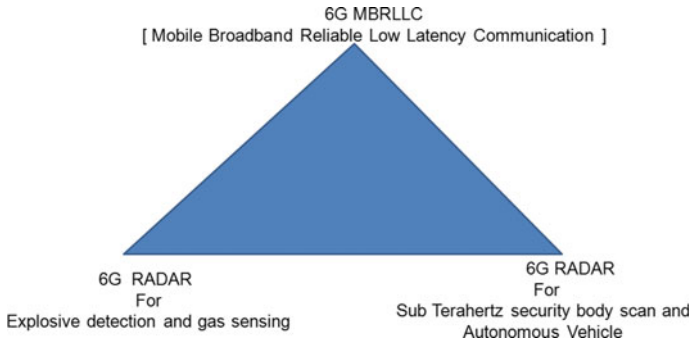


**Fig. 3** Author's Triangular use cases of 6G TEST BED using 140 GHz radio

terahertz wave radio is reviewed in the introductory article 1. The author and his team members both at University of Calcutta as well as Sikkim Manipal University are fully engaged in 'Millimetre wave and Sub Terahertz wave propagation studies and system development' since the year 1988 onwards. This will be detailed in article 2. Sub article 2.1 will discuss Generic Sub-Terahertz Ove The Air (OTA) Test bed for 6G mobile communication use cases and radar based sensing uses. The hardware architecture will be discussed along with the test bed photos. The Use cases of the Test Bed will be discussed in sub article 2.2. The four specific problems are highlighted and as solution, four experiments are conducted using the Test Bed which are tabulated in Table 1. Sub article 2.3–2.6 will elaborate the four experiments conducted. Finally, the chapter will be concluded in article 3.

## *2.1 Architecture of the Test Bed*

The Author's test bed as shown in Fig. 4a consists of a mixed signal generator MXG N5182 (Mixed signal Generator). This is used to produce a wideband IF cantered at 2 GHz with a modulation occupied bandwidth of approximately 120 MHz MXG composed of (i) Digital section (ii) Analog RF section up to frequency of 3 GHz. The Digital section is fully programmable using Keysight Systemvue software and any waveform of choice like FBMC, CP-OFDM communication waveform and also PMCW radar waveform can be easily generated. One D-Band up converter is used for up conversion of 2 GHz IF to RF, converting to a RF frequency range at 140 GHz. The Local Oscillator is produced by another vector signal generator set at 23 GHz. The 23 GHz LO is multiplied by a factor of 6–138 GHz, so we have a 2 GHz IF coming in. It's being mixed with a 138 GHz LO to produce an up converted product at 140 GHz. It is amplified and filtered using an amplifier and filter and then transmitted over the air with a horn antenna.

The transmitted signal is picked up by another horn antenna on the receive side. It is down converted back down to an IF using a down converter. The IF is then

fed into a Vector signal analyzer for reception and analysis of the received signal. The IF signal is digitized, analyzed and demodulated using Keysight Vector Signal Analysis software 89600. We have the 128 QAM received constellation diagram and extremely wide bandwidth of 120 MHz measured on VSA using over the air mode of more than 10 m distance. Lots of further challenges like source power, power amplifier, smart antenna, LNA and remedy to avoid propagation loss are involved for the increase of the distance. The Photograph of the Test Bed is shown in Fig. 4b, c, d, where Indoor Unit (IDU), Outdoor Unit 1 (ODU_1) and Outdoor Unit 2 (ODU_2) are shown separately.

The IDU part can be integrated inside an autonomous vehicle thus behaves as GREEN VEHICLE EMULATOR as shown in Fig. 4b. A metallic flat plate as the part of ODU_1 unit as in Fig. 4c will behave as Red Vehicle EMULATOR as RADAR target on road. Also placing another Communication Terminal as ODU_2 will behave as RSU (Roadside Unit) 6G V2X communicator (Fig. 4d). To achieve this future ultimate objective of 6G IRC mode of operation, the initial present work is mainly focussed on only (i) 6G RADAR mode (ii) 6G Communication mode separately with future extension to 6G_IRC (Integrated Radar Communication).

## *2.2 Use Cases of the Test Bed*

Presently, the test bed is intended to be used for three use cases as mentioned in Fig. 2 namely.

(i) USE CASE 1: 6G radar for security body scan and autonomous vehicle
(ii) USE CASE 2: 6G radar for smoke/fog sensing
(iii) USE CASE 3: 6G MBRLLC (Mobile Broad Band Low Latency Communication).

All the above use cases are experimented by the author either in simulation or in actual hardware emulation as discussed in detail in subsequent articles. Those experiments are conducted to solve the following highlighted problem. The problems and the solutions are tabulated in Table 2.

## *2.3 Hardware Experiment EXP 1 Using 6G Radar Test Bed for Motion Detection*

**Vibration Analysis and Target Identification using 140 GHz Radar**: Recently, TeraSense launched a product 'Terahertz security body scanner' [23] for effective body scanning for any hidden metallic objects like bomb, hand rifles and others which is too useful in airport entry security zone. While passing through the security area having motion of human, the doppler spectrum is more useful in analyzing the hidden metal within the body. In effect, it is a vibration analysis using Sub-Terahertz system.

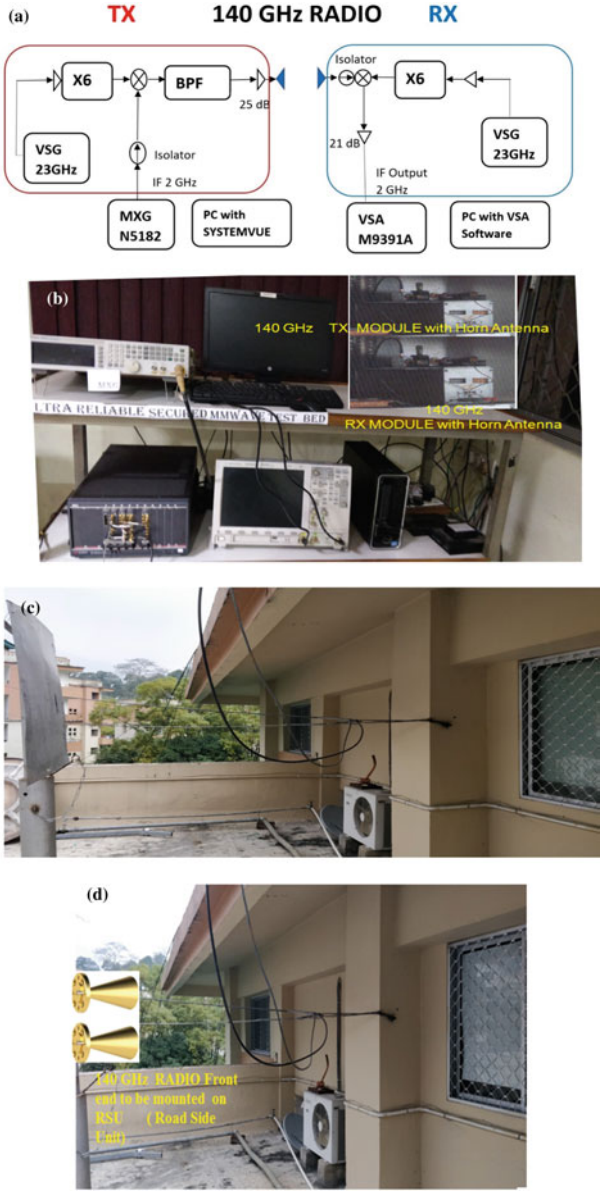


**Fig. 4** **a** Generic Block Diagram of 140 GHz Test Bed to be used as 'RADAR or 6G Communicator'. **b** Indoor Unit (IDU) of the Test Bed with 140 GHz TRANCEIVER EMULATING 'GREEN VEHICLE with 6G RADAR' on road of Fig. 2. **c** Outdoor Unit 1 (ODU_1) of the Test Bed with a FLAT Metal Plate EMULATING 'RED VEHICLE' on road of Fig. 2. **d** Outdoor Unit 2 (ODU_2) of the Test Bed with another 140 GHz Radio EMULATING 'RSU … Road Side Unit' on road of Fig. 2

**Table 2** The problems and the solutions utilizing author's Test BED

| Problems | Solution | Remarks |
|---|---|---|
| Problem1: security body scan of a Human passing across the Security Zone of an airport for motion detection | USE CASE 1: 6G radar for motion detection | Hardware experiment EXP 1 conducted at Author's premises using the test bed |
| Problem2: use of 6G radar in autonomous vehicle for road vehicle detection | USE CASE 1: 6G radar for road vehicle detection | Simulation experiment EXP 2 is conducted using Systemvue software |
| Problem3: use of 6G radar for smoke/fog sensing | USE CASE 2: 6G radar for smoke/fog sensing | Hardware experiment EXP 3 conducted at Author's premises using the test bed |
| Problem4: use of 6G MBRLLC | USE CASE 3: 6G MBRLLC | Simulation experiment EXP 4 is conducted using Systemvue software |

A similar experiment is also conducted by the author to emulate a metal detection and also its vibration analysis using 140 GHz radar. Figure 5a is the time domain behaviour of the backscatter signal from the metal scale when a 12 inch STEEL scale is vibrating only once in front of 140 GHz radar. A symmetry centred around the STATIC Position of the metallic scale with diminishing amplitude in received waveform is noticed as the scale was vibrated only once. The Metallic Steel scale is detected easily by the radar and vibration analysis is computed over the received data. Both the time and frequency domain plots are shown. With proper calibration, the size (RCS) of the metal scale can be measured accurately. The frequency domain plot gives the vibration frequency of the motion very accurately. Thus, using vibration analysis with proper calibration of the radar return, the exact metal is hidden within the body of a human while passing through the security area of the airport can be easily located.

## *2.4 Simulation Experiment (EXP 2) Using 6G Radar Test Bed for Road Vehicle Detection*

**Phased MIMO Automotive Radar**: In line up with success story of autonomous driving of google self driving car, SAE (Society of Automotive Engineers, a standardization body) has formulated 6 levels of driving automation. This autonomy in driving is being realized using different kinds of sensors like radar, lidar, camera and others. Radar specifically the mm-wave radars plays one of the major roles in such sensing activities. The 76–81 GHZ RF frequency is being used by Short range radar at present and putting four such MIMO radars at the four corners of the vehicle will help a lot in avoiding collision between road vehicles. In effect, the vehicle is protected by a radiation shield surrounding it. The radars will measure the distance

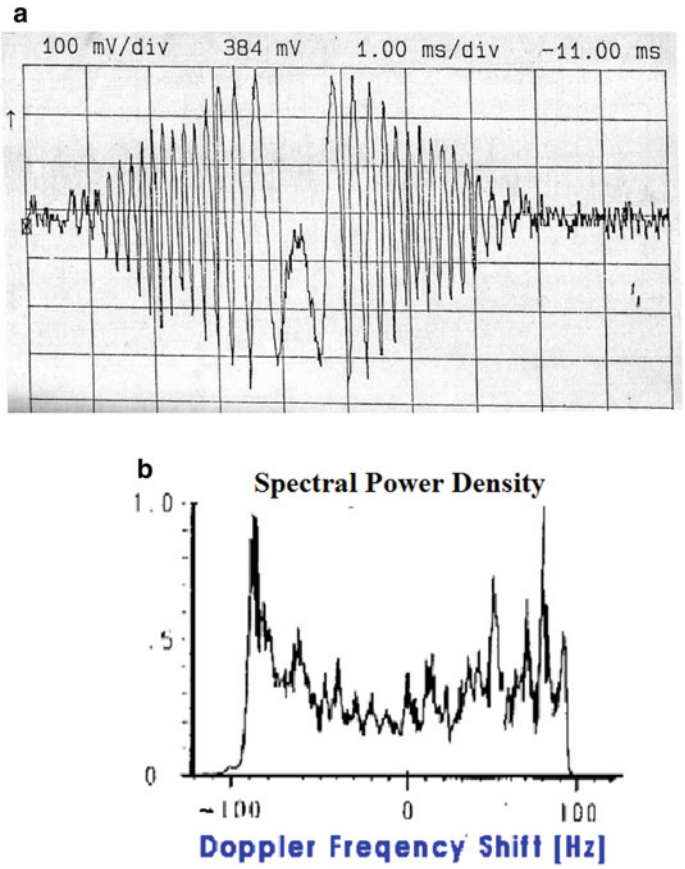


**Fig. 5** **a** Doppler Effects in Time domain on 140 GHz Radar return for Vibration Analysis of a 12 inch STEEL Scale with gradually diminishing amplitude. **b** Doppler Effects in Frequency domain on 140 GHz Radar return for Vibration Analysis

of separation between the vehicles and their velocities and also angular orientation. Those measurements will help vehicle to decide its control activities through the Actuators. So, here is the huge requirements of MIMO radars for autonomous vehicles and also SoC (System on Chip) for MIMO radars for performance improvement and lowering the cost of radars [24]. Successful attempts to develop SoC towards a $2 \times 2$ MIMO short range radar for autonomous vehicles are there and soon will be available commercially [25]. Those radars are governed by the following two formulae:

SNR at the radar receiver for SISO case for a target vehicle having radar cross section $\sigma$ at distance $R$ is given by

$$\text{SNR(SISO)} = \text{PTX} \cdot \text{GTX} \cdot \text{GRX} \cdot GP \cdot \lambda 2 \cdot \sigma / ((4\pi)3 \cdot R4 \cdot kB \cdot T \cdot BN$$

$$\cdot N\mathrm{FRX} \cdot \mathrm{LTX} \cdot \mathrm{LRX}), \tag{1}$$

where the variables are their usual meaning as per standard radar range equation. For the MIMO case when NTX and NRX are the number of transmitters and receivers, Eq. 1 will be modified as,

$$\mathrm{SNR(MIMO)} = \mathrm{SNR(SISO)} \cdot \mathrm{NTX} \cdot \mathrm{NRX}. \tag{2}$$

*Problem Definition: Definition*: 360° sensing from a vehicle for autonomous driving on road enabling safety cocoon.

*Solution Strategy*: MIMO radar sensors are to be put to have full coverage of 360° electromagnetic radiation and shielding of the vehicle.

*Objective*:

- Simulation of Automotive 4 * 4 MIMO Radar based on PMCW (Phase Modulated Continuous Wave) waveform at 140 GHz.
- The range and velocity of target vehicles will be measured.

*Detailed Methodology*: Keysight Systemvue is an electronic design automation (EDA) environment for electronic system-level (ESL) design which is used by the designer both for simulation as well as emulation of electronic systems like 5G/6G communication system, WiFi systems, Satellite systems, radar systems and others. The Systemvue software is a part of the Author's Test Bed at 140 GHz. Its Library is enriched with parts that are 'drag and drop' into the workspace. The simulation model is required to be built on the workspace which is composed of several parts and their interconnection. After proper selection of the parameters of the workspace variables, the model can be run for analysis. The different performances of the radar system like target range and velocity measurement, multiple target detection using CFAR algorithm can be measured and displayed on 2D/3D graphs for visualization. Following the above approach, this particular model is built up as shown in the Fig. 6.

*Workspace Description of the Simulation Mode*: This model is based on typical 3-layer radar simulation architecture. The baseband waveform design is based on PMCW, with 4 Tx channels modulated by different codes defined by Pseudo-random coding. The aim is to realize radar in complicated interference scenarios. With 4 Rx channels, the range and velocity of two target vehicles are conducted.

*Results*: Coded MIMO radar is too useful for improving radar performances. Transmit code of 140 GHz MIMO radar is recorded and is shown in Fig. 7. Two targets on road are detected using CFAR algorithm. Target range and velocity are measured using 140 GHz MIMO radar and is plotted and also shown in Fig. 8.

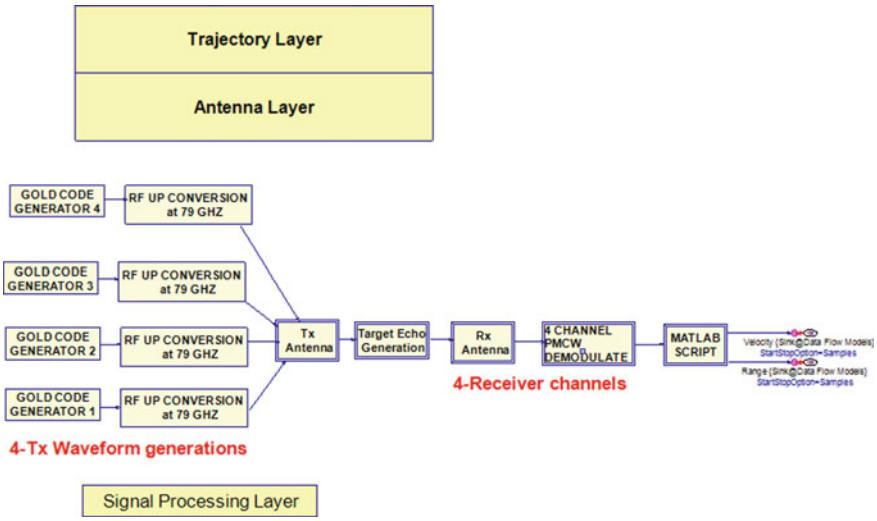


**Fig. 6** Systemvue simulation model of 140 GHz MIMO radar

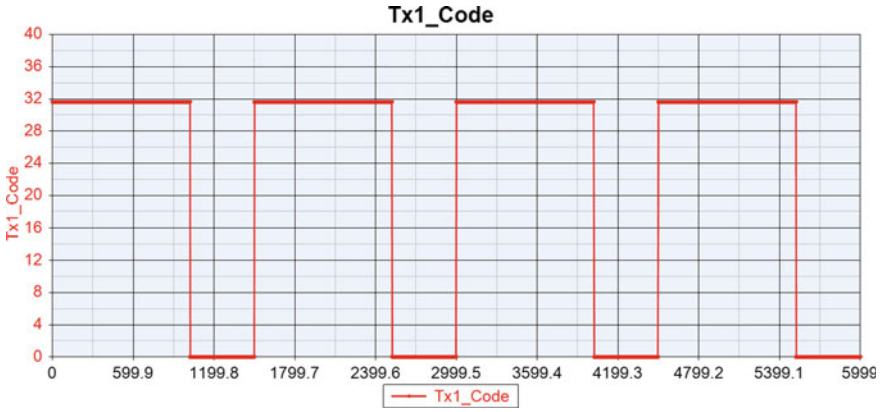


**Fig. 7** Transmit code of 140 GHz MIMO radar

## *2.5 Hardware Experiment (EXP 3) for Gas, Smoke and Fog Detection Using 140 GHz Radar Test Bed*

Millimetre wave and Terahertz waves are also best usable in sensing for (i) Air quality detection [26], (ii) Personal health monitoring system [27], (iii) Gesture detection and touchless smartphones [28], (iv) Explosive detection and gas sensing [29].

Exploiting, the wavelength of the sub terahertz 140 GHz radio with wavelength comparable to fog particle size, the fog and smoke detection is highly efficient and

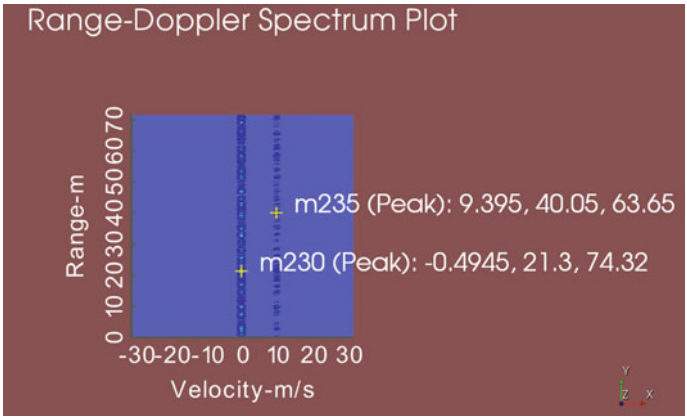


**Fig. 8** Target range and velocity detection of two vehicles on road using 140 GHz MIMO radar

useful for 140 GHz radar. With the same motivation, author has conducted experiments to detect the integrated fog/smoke of the atmosphere using the same radar set up at 140 GHz. This is a new innovation by the author as earlier they evolved radio systems having frequencies up to 100 GHz and fog detection was too inefficient by radio with frequency less than 100 GHz. The Author's Generic Test Bed configured for 140 GHz radar in BISTATIC RADAR mode which transmits 140 GHz radiation into the atmosphere and back scatter signal from atmospheric fog/smoke was received by 140 GHz receiver during winter. The variation of fog/smoke intensity was recorded as shown in Fig. 9 and the recorded pattern has five interesting regions

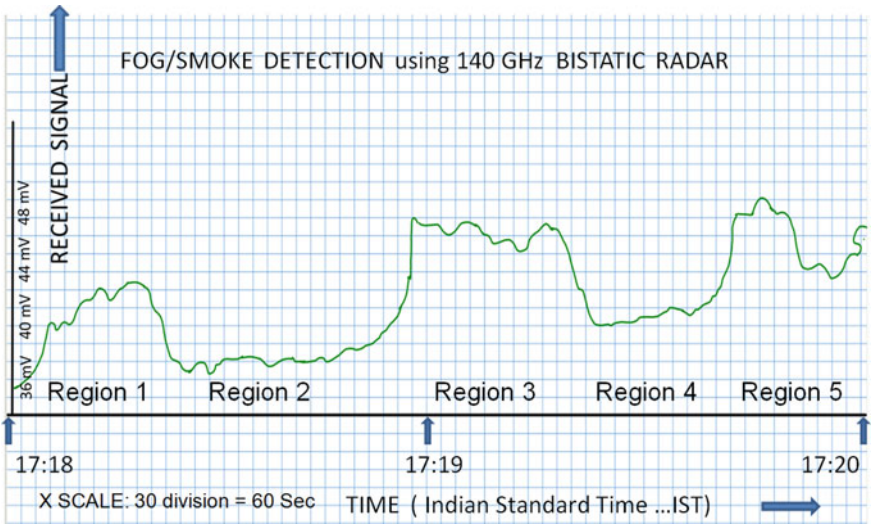


**Fig. 9** Fog/Smoke detection using 140 GHz Radar

**Table 3** Recorded Fog/SMOKE events detected by 140 GHz Radar

| Regions with voltage variation (mV) | Local Time (hr:min:sec) | Types of response | Remarks |
|---|---|---|---|
| Region 1: 36 to 41 | 17:18 to 17:18:22 [11 smallest division] | Gradually increasing during Build-up stages of Fog | FAST rise in FOG density |
| Region 2: 37 | 17:18:22 to 17:18:50 [14 smallest division] | Steady value | (i) Value almost constant at 37 mV (ii) SLOW rise in FOG density |
| Region 3: 37 to 42 with ripples | 17:18:50 to 17:19:22 [16 smallest division] | Gradually increasing during Build-up stages of Fog | FAST rise in FOG density |
| Region 4: 38 to 38.5 with ripple | 17:19:22 to 17:19:42 [10 smallest division] | Gradually increasing during Build-up stages of Fog | SLOW rise in FOG density |
| Region 5: 38 to 42.5 | 17:19:42 to 17:20:00 [9 smallest division] | Gradually increasing during Build-up stages of Fog | FAST rise in FOG density |

of operation during building up of Smoke/Fog at winter evening. The result is also tabulated in Table 3.

The same experiment is also useful in detecting any extraneous gas in a factory environment and IOT based control activities can be easily implemented after sensing such gases, thus ensuring SAFETY operation.

## *2.6 Simulation Experiment EXP 4: 140 GHz Radio Communication Test Bed*

*Qualcomm Approach of 5G based MIMO COMP Diversity in solving blockage by metals in the production line of a Smart Factory*: In the production line of a smart factory, the manufacturing processes are fully automated with the use of AI enabled edge servers and PLCs which are often connected wirelessly to the edge devices used to automate the process as shown in Fig. 11. Problem of radio signal blockage is very common due to movement of material handling vehicles creating impairments to the radio signal and reducing the reliability of the process. Qualcomm recently demonstrated a smart factory with 5G URLLC support where ultra reliability of 99.99% is achieved using COMP based MIMO diversity as shown in Fig. 10. COMP

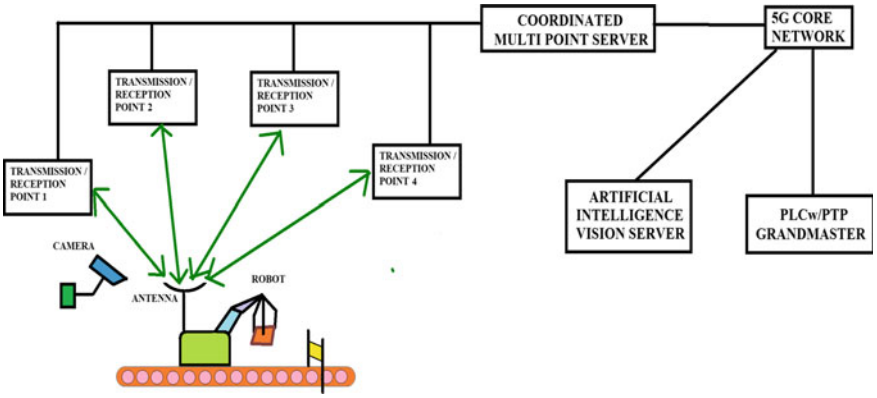


**Fig. 10** 5G URLLC system demo for SMART FACTORY (*Courtesy* QUALCOMM)

based MIMO diversity is the redundancy at the radio level and is used to solve the problem with 5G waveform.

As part of Qualcomm research and standardization, they have build liberal industry production lines involved the warehouses in San Diego whose architecture is shown in Fig. 11. Their little production line including a conveyor belt and cup of major components and right-hand side cameras taking all imagery and send it back to AI vision Centre. The vision Centre then analyzed what's going on and stand back in the direction of PLC which is to remotely control the behavioural robots and gates in a very precise time manner. Out of many objects moving over Conveyor belt, their objective was how many of the objects had been detected and how many objects have been missed.

Turn on focus to reliability one of the radio technology they are using in a demo is called quality multi point or COMP where one device is communicating to multiple points. It is very common in industry set up environments having a lot of metal structures either fixed or moving and when certain radio link pass gets blocked. The radio quality would be great and that is where the benefit of COMP comes in. In their set up, even though radio signal from one direction gets blocked there still signals

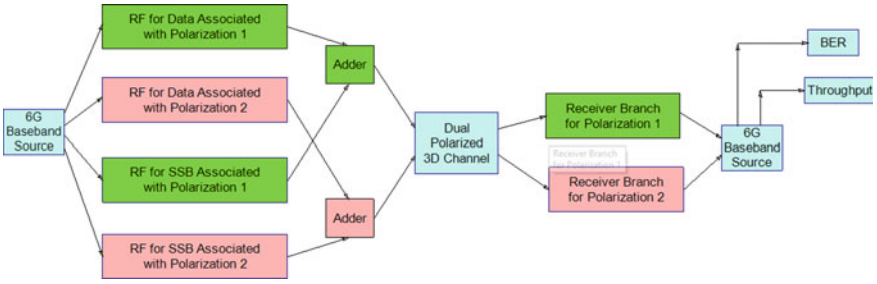


**Fig. 11** SIMULATION diagram of a 6G based MIMO COMP Diversity using 140 GHz RF carrier

coming from other direction creates redundancy as high as 99.9999% thus ensures reliable communications.

*Author's approach of 6G based MIMO COMP Diversity in solving signal blockage problem by metallic body of a material handling vehicle in a smart factory production line*: Similar problem of radio signal blockage in a smart factory environment is also considered by the author. One 140 GHz radio link is simulated by the author for COMP based MIMO diversity towards solution to the problem of radio signal blockage due to movement of material handling vehicles at the smart factory. The author has also worked on a similar problem using 6G based FBMC waveforms and special MIMO diversity where instead of repeating the systems at four places as in Fig. 11, dual polarized antenna integrated within one unit at 140 GHz radio carrier will be useful. Thus the use of dual polarized antenna along with FBMC waveform will help in reducing the cost and space saving and integrated to a single unit instead of four different radio unit placed at four spatially separated points. Author has evolved a Simulation model '6G MIMO diversity towards a solution to the problem of radio signal blockage due to movement of material handling vehicles at the smart factory using 140 GHz radio communication test bed. They are able to transmit both Video, Audio and Data through this model and receive the same with negligible distortion.

*Problem Definition*: problem of radio signal blockage in a smart factory environment with reducing reliability in automation process and degrading the performance.

*Solution Strategy*: 6G based FBMC waveform and special MIMO diversity with dual polarized 2X2 antenna with antenna beam formation.

*Objective*: Simulation of a Multimedia FBMC based 6G URLLC sub terahertz Link at 140 GHz.

*Detailed Methodology*: Keysight Systemvue software is again used in this model also and is a part of the Author's Test Bed at 140 GHz. Its Library is enriched with parts that are 'drag and drop' into the workspace. The simulation model is required to be built on the workspace which is composed of several parts and their interconnection. After proper selection of the parameters of the workspace variables, the model can be run for analysis. The different performances of the system like BER, Throughput, etc. can be measured and displayed on 2D/3D graphs for visualization.

Following the above approach, this particular model is built up by the author where the following Major parts list are being used:-

- Information Sources: Audio/Video (TV Video Pattern) and Data
- Modulation waveform: CP-OFDM and FBMC
- RF carrier: 140 GHz
- Antenna: MIMO (2X2) for Diversity reception and COMP realization and Antenna Beam formation [BF MRC Polarized Diversity Use case]
- Radio Channel: radio signal blockage due to movement of material handling vehicles at the smart factory with short distant communication with maximum distance 10 m
- Solution related to radio channel blockage: MIMO DIVERSITY reception with MRC (Maximum Ratio Combining)
- SMART ANTENNA Algorithm: Switched Beam

- Use Cases: This model is a solution towards the problem of radio signal blockage against movement of vehicle inside the production floor within a Factory.

Systemvue Modelling of 6G based MIMO COMP Diversity using 140 GHz RF carrier is shown in Fig. 11.

*Workspace Description of the Simulation Model (MIMO 2 × 2 BF MRC Polarized Diversity Case is included in above design)*: In the schematic, green part handles signals for the first polarization and pink part handles signals for the second polarization. Information pertinent to polarization is included in MIMO_3D Channel Configuration section.

Below are the details of these designs.

*MIMO 2X2 Beamfoming Polarized case*

- In this case, dual-polarized antenna arrays are deployed in both TX and RX sides. Only one channel direction is modelled in the 3D channel model and two streams of the MIMO transmission are transmitted in two polarizations with NumTxRFChains = 2 per polarization respectively.
- Four RF chains are deployed in TX side. Two are for one polarization and the other two are for the other polarization. One RF in the two RFs for whichever polarization is used for data transmission and the other one is for SSB transmission.
- Four RF chains (NumRxRFChains = 2) per polarization are also deployed in RX side. Two are for one polarization and the other two are for the other polarization, just as same as the deployment in TX side. Similar, regarding two RFs in RX side for one polarization, one is for data receiving and the other one is for SSB receiving.
- The channel is set up with only one path and is configured to Dual Polarized mode to accommodate 2 × 2 MIMO transmission.
- The following smart antenna parameters are set

  TxThetaTable = [90;90;90;90]/180 * pi;
  TxPhiTable = [60;20;340;300]/180 * pi;
  RxThetaTable = [30;30;30;30]/180 * pi;
  RxPhiTable = [60;20;340;300]/180 * pi;
  NumTxAnts = 8; % per polarization for TX
  NumRxAnts_x = 2; % per polarization for RX
  NumRxAnts_y = 2; % per polarization for RX
  NumRxAnts = NumRxAnts_x + NumRxAnts_y; % per polarization for RX.

- The channel is set up with only one path and is configured to Dual Polarized mode to accommodate 2 × 2 MIMO transmission. The 1-layer signal is demodulated upon signals from two polarizations by MRC algorithm in the Equalizer. Throughput curves are obtained based on MRC, branch #1 and branch #2 respectively, where MRC outperforms receiving only on branch #1 or branch #2 by 3 dB.

*Procedure of Smart antenna Beam acquisition and Beam Locking*: Smart antennas are in use for 6G communication using sub Terahertz waves. The performance of 6G

communication will be superb with the use of massive MIMO based smart antenna. But, in turn, it will increase the complexity in signal processing for smart antenna operation. The following three step procedure is mandatory for 6G MIMO beam formation application:

Procedure 1: Smart antenna Beam acquisition.

Procedure 2: Smart antenna Beam acquisition and Beam Locking.

Procedure 3: Data Communication over 6G radio.

Figure 12 pictorially depicts Smart antenna Beam acquisition and Beam Locking procedures.

Figure 12 is showing multiple simultaneous antenna beams (four has been shown in the figure as an example) will be radiated from the 6G base station. The 6G UE will receive radiated energy from all the beams and in turn, receiver will measure the beam powers of ALL the beams. The receiver will notify about the measured beam state information to the 6G base station through uplink (Procedure 1) and the base station will pass user data over this beam which has the maximum beam Index (Procedure 2). Thus, receiver will be locked to this beam having maximum energy of radiation and receive the data (Procedure 3). The simulated result from the above model following the above procedures is plotted and shown in Fig. 13. The maximum value measured from Beam with index 3 is also shown in Fig. 13.

*Further Experimental Results*: Two MIMO diversity Branches are modelled within the receiver. Thus the receiver in the above model is a diversity reception system having Branch 1 and 2 and also MRC (Maximum Ratio Combining algorithm) is implemented. The throughput is measured and plotted with variation of SNR as shown in Fig. 14. Three plots are shown and Throughput improvement at low SNR is noticed in the figure.

Finally, at the last step, Video pattern from a Video source is transmitted over the said 6G link and received successfully at the 6G receiver as shown in Fig. 15.

Thus, the 6G Communication model with (i) Video source, (ii) FBMC waveform, (iii) RF carrier using 140 GHz, (iv) MIMO Dual polarized SMART antenna with beam formation, (v) Diversity reception with MRC algorithm is successfully simulated using Systemvue software platform. Author is further motivated to extend the work for its actual hardware implementation and trials in a Smart Factory and test the

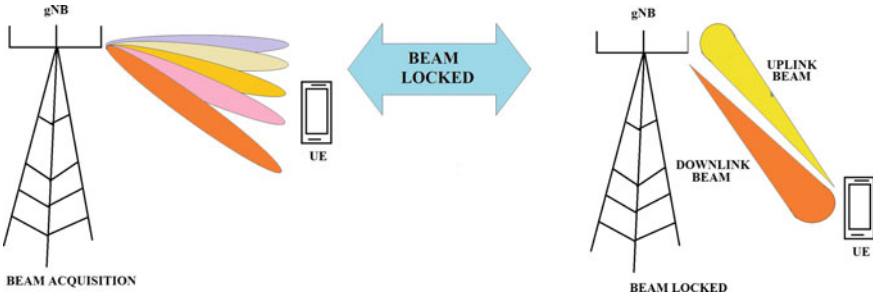


**Fig. 12** Smart antenna Beam acquisition and Beam Locking procedure

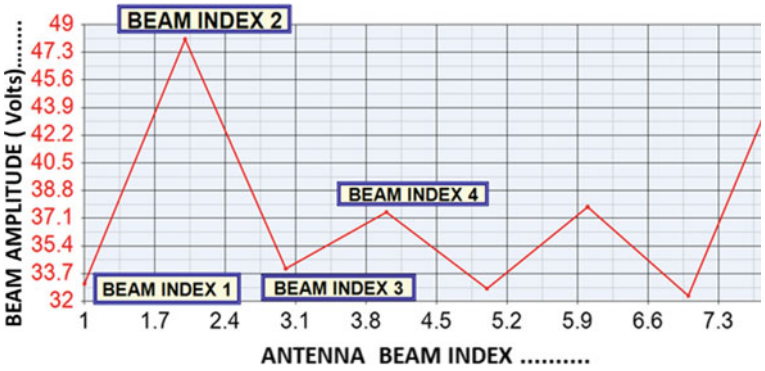


**Fig. 13** Smart antenna Beam acquisition and Beam Locking result

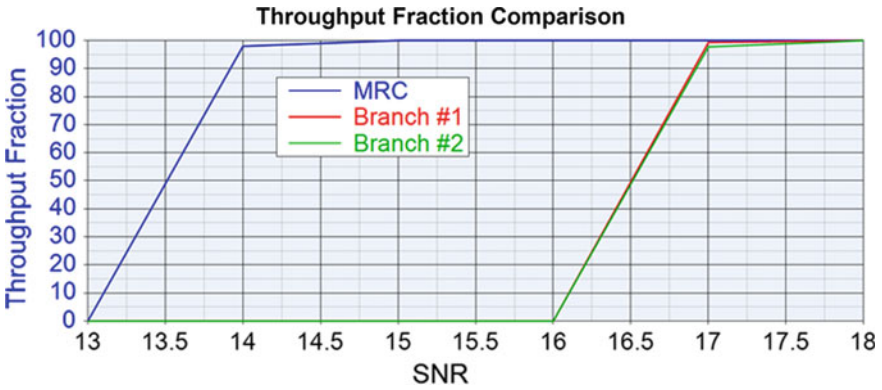


**Fig. 14** SNR improvement using MRC based signal processing within the receiver

reliability of the said link. Further, the authors are working towards the upgradation of the above systems to 220 GHz and Terahertz region to cater for new use cases in 6G area.

## 3 Summary

The recent literatures are reviewed thoroughly towards forthcoming 6G mobile and Radar uses of Sub-Terahertz waves. Overall technological challenges are discussed to formulate the research direction set by the author. 6G physical layer technologies are compared with reference to 5G physical layer technologies. FBMC waveform is becoming mandatory for 6G operation instead of CP-OFDM used by 5G. Similarly, by placing 4 MIMO radars at the four corners of a vehicle, an electromagnetic shield is surrounded around the vehicle. With continuous monitoring by radar signal

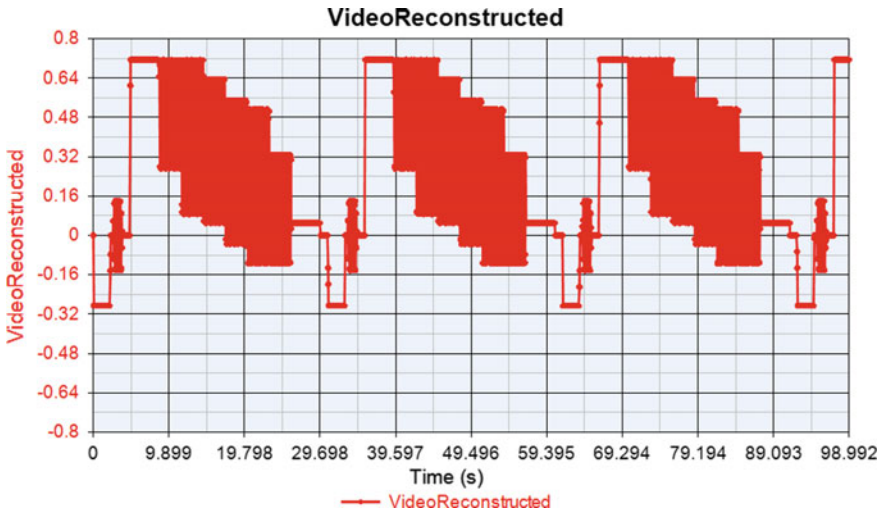


**Fig. 15** Excellent Video Pattern Reception at the 6G receiver

processing, any disturbances of the EM shield are noticed and actions towards collision avoidance are initiated. This will be best possible with D Band (110–170 GHz) Sub -terahertz radio. The author has simulated the same and results are highlighted. 140 GHz is also too useful in detecting weapon inside the jacket of a human while passing through the security zone of an airport. A similar situation is experimented by the author at their 140 GHZ test bed and vibration is detected by measuring the Doppler from a vibrating metal scale in front of 140 GHz radar.

In further experiments, they have detected fog in the atmosphere in the winter season and the growth status of the fog is noticed and reported using 140 GHz radar. In the fourth experiment for the communication use cases of the author's test bed, the model is developed exploiting FBMC waveform, Video Sources, 140 GHz radio, dual polarized smart antenna with switched beam and MRC combining for radio detection under the blockage condition of the radio in smart factory environment, thus improving the reliability of communication to a great extent. Thus, the generic 140 GHz test bed developed by the author is tested for four specific use cases as mentioned in the chapter and they have successfully experimented in solving specific problems as mentioned. With this success, the author is extending their test bed towards higher RF frequency of 220 GHz and above.

## References

1. Zhou Y, Liu L, Wang L et al (2020) Service-aware 6G: an intelligent and open network based on the convergence of communication, computing and caching. Digital Commun Networks 6(3):253–260

2. 5GIC Strategy Advisory Board, 6G WIRELES S A NEW STRATEGIC VIS ION. 6 G I C, University of Surrey (2020). Available from: https://www.surrey.ac.uk/sites/default/files/2020-11/6g-wireless-a-new-strategic-vision-paper.pdf. Accessed on Apr 2021
3. Saad W, Bennis M, Chen M (2020) A vision of 6G wireless systems: applications, trends, technologies, and open research problems. IEEE Network 34(3):134–142
4. Letaief KB, Chen W, Shi Y, Zhang J, Zhang WJA (2019) The roadmap to 6G: AI empowered wireless networks. IEEE Commun Mag 57(8):84–90
5. S. Raed, 6G wireless communications: future technologies and research challenges. In: International conference on electrical and computing technologies and applications (ICECTA), 19–20 November, 2019, pp 1–4
6. Piran MJ, Suh DY (2019) Learning-driven wireless communications, towards 6G. In: 2019 International conference on computing, electronics & communications engineering (iCCECE), London, UK, 2019, pp 219–224. https://doi.org/10.1109/iCCECE46942.2019.8941882.
7. Yang P, Xiao Y, Xiao M, Li S (2019) 6G Wireless communications: vision and potential techniques. IEEE Network 33(4):70–75
8. Chowdhury MZ, Shahjalal M, Ahmed S, Jang YM (2020) 6G Wireless communication systems: applications, requirements, technologies, challenges, and research directions. IEEE Open J Commun Soc 1:957–975
9. You X, Wang CX, Huang J et al (2021) Towards 6G wireless communication networks: vision, enabling technologies and new paradigm shifts. Sci China Inf Sci 64:110301
10. Yazar A, Arslan H (2020) A waveform parameter assignment framework for 6G with the role of machine learning. IEEE Open J Veh Technol 1:156–172
11. Online Content. Available from: https://www.slideshare.net/marwanhammouda/phydyas-09-ffilter-bank-multicarrier-fbmc-an-integrated-solution-to-spectrum-sensing-and-data-transmission-in-cognitive-radionetworksarhangboroujeny?qid=98bca999-3ebd-4178-9e7e-ce598865bc43&v=&b=&from_search=1. Accesses on Apr 2021
12. Cherubini G, Eleftheriou E, Olcer S (1999) Filtered multitone modulation for VDSL. Proc IEEE Globecom 2(1999):1139–1144
13. Saltzberg BR (1967) Performance of an efficient parallel data transmission systems. IEEE Trans Comm Tech 15(6):805–911
14. Farhang-Boroujeny B (2003) Multicarrier modulation with blind detection capability using cosine modulated filter banks. IEEE Trans Comm 51:2057–2070
15. Online Content. Available from: https://www.rohde-schwarz.com/us/about/news-press/all-news/rohde-schwarz-and-ihp-first-to-characterize-d-band-frequencies-in-over-the-air-test-setup-for-6g-and-automotive-radar-press-release-detailpage_229356-1003584.html. Accesses on Apr 2021
16. Zheng L, Lops M, Eldar YC, Wang X (2019) Radar and communication coexistence: an overview, advances in radar systems for modern civilian and commercial applications: part 2. IEEE Sign Process Mag 36(5):85–99
17. Gameiro A, Castanheira D, Sanson J, Monteiro PP (2018) Research challenges, trends and applications for future joint radar communications systems. Wireless Pers Commun 100:81–96
18. Mishra KV, Bhavani Shankar MR, Koivunen V, Ottersten B, Vorobyov SA (2019) Towards millimeter-wave joint radar communications. Advances in radar systems for modern civilian and commercial applications: part 2. IEEE Sign Process Mag 36(5):100–114
19. McCormick PM, Blunt SD, Metcalf JG (2017) Simultaneous radar and communications emissions from a common aperture, part I: theory. In: Proceedings of the IEEE radar conference 2017, pp 1685–1690
20. Hassanien A, Amin MG, Aboutanios E, Himed B (2019) Dual-function radar communication systems, advances in radar systems for modern civilian and commercial applications: part 2. IEEE Sign Process Mag 36(5):115–126
21. Kiviranta M, Moilanen I, Roivainen J (2019) 5G Radar: scenarios, numerology and simulations. In: International conference on military communications and information systems (ICMCIS). IEEE, New York, pp 1–4

22. Online Content. Available from: https://wireless.engineering.nyu.edu/terahertz-thz-communications-and-sensing/. Accesses on Apr 2021
23. Online Content. Available from: https://terasense.com/products/body-scanner/. Accesses on Apr 2021
24. Online Content. Available from: https://www.slideshare.net/Yole_Developpement/radar-and-wireless-for-automotive-market-and-technology-trends-2019-report-by-yole-dveloppement. Accesses on Apr 2021
25. Guermandi D et al (2016) A 79 GHz 2×2 MIMO PMCW radar SoC in 28 nm CMOS. In: IEEE Asian solid-state circuits conference (A-SSCC), Toyama, 2016, pp 105–108. https://doi.org/10.1109/ASSCC.2016.7844146
26. Tonouchi M (2007) Cutting-edge terahertz technology. Nature Photon 1(2):97
27. Teng X, Zhang Y, Poon CCY, Bonato P (2008) Wearable medical systems for p-Health. IEEE Rev Biomed Eng 1:62–74
28. Aggrawal H, Chen P, Assefzadeh MM, Jamali B, Babakhani A (2016) Gone in a picosecond: techniques for the generation and detection of picosecond pulses and their applications. IEEE Microwave Mag 17(12):24–38
29. Mittleman DM, Jacobsen RH, Neelamani R, Baraniuk RG, Nuss MC (1998) Gas sensing using terahertz time-domain spectroscopy. Appl Phys B: Lasers Opt 67(3):379–390

# THz Image Processing and Its Applications


**Bidyut Kumar Kundu and Pragti**

**Abstract** This chapter labels the recent advances of terahertz (THz or $10^{12}$ Hz) technology-based image processing and its applications. In short, the sandwiched regime between infrared and microwaves, bridging the gap amid optics and electronics is renowned as the THz. THz image processing deals with the interaction of matters in the sub-millimetre wavelength band (*ca.* 300 GHz to 3 THz) of a distinct electromagnetic spectrum indistinguishable from the other spectroscopic techniques. The THz regime also known as the "THz gap" for a long time as neither microwave nor optical devices could entirely subjugator this mysterious realm with its countless unseen scientific assets. Thus, the discovery of THz imaging techniques becomes successful to fill the gap. In general, the traditional THz technology can simultaneously acquire both image and spectral information to address various fields such as security, aerospace industries, medicine, materials science, biomedical imaging and others. The development and commercialization of THz imaging systems are now broadly accepted as the accessible alternative roots, such as electron lasers, Smith-Pur-cell emitters, backward wave oscillators, synchrotrons, are relatively expensive components. Therefore, THz image processing tries to find the solution through its generation, manipulation and detection of THz radiation to expand its usability as check-up tool for various imaging applications. For example, higher sensitivity of THz wave is convenient to investigate the specific behaviour of bio-molecules. In addition, advanced digital image processing algorithms in association with THz pulsed imaging (TPI) are effective for screening, diagnosis and treatment to examine the 3D structures of biological samples like cancer tumours.

B. K. Kundu (✉)
School of Applied Sciences, Centurion University of Technology and Management, Bhubaneswar, Odisha 752050, India
e-mail: bidyut.kundu@cutm.ac.in

Pragti
School of Basic Sciences, Discipline of Chemistry, Indian Institute of Technology Indore, Khandwa Road, Simrol, Indore 453552, India
e-mail: phd1801131009@iiti.ac.in



A. Acharyya et al. (eds.), *Generation, Detection and Processing of Terahertz Signals*, Lecture Notes in Electrical Engineering 794,
https://doi.org/10.1007/978-981-16-4947-9_9

Apart from that, THz spectrum might not only impact wireless network architectures (e.g. WLAN/WPAN/D2D) or security screening but also in aerospace industries using diode detectors through non-ionizing radiation. In contrast to X-rays, THz wave is completely harmless that can pass through clothing, objects and packages to recognize the inside materials and substances. At a glance, THz imaging along with detection technology contributes to identify opaque objects with clear borders, shaping this book a must-read for anybody in the arena of digital imaging and biomedical engineering.

**Keywords** THz spectroscopy · THz technology · THz image processing · THz applications

## 1 Introduction

In the recent decade, Terahertz science has progressively common day by day owing to the most part to the arrival of ultrashort-pulse optical device based time-domain spectroscopic analysis (TDS), that permits it conceivable for researchers to convey time-resolved "far-infrared" (FIR) lessons and to get spectroscopic analysis and their applications in the field of imaging and image processing within the sub-millimetre wavelength range (Fig. 1) [1, 2].

The development and commercialization of THz imaging systems are now broadly accepted as the accessible alternative roots, such as electron lasers, Smith-Pur-cell

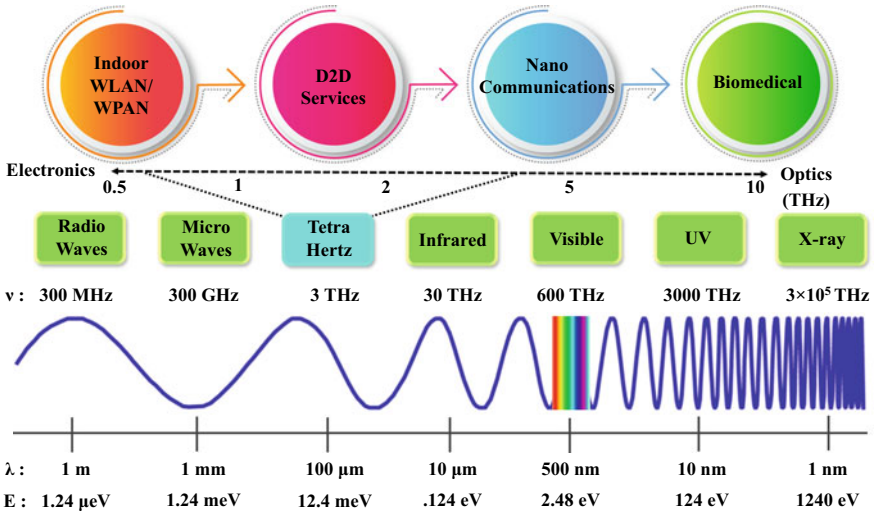


**Fig. 1** Electromagnetic spectrum

emitters, backward wave oscillators, synchrotrons, are relatively expensive components. Therefore, THz image processing tries to find the solution through its generation, manipulation and detection of THz radiation to expand its usability as check-up tool for various imaging applications.

Terahertz event surveys fundamental scientific benefits. Introduction of THz imaging systems can provide the answer to many spectroscopic limitations. The general objectives of this chapter are to assess the elementary theories of diverse kinds of THz foundations and detectors that are now thoughtful with THz radiation. The terahertz investigations are essential to be considered to accompanying crucial information. Thus, keeping in mind the growing interest in THz spectroscopy, this chapter will be sequenced as follows: Sect. 2 describes the background of THz spectroscopy. Sect. 3 briefly introduces Terahertz technology followed by THz image processing in the Sect. 4. This will follow up with THz technology-based applications in Sect. 5 that will be followed by conclusion in Sect. 6.

## 2 THz Spectroscopy

Terahertz wave is very sensitive to bio-molecules in the sub-millimetre wavelength band (*ca.* 300 GHz to 3 THz) [3], which offer several crucial medical applications. Moreover, the pulses of electromagnetic wave with an average power of 100 nW and a full-width half-maximum of 0.3 ps generally used for terahertz pulsed imaging (TPI) [4]. Fourier-transformed pulse or a photoconductive device can be convenient to coherently detect the pulses that provide a working frequency regime of 0.1–3.0 Terahertz [5]. While various methods like x-ray and ultrasound are failed to provide unique spectral information, terahertz imaging can be a proper solution furnishing a key advantage that is found that can possibly be employed to differentiate between the types of tissue [6]. The spectroscopic data may also be helpful for pharmaceutical applications—THz spectrographic analysis is ready to tell apart among polymorphic varieties of medicines. In fact, carbamazepine, a drug on the whole operated to deal with sufferers having psychological syndromes, transforms from shape III to shape I in a temperature-based method [7] (Fig. 2).

Terahertz radiations are non-invasive, penetrable and non-ionizing to numerous objects with a complexity of diffusion inferior to that of microwave radiation. THz spectra additionally tend to be terribly sensitive to numerous forms of resonances such as torsional, rotational, translational, vibrational and conformational states, empowering it to offer details on compounds, which are unapproachable with other imaging and analytical procedures (Fig. 3). These precise traits lead them to be appropriate for recognizing, analyzing, or imaging numerous materials. Despite Infrared and Raman spectroscopy, the improvement of strategies for generating, manipulating and detecting THz waves remains in its primary phases. However, THz wave was believed appropriate for image processing and other implementations, technologies to connect such competencies were realistically non-staying. On the other, the high frequency of terahertz cannot be estimated by an electronic counter used to record

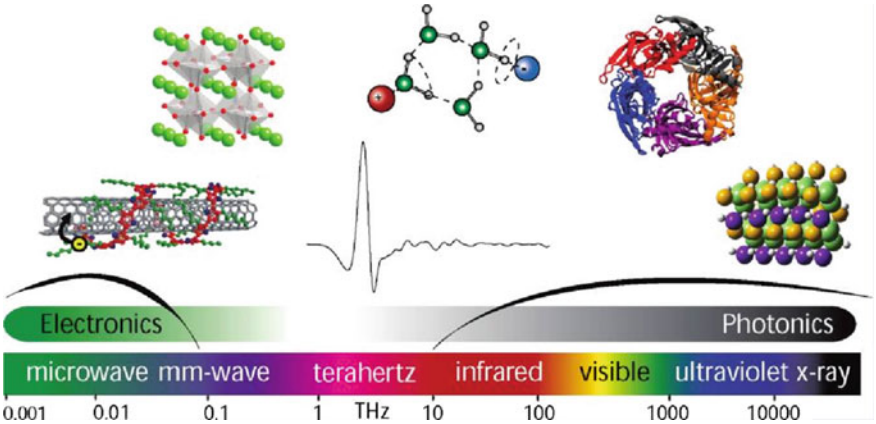


**Fig. 2** The THz scale based on the electromagnetic spectrum, with pictures featuring the large assortment of materials, molecules and phenomena, which THz spectroscopy can explore. Some examples of this kind are nano-materials and correlated electron materials; the charge carrier dynamics in semiconductors, hydration of solutes and liberational fashions in water and other liquids; and cooperative approaches in amino acid crystals and proteins. Reprinted with permission from [8]

optical radiations. Instead, different properties of wavelength and energy are used to characterize THz spectra. Significant advances in terahertz technology have led to more and more types of terahertz devices for different applications appearing for commercialization. This chapter introduces the use of THz image processing and the application of THz spectroscopy.

## 3 THz Technology

Although there is no precisely defined terahertz range, the accepted terahertz range is 300 to 3 GHz [3]. This parallels to wavelengths of 100 μm to 1 mm. This is a relatively unknown part of the electromagnetic spectrum called the "terahertz gap". Until recently, this gap was mainly due to the lack of light source and detector technology. Electromagnetic radiation (EM) with a wavelength longer than terahertz, antenna and waveguide tools can be presented for many years. Whereas for the wavelengths shorter than THz, optoelectronic and optical technologies have been applied for decades. These two technologies must be transported together to capture and study the THz regime, also stated as the far-infrared region.

THz radiation synthesis has been made conceivable by the advancement of three different strategies. These are:

1. Direct emission from far-infrared incoherent sources.
2. Up-conversion to terahertz frequencies from microwave frequencies [9].

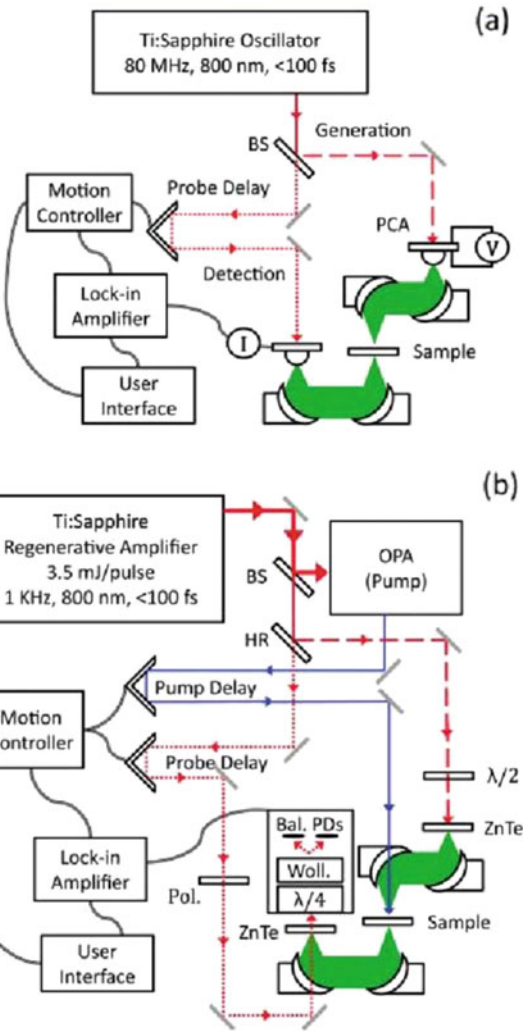


**Fig. 3** Characteristic transmission spectrometer flowchart of arrangements for **a** THz-TDS with photoconductive antennas and **b** TRTS with electro-optic production and recognition. Reprinted with permission from [8]

3. Coherent lasers down-conversion functioning in the adjacent IR to the THz band [10].

Figure 2 represents the THz-TDS in association to photoconductive antennas having characteristic transmission spectrometer configurations for TRTS generation and detection.

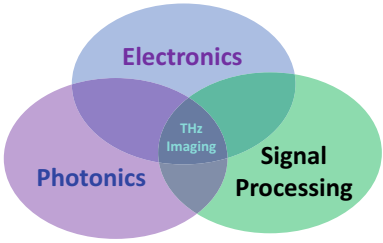


**Fig. 4** Counterparts for THz image processing

## 4 THz Image Processing

The components required for fruitful development of THz imaging is summarized in Fig. 4. It comprises the convergence of three units: electronics, photonics and signal processing.

Undoubtedly a portion of exertion has been devoted in the areas of electronics and photonics through the progress of production and identification technologies. Signal processing of THz data is the part that is least established [11]. Following are the main outcomes of this assignment, in this favour of THz spectroscopic imaging:

1. For significant development in THz image processing or THz imaging the key signal processing subjects that prerequisite to be talked about have been recognized and prospective lines of examination have been projected.
2. Introductory mathematical simulation and formulation outcomes have been gained for signal processing difficulties in Terahertz image modernization.

Moreover, in the typical working range of 0.3–5 THz, focal plane detector arrays are not yet accessible [12]. Antenna array mediated imaging by means of signal processing techniques is thus of great fit. Researchers established mathematical equations and primary explanations for complementary interferometric image modernization complications with antenna arrays [13]. Using MATLAB phantoms, computer simulations have also been achieved for tomographic renovation of complex-valued predictions.

## 5 THz Technology Applications

The aforesaid idiosyncratic competencies of terahertz radiations have been subjugated in a spare of applications in imaging and sensing. In general, THz wave applications are exploited in diverse areas including spectroscopy, photovoltaics, pharmacy, quality assurance, dentistry, medicine, communication, security screening and astronomy as depicted in Fig. 5.

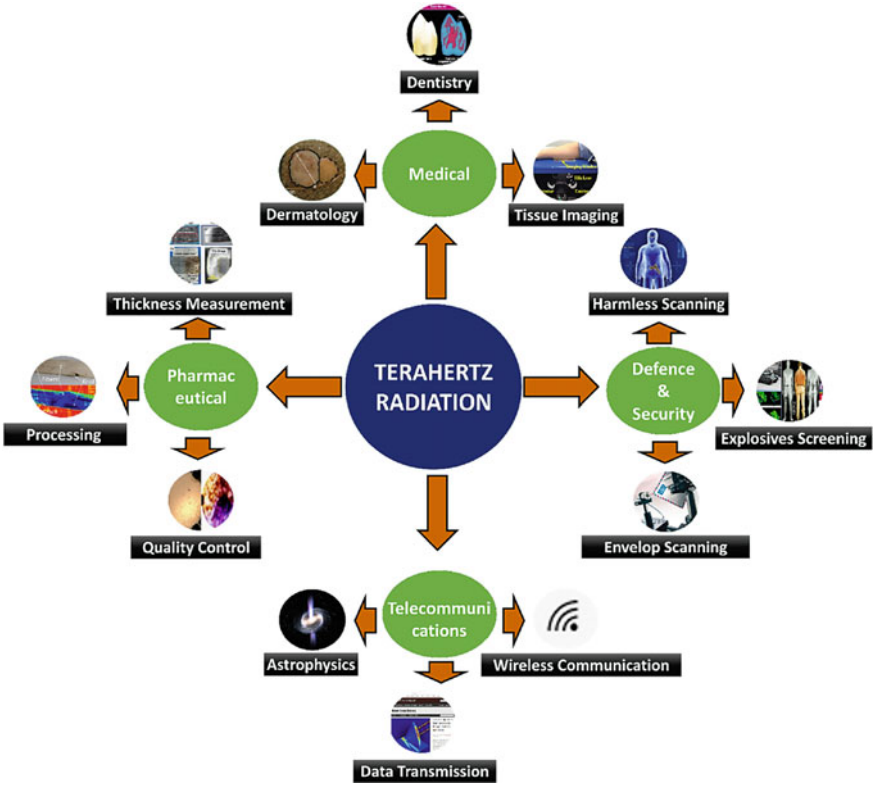


**Fig. 5** Applications of THz image processing. Reprinted with permission from ref [14]

## *5.1 THz Technology in Spectroscopic Analysis*

Spectroscopic characterization of numerous materials can be analyzed by using Terahertz radiation. The characterization of various compounds has been exploited by introducing the sensitivity and resonances effect of terahertz radiation in different molecules. Moreover, intra-molecular connections can be investigated with the help of Fourier transform infrared (FTIR) spectroscopic techniques but THz probes are exclusive in the intelligence that they probe the intermolecular and intra-molecular interactions and deliver characteristic information of material. In a recent report, terahertz time-domain spectroscopy of 1,3,5-trinitro-s-triazine has been studied by Huang et al. which displayed an absorption peak at 0.8 THz accountable to intermolecular accomplishment [15].

In addition, infrared spectroscopy (FTIR) was introduced to corroborate the results with THz study, which was approved by the same researcher for assessment [15]. Using terahertz time-domain spectroscopy, the spectral topographies of uric acid and glucose has been investigated Upadhya et al. The results show that the absorption

spectra of the two organic molecules were having unique features as a consequence of the intermolecular vibrational modes present in the compounds [16]. The spectral absorption topographies of a well-acknowledged illicit drug viz. methamphetamine has also been applied to study by Terahertz spectroscopy. Absorption spectra were traced to the cooperative vibrational modes estimated in the range of 0.2–2.6 THz corroborated with the experimental outcome of the molecule. Similarly, the investigation of time-domain THz spectroscopic measurement of 2,4-dinitrotoluene experimented for the same molecule in parallel with FTIR recording, which disclosed an improved association of outcomes of two procedures at lower frequencies range than at longer frequencies. The consequence gained experimentally interrelated well with theoretical analysis displaying that THz spectroscopy is an influential tool for perusing the low frequency modes of various molecules [17]. Apart from that, terahertz spectroscopy has been used to estimate some other compounds such as tryptophan [18] and trialanine, short-chain polypeptides [19].

Besides, the infrared spectra based on protein (bovine serum albumin, BSA)-complex interaction has been reported in one of our recent reports [20]. Though the information was not corroborated with THz spectral analysis. But, in a report, amplitude transmittance spectra of native-conformation and thermally denatured BSA protein interpreted using a THz-TDS system (Fig. 6).

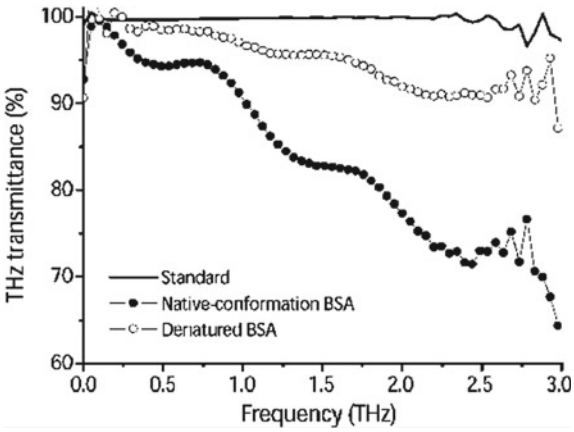


**Fig. 6** Applications to protein (here BSA) conformational analysis using a THz-TDS system. A standard sample with the solid curve shows THz transmittance without BSA, that of thermally denatured is denoted by open circles and the native conformation of BSA signified with solid circles. Reprinted with permission from ref [8]

## 5.2 THz Technology in Quality Control (QC)

The character of quality checks in the industry cannot be exaggerated and many methods and techniques are always being sight seen for use in the quality control of countless products. The analysis and characterization of numerous products can be done with the help of a powerful tool viz. THz time-domain spectroscopy. The assessment of several polymeric molecules along with a glass-fibre-reinforced epoxy composite and a polyethylene compound with silver-coated titanium dioxide nanospheres was utilized by Rutz et al. [21]. Terahertz radiation can also be useful for estimating the water content in various materials. The reduction of water to it has been subjugated for quality control in the paper manufacture process and the THz wave is also not clear to water [22]. Terahertz spectroscopy can also be introduced to evaluate the humidity level of papers. In addition, THz can also be applied to the measured mass of paper and thickness besides the access to the amount of water in papers [23]. THz imaging and spectroscopic techniques can also be helpful to monitor various food processes [24].

## 5.3 THz Technology in Photovoltaics

The construction of dye-sensitized solar cells on dye-sensitized titanium dioxide ($TiO_2$) can be analyzed through THz time-domain spectroscopy to acquire detailed spectroscopic information of the films [25]. Blackberry and pomegranate are the two natural dyes, which were inspected and extract an inorganic dye namely ruthenium bipyramidal complex (rubpy). From the observation, it was found that these two natural dyes having comparable spectral properties, which were dissimilar to that of the inorganic dye (rubpy).

THz reflectometry is also used in accumulation to the spectroscopic classification of photovoltaic compounds, to image photovoltaic compounds for identifying defects and flaws in the compounds, which could ultimately govern the competence of solar cells.

## 5.4 THz Technology in Pharmaceutical Industry

THz technology is oppressed in the pharmaceutical industry due to the exclusivity of its features [26–28]. THz radiations have the exceptional aptitude of powerful different classes of compounds, which are typically not clear to other procedures of electromagnetic fallout. The detection and quantification of hydrates or polymorphic systems can be explored by the applications of THz in pharmaceutical industry including novel active pharmaceutical constituents. The bioavailability, stability and production of drugs makes it easy to optimize the characterization via THz image

processing [29]. The thickness of coated pharmaceutical tablets and the quantification of the coating can be used by THz pulse imaging (TPI), which is reported by Russe et al. The common tomographic procedure and X-ray Micro tomography were screened to authenticate the outcomes of the tablet coated THz pulsed imaging.

## *5.5 THz Technology in Biomedical Applications*

The development of imaging and sensing purposes of new THz techniques have seen for the last couple of decades. Like X-ray, THz wave is proficient in producing 2D pictures of diverse types of matters owing to the circumstance that THz waves transportable through some materials like plastics and semiconductors but are not clear to the others such as polarizing and metallic materials. For medical imaging, THz radiations are superior over X-rays because they are non-ionizing and to a large degree innocuous to the receiver. THz radiations are presently beneath examination for routine as an imaging modality to envisage tumour or cancerous tissues. Cancer is the second foremost reason of death in the U.S. after cardiovascular disease as per the American Cancer Society and notes for approximately one in every four deaths. The current imaging methods are no sufficient to study early detection of disease, which could mean the variance between life and death for countless patients but there is a gap. Herein, novel THz spectroscopic lessons on cancer could possibly offer new procedures for the initial recognition of the disease. Indeed, THz radiation-based imaging and detection of cancerous cells and skin tissues thus has been a sharp upsurge in the amount of studies signifying its potential use [30–33]. The technique lends itself glowing to imaging utmost organic tissue as THz wave is voluntarily absorbed by polar liquids and/or water [31]. Furthermore, Woodward et al., able to discriminate basal cell carcinoma, a type of skin cancer, from healthy tissues with the help of Terahertz pulse imaging [32]. Breast cancer studies are also an example, which has also been tested through the THz pulse imaging [34]. Terahertz radiation is very essential to investigate an excessive quantity of bio-molecules such as proteins, amino acids/peptides, carbohydrates, RNA/ DNA, cells and tissues [35]. The absorption spectra in the terahertz frequency can be reflected in the low-frequency core helical vibration of DNA involving hydrogen bond of DNA base pairs [36]. Thus, for the characterization of biological compounds or bio-molecules, THz radiation can be utilized to get extreme level of sensitivity towards the study of bio-molecules.

**Dental Application**: Imaging with X-ray is the leading imaging method in dentistry. This is the key technology used to watch dental caries and set up treatment for implants, extractions, dentures and braces. Nevertheless, X-rays are especially ionizing and common contacts are negative to health. Thus, as an alternative imaging technique, Terahertz pulsed imaging (TPI) express inordinate prospective in dental diagnosis [37–40]. On the other, THz radiations are less hazardous, non-ionizing and low in energy. In contrast to different organic tissues with a large percent of water with the inclination for extensive absorption of THz wave, tooth have an enormously

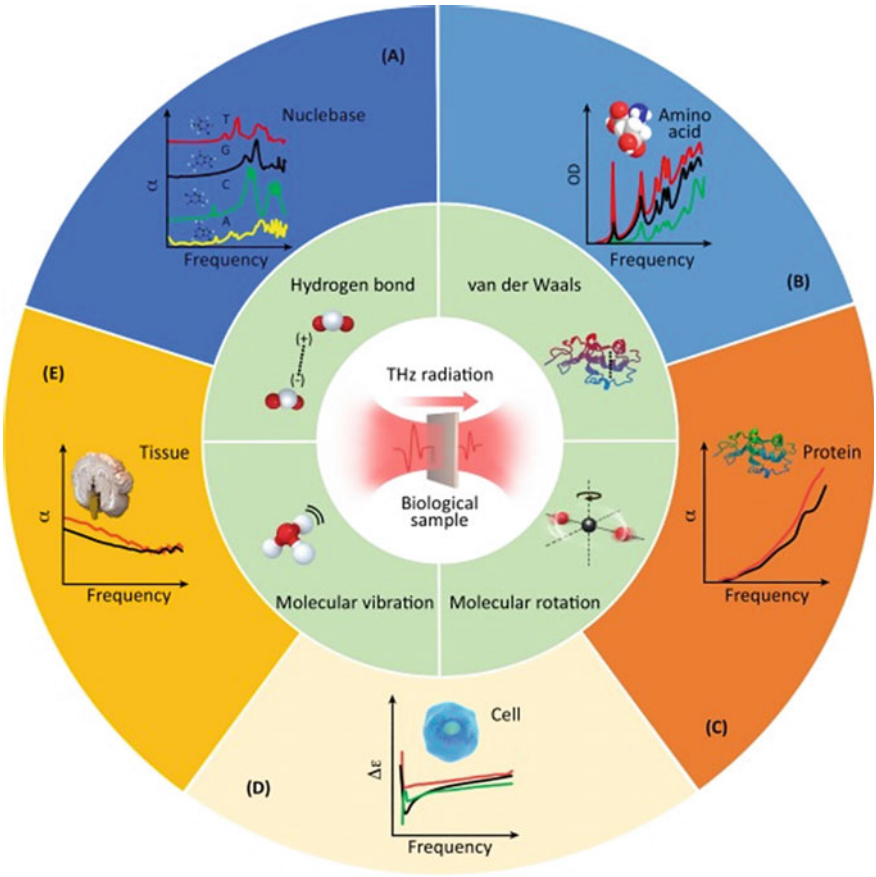


**Fig. 7** Terahertz spectroscopy in biomedical applications and image processing. Reprinted with permission from ref [41]

small water proportion, which drives it handy to photo tooth samples the usage of the THz pulsed imaging method (Fig. 7).

## *5.6 THz Technology in Security Screening*

Security screening is the most usual place programs of THz technology and image processing. Terahertz does nowadays no longer most effective supply statistics approximately the existence of hid objects however additionally has the ability to become aware of the composition of the substances as per requirement. In latest years several examinations have been performed at the functionality of terahertz to hit upon explosives at airports and different touchy places [42]. The gain of THz wave over

X-ray, extensively utilized for security screening because of its non-ionizing nature and low energy. The ionizing behaviour of X-rays forms the ordinary acquaintance of it, which by means is dangerous to people. The particular ability of Terahertz radiations to impale an extensive variety of packaging substances drives it feasible to hit upon explosives, weapons and doubtlessly explosive devices hid inside those substances [43].

### *5.7 THz Technology in Communication, Remote Sensing and Astronomy*

One different use of THz spectra is inside the place of wireless statistics communication. The THz radiation part of the electromagnetic radiations has proven to undertake as a bandwidth appropriate for statistics transmission. Ishagaki et al. have planned a THz oscillating resonate tunnelling diode that has the capacity to transmits a signal at 542 GHz with a statistics switches price of 3 Gbit/s. This kind of THz WIFI is constrained to a vicinity of 30 ft however has an ability to aid statistics fees of as much as a hundred Gbit/s. Remote sensing lets in the purchase of data approximately substances or places from a span, which will be from a plane or satellites. Terahertz radiation is one of the potential equipment for sporting out far off sensing. Lui et al. advanced a method primarily based on broadband THz radiation identification for far off sensing with which they had been capable of coming across coherent THz radiation at a separation of 10 m [44].

### *5.8 THz Technology in Some Other Applications*

Meta materials are substances that can be structurally regulated to have interaction in a selected manner to electromagnetic waves. Meta materials can also be represented by THz spectroscopy in a regular manner. Meta materials that can be mainly counterfeited to have interaction with THz radiation are mentioned to THz meta materials. THz spectroscopy additionally has the capacity to hit upon oil spills in water bodies [45, 46]. Gorenflo et al. decided the quantity and shape of water in oil-water complexes with the help of terahertz transmission spectroscopy, via way of means of tracking modifications in refractive index and absorption coefficient [45].

## 6 Summary

In the last couple of decades, a noteworthy development has been made on the Tetrahertz mediated technology for the production, manipulation and identification of

THz wave resulting in ever-growing applications of this technology in the research and industry. Herein, this chapter contributes towards the role of Terahertz image processing and THz technology along with its applications in numerous areas such as spectroscopic analysis, biomedical, pharmaceutical testing, oil spill characterization, astronomy, photovoltaic characterization, security screening, quality control and pharmaceutical industry. With the exponential development in analysis within the THz region, a tendency has been developed to anticipate additional proceedings in the implementation of THz technology within society.

**Acknowledgements** The first author gladly thanks his mother, Mrs. Champa Kundu for her constant moral support and encouragement to carry out this work.

## References

1. Safian R, Ghazi G, Mohammadian N (2019) Review of photomixing continuous-wave terahertz systems and current application trends in terahertz domain. Opt Eng 58:110901
2. Castro-Camus E, Alfaro M (2016) Photoconductive devices for terahertz pulsed spectroscopy: a review. Photonics Res 4:A36–A42
3. Ghasempour Y, Shrestha R, Charous A, Knightly E, Mittleman DM (2020) Single-shot link discovery for terahertz wireless networks. Nat Commun 11:1–6
4. Huang S, Wang Y, Yeung D, Ahuja A, Zhang Y, Pickwell-MacPherson E (2008) Tissue characterization using terahertz pulsed imaging in reflection geometry. Phys Med Biol 54:149
5. Spies JA, Neu J, Tayvah UT, Capobianco MD, Pattengale B, Ostresh S, Schmuttenmaer CA (2020) Terahertz spectroscopy of emerging materials. J Phys Chem C 124:22335–22346
6. Afsah-Hejri L, Hajeb P, Ara P, Ehsani RJ (2019) A comprehensive review on food applications of terahertz spectroscopy and imaging. Compr Rev Food Sci Food Saf 18:1563–1621
7. Kiang Y-H, Huq A, Stephens PW, Xu W (2003) Structure determination of enalapril maleate form II from high-resolution X-ray powder diffraction data. J Pharm Sci 92:1844–1853
8. Baxter JB, Guglietta GW (2011) Terahertz Spectroscopy. Anal Chem 83:4342–4368
9. Shi M, Yu M, Li G, Wang M (2020) A THz fourth-harmonic conversion system expanding microwave to THz band. Infrared Phys Technol 107:103217
10. Pistore V, Nong H, Vigneron P-B, Garrasi K, Houver S, Li L, Davies AG, Linfield EH, Tignon J, Mangeney J (2021) Millimeter wave photonics with terahertz semiconductor lasers. Nat Commun 12:1–7
11. Khabibullin RA, Morozov OG, Sakhabutdinov AJ, Nureev II, Kuznetsov AA (2018) Two-frequency radiation forming on chirped FBG for tuning terahertz carriers generation. In: 2018 Systems of signals generating and processing in the field of on board communications, IEEE, pp 1–4
12. Oda N, Kurashina S, Miyoshi M, Doi K, Ishi T, Sudou T, Morimoto T, Goto H, Sasaki T (2015) Microbolometer terahertz focal plane array and camera with improved sensitivity in the sub-terahertz region. J Infrared Millim Terahertz Waves 36:947–960
13. Guerboukha H, Nallappan K, Skorobogatiy M (2018) Toward real-time terahertz imaging. Adv Opt Photonics 10:843–938
14. Yakasai IK, Abas PE, Begum F (2021) Review of porous core photonic crystal fibers for terahertz waveguiding. Optik 229:166284
15. Huang F, Schulkin B, Altan H, Federici JF, Gary D, Barat R, Zimdars D, Chen M, Tanner D (2004) Terahertz study of 1, 3, 5-trinitro-s-triazine by time-domain and Fourier transform infrared spectroscopy. Appl Phys Lett 85:5535–5537

16. Upadhya P, Shen Y, Davies A, Linfield E (2003) Terahertz time-domain spectroscopy of glucose and uric acid. J Biol Phys 29:117–121
17. Chen Y, Liu H, Deng Y, Schauki D, Fitch MJ, Osiander R, Dodson C, Spicer JB, Shur M, Zhang X-C (2004) THz spectroscopic investigation of 2, 4-dinitrotoluene. Chem Phys Lett 400:357–361
18. Yu B, Zeng F, Yang Y, Xing Q, Chechin A, Xin X, Zeylikovich I, Alfano R (2004) Torsional vibrational modes of tryptophan studied by terahertz time-domain spectroscopy. Biophys J 86:1649–1654
19. Kutteruf M, Brown C, Iwaki L, Campbell M, Korter T, Heilweil E (2003) Terahertz spectroscopy of short-chain polypeptides. Chem Phys Lett 375:337–343
20. Kundu BK, Pragti, Mobin SM, Mukhopadhyay S (2020) Studies on the influence of the nuclearity of zinc(ii) hemi-salen complexes on some pivotal biological applications. Dalton Trans 49:15481–15503
21. Rutz F, Koch M, Khare S, Moneke M, Richter H, Ewert U, Waves M (2006) Terahertz quality control of polymeric products. Int J Infrared 27:547–556
22. Banerjee D, Von Spiegel W, Thomson M, Schabel S, Roskos H (2008) Diagnosing water content in paper by terahertz radiation. Opt Express 16:9060–9066
23. Hernandez-Serrano A, Corzo-Garcia S, Garcia-Sanchez E, Alfaro M, Castro-Camus E (2014) Quality control of leather by terahertz time-domain spectroscopy. Appl Opt 53:7872–7876
24. Gowen AA, O'Sullivan C, O'Donnell C (2012) Technology, Terahertz time domain spectroscopy and imaging: emerging techniques for food process monitoring and quality control. Trends Food Sci 25:40–46
25. Ghann W, Rahman A, Rahman A, Uddin J (2016) Interaction of sensitizing dyes with nanostructured TiO 2 film in Dye-Sensitized solar cells using terahertz spectroscopy. Sci Rep 6:1–11
26. Uddin J (2017) Terahertz (THz) spectroscopy: a cutting-edge technology. Wiley, Hoboken, NJ, USA, 2006
27. Taday PF (2004) Applications of terahertz spectroscopy to pharmaceutical sciences. Philos Trans R Soc London. Ser: Math Phys Eng Sci 362:351–364
28. Shen Y-C (2011) Terahertz pulsed spectroscopy and imaging for pharmaceutical applications: a review. Int J Pharm 417:48–60
29. McIntosh AI, Yang B, Goldup SM, Watkinson M, Donnan RS (2012) Terahertz spectroscopy: a powerful new tool for the chemical sciences? Chem Soc Rev 41:2072–2082
30. Rahman A, Frenchek S, Kilfoyle B, Patterkine L, Rahman A, Michniak-Kohn B (2012) Diffusion kinetics permeation concentration of human stratum corneum characterization by terahertz scanning reflectometry. Drug Dev Delivery
31. Pickwell E, Cole BE, Fitzgerald AJ, Pepper M, Wallace VPJPiM (2004) Biology, In vivo study of human skin using pulsed terahertz radiation. Phys Med 49, 1595
32. Woodward RM, Wallace VP, Pye RJ, Cole BE, Arnone DD, Linfield EH, Pepper M (2003) Terahertz pulse imaging of ex vivo basal cell carcinoma. J Investig Dermatol 120:72–78
33. Woodward RM, Cole BE, Wallace VP, Pye RJ, Arnone DD, Linfield EH, Pepper M (2002) Terahertz pulse imaging in reflection geometry of human skin cancer and skin tissue. Phys Med Biol 47:3853
34. Ashworth PC, Pickwell-MacPherson E, Provenzano E, Pinder SE, Purushotham AD, Pepper M, Wallace VP (2009) Terahertz pulsed spectroscopy of freshly excised human breast cancer. Opt Express 17:12444–12454
35. Plusquellic DF, Siegrist K, Heilweil EJ, Esenturk O (2007) Applications of terahertz spectroscopy in biosystems. Chem Phys Chem 8:2412–2431
36. Globus T, Woolard D, Khromova T, Crowe T, Bykhovskaia M, Gelmont B, Hesler J, Samuels A (2003) THz-spectroscopy of biological molecules. J Biol Phys 29:89–100
37. Crawley DA, Longbottom C, Cole BE, Ciesla CM, Arnone D, Wallace VP, Pepper M (2003) Terahertz pulse imaging: a pilot study of potential applications in dentistry. Caries Res 37:352–359

38. Crawley DA, Longbottom C, Wallace VP, Cole BE, Arnone DD, Pepper M (2003) Three-dimensional terahertz pulse imaging of dental tissue. J Biomed Opt 8:303–307
39. Sim YC, Park JY, Ahn K-M, Park C, Son J-H (2013) Terahertz imaging of excised oral cancer at frozen temperature. Biomed Opt Express 4:1413–1421
40. Kamburoğlu K, Yetimoğlu N (2014) Applications of terahertz imaging in medicine. OMICS J Radiol 3, e127
41. Yang X, Zhao X, Yang K, Liu Y, Liu Y, Fu W, Luo Y (2016) Biomedical applications of terahertz spectroscopy and imaging. Trends Biotechnol 34:810–824
42. Shen Y, Lo AT, Taday P, Cole B, Tribe W, Kemp M (2005) Detection and identification of explosives using terahertz pulsed spectroscopic imaging. Appl Phys Lett 86, 241116
43. Davies AG, Burnett AD, Fan W, Linfield EH, Cunningham JE (2008) Terahertz spectroscopy of explosives and drugs. Mater Today 11:18–26
44. Liu J, Dai J, Chin SL, Zhang X-C (2010) Broadband terahertz wave remote sensing using coherent manipulation of fluorescence from asymmetrically ionized gases. Nat Photonics 4:627
45. Gorenflo S, Tauer U, Hinkov I, Lambrecht A, Buchner R, Helm H (2006) Dielectric properties of oil–water complexes using terahertz transmission spectroscopy. Chem Phys Lett 421:494–498
46. Cunnell R, Luce T, Collins J, Rungsawang R, Freeman J, Beere H, Ritchie D, Gladden L, Johns M, Zeitler J (2009) Quantification of emulsified water content in oil using a terahertz quantum cascade laser. In: 2009 34th international conference on infrared, millimeter, and terahertz waves. IEEE, pp 1–2

# A DC Analysis of Single-Gate TFET Using InAs as Channel Material


**Jayabrata Goswami, Anuva Ganguly, Anirudhha Ghosal, and J. P. Banerjee**

**Abstract** The modeling and analysis of an n-type InAs-based tunnel field-effect transistor (TFET) have been carried out by using parabolic approximation technique. The basic parameters of the device have been outlined by shifting the channel length, keeping gate oxide thickness constant to achieve high ON to OFF current ratio ($I_{on}/I_{off}$) and low subthreshold swing (SS). The surface potential, device electric field and ON state or drain current are obtained from the analytical solution of 2D Poisson's condition subject to suitable boundary conditions by utilizing finite difference method (FDM).

**Keywords** TFET · Subthreshold slope · Tunneling probability

## 1 Introduction

Ordinary planar metal–oxide–semiconductor field-effect transistors (MOSFETs) are drawing closer the scaling limit as transistor measure proceeds to recoil. Short channel MOSFETs have a few restrictions such as leakage currents and less controllability of gate over the channel [1]. In arrange to have way better controllability of the channel multi gate structures such as DG MOSFET, FinFET, Silicon Nanowire Transistor, Tunnel Field Effect Transistors were presented. Tunnel FETs act as field impact transistor but utilize interband tunneling for carrier transport. As the device is turned on, the carriers tunnel through the boundary so that current can flow from source to drain side. So the device is off, the nearness of the boundary keeps the leakage current significantly low. So as the high-k gate dielectric increases the channel current of Tunnel FET. Since germanium (Ge) has smaller $E_G$ than Si, TFET with Ge as channel material can be used to increase the ON state current [2]. The OFF state current is however more in Ge TFETs than in Si TFETs which leads to lower ON–OFF current ratio.

J. Goswami (✉) · A. Ganguly · A. Ghosal · J. P. Banerjee
Institute of Radio Physics and Electronics, University of Calcutta, 92, APC Road, Kolkata 700009, India



A. Acharyya et al. (eds.), *Generation, Detection and Processing of Terahertz Signals*, Lecture Notes in Electrical Engineering 794,
https://doi.org/10.1007/978-981-16-4947-9_10

The reason of this chapter is to show a consider of the performance of TFET utilizing InAs as channel materials as respects on–off current proportion, subthreshold swing etc. Hence n-type InAs based TFETs are promising another era devices for ultra large scale integration also low power digital application.

## 2 Device Structure and Modeling for Low Power Operation

In Fig. 1, an n-type TFET as InAs channel material is considered in the present study. The source and drain sides are both heavily doped. The doping concentration of the device is p + source ($2.4 \times 10^{20}$ cm$^{-3}$), n channel ($10^{17}$ cm$^{-3}$) and *n*+ drain sides ($1.1 \times 10^{20}$ cm$^{-3}$). An oxide layer ($SiO_2$) of 2-nm thickness ($t_{OX}$) acts as dielectric material in between the gate and the channel. The two-dimensional Poisson condition is illuminated to urge the surface potential and electric field of the device. The substrate thickness ($t_{InAs}$) chosen is 4 nm.

The surface potential and device electric field are calculated by the following analytical solution of two-dimensional Poisson's equation [3]

$$\frac{\partial^2 \Phi(x,y)}{\partial x^2} + \frac{\partial^2 \Phi(x,y)}{\partial y^2} = \frac{qN_{\text{Channel}}}{\varepsilon_{\text{InAs}}}, \tag{1}$$

where $q$ and $\varepsilon_{InAs}$ are the electronic charge and permittivity of the device. The potential function is written as second-order polynomial, i.e.,

$$\Phi(x,y) = a_0(x) + a_1(x)y + a_2(x)y^2, \tag{2}$$

where $a_0, a_1$ and $a_2$ are subjective constants. So, the condition (1) is illuminated utilizing condition (2) taken after by fitting boundary conditions:

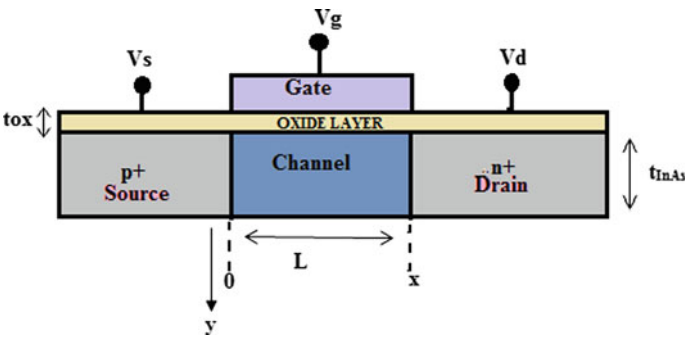


**Fig. 1** Schematic diagram of an n-type InAs TFET

(i) At the gate oxide interface, the electric flux is persistent, thus

$$\frac{\partial \Phi(x,y)}{\partial y} = \frac{\varepsilon_{\mathrm{OX}}}{\varepsilon_{\mathrm{InAs}}} \frac{\Phi_s(x) - v_g}{t_{\mathrm{OX}}}, y = 0. \tag{3}$$

(ii) At the back channel and back oxide interface, the electric flux is persistent, thus

$$\frac{\partial \Phi(x,y)}{\partial y} = 0, \quad y = t_{\mathrm{InAs}} \tag{4}$$

(iii) The potential at the source side and drain side is

$$\Phi(0,0) = \Phi_s(0) = V_{BI} \tag{5}$$

$$\Phi(L,0) = \Phi_S(L) = V_{BI} + V_{ds} \tag{6}$$

where $v_g = V_{gs} - \varphi_m + \chi + {}^{E_g}/_2$, $E_g$ is the energy band gap, $\varphi_m$ is the gate metal work function, $\chi$ is the electron affinity of InAs, and $V_{\mathrm{gs}}$ and $V_{\mathrm{ds}}$ are the gate–source voltage and drain–source voltage separately.

The constants $a_0(x), a_1(x)$ and $a_2(x)$ can be found from solution boundary condition Eqs. (3) and (4), and we get

$$a_0(x) = \Phi_S(x) \tag{7}$$

$$a_1(x) = \frac{\Phi_S(x) - v_g}{t_{OX}} \frac{\varepsilon_{OX}}{\varepsilon_{InAs}} \tag{8}$$

$$a_2(x) = \frac{1}{2t_S} \frac{\varepsilon_{OX}}{\varepsilon_{InAs}} \frac{v_g - \Phi_S(x)}{t_{InAs}} \tag{9}$$

Now putting the value of $a_0(x), a_1(x)$ and $a_2(x)$ in Eqs. (2) and (1), the following potential distribution function is written as

$$\Phi_S(x) = P \exp^{\lambda x} + U \exp^{-\lambda x} + v_g \tag{10}$$

where $\lambda = \sqrt{\frac{\varepsilon_{OX}}{\varepsilon_{InAs} t_{OX} t_{InAs}}}$ is the characteristic length of the device. The coefficients P and U are obtained as

$$P = \frac{-1}{(2\sinh(\lambda L))} \left[ V_{BI} \exp^{-\lambda L} - (V_{BI} + V_{ds}) + v_g (1 - \exp^{-\lambda L}) + V_{ds} \right] \tag{11}$$

$$U = \frac{1}{(2\sinh(\lambda L))} [V_{BI} \exp^{\lambda L} - (V_{BI} + V_{ds}) + v_g (1 - \exp^{\lambda L}) - V_{ds}] \tag{12}$$

Therefore, the electric field of the device is calculated from the following equations. The electric field along the $x$-axis is

$$E_x = -\frac{\partial \Phi_S(x)}{\partial x} = -(T\lambda \exp^{\lambda x} - U\lambda \exp^{-\lambda x}) \tag{13}$$

The electric field along $y$-axis is

$$E_y = -\frac{\partial \Phi_S(x)}{\partial y} = -(a_1(x) + 2ya_2(x)) \tag{14}$$

Hence, the overall electric field is written as

$$[E] = \sqrt{E_x^2 + E_y^2} \tag{15}$$

The tunneling probability, $T_{\mathrm{WKB}}$, in a triangular potential barrier of height of Eg is calculated by using WKB approximation [4, 5] according to which the tunneling probability is written as

$$T_{WKB} = \exp\left(-\frac{4\sqrt{2m^*_{\mathrm{reduce}}}E_g^{3/2}}{3q\hbar E}\right) \tag{16}$$

where $m^*_{reduce}$ is the reduce effective mass and $\hbar$ is the reduce Planck constant individually. So, the whole drain current is calculated from the following equations

$$\begin{aligned} I_{\mathrm{Drain}} &= \int q v_{\mathrm{group}}(k_x)\rho(k_x)(f_v - f_c)T_{WKB}dk_x \\ &= \frac{q^2}{\pi\hbar}T_{WKB}V_T \ln\left(\frac{1}{2}(1+\cosh)\frac{V_{\mathrm{Reverse}}}{V_T}\right) \end{aligned} \tag{17}$$

where $v_{group}(k_x)$ is the group velocity, $V_T$ is the thermal voltage and $f_v$ and $f_c$ are the Fermi–Dirac distributions at the valence band and conduction band individually [6]. In this chapter, drain current is calculated from both the analytical and numerical methods.

## 3 Simulation Results

The energy band diagram is first obtained from the simulation software to find out the OFF state leakage current by varying the gate length in the ranges 20 nm to 30 nm, respectively. The optimized value of channel length ($L$) is found to be 20 nm. The energy band diagrams in the OFF state ($V_{\mathrm{GS}} = 0$ V) and ON state ($V_{\mathrm{GS}}$

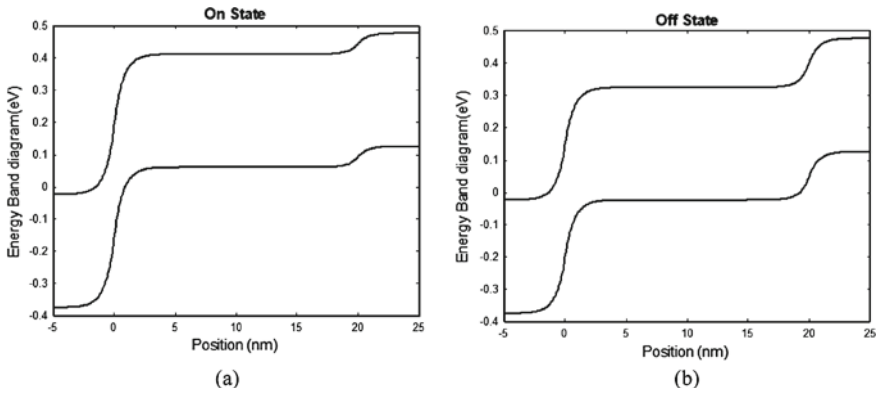


**Fig. 2** Energy band diagrams for an n-type InAs-based TFET at **a** ON state and **b** OFF state

$= 0.1$ V, $V_{DS} = 0.1$ V) for the optimized n-type InAs-based TFET are shown in Fig. 2a, b separately. The carrier interband tunneling in TFET is based on the variety of position of the energy band gap of the channel region with respect to the energy levels of source and drain sides. Therefore, the device surface potential and the electric field are shown in Fig. 3a, b separately. So, the tunneling probability of the device is shown in Fig. 4. As electric field increases, the barrier width decreases which leads to an exponential increase of tunneling probability. Figure 5a shows the plot of drain current versus gate–source voltage ($V_{GS}$) for the optimized n-type InAs TFET from which the magnitude of at $V_{GS} = 0.1$ V, whereas Fig. 5b shows ON–OFF current ratio of the aforementioned device structure.

The designed n-type InAs-based TFET at channel length 20 nm shows good switching property since the OFF state leakage current is very low and the ON–OFF current ratio is very high. The subthreshold swing (SS) is a vital parameter of low-power digital design application. The slope of the device is obtained from the

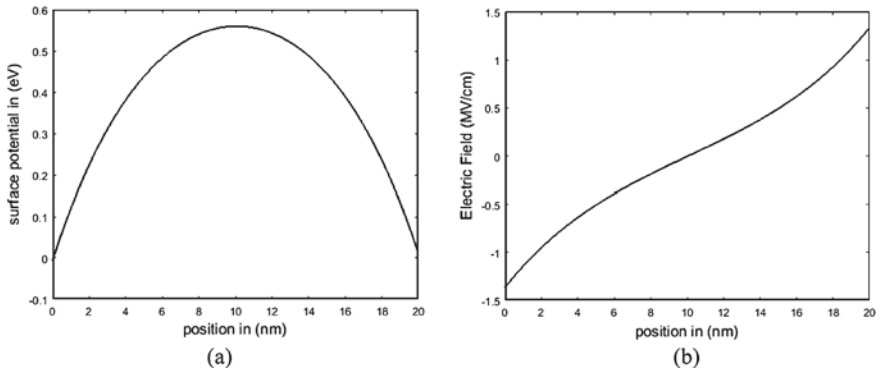


**Fig. 3** **a** Surface potential and **b** electric field of the *n*-type InAs-based TFET

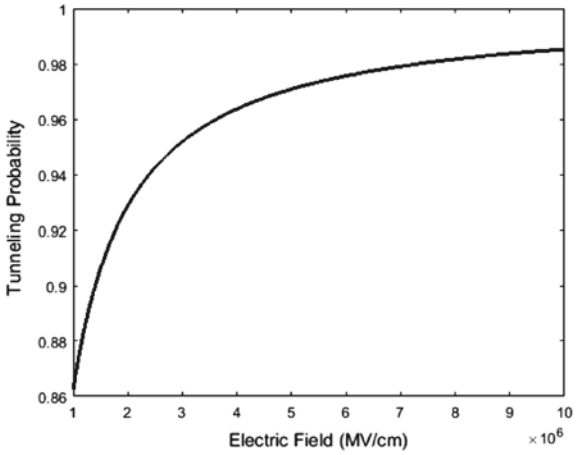


**Fig. 4** Shows that the tunneling probability of InAs based n-type TFET versus Electric Field

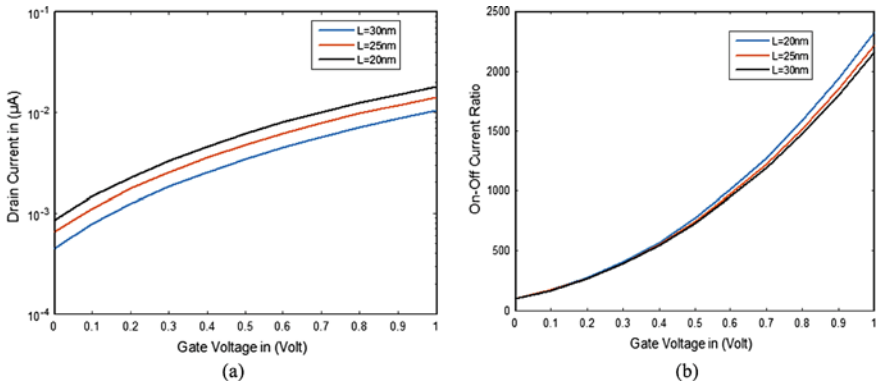


**Fig. 5** **a** Drain current versus gate–source voltage ($V_{gs}$) and **b** ON–OFF current ratio versus gate–source voltage ($V_{gs}$)

following equations. In a tunnel field-effect transistor, the subthreshold swing, SS, can be expressed in terms of transconductance ($g_m$) and subthreshold drain current ($I_D$) as follows [7].

$$\mathrm{SS} = \log 10 \left( \frac{\mathrm{I_D}}{\mathrm{g_m}} \right) \tag{18}$$

The calculated parameters such as current for ON state and OFF state, transistor ON–OFF ratio and subthreshold swing value of the optimized structure of an *n*-type InAs TFET have been given in Table 1.

**Table 1** Calculated parameters

| Optimized parameters: $L = 20$ nm, $t_{OX} = 2$ nm | |
|---|---|
| Performance parameters | Value |
| ON state current or drain current (ON state, $V_{GS} = 0.1$ V, $V_{DS} = 0.1$ V) | 6.1 mA |
| Leakage current (μA) | 4.48 μA |
| $I_{on}/I_{off}$ ratio | $10^3$ |
| Subthreshold swing (SS) | 21 mV/decade |

## 4 Summary

The analysis of an *n*-type InAs TFET has been carried out from the self-consistent solution of the 2D Poisson equation by using finite difference method. This $n^+$-channel tunnel field-effect transistor has been designed for optimum performance with regard to better ON to OFF current ratio and lower subthreshold swing of the device. The values of $I_{on}/I_{off}$ and SS for the optimized device are $10^3$ and 21 mV/decade when channel length is designed at 20 nm. Thus, the optimized n-type InAs TFET having the aforementioned structural parameters will be useful for low-power modern digital application.

## References

1. Jeon K et al (2010) SI tunnel transistors with a novel silicided source and 46 mV/dec swing. In: Symposium of VLSI technology, p 121
2. Toh E-H, Wang GH, Samudra G, Yeo Y-C (2008) Device physics and design of germanium tunneling field-effect transistor with source and drain engineering for low power and high performance applications. J Appl Phys 103(10):105–105
3. Goswami J, Ganguly A, Ghosal A, Banerjee JP (2021) A novel approach dual material double gate germanium-based TFET. In: Acharyya A, Das P (eds) Advanced materials for future terahertz devices, circuits and systems. Lecture notes in electrical engineering, vol 727. Springer, Singapore. https://doi.org/10.1007/978-981-33-4489-1_12
4. Jena D, Fang T, Zhang Q, Xing H (2008) Zener tunneling in semiconductor nanotube and graphene nanoribbon p-n junctions. Appl Phys Lett 93:112106
5. Khatami Y, Banerjee K (2009) Step subthershold slope n-type and p-type tunnel FET devices for low power and energy-efficient digital circuits. IEEE Trans Electron Devices 56(11):356–360
6. Landauer R (1957) Spatial variation of currents and fields due to localized scatterers in metallic conduction. IBM J Res Dev 1(3):223–231
7. Barboni L, Siniscalchi M, Rodriguez BS (2015) TFET based circuit design using the transconductance generation efficiency $g_m/I_d$ method. J Electr Dev Soc 3(3):1–12

# Cutting-Edge Technologies for Terahertz Wave Generation: A Brief History from the Inception Till the Present State of The Art


**Monisha Ghosh, Aritra Acharyya, and Arindam Biswas**

**Abstract** A short review on avalanche transit time devices has been presented in this chapter. From its first proposal till the state of the art, impact avalanche transit time (IMPATT) sources for the generation of terahertz (THz) waves have been briefly described. The noise outputs of the sources at different electromagnetic spectrum have been discussed. The details of deferent device structures, potential materials, popular simulation techniques, etc. are also appended in this chapter.

**Keywords** Avalanche noise · Lateral DDR structure · Wide bandgap semiconductors · Millimeter-wave · Terahertz regime

## 1 Introduction

IMPATT device is a microwave semiconductor device whose principle of operation is based on some basic physical phenomena like impact ionization, avalanche charge multiplication, and transit time of electrons and holes in a reverse biased *p–n* junction biased above the breakdown voltage. The mechanism giving rise to negative resistance is known as the avalanche transit time (ATT) action. This device is a leading solid-state device for generating high microwave (1–30 GHz), millimeter-wave (30–300 GHz) and THz (0.30–10 THz) power.

Shockley [1] in 1954 first introduced the origin of negative resistance within the high field region of reverse biased *p-n* junctions. First ancestor of IMPATT diode,

M. Ghosh
Department of Electronics and Communications Engineering, Supreme Knowledge Foundation Group of Institution, 1, Khan Road, Mankundu, Hooghly, West Bengal 712139, India
e-mail: monisha.ghosh@skf.edu.in

A. Acharyya (✉)
Department of Electronics and Communication Engineering, Cooch Behar Government Engineering College, Harinchawra, Ghughumari, Cooch Behar, West Bengal 736170, India

A. Biswas
Centre for Organic Spin-Tronics and Optoelectronics Devices (COSOD) and Mining Engineering Department, Kazi Nazrul University, Asansol, Burdwan, West Bengal 713340, India



A. Acharyya et al. (eds.), *Generation, Detection and Processing of Terahertz Signals*, Lecture Notes in Electrical Engineering 794,
https://doi.org/10.1007/978-981-16-4947-9_11

i.e., $p^+$-$n$-$i$-$n^+$ structured Read diode was proposed by Read [2] in the year 1958, and he established the initial theoretical explanation of the origin of negative resistance. The nearly intrinsic region (i.e., *i*-region) is used as the transit time drift zone for the injected carriers. Read diode languished in the literature as theoretical device for several years due to difficulty in growing the intrinsic layer. The oscillation from Read diode was first experimentally demonstrated by Lee et al. [3] in the year 1965. But they obtained very low microwave power output from the Read oscillator. In the same year, Johnston et al. reported the significant microwave power output from a $p^+$-$n$–$n^+$ structured reverse biased diode mounted in a suitable resonant cavity [4]. These two reports paved the way for the researchers in this field to come up with new ideas. Since then, the research and development of IMPATT diodes has indeed been phenomenal with the proposal of different types of doping profile, structure, and material operating from lower microwave to higher millimeter-wave frequency bands. In the year 1966, Misawa [5] proposed from his analytical work that negative resistance can be originated from reverse biased *p*–*n* junction of any arbitrary doping profile. Pioneering work on small-signal analysis of Read-type structure was carried out by Gilden and Hines [6] in the year 1966. They showed, when the nature of diode reactance alters from inductive to capacitive, the device resistance also becomes negative. They had assumed equal ionization rate of electrons and holes in their analysis. In 1967, Gummel and Blue [7] studied the avalanche noise in IMPATT sources by using small-signal model developed by them. The unequal ionization rate and drift velocity of electrons and holes were also used by Fisher [8] in his small-signal analysis during the same year. These pioneering works motivated several researchers in this field for designing and fabricating IMPATT devices for realizing high power, high efficiency microwave oscillators.

The effects of series resistance [9] and tunneling [10] on the performance of ATT sources were investigated several scientists. Culshaw [11] and Lee et al. [12] studied the effects of carrier diffusion and ionization rates of charge carriers on the performance of avalanche diodes. Pearsall et al. [13] in 1978 showed that impact ionization rates of hot carriers depend on the crystal orientation of the base semiconductor. In 1980, Lee and Sze [14] measured the dependence of breakdown characteristics of ATT device on crystal orientation of the base semiconductor. The process technology of IMPATT diodes based on Silicon as well as GaAs underwent remarkable improvement through accurate design of these devices in the decades of seventies and eighties.

## 2 Some Landmarks

Before 1970, single-drift, i.e., SD structured IMPATTs ($p^+$-$n$–$n^+$ or $n^+$-$p$-$p^+$ structure) with a single-drift region either for electrons (*n*-type) or for holes (*p*-type) and a single avalanche region were experimentally realized.

## 2.1 Proposal and Implementation of DDR Structure

First double-drift, i.e., DD structure ($p^+$-$p$-$n$–$n^+$) was proposed by Scharfetter et al. in 1970 [15]. DD structure possesses individual drift zones both for electrons and holes. This structure is much better than the earlier SD structure as regards power output, since both types of charge carriers take part in the mechanism of origination of negative resistance (unlike the SD structure in which either electron or hole gets the opportunity to be drifted and thereby originates the negative resistance). In the year 1970, Seidel et al. [16] fabricated both DD and SD diodes operating at 50 GHz. They realized 1.0 W power output with 14.2% efficient DD source and 0.53 watts power output SD source at 50 GHz. Later several confirmations regarding the superiority of DD diodes over their SD counterparts have been established in subsequent decades.

## 2.2 Noteworthy Numerical Simulation Methods

A universal small-signal simulation method was first proposed by Roy et al. [17] in the year 1979. They obtained the field, carrier, and current distributions and static parameters from the simulation of both DD and SD diodes. Later, Roy et al. [18] also formulated the universal small-signal model of IMPATTs. In the year 1991, Banerjee et al. [19] reported the theoretical designs of flat and low–high-low DD structures at V-band and studied the static and microwave properties of those. The theoretical results come with good agreement with the experimental results carried out on molecular beam epitaxy (MBE) grown Si diodes [19]. This agreement showed that the small-signal simulation method reported in [18] is accurate enough for predicting the realistic performance of the device.

## 2.3 Proposal of DAR Structure

Som et al. [20] proposed a completely different structure in 1974, which has two avalanche zones and a common drift region. This structure was given name double-avalanche region (DAR). Analysis of the DAR IMPATT diode was carried out by Dutta et al. [21] in 1982. Latter in 1991, Pati et al. [22] first investigated the characteristics of DAR IMPATTs by developing an in-house computer simulation method. Many interesting properties of DAR IMPATTs are further explored by several authors during last two decades [23, 24].

## 2.4 Further Advancements

In the year 1975, temperature effect on the ATT sources was studied by Takayama [25]. In the same year, Hirachi et al. [26] showed that the efficiency of mm-wave IMPATT diodes can be significantly improved by using ion-implantation method. Gupta [27] tried to develop an approximated method to find the carrier diffusion effect on the device performance. Chive et al. [28] studied the tunneling effect. Winterbon [29] explored the ion-implantation range and energy distribution for fabrication of IMPATT diodes. The limiting operation of silicon ATT oscillators as regards operating frequency was investigated by Doumitria et al. [30]. MM-wave multilayer epitaxial grown Si diode was demonstrated by Wan et al. [31] in the year 1975.

## 2.5 Upper Cut-Off Frequency Limit

In the year 2012, Acharyya et al. [32–34] proposed an avalanche response time-based simulation method for calculating the upper cut-off frequency limit ATT sources. Figures 1 and 2 show the high frequency performance limitations ATT sources based on different semiconductors; the performance of those was studied from avalanche response times ($\tau_A$) and corresponding transit time ($\tau_T$) at different mm-wave and THz frequencies. Same investigation has been illustrated in Fig. 3 for type-IIb diamond-based ATT source.

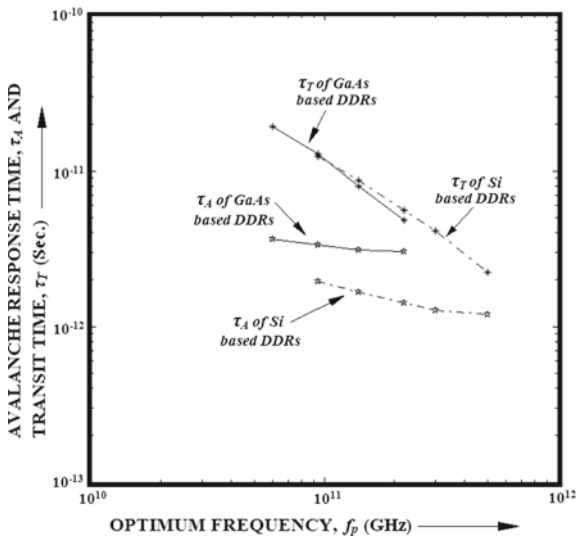


**Fig. 1** Variations of $\tau_A$ and $\tau_T$ with frequency in GaAs and Si diodes [32, 33]

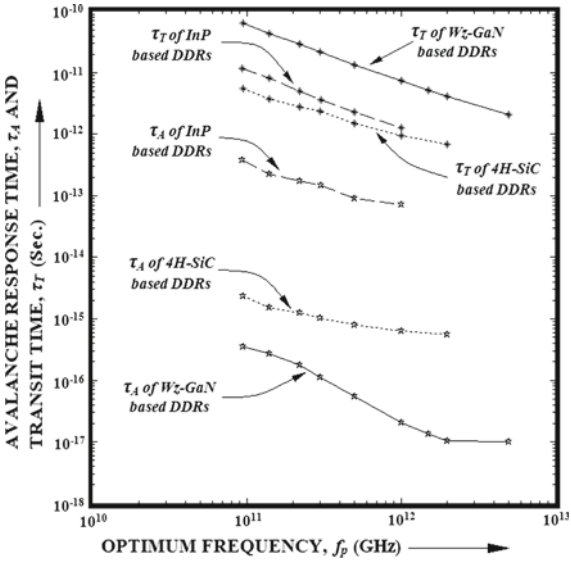


**Fig. 2** Variations of $\tau_A$ and $\tau_T$ with frequency in InP, 4H-SiC and Wz-GaN diodes [32, 33]

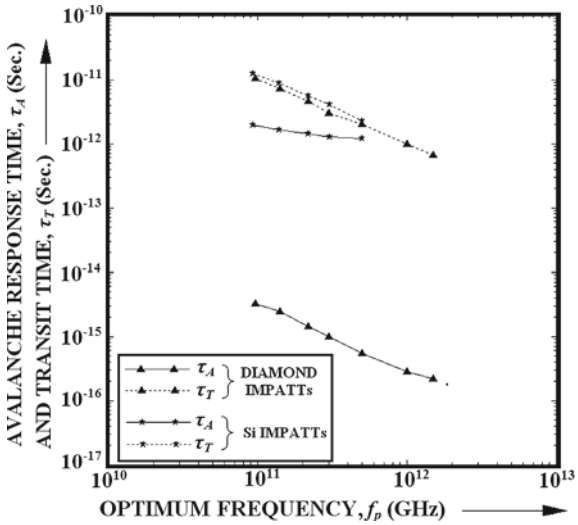


**Fig. 3** Variations of $\tau_A$ and $\tau_T$ with frequency in diamond and Si diodes [34]

## 3 MITATT and TUNNETT Modes

The effect of tunneling on the device performance was first elaborated by Kwok and Haddad [35]. Existence of both avalanche and tunneling generation in ATT sources constitutes mixed tunneling and avalanche transit time (MITATT) and tunnel transit time (TUNNETT) modes. Nishizawa et al. [36] studied the GaAs TUNNETT diodes. The dependency of three possible operating modes, such as (i) IMPATT, (ii) MITATT,

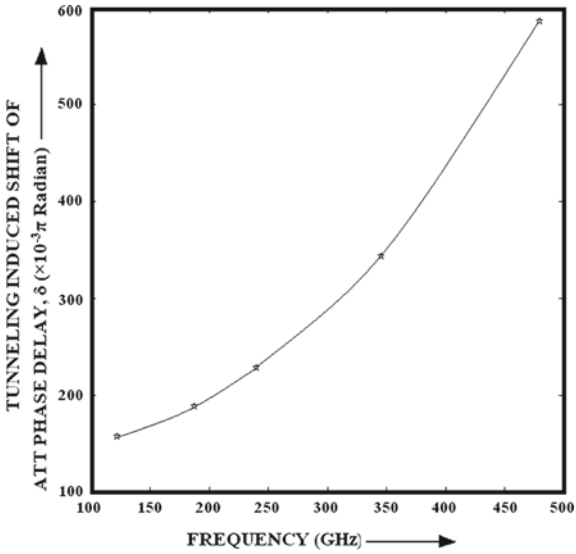


**Fig. 4** Frequency variation of tunneling induced shift of ATT phase delay [47]

and (iii) TUNNETT on the width of the device active region was first enlightened by Elta and Haddad [37, 38]. The device operates in normal IMPATT mode for avalanche region width (>200 nm) and TUNNETT mode for avalanche region width (<50 nm) while in MITATT mode, the avalanche region width lies between 50 and 200 nm. Deterioration of device performance due to tunneling was elaborate by Luy and Kuhn [39]. Simulation method for MITATT mode was later reported [40]. Elta and Haddad [41] and Kane [42] came to the same conclusion as concluded by Luy and Kuhn [39]; however, their studies provide much more insights to the said phenomena. Experimental works on TUNNETT mode were also carried out by Eisele and Haddad [43]. However, later studies show that appropriate design of the device may suppress the performance deterioration of ATT sources operating in MITATT mode [44]. Tunneling effect was more elaborately studied by Acharyya et al. in [45–47] in the recent years (example in Fig. 4).

## 4 Other Base Semiconductors

Initially, Si was the only material for fabricating IMPATTs. Using matured technology, Luy et al. in the year 1987 [48] and Wollitzer et al. in the year 1996 [49] experimentally realized Si-based DD sources at 94 and 140 GHz and obtained satisfactory performance.

### *4.1 GaAs*

At higher mm-wave frequencies, the performance of Si-based IMPATTs is limited as regards lower efficiency and power output. During early seventies to late nineties of the previous century, many researchers have studied the potentialities of group III-V material GaAs as the base semiconductor of ATT oscillators [50–60]. Out of those works, the experimental studies carried out by a few research groups are very significant, such as the reports of Eisele [54], Eisele [55] (proved the better noise performance of GaAs sources as compared to Si sources), Eisele and Haddad [56], Kearney et al. [57], Curow [58] (reported 400 mW peak output power with at 150 GHz), Tschernitz et al. [59], Tschernitz and Freyer [60], etc.

### *4.2 InP*

Another group III-V compound, i.e., InP was introduced for the fabrication of IMPATTs. Ion-implantation method was adopted by Berenz et al. [61] in the year 1978 for realizing SD diode based on InP. Later onwards, several studies on InP material established the fact that InP is better than Si as well as GaAs, as a based material of ATT device [62, 63]; some theoretical studies in recent years reveal that InP IMPATTs are also capable of delivering THz power [64–66]. However, due to the lack of technological advancements in InP process and fabrication technologies, InP could not replace Si and GaAs till date.

### *4.3 Wide Bandgap Semiconductors*

Some wide bandgap (WBG) semiconductors like diamond (C), SiC, GaN, etc. are the new generation materials which possess ultimate THz proficiencies [32–34, 67–70]. In the year 2001, two different research groups Yuan et al. [71] and Vassilevski et al. [72] attempted the fabrication of 4H-SiC-based modified SD diodes operating at X-band. However, they did not obtain the expected performance from their realized sources; lack of matured technology of 4H-SiC and not up to the mark quality of the 4H-SiC wafer used for those fabrications may be the cause of obtaining less power at X-band.

No attempt has yet been made by any researcher for fabricating GaN ATT device. Lack of matured technology of GaN is the main cause of it. However, this material has shown immense potentiality to be the ultimate base material for ATT devices operating at higher mm-wave and THz frequency bands [32] A small-signal simulation study based on drift–diffusion model [32] (Fig. 5). On the other hand, many researchers have suggested diamond as an extraordinary material for realizing mm-wave and THz devices [73–75].

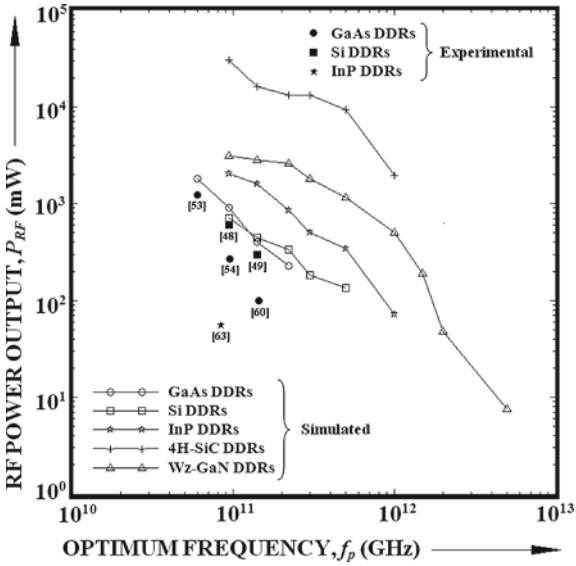


**Fig. 5** Power versus frequency graphs of GaAs, Si, InP, 4H-SiC, and Wz-GaN-based DD sources [32]

## 5 Effect on Photo-Irradiation on Impatt Oscillators

### *5.1 Photo-Irradiation on Vertical IMPATTs*

Carrier leakage current enhancements in the respective layers of ($p^+$- and $n^+$-layers, respectively) Si SD diodes were first experimentally reported by Vyas et al. [76] in the year 1977. Latter in the same year, Yen et al. [77] demonstrated the modulation of GaAs IMPATT diode oscillators by optical illumination. Many researchers have theoretically and experimentally verified the said phenomena during next few decades [78–89]. A theoretical model for analyzing the photo-irradiated Si DD diodes in two different optical illumination configurations (Fig. 6) such as (a) Top Mounted (TM) when the light is illuminated on $p^+$-layer and (b) Flip Chip (FC) when the light is illuminated on $n^+$-layer, at microwave/mm-wave/THz regime was proposed by Acharyya et al. [90] in 2012. They showed from simulation studies that better optical control of DDR IMPATTs based on Si may be achieved if the light is illuminated on the $p^+$-side of the device, i.e., when the photo-generated leakage current is electron dominated since the ionization rates of electrons are greater than those of holes in Si. The reverse results are obtained for IMPATTs based on InP, SiC, GaN, etc. for which hole ionization rates are more than electron ionization rates.

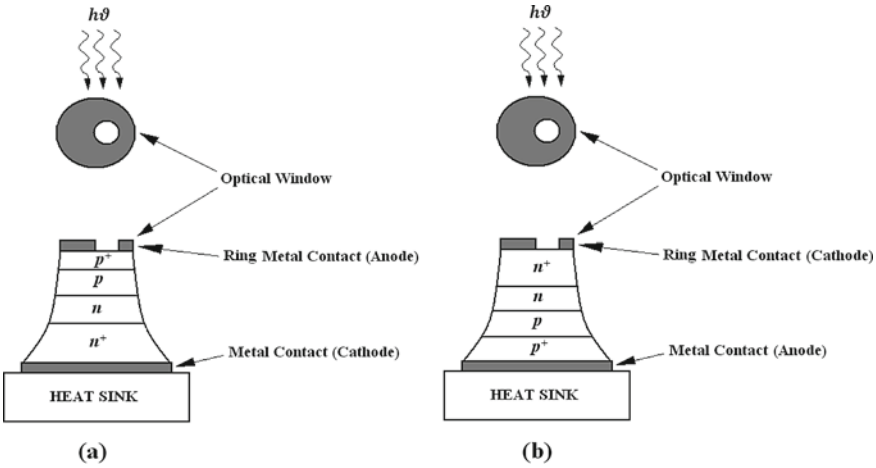


**Fig. 6** **a** TM and **b** FC vertical DDR IMPATT structures under optical illumination [90]

## 5.2 *Lateral IMPATT Oscillators for Better Optical Control*

Planer, mesa, and distributed structure of IMPATT diodes are also tested as the counterparts of conventional vertical SD and DD diodes [4, 91–97]. These structures are especially suitable for coupling optical energy into the electromagnetic oscillation of oscillators (for vertical structure, this coupling is difficult (see Fig. 6)). Moreover, these structures support the monolithic fabrication of the device, unlike the conservative vertical SD and DD structures; series power combination is also very convenient for these lateral structures. Diffused and buried geometry lateral SD diodes were first fabricated and tested by Stabile et al. [98] at X-band. Later 0.18 μm standard CMOS technology was used by Attar et al. [99–102] for fabricating lateral SD structure which were capable of oscillating up to W-band. Recently, Acharyya et al. [103] in 2012 proposed a lateral DD ($p^+$-$p$-$n$–$n^+$) IMPATT structure for better interaction between optical and electromagnetic waves as shown in Fig. 7. He also developed a simulation model [104] to study the optical modulation effect on the static and high frequency characteristics of lateral DDR IMPATTs and showed that better optical control of millimeter-wave properties of IMPATTs may be achieved if the device orientation is lateral instead of conventional vertical orientation.

## 5.3 *Avalanche Noise and Effect of Photo-Irradiation*

The applications of IMPATT diodes are however limited by the inherent noise which arises mainly due to the statistical nature of carrier generation by impact ionization. In 1965, Tager [105] obtained an approximate expression for the small-signal noise

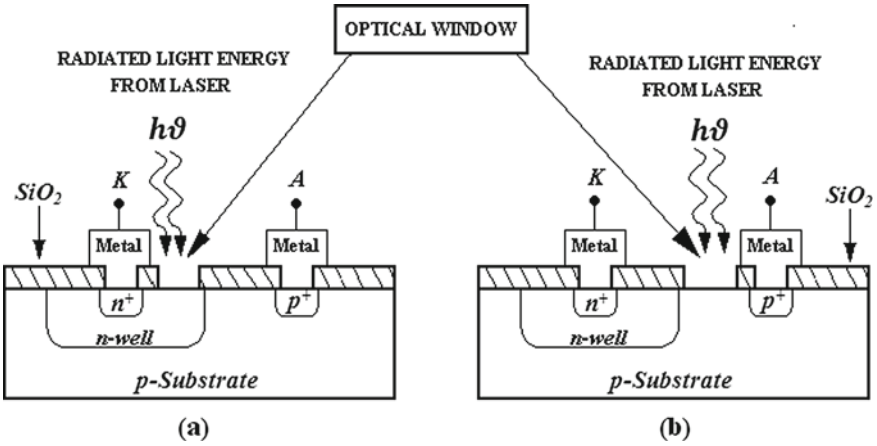


**Fig. 7** Photo-irradiation on **a** *n*-drift and **b** *p*-drift zones of lateral DD diode [103, 104]

spectrum. Hines [106] developed a small-signal theory for noise including interaction with external circuits. He obtained an expression for the noise current spectrum of a small-signal amplifier and calculated the noise figure. Gummel and Blue [7] in their work on avalanche noise of IMPATT diode generalized the theory applicable to arbitrary doping profile and incorporated realistic values of the ionization rates as a function of electric field. They assumed the field-independent saturated drift velocity of electrons and holes. They derived a general expression for the mean square open-circuit noise voltage in terms of Green's function. Large-signal noise properties of ATT sources were studied by Inkson [107] by using the "sharp-current-pulse approximation." Some significant works on the noise characterization of IMPATT oscillators were carried out by Haus et al. [108] and Kuvas [109]. In the year 1978, Etla and Haddad [110] in 1978 reported that a trade-off exists between noise and power under MITATT mode. Later several design methods were reported showing the reduction of noise in the device. Several authors reported that the pure TUNNETT mode operation provides lower noise at the expense of reduction of power output and efficiency.

In the year 1996, a new simulation technique to study the avalanche noise in MITATT mode operation of IMPATT devices was reported [111, 112], which enables one to design very low noise ATT source at mm-wave frequency bands. But the noise spectral densities as well as noise measure of the device were estimated without considering the effect of parasitic series resistance on the noise performance of the device. Recently, the author incorporated the effect of parasitic series resistance to estimate the noise spectral density as well as noise measure (Fig. 8) of Si DD sources at W-band [113, 114].

Millimeter-wave and noise properties of Si ~ $Si_{1-x}Ge_x$ heterojunction DDR MITATT devices at 94 GHz were studied by Banerjee et al. [115]. The effect of photo-irradiation on the noise performance of DDR MITATT device based on Si is

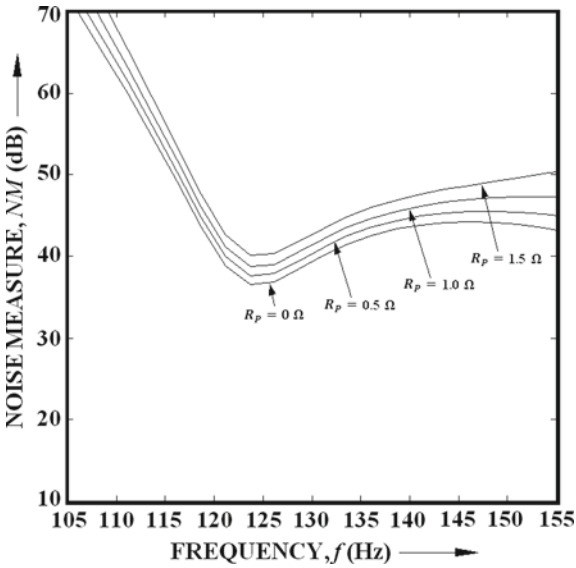


**Fig. 8** Noise measure versus frequency curves of DD Si ATT source [113]

first studied by Acharyya et al. [116, 117]. A model for the small-signal analysis of avalanche noise in DDR MITATT devices under optical illumination is proposed and simulation is carried out to study the noise properties of the device designed to operate at W-band. The results show that avalanche noise measures of optically illuminated FC and TM structures of Si DD diode are 37.1 dB and 40.2 dB, respectively, for the incident photon flux density of $10^{26}$ $m^{-2}$ $s^{-1}$ at 1000 nm wavelength near the bandgap absorption of Si while the noise measure of the same device under dark condition is 35 dB as shown in Figs. 9a and b.

## 6 Terahertz IMPATTs

The THz (i.e., 0.3–10 THz) sources are in great demand now-a-days for various applications such as THz imaging [118], spectroscopy [119], bio-sensing [120], quality inspection in various industrial branches [121–123], medical and pharmaceutical applications [124, 125], THz astronomy [126], etc. Recently, 1.9–2.7 THz cascaded frequency multiplier source is proposed [127–131] which can deliver 10–2 μW peak power. Also, some highly efficient THz devices are under development since last decade [132–140].

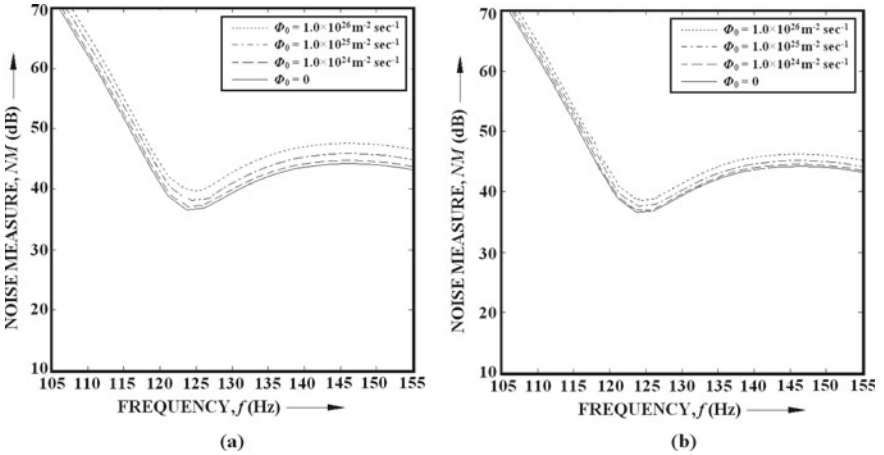


**Fig. 9** Effect of optical illumination on the noise measure versus frequency curves of **a** TM and **b** FC DD Si ATT source [116, 117]

## 6.1 *Figure of Merit Test of Different Semiconductor Materials*

Figure of merit (FOM) is a quantity used to characterize the performance of a device, system or method relative to its alternatives. In material science, FOMs are often used for a particular material in order to determine its relative utility for an application. A comparison of expected theoretical performances (i.e., FOMs) of different semiconductor materials is shown in Table 1. All the FOM values of the semiconductor materials are normalized with respected to the respective FOM values of Si in order to obtain a better comparative investigation.

It can be observed from Table 1 that the WBG semiconductors such as 4H-SiC ($E_g = 3.26$ eV), 6H-SiC ($E_g = 2.86$ eV), Wz-GaN ($E_g = 3.40$ eV), and diamond ($E_g = 5.48$ eV) clearly have much higher advantages like higher frequency of operation, higher switching speed, power dissipation capacity, power-switching product, etc. Moreover, Table 1 shows that WBG semiconductors excel their narrower bandgap (NBG) counterparts as regards the above said aspects.

## 6.2 *WBG Semiconductors*

Several reports suggest that WBG materials like SiC and GaN are best choices for fabricating ATT sources for generating THz frequencies [32, 33, 64–72]. Another very promising WBG material diamond recently attracted the researchers due to

**Table 1** Figure of merit (FOM) test [141]

| FOM | Si | GaAs | 6H-SiC | 4H-SiC | Wz-GaN | Diamond (C) |
|---|---|---|---|---|---|---|
| Johnson's figure of merit (JFOM) [142] | 1.0 | 1.8 | 277.8 | 215.1 | 215.1 | 81,000.0 |
| Baliga's figure of merit (BFOM) [143] | 1.0 | 14.8 | 125.3 | 223.1 | 186.7 | 25,106.0 |
| FET switching speed figure of merit (FSFOM) | 1.0 | 11.4 | 30.5 | 61.2 | 65.0 | 3595.0 |
| Bipolar switching speed figure of merit (BSFOM) | 1.0 | 1.6 | 13.1 | 12.9 | 52.5 | 2402.0 |
| FET power handling figure of merit (FPFOM) | 1.0 | 3.6 | 48.3 | 56.0 | 30.4 | 1476.0 |
| FET power-switching product (FTFOM): | 1.0 | 40.7 | 1470.5 | 3424.8 | 1973.6 | 5,304,459.0 |
| Bipolar power handling capability figure of merit (BPFOM) | 1.0 | 0.9 | 57.3 | 35.4 | 10.7 | 594.0 |
| Bipolar power-switching product (BTFOM) | 1.0 | 1.4 | 748.9 | 458.1 | 560.5 | 1,426,711.0 |

its favorable material properties and potentiality to generate RF power with significantly high DC to RF conversion efficiency at THz frequency regime up to 1.5 THz [34, 73–75].

## 7 Large-Signal Simulation

Small-signal simulations of ATT sources [5–8] are incapable of providing accurate information about the power delivery capability of the source; which can be acquired from the large-signal analysis [144]. Ground-breaking work on large-signal analysis of Read-type silicon IMPATT oscillator was done by Scharfetter et al. in 1969 [145]. Gupta et al. [146] in 1973 proposed a current-excited large-signal model of the device with a circuit model. Recently, Acharyya et al. [147–149] have developed a large-signal simulation method based on non-sinusoidal voltage excitation which is the most accurate one as regards its capability of predicting power and efficiency of mm-wave and THz ATT sources.

### *7.1 Diamond ATT Sources*

Recently, Acharyya et al. [34] have made an attempt to study the large-signal properties of DDR IMPATT devices based on type-IIb diamond at both mm-wave and THz

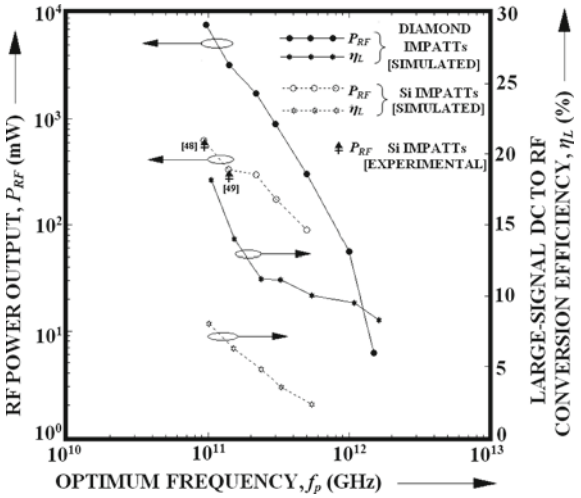


**Fig. 10** Power output and efficiency versus frequency graphs of Si and diamond DD sources [34]

frequencies. A rigorous large-signal simulation based on non-sinusoidal voltage excitation model developed earlier by the authors [147–149] is used to obtain the electric field snap-shots at different transit angles over consecutive cycles of oscillation. The large-signal negative conductance, power output, and conversion efficiency of both the devices are obtained at different voltage modulations. The large-signal simulation results show that the DDR Diamond IMPATT device delivers a peak RF power of 7.79 W with 18.17% conversion efficiency at 94 GHz while at 0.5 THz the peak power output and conversion efficiency decrease to 302.8 mW and 9.91%, respectively, taking 50% voltage modulation in both the cases. A comparative study of DDR IMPATTs based on diamond and Si shows that the former excels the later as regards high frequency-high power performance at both mm-wave and THz frequency bands (Fig. 10).

## *7.2 Group III–IV Compound Semiconductor-Based ATT Sources*

Acharyya et al. [150] have recently explored the potentiality of DD devices based on Wz-GaN as regards their performance. Large-signal simulation method developed by the authors [147–149] has been used to obtain the high frequency properties and performance of the device. The effect of band to band tunneling on the large-signal properties of the device at different mm-wave and THz frequencies is also investigated. Large-signal simulation results show that at mm-wave 94 GHz frequency the device delivers 3.73 W peak RF power ($P_{RF}$ in pure IMPATT mode and $P_{RF}^{'}$ in MITATT/TUNNETT mode) with around 21% conversion efficiency when the voltage modulation is 50%, whereas peak RF power output decreases to around

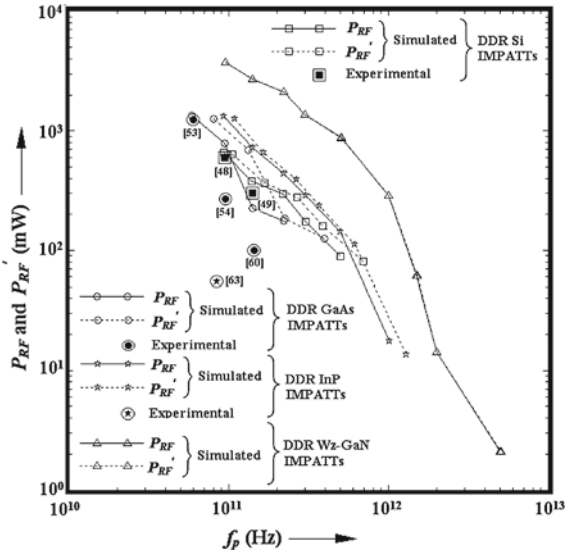


**Fig. 11** Power output and efficiency versus frequency graphs of Wz-GaN, Si, GaAs, and InP DD sources [150]

2.1 mW with 7.4% conversion efficiency at 5.0 THz for the same voltage modulation. A comparative study is presented in Fig. 11.

## 8 Series Resistance

Since the negative resistance of mm-wave and THz IMPATTs remains within the range of few ohms to few milli-ohms, the power loss in the inactive region of the device cannot be compensated fully by the external circuitry. This loss should be as small as possible in order to obtain nonzero output power from the device. The RF power is dissipated in the un-depleted region of the device since it contributes to the positive series resistance of the device. The series resistance originates not only from the un-swept epitaxial layer but also from the substrate and contact layers of the device. The negative resistance of millimeter-wave IMPATTs is in the range of few ohms, so the positive series resistance is to be kept to a minimum possible value by appropriate design of the structural, doping, and bias current parameters of the device. The direct measurement of series resistance is difficult [151] due to the errors associated with network analyzer. Further such measurement necessitates an accurate analysis of device-circuit interaction which is not an easy task.

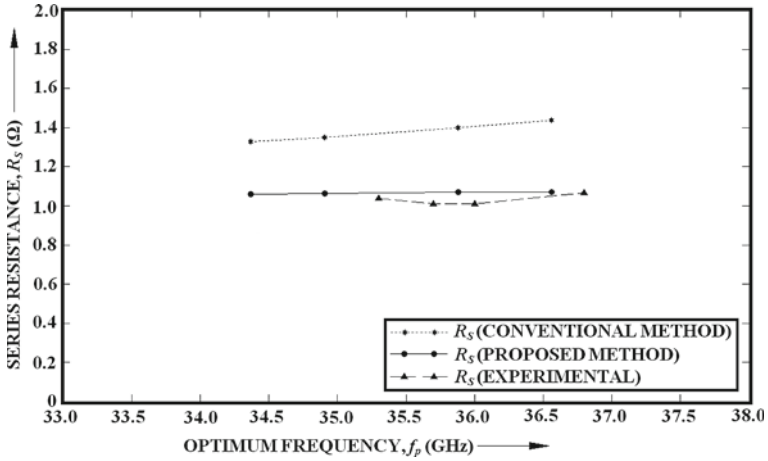


**Fig. 12** Series resistance versus frequency obtained from conventional method, proposed method [155, 156], and experimental measurement [154]

## *8.1 Experimental Determination of Series Resistance*

And indirect method was used by Adlerstein et al. [152] in the year 1983, for experimentally measuring the series resistance of DD GaAs IMPATT operating at 34–44 GHz. Some theoretical and experimental studies on the electrical series resistance of X- and Ka-band IMPATT diodes were also reported [153, 154]. The series resistance of Ka-band IMPATTs has been studied from small-signal simulation, and the reported [154] results have been compared with the experimental data.

## *8.2 A New Technique to Estimate the Series Resistance*

An interesting and very accurate method has been proposed by Acharyya et al. [155, 156] for estimating the series resistance of mm-wave IMPATTs from the large-signal electric field snap-shots at different phase angles of a full cycle of steady-state oscillation. The results show that the proposed method provides better and closer agreement with the experimental value [154] as compared to the conventional method (see Fig. 12).

## *8.3 Influence of Skin Effect*

Acharyya et al. [157] introduced the influence of skin effect in the method of estimating the series resistance. The series resistance estimated by including the skin

effect is in closer agreement with the experimental values as compared to that without including the same as shown in Figs. 13 and 14.

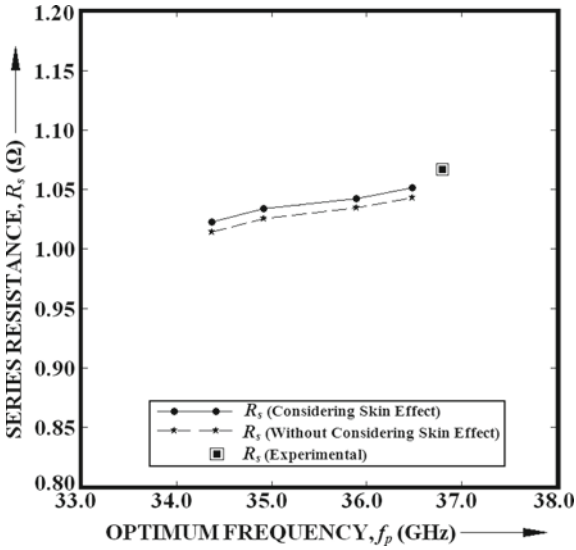


**Fig. 13** Series resistance of 35 GHz SDR Si IMPATT calculated by using the proposed method [157] and series resistance obtained from experimental measurement [154] versus frequency

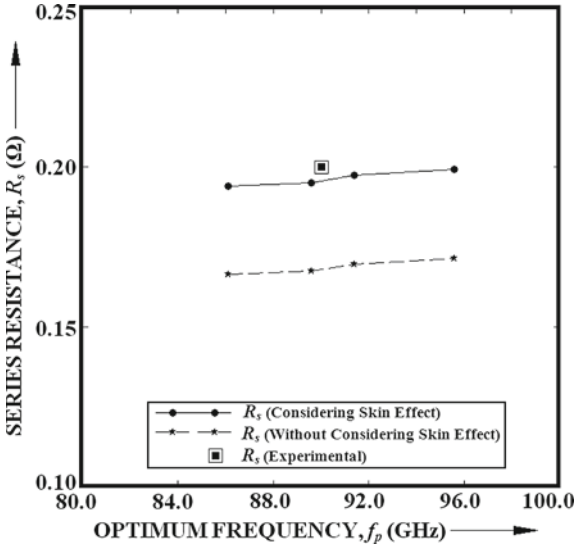


**Fig. 14** Series resistance of 94 GHz DDR Si IMPATT calculated by using the proposed method [157] and series resistance obtained from experimental measurement [48] versus frequency

## 9 Summary

A brief review of the progress and development of IMPATT device since its beginning till the present state of art is presented in this chapter. Various revolutionary aspects regarding IMPATT sources are discussed briefly. This review will be extremely helpful for the present researchers working in this field.

## References

1. Shockley W (1954) Negative resistance arising from transit time in semiconductor diodes. Bell Syst Tech J 33:799–826
2. Read WT (1958) A proposed high frequency negative resistance diode. Bell Syst Tech J 37:401
3. Lee CA, Batdrof RL, Weigman W, Kaminsky G (1965) The read diode an avalanching transit time negative resistance oscillator. Appl Phys Lett 6:89–91
4. Johnson RL, Deloach BC, Cohen BG (1965) A silicon diode microwave oscillator. Bell Syst Tech J 44:369–372
5. Misawa T (1966) The negative resistance in p-n junctions under avalanche breakdown conditions Part-1. IEEE Trans Electron Device 13:137–151
6. Gilden M, Hines ME (1966) Electronic tuning effects in read microwave avalanche diode. IEEE Trans Electron Devices 13:169–175
7. Gummel HK, Blue JL (1967) A small-signal theory of avalanche noise in IMPATT diodes. IEEE Trans Electron Devices 14:569–580
8. Fisher ST (1967) Small-signal impedance of avalanche junctions with unequal electron and hole ionization rates and drift velocities. IEEE Trans Electron Devices 14:313–322
9. Gewartowski JW (1968) The effect of series resistance on avalanche diode oscillator frequency. J Appl Phys 46:31
10. Kwok SP, Haddad GI (1972) Effect of tunnelling on an impatt oscillator. J Appl Phys 43:3824–3830
11. Culshaw B (1974) Effect of carrier diffusion on operation of avalanche diodes. Electron Lett 10:143SS
12. Lee CM, Seddik ME, Haddad GI (1974) Effect of ionisation rates on Si IMPATT diodes. IEEE Trans Electron Devices 21:808
13. Pearsall TP, Capasso F, Nahory RE, Pallock MA, Chelikowsky JR (1978) The band structure dependence of impact ionization by hot carriers in semiconductors: GaAs. Solid state Electron 21:297
14. Lee MH, Sze SM (1980) Orientation dependence of Breakdown voltage in GaAs. Solid State Electron 23:1007
15. Scharfetter DL, Evans WJ, Johnson HL (1970) Double drift region $p^+pnn^+$ avalanche diode oscillators. Proc IEEE (Lett) 50:1131
16. Seidel TE, Davis RE, Jglesias DE (1970) DDR ion-implanted ($p^+pnn^+$) mm-wave IMPATT diodes. Inst. Electron devices Meeting, Washington DC, USA, 28th–30th Oct 1970, pp 52
17. Roy SK, Sridharan M, Ghosh R, Pal BB (1979) Computer method for the dc field and carrier current profiles in the IMPATT device starting from the field extremum in the depletion layer. In: Miller JH (ed) Proceeding of the 1st conference on numerical analysis of semiconductor devices (NASECODE I). Dublin, Ireland, pp 266–274

18. Roy SK, Banerjee JP, Pati SP (1985) A computer analysis of the distribution of high frequency negative resistance in the depletion layer of IMPATT Diodes. In: Proceeding 4th conference on numerical analysis of semiconductor devices (NASECODE IV) (Dublin), Ireland, pp 494–500
19. Banerjee JP, Luy JF, Schaffler F (1991) Comparison of theoretical and experimental 60 GHz silicon IMPATT diode performance. Electron Lett 27:1049–1050
20. Som B, Pal BB, Roy SK (1974) A small-signal analysis of an IMPATT device having two avalanche layers interspaced by a drift layer. Solid State Electron 17:1029
21. Dutta DN, Pati SP, Banerjee JP, Pal BB, Roy SK (1982) Computer analysis of DC field and current density profiles of DAR Impatt diodes. IEEE Trans Electron Devices 29:677–632
22. Pati SP, Banerjee JP, Roy SP (1991) High frequency numerical analysis of DAR impatt diode. Semicond Sci Tech 6:777–783
23. Cruz RDL, Zemliak A, Alexander M (2004) Characteristics of the double avalanche region IMPATT diode in millimetric range. In: 14th international conference on electronics, communications and computers, 2004 (CONIELECOMP 2004), 16–18th Feb 2004, pp 223–227
24. Zemliak A, Ostrovsky A, Vergara S, Machusskiy E (2011) Analysis and optimization of a DAR IMPATT Diode for 330 GHz. In: CISST'11 proceedings of the 5th WSEAS international conference on circuits, systems, signal and telecommunications, pp 95–101
25. Takayama Y (1975) Effect of temperature on devices admittance of GaAs and Si IMPATT diodes. IEEE Trans Microw Theory Tech 23:673
26. Hirachi Y, Nishi H, Shireda M, Fukakawa Y (1975) Millimeter wave IMPATT diodes with improved efficiency by using ion-implanted ohmic contact. Proc IEEE Lett 63:1367–1367
27. Gupta MS (1975) A simple approximate method to estimate the effect of carrier diffusion in Impatt diodes. Solid State Electron 18:327
28. Chive M, Constant E, Lefebvre M, Ribetich JP (1975) Effect of tunneling on high efficiency Impatt avalanche diode. Proc IEEE (Lett) 63:824–826
29. Winterbon KB (1975) Ion implantation range and energy deposition distributions, vol. 2. New York, IFI/Plenum Press
30. Doumitria I, Salmer G, Constant E (1975) High frequency limitation of Silicon IMPATT diode velocity modulation. J Appl Phys 46:1831
31. Wan CP, Chang YS, Denoglar EJ (1975) Multilayer epitaxially grown silicon IMPATT diodes at millimeter wave frequencies. J Electron Mater 4(1):119–129
32. Acharyya A, Banerjee JP (2014) Prospects of IMPATT devices based on wide bandgap semiconductors as potential terahertz sources. Appl Nanosci 4:1–14
33. Acharyya A, Banerjee JP (2013) Potentiality of IMPATT devices as terahertz source: an avalanche response time based approach to determine the upper cut-off frequency limits. IETE J Res 59(2):118–127
34. Acharyya A, Mallik A, Banerjee D, Ganguli S, Das A, Dasgupta S, Banerjee JP (2014) Large-signal characterizations of DDR IMPATT devices based on group III-V semiconductors at millimeter-wave and terahertz frequencies. Journal of Semiconductors 35(8):084003-1-10
35. Kwok SP, Hadded GI (1972) Effects of tunnelling on an IMPATT oscillator. J Appl Phys 43:3824–3860
36. Nishizawa J, Motoya K, Okuno Y (1978) GaAs TUNNET diodes. IEEE Trans MTT 26(12):1029–1035
37. Elta EM, Hadded GI (1979) High frequency limitations of IMPATT, MITATT and TUNNET mode devices. IEEE Trans. on MTT 27:442
38. Elta EM, Hadded GI (1978) Mixed tunnelling and avalanche mechanism in *p-n* junctions and their effects on microwave transit-time devices. IEEE Trans Electron Devices 25(6):694–702
39. Luy JF, Kuehnf R (1989) Tunneling assisted IMPATT operation. IEEE Trans Electron Devices 36(3):589–595
40. Dash GN, Pati SP (1992) A generalized simulation method for IMPATT mode operation and studies on the influence of tunnel current on IMPATT properties. Semicond Sci Technol 7:222–230

41. Elta EM (1978) The effect of mixed tunneling and avalanche breakdown on microwave transit-time diodes. Ph.D. dissertation, Electron Physics Laboratory at the University of Michigan, Ann Arbor, MI, Tech Rep
42. Kane EO (1961) Theory of tunneling. J Appl Phys 32:83–91
43. Eisele H, Hadded GI (1995) GaAs TUNNETT diodes on diamond sink for 100 GHz and above. IEEE Trans MTT 43(1):210
44. Dash GN (1995) A new design approach for MITATT and TUNNETT mode devices. Solid State Electron 38:1381–1385
45. Acharyya A, Mukherjee M, Banerjee JP (2013) Effects of tunnelling current on mm-wave IMPATT devices. Int J Electron 102(9):1429–1456
46. Acharyya A, Mukherjee M, Banerjee JP (2011) Influence of tunnel current on DC and dynamic properties of silicon based terahertz IMPATT source. Terahertz Sci Technol 4(1):26–41
47. Acharyya A, Mukherjee M, Banerjee JP (2011) Studies on the millimeter-wave performance of MITATTs from avalanche transit time phase delay. In: Proceeding of IEEE applied electromagnetics conference 2011, Kolkata, India, 18–22 Dec 2011, pp 1–4
48. Luy JF, Casel A, Behr W, Kasper E (1987) A 90-GHz double-drift IMPATT diode made with Si MBE. IEEE Trans Electron Devices 34:1084–1089
49. Wollitzer M, Buchler J, Schafflr F, Luy JF (1996) D-band Si-IMPATT diodes with 300 mW CW output power at 140 GHz. Electron Lett 32:122–123
50. Huang HC (1973) A modified GaAs IMPATT structure for high-efficiency operation. IEEE Trans Electron Devices 20(5):482–486
51. Goldwasser RE, Rosztoczy FE (1974) High efficiency GaAs low-high-low IMPATTs. Appl Phys Lett 25:92
52. Bozler CO, Donelly JP, Murphy RA, Laton RW, Sudhury RN, Lindley WT (1976) High efficiency ion implanted Lo-hi-lo GaAs IMPATT diodes. Appl Phys Lett 29:123–125
53. Adlerstein MG, Chu SLG (1984) GaAs IMPATT diodes for 60 GHz. IEEE Electron Devices Let 5:97–98
54. Eisele H (1989) Selective etching technology for 94 GHz, GaAs IMPATT diodes on diamond heat sinks. Solid State Electron 32(3):253–257
55. Eisele H (1990) GaAs W-band IMPATT diode for very low noise oscillations. Electron Lett 26(2):109–110
56. Eisele H, Hadded GI (1992) GaAs single-drift flat profile IMPATT diodes for CW operation at D band. Electron Lett 28(23):2176–2177
57. Kearney MJ, Couch NR, Stephens JS, Smith RS (1992) Low noise, high efficiency GaAs IMPATT diodes at 30 GHz. Electron Lett 28(8):706–708
58. Curow M (1994) Proposed GaAs IMPATT device structure for D-band applications. Electron Lett 30(19):1629–1631
59. Tschernitz M, Freyer J, Grothe H (1994) GaAs read-type IMPATT diodes for D-band. Electron Lett 30(13):1070–1071
60. Tschernitz M, Freyer J (1995) 140 GHz GaAs double-read IMPATT diodes. Electron Lett 31(7):582–583
61. Berenz JJ, Fank FB, Hierl TL (1978) Ion-implanted p-n junction Indium-Phosphide IMPATT diodes. Electron Lett 14(21):683–684
62. Banerjee JP, Pati SP, Roy SK (1984) High frequency characterisation of double drift region InP and GaAs diode. Appl Phys A 48:437–443
63. Eisele H, Chen CC, Munns GO, Haddad GI (1996) The potential of InP IMPATT diodes as high-power millimeter-wave sources: First experimental results. IEEE MTT-S Inter Microwave Symp Dig 2:529–532
64. Mukherjee M, Banerjee S, Banerjee JP (2010) Dynamic characteristics of III-V and IV-IV semiconductor based transit time devices in the terahertz regime: a comparative analysis. Terahertz Sci Technol 3:98–109
65. Mukherjee M, Mazumder N, Roy SK, Goswami K (2007) Terahertz frequency performance of double drift IMPATT diode based on opto-sensitive semiconductor. In: Proceeding of Asia-Pacific microwave conference, pp 1–4

66. Acharyya A, Banerjee S, Banerjee JP (2012) Calculation of avalanche response time for determining the high frequency performance limitations of IMPATT devices. J Electron Dev 12:756–760
67. Mukherjee M, Mazumder N, Roy SK (2009) Prospects of 4H-SiC double drift region IMPATT device as a photo-sensitive high-power source at 0.7 terahertz frequency regime. Active Passive Electron Componen 1–9
68. Panda AK, Parida RK, Agarwala NC, Dash GN (2007) A comparative study on the high band gap materials (GaN and SiC)-based IMPATTs. In: Proceding of Asia-pacific microwave conference, pp 1–4
69. Panda AK, Pavlidis D, Alekseev E (2001) DC and high-frequency characteristics of GaN-based IMPATTs. IEEE Trans Electron Devices 48:820–823
70. Banerjee S, Mukherjee M, Banerjee JP (2010) Bias current optimization of Wurtzite-GaN DDR IMPATT diode for high power operation at THz frequencies. Int J Adv Sci Technol 16:12–20
71. Yuan L, James A, Cooper JA, Melloch MR, Webb KJ (2001) Experimental demonstration of a silicon carbide IMPATT oscillator. IEEE Electron Device Letter 22:266–268
72. Vassilevski KV, Zorenko AV, Zekentes K, Tsagaraki K, Bano E, Banc C, Lebedev A (2001) 4H-SiC IMPATT diode fabrication and testing. In: Technical digest of international conference on SiC and related materials, Tsukuba, Japan, pp 713–714
73. Trew RJ, Yan JB, Mock PM (1991) The potentiality of diamond and SiC electronic devices for microwave and millimeter-wave power applications. Proc IEEE 79(5):598–620
74. Osman MA, Andrews G, Kreskovsky JP, Grubin HL (1989) Numerical simulation studies of semiconducting diamond electronic devices. Final Report on Contract DNA001–87-C-0250, Defense Nuclear Agency 1989
75. Mock PM, Trew RJ (1989) RF performance characteristics of double-drift MM-wave diamond IMPATT diodes. In: Proceeding of IEEE/cornell conference advanced concepts in high-speed semiconductor devices and circuits, pp 383–389
76. Vyas HP, Gutmann RJ, Borrego JM (1977) Leakage current enhancement in IMPATT oscillator by photo-excitation. Eletron Lett 13:189–190
77. Yen HW, Barnoski MK, Hunsperger RG, Melville RT (1977) Switching of GaAs IMPATT diode oscillator by optical illumination. Appl Phys Lett 31:120–121
78. Schweighart A, Vyas HP, Borrego JM, Gutmann RJ (1978) Avalanche diode structure suitable for microwave-optical interaction. Solid-Sate Electron 21:1119–1121
79. Vyas HP, Gutmann RJ, Borrego JM (1979) Effect of hole versus electron photocurrent on microwave-optical interactions in impatt oscillators. IEEE Trans Electron Devices 26(3):232–234
80. Forrest JR, Seeds AJ (1978) Optical injection locking of impatt oscillators. Electron Lett 14(19):626–627
81. Seeds AJ, Augusto A (1990) Optical control of microwave semiconductor devices. IEEE Trans Microw Theory Tech 38(5):577–585
82. Mukherjee R, Banerjee JP (1994) Effect of electron and hole dominant photocurrent on the millimeter-wave properties of indium phosphide impatt diode at 94 GHz. Semicond Sci Technol 9:1–4
83. Mukherjee M, Majumder N (2007) Optically illuminated 4H-SiC terahertz IMPATT device. Egypt J Solids 30(1):87–101
84. Mukherjee M, Majumder N, Roy SK (2008) Prospects of 4H-SiC double drift region IMPATT device as a photo-sensitive high power source at 0.7 terahertz frequency regime. Active Passive Electron Compon 1–9
85. Mukherjee M, Roy SK (2009) Optically modulated III-V nitride-based top-mounted and flip-chip IMPATT oscillators at terahertz regime: studies on the shift of avalanche transit time phase delay due to photogenerated carriers. IEEE Trans Electron Device 56(7):1411–1417
86. Banerjee S, Chakrabarti I, Baidya R, Banerjee JP (2010) Studies on frequency chirping in optical illuminated α-Gallium Nitride Impatt Diodes at Sub-millimeter wave frequency. J Telecommun 3(2):1–8

87. Banerjee S, Banerjee JP (2010) Studies on Optical Modulation of III-V GaN and InP based DDR Impatt diode at Sub-millimeter wave frequency. Int J Eng Sci Technol 2(7):2790–2801
88. Mukhopadhyay J, Banerjee S, Banerjee JP (2010) A comparative study on indium phosphide and α-gallium nitride based impatt oscillators for terahertz communication. J Telecommun 3(1):14–21
89. Acharyya A, Banerjee JP (2011) A comparative study on the effect of optical illumination on $Si_{1-x}Ge_x$ and Si based DDR IMPATT diodes at W-Band. Iran J Electron Electr Eng 7(3):179–189
90. Acharyya A, Banerjee JP (2012) Analysis of photo-irradiated double-drift region silicon impact avalanche transit time devices in the millimeter-wave and terahertz regime. Terahertz Sci Technol 5(2):97–113
91. Midford TA, Bowers HC (1968) A two-port IMPATT diode travelling wave amplifier. Proc IEEE 56:1724–1725
92. Lee DH, Weller KP, Thrower WF (1978) Ion-implanted planner mesa IMPATT diodes for millimeter wavelengths. IEEE Trans Electron Devices 25:714–722
93. Bayraktaroglu B (1988) Monolithic 60 GHz GaAs IMPATT oscillators. IEEE Trans MTT 36(12):1925–1929
94. Lei WN, Stacey W, Brooks RC, Donegan K, Hoke WE (1988) Millimeter-wave monolithic GaAs IMPATT VCO. IEEE Trans MTT 36(12):1942–1947
95. Luy JF, Strohm KM, Benchler J (1988) Silicon monolithic mm-wave IMPATT Oscillator. In: Conference Paper, Microwave exhibition and publishers, Turnbridge Wells (UK), pp382–387
96. Bayraktaroglu B (1988) V-band monolithic IMPATT VCO. IEEE MTT-S Inter Microw Sympos Dig 2:687–690
97. Camilleri N, Bayraktaroglu B (1988) Monolithic millimeter-wave IMPATT oscillator and active antenna. IEEE MTT-S Inter Microw Symp Dig 2:955–958
98. Stabile PJ, Lalevic B (1989) Lateral IMPATT diodes. IEEE Trans Electron Devices 10(6):249–251
99. Al-Attar T, Mulligan M, Lee TH (2004) Lateral IMPATT diodes in standard CMOS technology. Int Electron Devices Meet Dig 459–462. *Washington, DC*, 13–14 Dec 2004
100. Al-Attar T, Mulligan M, Lee TH (2005) A 77 GHz monolithic IMPATT transmitter in standard CMOS technology. IEEE MTT-S Int Microwave Symp Dig Long Beach, CA, June 2005
101. Al-Attar T, Lee TH (2005) Monolithic integrated millimeter-wave IMPATT transmitter in standard cmos technology. IEEE Trans MTT 53(11):3557–3561
102. Al-Attar T (2011) CMOS diodes operating beyond avalanche frequency. In: 12th International symposium on quality electronic design (ISQED), 14–16 Mar 2011, pp 1–6
103. Acharyya A, Banerjee JP (2012) A proposed lateral DDR IMPATT structure for better millimeter-wave optical interaction. In: IEEE international conference on devices, circuits and systems 2012,Karunya University, Coimbatore, Tamil Nadu, India, 15–16 Mar 2012, pp 599–602
104. Acharyya A, Banerjee S, Banerjee JP (2012) Optical control of millimeter-wave lateral double-drift region silicon IMPATT device. Radioengineering 21(4):1208–1217
105. Tager AS (1965) Current fluctuations in semiconductor (dielectric) under the conditions of impact ionization and avalanche breakdown. Sov Phys Solid State 4:1919–1925
106. Hine ME (1966) Noise theory of Read type avalanche diode. IEEE Trans Electron Devices 13:57–60
107. Inkson JK (1958) Noise generation under large signal conditions in the Read micro-wave avalanche diode. Int J Electron 25:1–12
108. Haus HA, Statz H, Pucel PA (1971) Optimum noise measure of IMPATT diode. IEEE Trans MTT 19:801–8123
109. Kuvas RL (1972) Noise in IMPATT diodes Intrinsic properties. IEEE Trans Electron Devices 19:220–226
110. Elta ME, Haddad GI (1978) Mixed tunneling and avalanche mechanism in p-n junctions and their effects on microwave transit time devices. IEEE Trans Electron Devices 25:694–702

111. Dash GN, Mishra JK, Panda AK (1996) Noise in mixed tunneling avalanche transit time (MITATT) diodes. Solid-State Electron 39(10):1473–1479
112. Mishra JK, Panda AK, Dash GN (1997) An extremely low-noise heterojunction IMPATT. IEEE Trans Electron Devices 44(12):2143–2148
113. Acharyya A, Mukherjee M, Banerjee JP (2010) Noise performance of millimeter-wave silicon based mixed tunneling avalanche transit time.(MITATT) diode. Int J Electr Electron Eng 4(8):577–584
114. Acharyya A, Mukherjee M, Banerjee JP (2011) Noise in millimeter-wave mixed tunneling avalanche transit time diodes". Arch Appl Sci Res 3(1):250–266
115. Banerjee S, Acharyya A, Banerjee JP (2012) Millimeter-wave and noise properties of Si~$Si_{1-x}Ge_x$ heterojunction double-drift region MITATT devices at 94 GHz. In: IEEE Conference CODEC 2012, Kolkata, India, 17–19 Dec 2012, pp 1–4
116. Acharyya A, Banerjee S, Banerjee JP (2013) Effect of photo-irradiation on the noise properties of double-drift silicon MITATT device. Int J Electron 101(9):1270–1286
117. Banerjee S, Acharyya A, Mitra M (2012) Dependence of noise properties on photon flux incident on Silicon MITATT device at millimeter-wave window frequencies. Procedia Technol 4:431–436
118. Chan WL, Deibel J, Mittleman DM (2007) Imaging with terahertz radiation. Rep Prog Phys 70:1325–1379
119. Grischkowsky D, Keiding S, Exter M, Fattinger C (1990) Far-infrared time-domain spectroscopy with terahertz beams of dielectrics and semiconductors. J Opt Soc Am B 7:2006–2015
120. Debus C, Bolivar PH (2007) Frequency selective surfaces for high sensitivity terahertz sensing. Appl Phys Lett 91:184102
121. Yasui T, Yasuda T, Sawanaka K, Araki T (2005) Terahertz paintmeter for noncontact monitoring of thickness and drying progress in paint film. Appl Opt 44:6849–6856
122. Stoik CD, Bohn MJ, Blackshire JL (2008) Nondestructive evaluation of aircraft composites using transmissive terahertz time domain spectroscopy. Opt Expr 16:17039–17051
123. Jördens C, Koch M (2008) Detection of foreign bodies in chocolate with pulsed terahertz spectroscopy. Opt Eng 47:037003
124. Fitzgerald AJ, Cole BE, Taday PF (2005) Nondestructive analysis of tablet coating thicknesses using terahertz pulsed imaging. J Pharm Sci 94:177–183
125. Siegel PH (2004) Terahertz technology in biology and medicine. IEEE Trans Microw Theory Tech 52:2438–2447
126. Siegel PH (2007) THz instruments for space. IEEE Trans Antenn Propag 55:2957–2965
127. Ward J, Schlecht E, Chattopadhyay G, Maestrini A, Gill J, Maiwald F, Javadi H, Mehdi I (2004) Capability of THz sources based on schotiky diode frequency multiplier chains. IEEE MTT-S Dig 12:1587–1590
128. Heyminck S, Güsten R, Graf U, Stutzki J, Hartogh P, Hübers HW, Ricken O, Klein B (2009) GREAT: ready for early science aboard SOFIA. In: Proceding of 20th international symposium space THz technology, Charlottesville, VA, pp 315–317
129. Crowe TW, Hesler JL, Retzloff SA, Pouzou C, Schoenthal GS (2011) Solid state LO sources for greater than 2THz. In: 2011 ISSTT digest, 22nd symposium on space terahertz technology. Tucson Arizona, USA
130. Crowe TW, Hesler JL, Retzloff SA, Pouzou C, Hester JL (2011) Multiplier based sources for frequencies above 2 THz," In: 36th international conference on infrared, millimeter and terahertz sources (IRMMW-THz), pp 1–4
131. Maestrini A, Mehdi I, Siles JV, Ward J, Lin R, Thomas B, Lee C, Gill J, Chattopadhyay G, Schlecht E, Pearson J, Siegel P (2012) First demonstration of a tunable electronic source in the 2.5–2.7 THz Range. IEEE Trans Terahertz Sci Tech 3:112–123
132. Lynch SA et al (2005) Silicon quantum cascade lasers for THz sources. In: 18th annual meeting of the IEEE on lasers and electro-optics society. Leos 22–28 Oct 2005, pp 728–729

133. Seo M, Urteaga M, Hacker J, Young A, Griffith Z, Jain V, Pierson R, Rowell P, Skalare A, Peralta A, Lin R, Pukala D, Rodwell M (2011) InP HBT IC technology for terahertz frequencies: fundamental oscillators Up to 0.57 THz. IEEE J Solid-State Circuits 46(10):2203–2214
134. Gray WW, Kikushima L, Morentc NP, Wagner RJ (1969) Applying IMPATT power sources to modern microwave systems. IEEE J Solid-State Circuits 4:409–413
135. Chang Y, Hellum JM, Paul JA, Weller KP (1977) Millimeter-wave IMPATT sources for communication applications. IEEE MTT-S Inter Microw Symp Dig 4:216–219
136. Midford TA, Bernick RL (1979) Millimeter Wave CW IMPATT diodes and Oscillators. IEEE Trans Microw Theory Tech 27:483–492
137. Dalle C, Rolland P, Lieti G (1990) Flat doping profile double-drift silicon IMPATT for reliable CW high power high-efficiency generation in the 94-GHz window. IEEE Trans Electron Devices 37:227–236
138. Luschas M, Judaschke R, Luy JF (2002) Measurement results of packaged millimeter-wave silicon IMPATT diodes. In: Proceeding of 27th international conference on infrared and millimeter waves, conference digest, pp 135–136
139. Luschas M, Judaschke R, Luy JF (2002) Simulation and measurement results of 150 GHz integrated silicon IMPATT diodes. IEEE MTT-S Inter Microw Symp Dig 12:1269–1272
140. Shih HD, Bayraktaroglu B, Duncan WM (1983) Growth of millimeter-wave GaAs IMPATT structures by molecular beam epitaxy. J Vac Sc Technol B Microelectron Nanometer Struct 1:199–201
141. Shih HD, Bayraktaroglu B, Duncan WM (2021) Diamond a cut above the rest. Available from: http://www.akhantech.com/about.html. (Accessed on Apr 2021)
142. Johnson EO (1965) Physical limitations on frequency and power parameters of transistors. RCA Rev 26:163–177
143. Baliga BJ (1989) Power semiconductor device figure of merit for high-frequency applications. IEEE Electron Device Lett 10(10):455–457
144. Evans WJ, Haddad GI (1968) A large-signal analysis of IMPATT diodes. IEEE Trans Electron Devices 15(10):708–717
145. Scharfetter DL, Gummel HK (1969) Large-signal analysis of a silicon read diode oscillator. IEEE Trans Electron Devices 6(1):64–77
146. Gupta MS, Lomax RJ (1973) A current-excited large-signal analysis of IMPATT devices and its circuit implementations. IEEE Trans Electron Devices 20:395–399
147. Acharyya A, Banerjee S, Banerjee JP (2013) Effect of junction temperature on the large-signal properties of a 94 GHz silicon based double-drift region impact avalanche transit time device. J Semicond 34(2):024001–024012
148. Acharyya A, Banerjee S, Banerjee JP (2012) Large-signal simulation of 94 GHz pulsed DDR silicon IMPATTs including the temperature transient effect. Radioengineering 21(4):1218–1225
149. Acharyya A, Banerjee JP, Banerjee S (2012) Temperature transient effect on the large-signal properties and frequency chirping in pulsed silicon DDR IMPATTs at 94 GHz. In: IEEE Conference CODEC 2012, Kolkata, India, 17–19 Dec 2012, pp 5–7
150. Biswas A, Sinha S, Acharyya A, Banerjee A,.Pal S, Satoh H, Inokawa H (2018) 1.0 THz GaN IMPATT source: effect of parasitic series resistance. J Infrared Millimeter Terahertz Waves 39(10):954–974
151. Ray UC, Gupta AK (1988) Measurement of electrical series resistance of W-band Si IMPATT diode. In: 2nd Asia Pacific microwave conference proceedings, China, pp 434–437
152. Adlerstein MG, Holway LH, Chu SLG (1983) Measurement of series resistance in IMPATT diodes. IEEE Trans Electron Devices 30:179–182
153. Mitra M, Das M, Kar S, Roy SK (1993) A study of the electrical series resistance of Si IMPATT diodes. IEEE Trans Electron Devices 40:1890–1893
154. Pal TK (2009) Series resistance of silicon millimeter wave (Ka-band) IMPATT diodes. Def Sci J 59:189–193

155. Acharyya A, Banerjee S, Banerjee JP (2013) A proposed simulation technique to study the series resistance and related millimeter-wave properties of Ka-Band Si IMPATTs from the electric field snap-shots. Int J Microw Wirel Technol 5(1):91–100
156. Acharyya A, Banerjee S, Banerjee JP (2012) A proposed method to study the parasitic resistance of Ka-band silicon IMPATT diode from large-signal electric field snap-shots. In: IEEE conference CODIS-2012, Jadavpur University, W. B., India, 28–29 Dec 2012,pp 133–136
157. Acharyya A, Banerjee S, Banerjee JP (2013) Influence of skin effect on the series resistance of millimeter-wave IMPATT devices. J Comput Electron 12:511–525

# An Approximate Model for Analyzing Four-Terminal Lateral Single-Drift IMPATT-Based THz Radiators


**Subhashri Chatterjee and Aritra Acharyya**

**Abstract** An approximate model is presented in this chapter, which will be useful to study the static and dynamic performance of laterally oriented four-terminal single-drift (SD) IMPATT sources. This model is suitable for both sub-terahertz frequency and terahertz (THz) frequency of operation of the device. The details of the model are presented in this chapter; however, the simulation results are omitted from here due to the limitations in availability of space.

**Keywords** Analysis · Dynamic · IMPATT · Lateral · Terahertz

## 1 Introduction

The lateral orientation of IMPATT structure was first experimented by Stabile et al. [1]. They successfully realized SD planner diodes and obtained equivalent performance from this structure in comparison with the conventional vertically oriented structure. Standard 0.18 micron CMOS technology was used by Attar et al. for fabricating lateral SD diodes operating at W-band [2–5]. Primary advantage of this structure is the compatibility with monolithic integration technology. Photo-coupling with microwave oscillation and corresponding photonic–microwave interaction is also more convenient in this planner structure [6–8]. First, laterally oriented double-drift (DD) diode was proposed by Acharyya et al. in the year 2012 [6, 7]; two-dimensional dynamic simulation model was developed by them to study the sub-THz performance of Si DD diode oscillators.

S. Chatterjee
International Center for Materials Nanoarchitectectonics (MANA), National Institute for Material Science (NIMS), Tsukuba, Japan

Graduate School of Chemical Sciences and Engineering, Hokkaido University, Sapporo, Japan

A. Acharyya (✉)
Department of Electronics and Communication Engineering, Cooch Behar Government Engineering College, Cooch Behar, West Bengal, India



A. Acharyya et al. (eds.), *Generation, Detection and Processing of Terahertz Signals*, Lecture Notes in Electrical Engineering 794,
https://doi.org/10.1007/978-981-16-4947-9_12

Now, the planner structure promptly encourages one to append one or more additional terminals to SD IMPATT device in order to obtain one or more voltage-controlling external terminals. In this chapter, such two terminals, i.e., (i) gate and (ii) substrate terminals, are added to the lateral SD structure. An approximate model is presented to study the static and dynamic performance of laterally oriented four-terminal SD IMPATT sources. This model is suitable for both sub-THz frequency and THz frequency of operation of the device. The details of the model are presented in this chapter; however, the simulation results are omitted from here due to the limitations in availability of space.

## 2 Proposed Model

Four-terminal lateral SD $p^+pn^+$ and $n^+np^+$ structures are shown in Fig. 1. When a small positive gate voltage is applied to the gate terminal of the $p^+pn^+$ lateral SD IMPATT, due to downward vertical electric field ($\xi_v(z)$), majority carriers (holes) of the $p$-type substrate region will experience a force away from the oxide–semiconductor interface. As the holes are pushed away from the interface, a negative space charge region is created due to the immobile ionized acceptor atoms as shown in Fig. 1a. So, the effective $p$-type doping concentration of this region will decrease. Similarly, due to small negative gate voltage on the gate terminal of the $n^+np^+$ lateral SD IMPATT will create a positive space charge region due to immobile ionized donor atoms as shown in Fig. 1a; as a result of that $n$-type doping concentration of this region will decrease. Sufficiently, large positive and negative gate voltages will cause inverted oxide–semiconductor interface in lateral $p^+pn^+$ and $n^+np^+$ structures, respectively. In this section, a relationship between the applied gate voltage ($V_G$) and the effective doping concentration within the space charge region of the $p^+pn^+$ and $n^+np^+$ lateral SD IMPATTs is established.

Energy band diagrams of oxide-$p$-type and oxide-$n$-type semiconductor interfaces of lateral SD $p^+pn^+$ and $n^+np^+$ structures, respectively, are shown in Fig. 2a and b. The equilibrium hole and electron concentrations are respectively given by

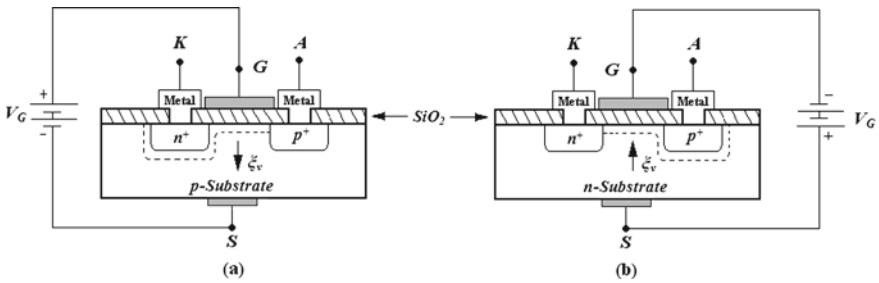


**Fig. 1** Four-terminal silicon-based lateral SD **a** $p^+pn^+$ and **b** $n^+np^+$ structures

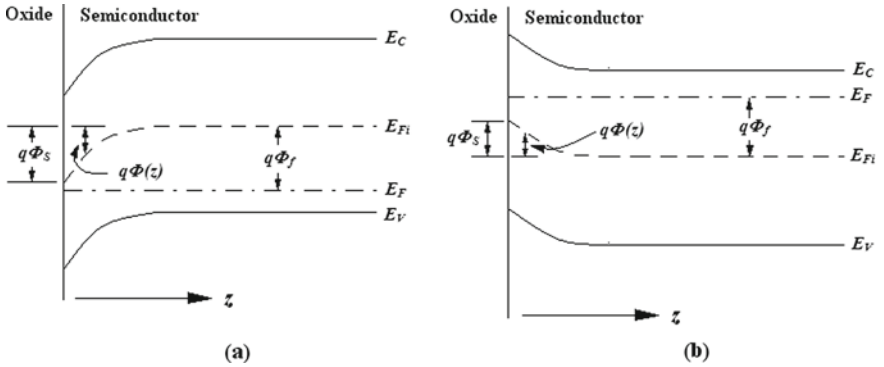


**Fig. 2** Energy band diagrams of **a** oxide-*p*-type and **b** oxide-*n*-type semiconductor interfaces at depletion

$$p_0 = n_i.\exp((E_i - E_F)/k_BT) = n_i.\exp\left(q\Phi_f/k_BT\right) = N_A, \tag{1}$$

$$n_0 = n_i.\exp((E_F - E_i)/k_BT) = n_i.\exp\left(-q\Phi_f/k_BT\right) = N_D. \tag{2}$$

The hole and electron concentrations at any distance $z$ from the oxide–semiconductor interface within the space charge region are given by

$$\begin{aligned} p(z) &= n_i.\exp\left(q\left(\Phi_f - \Phi(z)\right)/k_BT\right) = p_0.\exp(-q\Phi(z)/k_BT) \\ &= N_A.\exp(-q\Phi(z)/k_BT), \end{aligned} \tag{3}$$

$$\begin{aligned} n(z) &= n_i.\exp\left(-q\left(\Phi_f - \Phi(z)\right)/k_BT\right) \\ &= n_0.\exp(q\Phi(z)/k_BT) = N_D.\exp(q\Phi(z)/k_BT). \end{aligned} \tag{4}$$

Now, Eqs. (3) and (4) are combined with Poisson's equation to solve for $\Phi(z)$,

$$\begin{aligned} \frac{\partial \xi_v(z)}{\partial z} = \frac{\partial^2 \Phi(z)}{\partial z^2} &= -\frac{q}{\varepsilon_s}(N_D - N_A + p(z) - n(z)) \\ \Rightarrow \frac{\partial^2 \Phi(z)}{\partial z^2} &= \frac{\partial}{\partial z}\left(\frac{\partial \Phi(z)}{\partial z}\right) \\ = -\frac{q}{\varepsilon_s}&\left[N_A(\exp(-q\Phi(z)/k_BT) - 1)\right. \\ &\left. - N_D(\exp(q\Phi(z)/k_BT) - 1)\right], \end{aligned} \tag{5}$$

where $\varepsilon_s$ = permittivity of the semiconductor. Due to charge neutrality condition, $p_0 + N_D = n_0 + N_A$. Vertical electric field $\xi_v(z) = -\partial\Phi(z)/\partial z$.

Integrating Eq. (5) from the bulk (where the bands are flat, the electric fields are zero, and the carrier concentration is determined by doping concentration), toward the surface,

$$\int_0^{\frac{\partial\Phi(z)}{\partial z}} \left(\frac{\partial\Phi(z)}{\partial z}\right) d\left(\frac{\partial\Phi(z)}{\partial z}\right) = -\frac{q}{\varepsilon_s}$$

$$\int_0^{\Phi(z)} \left[N_A(\exp(-q\Phi(z)/k_BT) - 1) - N_D(\exp(q\Phi(z)/k_BT) - 1)\right] d\Phi(z)$$

$$\Rightarrow \xi_v(z) = \left\{\left(\frac{2k_BTN_A}{\varepsilon_s}\right)\left[\left(\exp\left(\frac{-q\Phi(z)}{k_BT}\right) + \frac{q\Phi(z)}{k_BT} - 1\right)\right.\right.$$

$$\left.\left. + \left(\frac{N_D}{N_A}\right)\left(\exp\left(\frac{q\Phi(z)}{k_BT}\right) - \frac{q\Phi(z)}{k_BT} - 1\right)\right]\right\}^{\frac{1}{2}}. \tag{6}$$

Equations (3) to (6) are written for lateral $p^+pn^+$ SD; for $n^+np^+$ SD, $\Phi(z)$ must be replaced by $-\Phi(z)$, since here the applied gate voltage is negative. At the oxide–semiconductor interface, i.e., at the surface where z = 0, the vertical electric field can be determined as

$$\xi_v(0) = \xi_s = \left\{\left(\frac{2k_BTN_A}{\varepsilon_s}\right)\left[\left(\exp\left(-\frac{q\Phi_s}{k_BT}\right) + \frac{q\Phi_s}{k_BT} - 1\right)\right.\right.$$

$$\left.\left. + \left(\frac{N_D}{N_A}\right)\left(\exp\left(\frac{q\Phi_s}{k_BT}\right) - \frac{q\Phi_s}{k_BT} - 1\right)\right]\right\}^{\frac{1}{2}} \text{for} p^+pn^+\text{SD}, \tag{7}$$

$$\xi_v(0) = \xi_s = \left\{\left(\frac{2k_BTN_A}{\varepsilon_s}\right)\left[\left(\exp\left(\frac{q\Phi_s}{k_BT}\right) - \frac{q\Phi_s}{k_BT} - 1\right)\right.\right.$$

$$\left.\left. + \left(\frac{N_D}{N_A}\right)\left(\exp\left(-\frac{q\Phi_s}{k_BT}\right) + \frac{q\Phi_s}{k_BT} - 1\right)\right]\right\}^{\frac{1}{2}} \text{for} n^+np^+\text{SD} \tag{8}$$

The relationship between the space charge per unit area to the electric displacement can be obtained from the Gauss's law at the surface, considering that the electric field or displacement deep into the substrate is zero

$$Q_S = -\varepsilon_s\xi_s \quad \text{for} p^+pn^+\text{SD} \quad \text{and} \quad Q_S = \varepsilon_s\xi_s \quad \text{for} n^+np^+\text{SD}. \tag{9}$$

The charge distribution, electric field, and electrostatic potential for depleted surface are sketched in Fig. 3 for both lateral SD $p^+pn^+$ and $n^+np^+$ structures. For simplicity, depletion approximation is considered, i.e., complete depletion for $0 < z < W_v$ and neutral material for $z > W_v$. In this case, the positive charge on the metal is balanced by the negative charge $Q_S = -qN_AW_v$ in the *p*-type semiconductor of $p^+pn^+$ structure and by the positive charge $Q_S = qN_DW_v$ in the *n*-type semiconductor

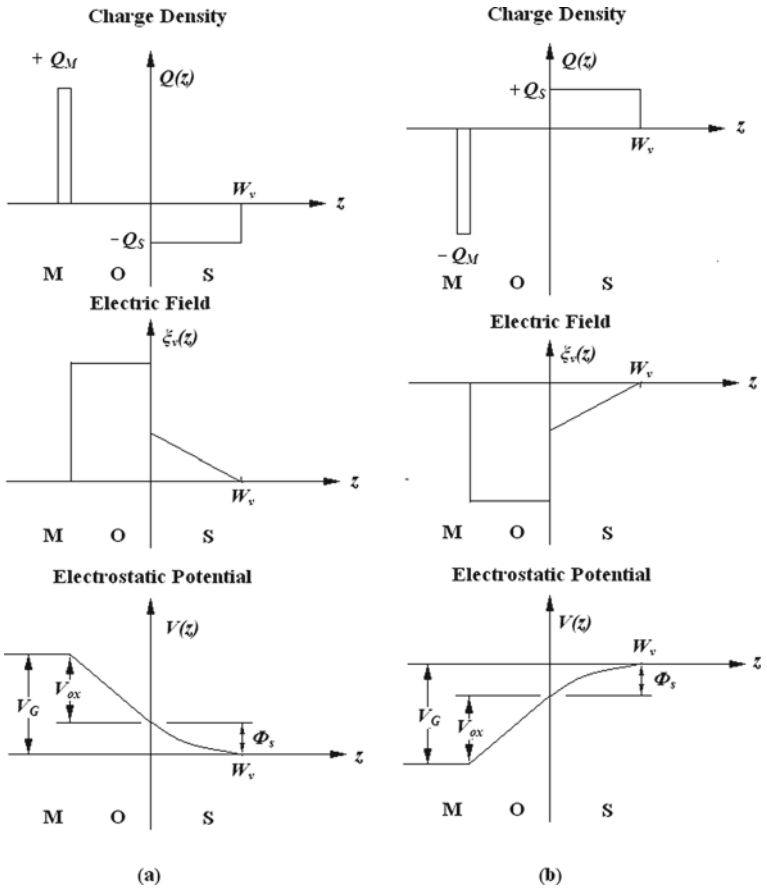


**Fig. 3** Approximated charge, electric field, and electrostatic potential distributions for depleted surface of lateral SD **a** $p^+pn^+$ and **b** $n^+np^+$ structures for applied gate voltage $V_G$

of $n^+np^+$ structure

$$Q_M = -Q_S = qN_A W_v \quad \text{for } p^+pn^+\text{SD} \quad \text{and}$$
$$Q_M = -Q_S = -qN_D W_v \quad \text{for } n^+np^+\text{SD}. \tag{10}$$

Using the depletion approximation, the value of $W_v$ can be determined as a function of $\Phi_s$. The result is same as the $n^+$-$p$/$p^+$-$n$ junction, for which the depletion region extends almost entirely into the $p$-region/$n$-region

$$W_v = \left[\frac{2\varepsilon_s \Phi_s}{qN_A}\right]^{\frac{1}{2}} \quad \text{for } p^+pn^+\text{SD} \quad \text{and} \quad W_v = \left[\frac{2\varepsilon_s \Phi_s}{qN_D}\right]^{\frac{1}{2}} \quad \text{for } n^+np^+\text{SD}. \tag{11}$$

From the potential distribution of Fig. 3, it can be observed that an applied voltage at gate terminal ($V_G$) appears partially across the oxide ($V_{ox}$) and partially across the depletion region of the semiconductor ($\Phi_s$). The voltage across the oxide layer is given by

$$V_{ox} = \frac{-Q_s t_{ox}}{\varepsilon_{ox}} = \frac{-Q_s}{C_{ox}} \quad \text{for} \, p^+pn^+\text{SD} \quad \text{and} \quad V_{ox} = \frac{Q_s t_{ox}}{\varepsilon_{ox}} = \frac{Q_s}{C_{ox}} \quad \text{for} \, n^+np^+\text{SD}, \tag{12}$$

where $\varepsilon_{ox}$ = permittivity of the oxide and $C_{ox} = (\varepsilon_{ox}/t_{ox})$ = oxide capacitance per unit area. So, the applied gate voltage is

$$|V_G| = |V_{ox}| + |\Phi_s| \quad \text{for both} \, p^+pn^+ \, \text{and} \, n^+np^+\text{SDs}. \tag{13}$$

Figure 4 shows the reverse-biased lateral SD $p^+pn^+$ and $n^+np^+$ structures. Due to increase of the positive or negative gate voltages in $p^+pn^+$ or $n^+np^+$ structures, respectively, the depletion region width ($W_v$) increases as shown in Fig. 4**a** and **b** until burly inversion is attained. After strong inversion, further increase in gate voltage results in stronger inversion rather than more depletion. Thus, the maximum depletion width is

$$\left.\begin{aligned} W_v(\max) &= \left[\frac{2\varepsilon_s \Phi_s(Inv)}{qN_A}\right]^{\frac{1}{2}} = \left[\frac{2\varepsilon_s(2\Phi_f)}{qN_A}\right]^{\frac{1}{2}} = 2\left[\frac{\varepsilon_s k_B T.\ln(N_A/n_i)}{qN_A}\right]^{\frac{1}{2}} \text{for} \, p^+pn^+\text{SD} \\ &\text{and} \\ W_v(\max) &= \left[\frac{2\varepsilon_s \Phi_s(Inv)}{qN_D}\right]^{\frac{1}{2}} = \left[\frac{2\varepsilon_s(2\Phi_f)}{qN_D}\right]^{\frac{1}{2}} = 2\left[\frac{\varepsilon_s k_B T.\ln(N_D/n_i)}{qN_D}\right]^{\frac{1}{2}} \text{for} \, n^+np^+\text{SD} \end{aligned}\right\} \tag{14}$$

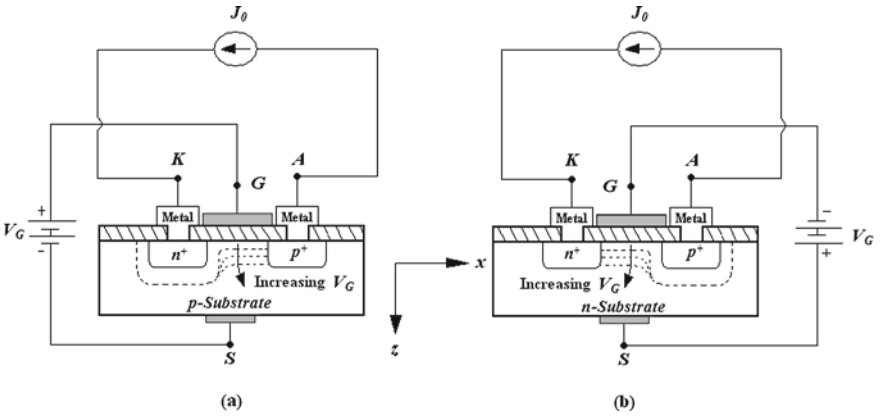


**Fig. 4** Reverse-biased lateral SD **a** $p^+pn^+$ and **b** $n^+np^+$ structures showing the increasing depletion region width due to increasing applied gate voltage $V_G$

Reverse-biased complimentary structures ($p^+pn^+$ and $n^+np^+$) are presented by one-dimensional (1D) models as shown in Fig. 5a and b; these can be used for the static and dynamic analysis. The following device equations will have to be simultaneously solved, subject to proper boundary conditions in order to obtain field, current, and carrier profiles:

$$\frac{d\xi(x)}{dx} = \frac{q}{\varepsilon_s}(N_D - N_A + p(x) - n(x)), \tag{15}$$

$$\frac{\partial J_n(x)}{\partial x} = -\frac{\partial J_p(x)}{\partial x} = q\big(n(x)\alpha_n(x)v_n(x) + p(x)\alpha_p(x)v_p(x)\big), \tag{16}$$

$$J_p(x) = qp(x)v_p(x) - qD_P\left(\frac{\partial p(x)}{\partial x}\right), \tag{17}$$

$$J_n(x) = qn(x)v_n(x) + qD_n\left(\frac{\partial n(x)}{\partial x}\right), \tag{18}$$

$$q\frac{\partial(p(x)-n(x))}{\partial x} = J_0\left(\frac{\alpha_n(x)}{v_n(x)} + \frac{\alpha_p(x)}{v_p(x)}\right) - \big(\alpha_n(x) - \alpha_p(x)\big)\left(\frac{J_p(x)}{v_p(x)} - \frac{J_n(x)}{v_n(x)}\right) + \left[J_p(x)\frac{\partial}{\partial\xi(x)}\left(\frac{1}{v_p(x)}\right) - J_n(x)\frac{\partial}{\partial\xi(x)}\left(\frac{1}{v_n(x)}\right)\right]\frac{\partial\xi(x)}{\partial x} \tag{19}$$

where the symbols $\alpha_n$, $\alpha_p$, $v_n$, $v_p$, $\mu_n$, $\mu_p$, etc., have their usual significance. For simplicity in 1D analysis, the authors have assumed $p(x) = p(x,z)|_{z=0}$ and $n(x) = n(x,z)|_{z=0}$; i.e., $p(x)$ and $n(x)$ are assumed as independent of $z$, having the constant values equal to values of $p(x)$ and $n(x)$ at surface ($z = 0$) throughout the space charge layer due to small gate voltage $V_G$.

The said boundary conditions for electric field are given by

$$\xi\big(W_p\big) = 0 \quad \text{for}\, p^+pn^+\,\text{SD} \quad \text{and} \quad \xi(-W_n) = 0 \quad \text{for}\, n^+np^+\text{SD}, \tag{20}$$

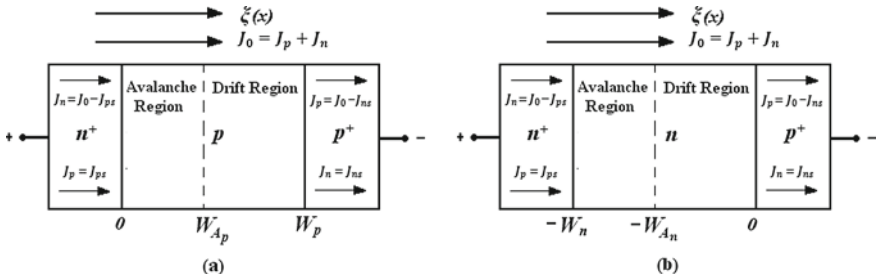


**Fig. 5** 1D model of $p^+pn^+$ and $n^+np^+$ structures

and current boundary conditions are given by

$$P(W_p) = \left(1 - \frac{2}{M_n}\right) \quad \text{for } p^+pn^+ \text{ SD} \quad \text{and}$$
$$P(-W_n) = \left(\frac{2}{M_p} - 1\right) \quad \text{for } n^+np^+\text{SD}, \tag{21}$$

where $M_n$ and $M_p$ are multiplication factors corresponding to electrons and holes and $M_n$ and $M_p$ tend to $10^6$ under breakdown condition.

The breakdown voltage can be obtained from

$$V_{\mathrm{B}} = \int_0^{W_p} \xi(x)\mathrm{d}x \quad \text{for } p^+pn^+ \text{ SD} \quad \text{and} \quad V_B = \int_{-W_n}^{0} \xi(x)\mathrm{d}x \quad \text{for } n^+np^+ \text{ SD}. \tag{22}$$

Conversion efficiency can be obtained from the semi-quantitative formula [9, 10]

$$\eta(\%) = \frac{2m}{\pi} \times \frac{V_{\mathrm{D}}}{V_{\mathrm{B}}}, \tag{23}$$

where $V_{\mathrm{D}}$ = voltage drop across the drift region, $V_{\mathrm{B}}$ = breakdown voltage, and $m$ = ½. The real part $R(x, \omega)$ and imaginary part $X(x, \omega)$ of the diode impedance $Z(x, \omega)$ can be obtained by solving the following second-order differential equations [11]

$$D^2R + \left[\alpha_n(x) - \alpha_p(x)\right]DR - 2\underline{r}\left(\frac{\omega}{\underline{v}}\right)DX + \left[\left(\frac{\omega^2}{\underline{v}^2}\right) - H(x)\right]R - 2\underline{\alpha}(x)\left(\frac{\omega}{\underline{v}}\right)X - 2\left(\frac{\underline{\alpha}(x)}{\underline{v}\varepsilon_s}\right) = 0, \tag{24}$$

$$D^2X + \left[\alpha_n(x) - \alpha_p(x)\right]DX + 2\underline{r}\left(\frac{\omega}{\underline{v}}\right)DR + \left[\left(\frac{\omega^2}{\underline{v}^2}\right) - H(x)\right]X + 2\underline{\alpha}(x)\left(\frac{\omega}{\underline{v}}\right)R + \left(\frac{\omega}{\underline{v}^2\varepsilon_s}\right) = 0, \tag{25}$$

where $\underline{v} = \left(v_{sp}v_{sn}\right)^{0.5}$, $\underline{\alpha}(x) = \left(\alpha_p(x)v_{sp} + \alpha_n(x)v_{sn}\right)/2\underline{v}$, $\underline{r} = \left(v_{sn} - v_{sp}\right)/2\underline{v}$, $H(x) = \left(J_0/\underline{v}\varepsilon\right)\left(2d\underline{\alpha}/d\xi + y.d\left(\alpha_n - \alpha_p\right)/d\xi\right)$, and $y = \underline{v}\varepsilon/J_0(d\xi_m/dx)$, and $D$ is the differential operator $\partial/\partial x$.

The boundary conditions for $R$ and $X$ at the $p^+p$ and $n^+n$ interfaces of reverse-biased $p^+pn^+$ and $n^+np^+$ structures are given by

$$DR - \frac{\omega X}{v_{sp}} = \left(\frac{1}{v_{sp}\varepsilon_s}\right) \text{and } DX + \frac{\omega R}{v_{sp}} = 0 \quad \text{at } x = W_p \text{i.e., at } p^+p \text{ interface} \tag{26}$$

$$DR + \frac{\omega X}{v_{sn}} = -\left(\frac{1}{v_{sn}\varepsilon_s}\right) \text{and}\, DX - \frac{\omega R}{v_{sn}} = 0 \quad \text{at} x = -W_n \text{i.e., at}\, n^+n \,\text{interface} \tag{27}$$

The device negative resistance ($Z_R$) and reactance ($Z_X$) are obtained from

$$Z_R = \int_0^{W_p} R(x)\mathrm{d}x \quad \text{and} \quad Z_X = \int_0^{W_p} X(x)\mathrm{d}x \quad \text{for}\, n^+np^+\text{SD} \tag{28}$$

$$Z_R = \int_{-W_n}^{0} R(x)\mathrm{d}x \quad \text{and} \quad Z_X = \int_{-W_n}^{0} X(x)\mathrm{d}x \quad \text{for}\, n^+np^+\text{SD} \tag{29}$$

The impedance of the device is given by $Z_D = Z_R + jZ_X$, and the device admittance is $Y_\mathrm{D} = 1/Z_\mathrm{D} = G + jB$. The negative conductance (–$G$) and associated susceptance ($B$) are obtained from

$$|G(\omega)| = \frac{Z_R}{\left(Z_R^2 + Z_X^2\right)} \quad \text{and} \quad |B(\omega)| = \frac{-Z_X}{\left(Z_R^2 + Z_X^2\right)} \tag{30}$$

The avalanche frequency ($f_a$) is the frequency at which the susceptance ($B$) changes its nature from inductive to capacitive. Again, it is the lowest frequency at which the real part ($G$) of admittance becomes negative and oscillation starts to build up in the circuit.

## 3 Summary

The planner structure promptly encourages one to append one or more additional terminals to SD IMPATT device in order to obtain one or more voltage-controlling external terminals. In this chapter, such two terminals, i.e., (i) gate and (ii) substrate terminals, are added to the lateral SD structure. An approximate model is presented to study the static and dynamic performance of laterally oriented four-terminal SD IMPATT sources. This model is suitable for both sub-THz frequency and THz frequency of operation of the device. The details of the model are presented in this chapter; however, the simulation results are omitted from here due to the limitations in availability of space.

## References

1. Stabile PJ, Lalevic B (1989) Lateral IMPATT diodes. IEEE Trans Electron devices 10(6):249–251
2. Al-Attar T, Mulligan M, Lee TH (2004) Lateral IMPATT diodes in standard CMOS technology. Int Electron Devices Meet Dig 459–462. Washington, DC, 13–14 Dec 2004
3. Al-Attar T, Mulligan M, Lee TH (2005) A 77 GHz monolithic IMPATT transmitter in standard CMOS technology. IEEE MTT-S Int Microwav Symp Dig Long Beach, CA
4. Al-Attar T, Lee TH (2005) Monolithic integrated millimeter-wave IMPATT transmitter in standard CMOS technology. IEEE Trans MTT 53(11):3557–3561
5. Al-Attar T (2011) CMOS diodes operating beyond avalanche frequency. In: 12th international symposium on quality electronic design (ISQED), 14–16 Mar 2011, pp 1–6
6. Acharyya A, Banerjee JP (2012) A proposed lateral DDR IMPATT structure for better millimeter-wave optical interaction. In: IEEE international conference on devices, circuits and systems 2012, Karunya University, Coimbatore, Tamil Nadu**,** India, pp 599–602, 15–16 Mar 2012
7. Acharyya A, Banerjee S, Banerjee JP (2012) Optical control of millimeter-wave lateral double-drift region silicon IMPATT device. Radioengineering 21(4):1208–1217
8. Acharyya A, Goswami J, Banerjee S, Banerjee JP (2014) Estimation of most favorable optical window position subject to achieve finest optical control of lateral DDR IMPATT diode designed to operate at W-band. Radioengineering 23(2):739–753
9. Scharfetter DL, Gummel HK (1969) Large-signal analysis of a silicon read diode oscillator. IEEE Trans Electron Devices 6(1):64–77
10. Scharfetter DL, Evans WJ, Johnson HL (1970) Double drift region $p^+pnn^+$ avalanche diode oscillators. Proc IEEE (Lett) 50:1131
11. Gummel HK, Blue JL (1967) A small-signal theory of avalanche noise in IMPATT diodes. IEEE Trans Electron Devices 14:569–580

# On Some Modern Simulation Techniques for Studying THz ATT Sources


**Monisha Ghosh, Aritra Acharyya, and Arindam Biswas**

**Abstract** Great demand of suitable terahertz (THz) sources requires optimized design and appropriate simulation tool for designing and investigating the device capability at the design spectrum before actual fabrication. Design and simulation of complex devices like THz avalanche transit time (ATT) diodes require comprehensive and accurate simulation model for small-signal, large-signal and noise simulation before the actual fabrication. This chapter is devoted to summarize these three types of simulation methodologies for THz ATT sources.

**Keywords** Simulation technique · Small-signal · Large-signal · Avalanche noise · Terahertz

## 1 Introduction

Solid-state semiconductor-based millimetre-wave and terahertz signal generators are the most commonly used sources for most of the modern-day wireless communication systems; the popularity of these spectrums are due to the availability of higher resolution as well as broader bandwidth. As a consequence of many advantages of solid-state sources, like lower weight and cost as well as better reliability, those have completely replaced earlier used vacuum tube devices in most of the applications. High power-efficient solid-state sources are now commercially available for various applications at mm-wave and THz regime. The fabrication technology of two

M. Ghosh
Department of Electronics and Communications Engineering, Supreme Knowledge Foundation Group of Institution, 1, Khan Road, Mankundu, Hooghly, West Bengal 712139, India
e-mail: monisha.ghosh@skf.edu.in

A. Acharyya (✉)
Department of Electronics and Communication Engineering, Cooch Behar Government Engineering College, Harinchawra, Ghughumari, Cooch Behar, West Bengal 736170, India

A. Biswas
Centre for Organic Spin-Tronics and Optoelectronics Devices (COSOD) and Mining Engineering Department, Kazi Nazrul University, Asansol, Burdwan, West Bengal 713340, India



A. Acharyya et al. (eds.), *Generation, Detection and Processing of Terahertz Signals*, Lecture Notes in Electrical Engineering 794,
https://doi.org/10.1007/978-981-16-4947-9_13

terminal devices like ATT and GUNN is compatible with microwave/mm-wave standard integrated-circuits process technology. The negative resistances in these devices are produced by different physical phenomena. Gunn diodes are known as transferred electron devices (TED) since the transfer of electrons from the central valley to the satellite valley in the conduction band of *n*-type bulk GaAs or InP under suitable biasing condition is responsible to produce negative resistance in these diodes. On the other hand, an appropriate phase lag (90°–270°) between the input voltage and external current produces negative resistance in ATT diode. Unlike Gunn diode, ATT diode can be fabricated from different semiconductors such as Si, GaAs, InP, SiC, GaN and type-IIb diamond; there is no restriction on the choice of semiconductor materials as regards their nature of the energy-band structure (wherther direct or indirect bandgap material).

The frequency or wavelength range, lies between 0.3 and 10 THz or 1000 μm to 30 μm, falls between electromagnetic mm-wave and optical infrared spectrums is usually regarded as THz domain. Various fields of modern research and development and industries like biotechnology, astronomy, spectroscopy, quality inspection, medical and pharmaceutical technology, etc. demand the THz waves of different frequencies and different intensity [1–8]; thus the requirement of high quality and high reliability THz sources is very high nowadays. The R&N of THz sources, detectors and other components are underway for implementation of THz system. Although, the primary disadvantage of high-power THz oscillators are their complexity, large weight and cryogenic operational temperature in most of the cases. Recently, 1.9–2.7 THz cascaded frequency multiplier source is proposed [9–13] which can deliver 10–2 μW peak power. Also, some highly efficient THz devices are under development since last decade [14–52].

This great demand of suitable THz sources requires optimized design and appropriate simulation tool for designing and investigating the device capability at the design spectrum before actual fabrication. Design and simulation of complex devices like THz avalanche transit time (ATT) diodes require comprehensive and accurate simulation model for small-signal, large-signal and noise simulation before the actual fabrication. This chapter is devoted to summarize these three types of simulation methodologies for THz IMPATT sources.

## 2 Overview of IMPATT Simulation

Several researchers have investigated [53–55] the DC and high frequency properties of IMPATT devices by using appropriate device model and analytical methods. The analytical methods involve several simplifying assumptions regarding the ionization rates and drift velocities of charge carriers in the semiconductor. These methods cannot provide accurate information regarding the high-frequency performance of IMPATTs under practical situation. Numerical simulation methods on the other hand are free from those simplifying assumptions and capable of predicting accurately the microwave and mm-wave properties of IMPATTs. In fact, accurate design of IMPATT

devices for specific applications in the mm-wave and sub-mm-wave frequencies relies mainly on the modelling and simulation techniques.

A simple DC and small-signal simulation method for design of IMPATTs was formulated by Roy et al. [56, 57], in which numerical computation begins from the location of field maximum, i.e. metallurgical junction of the device. The main advantages of this method over other existing methods are numerical stability and convergence. Later, this method was generalized for different structures, doping profiles and base semiconductors of IMPATT diodes. Various researchers studied the effects of space charge [58, 59], carrier diffusion [60] and band-to-band tunnelling [61] on the static and high frequency properties of IMPATT devices by using the above simulation method. The drift–diffusion model is used in most of the simulation methods for IMPATT devices in which one neglects the energy relaxation effects of charge carriers. Dalle et al. [62] used both drift–diffusion and energy-relaxation models to compare the accuracy of the two models with respect to the high frequency properties of mm-wave Si IMPATT diode at 94 GHz. They observed that the RF power level of the device estimated by those two models is comparable. However, energy-relaxation model tends to underestimate both the efficiency and the negative resistance of the device in comparison to the drift–diffusion model. Dalle et al. [62] found from the energy-relaxation model that the fundamental properties of IMPATT devices are not influenced by non-stationary effects.

Earlier, the authors have used classical drift–diffusion model to study the DC, small-signal and large-signal properties of DDR IMPATTs based on different semiconductor materials such as Si, GaAs, InP, 4H-SiC, Wz-GaN and diamond (type-IIb) designed to operate at different mm-wave and THz frequencies. A simulation method based on Gummel-Blue [63] technique and developed by Roy et al. [57] has been adopted by the author to study the small-signal properties of DDR IMPATTs based on different semiconductors. This method is discussed in detail in Chap. 4. The aforementioned method involves realistic field dependent ionization rates and drift velocities. The material parameters used in the present simulation study are given at a later section of this chapter. The velocity-overshoot in group III-V semiconductors (GaAs, InP, Wz-GaN, etc.) has also been included in the expression of field-dependent velocity.

Small-signal analysis and simulation studies of IMPATTs provide first order estimation of various high frequency properties of the device such as its negative resistance, RF power output, DC to RF conversion efficiency, etc. But the small-signal studies cannot accurately predict various high frequency parameters such as avalanche resonance frequency, optimum frequency, negative resistance, RF power output, DC to RF conversion efficiency, etc. Under actual operating condition, the device is embedded in resonant waveguide cavity, and those parameters depend strongly on the RF voltage swing. This dependence cannot be obtained from small-signal analysis. Thus, large-signal simulation is essential for accurate estimation of power and efficiency of the device.

A large-signal simulation method based on non-sinusoidal voltage excitation (NSVE) model has been developed by the authors to study the microwave and mm-wave properties of the device under realistic conditions. The authors have used the

said method to study the effects of various physical factors such as junction temperature, series resistance, skin depth, optical illumination, etc. on the RF performance of Si DDR IMPATTs operating at different mm-wave and THz frequency bands [64]. The authors have also studied the avalanche noise property of IMPATT diode and its dependence on the level of optical illumination. The large-signal properties of DDR IMPATTs based on type-IIb diamond and different group III–V semiconductors such as GaAs, InP and Wz-GaN have been studied by using large-signal simulation software [65, 66]. The validity of the large-signal program developed by the authors has been tested by comparing the large-signal simulation results with the corresponding experimental results. Further, the large-signal parameters tend to the small-signal ones under the limiting condition of very small voltage modulation. This also verifies the accuracy of the large-signal program.

In this chapter, the authors have presented the small-signal simulation method based on Gummel-Blue approach [63] in detail which has been further developed to study various RF properties of DDR IMPATT diode including the avalanche noise performance. A large-signal simulation method based on NSVE model developed by the author has been used to study the admittance, power output and conversion efficiency of the device based on different semiconductors at mm-wave and THz frequency bands. This method will be described in this chapter. Finally, the realistic experimental values of material parameters of different semiconductors such as Si, GaAs, InP, 4H-SiC, Wz-GaN and type-IIb diamond used in the simulation programs are given at the final section of this chapter.

## 3 Device Models

The single-drift (SD) and double-drift (DD) IMPATT models are illustrated in Fig. 1a, b. One-dimensional (1-D) models are sufficient for these two-terminal devices.

The net doping concentrations (i.e. $N(x) = N_D(x) - N_A(x)$) in different regions of $p^+$–$n$–$n^+$ SDR IMPATT device are given by

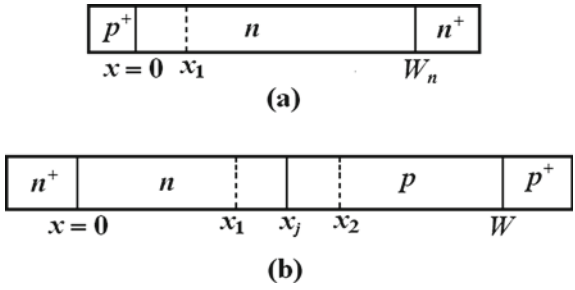


**Fig. 1** 1-D model of **a** SDR and **b** DDR IMPATT devices where the computation starts from the position of field maximum

$$\begin{aligned} N(x) &= -N_{p^+}\exp\left(-1.08\lambda_p(x) - 0.78\lambda_p(x)^2\right) && x \le 0 \\ &= N_D\left[1-\exp\left(\tfrac{x}{s}\right)\right] && 0 > x \ge x_1 \\ &= N_D && x_1 > x \ge W_n \\ &= N_{n^+}\exp\left(-1.08\lambda_n(x) - 0.78\lambda_n(x)^2\right) && x > W_n \end{aligned}, \tag{1}$$

where $N_D$ is the donor concentration, $W_n$ is the width of $n$-epitaxial layer and $N_{n^+}$ and $N_{p^+}p$ are the doping concentrations of $n^+$- and $^+$-layers. $\lambda_n(x)$ and $\lambda_p(x)$ are unite-less quantities expressed as $\lambda_n(x) = \lambda_p(x) = x/2\sqrt{(Dt_d)}$, where $D$ is a junction formation/epitaxial growth parameter, $t_d$ is the time of growth, and $s$ is an changeable parameter. The values of $\lambda_n(x)$ and $\lambda_p(x)$ as well as $Dt_d$ can be varied to optimize the doping profile of the diode. Doping profile may well represent a near abrupt doping profile by properly choosing the parameters, $\lambda_n(x)$, $\lambda_p(x)$ and $s$. The parameter $N(x)$ associated with different regions of the doping profile of $n^+$-$n$-$p$-$p^+$ DDR IMPATT device is given by

$$\begin{aligned} N(x) &= N_{n^+}\exp\left(-1.08\lambda_n(x) - 0.78\lambda_n(x)^2\right) && x \le 0 \\ &= N_D && 0 > x \ge x_1 \\ &= N_D\left[1-\exp\left(\tfrac{x}{s}\right)\right] && x_1 > x \ge x_j \\ &= -N_A\left[\exp\left(-\tfrac{x}{s}\right) - 1\right] && x_j > x \ge x_2 \\ &= -N_A && x_2 > x \ge W \\ &= -N_{p^+}\exp\left(-1.08\lambda_p(x) - 0.78\lambda_p(x)^2\right) && x > W \end{aligned}, \tag{2}$$

where $N_A$ is the acceptor concentration, $W_p$ is the width of $p$-epitaxial layer, and $x_j$ is the junction position.

## 4 DC Simulation Technique

The 1-D model and energy band diagram [61] of DD IMPATT device (reverse biased) considered in the simulation are shown in Fig. 2. The expression of mobile space charge is included in the fundamental device equation, i.e. Poisson's equation [67] without assuming the depletion approximation [58, 59] as given below

$$\frac{d\xi(x)}{dx} = \frac{q}{\varepsilon_s}(N_D(x) - N_A(x) + p(x) - n(x)), \tag{3}$$

where $\xi(x)$—electric field at $x$, $q = 1.6 \times 10^{-19}$ C = electronic charge, $p(x)$ — hole concentration, $n(x)$ —electron concentration, $N_D(x)$—ionized donor density, $N_A(x)$—ionized acceptor density and $\varepsilon_s$—permittivity of semiconductor material. The net impurity doping concentration at $x$ is $qN(x) = q(N_D(x) - N_A(x))$. The electric field due to mobile space charges $\xi_s(x)$ is given by

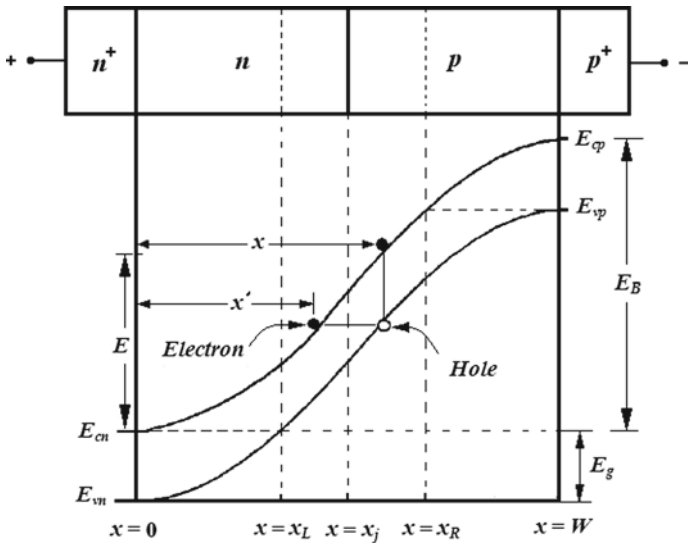


**Fig. 2** 1-D model and energy-band diagram of a reverse biased DD IMPATT [61]

$$\xi_s(x) = \xi(x) - \frac{q}{\varepsilon_s}\int N(x)\,dx. \tag{4}$$

The total bias current density is given by

$$J_0 = J_n(x) + J_p(x) + \frac{\partial}{\partial t}(\varepsilon_s \xi(x)) = q\big(v_p(x)p(x) + v_n(x)n(x)\big) + \frac{\partial}{\partial t}(\varepsilon_s \xi(x)), \tag{5}$$

where $J_p(x)$ and $J_n(x)$ are the hole and electron currents. The expressions for hole and electron concentrations at any space point $x$ are given by

$$p, n(x) = J_0 - \left(\frac{\partial}{\partial t} - \varepsilon_s v_{n,p}(x)\frac{\partial}{\partial x}\right)\xi_s(x) \Big/ q\big(v_p(x) + v_n(x)\big). \tag{6}$$

The continuity equations are as given by

$$\frac{\partial p(x)}{\partial t} = -\left(\frac{1}{q}\right)\left(\frac{\partial J_p(x)}{\partial x}\right) + G_{Ap}(x) + G_{Tp}(x) + \gamma_p(x) + R_p(x), \tag{7}$$

$$\frac{\partial n(x)}{\partial t} = \left(\frac{1}{q}\right)\left(\frac{\partial J_n(x)}{\partial x}\right) + G_{An}(x) + G_{Tn}(x) + \gamma_n(x) - R_n(x). \tag{8}$$

The avalanche generation rate of electron–hole pairs $G_A(x)$ is given by

$$G_A(x) = G_{An}(x) = G_{Ap}(x) = \alpha_n(x)v_n(x)n(x) + \alpha_p(x)v_p(x)p(x) \tag{9}$$

where $\alpha_n(x)$ and $\alpha_p(x)$ are the ionization rates of electrons and hole at $x$, respectively [68]. The combined continuity equation of electrons and holes is given by

$$\frac{\partial(p(x)+n(x))}{\partial t} + \frac{1}{q}\frac{\partial}{\partial x}\big(J_p(x) - J_n(x)\big) = 2(G_A(x) + \gamma(x)) + G_{Tn}(x) + G_{Tp}(x). \tag{10}$$

The tunnelling generation rate of electrons is given by [69, 70]

$$G_{Tn}(x) = a_T\xi^2(x)\exp\left(-\frac{b_T}{\xi(x)}\right). \tag{11}$$

The coefficients $a_T$ and $b_T$ in Eq. (11) are given by

$$a_T = \left(\frac{q^2}{8\pi^3\eta^2}\right)\left(\frac{2m_d^*}{E_g}\right)^{\frac{1}{2}} \quad \text{and} \quad b_T = \left(\frac{1}{2q\eta}\right)\left(\frac{m_d^* E_g^3}{2}\right)^{\frac{1}{2}}, \tag{12}$$

where $m_d{}^*$—density of state elective mass of charge carriers and $E_g$—bandgap. The tunnelling generation rate of holes can be determined from Fig. 2, where $G_{Tp}(x) = G_{Tn}(x')$. The relationship between $x$ and $x'$ is given by

$$x = x'\left(1 - \frac{E_g}{E}\right)^{-\frac{1}{2}} \quad \text{for } 0 \le x \le x_j, \tag{13}$$

$$x = W - (W - x')\left(1 + \frac{E_g}{E_B - E}\right)^{-\frac{1}{2}} \quad \text{for } x_j \le x \le W, \tag{14}$$

where $E$—energy measured from the bottom of the conduction band on the $n$-side and $E_g$—vertical difference between $x$ and $x'$ [61]. The particle current densities are

$$J_p(x) = qp(x)v_p(x) - qD_p\left(\frac{\partial p(x)}{\partial x}\right), \tag{15}$$

$$J_n(x) = qn(x)v_n(x) + qD_n\left(\frac{\partial n(x)}{\partial x}\right), \tag{16}$$

where $D_n$ and $D_p$—diffusion constants. The diffusion current components are much smaller in magnitude than the drift components in the drift layer of IMPATT diode. Thus, the 2nd terms on the RHS of Eqs. (13) and (14) may be neglected. The expressions for hole and electron current density are therefore given by

$$J_p(x) = qp(x)v_p(x) \quad \text{and} \quad J_n(x) = qn(x)v_n(x). \tag{17}$$

Under static condition, $\partial n/\partial t = \partial p/\partial t = 0$. Therefore, the continuity equations can be expressed as

$$\frac{dJ_p(x)}{dx} = \alpha_n(x)J_n(x) + \alpha_p(x)J_p(x) + qG_T(x') + q\gamma(x), \tag{18}$$

$$\frac{dJ_n(x)}{dx} = -\alpha_n(x)J_n(x) - \alpha_p(x)J_p(x) - qG_T(x) - q\gamma(x). \tag{19}$$

The normalized current density parameter is defined as $P(x) = (J_p(x) - J_n(x))/J_0$, where $J_0 = J_n(x) + J_p(x)$. By combining Eqs. (18) and (19) and then substituting the above defined parameter, the following equation is obtained

$$\frac{\partial P(x)}{\partial x} = \big(\alpha_n(x) + \alpha_p(x)\big) - \big(\alpha_n(x) - \alpha_p(x)\big)P(x) + \frac{q}{2J_0}\big(G_T(x) + G_T(x')\big) + \frac{2q}{J_0}\gamma(x). \tag{20}$$

The mobile space charge equation is obtained from Eqs. (18) and (19) [58, 59]

$$q\frac{\partial(p(x) - n(x))}{\partial x} = J_0\left(\frac{\alpha_n(x)}{v_n(x)} + \frac{\alpha_p(x)}{v_p(x)}\right) - q\big(\alpha_n(x) - \alpha_p(x)\big)(p(x) - n(x)) + q\left(\frac{G_T(x)}{v_n(x)} + \frac{G_T x'}{v_p(x)}\right) + q\gamma(x)\left(\frac{1}{v_n(x)} + \frac{1}{v_p(x)}\right) + \frac{\partial\xi(x)}{\partial x}K(x), \tag{21}$$

The drift velocity is not saturated throughout the space charge layer since the electric field near the edges of the layer is not high enough for velocity saturation. This necessitates the introduction of a correction term $K(x)$ which depends on the type of base material. In case of Si, the empirical relationship is given by [71, 72]

$$v_{n,p}(x) = v_{sn,sp}\left(1 - \exp\left(-\frac{\mu_{n,p}\xi}{v_{sn,sp}}\right)\right), \tag{22}$$

where $v_{sp}$ and $v_{sn}$—saturated drift velocities. The correction factor is expressed as

$$K(x) = \frac{J_p(x)\mu_p}{v_p(x)}\left(\frac{1}{v_{sp}} - \frac{1}{v_p(x)}\right) - \frac{J_n(x)\mu_n}{v_n(x)}\left(\frac{1}{v_{sn}} - \frac{1}{v_n(x)}\right), \tag{23}$$

Velocity-field relation for electrons in Group III-V semiconductors [73] is given by

$$v_n = \left( \frac{\mu_n \xi + v_{sn} \left( \frac{\xi}{\xi_c} \right)^4}{1 + \left( \frac{\xi}{\xi_c} \right)^4} \right), \tag{24}$$

where $\xi_c$—electric field associated with peak velocity-overshoot. Therefore, the correction factor is

$$\begin{aligned} K(x) = & \frac{J_p(x)\mu_p}{v_p(x)} \left( \frac{1}{v_{sp}} - \frac{1}{v_p(x)} \right) \\ & - \frac{J_n(x)\left(3(1 - (v_{sn}/v_n(x)))(\xi(x)/\xi_c)^4 - 1\right)}{v_n(x)\xi(x)\left(1 + (\xi(x)/\xi_c)^4\right)} \end{aligned}. \tag{25}$$

In the present simulation method, Eqs. (3), (20) and (21) are concurrently solved by 1-D finite difference method (FDM) subject to the boundary conditions of electric field and normalized current density at the depletion layer edges. The computation starts from the position of field maximum, $x = 0$, i.e. the edge of the $n^+$-$n$ interface and continues up to the edge of the $p$-epitaxial layer, i.e. $x = W$.

The field boundary conditions at $x = 0$ and $x = W$ (Fig. 1b) are

$$\xi(x = 0) = \xi(x = W) = 0. \tag{26}$$

Similarly, current the boundary conditions at $x = 0$ and $x = W$ (Fig. 1b) are

$$\left.\begin{aligned} P(x = 0) &= \left[ \left( \frac{2J_p(x = 0)}{J_0} \right) - 1 \right] \\ P(x = W) &= \left[ 1 - \left( \frac{2J_n(x = W)}{J_0} \right) \right] \end{aligned}\right\}. \tag{27}$$

The electric field profile, $\xi(x)$ and normalized current density profile, $P(x)$ in the active layer of the device are thus obtained.

## 5 Small-Signal Simulation Technique

The expressions of $p(x)$ and $n(x)$, i.e. Equation (6) are substituted in Eqs. (8) and (9) to obtain the time-dependent equation for small-signal simulation as follows [74]

$$\begin{aligned} & \left(D_x^2 - k(x)^2 + \left(\alpha_p(x) - \alpha_n(x) + 2r_n(x)k(x)\right)D_x + 2\overline{\alpha(x)}k(x)\right)\xi_s(x) \\ & = \frac{1}{\overline{v(x)}\varepsilon_s}\left(2\overline{\alpha(x)} - k(x)\right)J_0 + qr_p(x)G_T(x) + G_T x' + 2qr_p(x)\gamma(x) \end{aligned}, \tag{28}$$

where $\overline{v(x)} = \left(v_n(x)v_p(x)\right)^{\frac{1}{2}}$, $k(x) = \left(\overline{v(x)}\right)^{-1} D_t$, $\overline{\alpha(x)} = \left(\alpha_n(x)v_n(x) + \alpha_p(x)v_p(x)\right)/2\overline{v(x)}$ $r_n(x) = \left(v_n(x) - v_p(x)\right)/2\overline{v(x)}$, $r_p(x) = \left(v_n(x) + v_p(x)\right)/2\overline{v(x)}$, and $D_x \equiv \partial/\partial x$; $D_t \equiv \partial/\partial t$. Under small-signal condition, Eq. (3.28) reduces to

$$\left[\begin{array}{l} D_x^2 - k(x)^2 + \left(\alpha_p(x) - \alpha_n(x) + 2r_n(x)k(x)\right)D_x \\ \quad + 2\overline{\alpha(x)}k(x) - H(x) - \dfrac{qr_p(x)}{\overline{v(x)}\varepsilon_s}\left(G_T'(x) + G_T'(x')\right) \end{array}\right]$$

$$e = \frac{1}{\overline{v(x)}\varepsilon_s}\left[(2\bar{\alpha}(x) - k(x))j + 2qr_p(x)\gamma(x)\right] \tag{29}$$

where $H(x) = \left(2J_0/\overline{v(x)}\varepsilon_s\right)\partial\overline{\alpha(x)}/\partial\xi(x) + \left(\partial/\partial\xi(x)\right)\left(\alpha_p(x) - \alpha_n(x)\right)(D_x\xi_s(x))$. The alternating components of $\xi_s(x)$ and $J_0$ are $e$ and $j$, respectively. Now the boundary conditions can be evaluated from Eq. (3.29). In the $p$-drift region, total current is

$$J_0 = qv_p(x)p(x) + D_t(\varepsilon_s e). \tag{30}$$

Here, $qp(x) = Dx(\varepsilon se)$. The boundary condition at $x = W$ is obtained from Eqs. (3.29) and (3.30) as follows

$$\left(\frac{1}{v_p(x)}D_t + D_x\right)e = \frac{j}{v_p(x)\varepsilon_s} \quad \text{at } x = W. \tag{31}$$

Similarly, the boundary condition at $x = 0$ is

$$\left(-\frac{1}{v_n(x)}D_t + D_x\right)e = -\frac{j}{v_n(x)\varepsilon_s} \quad \text{at } x = 0. \tag{32}$$

Two second-order partial differential equations are formed in terms of real and imaginary parts of the total device impedance $Z(x,\omega)$ as [61]

$$\begin{aligned} D_x^2 R(x,\omega) + \left[\alpha_n(x) - \alpha_p(x)\right]D_x R(x,\omega) - 2r_n(x)\left(\frac{\omega}{\overline{v(x)}}\right)D_x X(x,\omega) \\ + \left[\left(\frac{\omega^2}{\overline{v(x)}^2}\right) - H(x) - \frac{qr_p(x)}{\overline{v(x)}\varepsilon_s}\left(G_T'(x) + G_T'(x')\right)R(x,\omega)\right] \\ - 2\overline{\alpha(x)}\left(\frac{\omega}{\overline{v(x)}}\right)X(x,\omega) - 2\left(\frac{\overline{\alpha(x)}}{\overline{v(x)}\varepsilon_s}\right) = 0, \end{aligned} \tag{33}$$

$$D_x^2 X(x,\omega) + \left[\alpha_n(x) - \alpha_p(x)\right] D_x X(x,\omega) + 2r_n\left(\frac{\omega}{\overline{v(x)}}\right) D_x R(x,\omega) + \left[\left(\frac{\omega^2}{\overline{v(x)}^2}\right) - H(x) - \frac{qr_p(x)}{\overline{v(x)}\varepsilon_s}\left(G_T'(x) + G_T'(x')\right)\right] X(x,\omega). + 2\overline{\alpha(x)}\left(\frac{\omega}{\overline{v(x)}}\right) R(x,\omega) + 2\left(\frac{\omega}{\overline{v(x)}^2 \varepsilon_s}\right) = 0 \tag{34}$$

The boundary conditions are given by

$$D_x R(x,\omega) + \frac{\omega X(x,\omega)}{v_{ns}} = -\left(\frac{1}{v_{ns}\varepsilon_s}\right) \quad \text{and} \quad D_x X(x,\omega) - \frac{\omega R(x,\omega)}{v_{ns}} = 0 \quad \text{at } x = 0, \tag{35}$$

$$D_x R(x,\omega) + \frac{\omega X(x,\omega)}{v_{ps}} = -\left(\frac{1}{v_{ps}\varepsilon_s}\right) \quad \text{and} \quad D_x X(x,\omega) - \frac{\omega R(x,\omega)}{v_{ps}} = 0 \quad \text{at } x = W, \tag{36}$$

Total device negative resistance ($Z_R(\omega)$) and reactance ($Z_X(\omega)$) for a particular frequency ($f = \omega/2\pi$) and bias current density ($J_0$) are then obtained from numerical integration of the $R(x,\omega)$- and $X(x,\omega)$-profiles over the entire space charge layer of the device, i.e. from $x = 0$ to $x = W$. Thus

$$Z_R(\omega) = \int_0^W R(x,\omega)dx \quad and \quad Z_X(\omega) = \int_0^W X(x,\omega)dx. \tag{37}$$

The total device impedance is

$$Z_D(\omega) = \int_0^W Z(x,\omega)dx = Z_R(\omega) + i\, Z_X(\omega). \tag{38}$$

The device admittance is

$$Y_D(\omega) = \frac{1}{Z_D(\omega)} = G(\omega) + i\, B(\omega) = \frac{1}{(Z_R(\omega) + i\, Z_X(\omega))}. \tag{39}$$

The negative conductance $G(\omega)$ and positive susceptance $B(\omega)$ are given by

$$\left.\begin{aligned} |-G(\omega)| &= Z_R(\omega)/\left(Z_R(\omega)^2 + Z_X(\omega)^2\right) \\ |B(\omega)| &= -Z_X(\omega)/\left(Z_R(\omega)^2 + Z_X(\omega)^2\right) \end{aligned}\right]. \tag{40}$$

The RF power output $P_{RF}$ from the device is obtained from

$$P_{RF} = \frac{1}{2}(V_{RF})^2 |G_p| A_j, \tag{41}$$

where $V_{RF}$—RF voltage given by $V_{RF} = m_x V_B$. Here, $m_x$—modulation index and $V_B$—breakdown voltage, $|G_p|$—peak negative conductance at optimum frequency ($f_p$), and $A_j$ is the effective junction area of the device.

## 6 Noise Simulation Technique

Starting from the small-signal noise field, $e_n(x,x') = e_{nr}(x,x') + j\, e_{ni}(x,x')$, two second order differential equations in the real ($e_{nr}(x,x')$) and imaginary ($e_{ni}(x,x')$) parts of the noise field $e_n(x,x')$ [74–78] are framed. These second order differential equations are given by

$$\begin{aligned} D^2 e_{nr}(x,x') + [\alpha_n(x) - \alpha_p(x)] D e_{nr}(x,x') - \frac{2r_n\omega}{\bar{v}} D e_{ni}(x,x') \\ + \left[\frac{\omega^2}{\bar{v}^2} - H(x) - \frac{q r_p}{\bar{v}\varepsilon}\left(G'_T(x) + G'_T(x')\right)\right] e_{nr}(x,x') \\ - \frac{2\bar{\alpha}(x)\omega}{\bar{v}} e_{ni}(x,x') = \frac{2q r_p \gamma(x')}{\bar{v}\varepsilon}, \end{aligned} \tag{42}$$

$$\begin{aligned} D^2 e_{ni}(x,x') + [\alpha_n(x) - \alpha_p(x)] D e_{ni}(x,x') + \frac{2r_n\omega}{\bar{v}} D e_{nr}(x,x') \\ + \left[\frac{\omega^2}{\bar{v}^2} - H(x) - \frac{q r_p}{\bar{v}\varepsilon}\left(G'_T(x) + G'_T(x')\right)\right] e_{ni}(x,x') \\ - \frac{2\bar{\alpha}(x)\omega}{\bar{v}} e_{nr}(x,x') = 0. \end{aligned} \tag{43}$$

Concurrent numerical solution of Eqs. (42) and (43) can be done [74–78] by using Runge–Kutta method. The boundary conditions at $x = 0$ and $x = W$

$$\left[-\frac{i\omega}{v_n} + D_x\right] e_n\left(x, x'\right) = 0 \qquad \text{at } x = 0, \tag{44}$$

$$\left[\frac{i\omega}{v_p} + D_x\right] e_n\left(x, x'\right) = 0 \qquad \text{at } x = W. \tag{45}$$

The terminal voltage $v_t(x')$ due to the noise source at $x'$, i.e.

$$v_t(x') = \int_{x=0}^{x=W} e_n(x, x')dx. \tag{46}$$

The transfer impedance is

$$z_t(x') = \frac{v_t(x')}{i_n(x')}, \tag{47}$$

where $i_n(x')$—average current generated in the interval $dx'$ due to $\gamma(x')$ located at $x'$. Now the mean-square noise voltage ($\langle {v_n}^2 \rangle$) is [63]

$$\langle v_n^2 \rangle = 2q^2.df.A_j \int |z_t(x')|^2 \gamma(x')dx', \tag{48}$$

The noise measure is given by [63, 79]

$$M_N = \frac{\langle v_n^2 \rangle / df}{4k_B T_j(-Z_R - R_S)}, \tag{49}$$

where $k_B = 1.38 \times 10^{-23}$ J K$^{-1}$—Boltzmann constant, $T_j$—junction temperature of the device in Kelvin (K) and $R_S$ is the series resistance of the device.

## 7 Large-Signal Simulation Technique

The time- and space-dependent device equations, i.e. Poisson's equation, current continuity equations and current density equations, are simultaneously solved subject to appropriate boundary conditions by using 1-D FDM [80]. These equations are given by

$$\frac{d\xi(x,t)}{dx} = \frac{q}{\varepsilon_s}(N_D - N_A + p(x,t) - n(x,t)), \tag{50}$$

$$\frac{\partial p(x,t)}{\partial t} = -\left(\frac{1}{q}\right)\frac{\partial J_p(x,t)}{\partial x} + G_{Ap}(x,t) + G_{Tp}(x,t), \tag{51}$$

$$\frac{\partial n(x,t)}{\partial t} = \left(\frac{1}{q}\right)\frac{\partial J_n(x,t)}{\partial x} + G_{An}(x,t) + G_{Tn}(x,t),, \tag{52}$$

$$J_p(x,t) = qp(x,t)v_p(x,t) - qD_p\left(\frac{\partial p(x,t)}{\partial x}\right), \tag{53}$$

$$J_n(x,t) = qn(x,t)v_n(x,t) + qD_n\left(\frac{\partial n(x,t)}{\partial x}\right), \tag{54}$$

The avalanche generation rates are given by

$$G_{An}(x,t) = G_{Ap}(x,t) = n(x,t)\alpha_n(x,t)v_n(x,t) + p(x,t)\alpha_p(x,t)v_p(x,t), \quad (55)$$

where $\alpha_n(x,t)$ and $\alpha_p(x,t)$ are the ionization rates and $v_n(x,t)$ and $v_p(x,t)$ are their drift velocities of charge carriers as functions of $x$ and $t$. The expression for band-to-band tunnelling generation rate of electrons is given in Eq. (11). The boundary conditions at $x = 0$ and $x = W$ at time $t$ are

$$\xi(x=0,t) = \xi(x=W,t) = 0 \quad (56)$$

$$\left.\begin{aligned} P(x=0) &= \left[\left(\frac{2J_p(x=0)}{J_0}\right) - 1\right] \\ P(x=W) &= \left[1 - \left(\frac{2J_n(x=W)}{J_0}\right)\right] \end{aligned}\right\}. \quad (57)$$

Time varying diode voltage ($V_t(t)$) and avalanche zone voltage are given by

$$V_t(t) = \int_0^W \xi(x,t)dx \quad \text{and} \quad V_a(t) = \int_{x_{A1}}^{x_{A2}} \xi(x,t)dx. \quad (58)$$

The DC values of the peak electric field ($\xi_P$), breakdown voltage ($V_B$) and avalanche zone voltage ($V_A$) drop are obtained as

$$\xi_P = \frac{1}{T}\int_0^T \xi_p(t)dt,\ V_B = \frac{1}{T}\int_0^T V_t(t)dt \quad \text{and} \quad V_A = \frac{1}{T}\int_0^T V_a(t)dt \quad (59)$$

A non-sinusoidal voltage excitation (NSVE) method is adopted in the proposed large-signal method. This voltage is given by

$$v_{rf}(t) = V_B \sum_{p=1}^{n} (m_x)^p \sin(2p\pi f_d t). \quad (60)$$

The voltage-driven IMPATT oscillator is shown in Fig. 3, where C is the coupling capacitor.

The large-signal program is run until the limit of one complete cycle (i.e. $0 \le \omega t \le 2\pi$) is reached. The simulation program is initially run for a number of consecutive cycles to verify the stability of oscillation. A constant direct current source is assumed to provide the necessary bias current density ($J_0$). The amplitude of the fundamental component of RF voltage is $V_{RF} = m_x V_B$. The Fourier analyses of terminal current ($j_t(t)$) and applied voltage ($v_{rf}(t)$) waveforms over a full oscillation cycle are carried out to obtain their frequency domain information. If the large-signal admittance be $Y_D(\omega)$, then the large-signal device impedance is obtained from

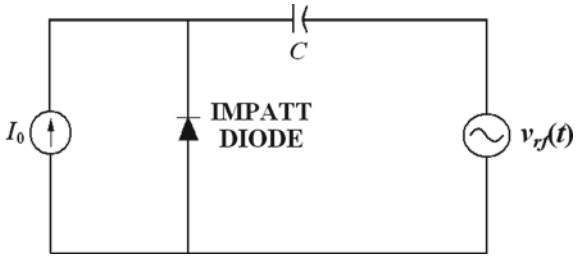


**Fig. 3** Voltage-driven IMPATT diode oscillator and associated circuit

$$Z_D(\omega) = \frac{1}{Y_D(\omega)} = \frac{1}{[G(\omega) + jB(\omega)]A_j} = Z_R(\omega) + i\, Z_X(\omega), \tag{61}$$

where $Z_R(\omega)$ and $Z_X(\omega)$—negative resistance and reactance of the device are given by

$$Z_R(\omega) = \frac{G(\omega)}{\left[G(\omega)^2 + B(\omega)^2\right]A_j} \quad \text{and} \quad Z_X(\omega) = \frac{-B(\omega)}{\left[G(\omega)^2 + B(\omega)^2\right]A_j}. \tag{62}$$

The RF power output is

$$P_{RF} = \frac{1}{2}(V_{RF})^2 \left|G_p\right| A_j, \tag{63}$$

The large-signal efficiency is

$$\eta_L = \frac{P_{RF}}{P_{DC}}. \tag{64}$$

where $P_{DC}$ is the input DC power given by $J_0 V_B A_j$ and $J_0$ is the DC bias current density. The flowchart shown in Fig. 4 illustrates the large-signal algorithm.

## 8 Material Parameters

Figure of merit (FOM) is a quantity used to characterize the performance of a device, system or method relative to its alternatives. In material science, FOMs are often used for a particular material in order to determine its relative utility for an application. A comparison of expected theoretical performances (i.e. FOMs) of different semiconductor materials is shown in Table 1. All the FOM values of the semiconductor materials are normalized with respected to the respective FOM values of Si in order to obtain a better comparative investigation. It can be observed from Table 1 that the WBG semiconductors such as 4H-SiC ($E_g = 3.26$ eV), 6H-SiC ($E_g = 2.86$ eV), Wz-GaN ($E_g = 3.40$ eV) and diamond ($E_g = 5.48$ eV) clearly have much higher

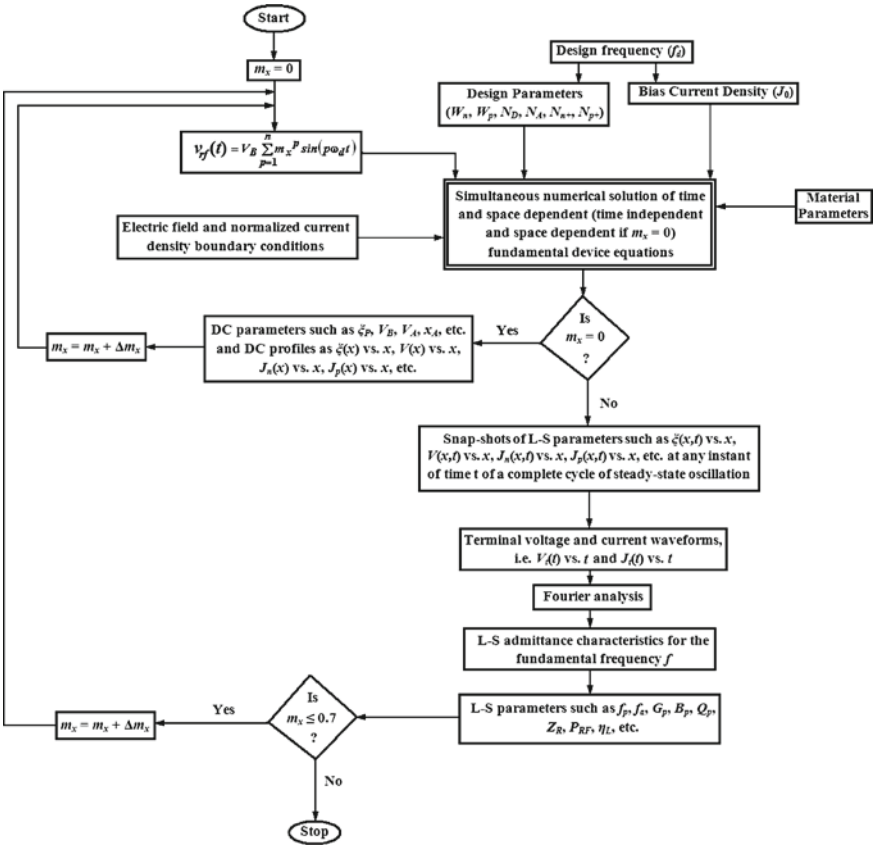


**Fig. 4** Flowchart of the large-signal (L-S) simulation software

advantages like higher frequency of operation, higher switching speed, power dissipation capacity, power-switching product, etc. Moreover, Table 1 shows that WBG semiconductors excel their narrower bandgap (NBG) counterparts as regards the above-said aspects.

## *8.1 Ionization Rates*

The parameters used to describe impact ionization phenomenon are the ionization rates $\alpha_n$ and $\alpha_p$ for electrons and holes, respectively. Ionization rates of charge carriers and its field and temperature dependences are important parameters which govern the DC and RF properties of IMPATT devices. The ionization rate is defined as the average number of ionizing collisions experienced by a single electron or hole per unit distance of travel in the direction of the electric field [68]. The ionization

**Table 1** Figure of merit (FOM) test [81]

| FOM | Si | GaAs | 6H-SiC | 4H-SiC | Wz-GaN | Diamond (C) |
|---|---|---|---|---|---|---|
| Johnson's figure of merit (JFOM) [81] | 1.0 | 1.8 | 277.8 | 215.1 | 215.1 | 81,000.0 |
| Baliga's figure of merit (BFOM) [82] | 1.0 | 14.8 | 125.3 | 223.1 | 186.7 | 25,106.0 |
| FET switching speed figure of merit (FSFOM) | 1.0 | 11.4 | 30.5 | 61.2 | 65.0 | 3595.0 |
| Bipolar switching speed figure of merit (BSFOM) | 1.0 | 1.6 | 13.1 | 12.9 | 52.5 | 2402.0 |
| FET power handling figure of merit (FPFOM) | 1.0 | 3.6 | 48.3 | 56.0 | 30.4 | 1476.0 |
| FET power switching product (FTFOM): | 1.0 | 40.7 | 1470.5 | 3424.8 | 1973.6 | 5,304,459.0 |
| Bipolar power handling capability figure of merit (BPFOM) | 1.0 | 0.9 | 57.3 | 35.4 | 10.7 | 594.0 |
| Bipolar power switching product (BTFOM) | 1.0 | 1.4 | 748.9 | 458.1 | 560.5 | 1,426,711.0 |

rates of electrons and holes (i.e. $\alpha_n$ and $\alpha_p$) in any semiconductor are exponentially increasing functions of electric field. The electric field dependence of ionization rates of electrons and holes in Si, GaAs, InP, Wz-GaN and type-IIb diamond can be represented by the following empirical relation following Shockley's model

$$\alpha_{n,p}(\xi) = A_{n,p} \exp\left[\left(\frac{-B_{n,p}}{\xi}\right)^m\right], \tag{65}$$

where $\xi$ is the electric field and the exponent, $m$ is 2.0 for GaAs only, but for other semiconductors, the exponent is 1.0. The ionization coefficients $A_{n,p}$ and $B_{n,p}$ for Si are taken from the experimental results reported by Grant in 1973 [83]. These coefficients were measured by Ito et al. in < 100 > GaAs for both low- and high-field ranges [84]. The ionization coefficients in < 100 > InP have been reported by Kao et al. [85] for the lower field range ($2.5 \times 10^7$–$5.0 \times 10^7$ V m$^{-1}$) and Umebu et al. [86] for the higher field range ($5.0 \times 10^7$–$8.0 \times 10^7$ V m$^{-1}$). The coefficients ($A_{n,p}$ and $B_{n,p}$) in Wz-GaN and type-IIb Diamond are obtained from the experimental report of Kunihiro et al. [87] and Konorova et al. [88], respectively. The field variation of carrier ionization rates in 4H-SiC is given by.

$$\alpha_n(\xi) = \left(\frac{\xi}{A_n}\right) \exp\left(\frac{-B_n}{\xi^2}\right) \quad \text{and} \quad \alpha_p(\xi) = \left(\frac{\xi}{7}\right) \exp\left[\frac{-1}{\left(A_p\xi^2 + B_p\xi\right)}\right]. \tag{66}$$

The ionization coefficients, $A_{n,p}$ and $B_{n,p}$, in 4H-SiC are taken from experimentally reported data of Konstantinov et al. [89] for a wide field range. Ionization rates of both

types of charge carriers in a semiconductor are also rapidly increasing functions of temperature. The carrier ionization rates in Si at different temperatures were reported by Grant [83] for both lower and higher field ranges. The following empirical relations for the field and temperature variations of electron and hole ionization rates fit very well with Grant's experimental results.

$$\alpha_n(\xi, T) = 6.2 \times 10^7 \left[ \exp\left\{ -\frac{\left(1.08 \times 10^8 + 1.3 \times 10^5 (T - 22)\right)}{\xi} \right\} \right]$$
$$\alpha_p(\xi, T) = 2.0 \times 10^8 \left[ \exp\left\{ -\frac{\left(1.97 \times 10^8 + 1.1 \times 10^5 (T - 22)\right)}{\xi} \right\} \right], \quad (67)$$
$$\text{for } 2.4 \times 10^7 \text{Vm}^{-1} < \xi < 5.3 \times 10^7 \text{Vm}^{-1}$$

$$\alpha_n(\xi, T) = 5.0 \times 10^7 \left[ \exp\left\{ -\frac{\left(9.90 \times 10^8 + 1.3 \times 10^5 (T - 22)\right)}{\xi} \right\} \right]$$
$$\alpha_p(\xi, T) = 5.6 \times 10^7 \left[ \exp\left\{ -\frac{\left(1.32 \times 10^8 + 1.1 \times 10^5 (T - 22)\right)}{\xi} \right\} \right]$$
$$\text{for } 5.3 \times 10^7 \text{Vm}^{-1} < \xi < 7.7 \times 10^7 \text{Vm}^{-1}, \quad (68)$$

where $T$ is the temperature in °C. The junction temperature of continuous-wave (CW) IMPATT diode is preferably kept close to 500 K. This is why the ionization coefficients of Si correspond to the junction temperature of 500 K in the present simulation study. The ionization coefficients $A_{n,p}$ and $B_{n,p}$ in < 100 > oriented GaAs was experimentally measured by Ito et al. [84]. These coefficients are determined from the measured ionization rates at temperature of 500 K over the lower field range of $2.5 \times 10^7 - 5.0 \times 10^7$ V m$^{-1}$ by Kao et al. [85] and higher field range of $5.0 \times 10^7 - 8.0 \times 10^7$ V m$^{-1}$ by Umebu et al. [86] in < 100 > oriented InP. The experimental values of ionization coefficients of Si, GaAs and InP are available at 500 K and given in Table 2. Simulation studies of IMPATT devices based on these semiconductors are carried out at a junction temperature of 500 K. The reported values of ionization coefficients of Wz-GaN, type-IIb diamond and 4H-SiC are available only at room temperature of 300 K but not at 500 K. The simulation studies of IMPATT devices based on those semiconductors are therefore carried out at room temperature (i.e. at

**Table 2** Ionization coefficients of electrons and holes in Si, GaAs and InP at 500 K

| Semiconductor material | Field range, $\xi$ ($\times 10^7$ V m$^{-1}$) | $A_n$ ($\times 10^9$ m$^{-1}$) | $B_n$ ($\times 10^9$ V m$^{-1}$) | $A_p$ ($\times 10^9$ m$^{-1}$) | $B_p$ ($\times 10^9$ V m$^{-1}$) |
|---|---|---|---|---|---|
| Si | 2.40 – 5.30 | 0.0620 | 0.1340 | 0.2000 | 0.2190 |
| | 5.30 – 7.70 | 0.0500 | 0.1250 | 0.0560 | 0.1540 |
| GaAs | 3.00 – 6.60 | 0.0184 | 0.0647 | 0.0184 | 0.0647 |
| InP | 2.50 – 8.00 | 0.7120 | 0.4070 | 3.5020 | 0.3852 |

**Table 3** Ionization coefficients of electrons and holes in Wz-GaN and type-IIb diamond at 300 K

| Semiconductor material | Field range, $\xi$ ($\times 10^7$ V m$^{-1}$) | $A_n$ ($\times 10^9$ m$^{-1}$) | $B_n$ ($\times 10^9$ V m$^{-1}$) | $A_p$ ($\times 10^9$ m$^{-1}$) | $B_p$ ($\times 10^9$ V m$^{-1}$) |
|---|---|---|---|---|---|
| Wz-GaN | 4.00 – 10.00 | 13.8000 | 1.4280 | 0.6867 | 0.8720 |
| | >10.00 | 12.2700 | 1.3630 | 0.3840 | 0.7950 |
| Type-IIb diamond | 1.00 – 10.00 | 19.3500 | 0.7490 | 19.3500 | 0.7490 |

**Table 4** Ionization coefficients of electrons and holes in 4H-SiC at 300 K

| Semiconductor material | Field range, $\xi$ ($\times 10^8$ V m$^{-1}$) | $A_n$ (V) | $B_n$ ($\times 10^{17}$ V$^2$ m$^{-2}$) | $A_p$ ($\times 10^{-18}$ V$^{-2}$ m$^2$) | $B_p$ ($\times 10^{-10}$ V$^{-1}$ m) * |
|---|---|---|---|---|---|
| 4H-SiC | 1.00 – 10.00 | 10.0000 | 4.0268 | 4.1915 | 4.6428 |

300 K) [87–89]. The values of $A_{n,p}$ and $B_{n,p}$ for Wz-GaN and type-IIb diamond are given in Table 3, and those for 4H-SiC are given in Table 4.

## 8.2 *Drift Velocities*

The field dependence of electron and hole drift velocity of group IV semiconductors such as Si and type-IIb diamond can be expressed by

$$v_{n,p}(\xi) = v_{sn,sp}\left[1 - \exp\left(\frac{-\mu_{n,p}\xi}{v_{sn,sp}}\right)\right]. \tag{69}$$

The values of saturated drift velocities of electrons and holes ($v_{sn}$ and $v_{sp}$) in Si are taken from the experimental data of Canali et al. [71]. The values of $v_{sn}$ and $v_{sp}$ in type-IIb diamond are taken from both experimental and theoretical data reported in [90, 91]. The negative differential mobility observed in the drift velocity versus electric field characteristics of group III-IV semiconductors such as GaAs, InP [92] and Wz-GaN [93] is taken into account in the computer simulation by using the following empirical relation.

$$v_n(\xi) = \frac{\left[\mu_n\xi + v_{sn}\left(\xi/\xi_c\right)^4\right]}{\left[1 + \left(\xi/\xi_c\right)^4\right]}, \tag{70}$$

The electron drift velocity attains a peak at a particular electric field called critical field, $\xi_c$ before saturation at high field. The drift velocity versus field characteristics of holes in GaAs, InP and Wz-GaN are similar to those for Si as expressed in Eq. (67). The electric field dependence of electron and hole drift velocity in 4H-SiC are given

**Table 5** Saturated drift velocities of electrons and holes in Si, GaAs, InP, Wz-GaN, diamond and 4H-SiC

| Saturated drift velocity | $T = 500$ K | | | $T = 300$ K | | |
|---|---|---|---|---|---|---|
| | Si | GaAs | InP | Wz-GaN | Diamond | 4H-SiC |
| $v_{sn}$ ($\times 10^5$ m s$^{-1}$) | 0.6430 | 0.5000 | 0.6000 | 3.0000 | 1.5000 | 2.1200 |
| $v_{sp}$ ($\times 10^5$ m s$^{-1}$) | 0.6340 | 0.5200 | 0.5680 | 0.7500 | 1.1700 | 1.0800 |

by [94]

$$v_{n,p}(\xi) = \left[\frac{\mu_{n,p}\xi}{\left(1 + \left(\mu_{n,p}\xi / v_{sn,sp}\right)^{\kappa}\right)}\right]^{1/\kappa}, \tag{71}$$

where the value of the constant $\kappa = 1.20$. The drift velocities of the charge carriers in a semiconductor are also strong functions of temperature. Carrier drift velocities versus electric field characteristics of Si for different temperature were studied by Canali et al. [71] in the year 1971. The empirical relations for the electron and hole drift velocities in Si with electric field and temperature can be expressed as [71]

$$v_n(\xi, T) = \frac{1.42 \times 10^7 \times T^{-2.42} \times \xi}{\left(1 + \left(\frac{\xi}{1.01 \times T^{1.55}}\right)^{0.0257 \times T^{0.66}}\right) \times \left(\frac{1}{0.0257 \times T^{0.66}}\right)}, \tag{72}$$

$$v_p(\xi, T) = \frac{1.31 \times 10^7 \times T^{-2.20} \times \xi}{\left(1 + \left(\frac{\xi}{1.24 \times T^{1.68}}\right)^{0.4600 \times T^{0.17}}\right) \times \left(\frac{1}{0.4600 \times T^{0.17}}\right)}, \tag{73}$$

where $T$ is the temperature in Kelvin (K). The junction temperature of IMPATT devices under CW operation are usually kept around 500 K by appropriate heat-sinking arrangements. Thus, the saturated drift velocities of both types of charge carriers ($v_{sn}$ and $v_{sp}$) measured at 500 K are used in the simulation studies. The reported values of $v_{sn}$ and $v_{sp}$ for Si, GaAs and InP at 500 K [71, 92] and for Wz-GaN, type-IIb diamond and 4H-SiC at 300 K are given in Table 5. These parameters are used in the simulation studies of IMPATT devices. The experimental data of $v_{sn}$ and $v_{sp}$ for Wz-GaN, type-IIb diamond and 4H-SiC are not available at 500 K. This has compelled the author to carry out simulation studies of IMPATT devices based on the above materials at a junction temperature of 300 K.

## *8.3 Other Parameters*

Table 6 shows some other material parameters used in the simulation such as bandgap ($E_g$), relative permittivity ($\varepsilon_r$), intrinsic carrier concentration ($n_i$), effective density

**Table 6** Important material parameters of Si, GaAs, InP, Wz-GaN, diamond and 4H-SiC [95, 96]

| Material parameter | | $T =$ 500 K | | | $T =$ 300 K | |
|---|---|---|---|---|---|---|
| | Si | GaAs | InP | Wz-GaN | Diamond | 4H-SiC |
| $E_g$ (eV) | 1.0465 | 1.3271 | 1.2729 | 3.4691 | 5.4800 | 3.1934 |
| ¶ $m_d{}^*$ ($\times m_0$) | 0.1370 | 0.0370 | 0.069 | 1.5000 | 0.5700 | 0.7700 |
| ¶¶ $\varepsilon_r$ | 11.7000 | 13.1000 | 14.0000 | 10.4000 | 5.7000 | 8.5884 |
| $n_i$ ($\times 10^{13}$ m$^{-3}$) | 859.5800 | 3.2393 | 11.4280 | $3.6114 \times 10^{-17}$ | $10^{-30}$ | $0.0161 \times 10^{-13}$ |
| $N_c$ ($\times 10^{25}$ m$^{-3}$) | 6.9318 | 0.0965 | 0.1229 | 0.2234 | 10.0000 | 1.6887 |
| $N_v$ ($\times 10^{25}$ m$^{-3}$) | 3.9131 | 2.0460 | 2.4597 | 4.6246 | 1.0000 | 2.4942 |
| $\mu_n$ (m$^2$ V$^{-1}$ s$^{-1}$) | 0.0500 | 0.4000 | 0.2760 | 0.1000 | 0.2200 | 0.1000 |
| $\mu_p$ (m$^2$ V$^{-1}$ s$^{-1}$) | 0.0180 | 0.0200 | 0.0090 | 0.0034 | 0.1800 | 0.0100 |
| $D_n$ ($\times 10^{-4}$ m$^2$ s$^{-1}$) | 11.0000 | 17.2000 | 11.9000 | 2.6000 | 57.0000 | 2.7100 |
| $D_p$ ($\times 10^{-4}$ m$^2$ s$^{-1}$) | 1.8900 | 8.6250 | 3.8812 | 0.8798 | 46.0000 | 2.5875 |
| $L_n$ ($\times 10^{-6}$ m) | 35.4000 | 70.0000 | 40.0000 | 6.5000 | – | 12.0000 |
| $L_p$ ($\times 10^{-6}$ m) | 10.0000 | 50.0000 | 25.0000 | 2.1000 | – | 1.5000 |
| $\xi_c$ ($\times 10^5$ V m$^{-1}$) | – – | 5.8000 | 11.0000 | 0.5000 | – | – |

¶ $m_0 = 9.1 \times 10^{-31}$ kg is the rest mass of an electron
¶¶ $\varepsilon_s = \varepsilon_r \varepsilon_0$ is the permittivity of the semiconductor material; where $\varepsilon_0 = 8.85 \times 10^{-12}$ F m$^{-1}$ is the permittivity of vacuum

of states of conduction and valance bands ($N_c$, $N_v$), density of state effective mass ($m_d{}^*$), mobilities ($\mu_n$, $\mu_p$), diffusion coefficients ($D_n$, $D_p$), diffusion lengths ($L_n$, $L_p$) and electric field corresponding to the peak drift velocity ($\xi_c$) of electrons in group III-V semiconductors for Si, GaAs, InP, Wz-GaN, type-IIb diamond and 4H-SiC. These parameters are taken from the available reports [95, 96].

## 9 Summary

Great demand of suitable THz sources requires optimized design and appropriate simulation tool for designing and investigating the device capability at the design spectrum before actual fabrication. Design and simulation of complex devices like THz ATT diodes requires comprehensive and accurate simulation model for small-signal, large-signal and noise simulation before the actual fabrication. This chapter is devoted to summarize these three types of simulation methodologies for THz ATT sources. Also, material properties of some promising materials for THz device fabrication are also included in this chapter.

## References


1. Siegel PH (2007) THz instruments for space. IEEE Trans Antenn Propag 55:2957–2965
2. Grischkowsky D, Keiding S, Exter M, Fattinger C (1990) Far-infrared time-domain spectroscopy with terahertz beams of dielectrics and semiconductors. J Opt Soc Am B 7:2006–2015
3. Debus C, Bolivar PH (2007) Frequency selective surfaces for high sensitivity terahertz sensing. Appl Phys Lett 91:184102
4. Yasui T, Yasuda T, Sawanaka K, Araki T (2005) Terahertz paintmeter for noncontact monitoring of thickness and drying progress in paint film. Appl Opt 44:6849–6856
5. Stoik CD, Bohn MJ, Blackshire JL (2008) Nondestructive evaluation of aircraft composites using transmissive terahertz time domain spectroscopy. Opt Express 16:17039–17051
6. Jördens C, Koch M (2008) Detection of foreign bodies in chocolate with pulsed terahertz spectroscopy. Opt Eng 47:037003
7. Fitzgerald AJ, Cole BE, Taday PF (2005) Nondestructive analysis of tablet coating thicknesses using terahertz pulsed imaging. J Pharm Sci 94:177–183
8. Siegel PH (2004) Terahertz technology in biology and medicine. IEEE Trans Microw Theory Tech 52:2438–2447
9. Ward J, Schlecht E, Chattopadhyay G, Maestrini A, Gill J, Maiwald F, Javadi H, Mehdi I (2004) Capability of THz sources based on schotiky diode frequency multiplier chains. IEEE MTT-S Digest 12:1587–1590
10. Heyminck S, Güsten R, Graf U, Stutzki J, Hartogh P, Hübers HW, Ricken O, Klein B (2009) GREAT: ready for early science aboard SOFIA. Proceeding 20th international symposium space THz techniques. Charlottesville, VA., pp 315–317
11. Crowe TW, Hesler JL, Retzloff SA, Pouzou C, Schoenthal GS (2011) Solid state LO sources for greater than 2THz. 2011 ISSTT digest, 22nd symposium on space terahertz technology. Tucson Arizona, USA
12. Crowe TW, Hesler JL, Retzloff SA, Pouzou C, Hester JL (2011) "Multiplier based sources for frequencies above 2 THz," 36th international conference on infrared, millimeter and terahertz sources (IRMMW-THz). p 1
13. Maestrini A, Mehdi I, Siles JV, Ward J, Lin R, Thomas B, Lee C, Gill J, Chattopadhyay G, Schlecht E, Pearson J, Siegel P (2012) First demonstration of a tunable electronic source in the 2.5 to 2.7 THz range. IEEE Trans Terahertz Sci Techn 3:112–123
14. Williams BS (2007) Terahertz quantum-cascade lasers. Nat Photonics 1:617–626
15. Lai R, Mei X, Deal W, Yoshida W, Kim Y, Liu P, Lee J, Uyeda J, Radisic V, Lange M, Gaier T, Samoska L, Fung A (2007)Sub 50 nm InP HEMT device with $f_{max}$ greater than 1 THz. In: Proceeding IEEE international electron devices meeting pp 609–611
16. Deal W, Mei X, Radisic V, Leong K, Sarkozy S, Gorospe B, Lee J, Liu P, Yoshida W, Zhou J, Lange M, Uyeda J, Lai R (2010) Demonstration of a 0.48 THz amplifier module using InP HEMT transistors. IEEE Microw Wireless Compon Lett 20(5):289–291
17. Urteaga M, Seo M, Hacker J, Griffith Z, Young A, Pierson R, Rowell P, Skalare A, Rodwell M (2010) InP HBT integrated circuit technology for terahertz frequencies. In: Proceeding IEEE compound semiconductor integrated circuit symposia. pp 1–4
18. Lobisser E, Griffith Z, Jain V, Thibeault B, Rodwell M, Loubychev D, Snyder A, Wu Y, Fastenau J, Liu A (May 2009) 200-nm InGaAs/InP type-I DHBT employing a dual-sidewall emitter process demonstrating $f_{max} >> 800$ GHz and $f_T = 360$ GHz. In: Proceeding IEEE international conference indium phosphide related materials. pp 16–19
19. Seo M, Urteaga M, Young A, Jain V, Griffith Z, Hacker J, Rowell P, Pierson R, Rodwell M (May 2010) 300 GHz fixed-frequency and voltage-controlled fundamental oscillators in an InP HBT process. In: IEEE MTT-S international microwave symposium digestivas. pp 272–275
20. Hacker J, Seo M, Young A, Griffith Z, Urteaga M, Reed T, Rodwell M (May 2010) THz MMICs based on InP HBT technology. In: IEEE MTT-S international microwave symposium digestivas. pp 1126–1129

21. Seo M, Urteaga M, Hacker J, Young A, Griffith Z, Jain V, Pierson R, Rowell P, Skalare A, Peralta A, Lin R, Pukala D, Rodwell M (2011) InP HBT IC technology for terahertz frequencies: fundamental oscillators up to 0.57 THz. IEEE J Solid-State Circ 46(10):2203–2214
22. Gray WW, Kikushima L, Morentc NP, Wagner RJ (1969) Applying IMPATT power sources to modern microwave systems. IEEE J Solid-State Circ 4:409–413
23. Chang Y, Hellum JM, Paul JA, Weller KP (1977) Millimeter-wave IMPATT sources for communication applications. IEEE MTT-S Int Microw Symp Dig 4:216–219
24. Midford TA, Bernick RL (1979) Millimeter wave CW IMPATT diodes and oscillators. IEEE Trans Microwave Theory Tech 27:483–492
25. Luy JF, Casel A, Behr W, Kasper E (1987) A 90-GHz double-drift IMPATT diode made with Si MBE. IEEE Trans Electron Devices 34:1084–1089
26. Wollitzer M, Buchler J, Schafflr F, Luy JF (1996) D-band Si-IMPATT diodes with 300 mW CW output power at 140 GHz. Electron Lett 32:122–123
27. Dalle C, Rolland P, Lieti G (1990) Flat doping profile double-drift silicon IMPATT for reliable CW high power high-efficiency generation in the 94-GHz window. IEEE Trans Electron Devices 37:227–236
28. Luschas M, Judaschke R, Luy JF (2002) Measurement results of packaged millimeter-wave silicon IMPATT diodes." In: Proceeding of 27th international conference on infrared and millimeter waves, conference digest. pp 135–136
29. Luschas M, Judaschke R, Luy JF (2002) Simulation and measurement results of 150 GHz integrated silicon IMPATT diodes". IEEE MTT-S Int Microw Symp Dig 12:1269–1272
30. Huang HC (1973) A modified GaAs IMPATT structure for high-efficiency operation. IEEE Trans Electron Dev 20(5):482–486
31. Goldwasser RE, Rosztoczy FE (1974) High efficiency GaAs low-high-low IMPATTs. Appl Phys Lett 25:92
32. Bozler CO, Donelly JP, Murphy RA, Laton RW, Sudhury RN, Lindley WT (1976) High efficiency ion implanted Lo-hi-lo GaAs IMPATT diodes. Appl Phys Lett 29:123–125
33. Eisele H (1989) Selective etching technology for 94 GHz, GaAs IMPATT diodes on diamond heat sinks. Solid State Electron 32(3):253–257
34. Eisele H (1990) GaAs W-band IMPATT diode for very low noise oscillations. Electron Lett 26(2):109–110
35. Eisele H, Hadded GI (1992) GaAs single-drift flat profile IMPATT diodes for CW operation at D band. Electron Lett 28(23):2176–2177
36. Kearney MJ, Couch NR, Stephens JS, Smith RS (1992) Low noise, high efficiency GaAs IMPATT diodes at 30GHz. Electron Lett 28(8):706–708
37. Curow M (1994) Proposed GaAs IMPATT device structure for D-band applications. Electronic Lett 30(19):1629–1631
38. Tschernitz M, Freyer J, Grothe H (1994) GaAs read-type IMPATT diodes for D-band. Electron Lett 30(13):1070–1071
39. Tschernitz M, Freyer J (1995) 140 GHz GaAs double-read IMPATT diodes. Electron Lett 31(7):582–583
40. Berenz JJ, Fank FB, Hierl TL (1978) Ion-implanted p-n junction Indium-phosphide IMPATT diodes. Electron Lett 14(21):683–684
41. Banerjee JP, Pati SP, Roy SK (1984) High frequency characterisation of double drift region InP and GaAs diode. Appl Phys A 48:437–443
42. Shih HD, Bayraktaroglu B, Duncan WM (1983) Growth of millimeter-wave GaAs IMPATT structures by molecular beam epitaxy. J Vacuum Sci Technol B: Microelectron Nanometer Struct 1:199–201
43. Mukherjee M, Mazumder N, Roy SK (2009) Prospects of 4H-SiC double drift region IMPATT device as a photo-sensitive high-power source at 0.7 THz frequency regime. Act Passive Electron Compon 2009:1–9
44. Panda AK, Parida RK, Agarwala NC, Dash GN (2007) A comparative study on the high band gap materials (GaN and SiC)-based IMPATTs. In: Proceeding of Asia-Pacific microwave conference. pp 1–4

45. Panda AK, Pavlidis D, Alekseev E (2001) DC and high-frequency characteristics of GaN-based IMPATTs. IEEE Trans Electron Dev 48:820–823
46. Banerjee S, Mukherjee M, Banerjee JP (2010) Bias current optimization of Wurtzite-GaN DDR IMPATT diode for high power operation at THz frequencies. Int J Adv Sci Technol 16:12–20
47. Acharyya A, Banerjee JP (2014) Prospects of IMPATT devices based on wide bandgap semiconductors as potential terahertz sources. Appl Nanosci 4:1–14
48. Acharyya A, Banerjee JP (2013) Potentiality of IMPATT devices as terahertz source: an avalanche response time based approach to determine the upper cut-off frequency limits. IETE J Res 59(2):118–127
49. Yuan L, James A, Cooper JA, Melloch MR, Webb KJ (2001) Experimental demonstration of a silicon carbide IMPATT oscillator. IEEE Electron Dev Lett 22:266–268
50. Vassilevski KV, Zorenko AV, Zekentes K, Tsagaraki K, Bano E, Banc C, Lebedev A (2001) 4H-SiC IMPATT diode fabrication and testing. Technical digest of international conference on SiC and related materials, Tsukuba, Japan. pp 713–714
51. Trew RJ, Yan JB, Mock PM (1991) The potentiality of diamond and SiC electronic devices for microwave and millimeter-wave power applications. Proc IEEE 79(5):598–620
52. Mock PM, Trew RJ (1989) RF performance characteristics of double-drift MM-wave diamond IMPATT diodes. In: Proceeding of IEEE/cornell conference advanced concepts in high-speed semiconductor devices and circuits. pp 383–389
53. Misawa T (1966) The negative resistance in p-n junctions under avalanche breakdown conditions Part-1. IEEE Trans Electron Device 13:137–151
54. Gilden M, Hines ME (1966) Electronic tuning effects in read microwave avalanche diode. IEEE Trans Electron Devices 13:169–175
55. Sze SM, Gibbons G (1966) Avalanche breakdown voltages of abrupt and linearly graded p-n junctions in Ge, Si GaAs and InP. Appl Phys Lett 8:111–112
56. Roy SK, Sridharan M, Ghosh R, Pal BB (1979) Computer method for the dc field and carrier current profiles in the IMPATT device starting from the field extremum in the depletion layer. In: Miller JH (ed) Proceeding of the 1st conference on numerical analysis of semiconductor devices (NASECODE I). Dublin, Ireland. pp 266–274
57. Roy SK, Banerjee JP, Pati SP (1985) A computer analysis of the distribution of high frequency negative resistance in the depletion layer of IMPATT diodes. In: Proceeding 4th conference on numerical analysis of semiconductor devices (NASECODE IV) (Dublin). Ireland. pp 494–500
58. Sridharan M, Roy SK (1978) Computer studies on the widening of the avalanche zone and decrease on efficiency in silicon X-band symmetrical DDR. Electron Lett 14:635–637
59. Sridharan M, Roy SK (1980) Effect of mobile space charge on the small signal admittance of silicon DDR. Solid State Electron 23:1001–1003
60. Dash GN, Pati SP (1991) Small-signal computer simulation of IMPATT diodes including carrier diffusion. Semicond Sci Technol 6:348–355
61. Dash GN, Pati SP (1992) A generalized simulation method for IMPATT mode operation and studies on the influence of tunnel current on IMPATT properties. Semicond Sci Technol 7:222–230
62. Dalle C, Rolland PA (1989) Drift-diffusion versus energy model for millimetre-wave IMPATT diodes modelling. Int J Numer Model Electron Networks Devices Fields 2:61–73
63. Gummel HK, Blue JL (1967) A small-signal theory of avalanche noise in IMPATT diodes. IEEE Trans Electron Devices 14:569–580
64. Acharyya A, Banerjee S, Banerjee JP (2013) Influence of skin effect on the series resistance of millimeter-wave of IMPATT devices. J Comput Electron 12(3):511–525
65. Acharyya A, Mallik A, Banerjee D, Ganguli S, Das A, Dasgupta S, Banerjee JP (2014) Large-signal characterizations of DDR IMPATT devices based on group III–V semiconductors at millimeter-wave and terahertz frequencies. J Semiconductors 35(8):084003–1–10
66. Acharyya A, Datta K, Ghosh R, Sarkar M, Sanyal R, Banerjee S, Banerjee JP (2013) Diamond based DDR IMPATTs: prospects and potentiality as millimeter-wave source at 94 GHz atmospheric window. Radioengineering 22(2):624–631
67. Sze SM (1981) Physics of semiconductor devices, 2nd edn. Wiley, New York, NY

68. G. Gibbons, Avalanche-diode Microwave Oscillators Oxford: Oxford University Press, pp. 13 and pp. 53, (1973)
69. Elta EM (1978) The effect of mixed tunneling and avalanche breakdown on microwave transit-time diodes. Ph.D. dissertation, electron physics laboratory, University of Michigan, annals Arbor, MI, Tech. Rep
70. Kane EO (1961) Theory of tunneling. J Appl Phys 32:83–91
71. Canali C, Ottaviani G, Quaranta AA (1971) Drift velocity of electrons and holes and associated anisotropic effects in silicon. J Phys Chem Solids 32:1707–1720
72. Dalal VL (1970) Hole velocity in *p*-GaAs. Appl Phys Lett 16:489–491
73. Houston PA, Evans AGR (1977) Electron drift velocity in *n*-GaAs at high electric field. Solid State Electron 20:197–204
74. Dash GN, Mishra JK, Panda AK (1996) Noise in mixed tunneling avalanche transit time (MITATT) diodes. Solid State Electron 39(10):1473–1479
75. Mishra JK, Panda AK, Dash GN (1997) An extremely low-noise heterojunction IMPATT. IEEE Trans Electron Devices 44(12):2143–2148
76. Acharyya A, Mukherjee M, Banerjee JP (2010) Noise performance of millimeter-wave silicon based mixed tunneling avalanche transit time (MITATT) diode international journal of electrical and electronics engineering 4(8):577–584
77. Acharyya A, Mukherjee M, Banerjee JP (2011) Noise in millimeter-wave mixed tunneling avalanche transit time diodes". Arch Appl Sci Res 3(1):250–266
78. Banerjee S, Acharyya A, Banerjee JP (Dec 17–19 2012) Millimeter-wave and noise properties of Si~$Si_{1-x}Ge_x$ heterojunction double-drift region MITATT devices at 94 GHz. IEEE Conference CODEC 2012, Kolkata, India. pp 1–4
79. Haus HA, Statz H, Pucel PA (1971) Optimum noise measure of IMPATT diode. IEEE Trans MTT 19:801–8123
80. Douglas J, Yuan Y (1987) Finite difference methods for the transient behavior of a semiconductor device. IMA Preprint Series#286, Institute for mathematics and its applications, University of Minnesota, Minnesota
81. Johnson EO (1965) Physical limitations on frequency and power parameters of transistors. RCA Rev 26:163–177
82. Baliga BJ (1989) Power semiconductor device figure of merit for high-frequency applications. Electron Device Lett 10(10):455–457
83. Grant WN (1973) Electron and hole ionization rates in epitaxial Silicon. Solid State Electron 16:1189–1203
84. Ito M, Kagawa S, Kaneda T, Yamaoka T (1978) Ionization rates for electrons and holes in GaAs. J Appl Phys 49:4607
85. Kao CW, Crowell CR (1980) Impact ionization by electrons and holes in InP. Solid State Electron 23:881–891
86. Umebu I, Chowdhury ANMM, Robson PN (1980) Ionization coefficients measured in abrupt InP junction. Appl Phys Lett 36:302–303
87. Kunihiro K, Kasahara K, Takahashi Y, Ohno Y (1999) Experimental evaluation of impact ionization coefficients in GaN. IEEE Electron Device Letter 20(12):608–610
88. Konorova EA, Kuznetsov YA, Sergienko VF, Tkachenko SD, Tsikunov AK, Spitsyn AV, Danyushevski YZ (1983) Impact ionization in semiconductor structures made of ion-implanted diamond. Sov Phys—Semicond 17:146
89. Konstantinov AO, Wahab Q, Nordell N, Lindefelt U (1997) Ionization rates and critical fields in 4H-silicon carbide. Appl Phys Lett 71:90–92
90. Ferry DK (1975) High-field transport in wide-bandgap semiconductors. Phys Rev B 12:2361
91. Canali C, Gatti E, Kozlov SF, Manfredi PF, Manfredotti C, Nava F, Quirini A (1979) Electrical properties and performances of neutral diamond nuclear radiation detectors. Nuclear Instrum Methods 160:73
92. Kramer B, Micrea A (1975) Determination of saturated electron velocity in GaAs. Appl Phys Lett 26:623–624

93. Shiyu SC, Wang G (2008) High-field properties of carrier transport in bulk wurtzite GaN: monte carlo perspective. J Appl Phys 103:703–708
94. Vassilevski KV, Zekentes K, Zorenko AV, Romanov LP (2000) Experimental determination of electron drift velocity in 4H-SiC $p^+$–$n$–$n^+$ avalanche diodes. IEEE Electron Dev Lett 21:485–487
95. Vassilevski KV, Zekentes K, Zorenko AV, Romanov LP, Electronic archive: new semiconductor materials, characteristics and properties. Available from: http://www.ioffe.ru/SVA/NSM/Semicond/index.html (Last accessed on: April 2021)
96. Zeghbroeck BV (2011) Principles of semiconductor devices. Colorado Press, USA

# Studies on Sub-Terahertz Performance of Avalanche Transit Time Sources


**Prajukta Mukherjee and Aritra Acharyya**

**Abstract** This chapter describes the procedure of estimating the degree of deterioration of the performance of avalanche transit time (ATT) sources due to instantaneous tunneling effect. The comparative study of Si, InP, GaAs and 4H-SiC ATT sources is presented. Tunneling-induced ATT phase delays in the oscillators are estimated and the degree of deterioration of the oscillators are interpreted via the estimated ATT phase delay at sub-terahertz frequency bands.

**Keywords** ATT phase delay · Sub-terahertz · MITATT · Tunneling

## 1 Introduction

ATT oscillators are the most powerful, efficient and popular solid-state sources for millimeter-wave or sub-terahertz (30–300 GHz) power generation [1–3]. Most convenient semiconductor material for fabricating IMPATT diodes is Si due to the existence of advanced technology associated with it [1, 4–7]. However, some group III–V compound semiconductors such as InP and GaAs have also show immense potentiality as base materials of IMPATT diodes especially operating at millimeter-wave (mm-wave) frequency regime [8–10]. At the beginning of this century, a wide bandgap (WBG) group IV–IV material, 4H-SiC attracted the attention of researchers for its extraordinary electronic properties. Some researchers have already made attempts to utilize the potentiality of 4H-SiC as fabricating 4H-SiC IMPATT diodes operating at microwave frequency bands [11, 12]. However, their attempts did not achieve significant success as a result of the unavailability of high quality 4H-SiC substrate at that time. However, several researchers have demonstrated the high power delivery capability of 4H-SiC IMPATT sources (in the order of watts) via simulation

P. Mukherjee
Department of Electrical Engineering, Cooch Behar Government Engineering College, Harinchawra, Ghughumari, Cooch Behar 736170, West Bengal, India

A. Acharyya (✉)
Department of Electronics and Communication Engineering, Cooch Behar Government Engineering College, Harinchawra, Ghughumari, Cooch Behar 736170, West Bengal, India



A. Acharyya et al. (eds.), *Generation, Detection and Processing of Terahertz Signals*, Lecture Notes in Electrical Engineering 794,
https://doi.org/10.1007/978-981-16-4947-9_14

experiments; while the power delivery capability of narrow bandgap (NBG) material (e.g. Si, InP, GaAs, etc.) based IMPATT sources is limited to in the order of few hundred milli-watts at mm-wave frequencies [13–16].

Since the IMPATT diodes operate under high reverse bias voltage above the breakdown condition, generation of EHPs occur near the junction primarily due to the charge multiplication due to the avalanche breakdown phenomena. However, in the mm-waves IMPATT diodes, the thickness of the depletion layer narrowed down to very low dimension, in the order of few sub-micrometers which, in turn, leads to very high electric field near the metallurgical junction of the device. Therefore, the thin depletion layer and high electric field originates ideal condition for direct band-to-band tunneling generation of EHPs near the junction. Thus, in mm-wave IMPATTs, EHPs are generated via two major processes, such as (i) avalanche generation and (ii) band-to-band tunneling generation; that is why the mode of operation of the device at these frequencies may be regarded as mixed tunneling avalanche transit time (MITATT mode) [17]. Out of these two generation mechanisms, avalanche generation introduces nearly 90° phase delay (known as avalanche delay) to the generated charge carriers with respect to the applied voltage which is necessary for the origination of negative resistance of the device required for IMPATT operation; however, being an instantaneous phenomena, band-to-band tunneling fails to provide the required phase delay to the charge carriers with respect to the applied bias voltage. Therefore, overall phase delay of the generated charge carriers reduces below 90° as a result of the band-to-band tunneling generation, which leads to reduction in the magnitude of negative resistance as well as power output of the source. The degree of tunneling generation increases significantly with increase of the frequency of operation of the device [17]. Thus the deterioration in the high frequency performance of IMPATT sources further increases as the frequency of operation increases.

This chapter describes the procedure of estimating the degree of deterioration of the performance of ATT (i.e., impact avalanche transit time (IMPATT)) sources due to instantaneous tunneling effect. An in-house simulation code developed by the authors based on self-consistent quantum drift–diffusion (SCQDD) model has been used to study the above-mentioned effect on the IMPATTs at 94 GHz. The comparative study of Si, InP, GaAs and 4H-SiC ATT sources is presented. Tunneling-induced ATT phase delays in the oscillators are estimated, and the degree of deterioration of the oscillators are interpreted via the estimated ATT phase delay at sub-terahertz frequency bands.

## 2 Tunneling

One-dimensional (1-D) simulation model of a reverse double-drift (DD) IMPATT device is illustrated in Fig. 1. The tunneling generation rate for electrons can be expressed as [18–20]

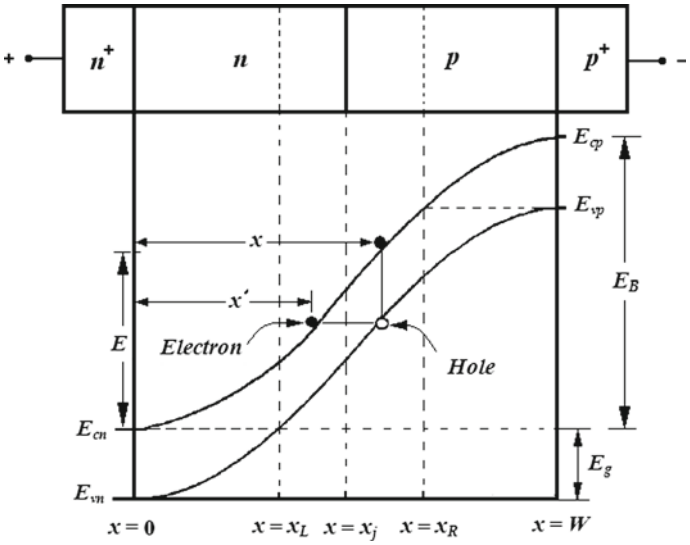


**Fig. 1** 1-D model and band-diagram of reverse biased DD IMPATT

$$g_{Tn}(x) = a_T \xi^2(x) \exp\left(-\frac{b_T}{\xi(x)}\right), \tag{1}$$

where

$$a_T = \frac{q^2}{8\pi^3\hbar^2}\left(\frac{2m^*}{E_g}\right)^{\frac{1}{2}} \quad \text{and} \quad b_T = \frac{1}{2q\hbar}\left(\frac{m^* E_g^3}{2}\right)^{\frac{1}{2}} \tag{2}$$

where $E_g$, $m^*$ and, $q = 1.6 \times 10^{-19}$ C are the bandgap, density state effective mass and electronic charge, respectively. From the band-diagram shown in Fig. 1, the tunneling generation rate of holes at $x$ can be associated with that of electrons at $x'$; the relation between the space points x and $x'$ can be obtained from

$$x' = x\left(1 - \frac{E_g}{E}\right)^{\frac{1}{2}} \quad \text{for} \quad 0 \le x \le x_j \tag{3}$$

$$x' = W - (W - x)\left(1 + \frac{E_g}{E_B - E}\right)^{\frac{1}{2}} \quad \text{for} \quad x_j \le x \le W \tag{4}$$

## 3 Design, Material Parameters and Simulation

Designs of the diodes are initially obtained from the formula of Sze and Ryder [21]. The initial designs are modified and finalized for 94 GHz operation by using a iterative simulation approach adopted from the small-signal model reported by Gummel and Blue [22]. The SCQDD model is used to study the static as well as high frequency performance of the sources at 94 GHz. The material parameters used in the simulation are taken from the trustworthy published literatures [23–32]. The effects of different quantum and classical phenomena have been incorporated in the simulation program [17, 34–38].

## 4 ATT Phase Delay Shift Due to Tunneling

The amount of ATT phase delay shift due to tunneling is estimated from the mutual shifts of negative resistivity peaks between the pure IMPATT mode and mixed tunneling ATT (MITATT) mode. The ATT phase delay at p-side of a DD diode is given by If the distances of the peaks from the junction on the *p*-side of ATT device in the avalanche and mixed mode are $x_{pa}$ and $x_{pm}$ and the corresponding optimum frequencies $f_a$ and $f_m$, respectively, then the phase delays on the *p*-side of the device at $x_{pa}$ and $x_{pm}$ for cases (i) and (ii), are obtained from the following relations:

$$\phi_{pa} = \left(\frac{2\pi x_{pa} f_a}{v_{ps}}\right), \quad \phi_{pm} = \left(\frac{2\pi x_{pm} f_m}{v_{ps}}\right), \tag{5}$$

where $x_{pa}$ and $x_{pm}$ are the position of the negative resistivity peaks at *p*-side in IMPATT and MITATT modes, respectively, and $f_a$ and $f_m$ are the corresponding frequencies. Likewise for *n*-side

$$\phi_{na} = \left(\frac{2\pi x_{na} f_a}{v_{ns}}\right), \quad \phi_{nm} = \left(\frac{2\pi x_{nm} f_m}{v_{ns}}\right), \tag{6}$$

where $x_{na}$ and $x_{nm}$ are the position of the negative resistivity peaks at *n*-side in IMPATT and MITATT modes, respectively. If $\phi_{pt}$ and $\phi_{nt}$ are the transit time phase delays, then the maximum power condition is given by $\phi_{pa} + \phi_{pt} = \phi_{na} + \phi_{nt} = \pi$. The shifts of ATT phase delays (in MITATT device) due to the effect of tunneling are determined from the following relations:

$$\delta_p = \phi_{pm} - \phi_{pa} \quad \text{on} p - \text{side}, \tag{7}$$

$$\delta_n = \phi_{nm} - \phi_{na} \quad \text{on} n - \text{side}. \tag{8}$$

The overall ATT phase delay shift is given by,

$$\delta = \frac{\delta_p + |\delta_n|}{2}. \tag{9}$$

## 5 Characteristics

The design parameters of the DD diodes are tabulated in Table 1. The junction diameter of the diodes is chosen to be $D_j = 35$ μm for 94 GHz operation [5].

The variations of avalanche and tunneling generation rates with frequency in the Si, InP, GaAs and SiC diodes are shown in Fig. 2. Rise of tunneling generation with field is found to be maximum GaAs diode and minimum in SiC diode; thus, the effect of tunneling on the performance of the sources will be accordingly. Also, SiC diode is found to be much higher field device as compared to others; it is obvious due to its wider bandgap.

Spatial variations of both avalanche and tunneling generation rates in the diodes are shown in Fig. 3. Internal distribution of avalanche and tunneling phenomena can be clearly understood from these plots and also Fig. 3 provides better insight to the comparison of avalanche and tunneling generation rates in the diodes than the Fig. 2. Ratio of peak tunneling generation rate and peak avalanche generation rates are listed in Table 2; which is also minimum for SiC diode. Thus, SiC diode must be least affected by the tunneling phenomena.

**Table 1** Design parameters

| Base material | $W_n$ (μm) | $W_p$ (μm) | $N_D$ ($\times 10^{23}$ $m^{-3}$) | $N_D$ ($\times 10^{23}$ $m^{-3}$) | $N_{n+}$, $N_{p+}$ ($\times 10^{26}$ $m^{-3}$) | $J_0$ ($\times 10^8$ A $m^{-2}$) |
|---|---|---|---|---|---|---|
| Si | 0.3900 | 0.3800 | 1.200 | 1.250 | 1.0 | 3.4 |
| InP | 0.3500 | 0.3520 | 1.600 | 1.600 | 1.0 | 1.4 |
| GaAs | 0.3200 | 0.3200 | 1.600 | 1.600 | 1.0 | 6.0 |
| 4H-SiC | 0.5500 | 0.5500 | 3.500 | 3.500 | 1.0 | 5.0 |

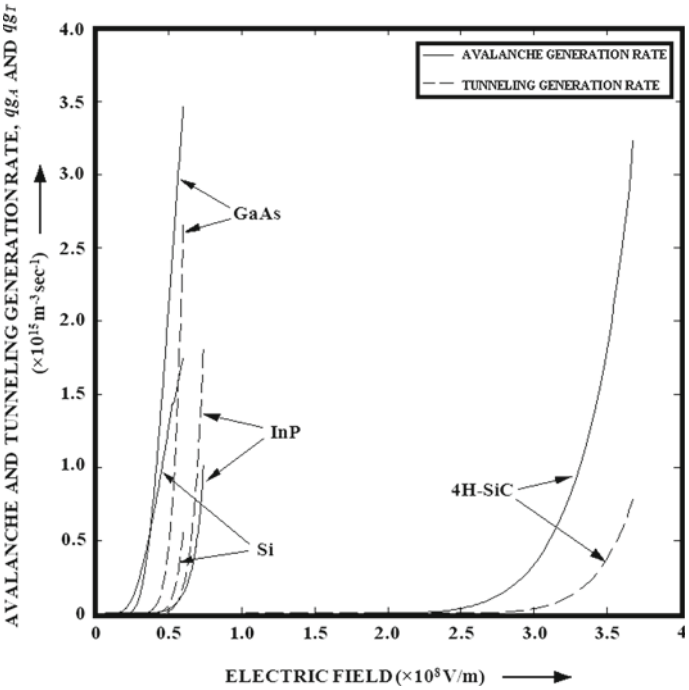


**Fig. 2** Avalanche and tunneling generation rates versus electric field

## *5.1 Effect of Tunneling*

Effects of tunneling on the static properties of the diodes are found to very nominal. However, those effects are found to be significant on the high frequency properties. A comparative study is presented in Table 3. Admittance characteristics and negative resistivity profiles of the diodes in both IMPATT and MITATT modes are shown in Figs. 4, 5, 6 and 7. It is observed that the high frequency performance of InP diode is significantly affected by tunneling; and the least affected diode is SiC.

## *5.2 ATT Phase Delay Shift Due to Tunneling*

Electron tunneling peak is generally attained near the *p*–*n* junction, while the hole tunneling generation peak is slightly shifted at the *p*-side. As a result of that the shift of negative resistivity profiles are observed to be having more right shift at *p*-side than the *n*-side. The procedure described in Sect. 4 is used to calculate the ATT phase

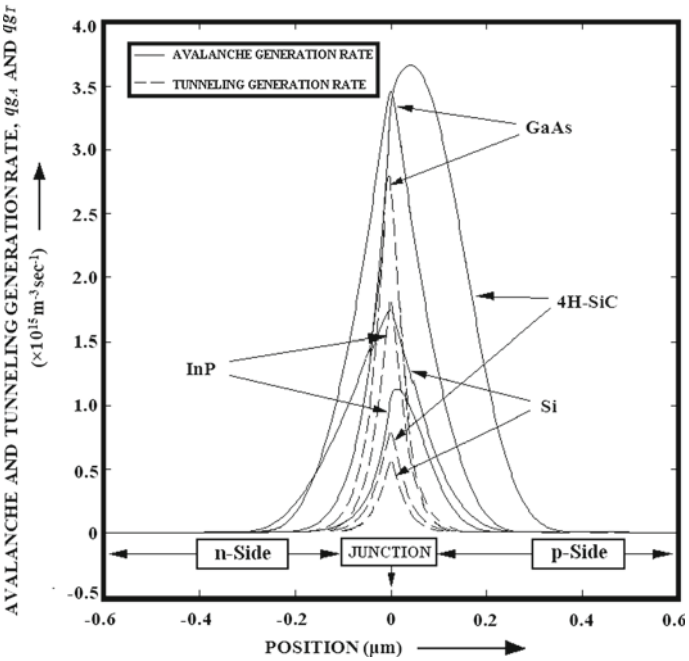


**Fig. 3** Spatial variations of avalanche and tunneling generation rates

**Table 2** Ratio of the peak tunneling generation rate to the maximum avalanche generation rate of the diodes

| Base material | $E_g$ (eV) | $m^*$ (Kg) | $f_d$ (GHz) | $g_{Tpeak}$ ($\times 10^{15}$ m$^{-3}$ s$^{-1}$) | ($g_{Tpeak}/g_{Apeak}$) |
|---|---|---|---|---|---|
| Si | 1.12 | 0.137 $m_0$ | 95 | 0.5529 | 0.31 |
| InP | 1.35 | 0.093 $m_0$ | 94 | 1.8019 | 1.59 |
| GaAs | 1.43 | 0.037 $m_0$ | 96 | 2.6568 | 0.76 |
| 4H-SiC | 3.23 | 0.390 $m_0$ | 94 | 0.7822 | 0.21 |

*Rest mass of an electron, $m_0 = 9.11 \times 10^{-31}$ kg

delay shift in the diodes due to tunneling. Results indicate the same observation which was stated in the earlier section, i.e., the ATT phase delay is significantly shifted in InP diode due to the highest level of tunneling, whereas said shift is minimum in SiC diode (Table 4 and Fig. 8).

**Table 3** Static and high frequency parameters

| Parameter | Si flat-DDR | | InP flat-DDR | | GaAs flat-DDR | | 4H-SiC flat-DDR | |
|---|---|---|---|---|---|---|---|---|
| | IMPATT | MITATT | IMPATT | MITATT | IMPATT | MITATT | IMPATT | IMPATT |
| $J_0$ ($\times 10^8$ A m$^{-2}$) | 3.4 | 3.4 | 1.4 | 1.4 | 6.0 | 6.0 | 5.0 | 5.0 |
| $\xi_m$ ($\times 10^7$ V m$^{-1}$) | 6.0125 | 5.9404 | 6.7499 | 6.1762 | 6.0192 | 5.8747 | 36.1247 | 35.5720 |
| $V_B$ (V) | 24.25 | 23.64 | 28.82 | 26.71 | 22.88 | 22.03 | 212.41 | 210.35 |
| $\eta$ (%) | 10.62 | 10.14 | 15.90 | 14.34 | 9.89 | 9.24 | 16.40 | 16.27 |
| $f_p$ (GHz) | 95 | 117 | 94 | 132 | 96 | 123 | 94 | 103 |
| $G_P$ ($\times 10^7$ S m$^{-2}$) | −4.3419 | −4.1676 | −8.2456 | −7.7174 | −6.0287 | −5.6971 | −6.2250 | −6.0687 |
| $B_P$ ($\times 10^7$ S m$^{-2}$) | 6.6244 | 7.7904 | 6.8436 | 7.8599 | 8.1159 | 10.1450 | 12.7510 | 13.7700 |
| $Q_P = (-B_P/G_P)$ | 1.53 | 1.86 | 0.83 | 1.19 | 1.35 | 1.78 | 2.05 | 2.27 |
| $Z_R$ ($\times 10^{-8}$ Ω m$^2$) | −0.6921 | −0.5340 | −0.7181 | −0.6360 | −0.5898 | −0.4208 | −0.3091 | −0.2680 |
| $P_{RF}$ (W) | 0.3192 | 0.2911 | 0.8563 | 0.6882 | 0.3946 | 0.3456 | 35.1070 | 33.5653 |

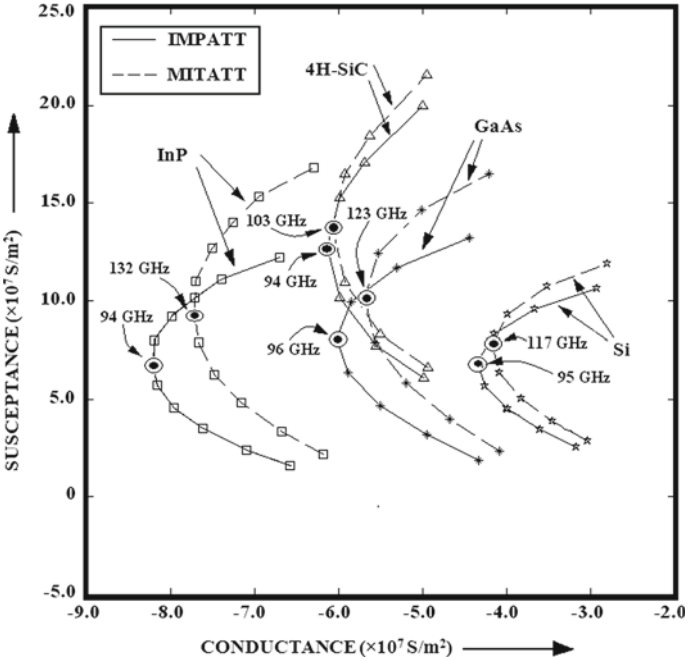


**Fig. 4** Admittance characteristics

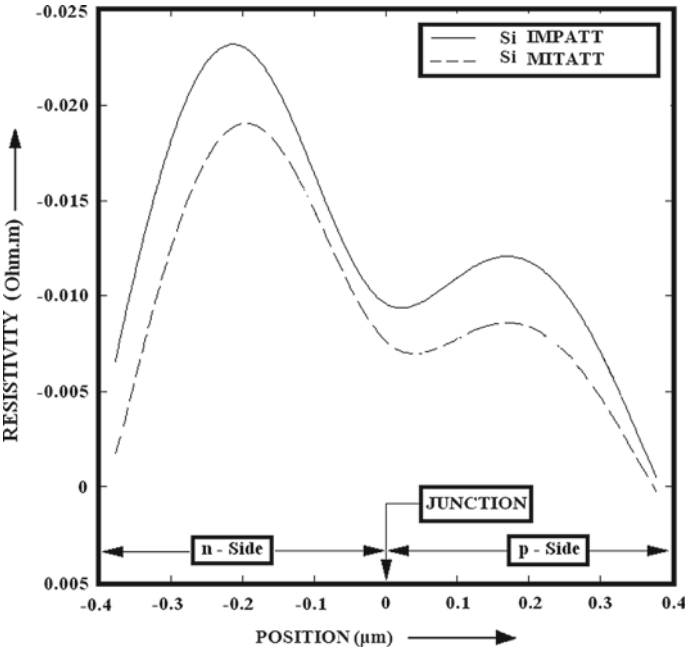


**Fig. 5** Negative resistivity profiles Si DD diode

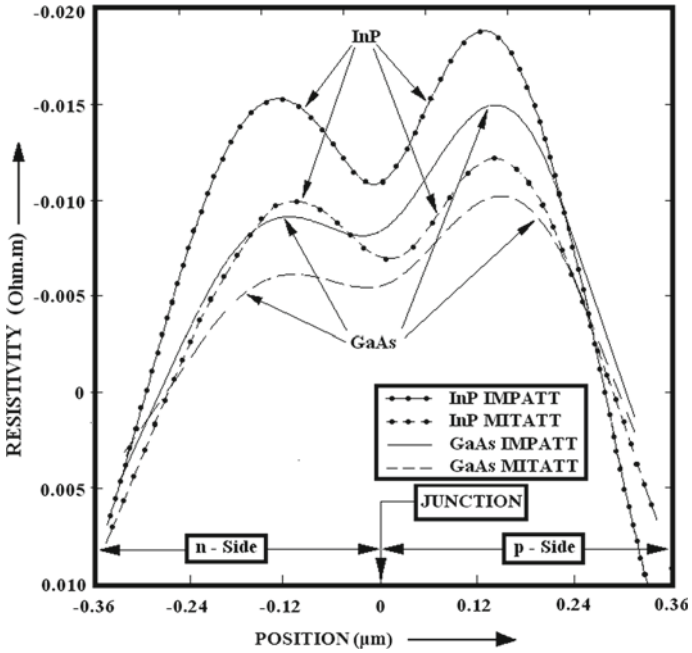


**Fig. 6** Negative resistivity profiles of InP and GaAs DD diodes

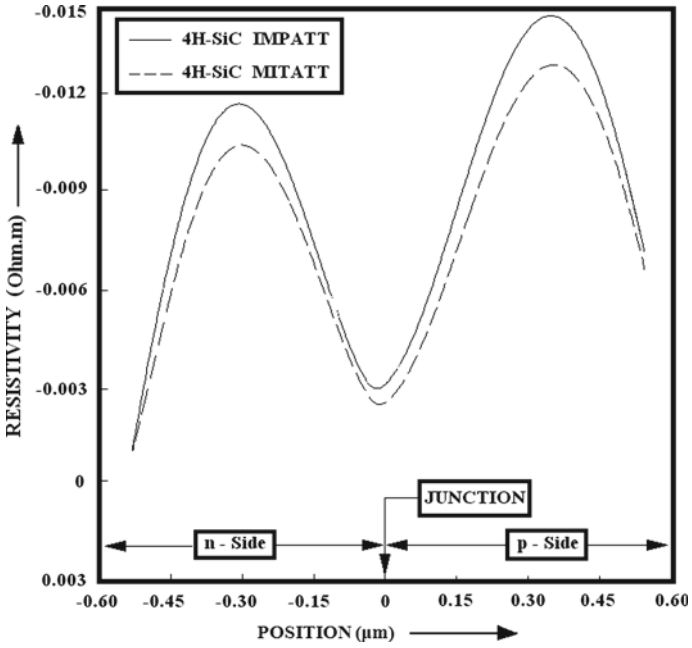


**Fig. 7** Negative resistivity profile of 4H-SiC DD diode

**Table 4** ATT phase delay shifts due to tunneling

| Base material | $\delta$ ($\times 10^{-3}$ $\pi$ rad.) |
|---|---|
| Si | 130.2 |
| InP | 257.6 |
| GaAs | 169.4 |
| 4H-SiC | 41.7 |

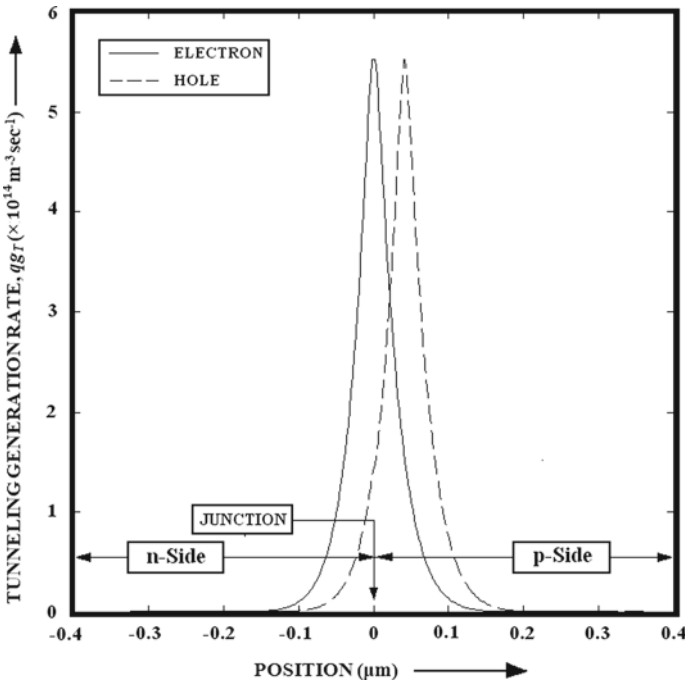


**Fig. 8** Spatial distribution of electro and hole tunneling generation rates in Si DD diodes

## 6 Summary

This chapter describes the procedure of estimating the degree of deterioration of the performance of IMPATT sources due to interband tunneling effect. An in-house simulation code developed by the authors based on SCQDD model has been used to study the above-mentioned effect on the IMPATTs at 94 GHz. The comparative study of Si, InP, GaAs and 4H-SiC ATT sources is presented. Tunneling induced ATT phase delays in the oscillators are estimated and the degree of deterioration of the oscillators are interpreted via the estimated ATT phase delay at sub-terahertz frequency bands. It is observed that the sub-terahertz performance of SiC diode is least affected due to the tunneling as compared to the other diodes. Thus, the choice

of wider bandgap material for fabricating IMPATT diodes should be prefer in order to eliminate the tunneling induced deterioration of high frequency performance of the oscillator.

## References


1. Midford TA, Bernick RL (1979) Millimeter wave CW IMPATT diodes and oscillators. IEEE Trans Microw Theory Tech 27:483–492
2. Gray WW, Kikushima L, Morentc NP, Wagner RJ (1969) Applying IMPATT power sources to modern microwave systems. IEEE J Solid-State Circ 4:409–413
3. Chang Y, Hellum JM, Paul JA, Weller KP (1977) Millimeter-wave IMPATT sources for communication applications. IEEE MTT-S Int Microw Symp Dig 216–219
4. Banerjee JP, Luy JR (1991) Comparison of theoretical and experimental 60 GHz silicon Impatt diode performance. Electron Lett 27(12):1049–1050
5. Luy JF, Casel A, Behr W, Kasper E (1987) A 90-GHz double-drift IMPATT diode made with Si MBE. IEEE Trans Electron Devices 34:1084–1089
6. Dalle C, Rolland P, Lieti G (1990) Flat doping profile double-drift silicon IMPATT for reliable CW high power high-efficiency generation in the 94-GHz window. IEEE Trans Electron Devices 37:227–236
7. Wollitzer M, Buchler J, Schafflr F, Luy JF (1996) D-band Si-IMPATT diodes with 300 mW CW output power at 140 GHz. Electron Lett 32:122–123
8. Eisele H (1989) Selective etching technology for 94 GHz, GaAs IMPATT diodes on diamond heat sinks. Solid State Electron 32(3):253–257
9. Eisele H, Hadded GI (1992) GaAs single-drift flat profile IMPATT diodes for CW operation at D band. Electron Lett 28(23):2176–2177
10. Eisele H, Chen CC, Munns GO, Haddad GI (1996) The potential of InP IMPATT diodes as high-power millimetre-wave sources: first experimental results. IEEE MTT-S Int Microw Symp Digest 2:529–532
11. Yuan L, James A, Cooper JA, Melloch MR, Webb KJ (2001) Experimental demonstration of a silicon carbide IMPATT oscillator. IEEE Electron Device Lett 22:266–268
12. Vassilevski KV, Zorenko AV, Zekentes K, Tsagaraki K, Bano E, Banc C, Lebedev A (2001) 4H-SiC IMPATT diode fabrication and testing. Technical digest of international conference on SiC and related materials. Tsukuba, Japan, pp 713–714
13. Acharyya A, Banerjee JP (2014) Prospects of IMPATT devices based on wide bandgap semiconductors as potential terahertz sources. Appl Nanosci 4:1–14
14. Acharyya A, Banerjee JP (2013) Potentiality of IMPATT devices as terahertz source: an avalanche response time based approach to determine the upper cut-off frequency limits. IETE J Res 59(2):118–127
15. Mukherjee M, Mazumder N, Roy SK (2009) Prospects of 4H-SiC double drift region IMPATT device as a photo-sensitive high-power source at 0.7 Thz frequency regime. Act Passive Electron Compon 2009:1–9
16. Acharyya A, Goswami J, Banerjee S, Banerjee JP (2015) Quantum corrected drift-diffusion model for terahertz IMPATTs based on different semiconductors. J Comput Electron 14:309–320
17. Acharyya A, Mukherjee M, Banerjee JP (2015) Effects of tunnelling current on mm-wave IMPATT devices. Int J Electron 102(9):1429–1456
18. Elta ME (1978) The effect of mixed tunneling and avalanche breakdown on microwave transit-time diodes. Ph.D. dissertation, electron physics Lab., University of Michigan, Annals Arbor, MI, Tech. Rep
19. Kane EO (1961) Theory of tunneling. J Appl Phys 32:83–91

20. Dash GN, Pati SP (1992) A generalized simulation method for MITATT-mode operation and studies on the influence of tunnel current on IMPATT properties. Semicond Sci Technol 7:222–230
21. Sze SM, Ryder RM (1971) Microwave avalanche diodes. Proceeding of IEEE, special issue on microwave semiconductor devices 59:1140–1154
22. Gummel HK, Blue JL (1967) A small-signal theory of avalanche noise in IMPATT diodes. IEEE Trans Electron Devices 14(9):569–580
23. Grant WN (1973) Electron and hole ionization rates in epitaxial silicon at high electric fields. Solid State Electron 16:1189–1203
24. Ito M, Kagawa S, Kaneda T, Yamaoka T (1978) Ionization rates for electrons and holes in GaAs. J Appl Phys 49:4607
25. Kao CW, Crowell CR (1980) Impact ionization by electrons and holes in InP. Solid State Electron 23:881–891
26. Umebu I, Chowdhury ANMM, Robson PN (1980) Ionization coefficients measured in abrupt InP junction. Appl Phys Lett 36:302–303
27. Konstantinov AO, Wahab Q, Nordell N, Lindefelt U (1997) Ionization rates and critical fields in 4H-silicon carbide. Appl Phys Lett 71:90–92
28. Canali C, Ottaviani G, Quaranta AA (1971) Drift velocity of electrons and holes and associated anisotropic effects in silicon. J Phys Chem Solids 32:1707–1720
29. Kramer B, Micrea A (1975) Determination of saturated electron velocity in GaAs. Appl Phys Lett 26:623–624
30. Vassilevski KV, Zekentes K, Zorenko AV, Romanov LP (2000) Experimental determination of electron drift velocity in 4H-SiC $p^+$–$n$–$n^+$ avalanche diodes. IEEE Electron Device Lett 21:485–487
31. Vassilevski KV, Zekentes K, Zorenko AV, Romanov LP, "Electronic archive: new semiconductor materials, characteristics and properties." Available from: http://www.ioffe.ru/SVA/NSM/Semicond/index.html (Last accessed on: May 2021)
32. Zeghbroeck BV (2011) Principles of semiconductor devices. Colorado Press, USA
33. Ghosh M, Ghosh S, Acharyya A (2017) Self-consistent quantum drift-diffusion model for multiple quantum well IMPATT diodes. J Comput Electron 15(4):1370–1387
34. Acharyya A, Chatterjee S, Goswami J, Banerjee S, Banerjee JP (2014) Quantum drift-diffusion model for IMPATT devices. J Comput Electron 13:739–752
35. Acharyya A, Ghosh S (2017) Dark current reduction in nano-avalanche photodiodes by incorporating multiple quantum barriers. Int J Electron 104(12):1957–1973
36. Dash GN, Pati SP (1991) Small-signal computer simulation of IMPATT diodes including carrier diffusion. Semicond Sci Technol 6:348–355
37. Acharyya A, Banerjee S, Banerjee JP (2013) Influence of skin effect on the series resistance of millimeter-wave of IMPATT devices. J Comput Electron 12:511–525
38. Acharyya A, Banerjee S, Banerjee JP (2013) A proposed simulation technique to study the series resistance and related millimeter-wave properties of Ka-Band Si IMPATTs from the electric field snap-shots. Int J Microw Wirel Technol 5(1):91–100

# Search of a Suitable Heterojunction Material System for Terahertz Wave Generation


**Aritra Acharyya**

**Abstract** In this chapter, a comparative study is carried out to find out a suitable heterojunction material system for generating sub-terahertz and terahertz (THz) power. Avalanche transit time (ATT) sources based on GaAs~$Al_xGa_{1-x}As$, Si~3C-SiC and GaN~$Al_xGa_{1-x}N$ heterojunctions are simulated, and their performances are compared at a wide range of frequency spectrum. Out of those potential heterostructures, GaN~$Al_xGa_{1-x}N$ is found to be most suitable one for realizing THz ATT oscillators.

**Keywords** ATT · AlGaAs · AlGaN · Heterojunction · SiC · Terahertz

## 1 Introduction

The ATT sources, especially impact avalanche ATT (IMPATT) oscillators, are generally noisy sources. Avalanche multiplication is the predominant mechanism of generating both signal and noise. However, by using heterostructures, the noise level of IMPATT sources can be significantly reduced [1, 2]. Also, the use of heterojunction reduces the tunneling-induced deterioration of the high-frequency performance of ATT sources [3].

On the other hand, the dimension of the ATT diodes shrinks exponentially with the increase of frequency of operation [4]. At THz frequency bands, dimension of the device shrinks to a few hundred nanometers [5, 6]. Due to the significant downscaling of the device dimensions, the breakdown voltage, magnitude of negative resistance, power output, etc., of the source also fall rapidly with the increase of operating frequency [7]. At the THz regime, the power output of double-drift (DD) IMPATT source becomes a few tens of milliwatts (mW) [8]. However, the rate of reduction of noise power per bandwidth (noise spectral density) in IMPATT diodes with operating frequency is not as sharp as it is for the rate of reduction in signal power. Therefore, the signal-to-noise ratio (SNR) becomes very small at

A. Acharyya (✉)
Department of Electronics and Communication Engineering, Cooch Behar Government Engineering College, West Bengal, Cooch Behar 736170, India



A. Acharyya et al. (eds.), *Generation, Detection and Processing of Terahertz Signals*, Lecture Notes in Electrical Engineering 794,
https://doi.org/10.1007/978-981-16-4947-9_15

THz frequencies and IMPATT sources effectively become a valueless random noise source. Thus, in order to realize a low noise and efficient THz IMPATT source, the use of heterojunction is indispensible.

In this chapter, a comparative study is carried out to find out a suitable heterojunction material system for generating sub-THz and THz power. Avalanche transit time (ATT) sources based on GaAs~$Al_xGa_{1-x}As$, Si~3C-SiC and GaN~$Al_xGa_{1-x}N$ heterojunctions are simulated, and their performances are compared at a wide range of frequency spectrum. Out of those potential heterostructures, GaN~$Al_xGa_{1-x}N$ is found to be most suitable one for realizing THz ATT oscillators.

## 2 GaAs~$Al_xGa_{1-x}As$ Heterojunction IMPATTs

The group III–V compound semiconductor, GaAs, is the second choice material (after Si) for fabricating IMPATT sources, since the 1970s [9–18]. However, due to the limitations in the carrier transport in this material, GaAs IMPATTs cannot operate efficiently beyond 200 GHz. In order to reduce the noise level, two types of anisotype heterojunction GaAs~$Al_xGa_{1-x}As$ DD IMPATTs can be realized as shown in Fig. 1. Here, $Al_xGa_{1-x}As$ is the wider bandgap material; therefore, the following combinations are possible if one uses four values of Al mole fraction $x = 0, 0.1, 0.2$ and 0.3:

(i) $n$-GaAs~$p$-GaAs (HMDD) → for $x = 0$,
(ii) $N$-$Al_{0.1}Ga_{0.9}As$~$p$-GaAs (HTDD1) → for $x = 0.1$,
(iii) $P$-$Al_{0.1}Ga_{0.9}As$~$n$-GaAs (HTDD2) → for $x = 0.1$,
(iv) $N$-$Al_{0.2}Ga_{0.8}As$~$p$-GaAs (HTDD3) → for $x = 0.2$,
(v) $P$-$Al_{0.2}Ga_{0.8}As$~$n$-GaAs (HTDD4) → for $x = 0.2$,
(vi) $N$-$Al_{0.3}Ga_{0.7}As$~$p$-GaAs (HTDD5) → for $x = 0.3$,

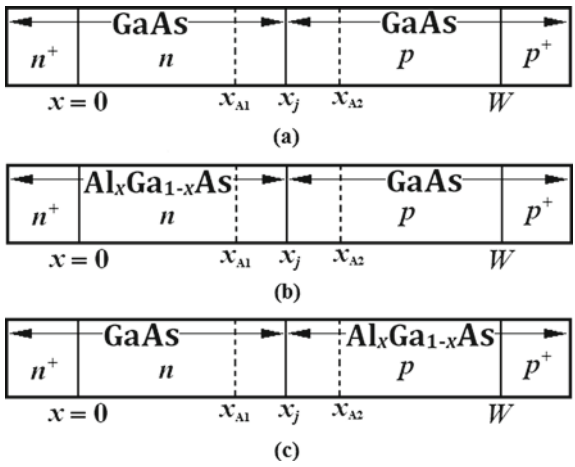


**Fig. 1** Types of homo- and heterojunction DD diodes based on GaAs~$Al_xGa_{1-x}As$ system

(vii) $P$-$Al_{0.3}Ga_{0.7}As$~$n$-GaAs (HTDD6) → for $x = 0.3$.

The large-signal characteristics of 60 GHz DD IMPATTs having above-mentioned structures are presented in this section. Admittance characteristics, power and efficiency versus RF voltage and mole fraction plots are shown in Figs. 2, 3 and 4. The results of small-signal noise analysis are shown in Figs. 5 and 6. Results purely

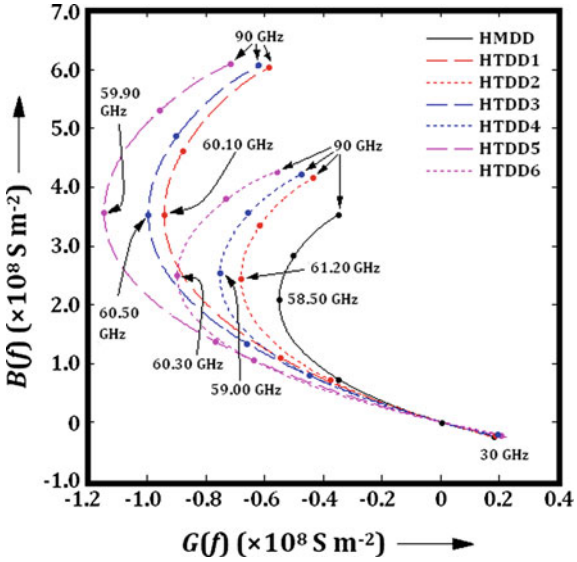


**Fig. 2** Admittance characteristics

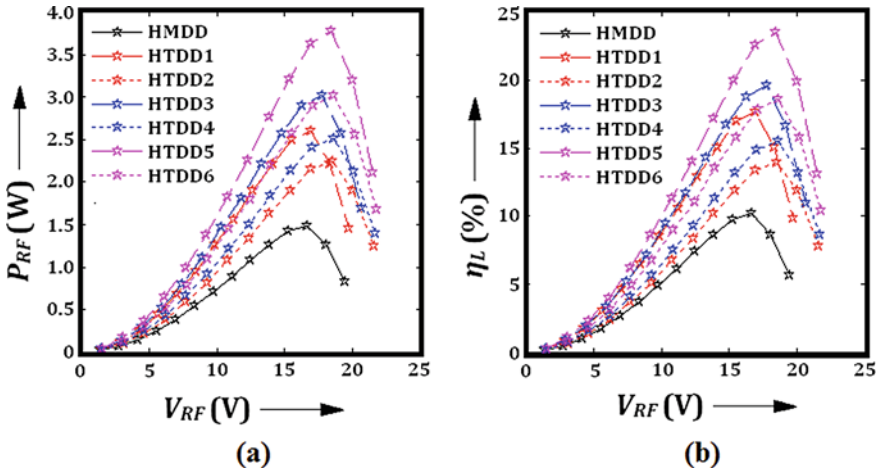


**Fig. 3** **a** Power and **b** efficiency versus RF voltage plots

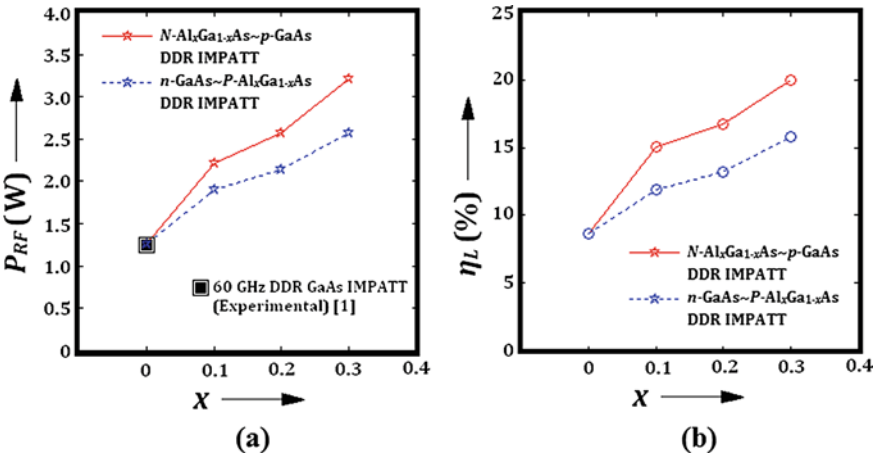


**Fig. 4** **a** Power and **b** efficiency versus Al mole fraction plots

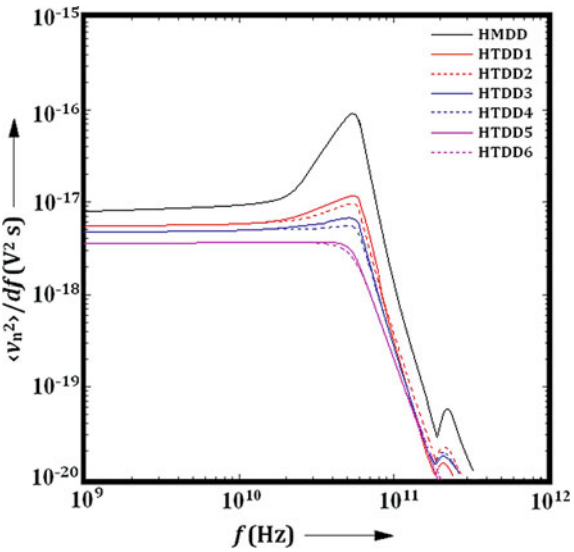


**Fig. 5** Noise spectral density versus frequency plots

indicate that heterojunction IMPATTs are more efficient and less noisy than the homojunction counterpart. The best heterostructure device among these is found to be $N$-$Al_{0.3}Ga_{0.7}As$~$p$-GaAs DD IMPATT.

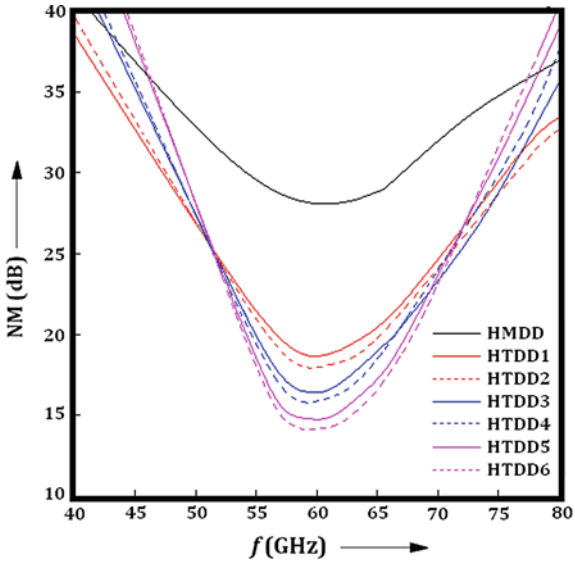


**Fig. 6** Noise measure versus frequency plots

## 3 Si~3C-SiC Heterojunction IMPATTs

Another very promising heterostructure is made of group IV–IV compound 3C-SiC and most popular semiconductor material Si (group IV). Two possible types of these anisotype heterojunction DD IMPATTs are based on *N*-3C-SiC~*p*-Si and *P*-3C-SiC~*n*-Si; performance of these two structure base IMPATTs is compared with Si and 3C-SiC-based homojunction DD IMPATTs at 94, 140, 220, 300 and 500 GHz (Fig. 7). The results of large-signal and noise analysis are presented in the form of graphs and plots in Figs. 8, 9, 10, 11, 12, 13, 14, 15, 16, 17 and 18. The *P*-3C-SiC~*n*-Si-based DD IMPATT oscillator is found to be the best one among all in terms of both efficiency and noise performance.

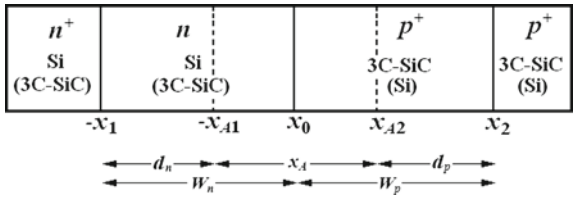


**Fig. 7** Model of Si~3C-SiC heterojunction DD diodes

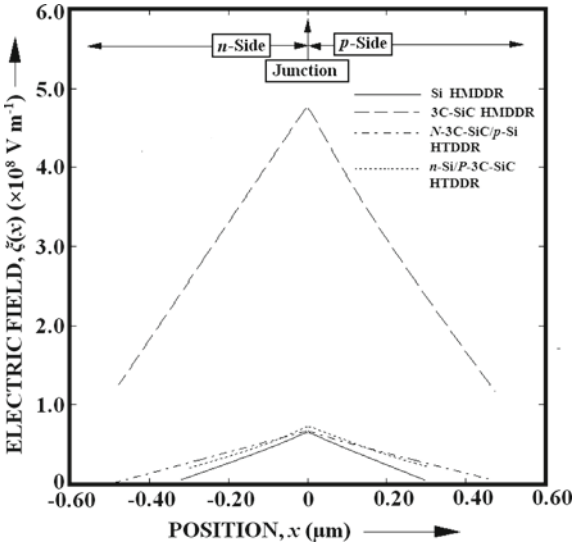


**Fig. 8** Electric field profiles of 94 GHz DD IMPATTs

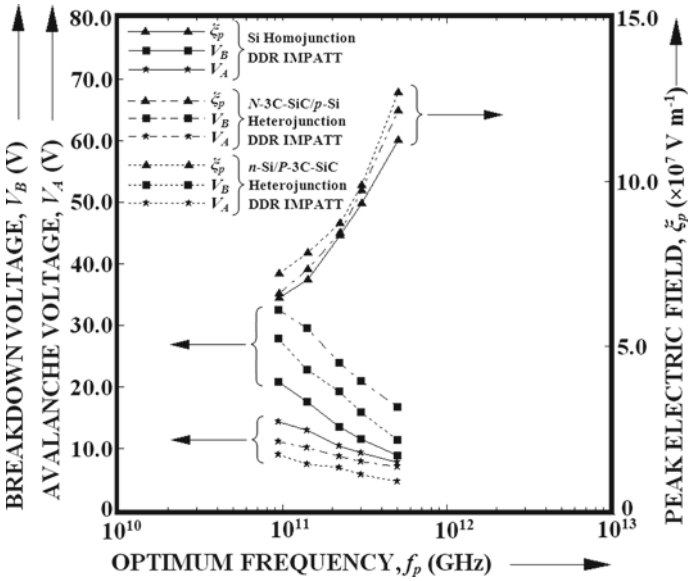


**Fig. 9** Breakdown voltage, avalanche voltage and peak electric field versus frequency plots of 94 GHz DD IMPATTs

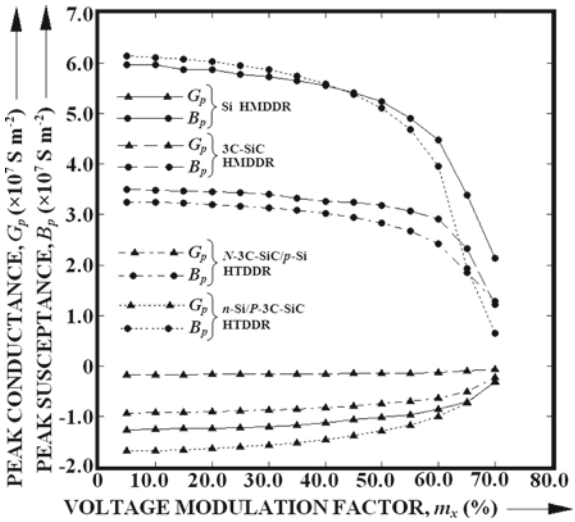


**Fig. 10** Peak negative conductance and susceptance versus voltage modulation factor plots of 94 GHz DD IMPATTs

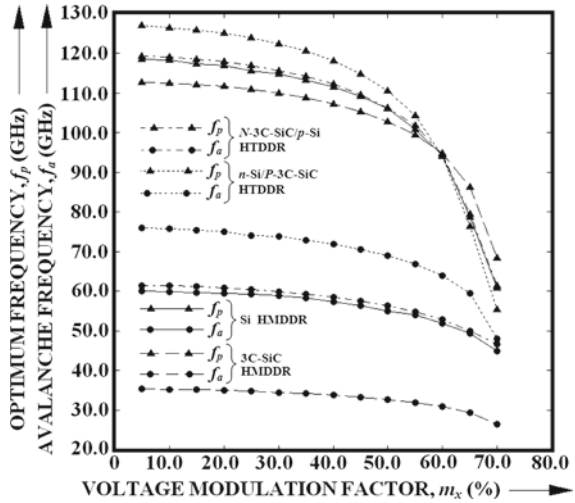


**Fig. 11** Avalanche resonance frequency and optimum frequency versus voltage modulation factor plots of 94 GHz DD IMPATTs

## 4 GaN~$Al_xGa_{1-x}N$ Heterojunction IMPATTs

The GaN is the highest potential material in terms of THz capabilities. Two anisotype heterostructure DD IMPATTs such as *P*-$Al_{0.4}Ga_{0.6}$ N~*n*-GaN (HTDD1) and *N*-$Al_{0.4}Ga_{0.6}$ N~*p*-GaN (HTDD2) are studies, and their performances are compared with GaN and $Al_{0.4}Ga_{0.6}$ N homojunction DD IMPATTs at 1.0 THz (Fig. 19). The static, large-signal and noise analysis results are presented in Figs. 20, 21, 22, 23,

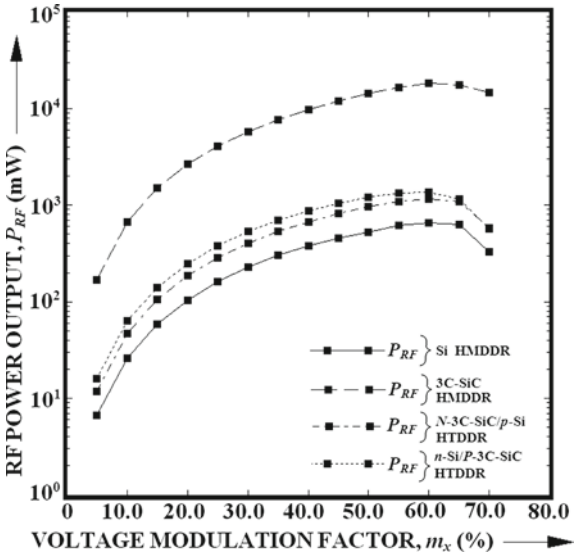


**Fig. 12** Power output versus voltage modulation factor plots of 94 GHz DD IMPATTs

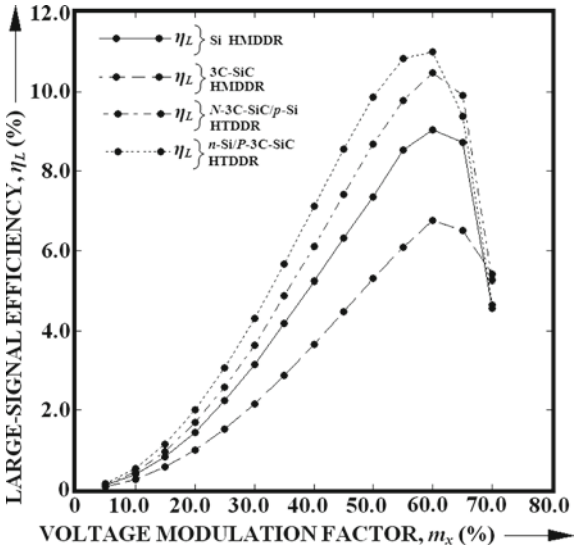


**Fig. 13** Efficiency versus voltage modulation factor plots of 94 GHz DD IMPATTs

24, 25 and 26. It is observed that the HTDD1, i.e., *P*-$Al_{0.4}Ga_{0.6}$ N~*n*-GaN-based DD IMPATT source, is the best heterostructure IMPATT among all in terms of highest efficiency, power output and lowest noise level.

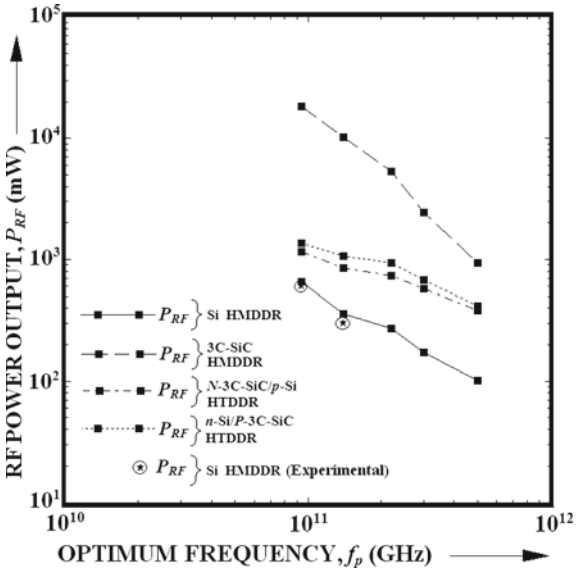


**Fig. 14** Power output versus frequency plots

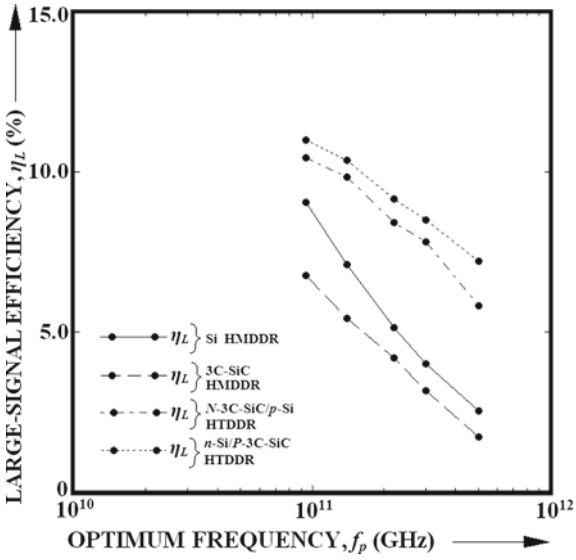


**Fig. 15** Efficiency versus frequency plots

## 5 Summary

In this chapter, a relative investigation is carried out to find out a suitable heterojunction material system for generating sufficient power at sub-THz and THz frequency bands. Avalanche transit time (ATT) sources based on GaAs~$Al_xGa_{1-x}As$, Si~3C-SiC and GaN~$Al_xGa_{1-x}N$ heterojunctions are simulated, and their performances are

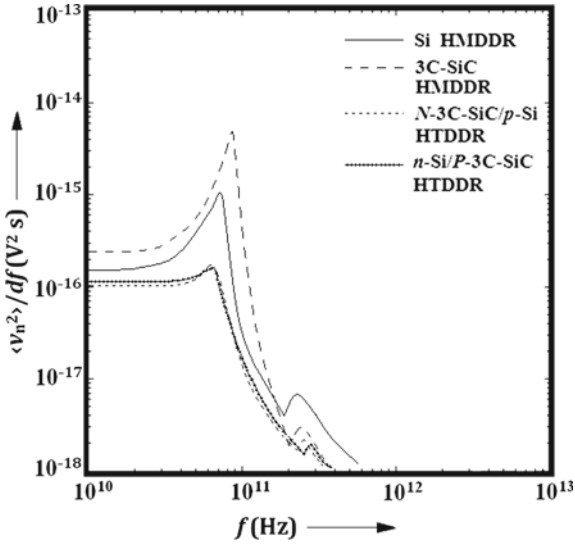


**Fig. 16** Noise spectral density versus frequency plots of 94 GHz DD IMPATTs

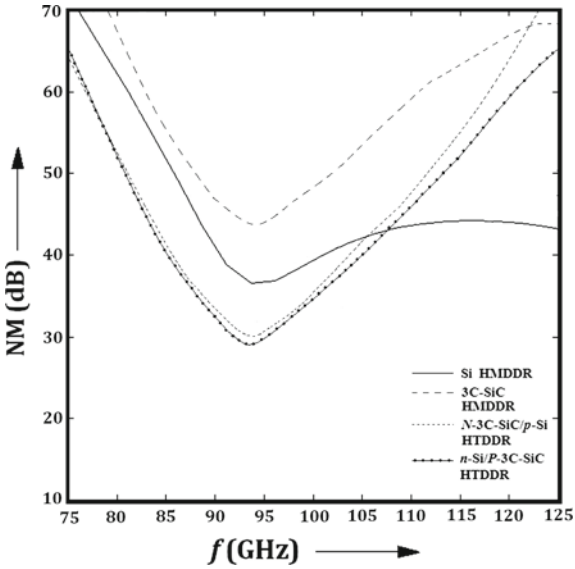


**Fig. 17** Noise measure versus frequency plots of 94 GHz DD IMPATTs

compared at a wide range of frequency spectrum. Out of those potential heterostructures, GaN~$Al_xGa_{1-x}N$ is found to be most suitable one for realizing THz ATT oscillators. Specifically, *N*-$Al_{0.4}Ga_{0.6}$ N~*p*-GaN material system is proved to be the best choice for fabricating sub-THz and THz DD IMPATT sources.

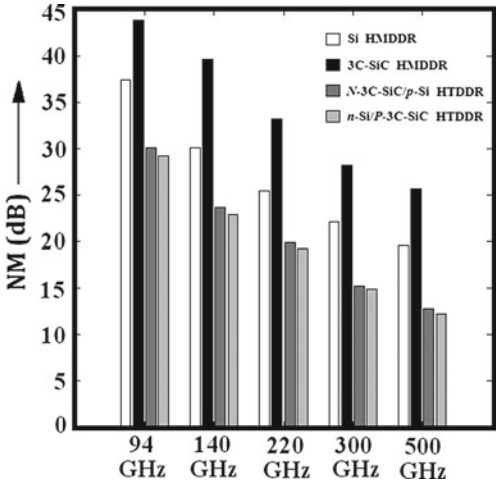


**Fig. 18** Bar graphs showing the improvement of noise measure due to the use of heterojunctions

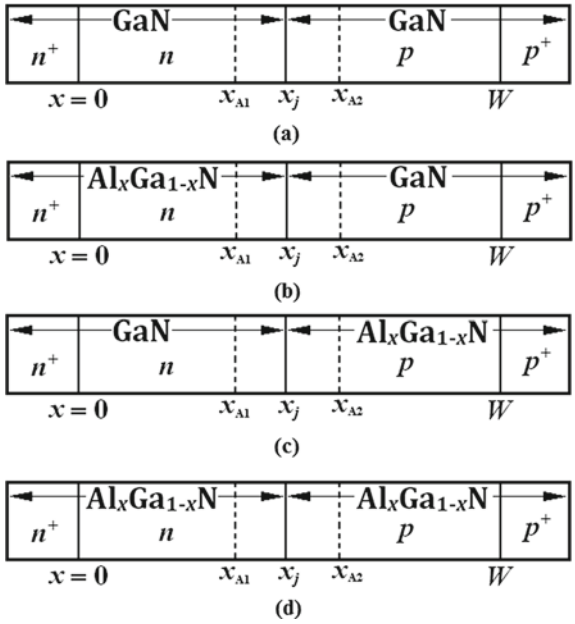


**Fig. 19** Types of homo- and heterojunction DD diodes based on GaN~$Al_xGa_{1-x}N$ system

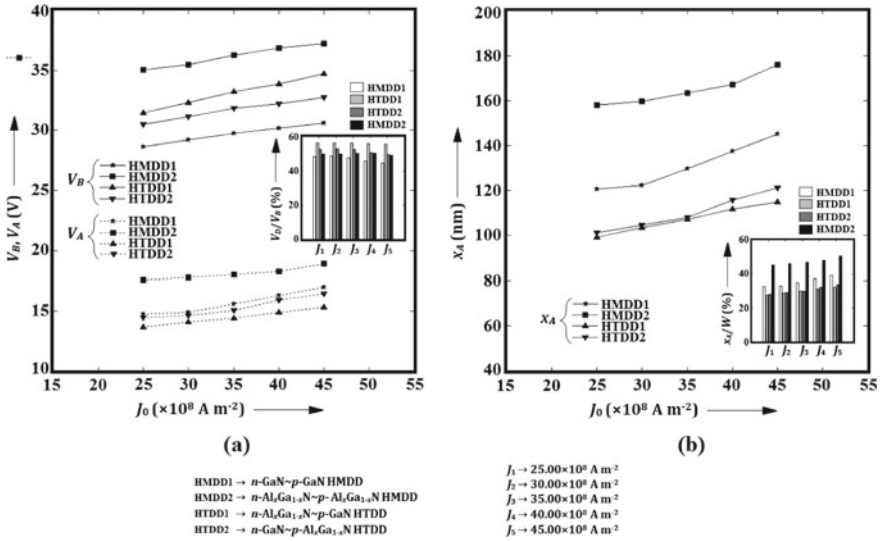


**Fig. 20** **a** Breakdown voltage and avalanche voltage and **b** avalanche width versus bias current density plots

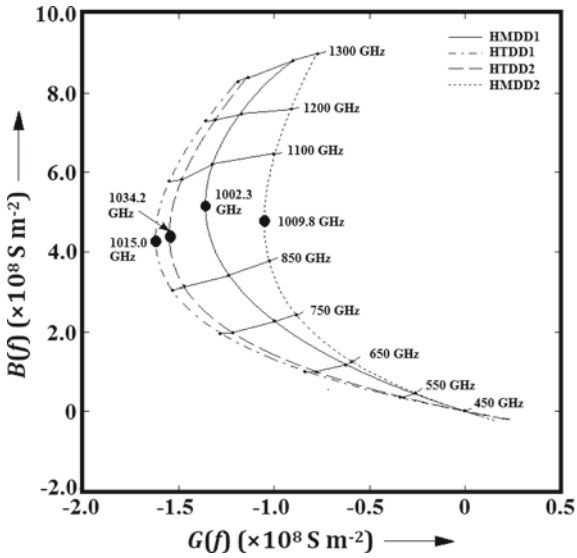


**Fig. 21** Admittance characteristics

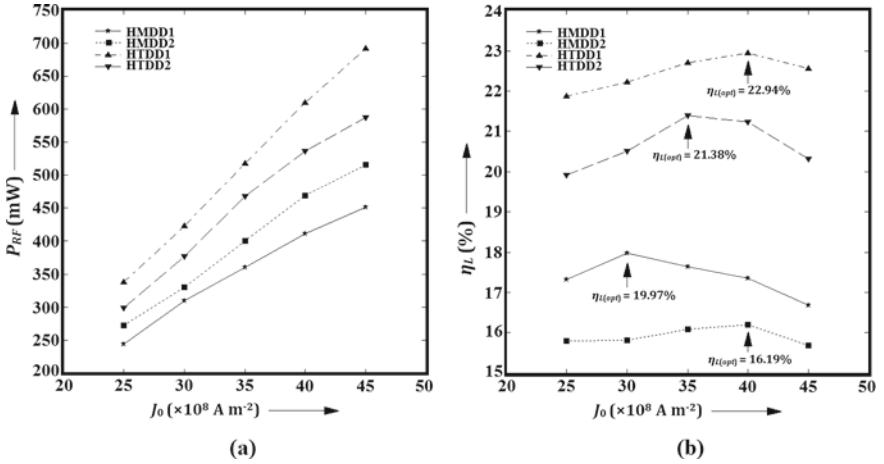


**Fig. 22** **a** Power output and **b** efficiency versus bias current density plots

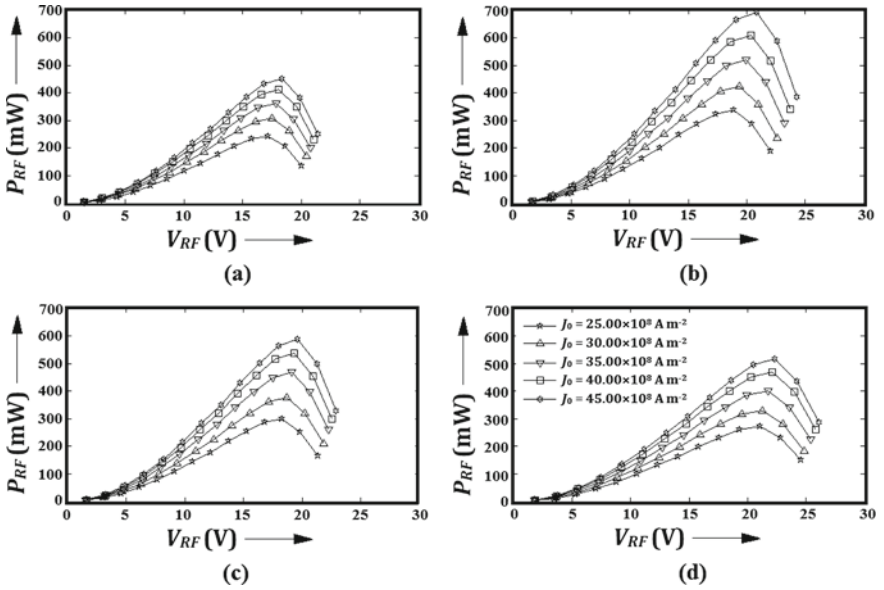


**Fig. 23** Power output versus RF voltage plots

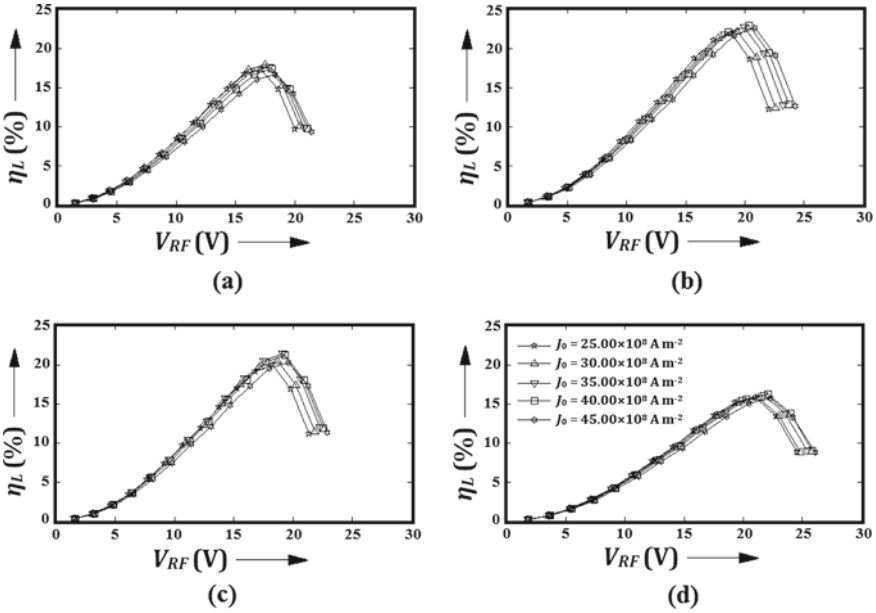


**Fig. 24** Efficiency versus RF voltage plots

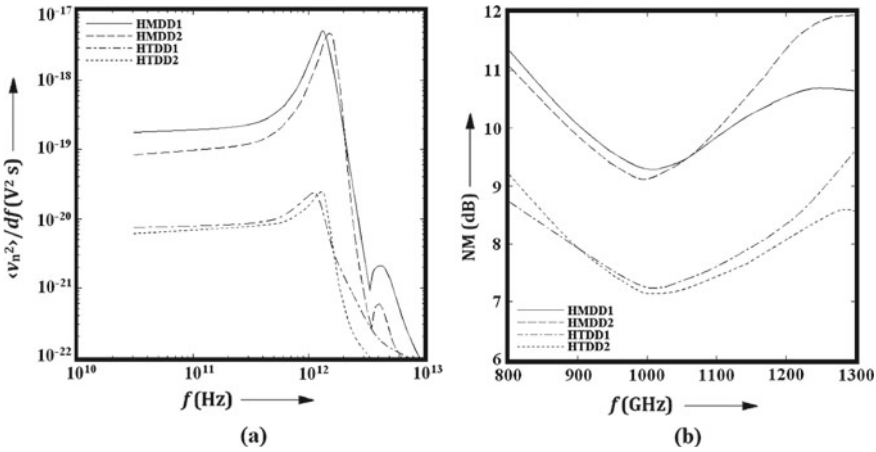


**Fig. 25** **a** Noise spectral density and **b** noise measure versus frequency plots

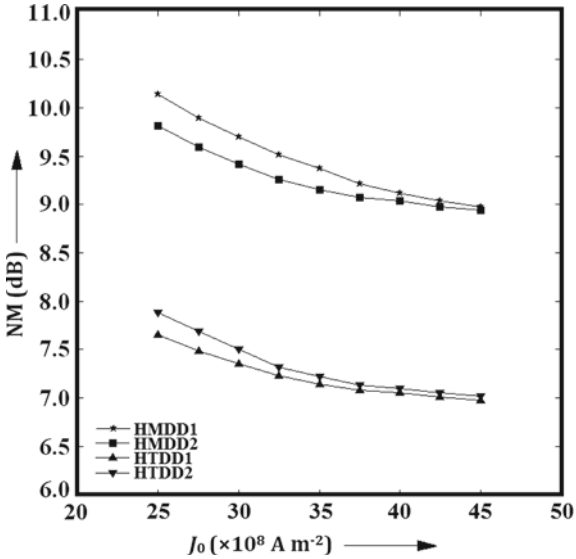


**Fig. 26** Noise measure versus bias current density plots

## References


1. Mishra JK, Panda AK, Dash GN (1997) An extremely low-noise heterojunction IMPATT. IEEE Trans Electron Dev 44(12):2143–2148
2. Banerjee S, Monojit M (2015) Heterojunction DDR THz IMPATT diodes based on $Al_xGa_{1-x}N$/GaN material system. J Semicond 36(6):064002-1-11
3. Banerjee S, Acharyya A, Banerjee JP (2013) Noise performance of heterojunction DDR MITATT devices based on $Si/Si_{1-x}Ge_x$ at Wband. Act Passive Electron Compon 2013(1):1–9
4. Sze SM (1981) Physics of semiconductor devices, 2nd edn. Wiley, New York
5. Acharyya A, Goswami J, Banerjee S, Banerjee JP (2015) Quantum corrected drift-diffusion model for terahertz IMPATTS based on different semiconductors. J Comput Electron 14(1):309–320
6. Acharyya A, Chatterjee S, Goswami J, Banerjee S, Banerjee JP (2014) Quantum drift-diffusion model for IMPATT devices. J Comput Electron 13(3):739–752
7. Acharyya A, Banerjee JP (2014) Prospects of IMPATT devices based on wide bandgap semiconductors as potential terahertz sources. Appl Nanosci 4:1–14
8. Acharyya A, Mallik A, Banerjee D, Ganguli S, Das A, Dasgupta S, Banerjee JP (2014) IMPATT devices based on group III-V compound semiconductors: prospects as potential terahertz radiators. HKIE Trans 21(3):135–147
9. Huang HC (1973) A modified GaAs IMPATT structure for high-efficiency operation. IEEE Trans on Electron Dev 20(5):482–486
10. Goldwasser RE, Rosztoczy FE (1974) High efficiency GaAs low-hig-low IMPATTs. Appl Phys Lett 25:92
11. Bozler CO, Donelly JP, Murphy RA, Laton RW, Sudhury RN, Lindley WT (1976) High efficiency ion implanted Lo-hi-lo GaAs IMPATT diodes. Appl Phys Lett 29:123
12. Eisele H (1989) Selective etching technology for 94 GHz, GaAs IMPATT diodes on diamond heat sinks. Solid State Electron 32(3):253–257
13. Eisele H (1990) GaAs W-band IMPATT diode for very low noise oscillations. Electron Lett 26(2):109–110
14. Eisele H, Hadded GI (1992) GaAs single-drift flat profile IMPATT diodes for CW operation at D band. Electron Lett 28(23):2176–2177

15. Kearney MJ, Couch NR, Stephens JS, Smith RS (1992) Low noise, high efficiency GaAs IMPATT diodes at 30 GHz. Electron Lett 28(8):706–708
16. Curow M (1994) Proposed GaAs IMPATT device structure for D-band applications. Electron Lett 30(19):1629–1631
17. Tschernitz M, Freyer J, Grothe H (1994) GaAs Read-type IMPATT diodes for D-band. Electron Lett 30(13):1070–1071
18. Tschernitz M, Freyer J (1995) 140 GHz GaAs double-Read IMPATT diodes. Electron Lett 31(7):582–583

# Applications of Si~3C-SiC Heterostructures in High-Frequency Electronics up to the Terahertz Spectrum


**Monisha Ghosh and Arindam Biswas**

**Abstract** Potentialities of semiconductor heterostructures based on Si~3C-SiC material system for realizing high-frequency electronic devices extended up to terahertz (THz) frequency spectrum are described in this chapter. Current mechanism of Si~3C-SiC heterojunctions has been discussed concisely. Applications of this heterostructure in different areas of electronics and optoelectronics like microelectromechanical systems (MEMS), energy conversion, photodetection, light emission, etc., have been discussed in this chapter. Lastly, the possibilities of realizing high power THz avalanche transit time oscillators based on Si~3C-SiC heterostructures have been discussed.

**Keywords** 3C-SiC · Heterojunction · Heterostructure · Si · THz

## 1 Introduction

A wide band gap material silicon carbide (SiC) performs significantly in high-power and high-temperature electronics applications due to its high thermal conductivity and high breakdown electrical field. SiC has similar crystal lattice structure as of silicon and diamond. Thus, SiC became a perfect semiconductor material between silicon and diamond. SiC is also considered as the only stable group IV–IV compound semiconductor, whereas no other combination of elements except C, Si, Ge, Sn exists in a defined lattice. The silicon atoms in the SiC crystal are surrounded by four carbon atoms in a tetrahedral arrangement or vice versa as shown in Fig. 1. The side of the tetrahedral is equal to the lattice constant *a*, which is approximately

M. Ghosh (✉)
Department of Electronics and Communications Engineering, Supreme Knowledge Foundation Group of Institution, 1, Khan Road, Mankundu, Hooghly, West Bengal 712139, India
e-mail: monisha.ghosh@skf.edu.in

A. Biswas
Centre for Organic Spin-tronics and Optoelectronics Devices (COSOD) and Mining Engineering Department, Kazi Nazrul University, Asansol, Burdwan, West Bengal 713340, India



A. Acharyya et al. (eds.), *Generation, Detection and Processing of Terahertz Signals*, Lecture Notes in Electrical Engineering 794,
https://doi.org/10.1007/978-981-16-4947-9_16

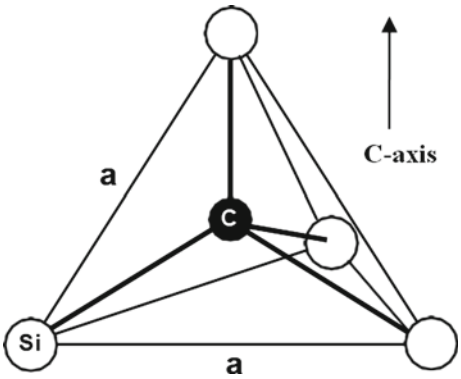


**Fig. 1** Tetrahedron covalent bond [2]

3.08 Å [1], and from geometrical considerations, the Si–C bond can then be calculated approximately to 1.89 Å. The Si–C bond is considered to be 88% covalent and 12% ionic, where Si is believed to be charged more positively [1]. The silicon and carbon's atomic orientation is acquired by rotating tetrahedron by 180° along its c-axis. The direction normal to the Si–C double-atomic layer is indicated by the c-axis as shown in the figure. In each layer, the silicon (or carbon) atoms have close-packed hexagonal arrangements. The silicon carbide crystal consists of two types of tetrahedrons. If another tetrahedron is rotated 180° along its c-axis, then the first one can be acquired, and when the c-axis is parallel to the mirror, the second one is mirror image of the other. The direction normal to the Si–C double-atomic layers is denoted by the c-axis. In each layer, the silicon (or carbon) atoms have close-packed hexagonal arrangement. At the time when the tetrahedral bonding scheme of the crystal is being maintained, each SiC bilayer can be located likely in any of the three positions with respect to the lattice. Sites to arrange the Si–C double-atomic layers can be of three kinds (A, B, and C), and each layer appears normal to the c-axis as shown in Fig. 2.

The Si and C bonding of atoms in adjacent bilayer planes is of either zinc blende (cubic) or wurtzite (hexagonal) nature depending on the stacking order. With respect to nearest neighbors, zinc blende bonds are turned 60°, while as shown in Fig. 3, hexagonal bonds are mirror images. A little altered atomic form is given by each kind of bonds which makes a few lattice difference from the existing polytypes with mixed bonding schemes, and also, it drops the overall crystal symmetry. These effects are important when considering the substitution impurity incorporation and electronic transport properties of SiC.

The purely cubic zinc blende structure, usually shortened as 3C-SiC (or beta SiC), is realized when the stacking is ABCABC (Fig. 4). Letter "C" indicates the crystal's overall cubic symmetry, and the three-bilayer periodicity of the stacking is referred by number "3". The only likely cubic polytype is 3C-SiC. Rest of the polytypes are likely to be combinations of the fundamental zinc blende and wurtzite bonds.

While 6H-SiC is two-thirds cubic, 4H-SiC is composed evenly by cubic and hexagonal bonds. Among more than 200 polytypes, single-crystalline cubic silicon carbide

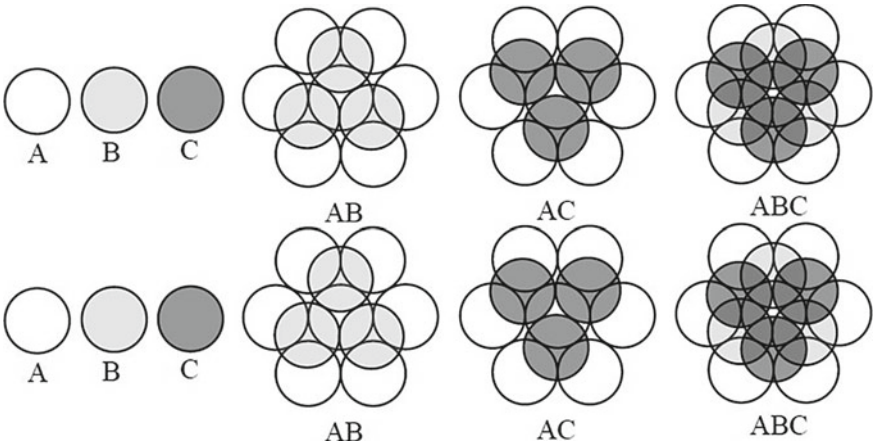


**Fig. 2** Atomic layers of SiC [3]

**Fig. 3** Zinc blende and wurtzite bond [3]

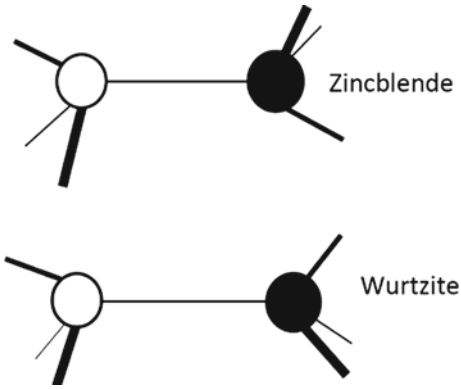


**Fig. 4** Purely cubic 3C-SiC polytype's crystal structure: All lattice sites (cubic symmetry referred as "k") are equivalents [3]

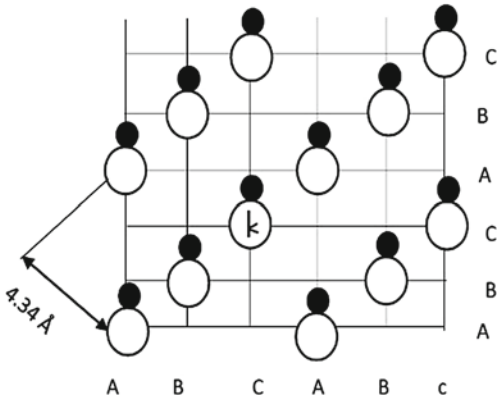

**Table 1** Comparison chart for electrical properties of Si with SiC polytypes [6]

| Properties | Si | 4H-SiC | 6H-SiC | 3C-SiC |
|---|---|---|---|---|
| Band gap energy (eV) | 1.12 | 3.26 | 3.03 | 2.40 |
| Relative dielectric | 11.90 | 9.70 | 9.66 | 9.72 |
| Saturation electron velocity | 1.00 | 2.00 | 2.00 | 2.50 |
| Intrinsic carrier concentration ( $cm^{-3}$) | $9.65 \times 10^{9}$ | $5 \times 10^{-9}$ | $1.6 \times 10^{-6}$ | $1.5 \times 10^{-1}$ |
| Thermal conductivity (W/cm K) | 1.31 | 4.9 | 4.9 | 3.2 |
| Electron mobility @ $N_D = 10^{16}$ $cm^{-3}$ [$cm^2$/Vs] | 1430 | 900 (∥c-axis) 800 (⊥c-axis) | 60 (∥c-axis) 400 (⊥c-axis) | 800 |
| Hole mobility @ $N_A = 10^{16}$ $cm^{-3}$ [$cm^2$/Vs] | 480 | 115 | 90 | 40 |
| Commercial wafer diameter (inches) | 12 | 3 | 3 | ? |
| Density (gm/$cm^3$) | 2.30 | 3.20 | 3.20 | 3.20 |
| Melting point (°C) | 1420 | 2830 | 2830 | 2830 |
| Bond length (Å) | 2.35 | 1.89 | 1.89 | 1.89 |
| Physical stability | Good | Excellent | Excellent | Excellent |

(3C-SiC) is drawing vital research interest because of its higher channel mobility and lower energy band gap that make it the most suitable polytype for developing electronic and optoelectronic devices [4]. 3C-SiC can be grown heteroepitaxially on different substrate materials. Additionally, production of device-grade 3C-SiC epilayers is being developed majorly in recent times. However, to decrease crystallographic structural errors in 3C-SiC epilayers is crucial before this polytype turns into a practical substitute to 4H- and 6H-SiC [5]. Table 1 shows the comparison between various properties of SiC polytypes [6]. Single-crystalline silicon carbide (3C-SiC) on the Si substrate has got momentous notices in recent years because of its low wafer cost and excellent mechanical, chemical, and optoelectronic properties. The applications of the structure are mainly focused on piezoresistive and pressure sensors, bio-microelectromechanical system, and photonics [7].

## 2 Electrical Properties of Si~3C-SiC Heterojunctions

Owing to the differing understanding of Si and C atoms within the SiC crystal lattice, each SiC polytype reveals exclusive elementary electrical and optical properties. The hetero-epitaxial growth of 3C-SiC on Si got vital interest for several decades due to availability of Si material and well-developed Si-orientated MEMS processing technologies. Because of its enormous energy band, exceptional mechanical properties, and higher chemical inertness, silicon carbide (SiC) is a potential material for applications used in harsh environments [8]. 3C-SiC films, typically, grow on Si substrates using low pressure/atmospheric pressure chemical vapor deposition

(LPCVD/APCVD) methods. SiC is amazing semiconductor to impart to silicon in heterojunction diode, due to its high thermal conductivity, chemical stability, and extensive band gap. Among existing SiC polytypes, only 3C-SiC has gainfully been developed on silicon substrates at lower temperatures than the silicon's melting point [9, 10]. The current mechanism irrespective of external transverse stress on the 3C-SiC [110] lattice orientation is reported in 2014 [11]. Due to the valance band offset between Si and SiC, the current flow in the heterojunction due to tunneling through the triangular barrier potential had been observed. When stress is enlarged from 0 to 308 MPa, the applied stress produces little changes in tunneling current. It is observed that increasing the voltage at 0.24 V in forward bias gives 10% of the maximum stress of 308 MPa. After applying stress, tunneling current gets increased and it also changes the out-of-plane effective mass and the effective tunneling barrier height of holes at top sub-bands of p-type Si [11]. A couple of studies find that in SiC/Si structures the space charge region is established by the relationship I~V1/2 [6], but a mechanism of excess tunneling to explain V–I characteristics of n-3C-SiC/Si heterojunctions is suggested by others [12]. The current density vs voltage characteristics at room temperature of a heterojunction diode is shown in Fig. 5 [6]. $J = J_0 \exp(qV/nkT)$ is the expression for forward bias current density (ideality factor $n = 1.2$). The forward bias current is prevailing by diffusion, but holds a recombination segment, which may happen at the SiC/Si interface. It is described by the specific ideality factor 1.2. At room temperature, it is found that the reverse saturation current density $J_0 = 0.1$ A/cm$^2$ after expanding the temperatures leads to uncover an actuation energy for $J_0$. The diode has incredible characteristics of reverse blocking without apparent breakdown to 200 V, with current density 1.3 mA/cm$^2$, and rectification ratio at $\pm 1$ V is 200,000.

Figure 6 [8] shows the temperature versus reverse current density at different voltage points. The doping concentration of SiC is higher than that of the silicon. Hence, in the silicon most electric field changes occur near the interface. It is reported that activation energy is reduced from 0.54 to 0.39 eV by increasing reverse bias from

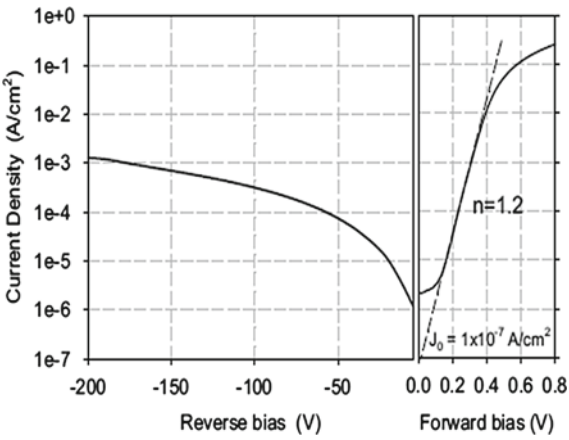


**Fig. 5** Forward and reverse bias V–I characteristics of n-3C-SiC/p-Si [8]

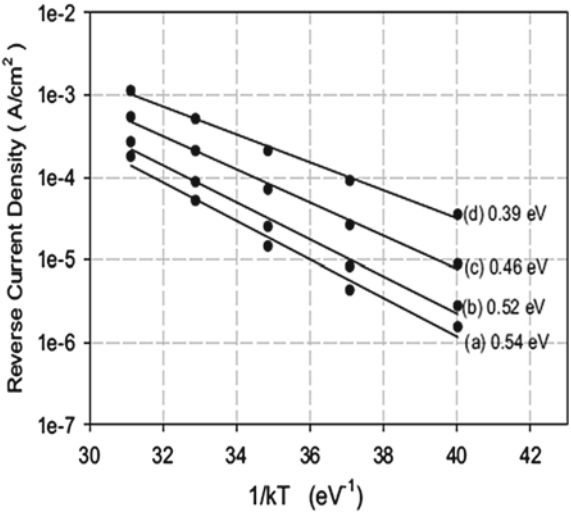


**Fig. 6** Reverse current density measure at various bias voltages [8]

5 to 40 V. Rather than simply trap-assisted thermal generation in the silicon depletion region or at the SiC/Si interface, the current generation is happening via a multistep mechanism at the SiC/Si interface. It is suggested by the mixture of temperature and field dependence. Energy band diagram of ideal heterojunction with zero bias conditions and with different values of 3C-SiC band gap and electron affinity gained in 2002 [10] is shown in Fig. 7 [8]. A current mechanism consisting of an electron tunneling from the valence band of silicon to a trap at the SiC/Si interface, followed by thermal emission into the conduction band of the SiC, was proposed to clarify the experimental results in reverse bias [8].

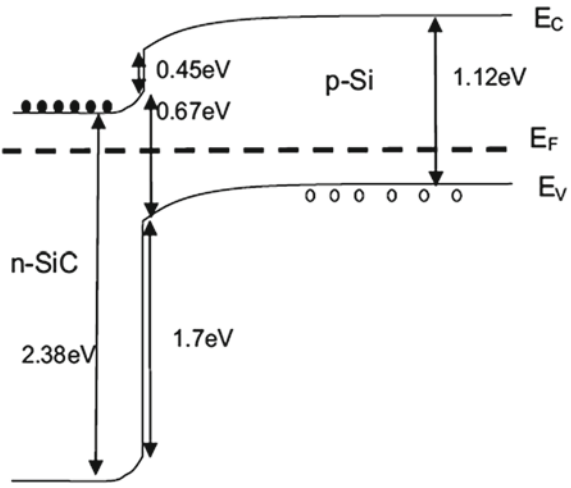


**Fig. 7** n-3C-SiC/p-Si heterojunction's band alignment diagram at zero bias [8]

The reverse bias current mechanism can be expressed by the relationships [13], where thermal emission time constant is expressed as

$$\tau_{\mathrm{e}} = \tau_{\mathrm{e0}} \cdot \exp\left[(E_{c,\mathrm{SiC}} - Et)/kT\right], \tag{1}$$

where $E_{c,\mathrm{SiC}}$ is the SiC conduction band energy, $E_t is$ trap energy, $\tau_{e0}$ is constant, $T$ is temperature, *and* $k$ is Boltzmann's constant. Tunneling process time constant is expressed as

$$\tau_t = \tau_{t0} \cdot \exp[(\Phi_B)/E_{\mathrm{si}}], \tag{2}$$

where $E_{\mathrm{Si}}$ is the electric field strength in the silicon at the heterojunction, $\Phi_B$ is the tunneling barrier height, *and* $\tau_{t0}$ is a constant. So, total time consuming for this two-step process is:

$$\tau = \tau_{\mathrm{e}} + \tau_t, \tag{3}$$

For the trap energy which gives the minimum value of τ, the reverse current density, $J_r$, will be:

$$J_r = (qN_t)/\tau, \tag{4}$$

where $N_t$ is trap density at that energy.

## 3 Optoelectronic Applications

For its stable and long-range ordered structures along with its optoelectronic properties, large thermal conductivity, hardness, and chemical reliability, SiC demands attention of the researchers. The intermediate state insertion into the energy band gap can potentially enhance the optoelectronic properties. Group-VIII transition metal impurity sets up a deeper band into the host energy band gap for ferromagnetic and antiferromagnetic spin alignments; this fact is reported in some cases. During a site deformation around the impurities or a Mott–Hubbard metal–insulator transition, the intermediate bands could split into two sub-bands. It is evident that these effects or a combination of them does not split the bands into energy band gap. So, more photon absorption channels are opened up by these deeper bands and hence boost the solar light absorption with respect to the host in solar cell devices [14]. Wideband photodetectors those convert incident photon energy into electrical signals are necessary for many applications including biomedical imaging, broadband optical communication, multispectral image sensors, and smart cities [15, 16]. The heterojunction also gives a high built-in potential, which is important to divide the photogenerated electrons ($e_{\mathrm{ph}}$)

and holes ($h_{ph}$) [17]. Consequently, the heterostructure shows an improved sensitivity over a wide spectral range. Due to the distinct optical properties of 3C-SiC and Si, the 3C-SiC/Si heterostructure could be an exceptional platform to expand broadband photodetectors. If a heterostructure illuminates non-uniformly, a lateral photovoltage generates parallel to the heterojunction [18]. The photovoltage originates from the lateral movement of the photogenerated carriers from the laser spot and recombines with the excited carriers away from the illumination point. The lateral photo effect (LPE) is used to measure the laser spot position between two contacts as the photovoltage varies linearly with the spot position and which is also sensitive to a very small displacement [19]. The position-sensitive detectors (PSDs) have many applications in optical engineering, process control, and triangulation-based distance sensors where precise automated control is essential. In 2018, at 1000 °C using epitaxial method of low pressure chemical vapor deposition technique, 3C-SiC/Si-based heterostructure photodetector operating in ultraviolet and visible spectrum has been developed [20], and as a result in dark conditions, the detector gives a rectification ratio of $1.03 \times 103$ and a reverse leakage current of $7.2 \times 10^{-6}$ A at 2 V. The reported device responsivity are $5.4 \times 10^{-2}$ A/W for visible spectrum of wavelength 635 nm and $3.18 \times 10^{-2}$ A/W for UV spectrum of wavelength 375 nm at 2.0 V reverse bias [20]. 3C-SiC-based single-mode optical waveguides and ring resonators applicable for telecommunication wavelength and leverage post-fabrication thermal annealing to minimize optical propagation losses were fabricated in 2020. Annealed optical resonators with yield quality factors more than 41,000, exhibit the propagation loss of 7 dB/cm, which is an improvement of 24 dB/cm as compared to the non-annealed chip [21].

## 4 THz Sources

Due to the improved noise performance, high frequency operation and high power capabilities make 3C-SiC/Si an appropriate material for terahertz sources like IMPATT diode. The Si~3C-SiC MQW DDR IMPATT diodes' self-consistent quantum drift-diffusion (SCQDD) mode developed by the authors was reported [22, 23]. Figure 8a, b shows the one-dimensional (1-D) *n*+–*n*–*p*–*p*+ structured MQB DDR IMPATT diode's cross-sectional view and the resultant simulation model utilized for the study [24].

Eighteen periods of MQWs which are made of alternative 3C-SiC and Si layers form the MQB DDR IMPATT structures. For appropriate high frequency applications, asymmetrical doping profile is generally considered; in this case the doping density of 3C-SiC quantum barrier layers are kept roughly double of the doping density of Si layers [22, 23]. Si~3C-SiC MQW DDR IMPATT diodes' design parameters are designed to operate at 94, 140, and 220 GHz and 0.30 and 0.50 THz as listed in Table 2 [24].

The material parameters of Si and 3C-SiC at room temperature, i.e., at 300 K, have been used in SCQDD simulation of Si~3C-SiC MQW DDR IMPATT diodes to work at 94, 140, and 220 GHz and 0.30 and 0.50 THz frequencies [25–30]. According

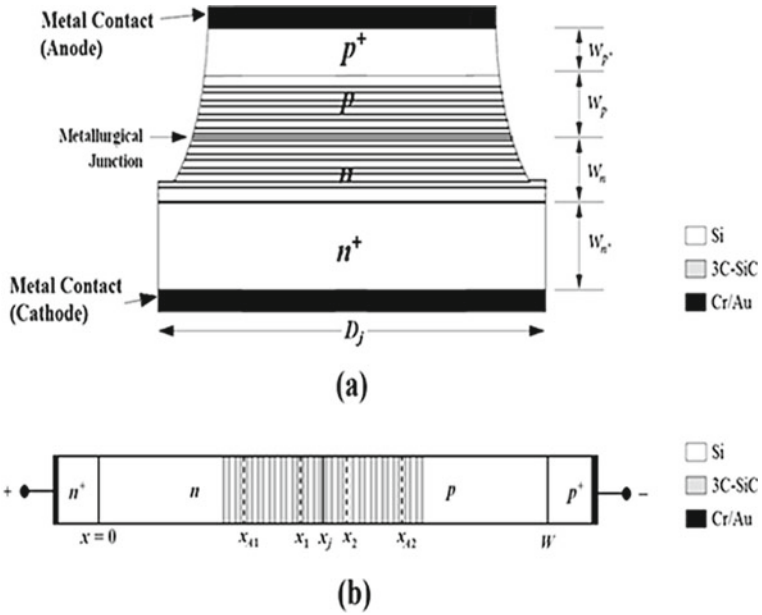


**Fig. 8** **a** $n^+$-$n$-$p$-$p^+$ structured MQB DDR IMPATT diode's cross-sectional view and **b** its resultant 1D mode [24]

**Table 2** Design parameters [24]

| Design parameters* | 94 GHz | 140 GHz | 220 GHz | 0.30 THz | 0.50 THz |
|---|---|---|---|---|---|
| $W_n$ (nm) | 370 | 249 | 161 | 116 | 68 |
| $W_p$ (nm) | 400 | 269 | 174 | 125 | 74 |
| $W1$ (nm) | 10.00 | 6.73 | 4.36 | 3.13 | 1.85 |
| $W2$ (nm) | 10.00 | 6.73 | 4.36 | 3.13 | 1.85 |
| $N_D1$ ($\times 10^{23}$ m$^{-3}$) | 1.50 | 2.25 | 4.94 | 7.50 | 18.75 |
| $N_D2$ ($\times 10^{23}$ m$^{-3}$) | 3.00 | 4.50 | 9.88 | 15.00 | 37.50 |
| $N_A1$ ($\times 10^{23}$ m$^{-3}$) | 1.25 | 2.10 | 4.59 | 7.30 | 16.20 |
| $N_A2$ ($\times 10^{23}$ m$^{-3}$) | 2.50 | 4.20 | 9.18 | 14.60 | 32.40 |
| $N_{n+}$ ($\times 10^{25}$ m$^{-3}$) | 5.00 | 5.00 | 5.00 | 5.00 | 5.00 |
| $N_{p+}$ ($\times 10^{25}$ m$^{-3}$) | 2.70 | 2.70 | 2.70 | 2.70 | 2.70 |
| $A_j$ ($\times 10^{-8}$ m$^{-2}$) | 9.6210 | 4.9090 | 3.1420 | 1.7670 | 0.7850 |
| $J0$ ($\times 10^{8}$ A m$^{-2}$) | 6.00 | 10.24 | 25.59 | 43.24 | 97.06 |

where $W_n$ is thickness of $n$-epitaxial layer, $W_p$ is thickness of $p$-epitaxial layer, $W1$ is thickness of quantum wells based on Si, $W2$ is thickness of quantum barriers based on 3C-SiC, $N_D1$ is donor concentration of Si layers at $n$-side, $N_D2$ is donor concentration of 3C-SiC layers at $n$-side, $N_A1$ is acceptor concentration of Si layers at $p$-side, $N_A2$ is acceptor concentration of 3C-SiC layers at $p$-side, $N_{n+}$ is donor concentration of $n^+$-contact layer, $N_{p+}$ is acceptor concentration of $p^+$-contact layer, $A_j$ is effective junction area, and $J0$ is optimum bias current density

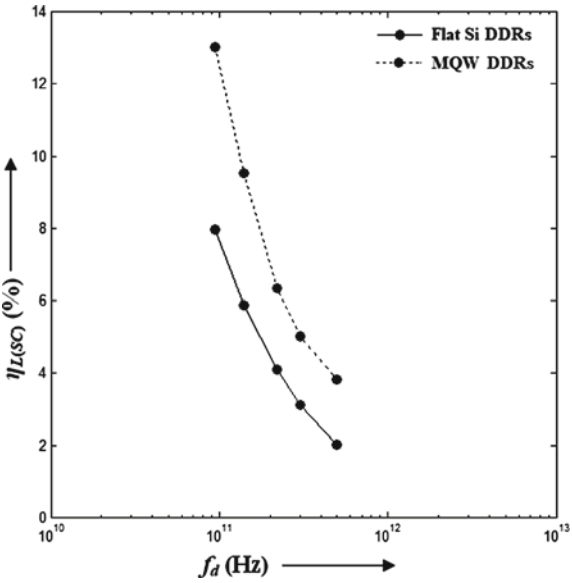


**Fig. 9** Flat Si DDR IMPATTs and MQW DDR IMPATTs' efficiency with operating frequency at respective optimum current densities [24]

to simulation result, Si~3C-SiC MQW IMPATT sources are capable to give notably higher RF output power with significantly lower noise level at mm wave and THz frequency bands comparing to conventional flat Si IMPATT sources. The variations of RF power output and DC-to-RF conversion efficiency of flat Si DDR and MQW DDR IMPATTs at unusual operating frequencies [24] are shown in Fig. 9. It is observed from Fig. 9 [24] that MQW DDRs are capable to deliver quite higher DC-to-RF conversion efficiency when comparing to flat Si DDRs at different frequencies mentioned in Fig. 9.

## 5 Other Applications

Despite optical applications, Si~3C~SiC is also utilized in biomedical purposes with particular importance for the most promising applications: in vivo glucose monitoring, biomedical implants for connecting the human nervous system to advanced prosthetics, and MEMS/NEMS research aimed at allowing for in vivo diagnostic and therapeutic systems for superior biomedical applications [31]. The generation of hydrogen for fuel cells and other "clean energy" applications are global priorities those have received an incredible amount of awareness during past decade [32]. 3C-SiC has been reported as a popular photo-electrode for several reasons [33–35]: 3C-SiC is chemically stable and has a band gap of ~2.3 eV which is proper for absorbing a part of visible spectrum.

## 6 Summary

Potentialities of semiconductor heterostructures based on Si~3C-SiC material system for realizing high-frequency electronic devices extended up to THz frequency spectrum are described in this chapter. Current mechanism of Si~3C-SiC heterojunctions has been discussed concisely. Applications of this heterostructure in different areas of electronics and optoelectronics like microelectromechanical systems (MEMS), energy conversion, photodetection, light emission, etc., have been discussed in this chapter. Lastly, the chances of realizing high-power THz avalanche transit time oscillators based on Si~3C-SiC heterostructures have been described.

## References

1. Knippenberg WF (1963) Growth phenomena in silicon carbide. Philips Res Rep 18:161–274
2. Henrik P et al (2012) Chloride-based CVD growth of silicon carbide for electronic applications. Chem Rev 112(4):2434–2453
3. Islam MR, Galib RH, Sarkar M, Chowdhury S (2018) Wide-bandgap semiconductor device technologies for high temperature and harsh environment applications. In: Sharif (ed), Harsh environment electronics. Interconnect materials and performance assessment, Chapter 1, Wiley Publication
4. Foisal MAR (2019) Optoelectronic effects in 3C-SiC/Si heterostructure and applications, PhD Thesis, School of Engineering & Built Environment
5. Pirouz P, Chorey C, Powell J (1987) Antiphase boundaries in epitaxially grown β-SiC. Appl Phys Lett 50(4):221–223
6. Maity NP (2011) 4H-SiC semiconductor based metal oxide semiconductor devices. In: 2011 international conference on future information technology IPCSIT (2011), IACSIT Press, Singapore 13, pp 1–4
7. Riduan A, Foisal M, Nguyen T, Dinh T, Nguyen TK, Tanner P, Streed EW, Dao DV (2019) 3C-SiC/Si heterostructure: an excellent platform for position-sensitive detectors based on photovoltaic effect. Appl Mater Interfaces 11(43):40980–40987
8. Tanner P, Dimitrijev S, Harrison HB (2008) Current mechanisms in n-SiC/p-Si heterojunctions. In: 2008 conference on optoelectronic and microelectronic materials and devices, Sydney, NSW, Australia, 28th July–1st Aug 2008, pp 1–4
9. Nagasawa H, Yagi K (1997) 3C-SiC single crystal films grown on 6-inch Si substrates. Phys Status Solidi B 202:335–340
10. Chassagne T, Ferro G, Chaussende D, Cauwet F, Monteil Y, Bouix J (2002) A comprehensive study of SiC growth processes in a VPE reactor. Thin Solid Films 402:83–89
11. Qamar A, Tanner P, Dao DV, Phan HP, Dinh T (2014) Electrical properties of p-type 3C-SiC/Si heterojunction diode under mechanical stress. IEEE Electron Device Lett 35(12):1293-1295)
12. Karazhanov SZ, Atabaev IG, Saliev TM, Kanaki EV, Dzhaksimov E (2001) Excess tunneling currents in p-Si-n-3C-SiC heterostructures. Semiconductor 35(1):75–77
13. Sze SM (1981) Physics of Semiconductor devices, 2nd edn. Wiley
14. Tablero C (2013) Optoelectronic application of the 3C-Silicon carbide with substitutional VIII-Group atoms. J Phys Chem C 117(42):21949–21954
15. Periyanagounder D, Gnanasekar P, Varadhan P, He J-H, Kulandaivel J (2018) High performance, self-powered photodetectors based on a graphene/silicon Schottky junction diode. J Mater Chem C 6:9545–9551
16. Ovanesyan Z, Mimun LC, Kumar GA, Yust BG, Dannangoda C, Martirosyan KS et al (2015) Depth-resolved multispectral sub-surface imaging using multifunctional upconversion phosphors with paramagnetic properties. ACS Appl Mater Interfaces 7:21465–21471

17. Li G, Suja M, Chen M, Bekyarova E, Haddon RC, Liu J et al (2017) Visible-blind UV photodetector based on single-walled carbon nanotube thin film/ZnO vertical heterostructures. ACS Appl Mater Interfaces 9:37094–37104
18. Wallmark JT (1957) A new semiconductor photocell using lateral photoeffect. Proc IRE 45:47483
19. Wang X, Zhou Q, Li H, Hu C, Zhang L, Zhang Y, Zhang Y, Sui Y, Song B (2018) Self-powered ultraviolet vertical and lateral photovoltaic effect with fast-relaxation time in $NdNiO_3$/Nb: $SrTiO_3$ heterojunctions. Appl Phys Lett 112:122103
20. Foisal ARM, Dinh T, Tanner P, Phan HP, Nguyen TK, Iacopi A, Streed EW, Dao DV (2018) Ultraviolet and visible photodetection using 3C-SiC, Si hetero-epitaxial junction. In: Sustainable design and manufacturing 2018. KES-SDM, 2018 smart innovation, systems and technologies 130. Springer, Cham.https://doi.org/10.1007/978-3-030-04290-5_22
21. Powell K, Ansari AS, Desai S, Austin M, Deng J, Sinclair N, Loncar M, Yi X (2020) High-Q suspended optical resonators in 3C silicon carbide obtained by thermal annealing. Opt Express 28(4):STu3P.3
22. Ghosh M, Ghosh S, Acharyya A (2017) Self-consistent quantum drift-diffusion model for multiple quantum well IMPATT diodes. J Comput Electron 15(4):1370–1387
23. Ghosh M, Ghosh S, Bandyopadhyay PK, Biswas A, Bhattacharjee AK, Acharyya A (2018) Noise performance of 94 GHz multiple quantum well double-drift region IMPATT sources. J Active Passive Electron Dev 13(2/3):195–207
24. Ghosh M, Biswas A, Acharyya A (2019) Terahertz radiators based on Si~3C-SiC MQW IMPATT diodes. Nanosci Nanotechnol Asia 9:1–12
25. Electronic archive: new semiconductor materials, characteristics and properties. Available from: http://www.ioffe.ru/SVA/NSM/Semicond/index.html. Last accessed on Apr 2021
26. Zeghbroeck BV (2011) Principles of semiconductor devices. Colorado Press, USA
27. Grant WN (1973) Electron and hole ionization rates in epitaxial silicon. Solid-State Electron 16:1189–1203
28. Canali C, Ottaviani G, Quaranta AA (1971) Drift velocity of electrons and holes and associated anisotropic effects in silicon. J Phys Chem Solids 32:1707–1720
29. Bellotti E, Nilsson HE, Brennan KF, Ruden PP (1999) Ensemble Monte Carlo calculation of hole transport in bulk 3C-SiC. J Appl Phys 85(6):3211–3217
30. Mickevicius R, Zhao JH (1998) Monte Carlo study of electron transport in SiC. J Appl Phys 83(6):3161–3167
31. Frewin CL, Reyes M, Register J, Thomas SW, Saddow SE (2014) 3C-SiC on Si: a versatile material for electronic, biomedical and clean energy applications. MRS Online Proc Libr Arch 1693:178–192
32. Lipman T (2011) An overview of hydrogen production and storage systems with renewable hydrogen case studies. Clean Energy States Alliance (2011). Available from: https://www.cesa.org/resource-library/resource/an-overview-of-hydrogen-production-and-storage-systems-with-renewable-hydrogen-case-studies/. Last accessed on Apr 2021
33. Ma QB, Kaiser B, Ziegler J, Fertig D, Jaegermann W (2012) XPS characterization and photoelectrochemical behaviour of p-type 3C-SiC films on p-Si substrates for solar water splitting. J Phys D Appl Phys 45:325101
34. Yasuda T, Kato M, Ichimura M, Hatayama T (2012) SiC photoelectrodes for a self-driven water-splitting cell. Appl Phys Lett 101(5):053902
35. Song JT, Mashiko H, Kamiya M, Nakamine Y, Ohtomo A, Iwasaki T, Hatano M (2013) Improved visible light driven photoelectrochemical properties of 3C-SiC semiconductor with Pt nanoparticles for hydrogen generation. Appl Phys Lett 103:213901-1-4

# Novel InAs/Si Heterojunction Dual-Gate Triple Metal P-i-N Tunneling Graphene Nanoribbon Field Effect Transistor (DG-TM-TGNFET) For High-Frequency Applications


**Ritam Dutta and Nitai Paitya**

**Abstract** The detail DC and AC analysis of a proposed novel Indium Arsenide (InAs)/Silicon (Si) heterojunction-based dual-gate triple metal P-i-N tunneling graphene nanoribbon field effect transistor (DG-TM-TGNFET) has been reported in this chapter. The novel heterojunction-based TFET structure with ultra-thin graphene nanoribbon placed over silicon channel has produced better digital and analog/RF performance, by means of which the proposed device can be useful for high-frequency (Tera Hertz) applications. A thorough investigation of analog/RF performance parameters viz. transconductance ($g_m$), overall gate capacitance ($C_{gg}$), gain bandwidth product (GBP) and cut-off frequency ($f_t$) has been derived, simulated, and compared with conventional all silicon homojunction-based dual-gate TFET structures. All simulation work has been performed by Silvaco simulator. The cut-off frequency ($f_t$) of DG-TM-TGNFET device has been observed as 0.349 THz which is suitable for high-frequency applications.

**Keywords** TFET · DG-TM-TGNFET · Transconductance · Gate capacitance · GBP · Cut-off frequency · Silvaco

## 1 Introduction

Now-a-days, tunnel field effect transistors (TFETs) are envisioned as the most encouraging candidate for high-frequency applications. There have been several advancements in CMOS technology found to be inculcated to surmount short-channel effects (SCE) and controlled leakage current ($I_{OFF}$). To cope up with continuous miniaturization in nano-device channel lengths, it is the tunnel FETs that utilized Quantum

R. Dutta (✉)
Center of Intelligent Systems and Robotics - ITER, Siksha 'O' Anusandhan (Deemed to be University), Bhubaneswar, Odisha 751030, India

N. Paitya
Department of Computer Science and Engineering, Sikkim Manipal Institute of Technology, Sikkim Manipal University, Sikkim 737136, India
e-mail: nitai.p@smit.smu.edu.in



A. Acharyya et al. (eds.), *Generation, Detection and Processing of Terahertz Signals*, Lecture Notes in Electrical Engineering 794,
https://doi.org/10.1007/978-981-16-4947-9_17

Mechanical Effect (QME) for band-to-band tunneling (BTBT). Moreover, TFET suffers poor drive current ($I_{ON}$). Therefore, many research works [1–6] to boost $I_{ON}$ in TFETs have been studied. With the advent of nanotechnology, several materials as well as device engineering have been performed in last few years to fulfill the TFET limitations. Lower-energy band gap compound materials, i.e., Indium Arsenide (InAs) at source for n-type TFET model has shown promising ON-state current compared to homojunction materials [7, 8].

This chapter showcased a proposed n-type dual-gate triple material P-i-N tunneling graphene nanoribbon FET (DG-TM-TGNFET) based on InAs/Si heterojunction at source–channel region, where the device performance has been thoroughly analyzed for DC as well as small signal performance for high frequency with low-power applications.

## 2 Device Structure and Simulation Strategy

### *2.1 Device Description*

The proposed DG-TM-TGNFET structure is showcased in Fig. 1 with ultra-thin graphene nanoribbon placed over silicon channel. InAs/Si based heterojunction helps to create better band to band tunneling (BTBT) at source–channel interface for our n-type dual-gated TFET device model.

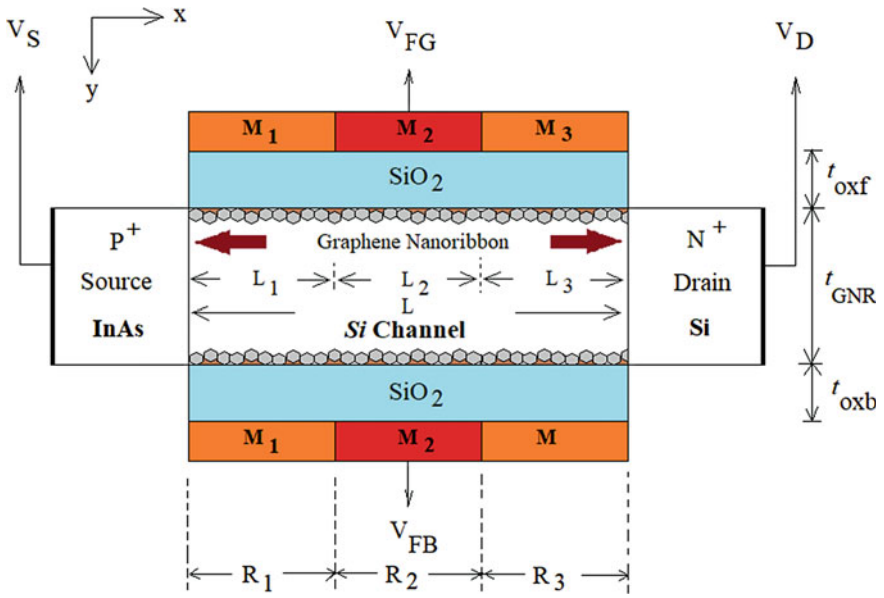


**Fig. 1** Schematic view of proposed DG-TM-TGNFET

**Table 1** Typical device and electrical parameters

| Device parameters | DG-TM-TGNFET model |
|---|---|
| Channel length (L) | 20 nm |
| Effective oxide thickness—front gate ($t_{oxf}$) | 2 nm |
| Effective oxide thickness—back gate ($t_{oxb}$) | 2 nm |
| Channel thickness ($t_{GNR}$) | 10 nm |
| $P^+$ source doping ($N_S$) | $10^{20}$ cm$^{-3}$ |
| $N^+$ drain doping ($N_D$) | $10^{18}$ cm$^{-3}$ |
| Intrinsic channel doping ($N_{ch}$) | $10^{14}$ cm$^{-3}$ |
| Metal 1 work-function ($\phi_{m1}$) | 4 eV |
| Metal 2 work-function ($\phi_{m2}$) | 4.8 eV |
| Metal 3 work-function ($\phi_{m3}$) | 4.5 eV |
| Gate–source voltage ($V_G$) | 0 to 1.5 V |
| Supply voltage ($V_{DD}$) | 0.5 V |

The incorporation of triple metal with three different metal work-function provides better drain current ($I_{ON}$), with optimized leakage current ($I_{OFF}$) and steeper subthreshold slope. High-switching ratio can be obtained by large ON-state current and small leakage current. Typical device and electrical parameter for DC analysis are being taken from recent established research works shown in Table 1.

## 2.2 *Mathematical Analysis for TCAD Simulation Framework*

The Poisson's equation is generally used to analyze the surface potential variation [9] along channel length. Here, for ease of calculations, two-dimensional parameters have been taken in Eq. (1).

$$\frac{\partial^2\psi(x,y)}{\partial x^2}+\frac{\partial^2\psi(x,y)}{\partial y^2}=\frac{qN_R}{\varepsilon_{GNR}} \quad for \quad 0\le x\le L, \quad 0\le y\le t_{GNR}, \tag{1}$$

where, $\psi(x,y)$ is the electrostatic potential, $\varepsilon_{GNR}$ is the permittivity of graphene used as nanoribbon, $q$ is the charge, and $N_R$ is the intrinsic doping concentration of specified region. The total intrinsic channel length is termed as $L$ has been segregated as three distinct equally lengthen regions for using three metal contacts; therefore, $L = L_1 + L_2 + L_3$ and $t_{GNR}$ are the thickness of the channel. To obtain surface potential at entire intrinsic channel surface, three regions have been approximated mentioning $R_1$, $R_2$ and $R_3$. Then, the Young's approximation [10] has been applied to obtain $\psi(x,y)$ by assuming the boundary conditions. Now, the electric field can be calculated from Eq. (2).

$$E_x = -\frac{\partial \psi(x,y)}{\partial x} \quad \text{and} \quad E_y = -\frac{\partial \psi(x,y)}{\partial y}. \tag{2}$$

And the total electric field would be:

$$E = \sqrt{{E_x}^2 + {E_y}^2}. \tag{3}$$

For ease of mathematical calculations, the entire electric field has been assumed as equally distributed. Therefore, Kane's model [11, 12] has been utilized to obtain the BTBT tunneling rate, using following mathematical equation.

$$G_{BTBT} = A_{\text{Kane}}\left(\varepsilon/\varepsilon_0\right)^P\right) - e^{(-B_{\text{Kane}}/\varepsilon)}, \tag{4}$$

where ε = dielectric material permittivity and $\varepsilon_0$ = relative permittivity, $P$ is the process parameter [13]. $A_{\text{Kane}}$ and $B_{\text{Kane}}$ are tunneling dependent parameters. The typical values of $A_{\text{Kane}}$ and $B_{\text{Kane}}$ are considered by default as $4 \times 10^{14}$ $\text{cm}^{-3}$ $\text{s}^{-1}$ and $1.9 \times 10^7$ V/cm, respectively. Here, in our model, InAs is used at source, to capitalize the direct band gap nature of this compound material. Now, integrating BTBT tunneling rate the tunneling current ($I_{\text{D}}$), i.e., drain current can be obtained using following equation.

$$I_{\text{D}} = q \int_{\substack{\text{TFET -} \\ \text{Volume}}} \left\{A_{\text{Kane}}\left(\varepsilon/\varepsilon_0\right)^P\right) - e^{(-B_{\text{Kane}}/\varepsilon)}\right\} \text{d}v \tag{5}$$

After getting the value of drain current, the transconductance ($g_{\text{m}}$) can also be found out using equation mentioned below.

$$g_{\text{m}} = (\text{d}I_{\text{D}}/\text{d}V_{\text{GS}})_{V_{\text{DS}}} \tag{6}$$

The proposed DG-TM-TGNFET is designed using TCAD device simulator. Shockley Read Hall (SRH) model is used to incorporate recombination effects. Band gap narrowing (BGN) model is used for BTBT at source–channel interface of our n-type device model [14, 15].

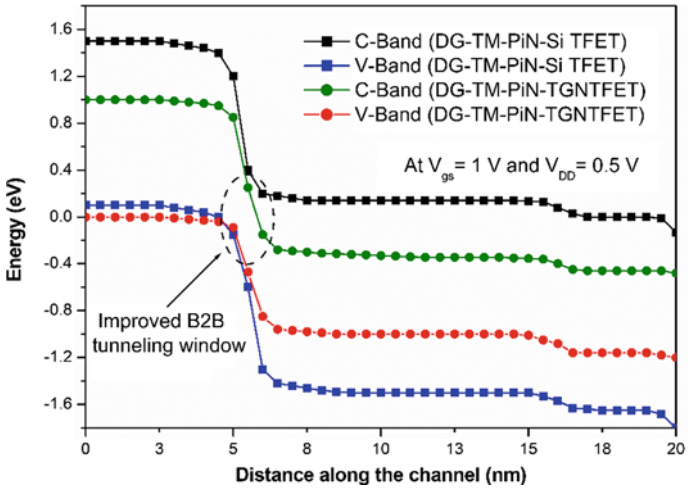


**Fig. 2** EBD Analysis of DG-TM-Si-TFET and DG-TM-TGNFET at $V_{gs} = 1$ V and $V_{DD} = 0.5$ V

## 3 Results and Discussion

### *3.1 The Energy Band Diagram (EBD) Analysis*

In our work, the energy bandgap analysis plays pivotal role in determining the BTBT rate, as graphene material has been incorporated over the intrinsic channel. This graphene layer is an edge-terminated graphene, known as graphene nanoribbons (GNR) to easily tune the carrier transport gaps and improve the ON/OFF current ratio (switching ratio). This technique is termed as quantum confinement effect which has been effective in GNRs. Therefore, from the energy band diagram analysis, the B2B, i.e., band-to-band tunneling window has been widened as shown in Fig. 2. The band bending results due to the variation in gate to source voltage ($V_{gs}$) from 0 to 1 V, keeping supply voltage ($V_{DD}$) as low as possible at 0.5 V.

### *3.2 Transfer Characteristics Analysis*

Figure 3 shows the $I_D - V_{GS}$ characteristics comparison between InAs/Si heterojunction-based DG-TM-TGNFET with orthodox all silicon (Si) homojunction-based DG-TM-Si-TFET model. At much lower supply voltage of 0.5 V, the steeper slope, i.e., subthreshold swing (SS) becomes 19.92 mV/decade which is much lower than the other. The $I_D$ has been recorded best at $1.12 \times 10^{-4}$ A/μm and leakage current ($I_{OFF}$) = $1.11 \times 10^{-16}$ A/μm. Here, the TFET with graphene nanoribbon structure developed better subthreshold swing (SS) of 19.92 mV/decade compared

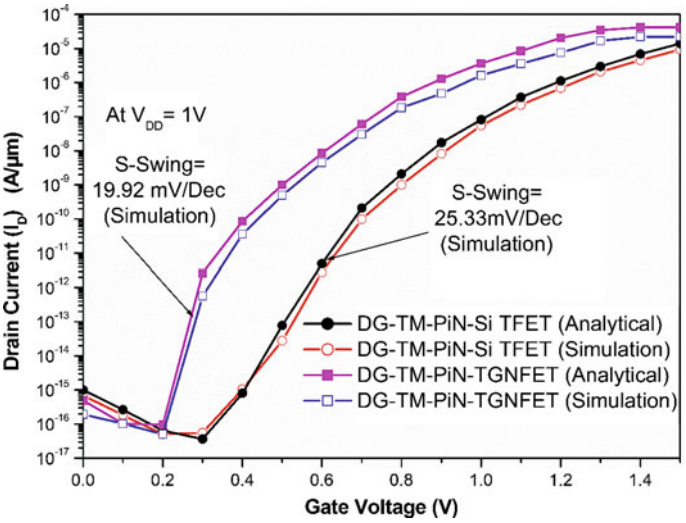


**Fig. 3** Transfer characteristics analysis of DG-TM-Si-TFET and DG-TM-TGNFET at $V_{DD}$ = 0.5 V

to orthodox all silicon homojunction-based TFET structure. Steeper slope ensures fast switching ON from OFF state of the proposed transistor model.

### *3.3 Surface Potential and Electric Field Distribution Analysis*

With variation in $V_{GS}$ from 0 to 1 V, keeping supply voltage as low as possible, the potential distribution along the surface area of our model has been depicted in Fig. 4, and compared with all silicon TFET model. The TCAD simulated results have been validated with analytical data. Figure 5 shows a lateral electric field (e-field) along *x*-axis channel to study short-channel effects. This confirms that the maximum lateral e-field distribution happens at source–channel interface for our n-type TFET device model. Higher e-field for DG-TM-TGNFET indicates higher BTBT rate at source–channel interface of our n-type tunnel FET device model (Fig. 6).

Though, the electric field variation hardly observed in vertical y-axis direction. Since our proposed device model is a structure laterally grown, therefore, the lateral electric field variation occurs much in comparison with vertical electric field distribution analysis.

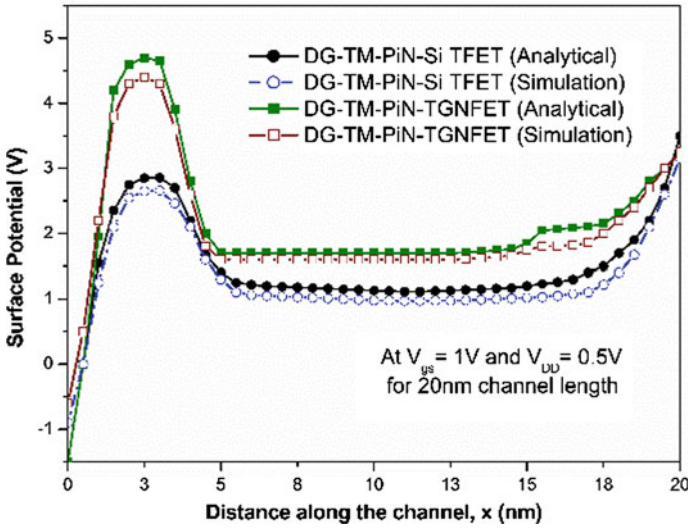


**Fig. 4** Surface potential variation of DG-TM-Si-TFET and DG-TM-TGNFET at $V_{DD} = 0.5$ V

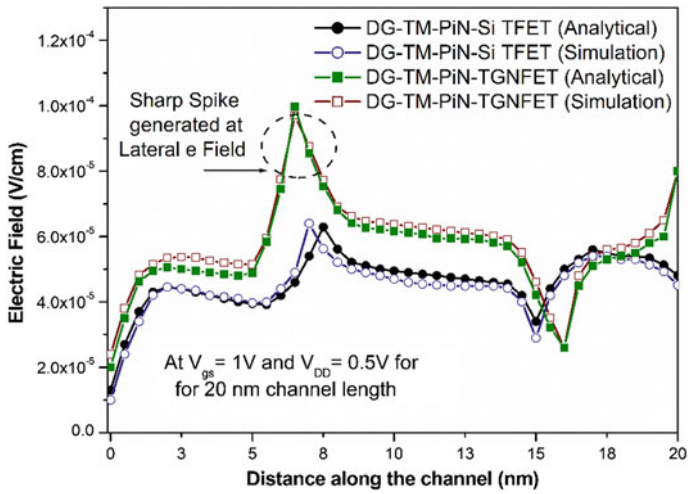


**Fig. 5** Lateral electric field profile for InAs/Si heterojunction P-i-N tunneling DG-TM-TGNFET keeping $V_{DD} = 0.5$ V compared with DG-TM-Si-TFET

## *3.4 Small Signal Analysis*

Now in this section, the proposed InAs/Si heterojunction-based DG-TM-TGNFET device model's small signal analysis has been investigated by analyzing analog/radio

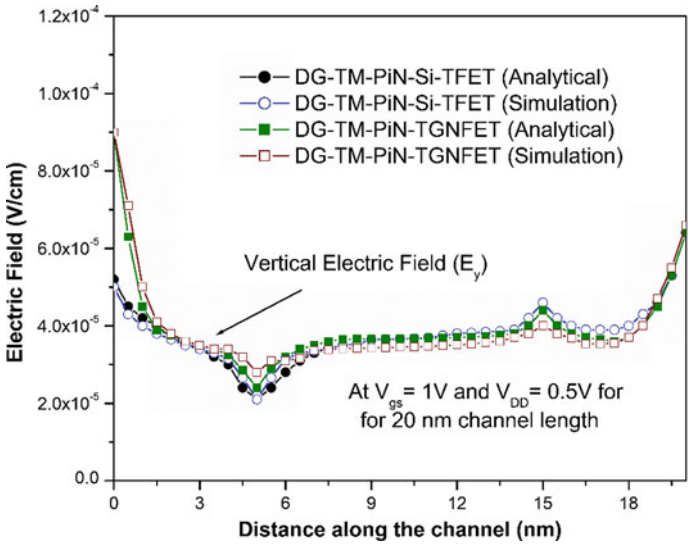


**Fig. 6** Vertical electric field profile for InAs/Si heterojunction P-i-N tunneling DG-TM-TGNFET keeping $V_{DD} = 0.5$ V compared with DG-TM-Si-TFET

frequency (RF) parameters. In the above section, we have already witnessed a considerable improvement in the direct current (DC) performance of the proposed TFET model. And due to channel length scaling ($L = 20$ nm) and deploying graphene material in terms of nanoribbon over the intrinsic channel, a sharp spike in lateral electric field has been identified. This results better tunneling current ($I_{ON}$) at source–channel junction for n-type DG-TM-TGNFET model. In this section, our proposed device model has been compared with dual-gated triple material all silicon TFET model, which includes transconductance ($g_m$), gate to drain capacitance ($C_{gd}$), gate to source capacitance ($C_{gs}$), cut-off frequency ($f_t$), gain bandwidth product (GBP) and maximum oscillation frequency ($f_{max}$).

All these figures of merits (FOM) have been evaluated at 1 MHz input frequency. The overall gate capacitance ($C_{gg}$) must be less for better device analog performance. For TFET devices, it has a miller capacitance, i.e., $C_{gd}$ behaves like parasitic capacitance at lower $V_{gs}$ and at higher $V_{gs}$, it acts like an inversion capacitance [16].

### 3.4.1 *Transconductance ($g_m$) Analysis*

Transconductance ($g_m$) is defined as the ratio of small change in output current to the small change in input voltage, i.e., gate voltage for TFET device. Now, after establishing the DC biasing, the transconductance ($g_m$) can be calculated from the transfer characteristics graph (Fig. 3); where the change in drain current ($I_D$) with respect to change in gate voltage ($V_{GS}$), keeping drain voltage ($V_{DS}$) constant, can be obtained using Eq. (6).

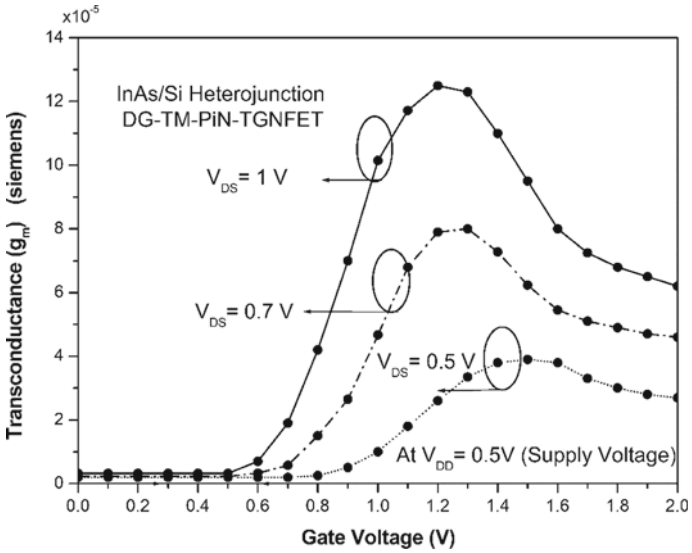


**Fig. 7** Transconductance analysis of DG-TM-TGNFET at 0.5 V supply voltage with varied $V_{DS}$ (0.5–1 V) at 0.5 V supply voltage

The transconductance ($g_m$) has been simulated and shown in Fig. 7. From the graphical representation, it is to be noted that at $V_{DD} = 0.5$ V and with varied drain–source potential ($V_{DS}$) from 1 to 0.5 V, and the subthreshold slope has got affected. Therefore, a minute calibration of $V_{DS}$ can provide steeper slope with controlled leakage current ($I_{OFF}$). Our device model provides transconductance of $12.82 \times 10^{-5}$ S at $V_{DS} = 1$ V and most importantly at considerably low-supply voltage of 0.5 V. Once the transconductance ($g_m$) is obtained, now the cut-off frequency ($f_t$) [17] can be very well obtained from Eq. (7). The cut-off frequency is defined as the frequency where the current gain becomes equal to unity.

$$f_t = \frac{g_m}{2\pi(C_{gs} + C_{gd})}, \tag{7}$$

$$So, f_t = \frac{g_m}{2\pi C_{gg}}, \tag{8}$$

where $g_m$ is the transconductance of the device; $C_{gs}$ and $C_{gd}$ are the capacitance values of gate-source and gate-drain regions, respectively. And the total gate capacitance ($C_{gg}$) is the summation of $C_{gs}$ and $C_{gd}$ of our InAs/Si heterojunction dual-gate triple material graphene nanoribbon based TFET model.

### 3.4.2 Capacitance–Voltage (C–V) Characteristics

Now, small signal alternating current (AC) simulation can be performed by keeping each gate bias of 1 MHz frequency source, from that the internal capacitances, i.e., $C_{gs}$ and $C_{gd}$ are extracted. $C_{gs}$ and $C_{gd}$ along with $g_m$ are employed to assess $f_t$. It is apparent [18] that lower the total gate capacitance ($C_{gg} = C_{gs} + C_{gd}$) and higher the transconductance ($g_m$) of TFET helps to attain superior high-frequency performance.

From Fig. 8, it can be observed that our device model, i.e., DG-TM-TGNFET produces very less $C_{gs}$ values with respect to $C_{gd}$. Now, with variation in drain-source voltage ($V_{DS}$) ranging from 1 to 0.7 V, the typical $C_{gd}$ can be lowered from $2 \times 10^{-16}$ F to $0.6 \times 10^{-16}$ F at 0.5 V of supply voltage. The TFET with graphene nanoribbon model can now be able to reduce the total gate capacitance ($C_{gg}$) with higher transconductance ($g_m$). The collective effort of rising $g_m$ with reducing $C_{gg}$ uplift the cut-off frequency. The DG-TM-TGNFET model delivers a cut-off frequency, $f_t = 0.349$ THz at $V_{DS} = 0.7$ V, $V_{DD} = 0.5$ V, which can be utilized for high-frequency applications.

$$\text{GBP} = \frac{g_m}{2\pi 10 C_{gd}}, \tag{10}$$

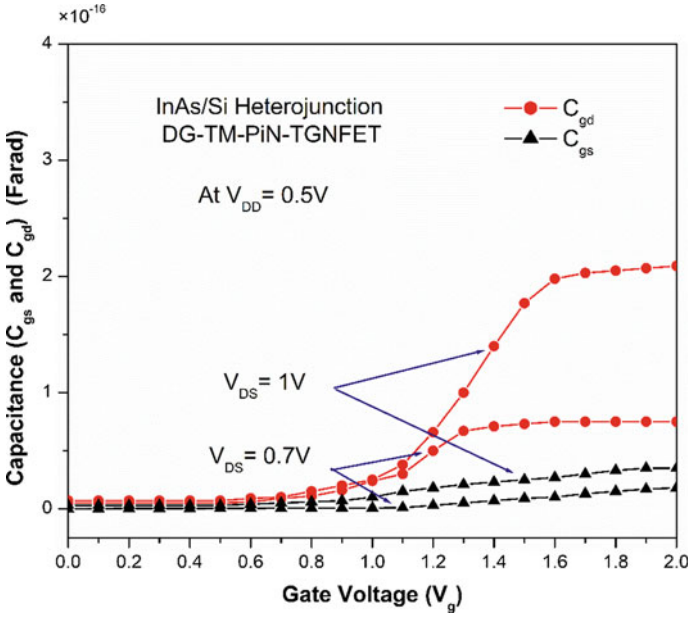


**Fig. 8** Capacitance–gate voltage (C–V) characteristics of InAs/Si Heterojunction DG-TM-TGNFET device with varied $V_{DS}$ (0.7–1 V) at 0.5 V supply voltage

$$f_{\max} = \frac{f_t}{8\pi \times C_{\mathrm{gd}} \times R_{\mathrm{gd}}}. \tag{11}$$

Moreover, the gain bandwidth product (GBP) and maximum oscillation frequency ($f_{\max}$) can be calculated from Eqs. (7) and (8), respectively. The $f_{\max}$ is calculated from Eq. (11), and optimum value of gate to drain resistance ($R_{\mathrm{gd}}$) has been considered as 1.2 KΩ for calculate maximum oscillation frequency [16].

## 4 Summary

The proposed device structure of InAs/Si heterojunction-based P-i-N tunneling DG-TM-TFET with graphene nanoribbon (DG-TM-TGNFET) has been undergone a thorough DC and AC analysis, to make the model suitable for high-frequency applications. The ultra-thin graphene nanoribbon lapping over the channel bends the conduction and valence bands to procure larger band-to-band tunneling (BTBT) window. By using this device, physics and mathematical calculation used for analytical modeling of the proposed device, and the electrical parameter analysis has been performed successfully. Where, larger spike has been observed in lateral electric field distribution analysis of the proposed model. At much lower supply voltage of 0.5 V, the steeper slope, i.e., subthreshold swing (SS) becomes 19.92 mV/decade which is much lower than the other. The $I_D$ has been recorded best at $1.12 \times 10^{-4}$ A/μm and leakage current ($I_{\mathrm{OFF}}$) = $1.11 \times 10^{-16}$ A/μm. In small signal analysis, the transconductance plays key role in determining the analog performance of the device. The DG-TM-TGNFET model provides transconductance ($g_m$) of $12.82 \times 10^{-5}$ S at $V_{\mathrm{DS}} = 1$ V and $V_{\mathrm{DD}} = 0.5$ V and cut-off frequency of 0.349 THz at $V_{\mathrm{DS}} = 0.7$ V, $V_{\mathrm{DD}} = 0.5$ V, which can be utilized for high-frequency applications. The gain bandwidth product (GBP) has been recorded as 40.8 GHz.

## References

1. Nirschl T, Henzler S, Fischer J et al (2006) Scaling properties of the tunneling field effect transistor (TFET): device and circuit. Solid State Electron 50(1):44–51
2. Zhang Q, Zhao W, Seabaugh A (2006) Low-subthreshold-swing tunnel transistors. IEEE Electron Device Lett 27(4):297–300
3. Choi WY, Park BG, Lee JD (2007) Tunneling field effect transistor (TFET) with subthreshold swing (SS) less than 60mV/dec. IEEE Electron Device Lett 28(8):743–745
4. Verhulst AS, Leonelli D, Rooyackers R, Groeseneke G (2011) Drain voltage dependent analytical model of tunnel field-effect transistors. J Appl Phys 110(2):024510
5. Brocard S, Pala M, Esseni D (2012) Design options for heterojunction tunnel FETs with high on current and steep sub-VT slope. In: Proceedings IEEE international electron devices meeting (IEDM). San Francisco, CA, USA, pp 1–4
6. Lee W, Choi WY (2011) Influence of inversion layer on tunneling field-effect transistors. IEEE Electron Device Lett 32(9):1191–1193

7. Tsen KT, Poweleit C, Ferry DK, Lu H, Schaff WJ (2005) Observation of large electron drift velocities in InN by ultrafast Raman spectroscopy. Appl Phys Lett 86(22):222103
8. O'Leary SK, Foutz BE, Shur MS, Eastman LF (2006) Potential performance of indium-nitride-based devices. Appl Phys Lett 88(15):152113
9. Shen C, Ong S-L, Heng C-H, Samudra G, Yeo YC (2008) A variational approach to the two-dimensional nonlinear Poisson's equation for the modeling of tunneling transistors. IEEE Electron Device Lett 29:1252–1255
10. Wisniewski P, Majkusiak M (2018) Modeling the tunnel field-effect transistor based on different tunneling path approaches. IEEE Trans Electron Devices 65(6):2626–2631
11. Kane EO (1961) Theory of tunneling. J Appl Phys 32(1):83–91
12. Bardon MG, Neves HP, Puers R, Van Hoof C (2010) Pseudo two - dimensional model for double-gate tunnel FETs considering the junctions depletion regions. IEEE Trans Electron Devices 57(4):827–834
13. Kane EO (1960) Zener tunneling in semiconductors. J Appl Phys Chem Solids 12(2):181–188
14. Khatami Y, Banerjee K (2010) Steep subthreshold slope n and p-type tunnel-FET devices for low-power and energy efficient digital circuits. IEEE Trans Electron Devices 56(11):2752–2761
15. A. S. Verhulst, D. Leonelli, R. Rooyackers, and G. Groeseneke, Drain voltage dependent analytical model of tunnel field-effect transistors. J. Appl. Phys. **110**(2), 024510 (2011)
16. Chandan V, Nigam K, Sharma D (2019) Approach on electrically doped TFET for suppression of ambipolar and improving RF performance. IET Circuits Devices Syst 13(6):787–792
17. Cho S, Lee JS, Kim KR, Park B-G, Harris JS, Kang IM (2012) Analyses on small-signal parameters and radio-frequency modeling of gate-all-around tunneling field effect transistors. IEEE Trans Electron Devices 58(12):4164–4171
18. Madan J, Chaujar R (2017) Numerical simulation of N+ source pocket PIN-GAA-tunnel FET: impact of interface trap charges and temperature. IEEE Trans Electron Devices 64(4):1482–1488

# Design and Simulation of Microstrip Antenna for Terahertz Applications


**Prashant Kumar Singh, Shashank Kumar Singh, Gufran Ahmad, Palash Das, Sandipan Mallik, Dilip Kumar Choudhary, Hare Krishna, Shivendra Pratap Singh, and Anjini Kumar Tiwary**

**Abstract** The imperative development in the wireless technology leads to the enormous research in least discovered range of terahertz (THz) frequencies. The spectrum for newer 5G technology and earlier generations of wireless communication is positioned in millimeter/microwave regime. However, regular escalating demand of high data speed requires the devices to work on higher frequencies. The nonionizing nature, low attenuation windows, and higher penetration properties makes THz regime as the prominent candidate for future wireless communication. The THz frequencies lie between microwave and photonic region in electromagnetic spectrum. The regular increasing demand of THz technology in various applications like military, medical, spectroscopy, imaging, sensing, material characterization, and communication makes it more attentive among THz research group. Most of the application needs a means of wireless data transmission and reception, which

P. K. Singh (✉) · S. K. Singh
University College of Engineering and Technology (UCET), VBU, Hazaribag, Jharkhand 825301, India

G. Ahmad
Department of Electrical Engineering, Dayalbagh Educational Institute, Agra 282005, India

P. Das
Department of Electronics and Communication Engineering, Cooch Behar Government Engineering College, West Bengal, Cooch Behar 736170, India

S. Mallik · S. P. Singh
Department of Electronics and Communication Engineering, National Institute of Science and Technology, Berhampur, Odisha 761008, India
e-mail: sandipan@nist.edu

D. K. Choudhary
Department of ETC, G H Raisoni College of Engineering, Nagpur, Maharashtra 440016, India

H. Krishna
Department of ECE, RTC Institute of Technology, Ranchi, Jharkhand 835219, India

A. K. Tiwary
Department of ECE, Birla Institute of Technology, Mesra, Jharkhand 835215, India
e-mail: aktiwary@bitmesra.ac.in



A. Acharyya et al. (eds.), *Generation, Detection and Processing of Terahertz Signals*, Lecture Notes in Electrical Engineering 794,
https://doi.org/10.1007/978-981-16-4947-9_18

is possible through the integration of antennas in the devices. The performance of wireless systems depends on the optimal design of the antenna. In THz regime, high path loss necessitates the designing of antenna with high-gain characteristic. In last decade, numerous THz antennas are proposed even though many challenges like suitable material selection, cost-effective design, precise fabrication, integration with existing device are still persist in this domain. The microstrip technology is a better candidate for THz antennas due to its features like easier integration, simple fabrication, low cost and light weight. Initially, this work provides a survey on recent literatures on THz antennas, challenges, fabrication techniques and measurement methods. Further, a microstrip antenna is presented for THz application. The proposed antenna is designed and simulated using electromagnetic simulation software HFSS. Finally, the chapter concludes the result of designed antenna and future research possibilities for THz antennas.

**Keywords** Antenna gain · Microstrip · Path loss · Terahertz antenna

## 1 Introduction

Future generation communication require ultra-high data rate, capacity, and hence bandwidth (BW); as the expected number of wireless devices with internet connectivity by 2025 is 75 billion, which is currently approximately 23 billion. The augmented and virtual reality traffic is also expected to rise 12-fold by 2022 as compared to 2017. Additionally, the dramatic advancement and increased number of handheld wireless smart devices popularized the multimedia services among individuals worldwide, which in turn increased the digital information and data consumption as compared to wired system. The exponential growth in the wireless data speed requirement, which is targeted towards terabits per second (Tbps) [1], urge to look over the higher frequency regions in spectrum for future communication devices. The mostly untouched terahertz (THz) region is gaining more attention among researchers due to its non-ionizing property. The THz spectrum sandwiched amid microwave and photonic band is also capable of high penetration and potential of high-resolution imaging [2].

In recent years, the THz imaging gets great attention in the applications like medical, quality control, security, and non-destructive evaluation due to its non-ionizing nature, which offers lesser damage compared to X-ray imaging to the human body; and high resolution capability than microwave systems. The technological trend noticed the design and development of the devices working in THz spectrum as one of the promising fields of research due to its applications in wireless communication industry for high speed, semiconductor industry for detection of defect, pharmaceutical industry for analyzing dosage, weapon and explosive detection, biomedical industry for noninvasive imaging, and so on [3, 4]. Many researchers had reported the involvement of THz technology in security screening, atmospheric and astronomic spectroscopy [3], chemical detection [5], quality control in pharmaceutical industries

[6], material research, and future radars and communication system [7]. The THz energy transmission and reception through space or materials is possible through the antenna, which makes it imperative component in THz technology. The regular development and advancement in technology has made possible the THz generation and detection [8–10]. This opens the door to work in previously inaccessible electromagnetic (EM) spectrum, which has great potential for radio astronomy, medical imaging, and high-speed wireless technology.

This chapter covers a concise review of regular development and advancement in the designing of THz antennas. Section 2 comprise of the challenges associated with THz components, selection of the materials, fabrication process technologies, measurement methods, and several antenna design technologies. A novel microstrip patch antenna (MPA) structure with co-axial fed proposed for future technology is discussed in Sect. 3. Finally, conclusive discussion and the future scope are presented in Sect. 4.

## 2 THz Antenna Review

The antennas are vital part of any wireless devices due to its capability of transmitting and receiving the EM signals. The regular escalation in the demand of high data speed, high resolution imaging, etc. needs to move in upper frequency spectrum. Due to least touched, the THz regime is a very promising candidate for the future systems. However, there are several challenges associated with the THz technology. Since last two decades, the new materials are investigated for better working in this spectrum with several fabrication and measurement methods. These are separately briefed in this section with various available THz antenna designs.

### *2.1 Challenges*

In last few years, numerous works had been done for the design and characterization of THz antennas. However, the THz antenna design are facing various challenges as compared to microwave antennas. It is well known that the device size is inversely proportional to the frequency, and hence, the antenna size for THz band is highly reduced, which limits the fabrication technology. Another challenge is the effective radiation [11]. The material selection is also one of the major issues for development of THz antenna. Even various process methods are available in literature, but none are standardized yet [12]. The high precision manufacturing process is required for both the antenna design as well as the integration of antenna with device circuit. The antennas at THz frequencies are facing several challenges like high path loss, costly fabrication process, and manufacturing tolerance due to very small size of the THz antennas. The high path loss at THz frequencies needs high gain antennas [13]. The antenna integration with THz components is also one of the vital challenges

[14] in THz technology. Though, there are also low loss windows in THz spectrum, which can be utilized for effective THz transmission and to improve the reliability of wireless link [15].

## 2.2 Material Selection

At THz frequencies, the conventional conductor/dielectric materials used for millimeter/microwave devices depict increased losses, which in turn reduces the efficiency and gain of the THz antennas. Hence, various new materials are investigated and used in the designing of THz antennas. Copper is the most common conducting material used in the previously reported THz antenna design. A comparison of copper (Cu), carbon nanotube, and graphene materials for THz antenna design is reported in different works [16]–[18] presented. This article presented a detailed analysis of material properties of above said materials to justify the selection of the materials for antenna fabrication. At THz frequencies, the conductivity of CNT is higher than the copper, which made it more suitable. However, the graphene is best one at THz due to its inherent material property, which supports very slow surface wave. The superiority of graphene in terms of size miniaturization, reflection coefficient, and directivity is further demonstrated by designing the traditional dipole antenna for resonant frequency of 1 THz.

## 2.3 Fabrication Process Technology

In order to fabricate the THz antennas with high accuracy and precision, the researchers have explored a number of different process technologies depending upon the complexity and size of the structures. Conventional micromachining technique had been utilized in low-THz antenna fabrication [19]. However, new fabrication techniques are needed for full utilization of THz range. Laser chemical vapor deposition (LCVD) micromachining technology [20] is presented for complex three-dimensional (3D) antenna fabrication. Using LCVD, a complex 3D antenna array can be directly developed over semiconductor substrate by growing carbon fibers through laser focusing. For the fabrication of graphene-based THz Vivaldi antenna [21], the CVD method is used to develop graphene sheet over arbitrary substrate [22]. Afterward, the graphene sheet is transferred to $SiO_2$ substrate using polymethyl methacrylate [23]. Further, focus ion beam (FIB) technology is used to etch the unwanted graphene surface with the precision of nanometer size [24].

The THz Antenna illustrated in Fig. 1 with all-dielectric electromagnetic crystal (EMXT) [25] is fabricated using 3D printing technique. The fast prototyping technology, polymer jetting [26] is used to fabricate this structure. The complex and arbitrarily shaped structures can be fabricated using polymer jetting technique. The process of the prototype fabrication can be summarized stepwise as:

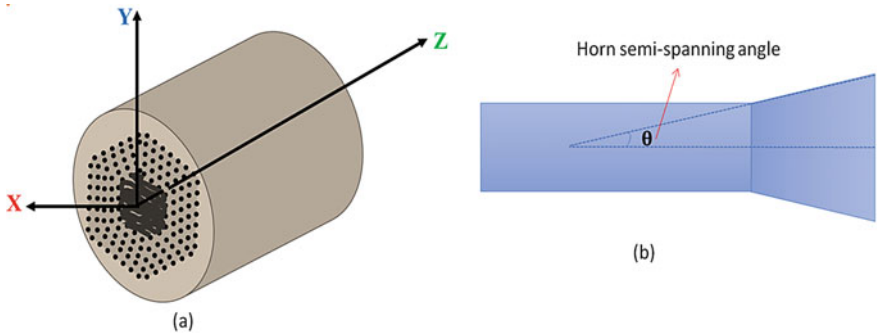


**Fig. 1** **a** An all-dielectric EMXT-based horn antenna, **b** inner EMXT horn schematic [25]

(a) To import 3D geometry of antenna structure into CAD program and convert it into layered slices.
(b) The actual antenna structure part is assigned as model material and other regions as support material (which is water soluble and gives support to the next slice).
(c) The data of each slice is sequentially sent to prototyping device, and then deposition and ultraviolet curing of each layer of polymer is performed.
(d) Further, support material is washed away by water jet with high pressure; which leaves only the required prototype structure.

The 3D printing and FIB are very popular fabrication process technologies for complex structure. For THz applications, a good and detailed review of the 3D printing technology is presented in [27]. This review chapter also presents a comparison table for several 3D printing technologies. The conventional fabrication techniques uses etching process; however, the 3D printing system, which encompasses a wide variety of additive manufacturing (AM) technique. Initially, 3D model is sliced in very thin 2D layers using the software tool, further 2D slice are deposited layer by layer using AM machine to create the designed object. General AM techniques are categorized into seven categories namely vat photopolymerization, sheet lamination, powder-bed fusion, material jetting, material extrusion, directed-energy deposition, and binder jetting [28]. The Si-based micromachining [29] is another process technology, which includes lithography, laser milling, and mold replication. Many other process technologies for THz application like milling, discharge, electroforming, and thick photoresist are well discussed and reviewed in [30].

## *2.4 Measurement and Characterization Methods*

Due to the perturbation and low bandwidth limitation, the conventional measuring system comprise of miniature antennas are not suitable for THz field measurements. To solve these problems several characterization and measurement techniques are

proposed in literature. The one solution to this issue is to use the electro-optic (EO) crystals in the sensors for measuring electric field. A free space optics-based EO sampling system [31] is used for detecting the THz pulses. In this system, the electric field is mapped by moving the antenna and fixing EO sensor at a particular position. In reference [32], a realistic measurement scheme with EO sampling probe is demonstrated, where EO sensor can be moved and also sensitivity is enhanced by minimizing the polarization effect in optical cable. Here, polarization controller elements are used in the EO probe. The optical elements used in the system, as shown in Fig. 2, are fixed inside the cylinder. The photo-detectors (PDs) are used to detect and convert the incoming signals into electrical, which is finally processed by oscilloscope or spectrum analyzer.

A method of characterizing or measuring the radiation pattern of EMXT THz horn antenna is presented in [25]. For characterization, two photoconductive antennas are used as receiver and transmitter, as shown in Fig. 3. The transmitting photoconductive antenna with EMXT antenna is fixed on the automated rotation stage to keep their relative positions unchanged.

A simple method for the impedance characterization of THz planar antenna is detailed in [33]. As the port geometry of THz antennas is in micron/submicron range; so, conventional probe characterization with large contact size is not possible. Here, the indirect impedance characterization method is used for measurement by using conventional probe at remote location on the plane of THz planar antenna.

For the characterization of on-chip dielectric resonator antenna (DRA) [34], a new comparison technique is presented due to unavailability of THz on-chip measurement systems. For demonstrating the gain enhancement of on-chip DRA as compared to on-chip patch antenna, two identical CMOS imagers are designed and integrated with these antennas individually. The comparison of the voltage responsivities at the output of the imagers demonstrates the gain enhancement of DRA.

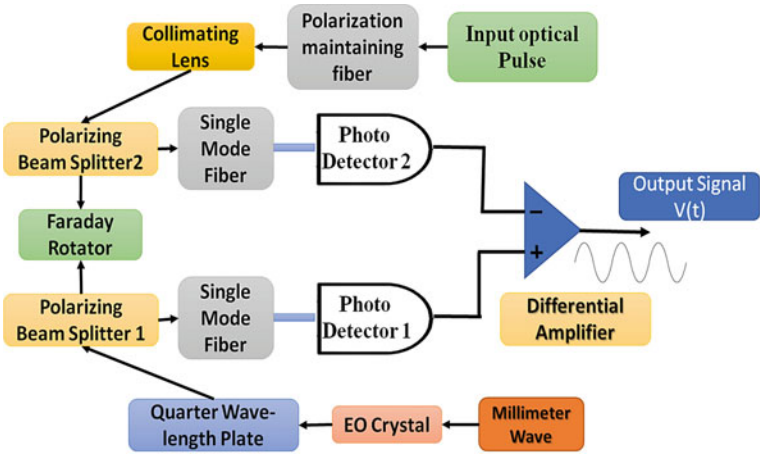


**Fig. 2** The block diagram of EO sampling system [32]

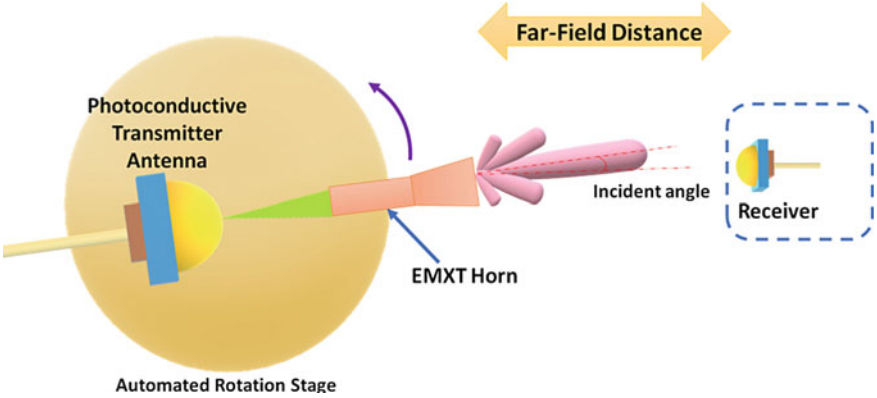


**Fig. 3** Schematic for the far-field pattern measurement of EMXT THz horn antenna [25]

## *2.5 THz Antennas*

At THz frequencies, the device size is very low and also it suffers from high atmospheric attenuation. To overcome the attenuation problem, many design methods are proposed to design antennas THz applications with increased gain. The size and complexity of antennas restricts the fabrication and measurements. However, as discussed, various methods are proposed by the researchers for the fabrication and measurements. As the THz device fabrication and characterization methods are not fully matured; many THz research groups have proposed only simulation and mathematical analysis of their designs. To improve the performance of THz antenna a number of methods, materials, designs are proposed in last two decade. This section reviews some of those THz antenna designs.

In reference [20], 3D helical antennas for 0.1–2.7 THz are demonstrated with single element and array configuration. The carbon fiber-based antenna is developed over three different substrates namely paper, steel, and silicon (Si) using LCVD technique. Here, a method to realize THz imaging device is also presented by fabricating arrayed pairs of antenna-microbolometer on same substrate. In this chapter, antenna is used as radiating element and MEMS microbolometer as THz detector.

A square spiral-shaped self-complementary antenna [35] over GaAs substrate with Si hyper-hemisphere on rear side of the substrate is proposed for THz application with high directivity. Like log-periodic and equiangular antennas [36], the self-complementary configuration also shows the possibility of frequency-insensitive antenna pattern and radiation resistance. This work presents a high value of radiation resistance (vary between approximately 100–250 Ω) for 0.1–1 THz, which violets the Booker's formula.

The electronic band-gap (EBG)/photonic band-gap (PBG) techniques [25, 37, 38] are also incorporated in THz antenna designs to improve the performance of the antennas. The EBG/PBG substrates are also incorporated in the implementation of THz antennas for better performance. The EBG/PBG substrates or crystals

are repeated arrangement of conductive or dielectric structures, which control the EM wave propagation for a range of frequencies depending upon the forbidden gap. The periodic arrangement configuration defines one, two, or three dimensional EBG/PBG. It suppresses the surface mode and redirects the radiation into substrate towards air-side. This in turn improves the directivity, gain, and bandwidth performance of the antenna. The work in [37] demonstrated the radiation efficiency, BW, and gain improvement in THz patch antenna over three-layer substrate through PBG in bottom substrate.

The EMXT as the substrate material for antenna had been employed [39] to enhance the efficiency, directivity, and bandwidth by suppressing the radiation in substrate side, substrate modes, and surface waves, as EMXT is a repeated arrangement of dielectric/metallic structures and possesses EBG feature. An EMXT-based highly directional horn antenna [25] for 0.1–0.19 THz frequency band is presented. This THz antenna is all-dielectric structure designed by flaring the straight circular EMXT waveguide into horn shape, as depicted in Fig. 1.

The photoconductive switch-based THz antennas [40] are proposed for high aperture and radiation efficiency, and directivity. This literature presented and compared simulation results of different photoconductive antennas. Here, the THz signal is generated by exposing the laser beam of very small time period (in the range of 100 fs) to the semiconductor across photoconductive gap (switch region) in the presence of an external electric field (developed between dc and ground) across the gap. In center-fed photoconductive dipole antenna [40], the legs of the dipole may work as its dc bias lines. In this chapter, authors initially reported a solo bowtie antenna for 1 THz resonating frequency. For exposing the laser beam in photoconductive gap, a cylindrical shaped structure is partially cut out through the substrate including ground plane. Further, in order to increase the directivity, the ground of the antenna is replaced by hemispherical Si lens. The directivity is further increased by integrating artificial magnetic conductor (AMC). This simplifies the antenna structure as it removes the hemispherical lens structure and becomes planar and hence reduces the fabrication complexity. Here, the AMC comprise of low-temperature grown Gallium-Arsenide (LT-GaAs) at the top of substrate, GaAs substrate and metamaterial-inspired structure consist of square loops at the ground. The incorporation of AMC had advantages of increased directivity, reduced fabrication complexity, reduced vertical size, and weight as compared to lens-based antenna, but it lowers the front-to-back ratio and increases side lobe levels (SLL). The bowtie antenna as unit element is not a good choice for THz array implementation, as the gain and impedance matching performance will decrease due to coupling between antenna elements on connecting ground and dc bias lines together (in order to array formation). So, THz dipole antenna with capacitive loading employing substrate-superstrate configuration is further introduced as a single element of antenna array. The capacitive loading is done by incorporating four rectangular patches on ground and dc bias lines of unit element. To reduce the coupling between antenna elements during array formation, the size is purposely increased four times as compared to previously designed bowtie antenna. Here, for efficient generation of electron–hole pair in photoconductive gap the cylindrical via partially through substrate including ground is modified to frustum shaped

via too. Additionally, this work reported and compared the performance of the linear array structure using capacitive loaded dipole elements, the capacitive loaded dipole antenna array with meta-films, grid antenna, and grid antenna arrays.

A metallic lens-based antenna [41] for 0.4125 THz operating frequency is reported, which is verified through simulation, fabrication, and measurement. The antenna comprise of H-plane horn, cavity, metallic lens (composed of metallic waveguides), and pyramidal horn. The H-plane horn is used to feed EM wave to metallic lens through small cavity. The widths of the metallic waveguides are kept different to transform the radiation phase of horn uniform at radiation plane. As metallic milling method is used to fabricate this antenna; hence, the three components namely feed horn, cavity, and metallic lens are intentionally designed with uniform small height to reduce the fabrication cost. To improve the radiation gain, a pyramidal horn is further integrated to the metallic lens; which will expand the E- and H-plane radiation apertures.

The graphene is also getting attention in the designing of THz antennas due to its monolayer thickness, complex conductivity and tuning property. The monolayer thickness allows to model accurate infinite thin surface, and complex conductivity allows the slow wave plasmonic propagation. The expression for this complex conductivity is given by Kubo formula, which depicts its dependencies on temperature, potential, frequency, and transport relaxation time [42]. This in turn allows employing graphene for reconfigurable/ tunable technologies.

In reference [43], the graphene is used as square patches for the first time in the designing of THz reflect-array, which is designed for 1.3 THz operating frequency. This reflect-array comprise of graphene patch elements (>25,000) over grounded substrate of quartz. The complex conductivity of graphene provides better BW and cross polarization performance with inter-element gap reduction. This work demonstrated the viability of utilization of graphene for future reconfigurable low cost reflect-arrays and highly directive antennas.

In reference [44], the tunable property of graphene is utilized in the designing of reconfigurable THz antenna with dual-band performance for the resonant frequencies of 4–5 and 6.5–7.5 THz. The reported antenna shows tunable range above 1 THz and wide BW for the dual frequency. The antenna configuration employs microstrip substrate over backing cavity with microstrip line fed patch printed over the substrate. The backing cavity patch [45, 46] enhances the performance of patch antenna in terms of improved matching, enhanced BW, reduced coupling and suppressed surface wave. The cross-sectional view of the reconfigurable dual-band patch antenna [44] is depicted in Fig. 4.

Here, the graphene stack is embedded in the cavity substrate by separating graphene sheets with $Al_2O_3$ layer. This stack connects the top and ground layer of the cavity. Several graphene stacks are embedded within this cavity along the circle with radii, $R_{outer}$. The electrostatic voltage is applied on the top and bottom layer of the cavity, which is connected through $Al_2O_3$ layer of the stack. The tuning capability of the graphene through change in electric field is used to implement the tunable backing cavity, which in turn utilized in the designing of dual-band reconfigurable

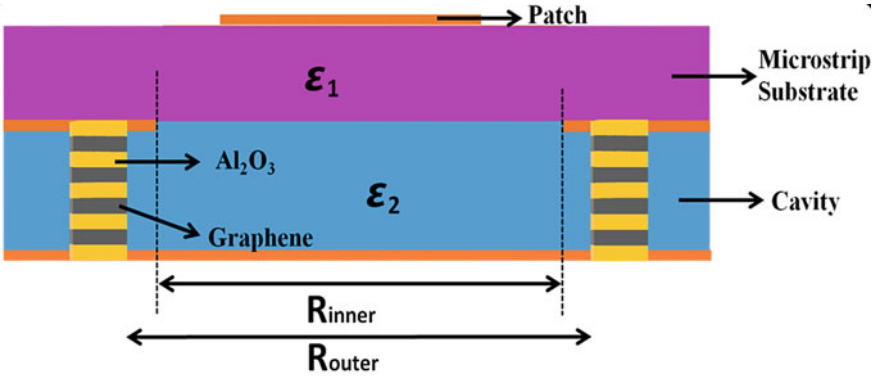


**Fig. 4** Cross-sectional view of the topology of graphene stacked backing cavity-based THz antenna [44]

antenna. The graphene stacks with different potentials in the reported antenna configuration may offer frequency and beam reconfiguration too. Graphene sheet is also utilized for the implementation of THz reconfigurable leaky wave antenna (LWA) [47]. The antenna cross-section topology is shown in Fig. 5. The reported LWA comprise of substrate-superstrate, ground, graphene sheet and extremely thin poly-Si layer. The graphene sheet and poly-Si layer are suitably placed inside the substrate as depicted in the figure. The poly-Si layer works as gate electrode, which tunes the conductivity of graphene based on the applied bias voltage. This chapter presented the fixed frequency beam scanning via changing the bias potential. The effect of graphene on the radiation and dispersion properties is also detailed with comparison of graphene-based substrate-superstrate (GSS) and graphene-based planar waveguide (GPW) structure. This study shows the superiority of GSS over GPW in terms of scanning range and directivity.

A dual-band graphene-based patch antenna array [38] is designed for 0.9039 and 0.9908 THz resonant frequencies, with high radiation performance using PBG and

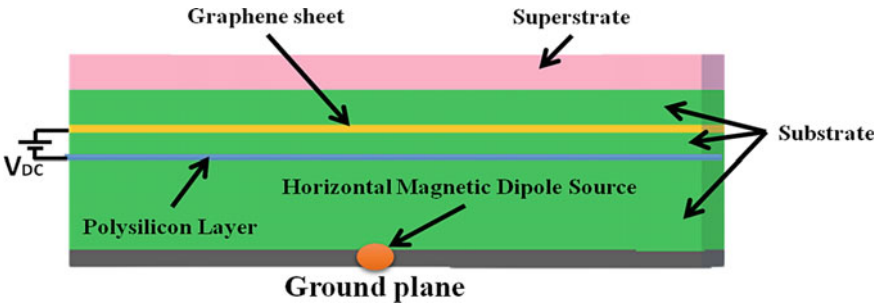


**Fig. 5** Cross-sectional view of graphene-based reconfigurable leaky wave antenna in substrate-superstrate configuration [47]

dielectric grating techniques. The leaky wave can be realized from travelling wave using the periodic dielectric grating [48] and the grating period ($G_p$) controls it. In THz regime, the periodic grating with ground plane illustrates several beaming performance. Figure 6 depicts the configuration of gratings with PBG substrate used in the design of antenna array [38]. This work presented dependency of return loss at resonating frequency on the grating period and performance improvement using the grating structure. The antenna array configuration comprises of conducting ground (first layer (at the bottom)), PBG substrate (second layer), periodic dielectric grating (third layer), silicon dioxide substrate (fourth layer), and graphene patches with microstrip line (both on the same plane at top layer (fifth layer)) for parasitic coupled feed as illustrated in Fig. 7. Here, the 2D graphene (single layer) is transformed to 3D by stacking 10 layers of graphene. The graphene is used as the material of microstrip feed line and patches for the miniaturization of array antenna and due to its unique material properties. The parasitic feed network reduces the structural complexity

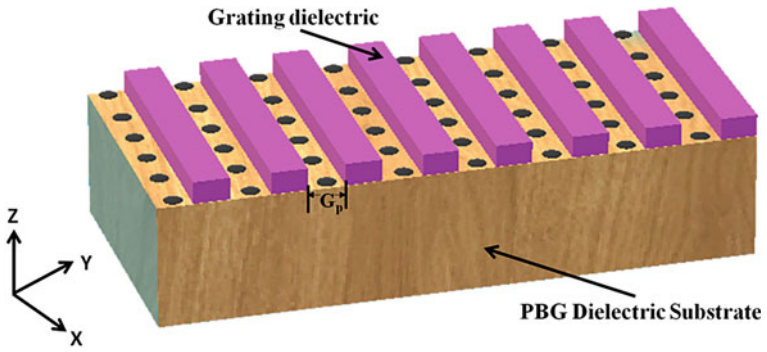


**Fig. 6** Topology of periodic grating over PBG substrate [38]

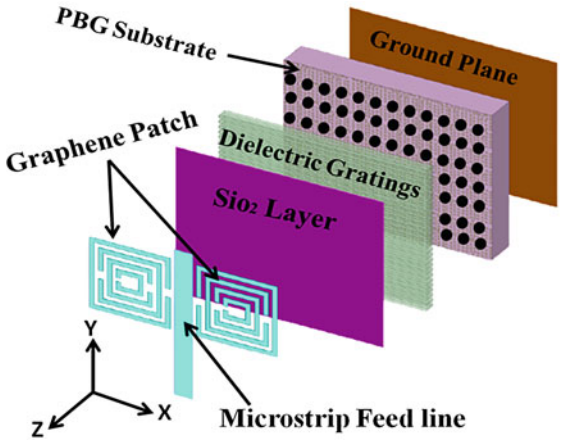


**Fig. 7** Schematic of the graphene-based antenna array with PBG and dielectric gratings [38]

as well as the conductor loss, which in turn improves radiation performance and impedance BW matching.

The accuracy of the imaging system is of utmost importance to precisely identify the smaller objects like skin, water content, weapons, and explosives [49], which needs the high-resolution image. The increase in resolution can be obtained by using THz imaging technology with wide BW. The THz device with wider BW is also a promising candidate to achieve more data rates for future wireless communication with high speed and quality. A graphene nonoribbon-based reconfigurable THz antenna [50] is reported, which shows wideband performance of 26% impedance BW at 1 THz center frequency. The antenna configuration is illustrated in Fig. 8. Here, reconfigurability is achieved by using the tuning capability of graphene material and applying the dc bias between top graphene nanoribbon-based patch (comprise of stack of 10 graphene layers) and polysilicon layer as depicted in Fig. 8. The ring structured patch is used in order to get increased BW. The rectangular double ring structure is used in this work, which resonates at two frequencies and hence further widens the BW of the antenna with efficient radiation.

A reconfigurable Vivaldi antenna [21] for THz application is also reported, which is designed by using graphene in place of metal at the top of $SiO_2$ dielectric. The feeding is done by microstrip line at the bottom of the substrate, which is terminated in a radial sector. Further, a novel graphene-metal-based hybrid structure is used in place of graphene at the top. This reduces the reflection coefficient; however, it demonstrates enhanced antenna gain and radiation efficiency.

The portable electronic devices are need of current era, which requires the integration of THz systems on the device. The CMOS technology has the potential to solve this problem and is a good candidate for lightweight on-chip THz devices. The THz antenna is one of the critical components of THz devices, and nowadays, many researchers are working in the designing of on-chip THz antennas. The simple on-chip patch antenna shows very low gain, which is due to very low separation between the patch and ground conductor. This in turn tightly bounds the EM fields and restricts effective radiation from the antenna. A low-cost DRA is proposed to enhance the gain of on-chip THz antenna [34]. A low loss and high impedance or

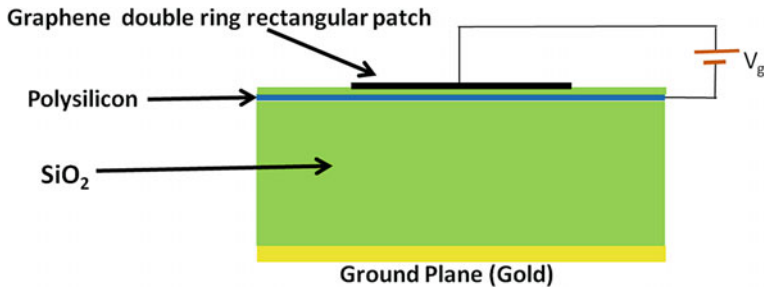


**Fig. 8** Reconfigurable graphene nanoribbon-based THz antenna schematic [50] with bias potential $V_g$

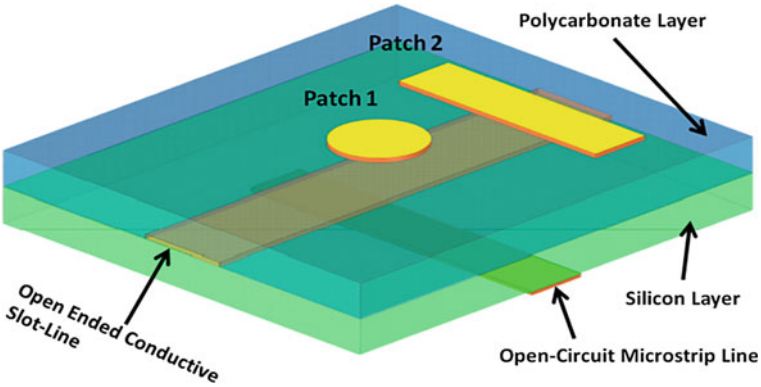


**Fig. 9** Aperture excited on-chip antenna element for array design [51]

resistivity Si material is used as the dielectric resonator (DR). The desired EM mode is excited through on-chip patch feeding realized in CMOS technology (0.18-μm). Here, higher order mode is excited (not fundamental mode) to increases the thickness of DR, which helps to make the fabrication feasible by Si wafer dicing technique. This enhances the gain of the antenna. The antenna efficiency is increased by including the ground plane to prevent the leakage of EM Field into lossy Si CMOS substrate. Further, this work demonstrated the THz transmissive imaging system by employing the CMOS imager integrated DRA.

The low profile, high gain Si-based on-chip antenna array for sub-THz application with simple design topology is investigated and verified through fabrication and measurements [51]. The reported array illustrates peak radiation efficiency and gain at 0.3 THz. The topology of unit element of the array is depicted in Fig. 9, which comprise of an open circuited metallic slot line sandwiched between two substrates namely Si and polycarbonate, a microstrip line (open ended) at the bottom of Si substrate placed orthogonal relative to conductive slot line, and two radiating patches (circular and rectangular) at the top of polycarbonate. The two patches are used in order to achieve circular polarization. The array is developed by using 15 unit elements over extended slot line with an orthogonally placed microstrip line at the center. Here, the high gain is realized by using aperture fed technique through conductive slot line to excite the antenna. Initially, microstrip line at the bottom of Si layer is excited, which couples the EM energy to slot line. Further, the signal is coupled to patch array through slot line. As part of the fabrication process, the sputter deposition technique is used for the conducting layers, and thermal compression with controlled annealing temperature to avoid fracturing is used for bonding substrates together.

In reference [52], CMOS integration compatible LWAs are presented for wideband operation. The antennas are double leaky slot lens antennas. One with center-fed

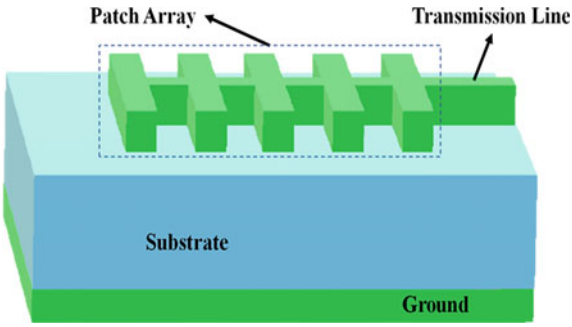


**Fig. 10** Series fed MPA array configuration [55]

configuration, which is operating over 0.2–0.6 THz, and other one is coplanar waveguide fed operates over 0.25–0.5 THz, which is developed for performance verification through fabrication and testing. Although, several design methods are developed and reported for the designing of antennas for THz appliances. However, considering several challenges in the THz antenna design, the microstrip patch antennas (MPA) looks one of the better candidates due to its easier integration and fabrication. In last few years, many MPAs are reported for THz application. In references [53] and [54], MPAs are successfully fabricated using simple etching process and tested up to 0.1 THz. The MPA array [55] comprises of series fed five symmetrical rectangular patches as shown in Fig. 10 is designed and reported for medical application. The liquid crystalline polymer is used as the substrate for designing this MPA. For cancer and vital sign detection, the MPA array is developed with resonating frequencies of 0.635 and 0.835 THz. For verification of the design approach used here is further done by fabricating and testing the prototype at 0.1 THz.

## 3 Proposed Patch Antenna

Initially, a simple circular patch structure, shown in Fig. 11, is designed for THz application. The substrate chosen for the antenna design is FR4 epoxy with the thickness ($H_s$) of 0.138 mm. The structure is fed with coaxial feeding technique and feeding point location is the center of the circular patch. The internal radius of probe and external radius of coaxial cable are 0.07 mm and 0.16 mm, respectively. The optimized value of radius of the circular patch is obtained as $R_1 = 0.14625$ mm for the resonance at 0.3 THz, which comes in low attenuation window of THz spectrum. The dimension of both $W_s$ and $L_s$ depicted in Fig. 11 are 0.6 mm.

This structure is simulated through HFSS software and the result of return loss (S11) is shown in Fig. 12. The S11 plot illustrate that the goal of antenna design are not met with it, and the return loss is above −8 dB. So, the efficient radiation will not take place.

Further, in order to achieve good return loss, VSWR and gain, a novel patch configuration is proposed for the THz antenna design. The proposed configuration

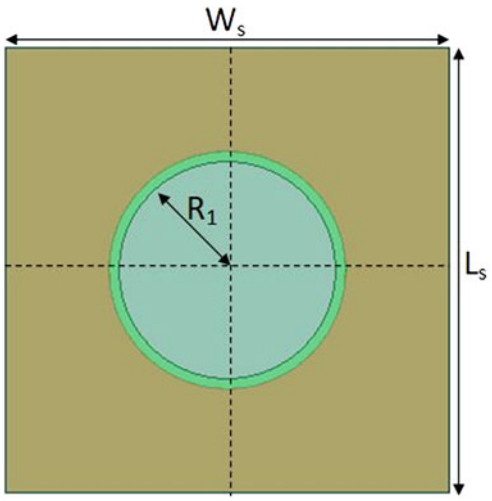


**Fig. 11** Top view of circular patch antenna

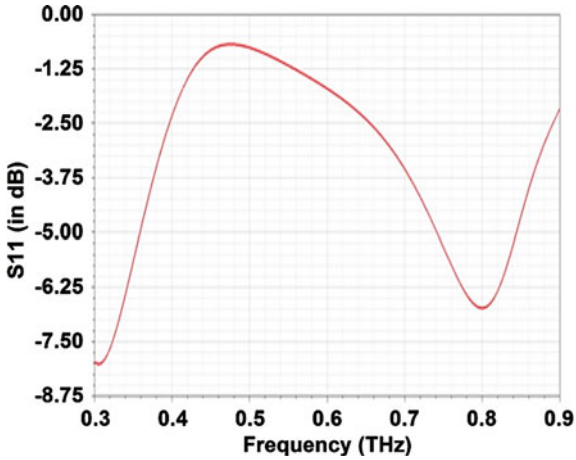


**Fig. 12** S11 parameter plot for the circular patch antenna

is achieved by etching out some portion from the conventional circular patch. The modification in design resulted in oppositely connected symmetrical circular strips to a circular patch as shown in Fig. 13a. Its 3D view as designed in the simulation software with coaxial feed is depicted in Fig. 13b. The circular strips in the figure are designated by outer radii $R_1$ and inner radii $R_2$. The outer arc length ($A$) of these strips can be calculated by using Eq. (1).

$$A = \text{spanning angle} \times R_1 \tag{1}$$

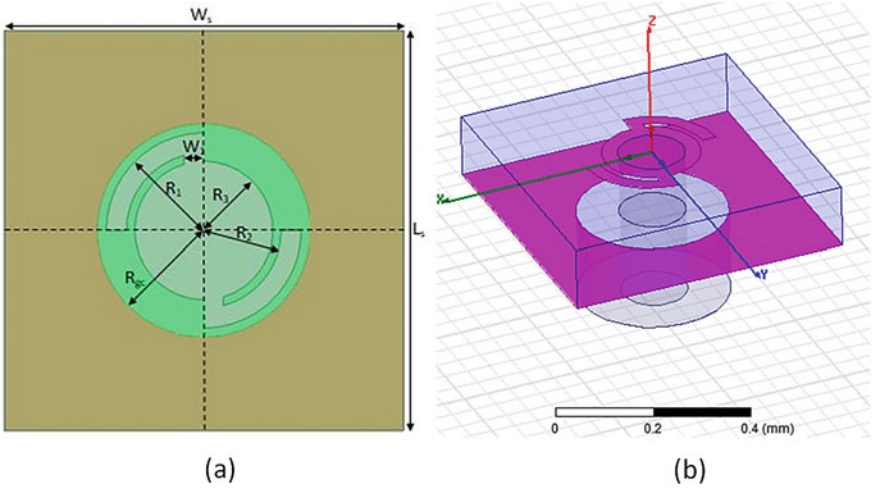


**Fig. 13** Proposed THz antenna configuration **a** top view, **b** side view of the proposed structure

In the proposed design, $R_1$, $W_s$, $L_s$, $H_s$, and the radii of coaxial cable and probe are kept same as for circular patch antenna. The other parameters in the proposed design are $R_2 = 0.11625$ mm, $R_3 = 0.10375$ mm, and $W = 0.03$ mm.

The simulated S11 plot of proposed antenna with different arc lengths is shown in Fig. 14. Three different arc lengths ($A$) are considered here to demonstrate the dependency of resonant frequency on it. It is obvious from the figure that the increase in the arc length decreases the resonant frequency with slight change in return loss; hence, one can control the resonant frequency by varying the arc length. For all the three lengths, the return loss is well below −30 dB with −10 dB BW in the range

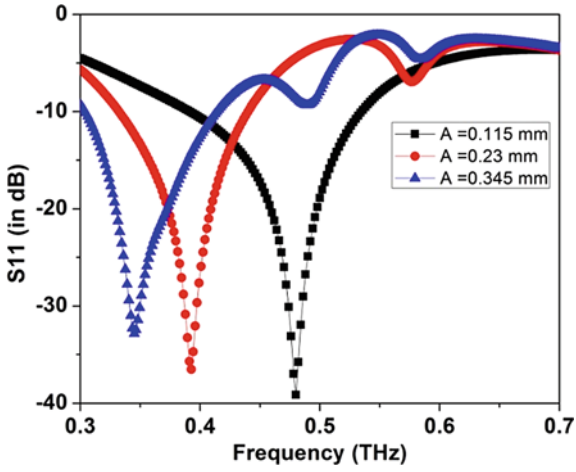


**Fig. 14** Simulation result of proposed THz antenna with variation in arc length of the circular strip

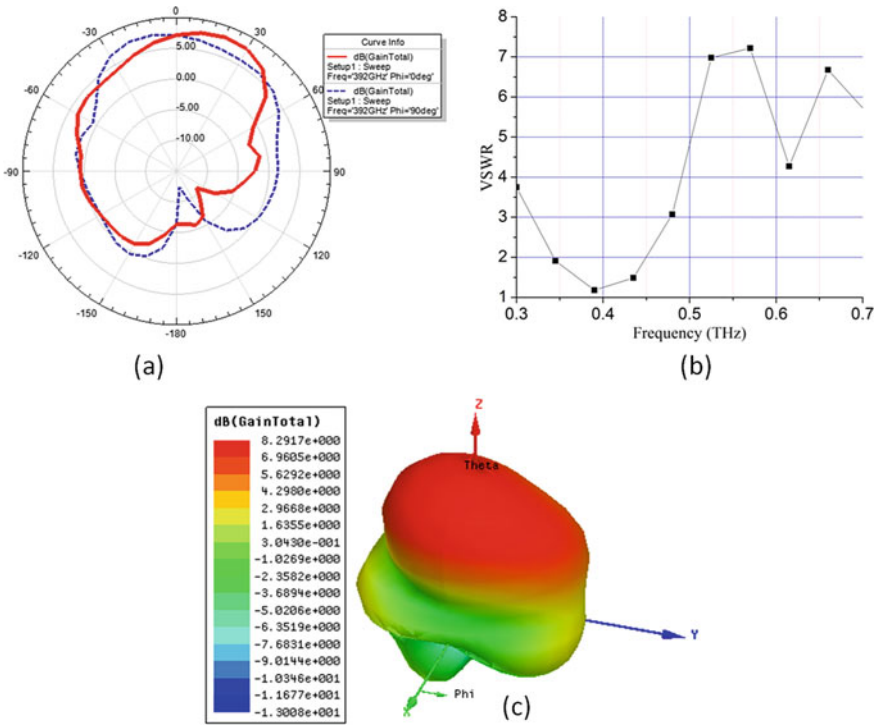


**Fig. 15** Simulated results of proposed THz antenna for outer arc length, A = 0.23 mm for 0.392 THz resonant frequency **a** radiation pattern, **b** VSWR plot, **c** 3D gain plot

of 0.1 THz. The resonant frequencies for A = 0.115 mm, 0.23 mm, and 0.345 mm are 0.48 THz, 0.392 THz, and 0.345 THz, respectively. For the configuration shown in Fig. 13a, i.e., A = 0.23 mm, the radiation pattern, VSWR, and 3D gain plot are illustrated in Fig. 15a, b, and c, respectively. These show the VSWR of 1.2 and peak gain of 8.2917 dB at the resonant frequency 0.392 THz, which illustrates very efficient radiation from the proposed antenna configuration.

## 4 Summary

This chapter reviewed and explored several THz antenna designs and methods used in challenges, material selection, fabrication process technologies, and characterization methods. The size of the antenna is fraction of wavelength of the signal to be transmitted or received, and the wavelength is inversely proportional to the operational frequency. That is, the increase in frequency reduces the dimension of the antenna. At THz frequency, this size is in the range of micro/nano- meter, and for this antenna size, it is very difficult to fabricate and characterize the designed THz

antennas with available conventional technologies. The integration of the antenna with the THz devices is also a challenge. Several solutions are presented and demonstrated by the researchers in past to solve these problems. Though, none of the process and characterization technology is standardized yet. The regular advancement in 3D printing/AM technology for the manufacturing looks to solve the fabrication problem and expected to provide low cost solution with high precision in future. The materials properties like dielectric constant, conductivity, and losses are also changed at these frequencies which needs the incorporation of new nanomaterials for the THz antenna designs. Out of the several materials, the graphene as conductor and $SiO_2$ as dielectric seems a competitive contender for future THz technology due to their better material properties at THz frequencies. Also, the graphene shows its capability of tuning the complex conductivity by using dc bias circuit, which is utilized in various works for the reconfigurability. The MPA incorporating the graphene as conductor, $SiO_2$ as dielectric and EBG/PBG patterns at the ground may be a contender for its employment in future THz devices due to its planar configuration, which provides simple and low-cost fabrication. This is also emerging as a popular technology for portable devices due to its light weight and compact size. It is also compatible for the integration with other THz system devices. The involvement of graphene and EBG/PBG ground helps to improve the gain, directivity, and efficiency of the antenna.

After the brief review, a planar novel microstrip patch structure is proposed for THz antenna design. The FR-4 substrate with dielectric constant of 4.5 and thickness of 0.138 mm is used for the proposed design. The proposed MPA illustrates very good return loss of −39 dB with 8.2917 dB peak gain and 1.2 VSWR at resonant frequency 0.392 THz with BW above 0.1 THz for outer arc length, $A = 0.23$ mm. The simulated results demonstrate the suitability of proposed structure for future THz devices. The planar configuration is used here for the proposed antenna design, due to its simple fabrication process, light weight, easier integration with other devices, etc.

In future, the extended work with improved performance parameters and proposed patch for THz application will be reported. In order to further improve the performance, EBG/PBG techniques with different conductor and dielectric material and array configuration will be incorporated.

## References

1. Jamshed MA, Nauman A, Abbasi MAB, Kim SW (2020) Antenna Selection and Designing for THz Applications: Suitability and Performance Evaluation: A Survey. IEEE Access 8:113246–113261
2. Mukherjee P, Gupta B (2008) Terahertz (THz) frequency sources and antennas-A brief review. Int J Infrared Millimeter Waves 29(12):1091–1102
3. Siegel PH (2002) Terahertz technology. IEEE Trans Microw Theory Tech 50(3):910–928
4. Song H-J, Nagatsuma T (2011) Present and future of terahertz communications. IEEE Trans. terahertz Sci. Technol. 1(1):256–263
5. Siegel PH (2004) Terahertz technology in biology and medicine. IEEE Trans Microw Theory Tech 52(10):2438–2447

6. Ferguson B, Zhang X-C (2002) Materials for terahertz science and technology. Nat Mater 1(1):26–33
7. Fitch MJ, Osiander R (2004) Terahertz waves for communications and sensing. Johns Hopkins APL Tech. Dig. 25(4):348–355
8. Dhillon SS et al (2017) The 2017 terahertz science and technology roadmap. J Phys D Appl Phys 50(4):43001
9. R. Al Hadi et al., A 1 k-pixel video camera for 0.7–1.1 terahertz imaging applications in 65-nm CMOS. IEEE J. Solid-State Circuits 47(12), 2999–3012 (2012)
10. Mueller ER (2003) Terahertz radiation: Applications and sources. Ind Phys 9(4):27–30
11. T. Nagatsuma, Antenna technologies for terahertz communications. in 2018 International Symposium on Antennas and Propagation (ISAP), (2018), pp. 1–2
12. He Y, Chen Y, Zhang L, Wong S-W, Chen ZN (2020) An overview of terahertz antennas. China Commun. 17(7):124–165
13. K. R. Jha and G. Singh, Improved performance analysis of square patch microstrip antenna at terahertz frequency. in 2009 International Conference on Advances in Recent Technologies in Communication and Computing, (2009), pp. 676–679
14. E. Seok et al., A 410 GHz CMOS push-push oscillator with an on-chip patch antenna. in 2008 IEEE International Solid-State Circuits Conference-Digest of Technical Papers, (2008), pp. 472–629
15. Huang K-C, Wang Z (2011) Terahertz terabit wireless communication. IEEE Microw Mag 12(4):108–116
16. Dash S, Patnaik A (2018) Material selection for TH z antennas. Microw Opt Technol Lett 60(5):1183–1187
17. Keller SD, Zaghloul AI, Shanov V, Schulz MJ, Mast DB, Alvarez NT (2014) Electromagnetic simulation and measurement of carbon nanotube thread dipole antennas. IEEE Trans Nanotechnol 13(2):394–403
18. Choi S, Sarabandi K (2010) Performance assessment of bundled carbon nanotube for antenna applications at terahertz frequencies and higher. IEEE Trans Antennas Propag 59(3):802–809
19. Katehi LPB, Rebeiz GM, Weller TM, Drayton RF, Cheng H-J, Whitaker JF (1993) Micromachined circuits for millimeter-and sub-millimeter-wave applications. IEEE Antennas Propag Mag 35(5):9–17
20. Dean RN Jr, Nordine PC, Christodoulou CG (2000) 3-D helical THz antennas. Microw Opt Technol Lett 24(2):106–111
21. J. Jin, Z. Cheng, J. Chen, T. Zhou, C. Wu, and C. Xu, Reconfigurable terahertz Vivaldi antenna based on a hybrid graphene-metal structure. Int. J. RF Microw. Comput. Eng. 30(5), e22175 (2020)
22. Saeed M, Hamed A, Wang Z, Shaygan M, Neumaier D, Negra R (2018) Metal–insulator–graphene diode mixer based on CVD graphene-on-glass. IEEE Electron Device Lett 39(7):1104–1107
23. Zhang B, Jornet JM, Akyildiz IF, Wu ZP (2019) Mutual coupling reduction for ultra-dense multi-band plasmonic nano-antenna arrays using graphene-based frequency selective surface. IEEE Access 7:33214–33225
24. Zakrajsek L, Einarsson E, Thawdar N, Medley M, Jornet JM (2016) Lithographically defined plasmonic graphene antennas for terahertz-band communication. IEEE Antennas Wirel Propag Lett 15:1553–1556
25. Wu Z, Liang M, Ng W-R, Gehm M, Xin H (2012) Terahertz horn antenna based on hollow-core electromagnetic crystal (EMXT) structure. IEEE Trans Antennas Propag 60(12):5557–5563
26. Wu Z, Ng W-R, Gehm ME, Xin H (2011) Terahertz electromagnetic crystal waveguide fabricated by polymer jetting rapid prototyping. Opt Express 19(5):3962–3972
27. J. Sun and F. Hu, Three-dimensional printing technologies for terahertz applications: A review. Int. J. RF Microw. Comput. Eng. 30(1), e21983 (2020)
28. I. Astm, ASTM52900–15 standard terminology for additive manufacturing—general principles—terminology. ASTM Int. West Conshohocken, PA 3(4), 5 (2015)

29. Lubecke VM, Mizuno K, Rebeiz GM (1998) Micromachining for terahertz applications. IEEE Trans Microw Theory Tech 46(11):1821–1831
30. Chattopadhyay G, Reck T, Lee C, Jung-Kubiak C (2017) Micromachined packaging for terahertz systems. Proc. of IEEE 105(6):1139–1150
31. Wu Q, Zhang X-C (1996) Design and characterization of traveling-wave electrooptic terahertz sensors. IEEE J Sel Top Quantum Electron 2(3):693–700
32. H. Togo, A. Sasaki, A. Hirata, and T. Nagatsuma, Characterization of millimeter-wave antenna using photonic measurement techniques. Int. J. RF Microw. Comput. Eng. Co-sponsored by Cent. Adv. Manuf. Packag. Microwave, Opt. Digit. Electron. Univ. Color. Boulder 14(3), 290–297 (2004)
33. Topalli K, Trichopoulos GC, Sertel K (2011) An indirect impedance characterization method for monolithic THz antennas using coplanar probe measurements. IEEE Antennas Wirel Propag Lett 11:3–5
34. Li C-H, Chiu T-Y (2017) 340 GHz low-cost and high-gain on-chip higher order mode dielectric resonator antenna for THz applications. IEEE Trans. Terahertz Sci. Technol. 7(3):284–294
35. Brown ER, Lee AWM, Navi BS, Bjarnason JE (2006) Characterization of a planar self-complementary square-spiral antenna in the THz region. Microw Opt Technol Lett 48(3):524–529
36. V. H. Rumsey, Frequency independent antennas. Academic Press (New York, 1966)
37. A. Sharma, G. Singh, and D. S. Chauhan, Design considerations to improve the performance of a rectangular microstrip patch antenna at THz frequency. in 2008 33rd International Conference on Infrared, Millimeter and Terahertz Waves, (2008), pp. 1–2.
38. Kushwaha RK, Karuppanan P (2020) Parasitic-coupled high-gain graphene antenna employed on PBG dielectric grating substrate for THz applications. Microw Opt Technol Lett 62(1):439–447
39. K. C. Huie, Microstrip antennas: broadband radiation patterns using photonic crystal substrates. Virginia Tech (2002)
40. Zhu N, Ziolkowski RW (2013) Photoconductive THz antenna designs with high radiation efficiency, high directivity, and high aperture efficiency. IEEE Trans. terahertz Sci. Technol. 3(6):721–730
41. Hao Z-C, Wang J, Yuan Q, Hong W (2017) Development of a low-cost THz metallic lens antenna. IEEE Antennas Wirel Propag Lett 16:1751–1754
42. Hanson GW (2008) Dyadic Green's functions and guided surface waves for a surface conductivity model of graphene. J Appl Phys 103(6):64302
43. Carrasco E, Perruisseau-Carrier J (2013) IEEE Antennas Wirel Propag Lett 12:253–256
44. Dong Y, Liu P, Yu D, Li G, Tao F (2016) Dual-band reconfigurable terahertz patch antenna with graphene-stack-based backing cavity. IEEE Antennas Wirel Propag Lett 15:1541–1544
45. Awida MH, Suleiman SH, Fathy AE (2011) Substrate-integrated cavity-backed patch arrays: A low-cost approach for bandwidth enhancement. IEEE Trans Antennas Propag 59(4):1155–1163
46. Awida MH, Fathy AE (2012) Design guidelines of substrate-integrated cavity-backed patch antennas. IET microwaves, antennas Propag 6(2):151–157
47. Fuscaldo W, Burghignoli P, Baccarelli P, Galli A (2016) A reconfigurable substrate–superstrate graphene-based leaky-wave THz antenna. IEEE Antennas Wirel Propag Lett 15:1545–1548
48. Li J, He M, Wu C, Zhang C (2017) Radiation-pattern-reconfigurable graphene leaky-wave antenna at terahertz band based on dielectric grating structure. IEEE Antennas Wirel Propag Lett 16:1771–1775
49. Malhotra I, Jha KR, Singh G (2018) Terahertz antenna technology for imaging applications: A technical review. Int J Microw Wirel Technol 10(3):271
50. M.-R. Nickpay, M. Danaie, and A. Shahzadi, Wideband rectangular double-ring nanoribbon graphene-based antenna for terahertz communications. IETE J. Res., 1–10 (2019)
51. Alibakhshikenari M et al (2020) High-gain on-chip antenna design on silicon layer with aperture excitation for terahertz applications. IEEE Antennas Wirel Propag Lett 19(9):1576–1580
52. van Berkel S et al (2020) Wideband Double Leaky Slot Lens Antennas in CMOS Technology at Submillimeter Wavelengths. IEEE Trans. Terahertz Sci. Technol. 10(5):540–553

53. Rabbani MS, Ghafouri-Shiraz H (2016) Improvement of microstrip patch antenna gain and bandwidth at 60 GHz and X bands for wireless applications. IET Microwaves, Antennas Propag 10(11):1167–1173
54. Rabbani MS, Ghafouri-Shiraz H (2015) Improvement of microstrip antenna's bandwidth and fabrication tolerance at terahertz frequency bands. IET Microwaves Antennas Propag 10(11):1167–1173
55. Rabbani MS, Ghafouri-Shiraz H (2017) Liquid crystalline polymer substrate-based THz microstrip antenna arrays for medical applications. IEEE Antennas Wirel Propag Lett 16:1533–1536

# Trends in Terahertz Biomedical Applications


**Debabrata Samanta, M. P. Karthikeyan, Daksh Agarwal, Arindam Biswas, Aritra Acharyya, and Amit Banerjee**

**Abstract** Terahertz radiation has drawn enormous attention in recent times due to its various application possibilities. This chapter reviews various emerging trends and well-established technologies in Terahertz biomedical. Due to its extraordinary sensing capabilities, non-invasive, non-ionizing properties, sensitive instrumentations for spectroscopy and imaging, Terahertz has found various biomedical sensing applications from biomolecules, proteins to cells and tissues. This chapter highlights terahertz device engineering, system technologies, range of materials, aiming at various biomedical applications. It also includes emerging topics such as terahertz biomedical imaging, pattern recognition and tomographic reconstruction by machine learning and artificial intelligence, for possible biomedical imaging applications.

**Keywords** Biomedical imaging · Terahertz · Non-invasive · Non-ionizing · Tomography

D. Samanta (✉)
Department of Computer Science, CHRIST (Deemed to be) University, Bangalore, Karnataka, India

M. P. Karthikeyan
Department of Computer Science, PPG College of Arts and Science, Coimbatore, India

D. Agarwal
Department of Materials Science and Engineering, University of Pennsylvania, Philadelphia, PA 19104, USA

Currently At Lam Research Corporation, Fremont, CA 94538, USA

A. Biswas
Mining Engineering Department, Centre for Organic Spin-Tronics and Optoelectronics Devices (COSOD), Kazi Nazrul University, Asansol, Burdwan, West Bengal 713340, India

A. Acharyya
Department of Electronics and Communication Engineering, Cooch Behar Government Engineering College, Harinchawra, GhughumariWest Bengal, Cooch Behar 736170, India

A. Banerjee (✉)
Physics Department, Bidhan Chandra College, Asansol, West Bengal 713303, India



A. Acharyya et al. (eds.), *Generation, Detection and Processing of Terahertz Signals*, Lecture Notes in Electrical Engineering 794,
https://doi.org/10.1007/978-981-16-4947-9_19

## 1 Terahertz Radiation and Devices

Terahertz (THz) radiation has drawn immense attention due to a vast range of possible applications. However, THz waves are not suitable for terrestrial radio applications because of strong absorption by atmospheric gases leading to high attenuation within a few metres in ambiance. THz radiation unlike X-rays is non-ionizing and hence does not harm live cells. But THz wave said in the production of high-resolution images. This radiation can be used to characterize materials, inspect layers, detect bombs, expose secret arms, inspect tiles on the space shuttle for defects, and detect skin cancer and tooth decay. THz technology has many uses in surveillance, pathogen detection, information science, biology, medicine, astronomy, and environmental science. For successful implementation of THz technology, suitable THz sources as well as compact and efficient detectors need to be developed.

Currently, various semiconductor devices like quantum cascade lasers (QCLs), high electron mobility transistors (HEMTs) and hetero junction bipolar transistors (HBTs) have evolved as potential THz sources. However, there is still need for compact, cost-effective, efficient and powerful solid-state source at this frequency range. Impact Avalanche Transit Time (IMPATT) devices based on wide bandgap semiconductors like GaN are found to generate appreciable power at THz band and have been proposed by the authors [1–3].

While photon detectors in the visible spectrum have been around for a long time, detectors in the THz range are much harder to build. This is because the photon energy in the visible spectrum is typically of the energy range ~1.6 to 3.3 eV, while THz photon energy is in the range ~0.41 to 41 meV, which is of the order of room temperature energy (~25 meV). Thus, ambient noise is of the same or higher order as the energy of THz photons, making it tough to build detectors in the THz range. However, significant progress has been made in developing THz detectors in recent decades [4, 5]. THz detectors that are available today can be broadly categorized into five main kinds based on the mechanism used for detection [6]: (a) THz radiation heats a material leading to change in a physical property (e.g. Golay cell, thermocouples, bolometers, pyro-electric detectors), (b) THz radiation interacts with plasmons in a medium (FETs), (c) THz radiation induces an electron transition (e.g. Schottky Barrier diodes (SBDs), photo-detectors), (d) THz radiation is mixed with reference radiation in a nonlinear medium (heterodyne detection, laser feedback interferometer), (e) THz radiation interacts with ultrashort optical pulses (optical rectification). Of this bolometer, thermocouples, Plasmon-based detectors and SBD have drawn significant interest because of their applications in broadband THz imaging. Heterodyne detection and laser feedback interferometer are narrowband, precise techniques and have also been used for imaging applications in the field of astronomy [7]. Various possible application of THz technology has been projected with schematics in Fig. 1 along with THz spectrum with THz distance in Fig. 2. The following sections of this article review the recent developments in THz biomedical applications, mainly. The prospects of medical application of THz have been highlighted in Fig. 3 and Table 1.

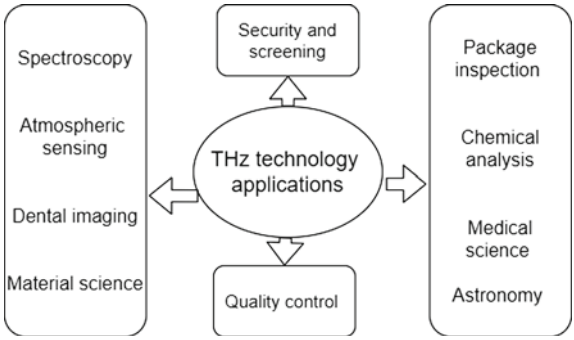


**Fig. 1** Various applications of THz technology

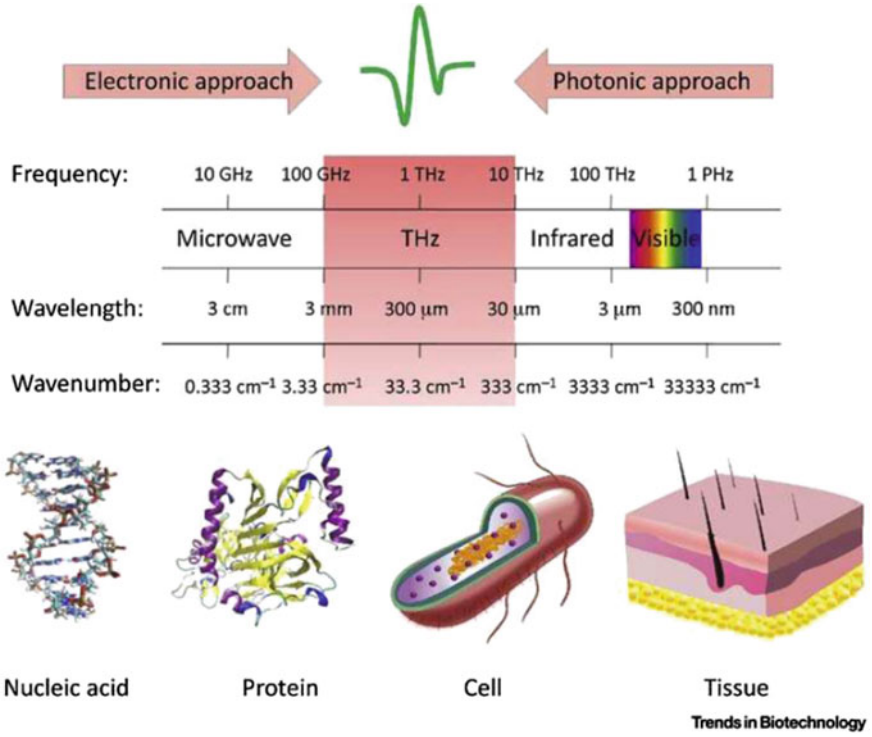


**Fig. 2** The terahertz (THz) spectrum, includes the "THz distance". THz technology is being used to detect a wide range of biomaterials, biomolecules, nucleic acids, and proteins at the cellular and tissue levels. Reproduced with permission from X. Yang, X. Zhao, K. Yang, Y. Liu, Y. Liu, W. Fu, Y. Luo, Biomedical applications of terahertz spectroscopy and imaging, Trends in Biotechnology 34(10), 810–824 (2016)

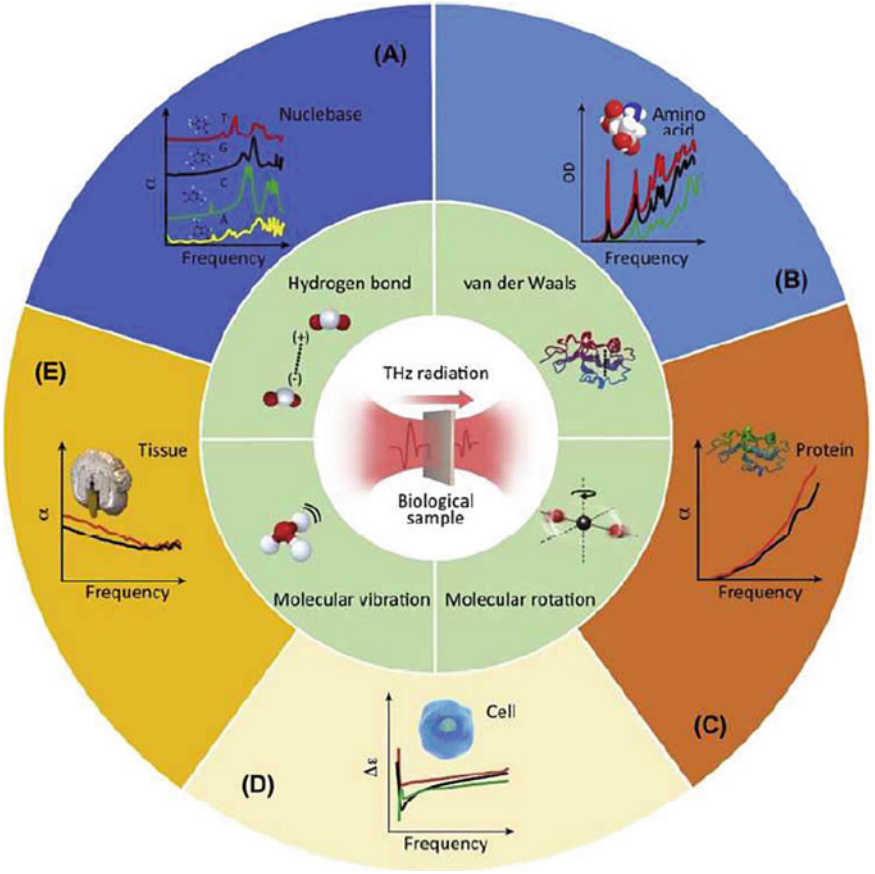


**Fig. 3** Terahertz (THz) spectroscopy has the potential to be used in biomedicine. THz can couple with low-frequency molecular rotations and vibrations of biomaterials, hydrogen bonds, weak interactions, and van der Waals interactions in the THz range, so it can be used for biomolecular probing, as shown in (A) THz absorption (absorption coefficient a) for the nucleobases adenosine (A), cytosine (C), guanine (G), and threonine (7) at 10 K. (B) OD of L-glutamic acid with THz (at different concentrations: 0.314 [green], 0.585 [black], and 0.837 mol [red]), found to be linearly proportional to concentration with notable and distinct peaks at 1.22, 2.03, 2.46, 2.68, 2.80, and 3.24 THz. THz absorption coefficient (a) at 270 K for lysozyme (HEWL, egg white) solution (red) and HEWL I triacetylglucosamine solution (black). (D) Dielectric constants of distilled water and cultured human cancer cells, such as DLD-1 (red), HEK293 (black), and HeLa (blue) (green). (E) A comparison of the absorption coefficient (a) of paraffin-embedded brain gliomas (red) and normal tissues (black) reveals that x for glioma tissue is higher than for normal tissue below 1 THz, but not at higher frequencies [ reproduced with permission from X. Yang, X. Zhao, K. Yang, Y. Liu, Y. Liu, W. Fu, Y. Luo, Biomedical applications of terahertz spectroscopy and imaging, Trends in Biotechnology 34(10), 810–824 (2016)]

**Table 1** Various characteristics of THz spectroscopy for cell detection

| Features | Explanation | Benefits | References |
|---|---|---|---|
| Low photon energy | THz radiation is insufficient to cause chemical damage to molecules, or knock particles out of atoms | Non-invasive method | C. Yu et al. Quantitative Imaging in Medicine and Surgery, 2012,2, 33–45 |
| Sensitive to water molecules | Water molecules are significantly more absorptive than common macromolecules | Monitoring cellular activity and accessing the living state of cell according to different hydration | X. Yang et al. Journal of Biophotonics, 2016, 9, 1050–1058 |
| Precision of data analysis | Both amplitude and phase of the THz radiation can be obtained simultaneously | Precision analysis of spectral parameters | J.E. Haddad et al. Trends in Analytical Chemistry, 2013, 44, 98–105 |
| Spectral fingerprint | THz spectroscopies of different cells are unique and can be utilized as fingerprint | Distinguish different cells | C. Wang et al. Journal of Biophotonics, 2010, 3, 641–645 |

Reproduced from L. Yu, L. Hao, T. Meiqiong, H. Jiaoqi, L. Wei, D. Jinying, C. Xueping, F. Weiling, Z. Yang, The medical application of terahertz technology in non-invasive detection of cells and tissues: opportunities and challenges, RSC Advances 9 (2019) 9354, under creative commons attribution-noncommercial 3.0 unported licence

The authors have reported high-performance on-chip integrable uncooled terahertz microbolometer arrays with nanoscale meander-shaped Ti thermistors, fabricated and compatible with state-of-the-art and medium-scale semiconductor device processes. The reports cover the width dependence of the temperature coefficient of resistance (TCR) and resistivity (ρ) for platinum (Pt) and titanium (Ti) thermistor used in the room temperature antenna-coupled terahertz microbolometer [8]. Further highlighted characterization of platinum and titanium thermistors for terahertz antenna-coupled bolometers, exploring the reason for the narrow width effect in thin metal lines, correlated with reduced grain size due to reduction of width. Further proposing the optimum value of thermistor width considering design requirement and used for the fabrication of microbolometers [9]. Also highlights the optimization of the narrow width effect on TCR of metal interconnects in nanometer dimensions of the thermistor used in terahertz microbolometer arrays [10]. Also reports the design and fabrication schemes of performance improvement of on-chip integrable terahertz microbolometer arrays using nanoscale meander titanium thermistor [11]. A performance comparison of SOI-based temperature sensors for room temperature terahertz operation in antenna-coupled bolometers, MOSFET, PN junction diode and resistor have been also reported [12]. Further, the possibility of chip-integrated medical devices for terahertz screening was explored based on authors' previous

reports. The authors have highlighted the prospects in medical applications of terahertz waves [13]. The idea of medical imaging, artificial intelligence, Internet of things and wearable devices in terahertz healthcare technologies was also reported [14, 15] along with the emerging trends in Internet of things and big data analytics for biomedical and healthcare technologies which is vital for the healthcare applications of the devices proposed [16] along with the concept of application of flexible and 2D materials in THz detection [17]. An implementation of the tunable graphene nanopatch antenna with chip-integrated terahertz detector arrays for cancer imaging has also been reported very recently by the authors [18]. Figure 4 shows a Terahertz microbolometer reported by the authors with nanoscale Ti meander thermistors that delivered high responsively in unit devices with scope for further miniaturization with significant potential for application as on-chip integrable detector arrays.

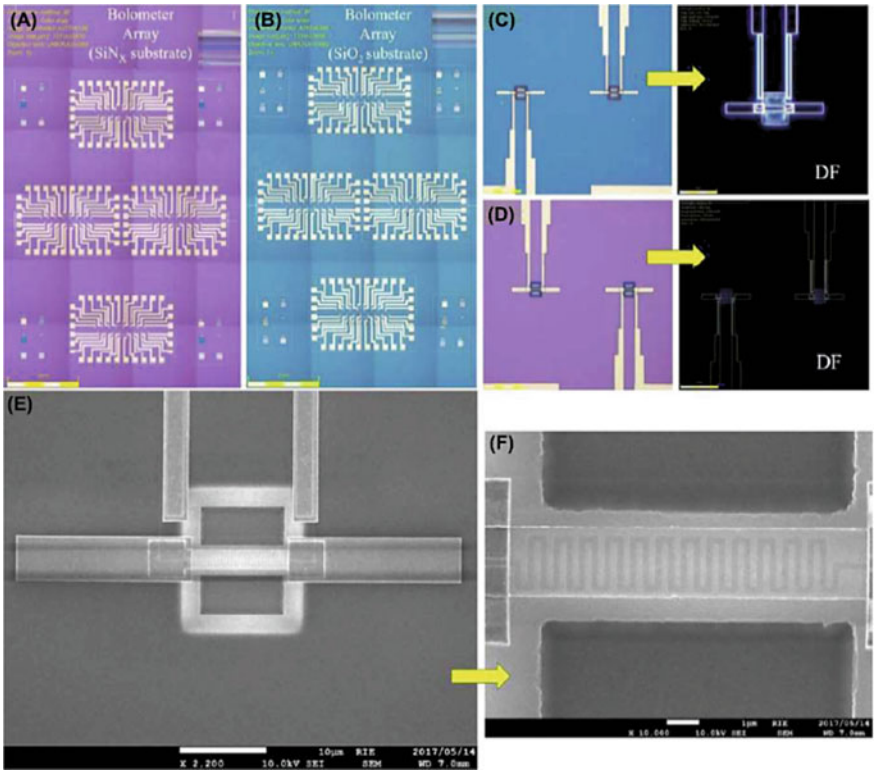


**Fig. 4** Optical microscopes **a**, **b** images of Ti-based uncooled antenna-coupled THz microbolometer arrays on SiN,, and $SiO_2$ substrates with thermistor design widths of 0.1 and 0.2 pm. **b**, **c**, **d** With dark-field vision, enlarged optical microscope images of a series of microbolometers. **e**, **f** An expanded view of a FE-SEM microbolometer system with a heater and a meander-structured thermistor floating above the cavity. Reproduced from A. Banenee. H. Satoh, D. Elamaran, Y. Sharma. N. Hiromoto. H. Inokawa, Performance improvement of on-chip integrable terahertz microbolometer arrays using nanoscale meander titanium thermistor, Journal of Applied Physics 125, 214502 (2019)

## 2 Terahertz Imaging Devices

THz imaging has significant advantages over other imaging methods because of which they have found numerous applications ranging from healthcare, defence and security, astronomy and manufacturing [19, 20]. THz imaging provides information that is complimentary to most imaging methods such as using X-Ray, UV, visible or IR for imaging. Most common packaging materials such as paper and plastics are transparent in the THz range which makes it is possible to image contents inside a package without opening it. Recent measurements in near field have shown that diffraction limited resolution can also be overcome to achieve good resolution [21]. THz radiation provides better resolution compared to other shorter frequency imaging methods because of shorter wavelength. Since THz photons are of much lower energy compared to X-Rays and are no ionizing, they provide a non-destructive, non-invasive method to image biological samples. For example, THz imaging has been used to detect cancer with possibility to achieve micron level resolution and to evaluate frost damage in barley [22, 23]. Cameras for THz imaging have employed both single pixel and multipage sensors depending on imaging applications. Single pixel cameras are preferred over multipage camera because of their reduced cost and superior durability; however, they require more time to raster-scan a sample in order to generate a two-dimensional image. This also makes them less suitable for applications involving moving objects. Some of the multipage camera technologies such as bolometer arrays are easier to integrate with CMOS technology and provide benefits of ease of manufacturing and cost efficiency which has been a major driver in various device fabrication and integration schemes [24, 25]. In the below section we will look at some of the recent developments in single pixel and multi-pixel cameras followed by a few commercial applications.

Single pixel detectors made of active meta-materials serve as real-time tuneable, spectrally sensitive spatial masks for terahertz imaging using compressive techniques, allowing for high-frame rate, high-fidelity images [26]. Monolayer graphene on a high resistance Si substrate illuminated by a coded laser beam was used to achieve Fourier single pixel imaging, allowing for high quality THz images to be produced with a small number of measurements [27]. By projecting a time-varying intense optical pattern onto a Si wafer that spatially modulates the transmission of synchronous THz radiation for applications in defect detection in circuitry wiring of a few micrometres in size, single pixel imaging with sub-wavelength resolution has also been demonstrated [27]. By refining the modulation geometry and post-processing algorithms, Stantchev et al. were able to demonstrate the acquisition of a THz-video ($32 \times 32$ pixels at 6 frames per second) in real time using a single pixel fibre-coupled photoconductive THz detector [28]. Semiconductor nano-wires provide an interesting platform for device fabrication because of enhanced properties, simple one-dimensional cylindrical geometry and ease of growth and integration [29, 30]. Semiconductor nano-wires have been used to make FET transistors for imaging with high responsively and low noise equivalent power (NEP) [31]. Ravaro et al. [32] used nano-wire as a transistor channel in a FET coupled to a bow-tie antenna

and increased the THz detection capability to 2.8 THz with a responsively 5 V/W bandwidth 100 kHz, thus proving the full potential of such approach for the detection of THz quantum cascade lasers. While single pixel cameras have made remarkable progress, they suffer from the larger acquisition times for a 2D image generation. Multi-pixel cameras employ array detectors and generate a two-dimensional image in a single snapshot. An array detector typically consists of an array of metal antennas coupled to either SBDs [33], FETs [34, 35] or bolometer [36]. Many THz array detectors employ SOI substrates and their CMOS integration has been extensively studied [37, 38].

THz technology has also been commercialized with multiples devices available commercially. Terasense [39] makes THz cameras, source, scanner, detectors and antennas. Terasense camera generates THz images in the range of 0.05THz to 1THzwith pixel resolution ranging from 256 pixels (16 $\times$ 16 or 256 $\times$ 1 array) to 4096 pixels (64 $\times$ 64 array), NEP of 1 nm/$\sqrt{}$Hz, and room temperature responsively of 50 kV/W. The device size is of the order of ten cm with image acquisition rate of up to 5000 fps for some models. The cameras use Terasense patented technology involving an array of plasmonic semiconductor detectors [40]. Thruvision [41] makes THz cameras employing heterodyne detection using GaAs Schottky diode mixer [42] for screening moving passengers at standoff range for applications in airport screening, counter-terrorism, and prevention of smuggling of drugs, cash and other prohibited items. These scanners also allow for detection of suicide vests and assault weapons from a distance from 3 to 8 m [43]. This camera uses THz radiation at 0.25THz, works below 28∘C and captures 6fps. On a stationary person 6 m away, it can detect an object of size 5 $\times$ 5 cm. Other cameras built for applications in distribution and fulfilment centres for theft prevention can detect objects as small as 3 $\times$ 3 cm hidden under clothing [44, 45].

## 3 Terahertz Medical Image Processing

Extensive literature survey has been carried out on THz medical image processing in this report. Peter et al. [46] reported a comprehensive idea on the impact of biology and medicine utilizing THz technology. They reviewed terahertz applications in the natural and clinical sciences. Further working at extended wavelength than infrared (IR) frequencies were investigated with attention on frequencies from 300 GHz to 3 THz the submillimetre-band.

Liu et al. [27] examined the clinical use of terahertz innovation in non-obtrusive identification of tissues and cells. In this work, the researchers summed up the points of interest and advances accomplished in THz spectroscopy for platelet recognition, disease cell portrayal, bacterial identification and organic tissue separation, further presenting THz frameworks for imaging of tissues. They featured the impacts of THz radiation and difficulties in techniques to accelerate future clinical applications. Recently, observing slight change [47] in malignancy cells at a beginning phase has been recognized with THz spectroscopy with trademark cancer spectral lines.

THz spectroscopic frameworks have shown application for estimating slight changes in cell monolayer, identifying quantitative examination of disease cells [48]. THz spectroscopy can be used for identifying intracellular hydration in malignancy cells [49]. Due to limited penetration depth of the THz radiation, it is most effective for scanning teeth and skin. Also, THz attenuation is insignificant to water substance [47] and this has prompted concern in the examination of hydration of tissues. The skin comprises of perhaps the biggest organ of the body for reflection imaging. It is made out of a few layers: dermis, epidermis and hypodermis (or sub-cutaneous tissues). This layered construction is interesting for reflection imaging as there are boundaries between materials with different properties that cause the impression of THz. Estimations on model of human dermis have revealed that the skin constituents could be separated by Terahertz pulsed imaging (TPI). Trademark changes are created in images of the skin utilizing ultrasound or Magnetic resonance imaging (MRI) due to infections, e.g. psoriasis where there is thickening of the epidermis. The potential offered by TPI is for estimation that is less expensive than MRI and does not need connection with the skin as ultrasound ensures [50]. Similar to skin, teeth are interesting for terahertz imaging (Fig. 5).

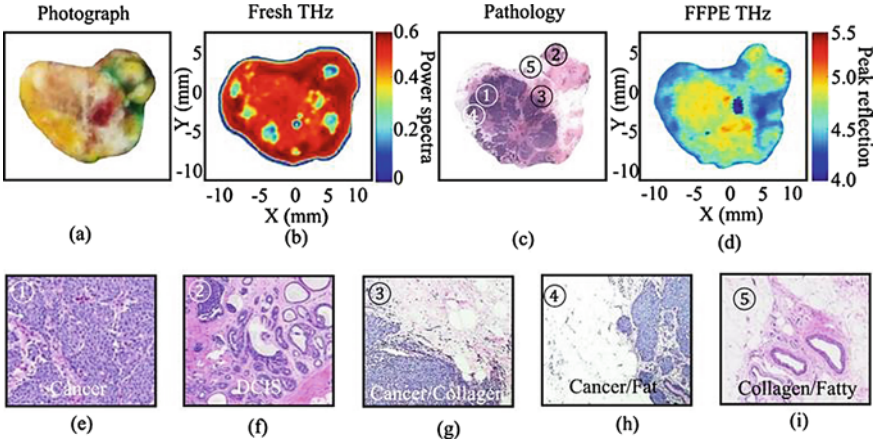


**Fig. 5** THz photographs of breast cancer tissue from a human. **a** A photograph of freshly harvested tissue. **b** A spectral power representation of the frequency domain THz image of fresh tissue. **c** A low-resolution pathology image. **d** THz picture of FFPE block tissue in the time domain. **e** A high-resolution pathology picture of the cancer area labelled 1 in (**c**). **f** In (**c**), the high-resolution pathology picture of the DCIS area is labelled as 2. **g** In (**c**), the high-resolution pathology picture of the cancer-collagen region is labelled as 3. **h** In (**c**), a high-resolution pathology picture of the cancer-fat area. **i** The collagen-fatty region is marked as 5 in this high-resolution pathology picture (**c**). Reproduced with permission from El-Shenawee, Magda, et al., Cancer Detection in Excised Breast Tumours Using Terahertz Imaging and Spectroscopy. Biomedical Spectroscopy and Imaging 8(1–2), 1–9 (2019)

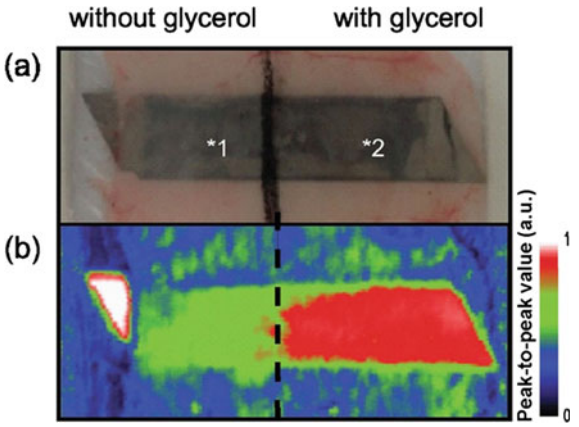


**Fig. 6** Using glycerol as a penetration-enhancing agent, the penetration depth of THz radiation was increased. The photos are 5 3 $cm^2$ in scale. **a** A visible image of a metal goal under a mouse's abdominal tissue. **b** Glycerol was used to treat the tissue on the right side, which has a lower absorption and phase delay when exposed to THz radiation. In THz imaging, the procedure resulted in increased contrast. Reproduced with permission from Oh et al., Opt. Express 21, 21299 (2013)

## 4 Detection of Cancer

Epithelial tissues are responsible for more than 80% of all adult cancers, including skin, bowel, lung, breast, bladder cancers. THz radiation has been shown in some studies to be able to differentiate between cancerous and healthy tissue [51]. Although the precise cause is unclear, it is generally assumed that the dissimilar water comfortable of these tissues is the primary reason and orientation therein. Deep body penetration is also difficult due to the high THz absorption in aqueous media. As a result, deep in vivo cases are still scarce, despite the fact that many research studies are currently underway around the world. Ex vivo applications with skin-deep tests are feasible with today's up to date THz imaging structures [52, 53] (Fig. 6).

## 5 Skin Cancer

THz radiation has been productively utilized to image human skin at a penetration depth of just a few millimetres. As a result, numerous studies have been conducted on the early detection and diagnosis of skin cancers [1, 54]. Ex vivo biopsies of abnormal skin tissues are expected to be reduced or eliminated with this technology. Early detection also decreases the risk of these tumours, as they are able to previously be easily indulgenced and costs of care. Some skin cancers are noticeable to the trained eye, but others, especially those that are small and flat, are not. THz imaging

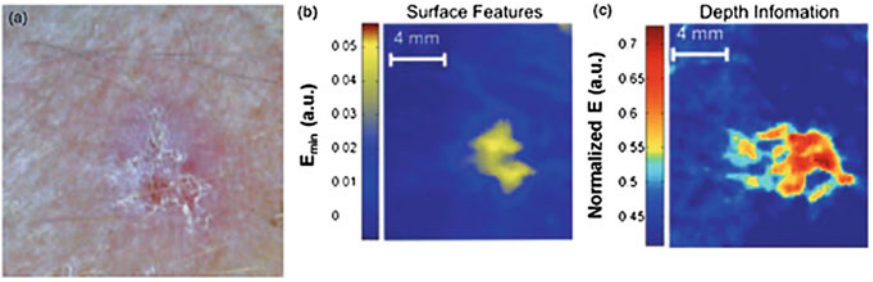


**Fig. 7** THz photographs of a nodular basal cell carcinoma (BCC, skin cancer) on a patient's arm taken in real time. **a** A photo of a cancerous lesion. **b** THz image of (**a**) derived from the THz waveform's minimum value. The picture depicts the lesion's surface. **c** THz representation of the tumour at a depth of 250 m. THz diagnostic imaging offers precise skin cancer information. Reproduced with permission from Wallace et al., Br. J. Dermatol. 151, 424 (2004)

can detect cancers at an early stage due to its ability to distinguish the supernatural signatures of plane proteins that are markers for some cancers [2, 3] (Fig. 7).

## 6 Inspection of Wounds and Burns

THz imaging has been used to non-invasively assess wounds and injuries, primarily using a THz tomography unit. THz tomography is used to create an axial illustration of a multilayered entity. The mirrored THz pulse train is calculated and analysed after a THz pulse is shined on the point of interest. Each layer is a distorted pulse that contains details about its depth and optical belongings. The depth and properties of the blaze injury decide the form and size of each replicated pulse when THz tomography is used for noncontact scrutiny of skin burn injuries [8]. A plastic over-layer (e.g. Polystyrene) can be used to the surface to provide a guide for the signal analysis. Areas of burned and unburned have slightly different THz reflectivity (Fig. 8).

This type of processing is also achievable under layers of medical bandage and cotton [9, 10]. THz imaging in three dimensions (3D) of dental X-rays can help dentists identify a number of issues, including tooth decay and enamel loss. THz radiation is attenuated more in decayed enamel than in healthy enamel, resulting in a distinct contrast in the THz image. The difference in refractive index between the enamel and dentine tissues is exploited in THz imaging. X-rays are also the most modern method of dental imaging. X-rays, on the other hand, are unsuccessful at detecting early stage tooth decay, since tissue damage is easily healed [11].

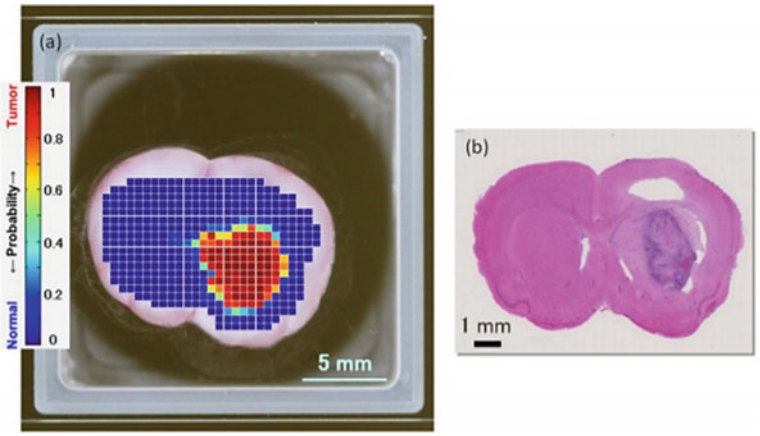


**Fig. 8** THz spectroscopy and HE-stained (hematoxylin and eosin) picture of the same tissue segment using separate techniques [54]. Based on the different refractive indexes of tumour and normal tissue regions, the THz image was generated by computing a tumour likelihood, where zero corresponds to healthy tissue. The tumour region is depicted in red in (**a**), which corresponds to the dark purple area in the HE-stained picture (**b**). Reproduced with permission from Brain tumour imaging of rat fresh tissue using terahertz spectroscopy, Sayuri Yamaguchi, Yasuko Fukushi, Oichi Kubota, TakeakiItsuji, Toshihiko Ouchi & Seiji Yamamoto, Scientific Reports, volume 6, Article number: 30124 (2016), under a Creative Commons Attribution 4.0 International License

## 7 Summary

THz has a variety of uses, including the identification of concealed objects for protection and inspection, non-destructive tests, also medical imaging diagnostics. THz radiation is non-harmful for cells, has wide range of spectroscopic signatures for biomolecules with enormous biomedical application advantage as described in this chapter. However, the lack of appropriate parts, complicated, costly hardware configurations, hardware and software integration, also low power THz sources, sensitivity of detectors, substantial water absorptions, and low penetration depths to achieve high-performance imaging have hindered the mass-market introduction of THz medical imaging.

## References

1. Biswas A, Sinha S, Acharyya A, Banerjee A, Pal S, Satoh H, Inokawa H (2018) 1.0 THz GaN IMPATT source: effect of parasitic series resistance. J Infrared Millimeter Terahertz Waves 39(10):954–974
2. Acharyya A, Biswas A, Sarkar B, Banerjee A, Inokawa H (2021) Terahertz radiation from gallium phosphide avalanche transit time sources. In: Emerging trends in terahertz engineering and system technologies. Springer Nature, ISBN 978-981-15-9765-7

3. Banerjee P, Acharyya A, Biswas A, Bhattacharjee AK, Banerjee A, Inokawa H (2018) Noise performance of magnetic field tunable avalanche transit time source. Int J Electron Commun Eng 12(10):718–728
4. Martyniuk P, Antoszewski J, Martyniuk M, Faraone L, Rogalski A (2014) New concepts in infrared photodetector designs. Appl Phys Rev 1:041102
5. Dhillon SS et al (2017) The 2017 terahertz science and technology roadmap. J Phys D Appl Phys 50:043001
6. Lewis RA (2019) A review of terahertz detectors. J Phys D Appl Phys 52:433001
7. Graf UU, Honingh CE, Jacobs K, Stutzki J (2015) Terahertz heterodyne array receivers for astronomy. J Infrared Milli Terahz Waves 36:896–921
8. Banerjee A, Satoh H, Tiwari A, et al (2017) Width dependence of platinum and titanium thermistor characteristics for application in room-temperature antenna-coupled terahertz microbolometer. Jpn J Appl Phys 56:04CC07
9. Banerjee A, Satoh H, Sharma Y, Hiromoto N, Inokawa H (2018) Characterization of platinum and titanium thermistors for terahertz antenna-coupled bolometer applications. Sens Actuators A Phys 273:49–57
10. Banerjee A, Satoh H, Elamaran D, Sharma Y, Hiromoto N, Inokawa H (2018) Optimization of narrow width effect on titanium thermistor in uncooled antenna-coupled terahertz microbolometer. Jpn J Appl Phys 57:04FC09
11. Banerjee A, Satoh H, Elamaran D, Sharma Y, Hiromoto N, Inokawa H (2019) Performance improvement of on-chip integrable terahertz microbolometer arrays using nanoscale meander titanium thermistor. J Appl Phys 125:214502
12. Elamaran D, Suzuki Y, Satoh H, Banerjee A, Hiromoto N, Inokawa H (2020) Performance comparison of SOI-based temperature sensors for room-temperature terahertz antenna-coupled bolometers: MOSFET, PN junction diode and resistor. Micromachines 11(8):718
13. Banerjee A, Vajandar S, Basu T (2020) Prospects in medical applications of terahertz waves. In: Banerjee A, Chakraborty B, Inokawa H, Roy JN (eds) Terahertz biomedical and healthcare technologies materials to devices. Elsevier, Amsterdam, Netherlands, pp 145–165
14. Banerjee A, Chakraborty C, Rathi M (2020) Medical imaging, artificial intelligence, internet of things, wearable devices in Terahertz healthcare technologies. In: Banerjee A, Chakraborty B, Inokawa H, Roy JN (eds) Terahertz biomedical and healthcare technologies materials to devices. Elsevier, Amsterdam, Netherlands, pp 225–239
15. Karthikeyan MP, Samanta D, Banerjee A, Roy A, Inokawa H (2021) Design and development of terahertz medical screening devices. In: Trends in wireless communication and information security, Lecture notes in electrical engineering. Springer Nature, ISSN 1876-1100
16. Banerjee A, Chakraborty C, Kumar A, Biswas D (2020) Emerging trends in IoT and big data analytics for biomedical and health care technologies. In: Balas VE, Solanki VK, Kumar R, Khari M (eds) Handbook of data science approaches for biomedical engineering. Academic Press, MA, USA, pp 121–152
17. Basu T, Banerjee A, Vajandar S (2020) 2D materials as THz generators, detectors, and modulators: potential candidates for biomedical applications. In: Banerjee A, Chakraborty B, Inokawa H, Roy JN (eds) Terahertz biomedical and healthcare technologies. Elsevier, Amsterdam, Netherlands, pp 75–87
18. Samanta D, Karthikeyan MP, Banerjee A, Inokawa H (2021) Tunable graphene nanopatch antenna design for on-chip integrated terahertz detector arrays with potential application in cancer imaging. Nanomedicine 16(12):1035–1047
19. Bogue R (2018) Sensing with terahertz radiation: a review of recent progress. Sens Rev 38:216–222
20. Zhang M, Yeow JTW (2016) Nanotechnology-based terahertz biological sensing: a review of its current state and things to come. IEEE Nanotechnol Mag 10:30–38
21. Stantchev RI et al (2016) Noninvasive, near-field terahertz imaging of hidden objects using a single-pixel detector. Sci Adv 2:e1600190
22. Yu C, Fan S, Sun Y, Pickwell-MacPherson E (2012) The potential of terahertz imaging for cancer diagnosis: a review of investigations to date. Quant Imaging Med Surg 2:33–45

23. Lee WSL, Withayachumnanku AFW, Able JA (2020) Assessing frost damage in barley using terahertz imaging. Opt Express 28 (21):30644
24. Berger JS (2020) Self-aligned on-chip coupled photonic devices using individual cadmium sulfide nanobelts. Nano Res 13(5):1413–1418
25. Agarwal D et al (2019) Nanocavity-enhanced giant stimulated raman scattering in Si nanowires in the visible light region. Nano Lett 19:1204–1209
26. Watts CM et al (2014) Terahertz compressive imaging with metamaterial spatial light modulators. Nat Photonics 8:605–609
27. Liu W, Lu Y, Zhou Z, Li G (2019) Fourier single-pixel imaging in the terahertz regime. Appl Phys Lett 115:021101
28. Stantchev RI, Yu X, Blu T, Pickwell-MacPherson E (2020) Real-time terahertz imaging with a single-pixel detector. Nat Commun 11:2535
29. Agarwal D, Yoo J, Pan A, Agarwal R (2019) Cavity engineering of photon−phonon interactions in Si nanocavities. Nano Lett 19:7950–7956
30. Agarwal D et al (2017) Engineering localized surface plasmon interactions in gold by silicon nanowire for enhanced heating and photocatalysis. Nano Lett 17:1839–1845
31. Romeo L et al (2013) Nanowire-based field effect transistors for terahertz detection and imaging systems Nanotechnology 24:214005
32. Ravaro M et al (2014) Detection of a 2.8 THz quantum cascade laser with a semiconductor nanowire field-effect transistor coupled to a bow-tie antenna. Appl Phys Lett 104:083116
33. Han R et al (2013) Active terahertz imaging using Schottky Diodes in CMOS: array and 860-GHz pixel. IEEE J Solid-State Circ 48:2296–2308
34. Knap W et al (2004) Plasma wave detection of sub-terahertz and terahertz radiation by silicon field-effect transistors. Appl Phys Lett 85:675–677
35. Tauk R, et al (2006) Plasma wave detection of terahertz radiation by silicon field e_ects transistors: Responsivity and noise equivalent power. Appl Phys Lett 89:253511
36. Elamaran D et al (2020) Performance comparison of SOI-based temperature sensors for room-temperature terahertz antenna-coupled bolometers: MOSFET PN junction diode and resistor. Micromachines 11:718
37. Perenzoni D, Perenzoni M, Gonzo L, Capobianco AD, Sacchetto F (2010) Analysis and design of a CMOS-based terahertz sensor and readout. Opt Sens Detect 7726:772618
38. Schuster F et al (2011) Broadband terahertz imaging with highly sensitive silicon CMOS detectors. Opt Express 19:7827–7832
39. www.terasense.com
40. Muravev VM, Gusikhin PA, Andreev IV, Kukushkin IV (2015) Novel relativistic plasma excitations in a gated two-dimensional electron system. Phys Rev Lett 114:106805
41. www.thruvision.com
42. Kowalski M, Piszczek M, Palka N, Szustakowski M (2012) Improvement of passive THz camera images. Proc SPIE8544, 85440N
43. Siegel PH (2004) Terahertz technology in biology and medicine. IEEE Trans Microw Theory Tech 52(10):2438–2447. https://doi.org/10.1109/TMTT.2004.835916
44. Markelz A, Whitmore S, Hillebrecht J, Birge R (2002) THz time domainspectroscopy of bimolecular conformational modes. Phys Med Biol 47(21):3797–3805
45. Mickan SP, Menikhu A, Liu H, Mannella CA, MacColl R, Abbott D, Munch J, Zhang X-C (2002) Label-free bioaffinity detection using terahertz technology. Phys Med Biol 47(21):3789–3795
46. Hartwick TS, Hodges DT, Barker DH, Foote FB (1976) Far infraredimagery. Appl Opt 15(8):1919–1922
47. Khadri SKA, et al (2014) Approach of message communication using fibonacci series: in cryptology. In: Lecture notes on information theory. https://doi.org/10.12720/lnit.2.2.168-171
48. Samanta D, Paul M, Khutubuddin S, Khadri A (2013) Message communication using phase shifting method (PSM). Int J Adv Res Comput Sci 4(11):9–11. https://doi.org/10.26483/ijarcs.v4i11.1936

49. Mukherjee M, Samanta D (2014) Fibonacci based text hiding using image cryptography. In: Lecture notes on information theory, vol 2, no 2, pp 172-–176. https://doi.org/10.12720/lnit.2.2.172-176
50. Khadri SKA et al (2016) Message encryption using pascal triangle multiplication. Cryptol Asian J Math Comput Res 13(4): 262–270
51. Jaferi F, Saeid KT, Borah L, Samanta D (2016) Recognition of potential drug-drug interactions in diabetic's patients in hospital pharmacy. Int J Control Theor Appl 10(9): 481–487. ISSN : 0974-5572
52. Kuchy SA, Khadri SKA, Mukherjee M, Samanta D, Le D-N (2017) An aggregation approach based on elasticsearch. J Eng Appl Sci 12:9451–9454. https://doi.org/10.36478/jeasci.2017.9451.9454
53. Manu MK, Roy S, Samanta D (2018) Effects of liver cancer drugs on cellular energy metabolism in hepatocellular carcinoma cells. Int J Pharmaceut Res 10(3). https://doi.org/10.31838/ijpr/2018.10.03.079. ISSN -0975-2366
54. Yamaguchi S, Yamaguchi S, Fukushi Y, Kubota O, Itsuji T, Ouchi T, Yamamoto S (2016) Brain tumor imaging of rat fresh tissue using terahertz spectroscopy. Sci Rep 6:30124

# The Elastic Constants in Opto-electronic Materials Under Terahertz Frequency


**R. Paul, J. Pal, S. Chakrabarti, B. Chatterjee, P. K. Das, T. Basu, and K. P. Ghatak**

**Abstract** In this chapter, we study the carrier contribution to the 2nd and 3rd order elastic constants ($\phi_1$ and $\phi_2$) in opto-electronic materials in terahertz frequency by taking the bulk of various opto-electronic compounds. The influence of magnetic quantization, 1D quantization and 2D quantization has also been studied in this context. It appears that both $\phi_1$ and $\phi_2$ changes with wave length, intensity, electron statistics, alloy composition and nano thickness in different ways for all the opto-electronic compounds as considered here and the influence of quantization of band state is also being apparent from all the figures.

**Keywords** Carrier contribution · Elastic constants · Opto-electronic materials · Terahertz frequency

R. Paul · S. Chakrabarti
Department of Computer Science and Engineering, Institute of Engineering and Management & University of Engineering and Management, Kolkata, India
e-mail: rajashree.paul@uem.edu.in

S. Chakrabarti
e-mail: satyajit.chakrabarti@iemcal.com

J. Pal
Department of Physics, Meghnad Saha Institute of Technology, Nazirabad, Uchepota, Anandapur, Kolkata 700150, India

B. Chatterjee
Department of Computer Science and Engineering, University of Engineering and Management, Jaipur, Rajasthan 303807, India
e-mail: biswajoy.chaterjee@iemcal.com

P. K. Das · T. Basu · K. P. Ghatak (✉)
Department of Basic Science and Humanities, Institute of Engineering and Management & University of Engineering and Management, Kolkata, India

P. K. Das
e-mail: prabir.das@iemcal.com

T. Basu
e-mail: tina.de@iemcal.com



A. Acharyya et al. (eds.), *Generation, Detection and Processing of Terahertz Signals*, Lecture Notes in Electrical Engineering 794,
https://doi.org/10.1007/978-981-16-4947-9_20

## 1 Introduction

Recently the different electronic properties of quantized materials have widely been studied [1–30]. The elastic constants are a very important mechanical property of stressed devices [31–50] and in this chapter, we study the carrier contribution to the 2nd and 3rd order elastic constants ($\phi_1$ and $\phi_2$) in opto-electronic compounds in terahertz frequency. The influence of magnetic quantization, 1D quantization and 2D quantization has also been studied in this context. The effect of wave length, intensity, electron statistics, alloy composition and nano thickness on $\phi_1$ and $\phi_2$ have been investigated. The influence of magnetic quantization, 1D quantization and 2D quantization has also been studied in this context.

## 2 Results and Discussion

Figures 1, 2, 3, 4, 5, 6, 7, 8, 9, 10, 11, 12, 13, 14, 15, 16, 17, 18, 19, 20, 21, 22, 23, 24, 25, 26, 27, 28, 29, 30, 31, 32, 33, 34, 35, 36, 37, 38, 39, 40, 41, 42, 43, 44 and 45 exhibit the plots of normalized $\phi_1$ and $\phi_2$ against normalized electron statistics ($n_0$), intensity ($I$), wave length ($\lambda$), alloy composition ($x$, $y$), magnetic field ($B$) and film thickness ($d_y$) respectively. For the purpose of condensation, the HD materials $InAs$, $InSb$, $Hg_{1-x}Cd_xTe$, $In_{1-x}Ga_xAs_yP_{1-y}$ are denoted by $P$, $Q$, $R$ *and* $S$ respectively. From the said figures we observe the following:

1. Both $\phi_1$ and $\phi_2$ increase with increasing electron statistics, intensity, wave length and alloy composition respectively.
2. They oscillate with $1/B$ due to SdH effect.
3. In quantum wells, both of them oscillate with film thickness.

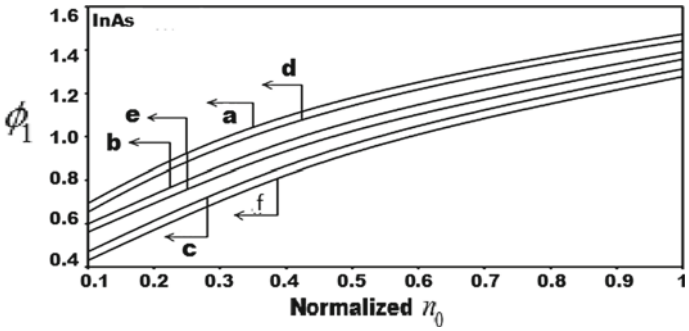


**Fig. 1** $\phi_1$ against $n_0$ for $P$ under terahertz frequency have been drawn where **a**, **b** and **c** represent the perturbed three band Kane model, two band Kane model and wide gap model respectively. The **d**, **e** and **f** exhibit the same when $I = 0$

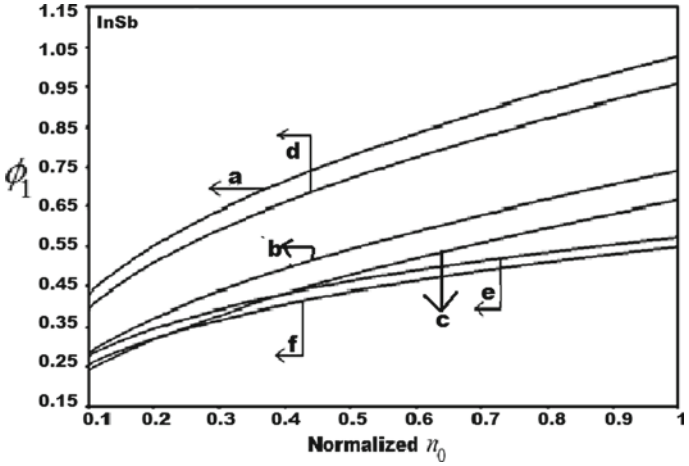


**Fig. 2** Plots of Fig. 1 for $Q$

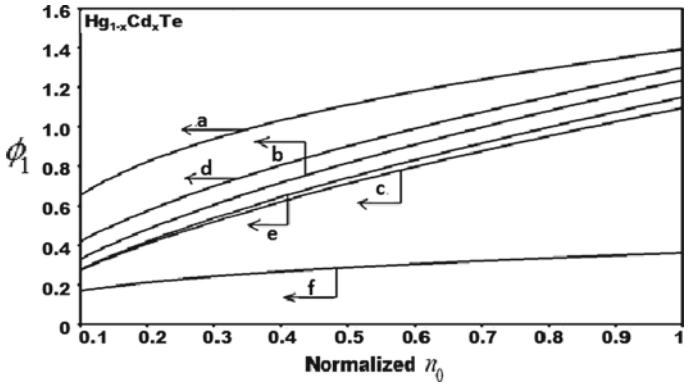


**Fig. 3** Plots of Fig. 1 for $R$

## 3 Summary

In this chapter, we study the carrier contribution to the 2nd and 3rd order elastic constants ($\phi_1$ and $\phi_2$) in opto-electronic materials in terahertz frequency by taking the bulk of various opto-electronic compounds. The influence of magnetic quantization, 1D quantization and 2D quantization has also been studied in this context. It appears that both $\phi_1$ and $\phi_2$ changes with wave length, intensity, electron statistics, alloy composition and nano thickness in different ways for all the opto-electronic compounds as considered here and the influence of quantization of band state is also being apparent from all the figures.

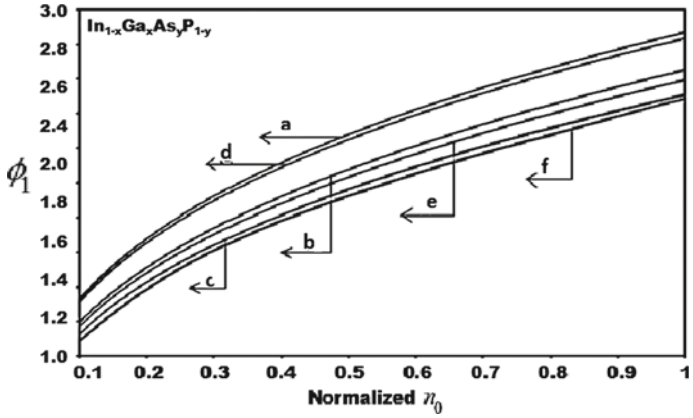


**Fig. 4** Plots of Fig. 1 for $S$

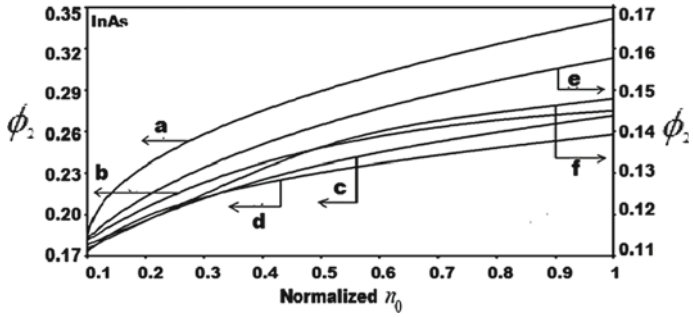


**Fig. 5** Plots of $\phi_2$ for the materials of Fig. 1 for $P$

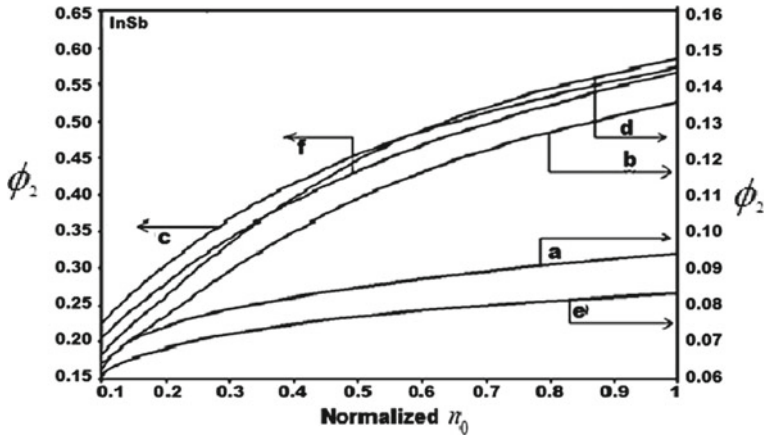


**Fig. 6** Plots of Fig. 5 for $Q$

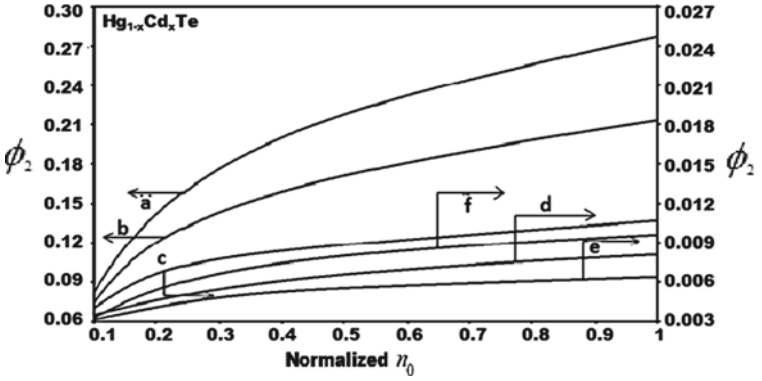


**Fig. 7** Plots of Fig. 5 for $R$

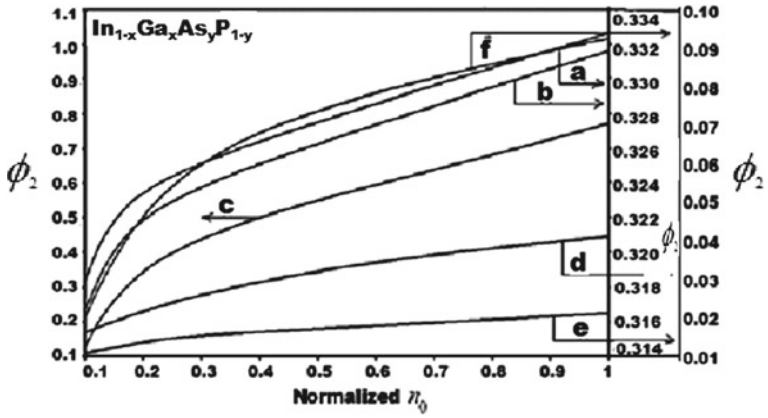


**Fig. 8** Plots of Fig. 5 for $S$

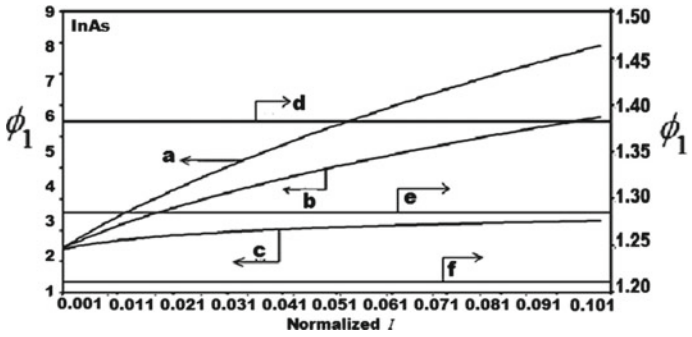


**Fig. 9** Plots of $\phi_1$ against $I$ for $P$

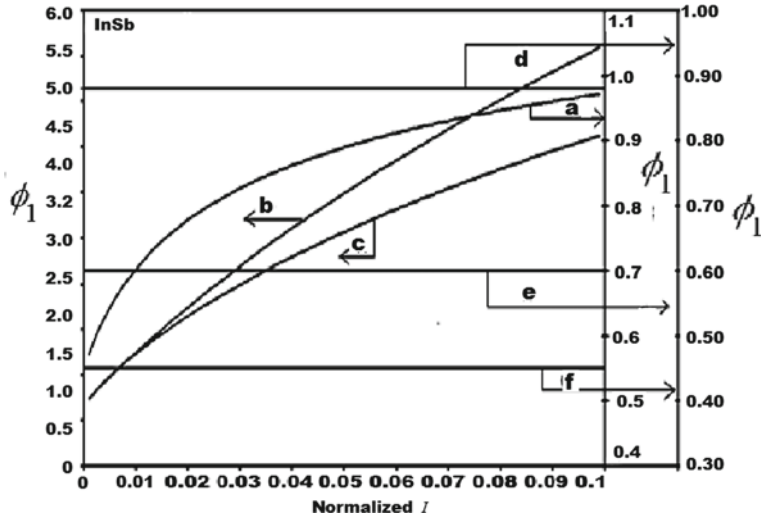


**Fig. 10** Plots of Fig. 9 for $Q$

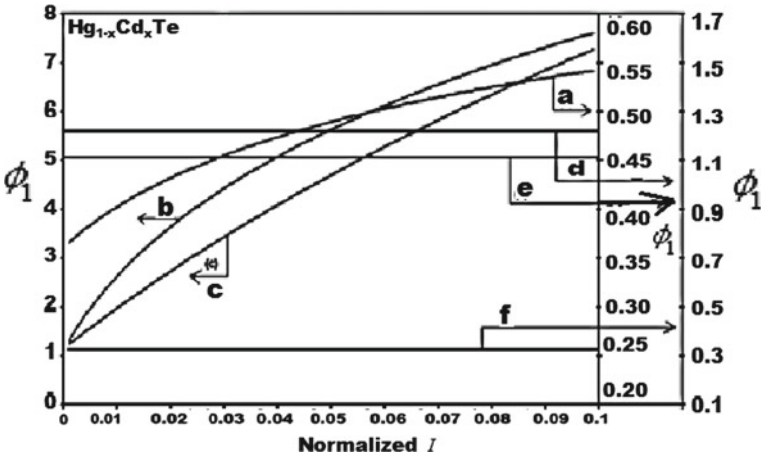


**Fig. 11** Plots of Fig. 9 for $R$

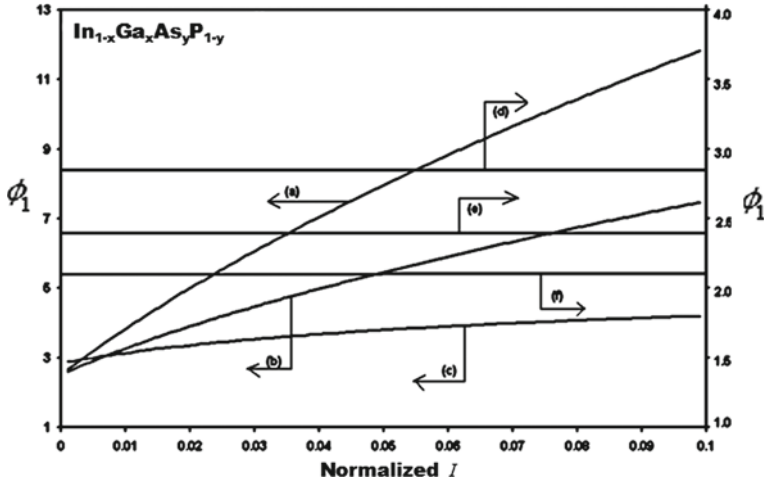


**Fig. 12** Plots of Fig. 9 for $S$

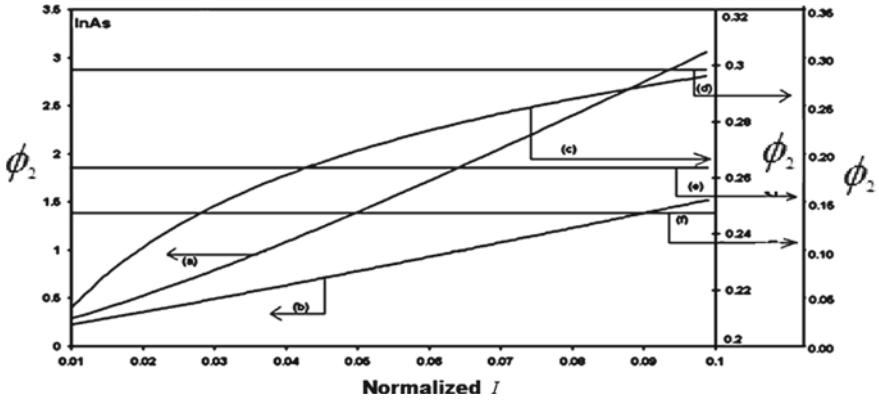


**Fig. 13** Plots of $\phi_2$ against $I$ for $P$

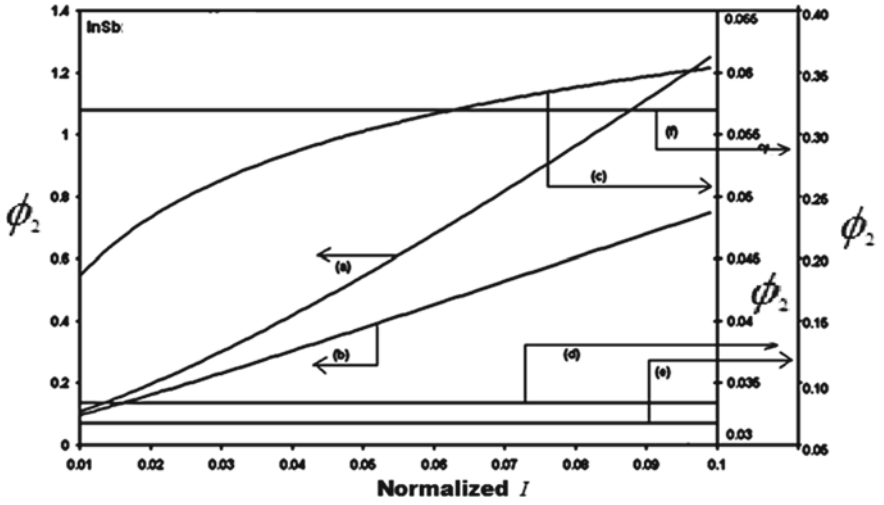


**Fig. 14** Plots of Fig. 13 for $Q$

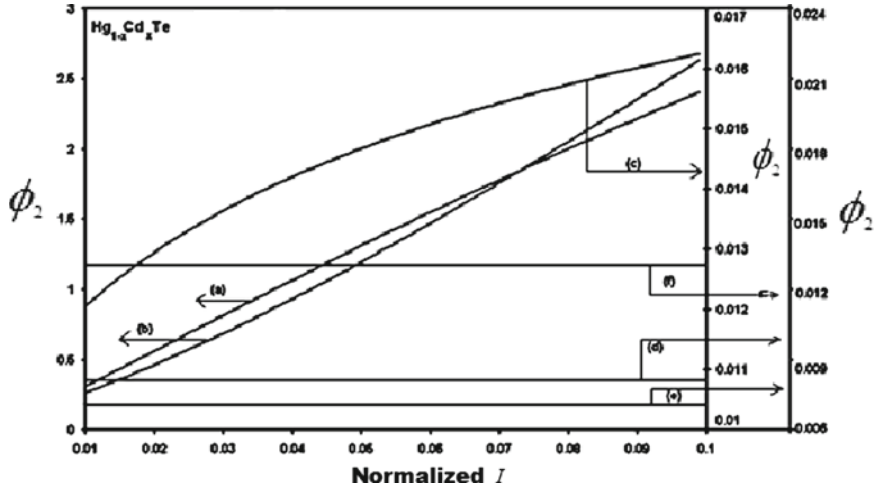


**Fig. 15** Plots of Fig. 13 for $R$

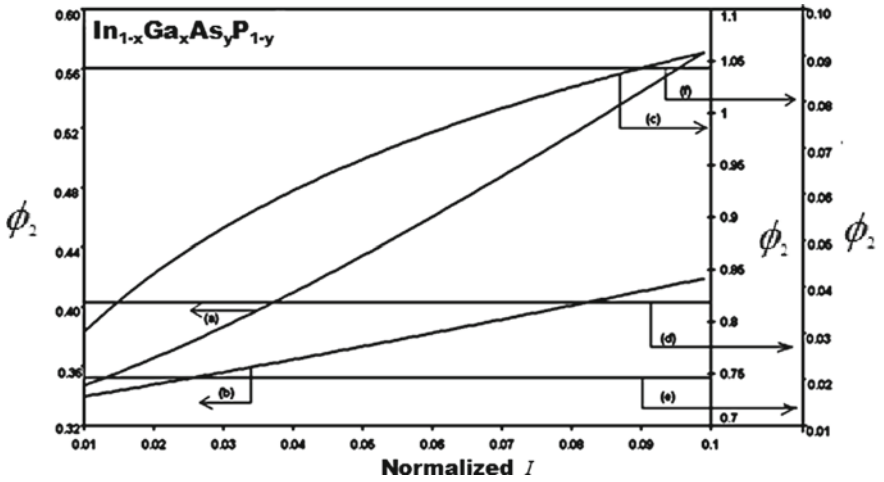


**Fig. 16** Plots of Fig. 13 for *S*

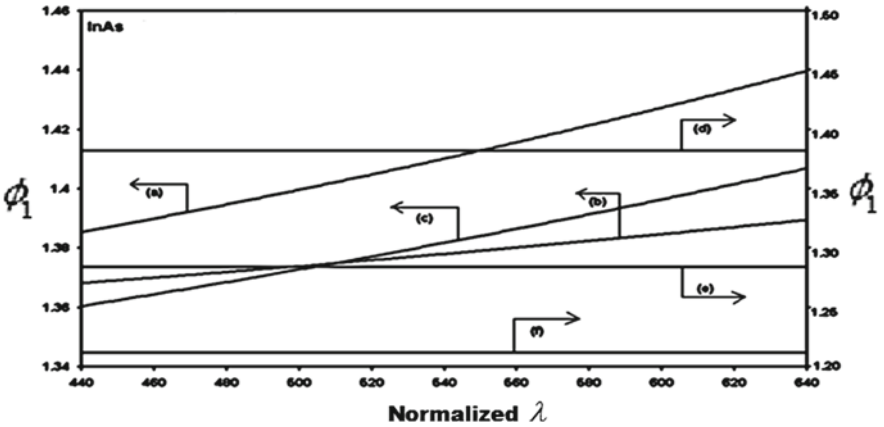


**Fig. 17** Plots of $\phi_1$ against λ for *P*

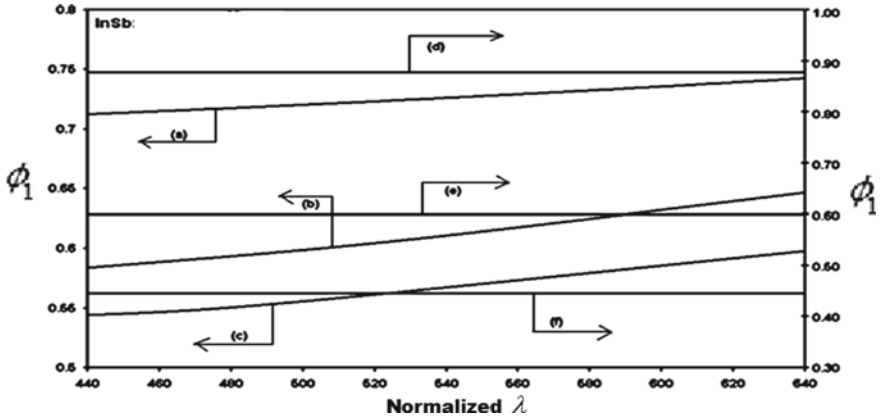


**Fig. 18** Plots of Fig. 17 for $Q$

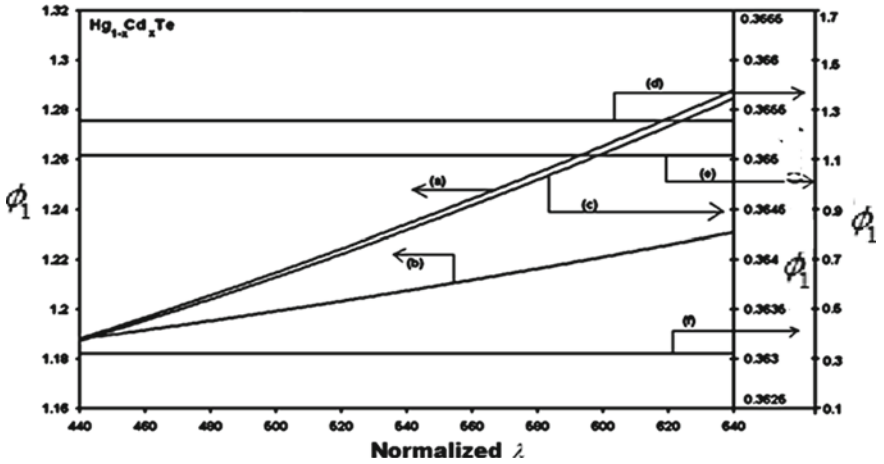


**Fig. 19** Plots of Fig. 17 for $R$

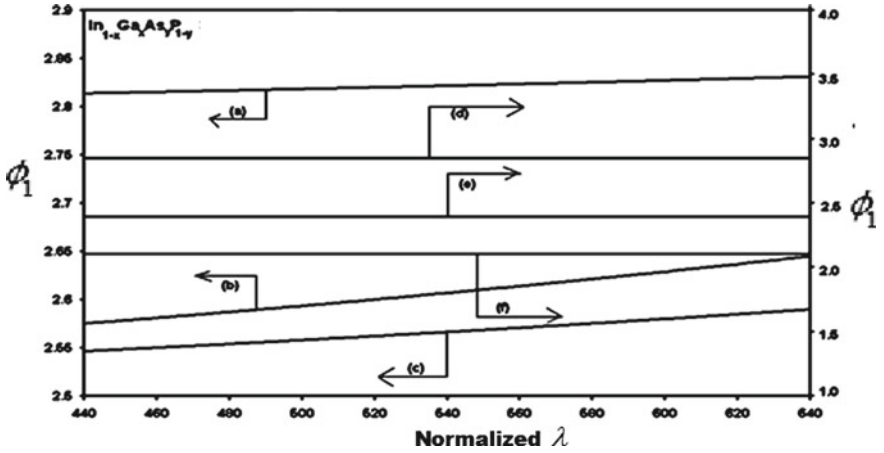


**Fig. 20** Plots of Fig. 17 for *S*

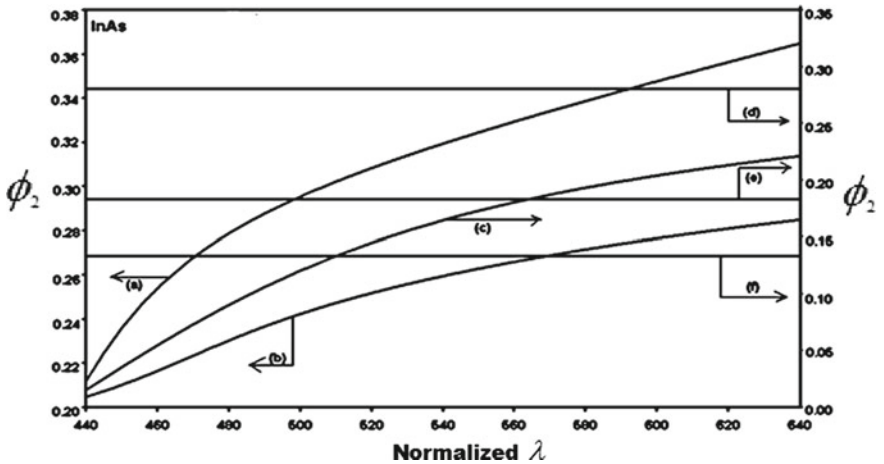


**Fig. 21** Plots of $\phi_2$ against λ for *P*

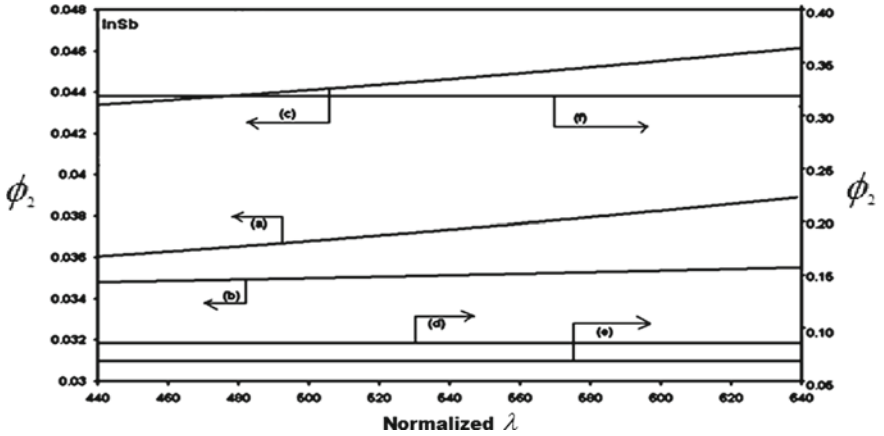


**Fig. 22** Plots of Fig. 21 for $Q$

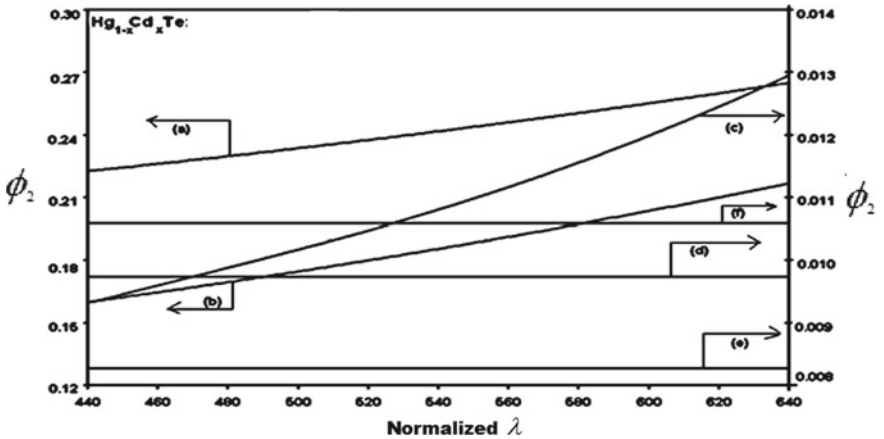


**Fig. 23** Plots of Fig. 21 for $R$

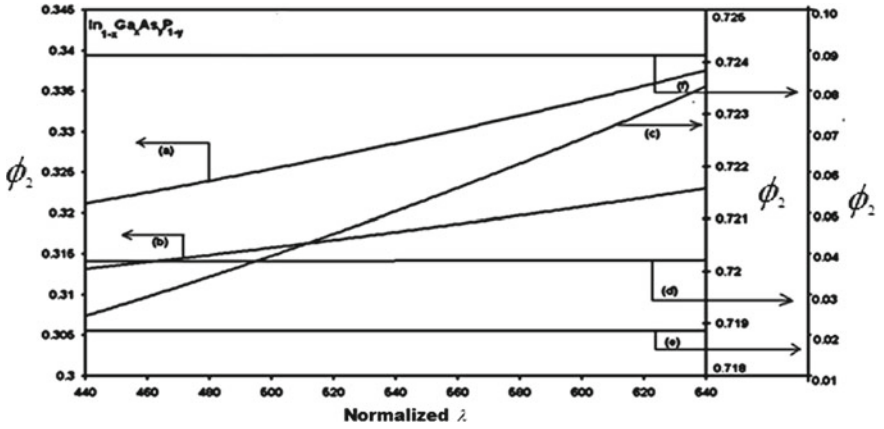


**Fig. 24** Plots of Fig. 21 for *S*

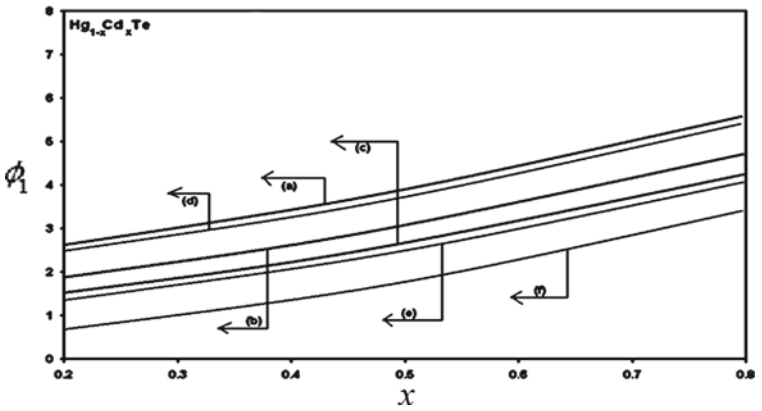


**Fig. 25** Plots of $\phi_1$ against $x$ for $R$

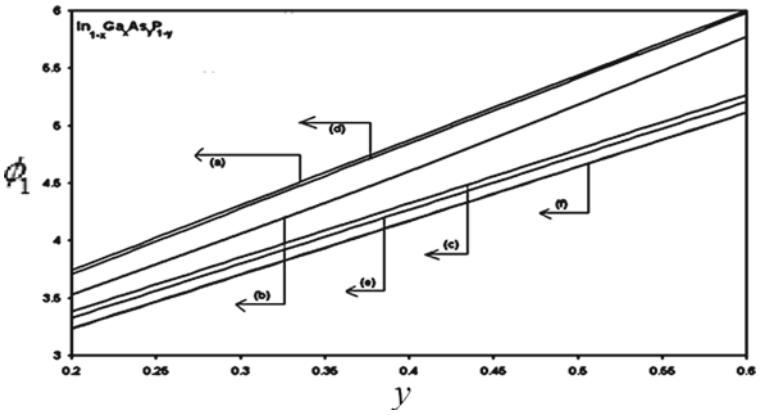


**Fig. 26** Plots of $\phi_1$ against $y$ for $S$

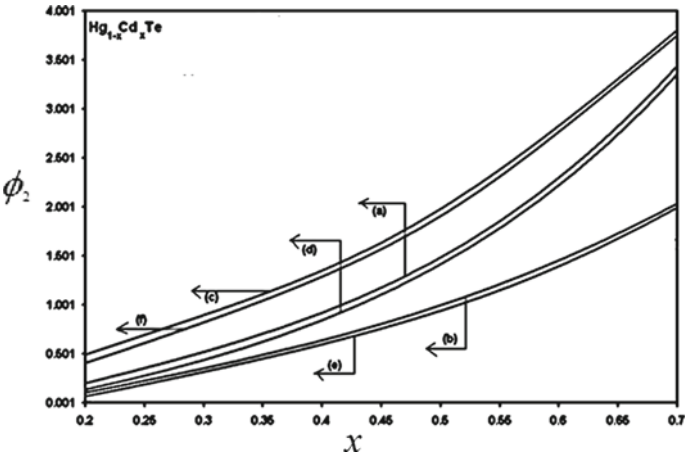


**Fig. 27** Plots of Fig. 25 for $R$

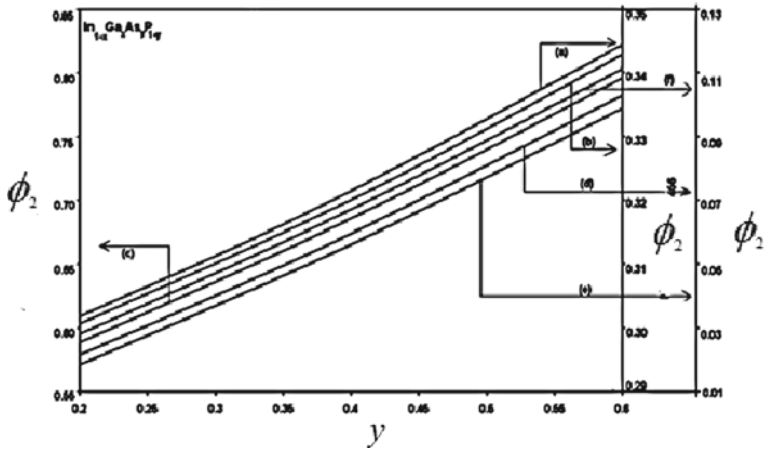


**Fig. 28** Plots of Fig. 26 for $S$

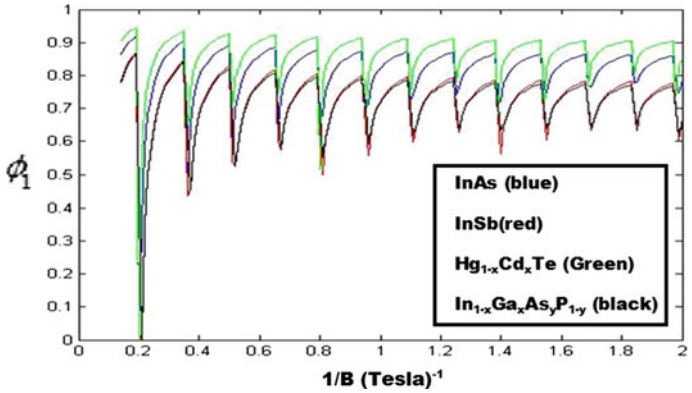


**Fig. 29** Plot of the $\phi_1$ against $1/B$ for $P$(blue), $Q$(red), $R$ (green) and $S$ (black) under the combining influences of $B$ and terahertz frequency respectively

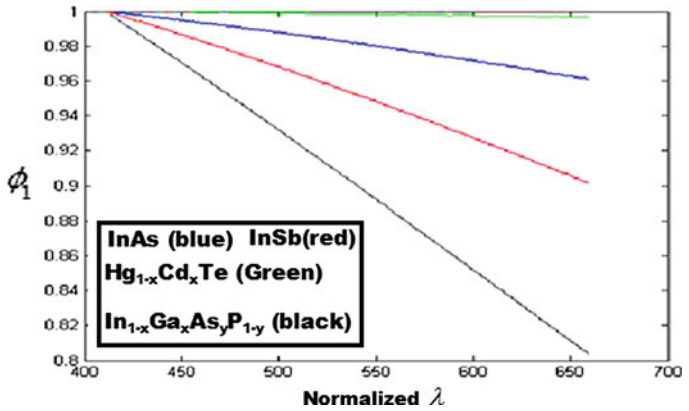


**Fig. 30** Plots of $\phi_1$ against normalized $\lambda$ for all curves of Fig. 29

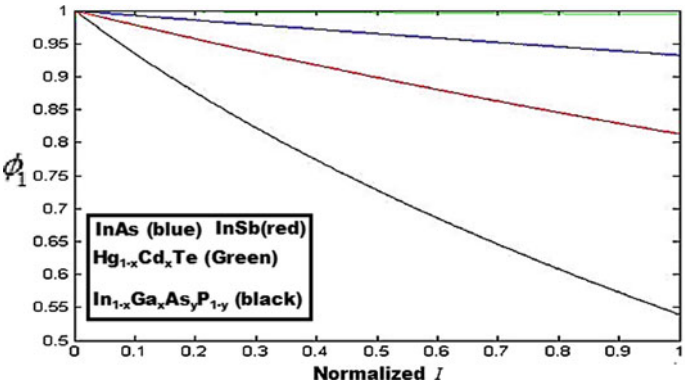


**Fig. 31** Plots of $\phi_1$ against normalized $I$ for all curves of Fig. 29

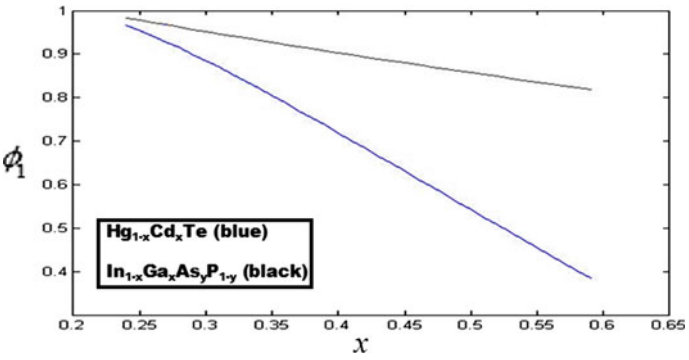


**Fig. 32** Plots of $\phi_1$ against $x$ for the two cases of Fig. 29 which are applicable for $R$ and $S$ respectively

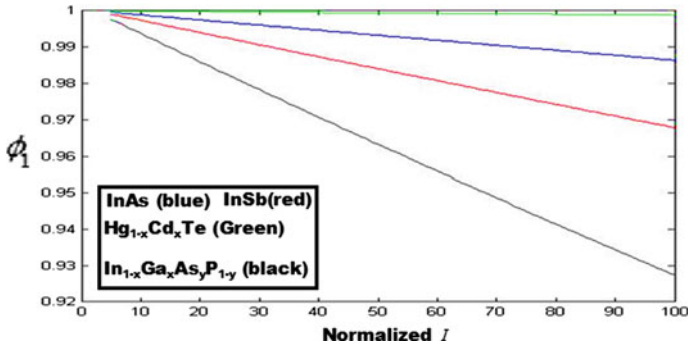


**Fig. 33** Plots of $\phi_1$ against normalized $I$ in quantum wells for all curves of Fig. 29

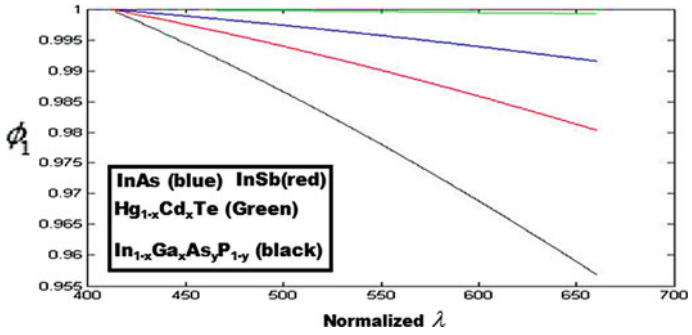


**Fig. 34** Plots of $\phi_1$ against normalized λ in quantum wells for all curves of Fig. 29

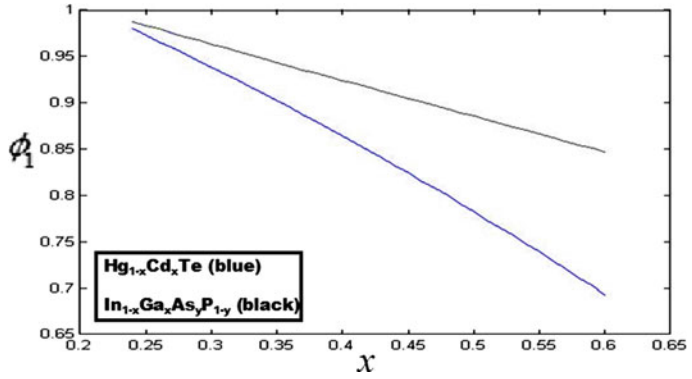


**Fig. 35** Plots of $\phi_1$ against $x$ for the two cases of Fig. 29 which are applicable for quantum wells of $R$ and $S$ respectively

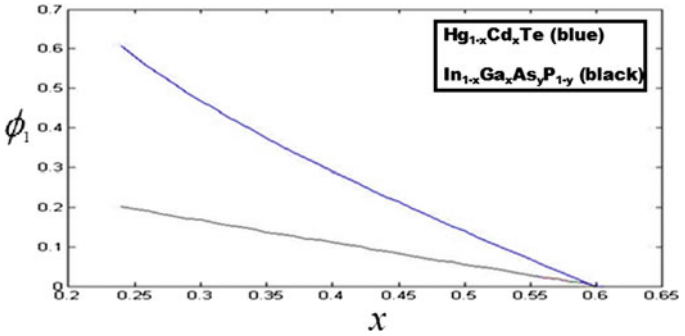


**Fig. 36** Plot of $\phi_1$ against $x$ for the two cases of Fig. 29 which are applicable for 1D $R$ and $S$ respectively

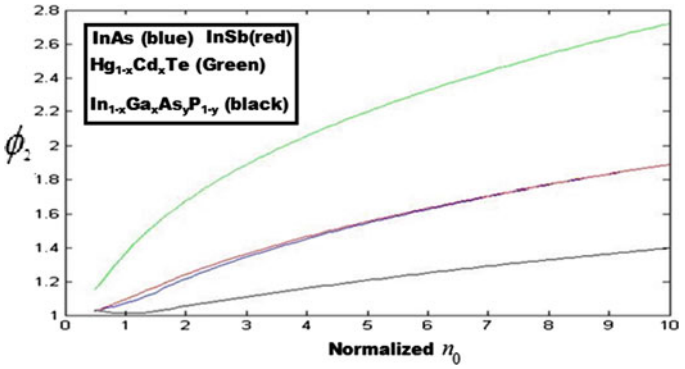


**Fig. 37** Plots of $\phi_2$ against normalized $n_0$ for $P$, $Q$, $R$ *and* $S$ of Fig. 5

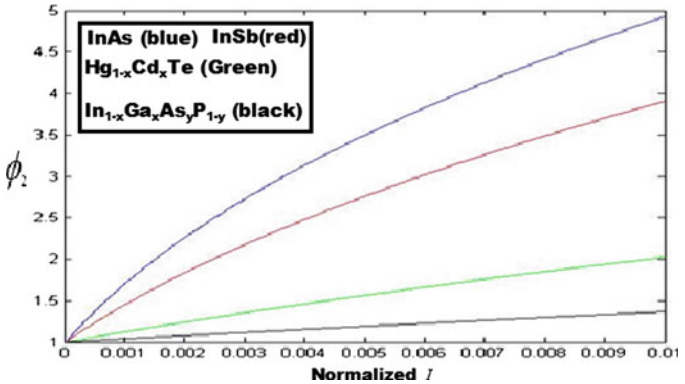


**Fig. 38** Plots of $\phi_2$ against normalized $I$ for $P$, $Q$, $R$ *and* $S$ of Fig. 13

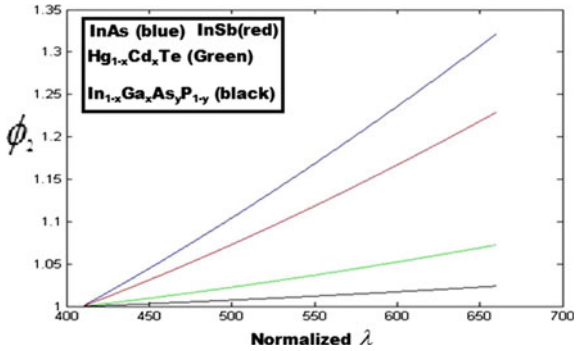


**Fig. 39** Plots of $\phi_2$ against normalized λ for $P$, $Q$, $R$ *and* $S$ of Fig. 22

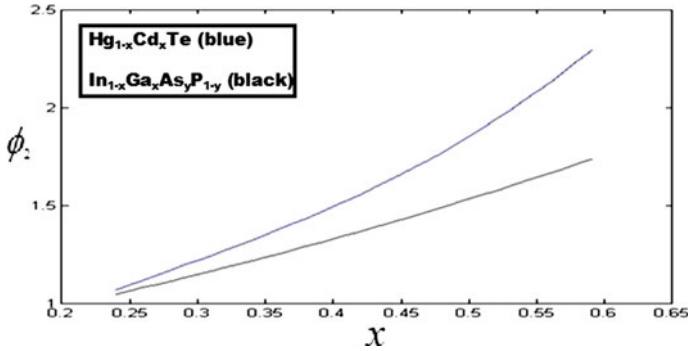


**Fig. 40** Plots of $\phi_2$ against normalized $x$ for $R$ *and* $S$ of Fig. 27

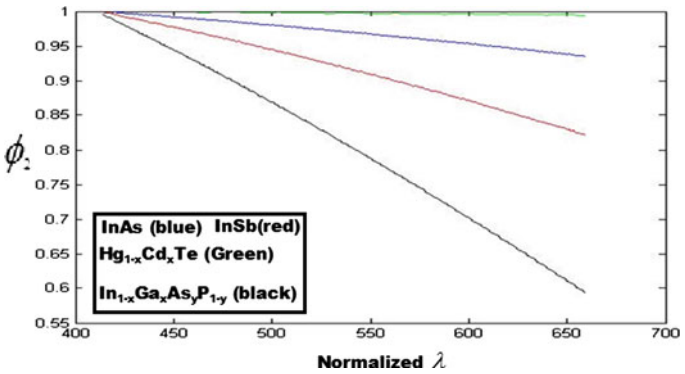


**Fig. 41** Plots of $\phi_2$ against normalized λ for $P$, $Q$, $R$ *and* $S$ of Fig. 39

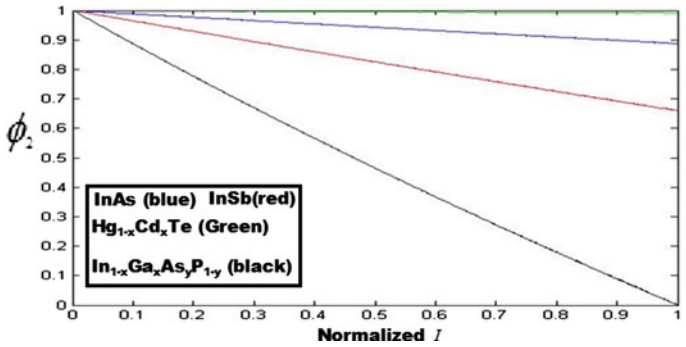


**Fig. 42** Plots of $\phi_2$ against normalized $I$ for $P$, $Q$, $R$ *and* $S$ of Fig. 13

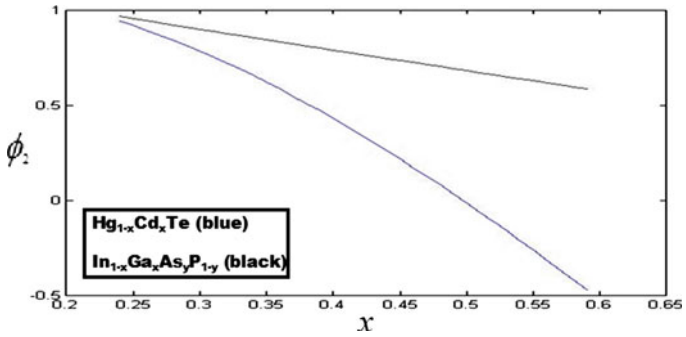


**Fig. 43** Plots of $\phi_2$ against normalized $\lambda$ for $R$ *and* $S$ of Fig. 27

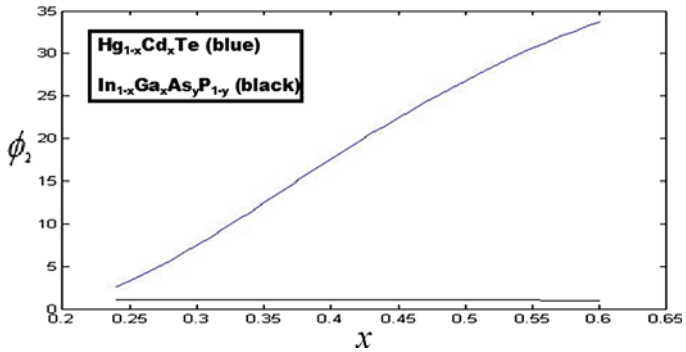


**Fig. 44** Plots of $\phi_2$ against normalized $x$ for quantum wells of $R$ *and* $S$ of Fig. 27

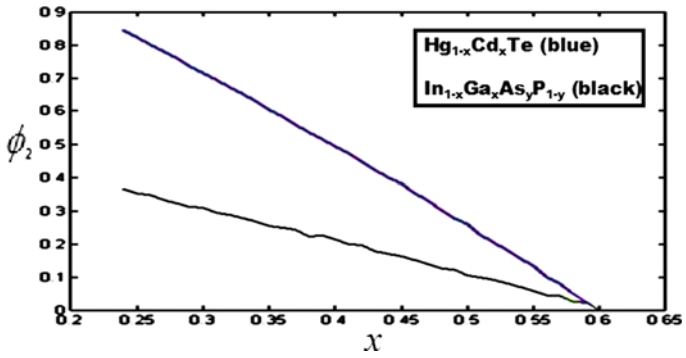


**Fig. 45** Plots of $\phi_2$ against normalized $x$ for 1D $R$ *and* $S$ of Fig. 27

## References


1. Ghatak KP, Mitra M (2020) Quantization and entropy, series in nanomaterials **2**. De Guyter, Germany
2. Ghatak KP (2020) Quantum wires: an overview. Series in nanotechnology science and technology, Nova, USA
3. Ghatak KP, Bhattacharya S, De D (2009) Einstein relation in compound semiconductors and their heterostructures, vol 116. Springer Series in Materials Science, Springer
4. Ghatak KP, De D, Bhattacharya S (2009) Photoemission from optoelectronic materials and their nanostructures. Springer Series in Nanostructure Science and Technology, Springer
5. Ghatak KP, Bhattacharya S (2020) Thermo electric power in nano structured materials strong magnetic fields, vol 137. Springer Series in Materials Science
6. Bhattacharya S, Ghatak KP (2012) Fowler-Nordheim Field Emission: Effects in semiconductor nanostructures, vol 170. Springer Series in Solid state Sciences**,** pp 1–12
7. Bhattacharya S, Ghatak KP (2013) Effective electron mass in low dimensional semiconductors, vol 167. Springer Series in Materials Sciences
8. Ghatak KP, Bhattacharya S (2014) Debye screening length: effects of nanostructured materials, vol 255. Springer Tracts in Modern Physics, Springer
9. Ghatak KP, Bhattacharya S (2015) Heavily doped 2D quantized structures and the Einstein relation, vol 260. Springer Tracts in Modern Physics, Springer
10. Ghatak KP (2015) Einstein's Photo-emission: emission from heavily doped quantized structures, vol 262. Springer Tracts in Modern Physics, Springer
11. Ghatak KP (2016) Dispersion relations in heavily—doped nanostructures, vol 265. Springer Tracts in Modern Physics
12. Ghatak KP (2016) Magneto thermoelectric power in heavily doped quantized structures, vol 7. Series on the Foundations of Natural Science and Technology. World Scientific
13. Ghatak KP (2017) Quantum effects, heavy doping, and the effective mass, vol 8. Series on the Foundations of Natural Science and Technology. World Scientific
14. Seikh AH, Alharthi N, Bose PK, Ghatak KP (2020) Emerging trends in terahertz solid-state physics and devices. Springer, Singapore, pp-85–106; Debbarma M, Das S, Pal J, Debbarma S, Paul R, Das PK, Dutta T, Ghatak KP (2019) Adv Sci Eng Med 11:1161; Ghatak KP, Chakrabarti S, Chatterjee B, Debbarma M, Debbarma N (2019) Adv Sci Eng Med 11:914
15. Biswas SK, Pradhan AK, Bhattacharya K, Maiti S, Mitra M, Chakrabarti S, Chatterjee B, Ghatak KP (2019) Adv Sci Eng Med **11**:977; Paul R, Das PK, Mitra M, Ghatak KP (2019) Adv Sci Eng Med 11:903. Das PK, Ghatak KP (2019) J Nanosci Nanotechnol 19:2909

16. Ghatak KP, Chakrabarti S, Chatterjee B (2018) Mater Focus 7:361; Ghatak KP, Chakrabarti S, Chatterjee B, Das PK, Dutta P, Halder A (2018) Mater Focus **7**:390; Singh SL, Singh SB, Ghatak KB (2018) J Nanosci Nanotechnol 18:2856
17. Ghatak KP, Mitra M, Paul R, Chakrabarti S (2017) J Comput Theoret Nanosci 14:2138; Chatterjee B, Debbarma N, Mitra M, Datta T, Ghatak KP (2017) J Nanosci Nanotechnol 17:3352; Ghatak KP, De D (2017) Mater Focus 6:114
18. Das PK, Dutta P, Halder A, Pal J, Debbarma N, Debbarma S, Ghatak KP (2017) Mater Focus 6:167; Das PK, Dutta P, Halder A, Bhattacharjee R, Ghatak KP (2017) Mater Focus 6:133; Ghatak KP, Mitra M, Paul R, Chakrabrati S, Mallik BB, Mallik PB (2017) J Nano Sci Nano Technol
19. Bhattacharjee R, Ghatak KP (2017) J Nanosci Nanotechnol 17: 640; Mitra M, Sen TN, Datta T, Bhattacharjee R, Singh LS, Ghatak KP (2017) J Nanosci Nanotechnol 17:256; Sen TN, Ghatak KP (2016) Quantum Matter 5:732
20. Sen TN, Ghatak KP (2016) Quantum Matter 5:721; Ghatak KP, Sarkar K, Chakrabarti S, Kumar M, Debbarma M, Sen TN, Chakraborty M (2016) Rev Theoret Sci 4:199; Bhattacharya R, Sarkar K, Kumar M, Chatterjee B, Ghatak KP (2016) Quantum Matter 5:557
21. Ghatak KP, Sarkar K, Debbarma N, Suraj Singh L (2016) Quantum Matter 5:427. Ghatak KP, De D (2016) J Nanoeng Nanomanuf 6:1; Biswas SK, Mitra M, Ghatak KP (2016) J Nanoeng Nanomanuf 6:63
22. Chakrabarti S, Chakraborty M, Ghatak KP (2016) Rev Theoret Sci 4:10–66. Paitya N, Ghatak KP (2016) Quantum Matter 5:191; Chatterjee B, Chakrabarti S, Sen SK, Mitra M, Ghatak KP (2016) Quantum Matter 5:85; Mitra M, Chakraborty M, Debbarma S, Chakraborty S, Sen SK, Chatterjee B, Ghatak KP (2016) Quantum Matter 5:58
23. Sen TN, Ghatak KP (2016) J Nanosci Nanotechnol 16:1229; Debbarma S, Ghatak KP (2016) J Nanosci Nanotechnol 16:1095; Chatterjee B, Chakrabarti S, Chakraborty M, Ghatak KP (2015) Rev Theoret Sci 3:428
24. Adhikari SM, Ghatak KP (2015) Quantum Matter 4:599; Chakrabarti S, Chatterjee B, Debbarma S, Ghatak KP (2015) J Nanoscie Nanotechnol 15:6460; Adhikari SM, Karmakar A, Ghatak KP (2015) Rev Theoret Sci 3:273
25. Mitra M, Chatterjee B, Ghatak KP (2015) J Comput Theoret Nanosci 12:1527; Mitra M, Chakrabarti S, Chakraborty M, Debbarma S, Ghatak KP (2015) J Comput Theoret Nanosci 12:1898; Ghatak KP, Singh LS, Sarkar K, Debbarma N, Debbarma M (2015) Mater Focus 4:85
26. Chakraborty M, Ghatak KP (2015) Quantum Matter 4:104; Sarkar K, Chakraborty M, Chakravarti S, Chatterjee B, Ghatak KP (2015) J Nanoeng Nanomanf 5:43; Debbarma S, Ghatak KP (2015) Rev Theoret Sci 3:16
27. Adhikari SM, Karmakar A, Ghatak KP (2014) J Comput Theoret Nanosci 11:2499; Chatterjee B, Debbarma N, Debbarma S, Chakrabarti S, Ghatak KP (2014) Adv Sci Eng Med 6:1177; Debbarma S, Chakravarti S, Debbarma N, Mitra M, Ghatak KP (2014) J Adv Phys 3:213
28. Debbarma S, N Debbarma, B Chatterjee, SM Adhikari and Ghatak KP, Adv Sci Eng Med 6:1024; Chakrabarti S, Sen SK, Chakraborty S, Singh LS, Ghatak KP (2014) Adv Sci Eng Med 6(9):1042; Adhikari SM, Sakar A, Ghatak KP (2013) Quantum Matter 2:455
29. Bhattachrya S, Paitya N, Ghatak KP (2013) J Comput Theoret Nanosci 10:1999; Paitya N, Ghatak KP (2013) Rev Theoret Sci 1:165; Adhikari SM, Ghatak KP (2013) Quantum Matter 2:296
30. Adhikari SM, Ghatak KP (2013) J Adv Phys 2:130; Ghatak KP, Bose PK, Bhattacharya S, Bhattacharjee A, De D, Ghosh S, Debbarma S, Paitya N (2013) Quantum Matter 2:83; Adhikari SM, De D, Baruah JK, Chowdhury S, Ghatak KP (2013) Adv Sci Focus 1:57
31. Ghatak KP, Biswas SK, De D, Ghosal S, Chatterjee S (2004) Physica B Condens Matter 353:127; Chakraborty PK, Biswas SK, Ghatak KP (2004) Physica B Condens Matter 352:111; Chakraborty PK, Singh LJ, Ghatak KP (2004) J Appl Phys 95:5311
32. Chakraborty PK, Datta GC, Ghatak KP (2003) Physica B Conden Matter 339:198; PK Chakraborty, B Nag, Ghatak KP (2003) J Phys Chem Solids 64:2191; Choudhury S, Singh LJ, Ghatak KP (2003) Nanotechnology 15:180

33. Chakraborty PK, Datta GC, Ghatak KP (2003) Physica Scripta 68:368; Chakraborty PK, Datta GC, Ghatak KP (2003) Physica Scripta 68:368; Chakraborty PK, Ghatak KP (2001) Phys Lett A 288:335
34. Chakraborty PK, Ghatak KP (2001) J Phys Chem Solids 62:1061; Ghatak KP, Siddiqui JY, Nag B (2001) Phys Lett A 282:428; Chakraborty PK, Ghatak KP (2001) J Appl Phys 89:1075
35. Chakraborty PK, Ghatak KP (1999) J Phys D Appl Phys 32:2438; Chakraborty PK, Ghatak KP (1999) J Phys D Appl Phys 32:2438; Ghatak KP (1999) J Wave Mater Interact 14:157
36. Ghatak KP, Nag B (1998) Nanostructured Mater 10:923; Nag B, Ghatak KP (1998) J Phys Chem Solids 59:71; Ghatak KP, Nag B (1998) J Phys Chem Solids 59:411
37. Ghatak KP, B Nag, physica status solidi (b),205, 519, (1998).Ghatak KP, Dutta S, Basu DK, Nag B (1998) Il Nuovo Cimento D 20:227. Ghatak KP, Banerjee JP, Nag B (1998) J Appl Phys 83:1420
38. Nag B, Ghatak KP (1998) Nonlinear Optics-Reading 19:1; Banerjee JP, Ghosh S, Nag B, Ghatak KP (1997) Int J Electron 8:35; Nag B, Ghatak KP (1997) J Phys Chem Solids 58:427
39. Ghatak KP, Basu DK, Nag B (1997) J Phys Chem Solids 58:133; Ghatak KP, Bose PK (1997) J Wave Mater Interact 12:96; Bose PK, Ghatak KP (1997) J Wave Mater Interact 12:67
40. Ghatak KP, Bose PK (1997) J Wave Mater Interact 12:60; Ghatak KP, Bose PK (1997) J Wave Mater Interact 12:53; Ghatak KP, Nag B (1997) J Wave Mater Interact 12:85
41. Mitra B, Basu DK, Nag B, Ghatak KP (1997) Nonlinear Optics-Reading 17:171; Ghatak KP, Bose PK, Majumder G (1997) MRS Proc 484:673; Ghatak KP, Bose PK, Majumder G (1997) MRS Proc 494:157
42. Ghatak KP, Mitra B, Nag B (1996) Physica Status Solidi (B) 199:95; Ghatak KP, Basu DK, Basu D, Nag B (1996) Il Nuovo Cimento D 18:947; Ghatak KP, Banerjee JP, Bhattacharyya D, Nag B (1996) Nanotechnology 7:110
43. Ghatak KP, De B, Nag B, Chakraborty PK (1996) Nonlinear Optics 16:221; Ghatak KP, Dutta S, Ali A, Banerjee S, Nag B (1996) J Wave Mater Interact 11:127; Chakrabarty PK, Nag B, Dutta S, Ghatak KP (1996) J Wave Mater Interact 11:55
44. Nag B, Chakrabarty PK, Ghatak KP (1996) J Wave Mater Interact 11:211; Ghatak KP, Chakrabarty PK, Nag B (1996) J Wave Mater Interact 11:159; Ghatak KP, Mitra B, Nag B (1996) Physica Status Solidi (B) 199:95
45. Ghatak KP, Basu DK, Basu D, Nag B (1996) Il Nuovo Cimento D 18:947; Ghatak KP, Banerjee JP, Bhattacharyya D, Nag B (1996) Nanotechnology 7:110; Ghatak KP, De B, Nag B, Chakraborty PK (1996) Nonlinear Opt 16:221
46. Ghatak KP, Banik SN (1996) FIZIKA A-ZAGREB 5:31; Ghatak KP, Beta S, Ali A, Nag B (1996) FIZIKA A- ZAGREB 5:111; Ghatak KP, De B, Nag B, Chakraborty PK (1996) Nonlinear Optics- Reading 16:221
47. Ghatak KP, Bhattacharya D, Basu D, Nag B (1995) Physica Status Solidi, (B) 191:141; Bhattacharyya D, Ghatak KP (1995) Physica Status Solidi, (B) 187:523; Ghatak KP, Banik SN (1995) FIZIKA A 4: 33
48. Ghatak KP, Nag B, Mazumder G (1995) MRS Proc 379:109; Ghatak KP, Bhattacharyya D (1995) Physica Scripta 52:343; Ghatak KP, Mondal M (1994) Physica Status Solidi (B) 185:K5; Ghatak KP, Biswas SN (1994) Solid-state Electron 37:1437
49. Ghatak KP (1994) Acta Physica Hungarica 74:257; Ghatak KP (1994) Acta Physica Hungarica 74:167; Ghatak KP, Bhattacharyya D (1994) Phys Lett A 184:366; Banik S, Ghatak KP, Biswas S (1994) Fizika A 3:77
50. Ghatak KP, De B (1994) MRS Proc 299:65; Ghatak KP, Banik SN, Fizika A 3:127; Ghatak KP, Banik SN, FIZIKA A 3:155; Banik S, Ghatak KP, Biswas S (1994) FIZIKA A 3(2):77 ; Ghatak KP, Bhattacharyya D, Physica Status Solidi (B) 181:127; Ghatak KP, Biswas S (1994) Fizika A 3:7; Ghatak KP, Bhattacharyya D, Physica Status Solidi (B) 179:383; Chakraborty PK, Ghatak KP (1996) J Appl Phys 74:3246

# Screening Length, Terahertz Frequency and Opto-electronic Compounds


**R. Paul, J. Pal, S. Chakrabarti, B. Chatterjee, P. K. Das, T. Basu, and K. P. Ghatak**

**Abstract** In this chapter, we study the influences of size quantization, magnetic quantization, cross-fields configurations and inversion layers on the screening length (SL) in opto-electronic compounds. We note that the screening length oscillates with inverse quantizing magnetic field under magnetic quantization due to SdH effect, exhibits quantum jumps with nano-thickness under size quantization and changes with alloy composition, electron statistics and electric field in various manners for different types of opto-electronic compounds as considered here. All the results in the absence of terahertz frequency have further been plotted to exhibit the mathematical compatibility in this context.

R. Paul · S. Chakrabarti
Department of Computer Science and Engineering, Institute of Engineering and Management & University of Engineering and Management, Kolkata, India
e-mail: rajashree.paul@uem.edu.in

S. Chakrabarti
e-mail: satyajit.chakrabarti@iemcal.com

J. Pal
Department of Physics, Meghnad Saha Institute of Technology, Nazirabad, P.O. Uchepota, Anandapur, Kolkata 700150, India

B. Chatterjee
Department of Computer Science and Engineering, University of Engineering and Management, Jaipur, Rajasthan 303807, India
e-mail: biswajoy.chaterjee@iemcal.com

P. K. Das · T. Basu · K. P. Ghatak (✉)
Department of Basic Science and Humanities, Institute of Engineering and Management & University of Engineering and Management, Kolkata, India

P. K. Das
e-mail: prabir.das@iemcal.com

T. Basu
e-mail: tina.de@iemcal.com



A. Acharyya et al. (eds.), *Generation, Detection and Processing of Terahertz Signals*, Lecture Notes in Electrical Engineering 794,
https://doi.org/10.1007/978-981-16-4947-9_21

**Keywords** Screening length · Terahertz frequency · Opto-electronic compounds · Magnetic quantization · Size quantization · Cross-fields configurations · Inversion layers

## 1 Introduction

In recent years, various physical properties of nano-devices have been extensively investigated [1–30]. The impact of the concept of SL in solid-state devices has been widely studied [31–50]. The classical expressions of SL (denoted by $L_D$) in wide gap materials under two extreme conditions of degeneracy are given by $L_D = [\varepsilon_{sc} k_B T/(e^2 n_0)]^{1/2}$ and $L_D = (\pi^{2/3}\hbar\sqrt{\varepsilon_{sc}})(e g_v^{1/3} 3^{1/6} n_0^{1/6}\sqrt{m_c})^{-1}$, respectively, where the notations have their usual meaning. Under non-degenerate condition, $L_D$ is temperature dependent, whereas under the condition of extreme degeneracy, the SL is independent of temperature. In this chapter, we study the influences of size quantization, magnetic quantization, cross-field configurations and inversion layers on the SL in opto-electronic compounds.

## 2 Results and Discussion

Figures 1, 2, 3, 4, 5, 6, 7, 8, 9, 10, 11, 12, 13, 14, 15, 16, 17, 18, 19, 20, 21, 22, 23, 24, 25, 26, 27, 28, 29, 30, 31, 32, 33, 34, 35, 36, 37, 38, 39, 40, 41, 42, 43, 44, 45, 46, 47, 48, 49, 50, 51, 52, 53, 54, 55, 56, 57, 58, 59, 60, 61, 62, 63, 64, 65 and 66 exhibit the plots of normalized SL is (denoted by $\phi_3$) against normalized electron

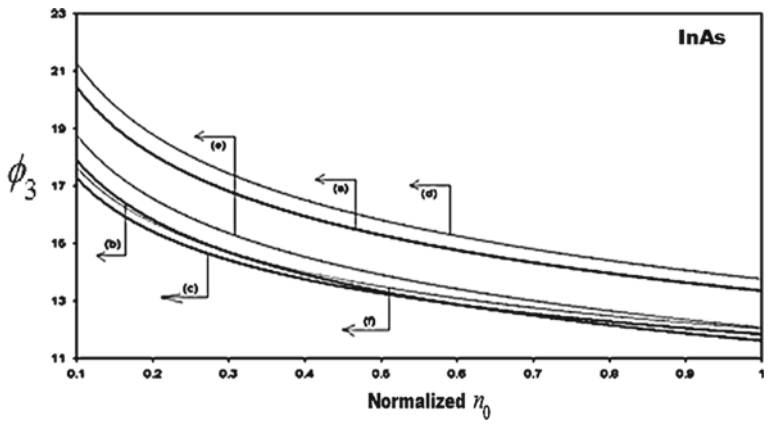


**Fig. 1** $\phi_3$ Against normalized $n_0$ for $W$ in the presence of terahertz frequency. The (a), (b) and (c) represent the three and two band models of Kane and together with wide bands, respectively. The (d), (e) and (f) represent the same when $I = 0$. The (g) exhibits the classical expression

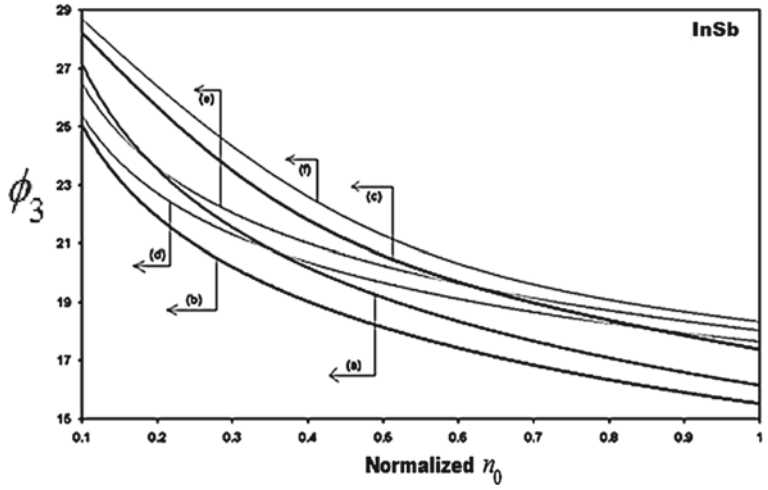


**Fig. 2** Plot of Fig. 1 for $X$

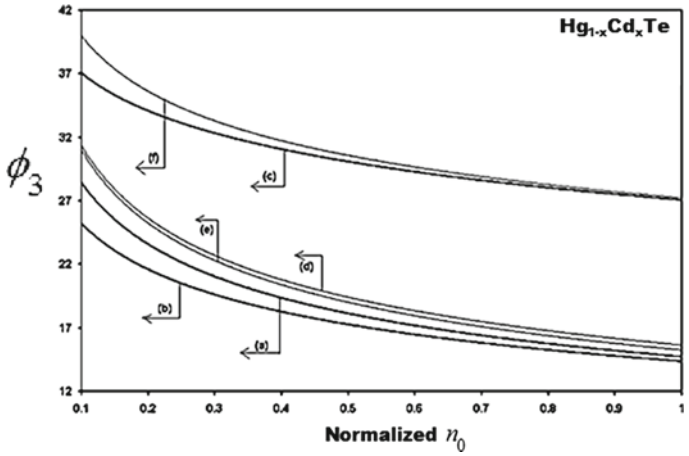


**Fig. 3** Plot of Fig. 1 for $Y$

statistics, intensity, wave length, alloy composition, magnetic field, film thickness and electric field, respectively. For the purpose of condensation, the HD materials $InAs$, $InSb$, $Hg_{1-x}Cd_xTe$, $In_{1-x}Ga_xAs_yP_{1-y}$ are denoted by $W$, $X$, $Y$ and $Z$, respectively. From the said figures, we observe the following:

1. The SL decreases with increasing electron statistics, intensity, wave length, alloy composition, respectively.
2. The SL oscillates with $1/B$ due to SdH effect.
3. In quantum wells, the SL exhibits quantum jumps with nano-thickness.
4. The specific magnitude of SL band structure dependent.

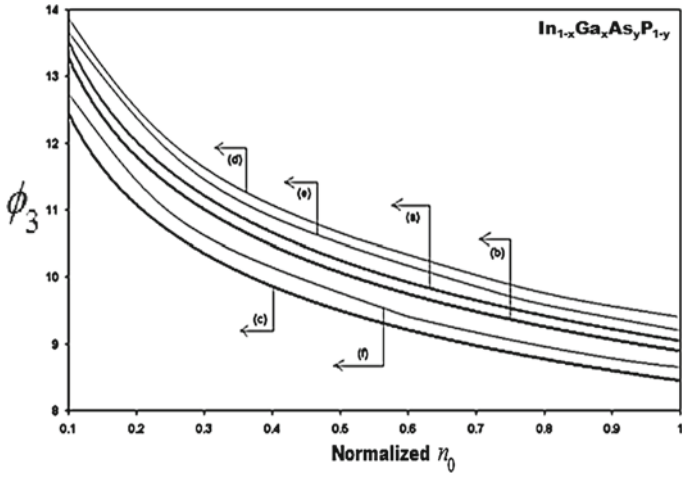


**Fig. 4** Plot of Fig. 1 for $Z$

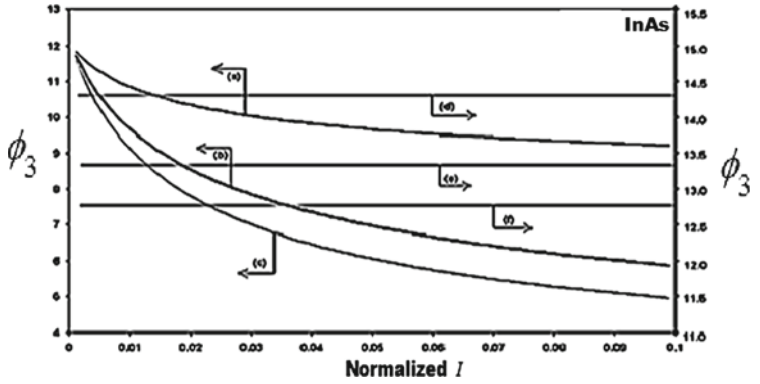


**Fig. 5** Plot of $\phi_3$ against $I$ for $W$

## 3 Summary

In this chapter, we study the influences of size quantization, magnetic quantization, cross-fields configurations and inversion layers on the screening length (SL) in opto-electronic compounds. We note that the screening length oscillates with inverse quantizing magnetic field under magnetic quantization due to SdH effect, exhibits quantum jumps with nano-thickness under size quantization and changes with alloy composition, electron statistics and electric field in various manners for different types of opto-electronic compounds as considered here. All the results in the absence of terahertz frequency have further been plotted to exhibit the mathematical compatibility in this context.

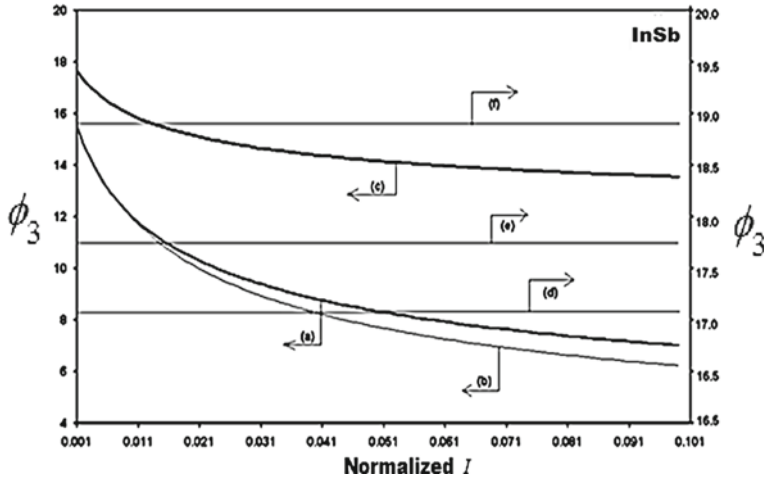


**Fig. 6** Plot of Fig. 5 for $X$

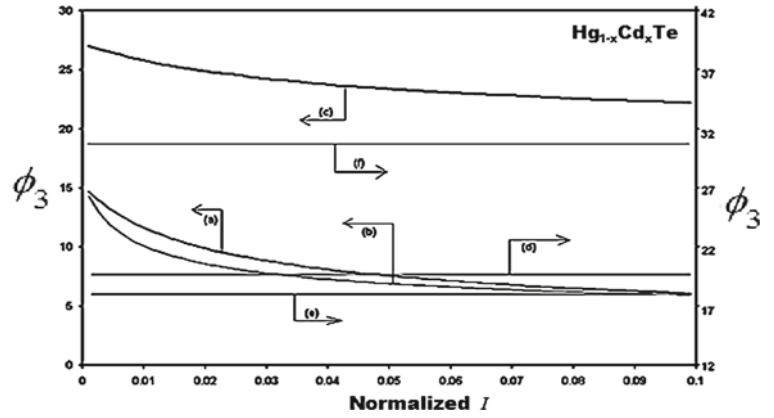


**Fig. 7** Plot of Fig. 5 for $Y$

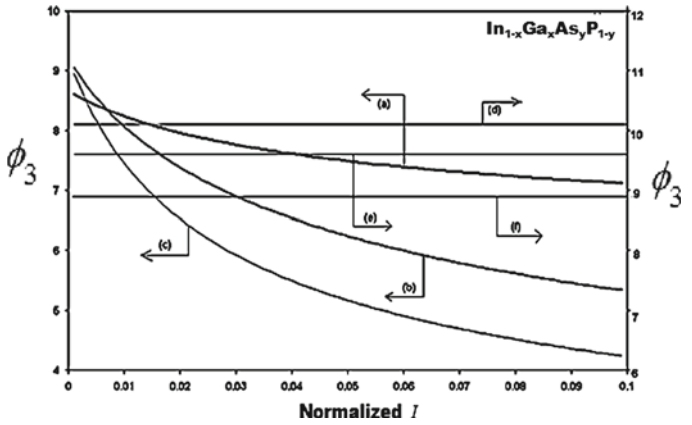


**Fig. 8** Plot of Fig. 5 for $Z$

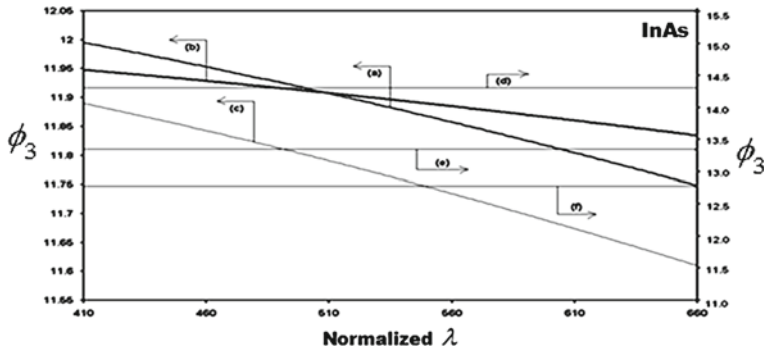


**Fig. 9** Plot of $\phi_3$ against λ for $W$

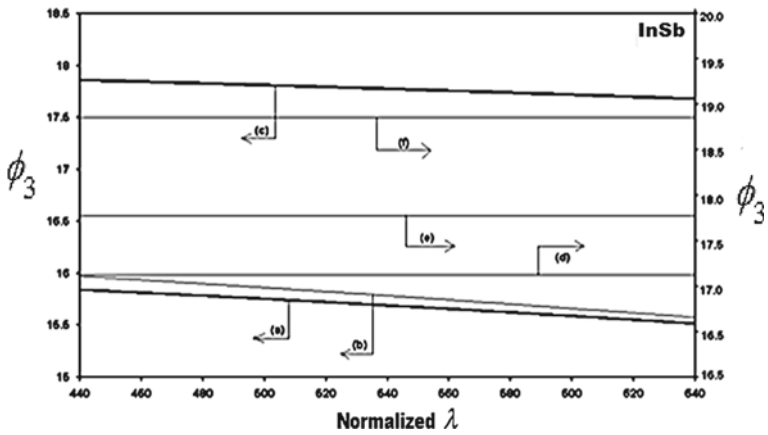


**Fig. 10** Plot of Fig. 9 for $X$

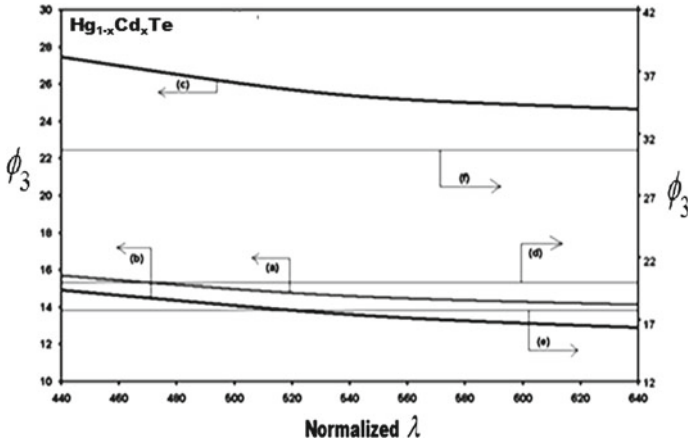


**Fig. 11** Plot of Fig. 9 for *Y*

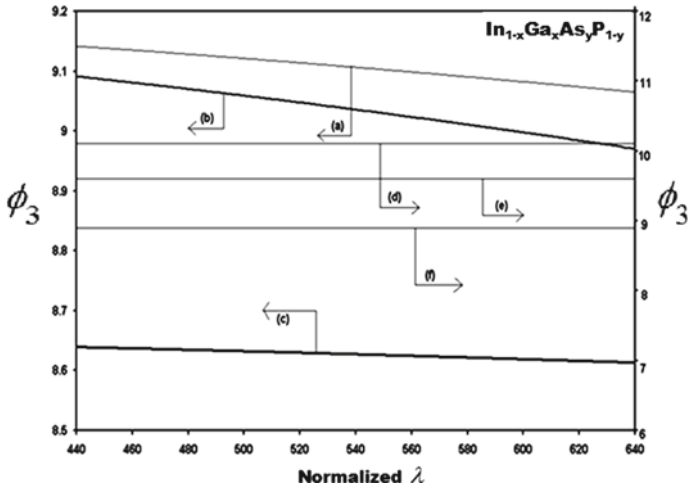


**Fig. 12** Plot of Fig. 9 for *Z*

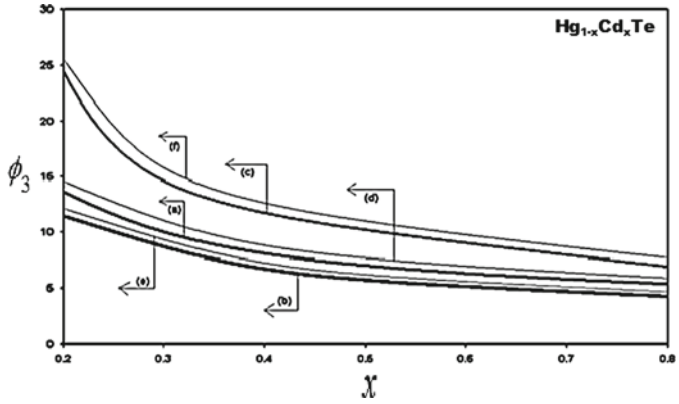


**Fig. 13** Plot of $\phi_3$ against $x$ for $Y$

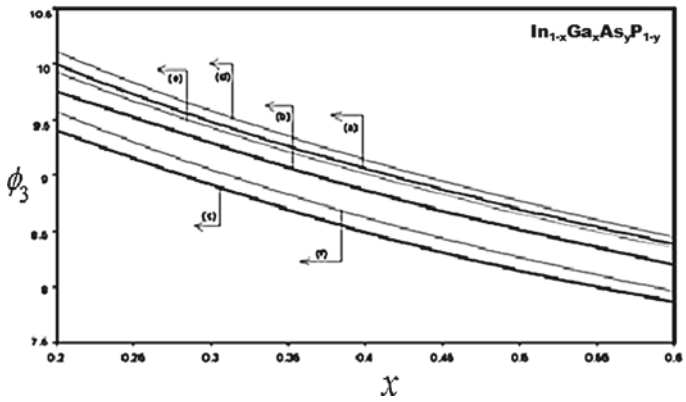


**Fig. 14** Plot of Fig. 13 for $Z$

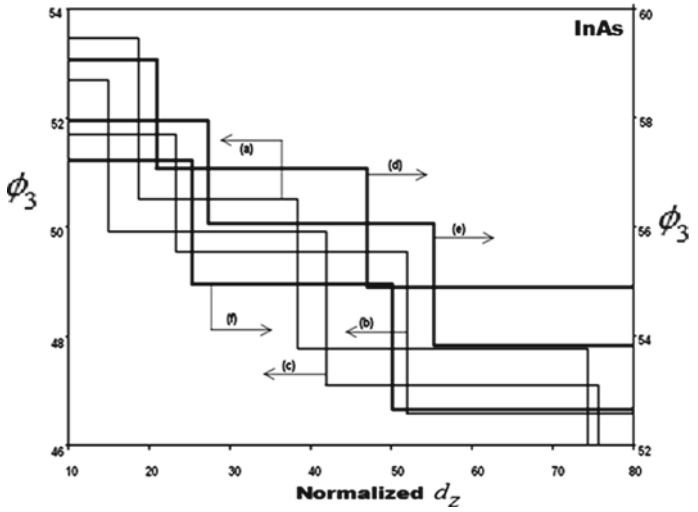


**Fig. 15** Plot of $\phi_3$ against $d_z$ for QWs of $W$

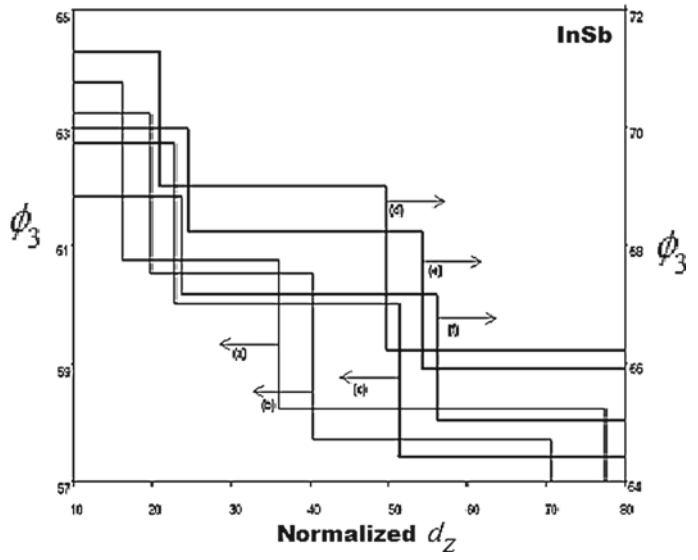


**Fig. 16** Plot of Fig. 15 for $X$

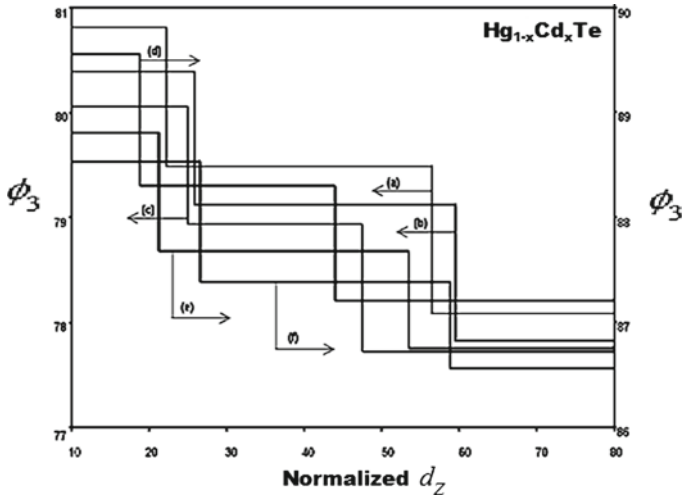


**Fig. 17** Plot of Fig. 15 for *Y*

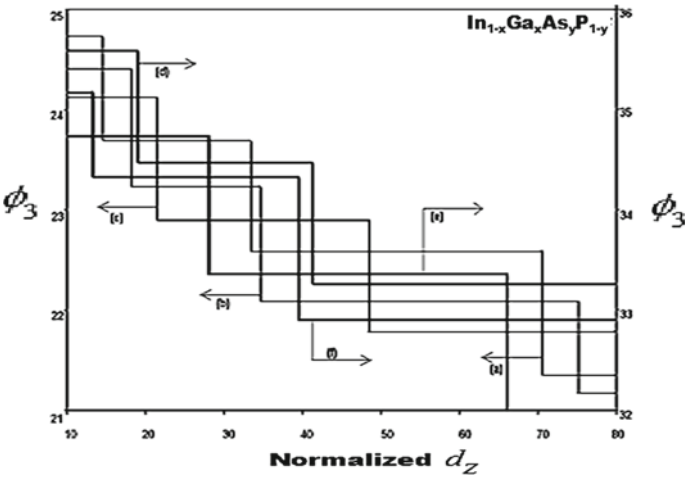


**Fig. 18** Plot of Fig. 15 for *Z*

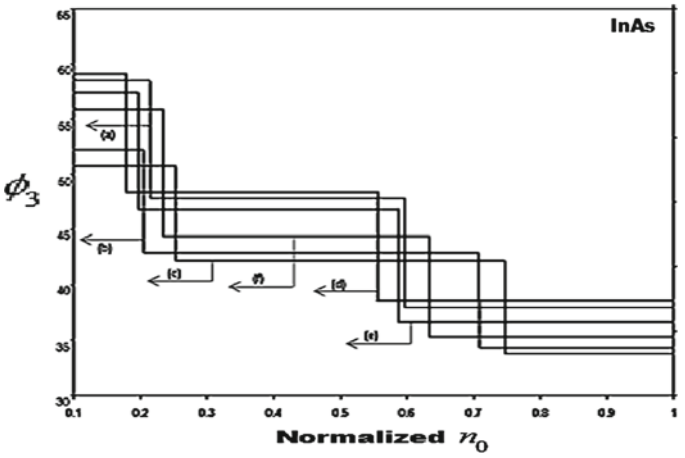


**Fig. 19** Plot of $\phi_3$ against $n_0$ for 2D *W*

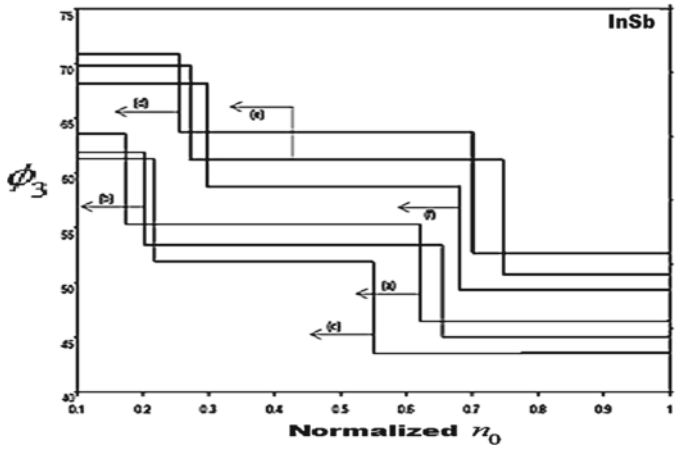


**Fig. 20** Plot of Fig. 19 for 2D *X*

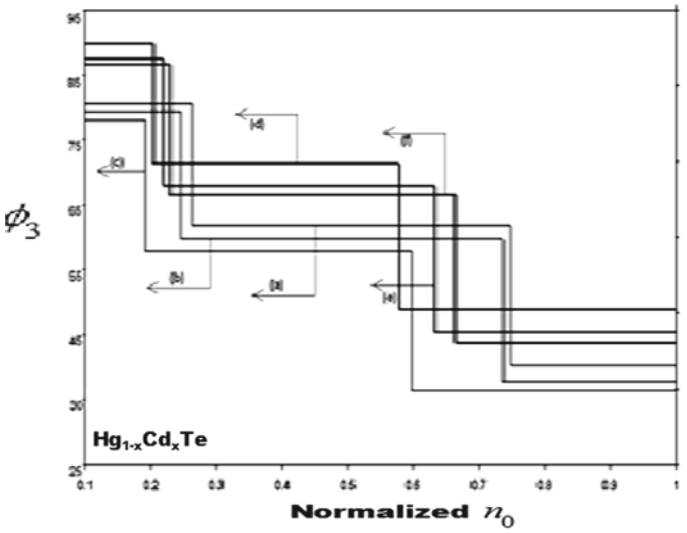


**Fig. 21** Plot of Fig. 19 for 2D *Y*

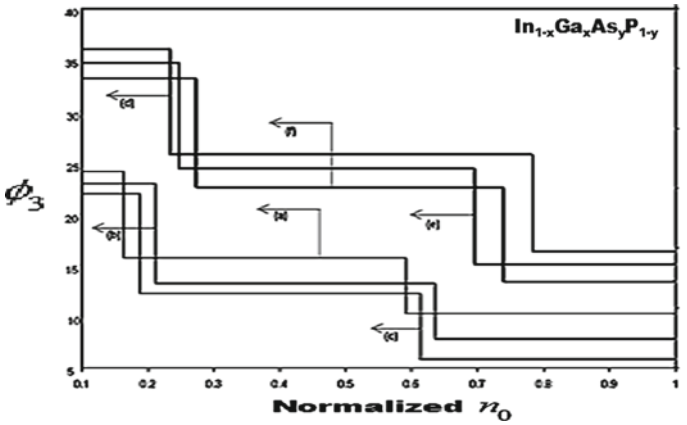


**Fig. 22** Plot of Fig. 19 for 2D *Z*

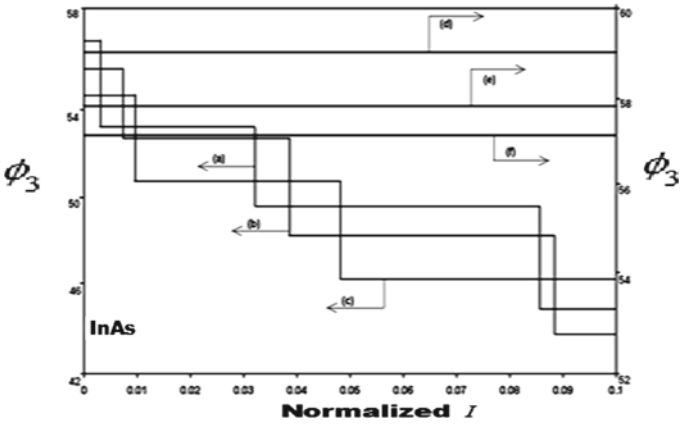


**Fig. 23** Plot of $\phi_3$ against $I$ for 2D $W$

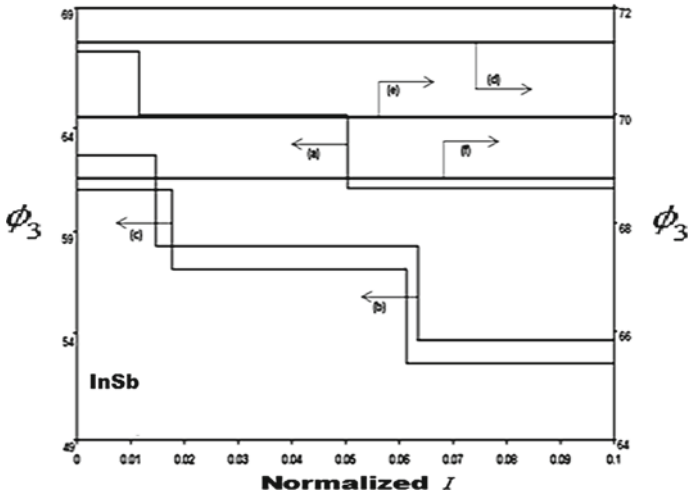


**Fig. 24** Plot of Fig. 23 for 2D $X$

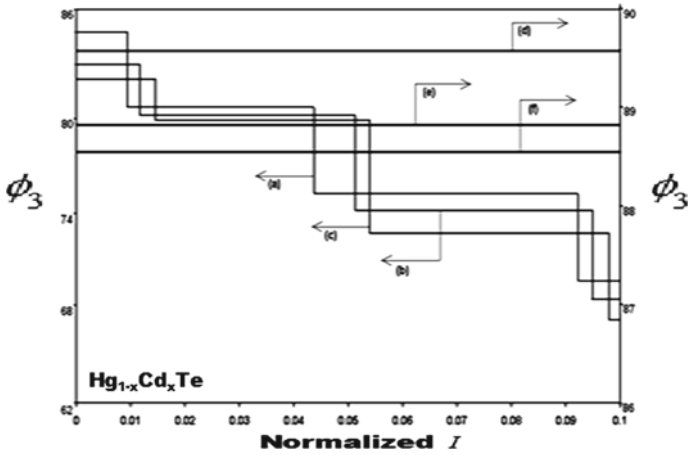


**Fig. 25** Plot of Fig. 23 for 2D $Y$

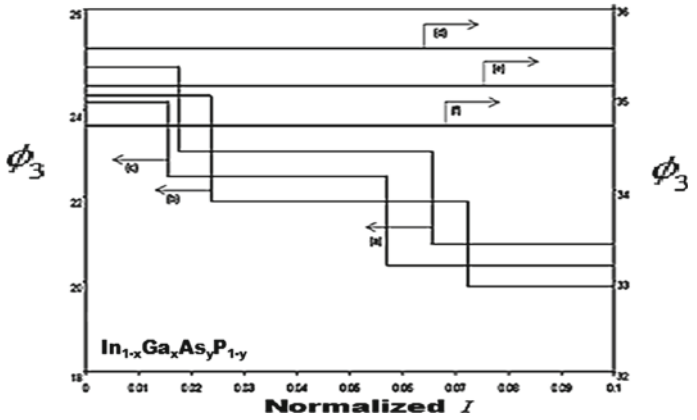


**Fig. 26** Plot of Fig. 23 for 2D $Z$

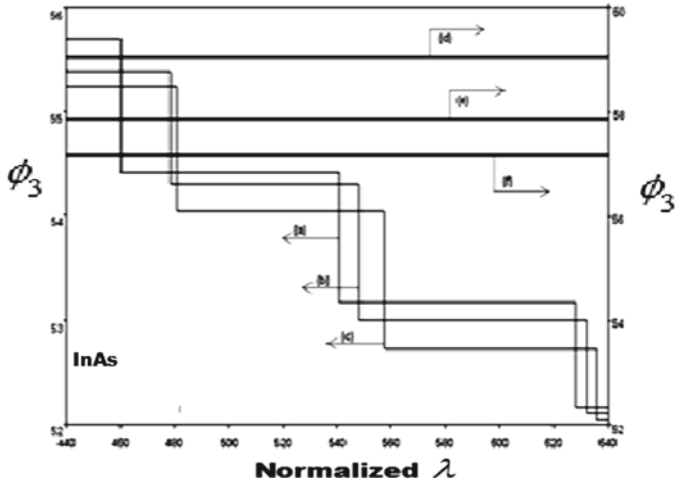


**Fig. 27** Plot of $\phi_3$ against λ for 2D *W*

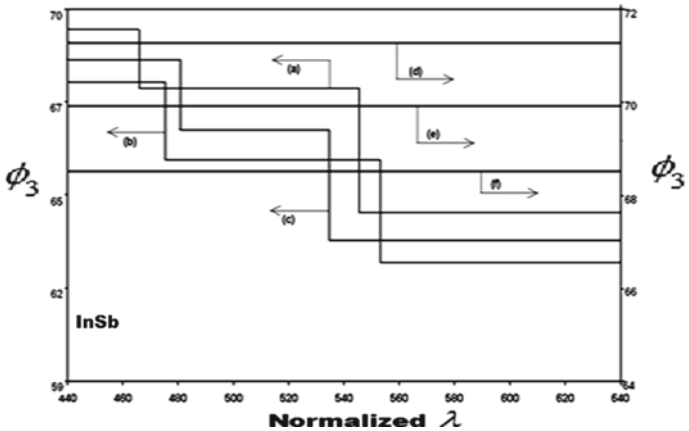


**Fig. 28** Plot of Fig. 27 for 2D *X*

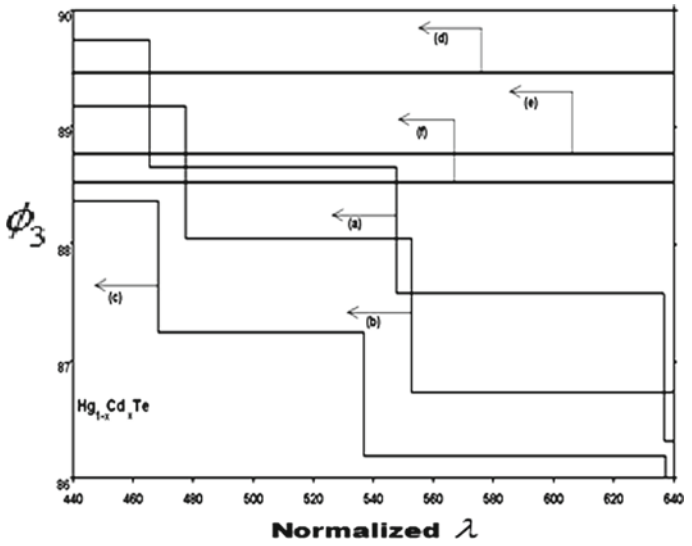


**Fig. 29** Plot of Fig. 27 for 2D *Y*

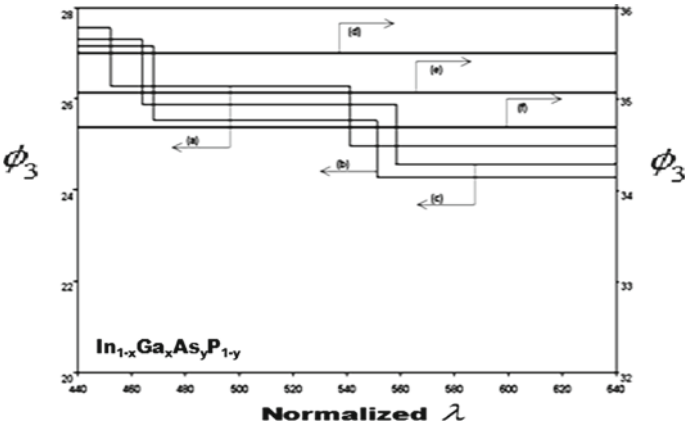


**Fig. 30** Plot of Fig. 27 for 2D *Z*

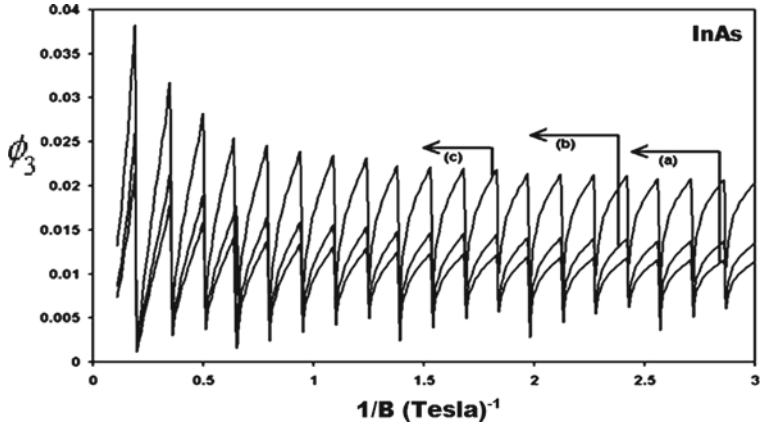


**Fig. 31** $\phi_3$ against $1/B$ for $W$

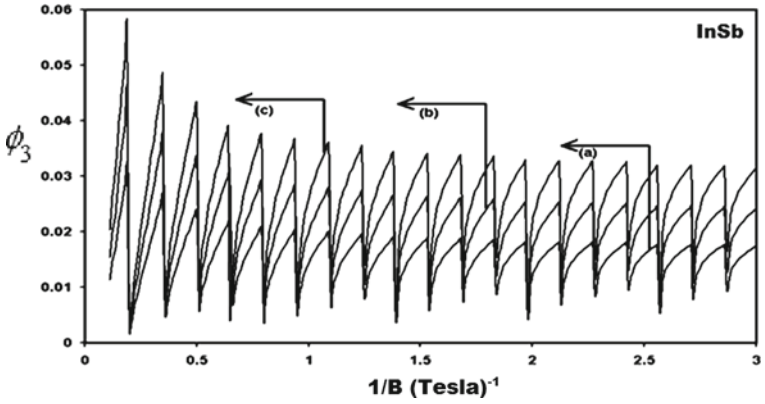


**Fig. 32** Plot of Fig. 31 for $X$

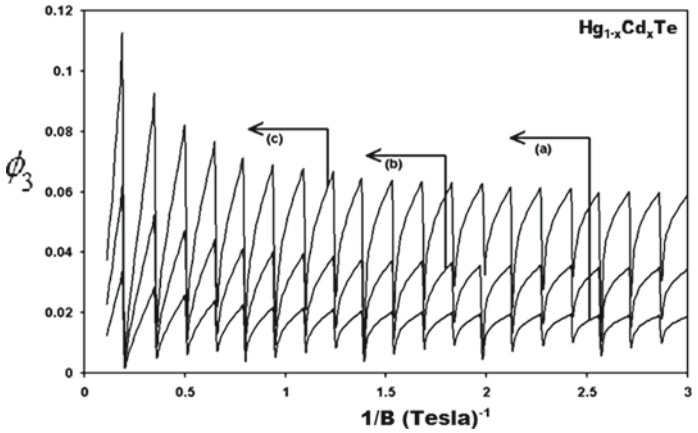


**Fig. 33** Plot of Fig. 31 for *Y*

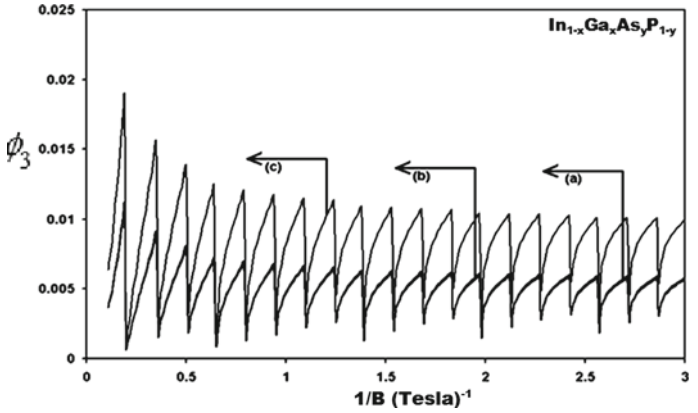


**Fig. 34** Plot of Fig. 31 for *Z*

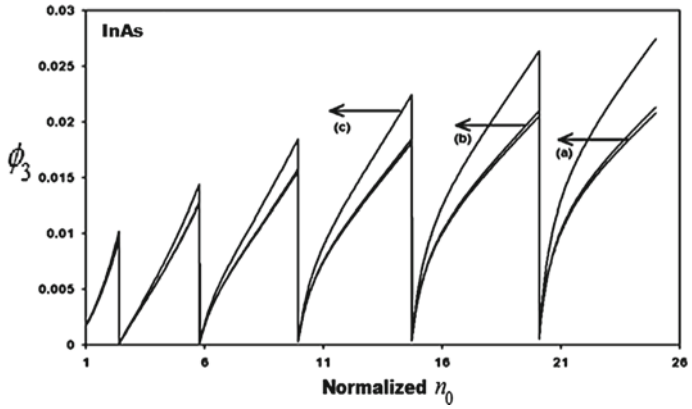


**Fig. 35** $\phi_3$ against $n_0$ for QWs of $W$

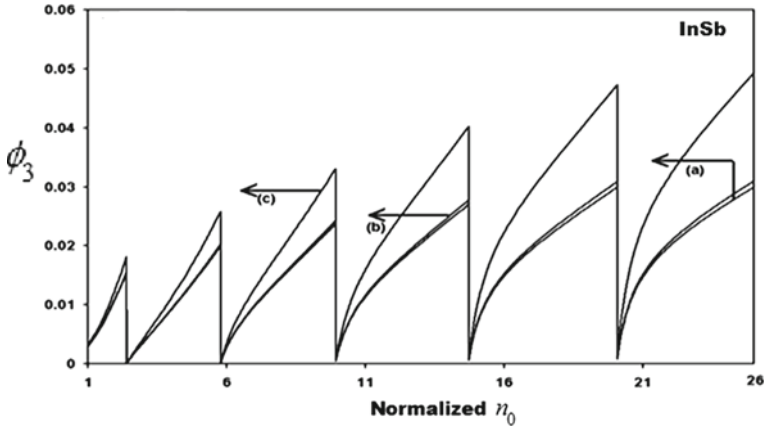


**Fig. 36** Plot of Fig. 35 for $X$

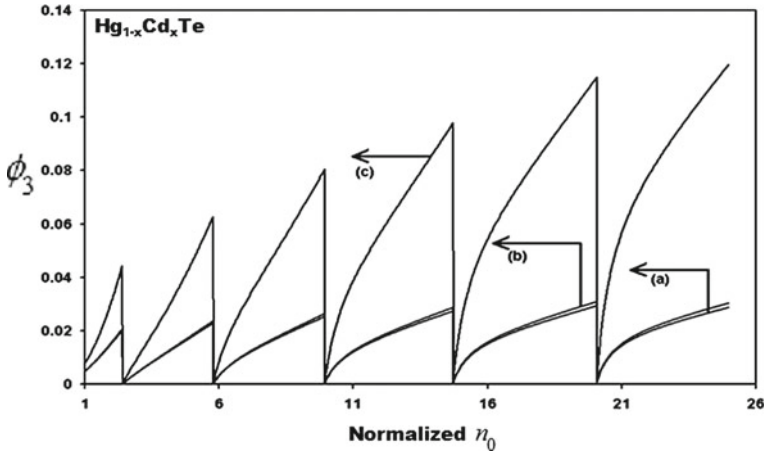


**Fig. 37** Plot of Fig. 35 for *Y*

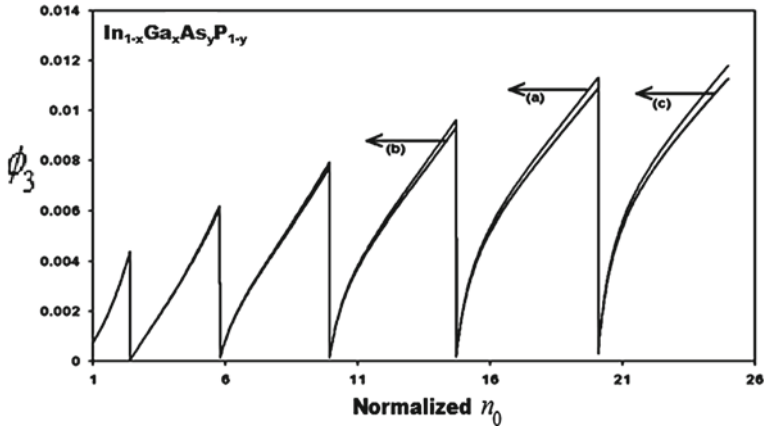


**Fig. 38** Plot of Fig. 35 for *Z*

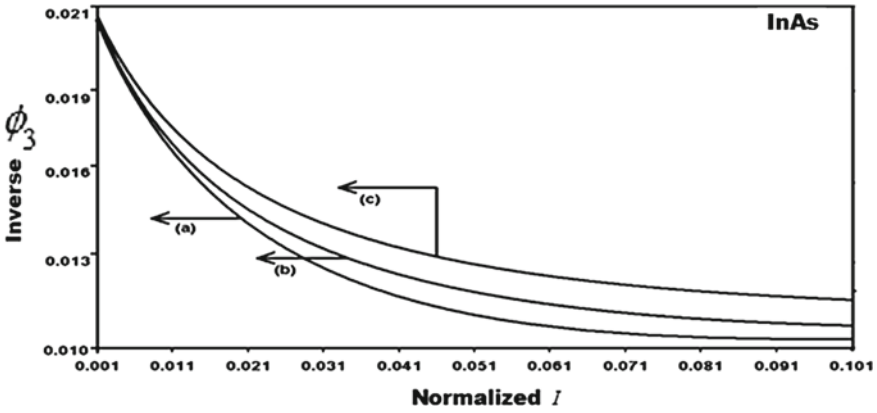


**Fig. 39** Plot of inverse $\phi_3$ against $I$ for $W$

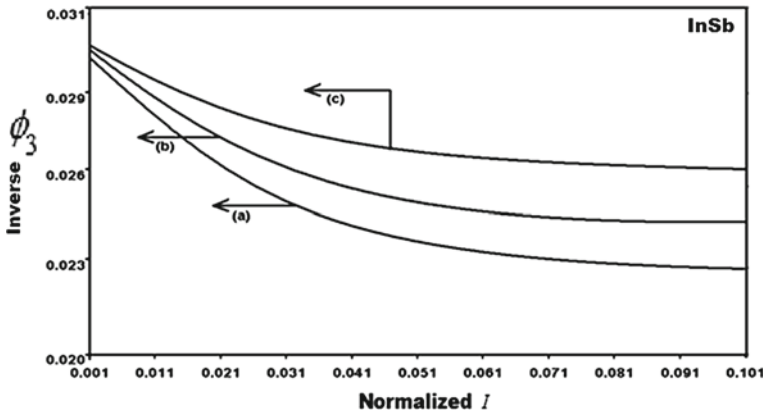


**Fig. 40** Plot of Fig. 39 for $X$

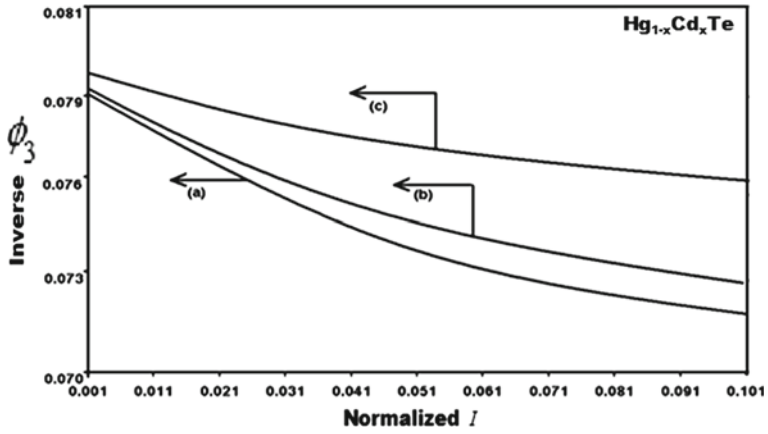


**Fig. 41** Plot of Fig. 39 for $Y$

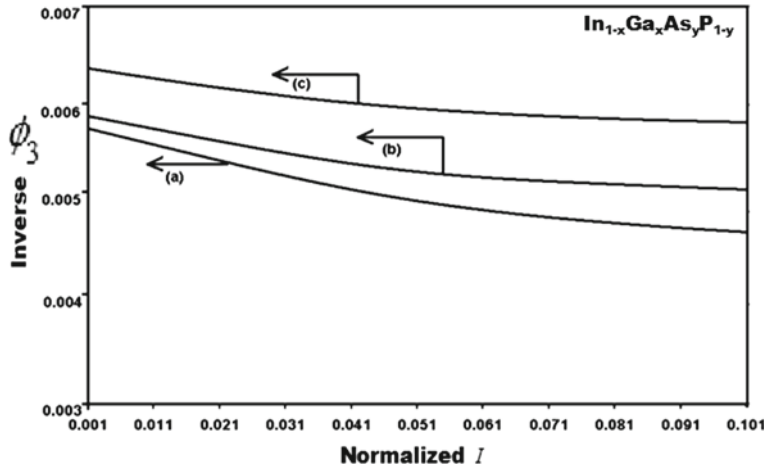


**Fig. 42** Plot of Fig. 39 for $Z$

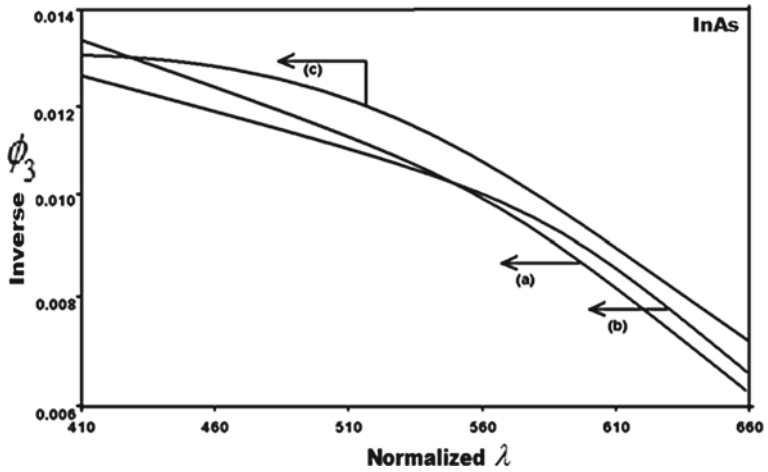


**Fig. 43** Plot of $\phi_3$ against λ for *W*

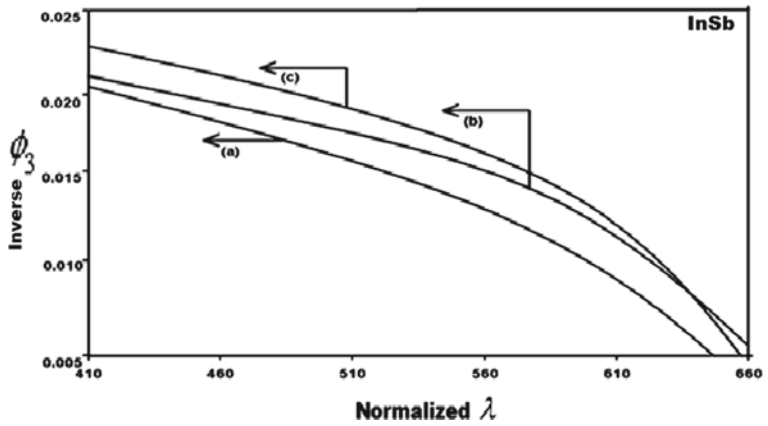


**Fig. 44** Plot of Fig. 43 for *X*

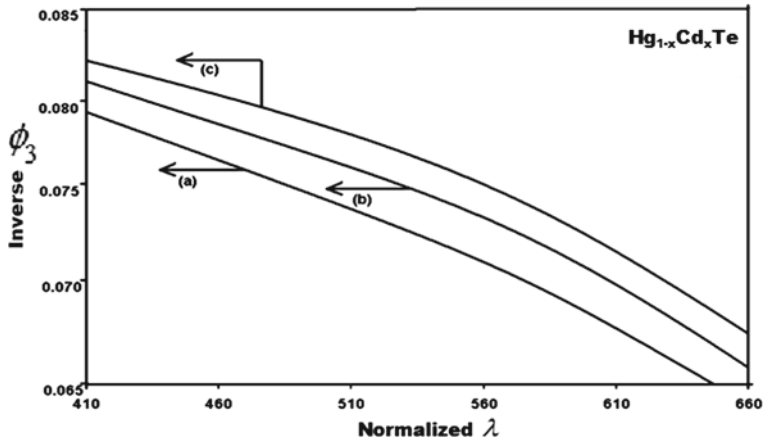


**Fig. 45** Plot of Fig. 43 for *Y*

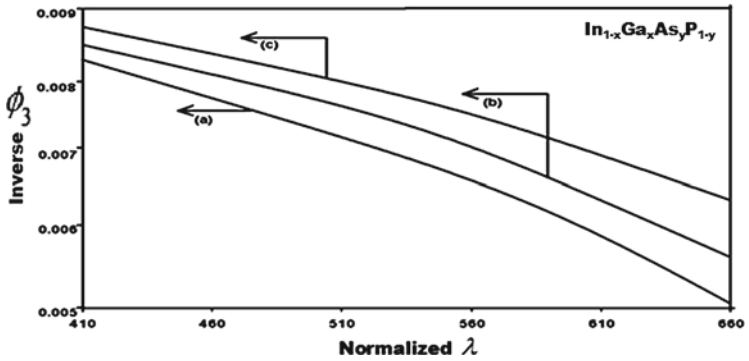


**Fig. 46** Plot of Fig. 43 for *Z*

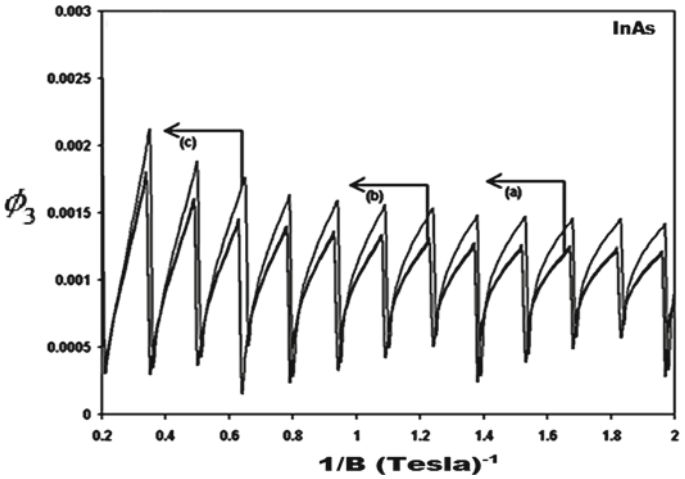


**Fig. 47** Plot of $\phi_3$ against $1/B$ for $W$ under cross-fields configuration

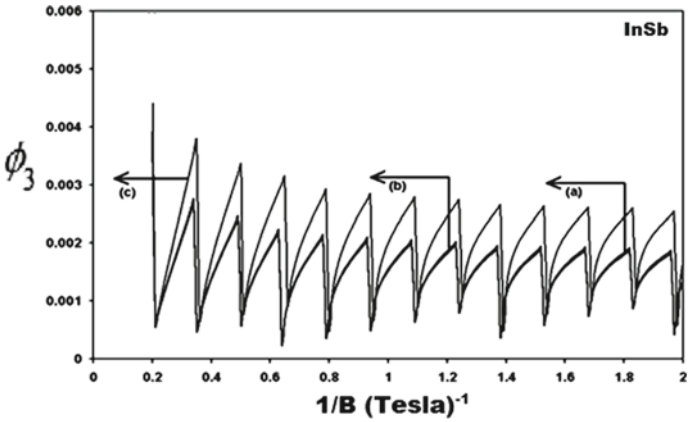


**Fig. 48** Plot of Fig. 47 for $X$

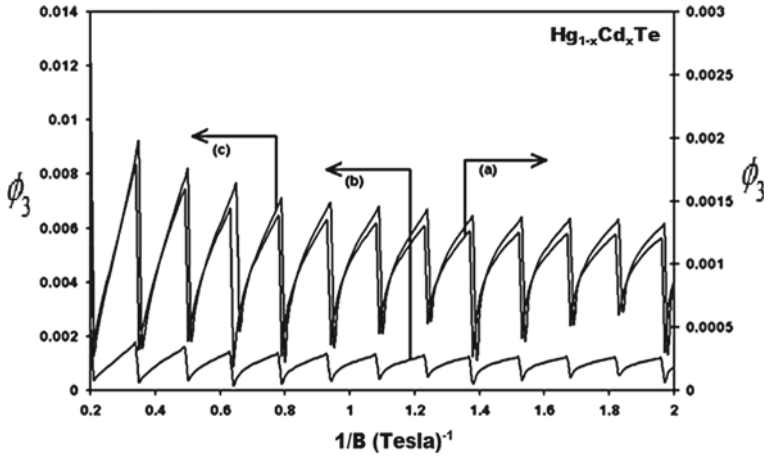


**Fig. 49** Plot of Fig. 43 for *Y*

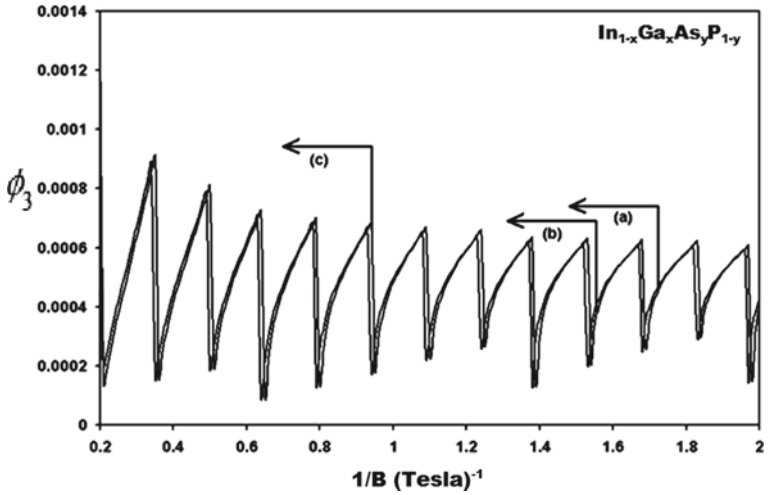


**Fig. 50** Plot of Fig. 43 for *Z*

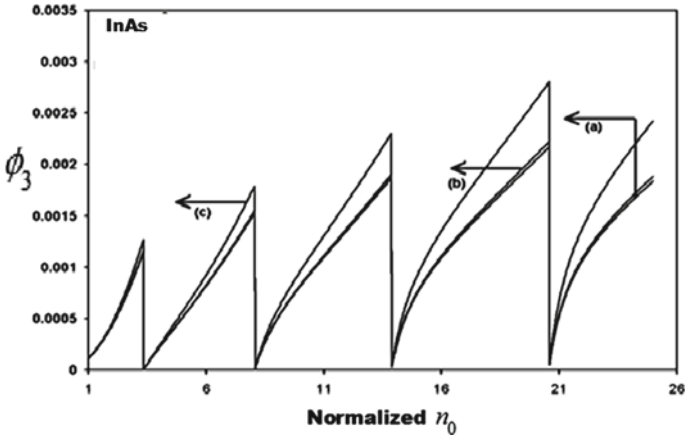


**Fig. 51** Plot of $\phi_3$ against $n_0$ for $W$ under cross-field configuration

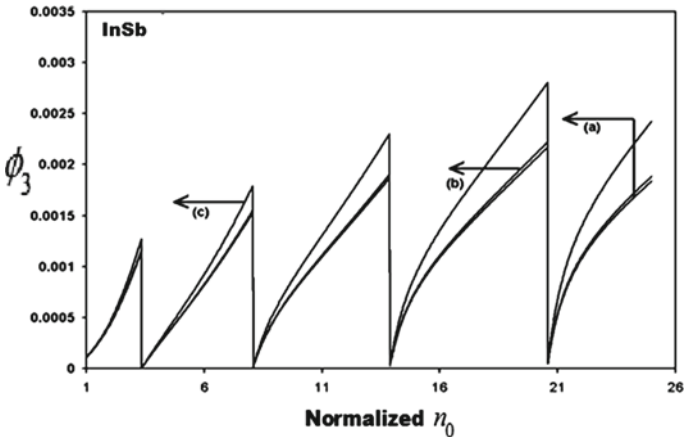


**Fig. 52** Plot of Fig. 51 for $X$

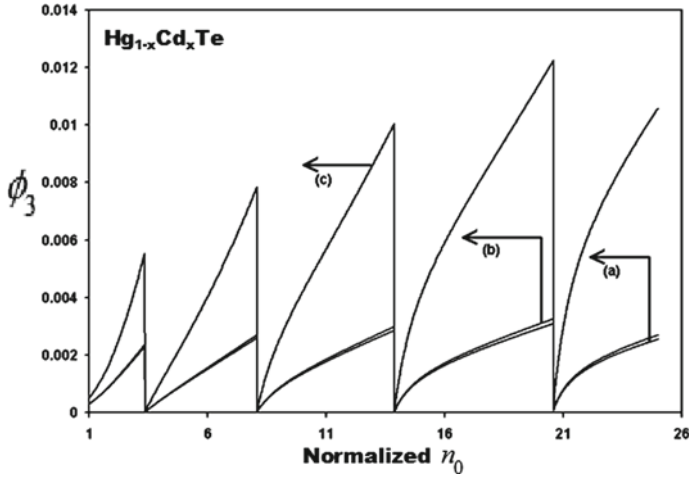


**Fig. 53** Plot of Fig. 51 for *Y*

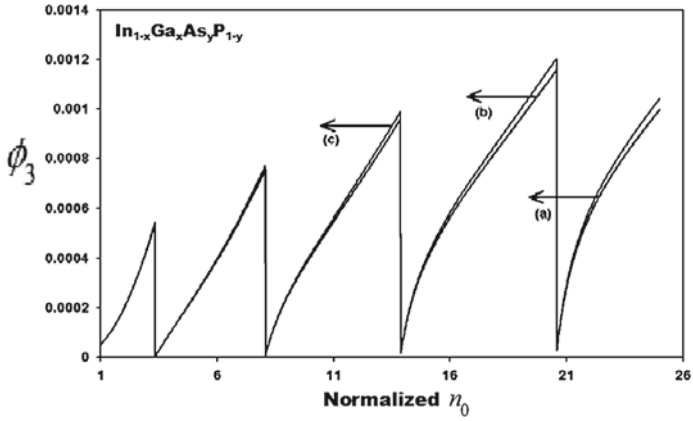


**Fig. 54** Plot of Fig. 51 for *Z*

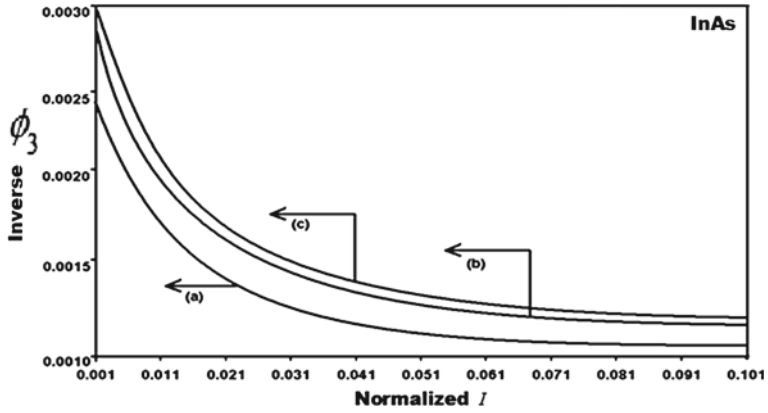


**Fig. 55** Plot of $\phi_3$ against $I$ for $W$ under cross-field configuration

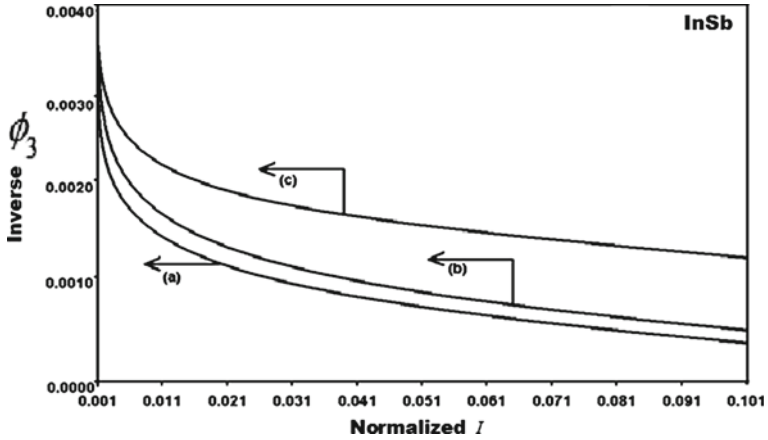


**Fig. 56** Plot of Fig. 55 for $X$

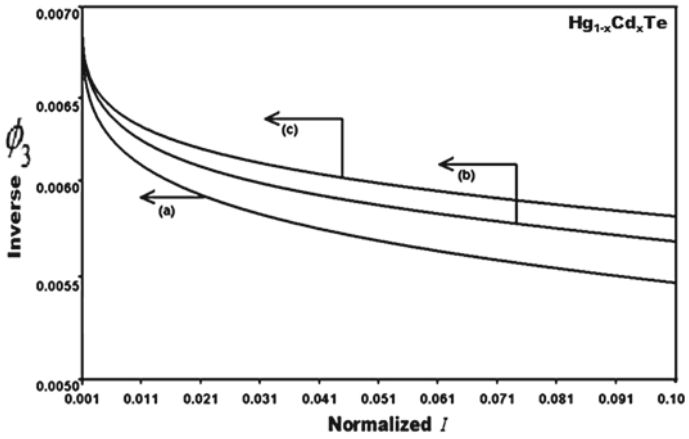


**Fig. 57** Plot of Fig. 55 for $Y$

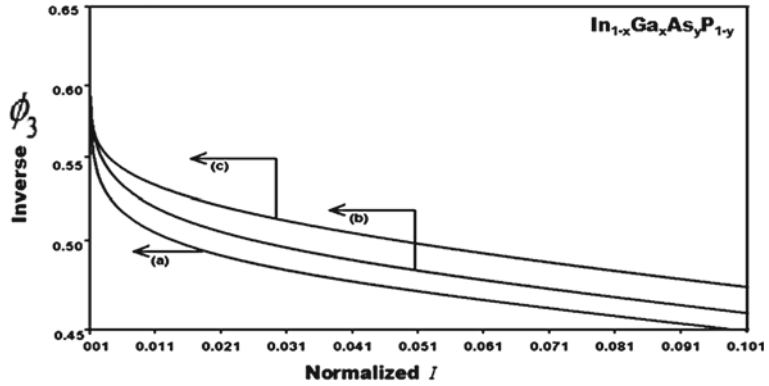


**Fig. 58** Plot of Fig. 55 for $Z$

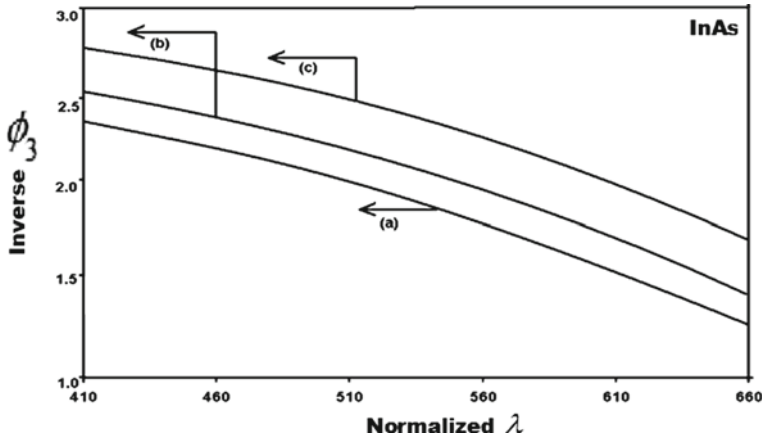


**Fig. 59** Plot of $\phi_3$ against λ for $W$ under cross-field configuration

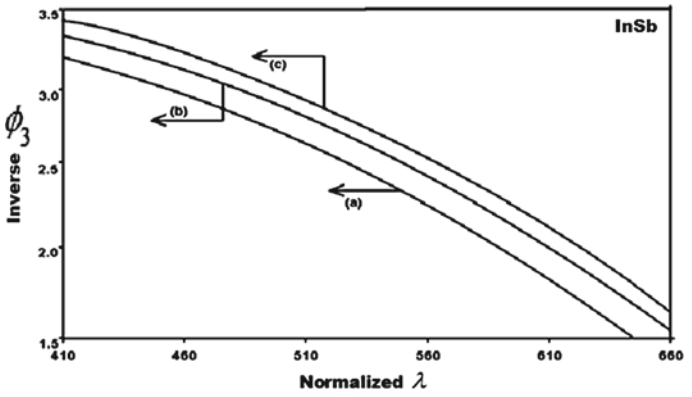


**Fig. 60** Plot of Fig. 59 for $X$

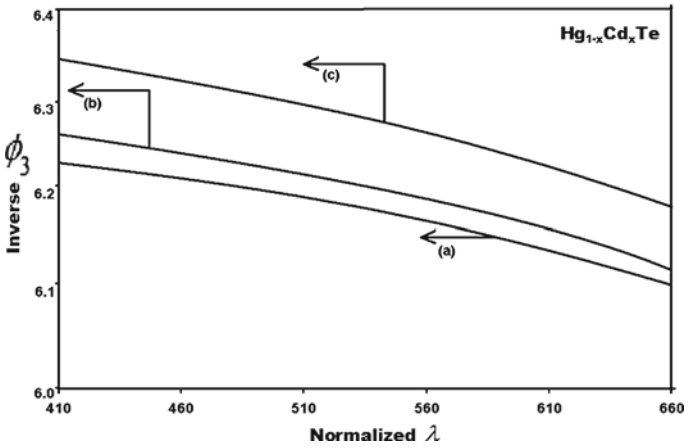


**Fig. 61** Plot of Fig. 59 for *Y*

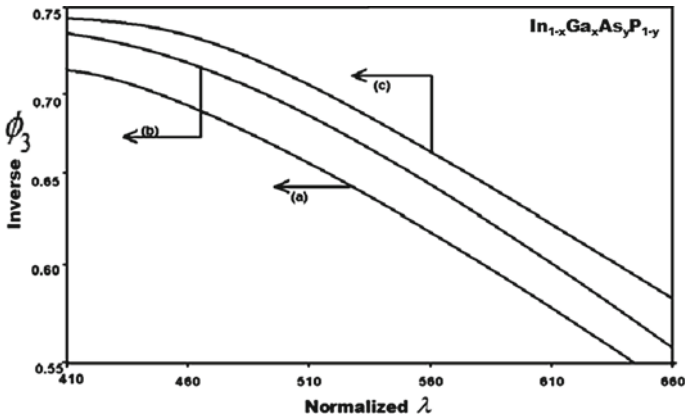


**Fig. 62** Plot of Fig. 59 for *Z*

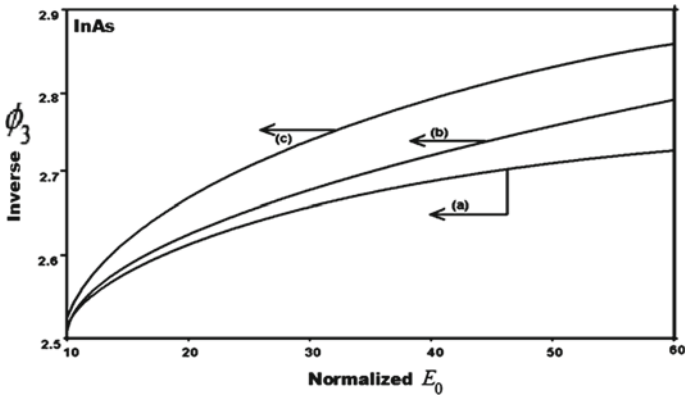


**Fig. 63** Plot of $\phi_3$ against $E_0$ for $W$ under cross-field configuration

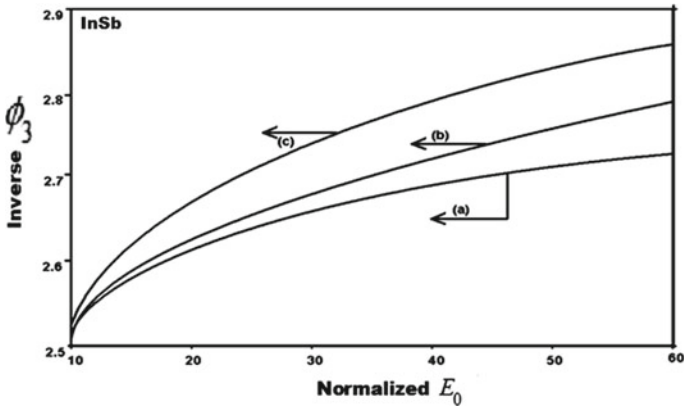


**Fig. 64** Plot of Fig. 63 for $X$

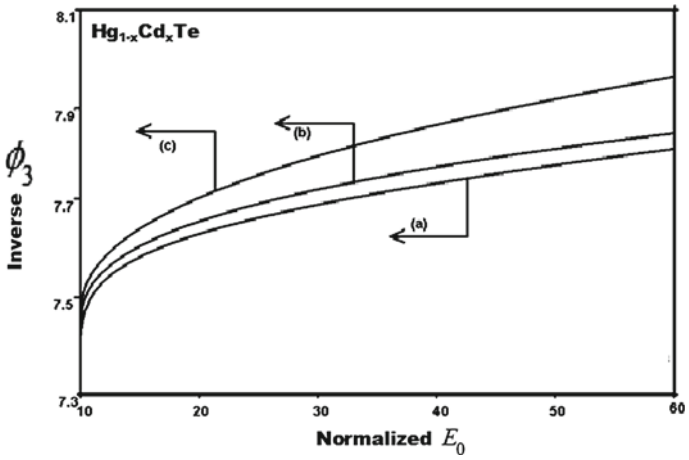


**Fig. 65** Plot of Fig. 63 for *Y*

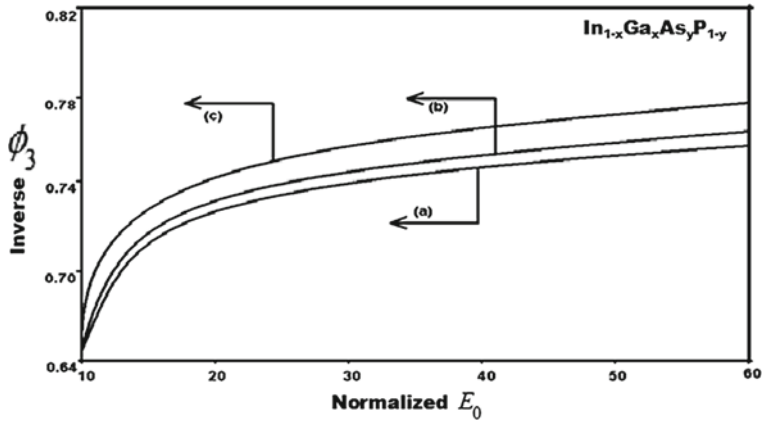


**Fig. 66** Plot of Fig. 63 for *Z*

**Acknowledgements** The authors are grateful to Prof. Dr. S. Chakrabarti, President of IEM UEM Group, India, for his constant encouragement and inspiration in this context.

## References

1. Bhattacharya S, Ghatak KP (2012) Fowler-Nordheim field emission: effects in semiconductor nanostructures. Springer series in solid state sciences (vol 170). Springer; Seikh AH, Alharthi N, Bose PK, Ghatak KP (2020) Emerging trends in terahertz solid-state physics and devices. Springer, Singapore, pp 85–106

2. Ghatak KP, Mitra M (2020) Quantization and entropy. Series in nanomaterials (vol 2). De Gruyter, Germany
3. Ghatak KP (2020) Quantum wires: an overview. Series in nanotechnology science and technology. Nova, USA
4. Ghatak KP, Bhattacharya S, De D (2009) Einstein relation in compound semiconductors and their heterostructures. Springer series in materials science (vol 116). Springer
5. Ghatak KP, De D, Bhattacharya S (2009) Photoemission from optoelectronic materials and their nanostructures. Springer series in nanostructure science and technology. Springer
6. Ghatak KP, Bhattacharya S (2010) Thermo electric power in nano structured materials strong magnetic fields. Springer series in materials science (vol 137). Springer
7. Ghatak KP, Mitra M (2020) Electronic properties. Series in nanomaterials (vol 1). De Gruyter, Germany
8. Bhattacharya S, Ghatak KP (2013) Effective electron mass in low dimensional semiconductors. Springer series in materials sciences (vol 167). Springer
9. Ghatak KP, Bhattacharya S (2015) Heavily doped 2D quantized structures and the Einstein relation. Springer tracts in modern physics (vol 260). Springer
10. Ghatak KP (2015) Einstein's photo-emission: emission from heavily doped quantized structures. Springer tracts in modern physics (vol 262). Springer
11. Ghatak KP (2016) Dispersion relations in heavily-doped nanostructures. Springer tracts in modern physics (vol 265). Springer
12. Ghatak KP (2016) Magneto thermoelectric power in heavily doped quantized structures. Series on the foundations of natural science and technology (vol 7). World Scientific
13. Ghatak KP (2017) Quantum effects, heavy doping, and the effective mass. Series on the foundations of natural science and technology (vol 8). World Scientific
14. Debbarma M, Das S, Pal J, Debbarma S, Paul R, Das PK, Dutta T, Ghatak KP (2019) Gate capacitance in quantum metal-oxide-semiconductor field-effect transistor devices of technologically important materials. Adv Sci, Eng Med 11:1161; Ghatak KP, Chakrabarti S, Chatterjee B, Debbarma M, Debbarma N (2019) The energy-wave vector relations and the density-of-states function in heavily doped non-parabolic materials. Adv Sci, Eng Med 11:914
15. Biswas SK, Pradhan AK, Bhattacharya K, Maiti S, Mitra M, Chakrabarti S, Chatterjee B, Ghatak KP (2019) On the electron energy spectrum in quantum wells of heavily doped III–V materials in the presence of an arbitrarily oriented magnetic field. Adv Sci, Eng Med 11:977; Paul R, Das PK, Mitra M, Ghatak KP (2019) Heisenberg's uncertainty principle and the gate capacitance in quantum metal oxide silicon field effect transistor devices. Adv Sci, Eng Med 11:903; Das PK, Ghatak KP (2019) Dimension dependent density-of-states function and the radiation laws. J Nanosci Nanotechnol 19:2909
16. Ghatak KP, Chakrabarti S, Chatterjee B (2018) Influence of intense electric field on the screening length in opto-electronic materials. Mater Focus 7:390; Singh SL, Singh SB, Ghatak KP (2018) 2D effective electron mass at the fermi level in accumulation and inversion layers of mosfet nano devices. J Nanosci Nanotechnol 18:2856
17. Ghatak KP, Mitra M, Paul R, Chakrabarti S (2017) Intense light waves, heavily doped kane type opto electronic nano-structures, carrier contribution to the elastic constants and all that. J Comput Theor Nanosci 14:2138; Chatterjee B, Debbarma N, Mitra M, Datta T, Ghatak KP (2017) 2D effective electron mass at the fermi level in accumulation and inversion layers of mosfet nano devices. J Comput Theor Nanosci 17:3352; Ghatak KP, De D (2017) A special section on physical properties of low dimensional heavily doped materials. Mater Focus 6:114
18. Das PK, Dutta P, Halder A, Pal J, Debbarma N, Debbarma S, Ghatak KP (2017) Heavily doped single quantum wells and the effective mass. Mater Focus 6:167; Das PK, Dutta P, Halder A, Bhattacharjee R, Ghatak KP (2017) Can photons affect the entropy?. Mater Focus 6:133
19. Bhattacharjee R, Ghatak KP (2017) Entropy, electric field and heavily doped nanowires. J Nanosci Nanotechnol 17:640; Mitra M, Sen TN, Datta T, Bhattacharjee R, Singh LS, Ghatak KP (2017) Heisenberg's uncertainty principle, intense electric field, heavily doped optoelectronic quantized structures and the electron statistics. J Nanosci Nanotechnol 17: 256; Sen TN, Ghatak KP (2016) Einstein's photoemission and the richardson-dushman formula. Quantum Matter 5:732

20. Sen TN, Ghatak KP (2016) On the simplest derivation of einstein's E= $MC^2$ without using relativity for only photons and under stationary frame of reference. Quantum Matter 5:721; Ghatak KP, Sarkar K, Chakrabarti S, Kumar M, Debbarma M, Sen TN, Chakraborty M (2016) Heavily doped quantum wells and the magneto-thermoelectric power. Rev Theor Sci 4:199; Bhattacharya R, Sarkar K, Kumar M, Chatterjee B, Ghatak KP (2016) Nanostructures, magnetic field and electron energy spectra. Quantum Matter 5:557
21. Ghatak KP, Sarkar K, Debbarma N, Singh LS (2016) Dispersion relations of heavily doped quantum wells. Quantum Matter 5:427; Ghatak KP, De D (2016) A special issue on electronic properties of nano-structured materials. J Nanoeng Nanomanuf 6:1; Biswas SK, Mitra M, Ghatak KP (2016) Thermo power, large magnetic field, quantized structures and all that. J Nanoeng Nanomanuf 6:63
22. Chakrabarti S, Chakraborty M, Ghatak KP (2016) Einstein and his photoemission from heavily doped quantum wells. Rev Theor Sci 4:10–66; Paitya N, Ghatak KP (2016) Analysis of screening length in doping superlattices. Quantum Matter 5:191; Chatterjee B, Chakrabarti S, Sen SK, Mitra M, Ghatak KP (2016) Influence of parallel electric and magnetic fields on the carrier contribution to the elastic constants in kane type semiconductors. Quantum Matter 5:85; Mitra M, Chakraborty M, Debbarma S, Chakraborty S, Sen SK, Chatterjee B, Ghatak KP (2016) On the carrier contribution to the elastic constants in ultra-thin films of III–V and optoelectronic materials in the presence of intense electric field. Quantum Matter 5:58
23. Sen TN, Ghatak KP (2016) Einstein's 1d photo emission and the von klitzing constant. J Nanosci, Nanotechnol 16:1229; Debbarma S, Ghatak KP (2016) Einstein's photoemission from quantum confined superlattices. J Nanosci, Nanotechnol 16:1095; Chatterjee B, Chakrabarti S, Chakraborty M, Ghatak KP (2015) Heavily doped semiconductors and the diffusion coefficient to mobility relationship. Rev Theor Sci 3:428
24. Adhikari SM, Ghatak KP (2015) Effect of intense electric field on the debye screening length in III–V, ternary and quaternary semiconductors: simplified theory, relative assessment and suggestion for experimental determination. Quantum Matter 4:599; Chakrabarti S, Chatterjee B, Debbarma S, Ghatak KP (2015) Two dimensional effective electron mass at the fermi level in quantum wells of III–V, ternary and quaternary semiconductors. J Nanosci Nanotechnol 15:6460; Adhikari SM, Karmakar A, Ghatak KP (2015) Quantization and screening length. Rev Theor Sci 3:273
25. Mitra M, Chatterjee B, Ghatak KP (2015) 2D Einstein Relation in Quantum Wells Under Strong Electric Field. J Comput Theor Nanosci 12:1527; Mitra M, Chakrabarti S, Chakraborty M, Debbarma S, Ghatak KP (2015) 2D screening length in ultrathin films under intense electric field. J Comput Theor Nanosci 12:1898; Ghatak KP, Singh LS, Sarkar K, Debbarma N, Debbarma M (2015) Light, Einstein relation, quantization and the heavily doped opto-electronic materials. Mater Focus 4:85
26. Chakraborty M, Ghatak KP (2015) The screening length in doping superlattices. Quantum Matter 4:104. Sarkar K, Chakraborty M, Chakravarti S, Chatterjee B, Ghatak KP (2015) Quantum confined heavily doped optoelectronic materials and the einstein's photoemission. J Nanoeng Nanomanuf 5:43; Debbarma S, Ghatak KP (2015) Quantum confinement and the diffusivity mobility ratio. Rev Theor Sci 3:16
27. Adhikari SM, Karmakar A, Ghatak KP (2014) Diffusivity-mobility ratio in heavily doped quantum wells under intense light waves. J Comput Theor Nanosci 11:2499; Chatterjee B, Debbarma N, Debbarma S, Chakrabarti S, Ghatak KP (2014) Influence of parallel electric and magnetic fields on the einstein relation in kane type semiconductors. Adv Sci Eng Med 6:1177; Debbarma S, Chakravarti S, Debbarma N, Mitra M, Ghatak KP (2014) Influence of parallel electric and quantizing magnetic fields on the screening length in III–V, ternary and quaternary semiconductor. J Adv Phys 3:213
28. Debbarma S, Debbarma N, Chatterjee B, Adhikari SM, Ghatak KP (2014) Can photon influence the screening length in heavily doped quantum wells?. Adv Sci Eng Med 6:1024; Chakrabarti S, Sen SK, Chakraborty S, Singh LS, Ghatak KP (2014) Einstein relation in heavily doped quantum wires superlattices with graded interfaces: simplified theory and suggestion for experimental determination. Adv Sci Eng Med 6(9):1042; Adhikari SM, Sakar A, Ghatak KP (2013)

Simple theoretical analysis of the field emission from quantum wire effective mass superlattices of heavily doped materials. Quantum Matter 2:455
29. Bhattachrya S, Paitya N, Ghatak KP (2013) Simple theoretical analysis of the effective electron mass in semiconductor nanowires. J Comput Theor Nanosci 10:1999; Paitya N, Ghatak KP (2013) Quantization and carrier mass. Rev Theor Sci 1:165; Adhikari SM, Ghatak KP (2013) On the diffusivity mobility ratio in III–V, ternary and quaternary materials in the presence of intense electric field. Quantum Matter 2:296
30. Landsberg PT (1981) Einstein and statistical thermodynamics. III. The diffusion-mobility relation in semiconductors. Eur J Phys 2:213
31. Dingle RB (1955) Philos Mag 46:813; Redfield D, Afromowitz MA (1969) ibid. 19:831; Casey HC, Stern F (1976) Concentration-dependent absorption and spontaneous emission of heavily doped GaAs. J Appl Phys 47:631; SN Mohammad (1980) Fermi energy and Fermi-Dirac integrals for zincblende-symmetry narrow-gap semiconductors with spherical energy bands. J Phys C 13:2685
32. Ghatak KP, Bhattacharya S, Pahari S, Mitra SN, Bose PK, De D (2009) The carrier contribution to the elastic constants in III–V, ternary and quaternary materials in the presence of light waves: Simplified theory, relative comparison and a suggestion for experimental determination. J Phys Chem Sol 70:122; Ghatak KP, Siddiqui JY, Nag B (2001) A simplified analysis of the electronic contribution to the elastic constants in ultrathin films of stressed semiconductors under magnetic quantization. Phys Lett, Sect A: Gen, At Solid State Phys 282:428. Nag B, Ghatak KP (1997) A simple theoretical analysis of the carrier contribution to the elastic constants in quantum wires of IV–VI semiconductors in the presence of a parallel magnetic field. J Phys Chem Sol 58:427
33. Ghatak KP, Banerjee JP, Nag B (1998) The carrier contribution to the elastic constants in small-gap materials. J Appl Phys 83:1420; Ghatak KP, Nag B (1998) On the carrier contribution to the elastic constants in ultrathin films of bismuth under quantizing magnetic field. Nanostruc Mater 10:923; Ghatak KP, Banerjee JP, Bhattacharyya D, Nag B (1996) The electronic contribution to the elastic constants in ultrathin films of ternary and quaternary alloys in the presence of an arbitrarily oriented magnetic field: theory and suggestion for experimental determination. Nanotechnol 7:110
34. Nag B, Ghatak KP (1996) On the carrier contribution to the elastic constants in ultrathin films of IV-VI compounds in the presence of a parallel magnetic field. Phys Scr 54:657; Sreedhar AK, Gupta SC (1972) Phys Rev B 5:3160; Keyes RW (1961) IBM J Res Develop 5:266; Nag B, Ghatak KP (1996) Phys Scr 54:657; Sreedhar AK, Gupta SC (1972) Phys Rev B 5:3160; Keyes RW (1967) Solid State Phys 20:37; Bhattacharya S, Chowdhury S, Ghoshal S, Biswas SK, De D, Ghatak KP (2006) The carrier contribution to the elastic constants in cylindrical quantum dot of optoelectronic materials in the presence of crossed electric and magnetic fields: simplified theory and a suggestion for experimental determination. J Comput Theor Nanosci 3:423
35. Chowdhary S, Singh LJ, Ghatak KP (2005) The electronic contribution to the elastic constants in strained layer quantum well superlattices of non-parabolic semiconductors with graded interfaces under magnetic quantization: Simplified theory and suggestion for experimental determination. Phys B: Condens Matter 365:5; Singh LJ, Choudhary S, Mallik A, Ghatak KP (2005) Electronic contribution to the elastic constants in strained layer quantum dot superlattices of non-parabolic semiconductors with graded interfaces. J Comput Theor Nanosci 2:287; Nag B, Ghatak KP (1998) Mol Cryst Liq Cryst Sci Technol Sect B: Nonlinear Opt 19:1; Ghatak KP, Basu DK, Nag B (1997) On a simplified analysis of the carrier contribution to the elastic constants in semiconductor superlattices in the presence of crossed electric and quantizing magnetic fields. J Phys Chem Sol 58:133
36. Ghatak KP, Banerjee JP, Goswami B, Nag B (1996) Mol Cryst Liq Cryst Sci Technol Sect B: Nonlinear Opt 16:241; Ghatak KP, Banerjee JP, Mitra M, Nag B (1996) Mol Cryst Liq Cryst Sci Technol Sect B: Nonlinear Opt 17:193; Ghatak KP, Mitra B(1992) A simple analysis of the electronic contribution to the elastic constants in stressed Kane type semiconductors. Phys Scr 46:182

37. Ghatak KP, Bhattacharya S (2007) Influence of light on the Debye screening length in III–V, ternary, and quaternary materials. J Appl Phys 102:073704; Mondal M, Ghatak KP (1984) The debye screening length in degenerate n-Cd3As2 in the presence of an arbitrarily oriented quantizing magnetic field. Phys Lett 102A:54; Bhattacharya S, Paul NC, Ghatak KP (2008) Influence of light on the Debye screening length in ultrathin films of optoelectronic materials. Physica B 403:4139; Ghatak KP, Bhattacharya S, Saikia H, Baruah D, Saikia A, Singh KM, Ali A, Mitra SN, Bose PK, Sinha A (2006) The Debye screening length in ultrathin films of nonlinear optical, optoelectronic, and related materials: Simplified theory and suggestion for experimental determination. J Comput Theor Nanosci 3:727
38. Chakraborty PK, Datta GC, Ghatak KP (2003) A simple theoretical analysis of the effective electron mass in heavily doped III–V semiconductors in the presence of band-tails. Phys Scr 68:368; Kane EO (1985) Solid-State Electron 28:3; Zawadzki W (1982) Handbook on semiconductors, Paul W (ed) North Holland, New York 1, p 715
39. Chakravarti AN, Mukherjee D (1975) Screening length under magnetic quantization. Phys Lett 53A:403; Mitra B, Basu DK, Nag B, Ghatak KP (1997) On the screening length in nonlinear optical and optoelectronic materials: theory and suggestion for experimental determination: part-I. Nonlinear Opt 17:171; Mondal M, Ghatak KP (1986) Phys Status Solidi B 135:239
40. Chakravarti AN, Swaminathan S (1974) Screening length in degenerate semiconductors. Phys Status Solidi A 23:K191; Chakravarti AN ibid. 25:K105; Chakravarti AN, Ghatak KP, Ghosh KK, Dhar A (1981) Effect of carrier degeneracy on the screening length in n-Cd3As2. Phys Status Solidi B 103:K55. Ando T, Fowler AH, Stern F (1982) Rev Mod Phys 54:437; Basu PK (2001) Optical processes in semiconductors. Oxford University Press, New York
41. Kampf N, Ben-Yaakov D, Andelman D, Safran SA, Klein J (2009) Direct measurement of sub-debye-length attraction between oppositely charged surfaces. Phys Rev Lett 103:118304; Arnold P, YafFe LG (1995) Non-Abelian Debye screening length beyond leading order. Phys Rev D 52:7208; Kulkarni GS, Zhong Z (2012) Detection beyond the Debye screening length in a high-frequency nanoelectronic biosensor. Nano Lett 12:719; Stern E, Wagner R, Sigworth FJ, Breaker R, Fahmy TM, Reed MA (2007) Importance of the Debye screening length on nanowire field effect transistor sensors. Nano Lett 7:3405
42. Chakravarti AN, Mukherji D (1975) Influence of magnetic quantization on the diffusivity of the carriers in degenerate semiconductors. Phys Lett A 53:57; Zawadzki W (1974) Electron transport phenomena in small-gap semiconductors. Adv Phys 23:435; Paitya N, Ghatak KP (2016) Analysis of screening length in doping superlattices. Quantum Matter 5:191; Ghatak KP, Chakrabarti S, Chatterjee B, Das PK, Dutta P, Halder A (2018) Influence of intense electric field on the screening length in opto-electronic materials. Mater Focus 7:390
43. Ghatak KP, Mitra M (2018) Nanomaterials, Heisenberg's uncertainty principle and the screening length in heavily doped optoelectronic nano materials in the presence of intense light waves (vol 1). De Gruyter, Germany, pp 273–274
44. Adhikari SM, Ghatak KP (2015) Effect of intense electric field on the debye screening length in III–V, ternary and quaternary semiconductors: simplified theory, relative assessment and suggestion for experimental determination. Quantum Matter 4:599; Ghatak KP, Dutta S, Ali A, Banerjee S, Nag B (1996) On the screening length in quantized II-VI materials. J Wave Mater Interact 11:127; 38. PK Chakrabarty, B Nag, S Dutta, KP Ghatak (1996) On the debye screening length in ultrathin films of IV-VI compounds in the presence of a parallel magnetic field: theory and suggestion for experimental determination. J Wave Mater Interact 11:55
45. Ghatak KP, Bhattacharya S (2013) The DSL in NIPI structures of non-parabolic semiconductors, Debye screening length (vol 265). Springer tracts in modern physics. Springer-Verlag, Germany, pp 63–76
46. Adhikari SM, Karmakar A, Ghatak KP (2015) Quantization and screening length. Rev Theor Sci 3:273; Chakraborty M, Ghatak KP (2015) The screening length in doping superlattices. Quantum Matter 4:104; Mitra B, Basu DK, Nag B, Ghatak KP (1997) On the screening length in nonlinear optical and optoelectronic materials: theory and suggestion for experimental determination: part-I. Nonlinear Opt-Read 17:171; Mitra M, Chakrabarti S, Chakraborty M, Debbarma

S, Ghatak KP (2015) Screening length in ultrathin films under intense electric field. J Computat Theor Nanosci 12:1898

47. Debbarma S, Chakravarti S, Debbarma N, Mitra M, Ghatak KP (2014) Influence of parallel electric and quantizing magnetic fields on the screening length in III–V, ternary and quaternary semiconductors. J Adv Phys 3:213; Debbarma S, Debbarma N, Chatterjee B, Adhikari SM, Ghatak KP (2008) Can photon influence the screening length in heavily doped quantum wells?. Adv Sci, Eng Med 6:1024; Bhattacharya S, Paul NC, De D, Ghatak D (2008) Influence of light on the Debye screening length in ultrathin films of optoelectronic materials. Phys B: Condens Matter 403:4139
48. Ghatak KP, Bhattacharya S (2007) J Appl Phys 102:073704; Ghatak KP, Bhattacharya S, Saikia H, Baruah D, Saikia A, Singh KM, Ali A, Mitra SN, Bose PK, Sinha A (2006) The Debye screening length in ultrathin films of nonlinear optical, optoelectronic, and related materials: Simplified theory and suggestion for experimental determination. J Comput Theor Nanosci 3:727
49. Ghatak KP, Chakrabarti S, Chatterjee B (2018) Influence of size quantization on the screening length in non-parabolic semiconductors. Mater Focus 7:390; Paul R, Mitra M, Chatterjee B, Pal J, Singh SL, Singh SB, Chakrabarti S (2018) Mater Focus 7:363; Ghatak KP, Chakrabarti S, Chatterjee B, Das PK, Dutta P, Halder A (2018) Mater Focus 7:39
50. Biswas SK, Mondal S, Bhattacharyya K, Pradhan AK, Pal J (2018) screening length in doping superlattices. Mater Focus 7:405; Singh LS, Singh SB, Paul R, Mitra M (2018) Heisenberg's uncertainty principle and the screening length. Mater Focus 7:413; Debbarma M, Debbarma S, Debbarma N (2018) The screening length, 2D opto-electronic materials. Mater Focus 7:424